UNIVERSIDAD COMPLUTENSE DE MADRID

FACULTAD DE CIENCIAS FÍSICAS
Departamento de Astrofísica y Ciencias de la Atmósfera

TESIS DOCTORAL

Propiedades e historias de formación estelar de galaxias enanas a baja masa con formación estelar a desplazamientos al rojo intermedios

Properties and star formation histories of dwarf low-mass star-forming galaxies at intermediate redshifts

MEMORIA PARA OPTAR AL GRADO DE DOCTOR

PRESENTADA POR

Lucía Rodríguez Muñoz

Director

Jesús Gallego Maestro

Madrid, 2016

UNIVERSIDAD COMPLUTENSE DE MADRID

FACULTAD DE CIENCIAS FÍSICAS
DEPARTAMENTO DE ASTROFÍSICA Y CIENCIAS DE LA ATMÓSFERA

Propiedades e Historias de Formación Estelar de Galaxias Enanas de Baja Masa con Formación Estelar a Desplazamientos al Rojo Intermedios

Properties and Star Formation Histories of Dwarf Low-Mass Star-Forming Galaxies at Intermediate Redshifts

Dirigida por:

Dr. Jesús Gallego Maestro
Profesor Titular UCM

Memoria presentada por:

D. Lucía Rodríguez-Muñoz
para aspirar al grado de Doctora en Astrofísica
2015

Anyhow, I sat by your side, by the water.
You taught me the names of the stars overhead that I wrote down in my ledger.
Though all that I knew of the rote universe were those Pleiades loosed in December,
I promised you I'd set them to verse so I'd always remember.

Joanna Newsom, *Emily*

Small is beautiful

E.F. Schumacher

A Juan & Montserrat
A Irene

Contents

Agradecimientos

Sin duda éste podría ser el capítulo más extenso de esta *Tesis*. En un trabajo que se prolonga durante años, en el que uno se implica tanto, al que uno dedica tanto esfuerzo e ilusión, el número de personas que contribuyen tanto en el ámbito profesional, como en el personal, en la luz, o en la sombra, es casi innumerable.

En primer lugar me gustaría agradecer a mi director, Jesús Gallego, el haberme abierto las puertas a la investigación y haber confiado en mí, dándome la oportunidad de incorporarme al Grupo de Astrofísica Extragaláctica e Instrumentación de la Universidad Complutense de Madrid (GUAIX). Gracias por las muchas enseñanzas y maravillosas experiencias. Sin duda, han sido unos años inolvidables. Gracias por todo.

Mil gracias a todos los compañeros con los que he compartido la vida a diario, con lo que ello conlleva: las frustraciones y las alegrías. Las de todos. Realmente, no sé si he logrado transmitiros todo lo que habéis significado para mí en estos años. Raffaella, simplemente no se me ocurre una compañera mejor para esta experiencia. Gracias por los *momentazzos*, que han sido muchos, por tu humor, por tu fuerza, y por estar ahí cuando lo he necesitado... Ya te echo de menos! Néstor y Alex, gracias por el apoyo, por la ayuda, por el intercambio de ideas, inquietudes, e ilusiones, por compartir vuestros días conmigo y dejar que compartiera los mios con vosotros, no sólo en el ámbito profesional. Alex, Jaime I., Cristina, Raúl, y Paco, gracias por todo el cariño que me habéis mostrado, sabéis que es recíproco. Mis primeros compañeros de despacho Juan Carlos, Guillermo y Elisa. Gracias por la bienvenida y vuestra valiosa ayuda siempre que la necesité. Pablo y Sergio, sin duda sabéis que esta *Tesis* no habría sido posible sin vuestra ayuda. Por dedicarme tiempo, por hacerme reir, por vuestros consejos y apoyo, por las muchas conversaciones, y por todo lo que me habéis enseñado, os doy mil gracias. Armando y África, gracias por las risas, el apoyo, y la energía. Por todo, que ha sido mucho. Víctor y Antonio C., gracias por vuestra complicidad y sentido del humor. Lástima no haber tenido tiempo de disfrutaros más. Carmen, gracias por recordarme que es el camino a *Ítaca*[1] lo que merece la pena y no sólo llegar a ella. Nicolás, gracias por estar disponible, por tu amabilidad, por ser un profesor fabuloso y por *R*! Jaime Z., gracias por tu entusiasmo y por hacernos disfrutar a todos los que tenemos la suerte de ser tus alumnos y/o tus compañeros. A Javier, gracias por ser un magnífico profesor y por estar ahí en todas las jornadas de lucha por la ciencia y la universidad pública. Gracias también a los últimos fichajes estrella: Belén, Helena, Pilar y Carlos. Gracias por vuestra energía, cercanía, y esos ánimos y fuerza. Ainhoa, gracias por la paciencia y por ser una compañera simplemente encantadora. A Antonio y Eugenia, por estar siempre dispuestos a ayudarme con una sonrisa.

También me gustaría agradecer la amable acogida desde el primer minuto al resto de com-

[1] *Ítaca*, Constantino Cavafis.

pañeros del departamento: Manuel Rego, María José Fernández Figueroa, Manuel Cornide, Elisa de Castro, David Montes. Por supuesto, también mi agradecimiento a José Antonio, Javi G. e Inés, por su amabilidad, y a Hugo, Javi, Miguel Ángel, Miriam, y Víctor por los buenos momentos compartidos. Gracias también a Maleni, por todo su cariño.

No me gustaría dejar de mencionar tampoco a los fantásticos compañeros del área de atmósfera. Chicos, sois encantadores.

Gracias también al resto de compañeros con los que he compartido momentos inolvidables dentro y fuera de la facultad: Marta Á. y Álvaro, Mariano, “Cahlo", Íñigo, Coumba, Ibrahima, Jesús, Belén y Luis, Ana, Elsa y Luis D., Julian, Roberto, Marta, Jon, Javi P., Juan, Javi, Joserra, José Luis y Valeria, Manu, y Pedro.

I would like now to dedicate next paragraphs to some of the most rewarding moments along my PhD: my stays in my beloved Marseille. Both of them were crucial for my work, sate of mind, and in general, my personal living experience.

Firstly, I would like to thank Olivier Le Fèvre, who first gave me the chance to work at the Laboratoire d'Astrophysique de Marseille (LAM). The hospitality of LAM PhD students, postdocs, faculty members, and staff made it easy to feel at home in barely a few minutes. In particular, I would like to mention Anna, Bin-wei (and family), Carlos, Javi, Sam, Mario, Wang Xin, and Firas (the sunset seekers!), Matvey, Brian, Pol, Elysse, Francesca, Aurelie, Alessandro, Vincent, Laurent, and a long etcetera... Thanks to all of you!

I would like to make a very special mention for Laurence Tresse. Thanks for sitting next to me checking spectra until our eyes saw UFOs in the window. Thanks for being a source of strength and motivation, and for your support. Thanks for everything.

When I come back to Marseille or when I see you guys, I always feel I saw you actually yesterday. For this reason, *goodbye* cannot be used as a farewell between us or between Marseille and myself. It is always a *see you tomorrow*.

This work would not have been possible without the spectroscopic observations carried out at the Very Large Telescope in 2011 and 2012. I would like to thank those that made them possible with their professional work: Dieter Nuernberger, Willem-Jan de Wit, and Pierre Vernazza. Furthermore, I acknowledge ESO members Caroline Foster and Fernando Selman for their important data assessment.

Quiero también agradecer a mis viejos y no tan viejos amigos, los que han estado cerca y lejos, pero han estado siempre. Rocío, mi segunda hermana, y Riqui. Fran y Celia, David, Santi, Rosa, Susana, Javi, Clara y Pilar. Agradeceros lo que he aprendido con vosotros y los momentos que hemos compartido, me parece una tarea completamente imposible. Simplemente dejadme deciros que me siento afortunada por contar con vuestra amistad y cariño. No dudo de

la existencia de vida en otros sistemas solares en el Universo. Pero dudo, y mucho, que pudiera encontrar en ninguno de ellos especímenes como vosotros.

Me gustaría agradecer también a mi increíble familia, que siempre ha estado ahí, haciendo mis días más felices, apoyándome, animándome, haciendo que creyera en mí misma cuando he dejado de hacerlo, haciéndome disfrutar, reír a carcajadas, y por qué no decirlo, dándome de comer los mejores manjares del planeta Tierra. Mi padre, Juan. Mi hermana del alma, Irene, y Luís. Mis abuelos, Margarita y Juan. Mis tíos Rosa y Ángel, y mis primos Rodrígo y María. Mis tíos Marga y Juan Carlos, Alicia y Quique, Pedro y Laura, y mis primos Fernando y Carmen, Alejandro, María, Guillermo, Carlota y Martina. Por supuesto también a Beatriz, Nerea, Marta y Gerson. Mi familia malagueña, María José y Miguel, María y Guti, y mi familia de Alcalá de Henares, Cristina, Yolanda, Ángel, Marina y Paula, y Enrique.

No tengo que decir más. Lo sabéis. Os quiero.

Me gustaría hacer una mención especial a algunas personas con las que no puedo compartir este momento, y con las que, desgraciadamente, tampoco he podido compartir estos últimos años. Mis abuelos maternos, Juliana y Jesús, que me enseñaron tanto de todo lo que verdaderamente es importante. Y mi maravillosa madre, Montserrat, a quien a veces me sorprendo esperando encontrar allá en la distancia tras una galaxia, sonriéndome desde los confines del Universo. Gracias por todos los recuerdos.

Por último, quiero no sólo agradecer sino también abrazar con estas palabras a mi compañero de viaje, sin duda alguna, el que sé ha sido y será el mayor de mis descubrimientos. Gracias por todos los días, Jorge.

Gracias a todos, gracias siempre.

Madrid, 9 de Junio de 2015

Resumen

La formación y evolución de galaxias es una de las áreas más activas de la astrofísica moderna. En los últimos años, la profundización de nuestro conocimiento y comprensión sobre cómo la población de galaxias evoluciona desde el universo primitivo hasta nuestro entorno más cercano, ha sido posible gracias al crucial desarrollo de la instrumentación astronómica, los grandes muestreos fotométricos y espectroscópicos llevados a cabo en regiones del cielo extensas, y el desarrollo de simulaciones y modelos teóricos, así como nuestra capacidad de computación.

En este contexto, esta *Tesis* aborda el reto de estudiar una de las más fascinantes poblaciones de galaxias, las galaxias de baja masa, también conocidas como *enanas*. Entre ellas, las galaxias de baja masa con formación estelar (LMSFGs) son los objetos que más se asemejan a lo que creemos debió ser la primera generación de galaxias primitivas. Sus propiedades físicas las hacen interesantes laboratorios para el estudio de la formación estelar en épocas del Universo que aún hoy no podemos observar directamente. Sin embargo, debido a su baja luminosidad intrínseca, y por tanto, las dificultades inherentes a su observación, las LMSFGs siguen siendo una población en gran medida desconocida, especialmente a medida que nos movemos a desplazamientos al rojo mayores.

La época en las que las LMSFGs forman la mayor parte de sus estrellas es aún incierta. Mientras algunos modelos predicen una formación temprana, otros favorecen un escenario en el que su formación se retrasa a épocas más tardías del Universo. El objetivo de esta *Tesis* es mejorar nuestro conocimiento sobre las historias de formación estelar y la naturaleza de este tipo de objetos.

Para ello hemos construído una muestra de candidatos a LMSFG situados a desplazamientos al rojo intermedios en el Extended-Chandra Deep Field-South, utilizando paralelamente una selección en masa estelar y una selección basada en las propiedades de las galaxias azules y compactas (BCDs), caracterizadas por un brote muy intenso de formación estelar.

Posteriormente hemos llevado a cabo espectroscopía profunda de nuestra muestra con el espectrógrafo óptico multi-objeto VIMOS en el VLT (Very Large Telescope; European Southern Observatory, ESO, Paranal, Chile). De estos datos hemos extraído para 94 galaxias desplazamientos al rojo espectroscópicos y medidas de líneas de emisión, entre ellas [OII]$\lambda\lambda$3727, Hβ, y [OIII]$\lambda\lambda$4959,5007.

Nuestro ulterior análisis de la muestra de galaxias espectroscópicamente confirmadas se ha basado principalmente en dos aproximaciones diferentes. Por un lado, hemos estimado sus propiedades físicas (masa estelar, M_*, tasa de formación estelar, SFR, y tasa de formación estelar específica, sSFR) e historias de formación estelar (SFHs) modelando sus distribuciones espectrales de energía (SEDs). Para el ajuste de las SEDs hemos utilizado una técnica que, por un lado, combina datos fotométricos y espectroscópicos de forma consistente, y por otro lado, utiliza SFHs

que incluyen variaciones de la SFR no uniformes en función del tiempo. Por otro lado, hemos obtenido las propiedades físicas del medio interestelar de cada objeto (e.g., metalicidad, extinción, excitación) a través del estudio de las líneas de emisión de los espectros VIMOS.

Nuestra muestra final de galaxias enanas está formada por 91 sistemas con masas estelares $7.0<\log M_*/M_\odot<9.5$, localizados a desplazamientos al rojo entre 0.1 y 1.3. La muestra presenta valores típicos de SFR consistentes con la secuencia principal de las galaxias con formación estelar a lo largo de dos órdenes de magnitud en masa, y elevadas sSFRs. Por otro lado, y de forma general, la muestra se caracteriza por líneas de emisión intensas, baja metalicidad, y elevado estado de excitación del medio interestelar. Estas propiedades son típicas de otros muestreos de enanas con formación estelar seleccionadas de acuerdo a la intensidad de líneas de emisión, color azul, o elevado brillo superficial, y se asemejan a las de algunas poblaciones de galaxias a grandes desplazamientos al rojo (e.g., emisores Lyα). Sin embargo, pensamos que debido a la selección en masa que utilizamos, nuestra muestra incluye además galaxias en condiciones menos extremas, principalmente en términos de sSFR. Esto nos indica que no todas las galaxias de nuestro estudio están atravesando un periodo de formación estelar extremadamente intenso. Una posible interpretación de estas propiedades es que estamos viendo un mismo tipo de objeto en diferentes estados evolutivos. Esta hipótesis encajaría dentro de un escenario evolutivo dominado por procesos estocásticos (el más probable para este tipo de galaxias según los modelos teóricos), en el que las enanas atraviesan diferentes fases de formación estelar con mayor y menor intensidad, y periodos de mayor quiescencia. Sin embargo, las SFHs que utilizamos en nuestra metodología no permiten acotar otros posibles brotes de formación estelar en la historia de estas galaxias más allá del actual. En cualquier caso, y a pesar de las diferencias individuales, la SFH promedio que obtenemos para nuestra muestra sugiriere un escenario de formación en general tardío y rápido ($\sim$2 Gyr anteriores a su observación) para este tipo de sistemas.

Summary

The formation and evolution of galaxies is one of the most active areas in modern astrophysics. In the last years, the development of astronomical facilities and instrumentation, the large and deep photometric and spectroscopic surveys, the development of models and simulations, and our increasing computing capabilities, have lead to an extraordinary deepening of our knowledge on how the population of galaxies evolves from the primitive universe to our nearby neighborhood.

In this context, this *Thesis* addresses the challenge of studying one of the most intriguing populations of galaxies, low mass galaxies, also referred to as *dwarfs*.

Low-mass star-forming galaxies (LMSFGs) are the systems that we think best resemble the first generation of primitive galaxies. Their physical properties make them interesting laboratories for the study of the star formation processes that take place in epochs of the Universe we are still not able to observe directly. However, due to their intrinsic low luminosity, and therefore, the inherent difficulties of their observation, LMSFGs are still nowadays a greatly unknown population, specially at intermediate to high redshifts.

The epoch when low-mass star-forming galaxies (LMSFGs) form the bulk of their stellar mass is still uncertain. While some models predict an early formation, others favor a delayed scenario until later ages of the Universe. In this *Thesis* we present improved constraints on the star formation histories (SFHs) and nature of these objects.

To this aim, we have built a sample of candidates to LMSFG located at intermediate redshifts in the Extended-Chandra Deep Field-South, using both a stellar mass criteria, and a selection based on the properties of *blue compact dwarfs* (BCDs), galaxies characterized by a strong starburst.

Subsequently, we have carried out deep spectroscopy of our sample with VIMOS at the Very Large Telescope. From these data we have obtained spectroscopic redshifts and emission lines measurements (e.g., [OII]$\lambda\lambda$3727, Hβ, and [OIII]$\lambda\lambda$4959,5007) for 94 galaxies.

Our final analysis of the sample of spectroscopically confirmed galaxies has been based on two alternative approaches. On the one hand, we have estimated their physical properties (stellar mass, M_*, star formation rate, SFR, and specific star formation rate, sSFR), and star formation histories (SFHs) by modeling their spectral energy distributions (SEDs). For the SED-fitting we have used a novel approach that (1) consistently combines photometric and spectroscopic data, and (2) uses physically-motivated SFHs with non-uniform variations of the SFR as a function of time. On the other hand, we have obtained the physical properties of their interstellar medium (metallicities, extinction, excitation) through the analysis of the emission lines in the VIMOS spectra.

The final sample of dwarfs is conformed of 91 objects with stellar masses $7.0<\log M_*/M_\odot<9.5$, located at redshifts between 0.1 and 1.3. The sample presents typical values of SFR consistent with the main sequence of star forming galaxies over 2 dex in stellar mass, and high sSFR. Besides, and broadly, the sample is characterized by strong emission lines, low metallicity, and an enhanced level of excitation. These properties are also found by other surveys of star-forming dwarfs in which galaxies are selected by emission lines, blue color, or surface brightness. Furthermore, they resemble the properties of high redshift galaxies (e.g., Lyα emitters). Nevertheless, we think that due to our mass selection, our sample includes also galaxies characterized by less extreme conditions, mainly in terms of sSFR. This could indicate that not all the galaxies included in our sample are undergoing a starburst. A possible interpretation of these results is that we are actually observing the same type of object in different evolutionary stages. This hypothesis would be compatible with evolution scenarios dominated by stochastic processes, in which dwarfs go through star formation processes of different intensity and quiescence periods. Theoretical models predict stochastic SFHs as the most probable for dwarf galaxies. However, our SED-fitting approach do not allow us to constrain other starbursts besides the present one. In any case, and despite the individual differences, the average SFH that we obtain suggests a late and fast ($\sim$2 Gyr prior their observation) assembly scenario for this type of system.

List of Figures

List of Tables

1

Introduction

1.1 Formation and Evolution of Galaxies

Astronomy has come a long way since the existence of systems far outside the Milky Way was first probed (Hubble 1925), barely a century ago. The responsible for this giant step in our conception of the Universe was Edwin Hubble, who measured the distance to Andromeda using Cepheids in 1923. Since those very first days of Extragalactic Astrophysics, our knowledge about the galactic systems beyond the borders of our very local neighborhood has undergone an exponential increase.

Indeed, deepening our understanding about how galaxies assemble along cosmic times has required a great development of both observational and theoretical approaches:

- On the one hand, the observing surveys carried out with space and ground-based telescopes in the last two decades have played a major role in this our great and challenging quest for answers to the questions about the formation and evolution of galaxies, that still nowadays remain open. As if they were panoramic viewpoints facing the history of the Universe, they have revealed populations of galaxies out to the very early times (e.g., the $z \sim 11$ galaxy candidate found by Coe et al., 2013). The thorough multi-wavelength coverage of extended areas of sky is extremely important because it allows the characterization of the galaxies which populate them. In particular, fitting the photometry that traces their Spectral Energy Distributions (SEDs) with spectral models permits estimations of physical parameters and redshift (photometric redshifts; z_{phot}). Some remarkable examples of such kind of projects are the Hubble Deep Field (HDF) observations (Williams et al., 1996), Great Observatories Optical Deep Survey (GOODS; Giavalisco et al. 2004), VIMOS-VLT Deep Survey (VVDS; Le Fèvre et al. 2005), All-wavelength Extended Groth strip International Survey (AEGIS; Davis et al. 2007), Cosmic Evolution Survey (COSMOS; Scoville et al. 2007), and The Cosmic Assembly Near-infrarred Deep Extragalactic Legacy Survey (CANDELS; Grogin et al., 2011; Koekemoer et al., 2011). The collective effort of the scientific community deciphering the huge amount of data collected by these projects, has led to a knowledge revolution on how galaxy assemble their stellar mass.

- On the other hand, cosmological simulations and models have become an important driver for further advancing galaxy formation theory (Springel, 2012). Not only do they help us establishing and validating the cosmological paradigm, but also guiding us in our interpretation of the observational data nowadays available. In particular, semi-analytic models have been able to produce a globally successful description of galaxy formation, while numerical

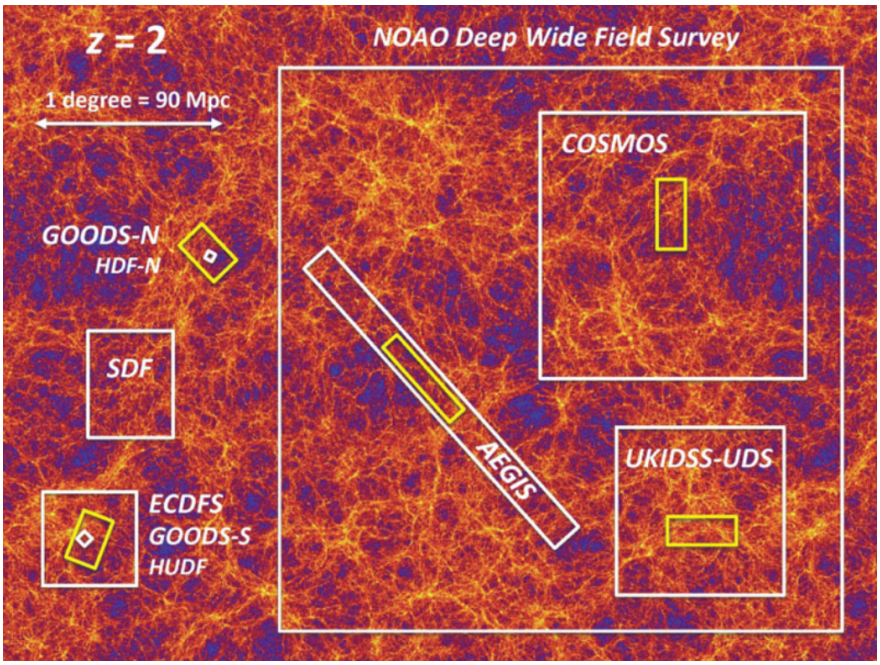

Figure 1.1: Figure 6 published by Madau and Dickinson 2014. Summary and size comparison between some of the most important surveys of the distant universe. The image in the background shows a cosmological N-body simulation performed within the MultiDark[2] project, viewd at z =2.

simulations have led to significant progress in our understanding of the non-linear regime of structure formation in dark matter and the complex processes involved in galaxy formation (e.g., self-gravity of dark matter and gas, dynamics of dark matter, hydrodynamical shocks in the gas, turbulence, radiative cooling and heating processes, stars formation and evolution, supernovae, black hole accretion, and magnetohydrodynamics). Among the exceptional projects developed in the last decade, we highlight the Millennium simulations[3] (Springel et al., 2005) that "used more than 10 billion particles to trace the evolution of the matter distribution in a cubic region of the Universe over 2 billion light-years on a side".

However, and despite the astounding advances, our picture of galaxy evolution still presents some blurred areas. Taghizadeh-Popp et al. (2015) precisely highlights two major reasons.

- First, from the observational perspective "the samples of high-redshift galaxies have been severely edited by selection effects, primarily limits on flux and surface brightness, effectively biasing the observable universe toward bright, compact galaxies". Among the disadvantaged systems we highlight *dwarf galaxies* (DGs; defined as low-mass/luminosity galaxies), which happen to be the most numerous population of galaxies in the Universe, as the stellar mass functions reveal (Figure 1.4), and have only been started to be observable at intermediate to high redshifts after the recent multiwavelength deep surveys. It is worth mentioning in any case that most of these surveys are mainly designed to reach the most distant galaxies, rather than intrinsically faint systems. For this reason, for instance, despite this observational progress, there is still a lack of DGs in spectroscopic surveys. Obviously, this also lead to a lack of observational constraints available for cosmological simulations.

[3]http://www.mpa-garching.mpg.de/galform/virgo/millennium/

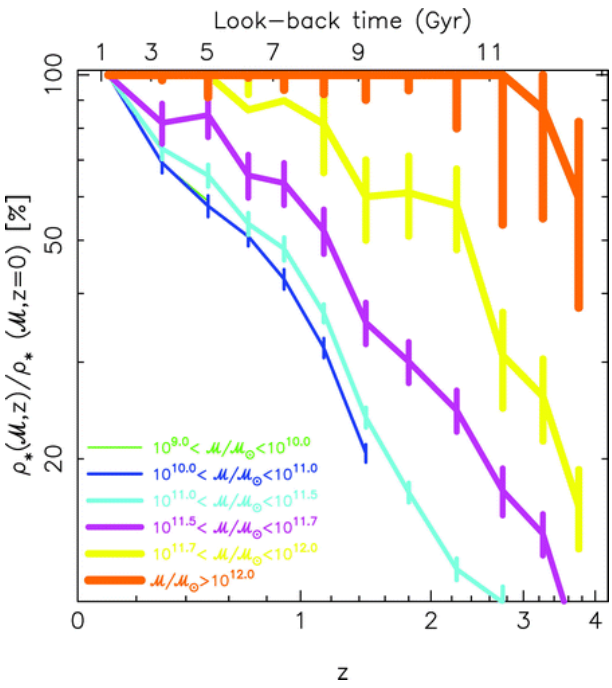

Figure 1.2: Figure 6 published by Pérez-González et al. 2008 presenting the fraction of the local stellar mass density already assembled at a given redshift within galaxies in a certain stellar mass bin (color coded). As an evidence of downsizing, the most massive systems form first and rapidly.

- On the theoretical side, "there are still many significant gaps in our understanding of the physical processes that affect the baryonic components of galaxies (stars, gas, and dust) and the radiation they emit. These uncertainties are reflected in the many free parameters of the semi-analytical models and in the analogous sub-grid physics of the hydrodynamical models". Indeed, models and simulations still struggle to reproduce the formation of galaxies due to the distinct evolution of baryonic and dark matter. See Springel (2012) for a review on the present and future challenges in cosmological simulations.

1.2 General Stellar Mass Assembly Scenario

Nowadays, the most widely accepted cosmological paradigm is the so called standard cosmological model, or Λ-Cold Dark Matter (ΛCDM) cosmology (e.g., Peebles, 1982; Blumenthal et al., 1984). This paradigm relies on the accelerating expansion of the Universe due to an unknown dark energy (represented by the constant Λ), and on the presence of a large amount of weakly interacting particles, referred to as dark matter (DM).

In the ΛCDM context, structure formation follows a hierarchical scheme in which low-mass DM halos assemble first in the history of the Universe. Most of these first halos merged to form

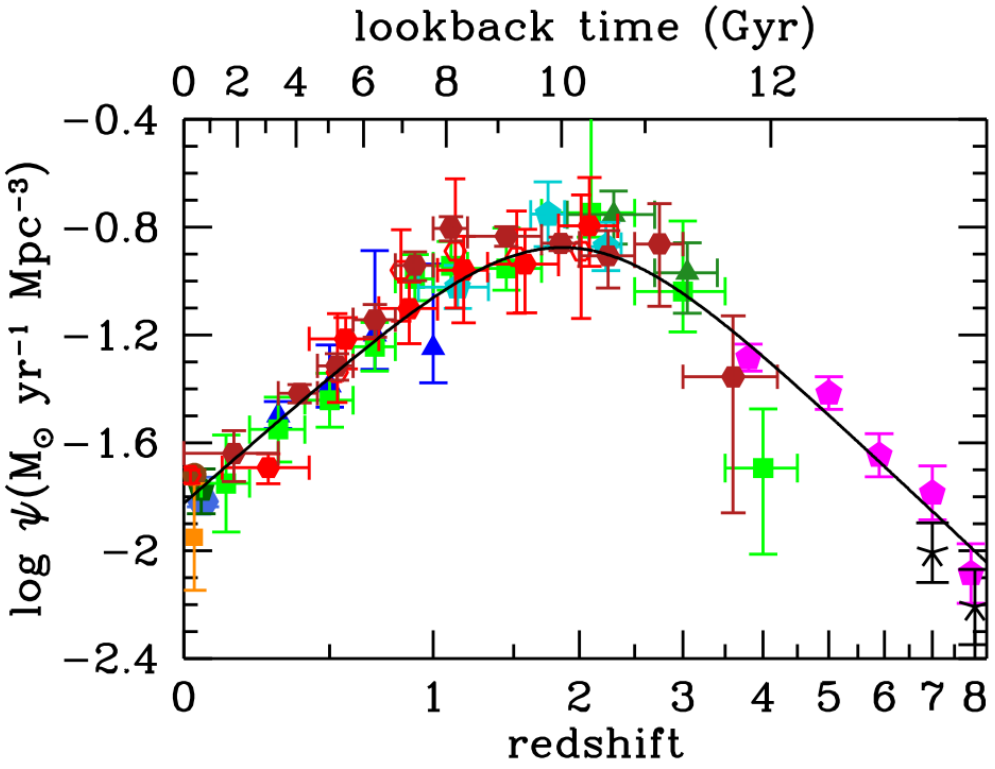

Figure 1.3: The history of cosmic star formation from FUV and IR rest-frame measurements (Figure 9 in Madau and Dickinson, 2014). The solid curve plots the best-fit SFRD. UV data: Blue-gray hexagon from Wyder et al., 2005; Blue triangles from Schiminovich et al., 2005; Dark green pentagon from Robotham and Driver, 2011; Green squares from Cucciati et al., 2012; Turquoise pentagons from Dahlen et al., 2007; Dark green triangles from Reddy and Steidel, 2009; Magenta pentagons from Bouwens et al., 2012b,a; Black crosses from Schenker et al., 2013. IR data: brown circle from Sanders et al. (2003); dark orange square from Takeuchi et al., 2003; red open hexagons from Magnelli et al., 2011; red filled hexagons from Magnelli et al., 2013; dark red filled hexagons from Gruppioni et al., 2013.

larger structures. Assuming that the distribution of baryonic mass traces the distribution of DM, then naively we would expect a similar behavior for the formation of the galaxies, with low-mass galaxies lying within the early low-mass DM halos merging to form more massive galaxies, giving rise to the Hubble sequence we see today. Nevertheless, the physical processes that govern the baryonic and DM interactions are too different for this simple image to be realistic. Not in vain have numerous studies identified a reversed trend in the evolution of galaxies, in which the most massive galaxies are formed earlier than less massive systems (Figure 1.2; e.g., Heavens et al., 2004; Juneau et al., 2005; Bauer et al., 2005; Pérez-González et al., 2005; Bundy et al., 2006; Tresse et al., 2007; Pérez-González et al., 2008). This trend is known as *downsizing* (Cowie et al., 1996). In this way, over the last 8 Gyr a large fraction of low-mass galaxies are still seen rapidly assembling most of their present-day stellar mass.

An alternative perspective of the stellar mass assembly of the galaxies in the Universe can be achieved through the study of the evolution of the star formation rate density, obtained as the average star formation rate (SFR) per unit comoving volume, with cosmic time. The state-of-the-art surveys shown in Figure 1.3 (Madau and Dickinson, 2014) provide a remarkably consistent picture of the cosmic star formation history (SFH) with a first rising trend between redshifts $3<z\lesssim8$, that slows and peaks at some point between $z=2$ and 1.5. Afterwards, the trend is followed by a decline

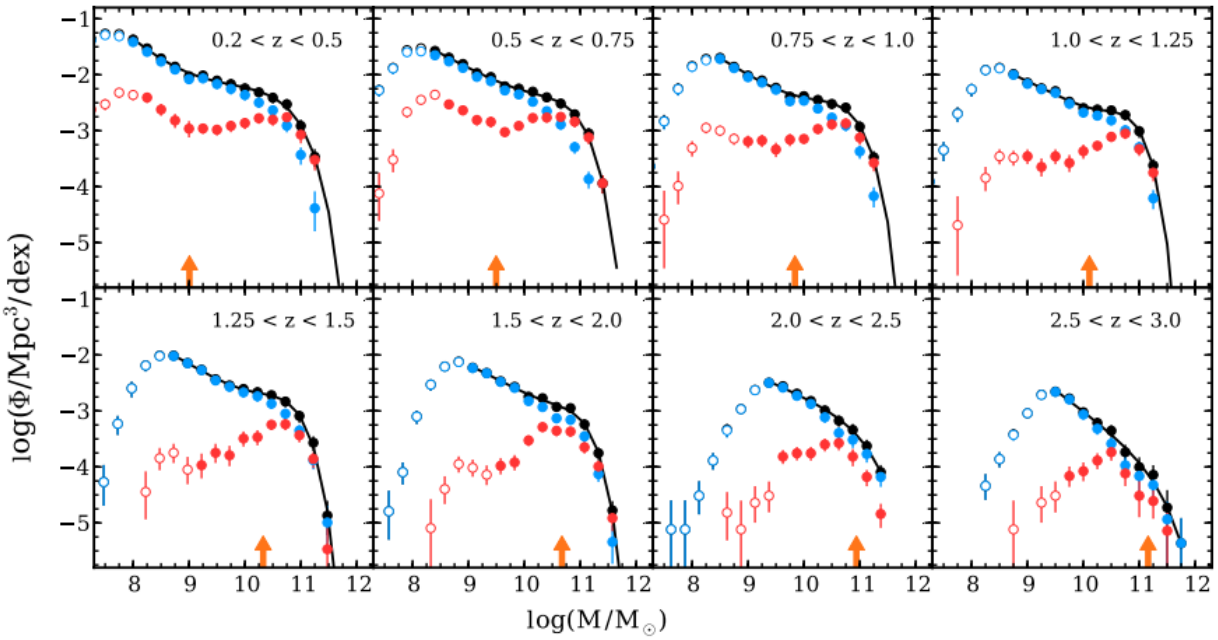

Figure 1.4: The evolution of the stellar mass fuction (Figure 7 in Tomczak et al. 2014). The plots show the stellar mass functions in sequential redshift bins for all (black), star-forming (blue), and quiescent (red) galaxies. Open symbols correspond to data below the completeness limit.

of an order of magnitude down to the values measured locally.

Another interesting tool to explore galaxy growth and evolution is the galaxy stellar mass function (SMFs; Pérez-González et al. 2008; Drory et al. 2009; Ilbert et al. 2010; Moustakas et al. 2013; Ilbert et al. 2013). In Figure 1.4 we show the SMFs found by Tomczak et al. 2014 for 8 different redshift ranges between 0.2 and 3.0, using the FourStar Galaxy Evolution Survey[4] (ZFOURGE). In each case, the SMF describes the number density of galaxies (black) per stellar mass bin. Also, the total galaxy sample is divided into star-forming (blue) and not star-forming (red) systems. By investigating the evolution of the SMF for different galaxy populations we can unveil the physical processes which govern stellar mass growth, and how they affect each type of galaxy. The analysis of the SMF has enable, e.g., the identification of a rapid growth of very massive galaxies in the first 1.5 Gyr of cosmic history (Stefanon et al. 2015). In the case of the low-mass end of the SMF, for instance, we can clearly see that it is dominated by star-forming galaxies with very blue colors at all redshifts, and that it varies very slightly with time. The low-mass end of the SMF for quiescent galaxies, on the contrary, evolves drastically since $z\sim2$, which has been interpreted as the probe for a large ammount of dwarfs being quenched by falling within high density environments.

[4]http://zfourge.tamu.edu/

1.3 Dwarf Galaxies

There is not a unique definition of DG in the literature. In fact, the criteria used to identify this kind of objects has evolved with our ability to observe them and infer their properties. First definitions were mainly based on small sizes (e.g., Hodge, 1971), low luminosity (e.g., Sandage and Binggeli, 1984), or a combination of both (e.g., Tammann, 1994). However, already in this later work, the author explains that these definitions are in any case artificial, as their are not based on the real nature of these systems. In deed, Tammann (1994) claims that the "physical meaning of dwarfs is probably much deeper". Then, the key points arise naturally: what are all the physical properties that distinguish a dwarf from a giant galaxy?, are their differences linked to their very nature or merely due to the amount of baryonic matter they host? Following the review published by Mateo (1998), Tolstoy et al. (2009) claim that there are no reasons to consider DGs in any way special systems, but simply smaller scale versions of the giant galaxy population, for which formation and evolutive processes may behave differently. They base this statement on the fact that the main properties of galaxies correlate with mass and luminosity continuously all the way from the biggest to the smallest galaxies. In this work we use the term *dwarf* as synonymous of *low-mass galaxy*.

In this period of rapid flourishing of Extragalactic Astrophysics, dwarf systems appear still as one of the most poorly known galaxy species. Despite the *a priori* simplicity of DGs compared to their more massive relatives and their larger number, how and when these objects acquire their stellar mass is still a source of debate.

The intrinsic low luminosity characteristic of low-mass systems has implied an additional difficulty for the research of DGs with respect the study of giant galaxies. Indeed, galaxy samples selected at any wavelength are conformed inevitably by flux limited samples of galaxies. To overcome such observational limitations, studies of dwarfs were historically biased to low redshifts or clusters, where the effect of magnification could help to reach fainter galaxies.

Hence, the most detailed studies of dwarfs have been carried out in the Local Universe, where the proximity of the Local Group galaxies enables the analysis of their inner structure and components (e.g., their resolved stellar populations). Tolstoy et al. (2009) reviewed the properties (e.g., SFH, abundances and kinematics) of the DGs in the Local Group. Some other remarkable projects in this line are: the Local Cosmology from Isolated Dwarfs project (LCID; Gallart, 2012), the ACS Nearby Galaxy Survey Treasury (Dalcanton et al., 2009; Weisz et al., 2011a), and the series of interesting works recently published by Weisz et al. on the SFHs of Local Group DGs (Weisz et al., 2014a,b).

There are different reasons why these detailed studies are not enough to decipher the formation and evolution of the whole dwarf population. On the one hand, the properties of local dwarfs are not proved to be representative of the whole dwarfs population (van den Bergh, 2000). On the other hand, their necessarily more evolved stellar populations, compared to those found in higher redshift galaxies, prevent from reaching certain levels of accuracy in the formation redshifts derived due to the little evolution in their photometric properties (Gil de Paz and Madore, 2002).

Given their low masses, dwarfs are characterized by shallow gravitational potentials. This makes them extremely vulnerable to the impact of different internal and external processes, such as feedback or interactions with the intergalactic medium of nearby neighbors. The role of environment has been deduced from the observed, morphology-density relationship, in which red,

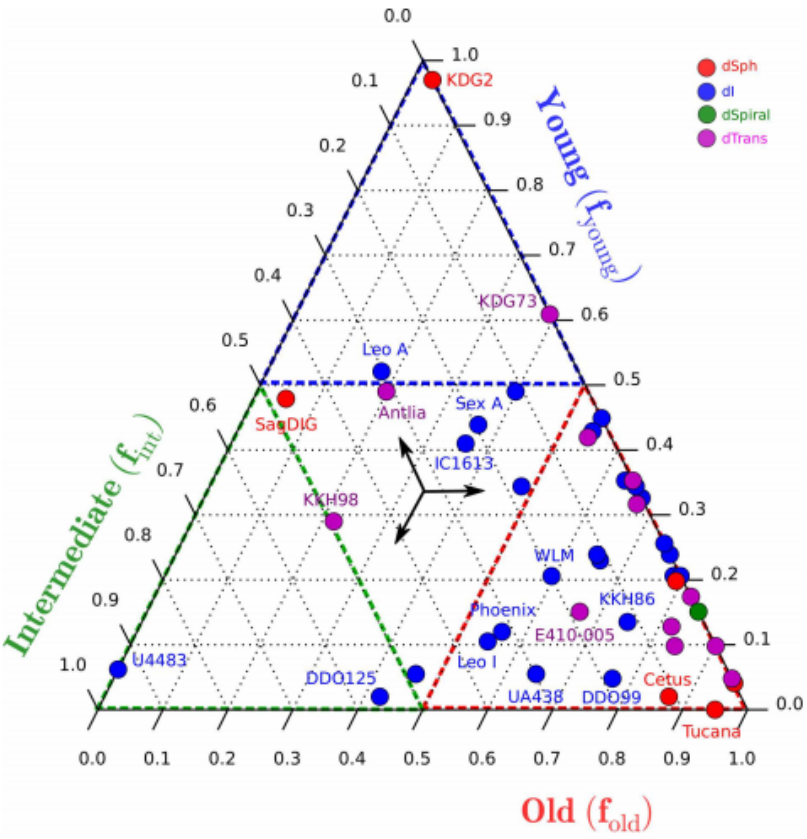

Figure 1.5: Ternary diagram summarizing the SFHs of the sample of nearby isolated dwarf galaxies by Benítez-Llambay et al. 2015, see their Figure 3 and Table 2. The three coordinates in this plot indicate the average SFR in the earliest 4 Gyr (old), at times between 4 and 8 Gyr (intermediate) and at t > 8 Gyr (young). These rates are normalized to the average SFR of each dwarf. The central point in this diagram correspond to a galaxy with constant SFR. The arrows emanating from it show how to read coordinates in each of the three axes. Galaxies are coloured by their morphological types (Weisz et al. 2011): dwarf spheroidals, dwarf irregulars, dwarf spirals, and dwarf transition systems are red, blue, green, and pink, respectively. The coloured highlighted triangles represent the areas where old (red), intermediate (green) and young (blue) stellar components dominate.

gas-poor, non-star forming DGs are predominantly found in close proximity to a massive host, while blue, gas-rich, star-forming dwarfs are preferentially located in lower density environments (e.g., Hodge, 1971; Mateo, 1998; van den Bergh, 2000; Tolstoy et al., 2009; Weisz et al., 2011b). For this reason, quenching in low-mass galaxies seems to be governed by the environmental impact, while massive galaxies follow a slef-quenched scenario. In fact, Geha et al. (2012) studied a sample of ∼10.000 dwarfs from the Sloan Digital Sky Survey (SDSS) Data Release 8, and concluded that galaxies with $7<\log M_*/M_\odot<9$ are always (except a negligible 0.06%) star-forming when they are located further than 1.5 Mpc away from the nearer massive galaxy. Indeed, dwarfs intrinsic evolutionary paths can be completely masked by these processes (e.g. Grebel and Gallagher, 2004).

Therefore, **obtaining observational constraints for dwarf objects beyond the Local Universe and in the field appears as a high priority objective for the progress in our knowledge about this elusive population**. Not in vane have a number of recent works targeted precisely low-mass galaxies at intermediate to high redshifts (e.g. Barazza et al., 2006; van der Wel et al., 2011; Henry et al., 2013b; Amorín et al., 2014a,b,c; Atek et al., 2014; Kochiashvili et al., 2015),

Figure 1.6: I Zw 18 observed by Izotov and Thuan (2004) with WFPC2 on *HST*/ACS.

now observable thanks to recent deep photometric surveys.

1.3.1 Star-forming Dwarf Galaxies

DGs span a wide range of physical characteristics and occupy a diverse set of environments (e.g., Hodge, 1971; Mateo, 1998). Among them, star-forming low-mass galaxies (LMSFGs) turn out to be of special interest for different reasons:

- They provide an ideal and simpler laboratory for studying SF processes in galaxies.
- They enable tracing low-mass galaxies at increasing redshifts thanks to their emission lines (Lee et al., 2000) and enhanced surface brightness.
- They resemble the primordial entities in the hierarchical galaxy formation scenarios due to their properties: low stellar mass, high gas content, low metallicities, highly excited inter stellar medium, and active star formation (SF). These characteristics make them the perfect laboratory to study how chemical enrichment, massive stars formation, and feedback processes take place in their high redshift analogous galaxies, e.g., Lyman-break galaxies and Lyman-α emitters (e.g., Pettini et al., 2001).

In the nearby Universe, one of the best examples of these candidates to primeval galaxies (Searle and Sargent, 1972) is I Zw 18 (Zwicky 1966, Sargent and Searle 1970; Figure 1.6). This galaxy is known for being one of the least metallic ($\sim 1/50$ $Z_{\odot}$; e.g., Izotov et al. 1999) blue compact dwarf galaxy ever observed, and probably the clearest candidate to primeval galaxy still assembling its stellar mass. It has even been claimed that this galaxy presents population III stars born in quasi-pristine gas (Heap et al., 2015).

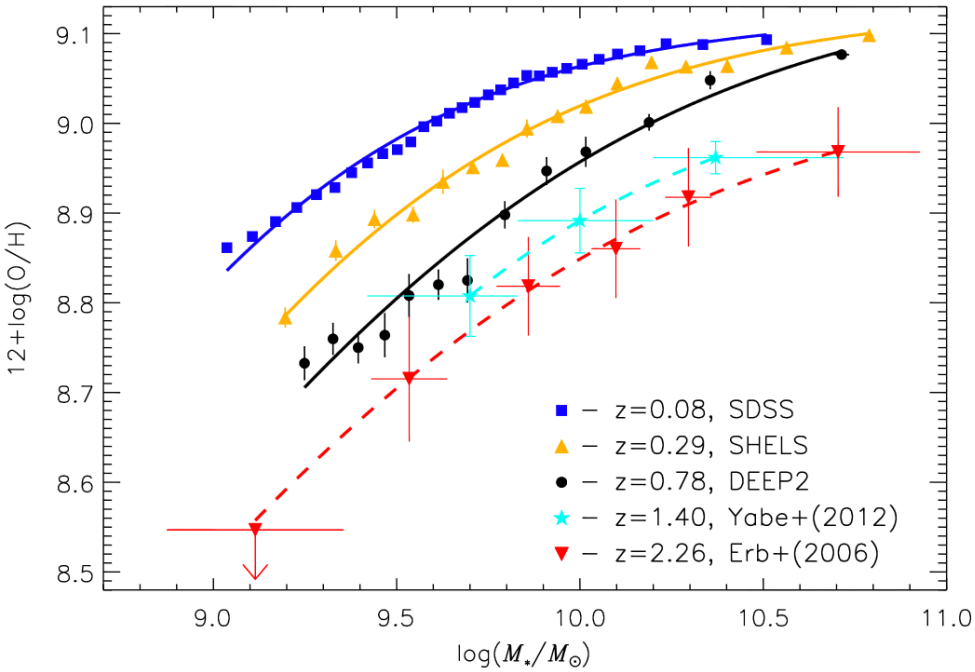

Figure 1.7: MZ relation at different redshifts. Figure 2 by Zahid et al. (2013) in which they indicate metallicities determined using the KK04 strong-line method with solid lines and metallicities converted using the formula of Kewley and Ellison (2008) with dashed curves.

LMSFGs include a rare population of extreme emission-line galaxies (EELGs), which are thought to present the largest nebular content and lowest metal abundances (e.g., Kniazev et al., 2003, 2004; Papaderos et al., 2008; Hu et al., 2009; Atek et al., 2011; Morales-Luis et al., 2011). Due to their large equivalent widths (EWs), and thanks to deep spectroscopic and photometric surveys the study of these systems has been extented to $z\sim1$ (e.g., Hoyos et al., 2005; Ly et al., 2014; Amorín et al., 2014b), and beyond (e.g., van der Wel et al., 2011; Maseda et al., 2013; Amorín et al., 2014a; Kochiashvili et al., 2015). This population of EELGs dominates the samples of DGs studied at intermediate to high redshifts. For this reason, despite the great recent efforts, it appears clear that there is still a whole low-mass universe to be explored.

1.3.1.1 Mass-Metallicity Relation

The correlation between galaxy stellar masses and gasphase metallicities (mass–metallicity relation, MZ), and its evolution with redshift, has long been considered an extremely usefull tool to understand the evolution in galaxies. Indeed, chemical enrichment is itself a product of galaxy evolution processes, as it reflects the balance between gaseous inflows, outflows, and star formation. For instance, feedback caused by stellar winds, supernovae, and supermassive black holes is often used to explain a variety of observations, from luminosity and stellar mass functions to the enrichment and reionization of the intergalactic medium. However, a complete physical picture of these feedback processes is still debated, partially due to the lack of observational constraints. MZ depicts a increasing trend with more massive galaxies presenting higher values of metallicity. The low metallicities characteristic of low-mass galaxies can be interpreted as a consequence of: (1) a lack of evolution; (2) outflows of enriched material driven by supernova; (3) infall of metal-poor gas. The MZ has been identified down to stellar masses $\sim10^9$ $M_\odot$ up to $z\sim2.5$, and down

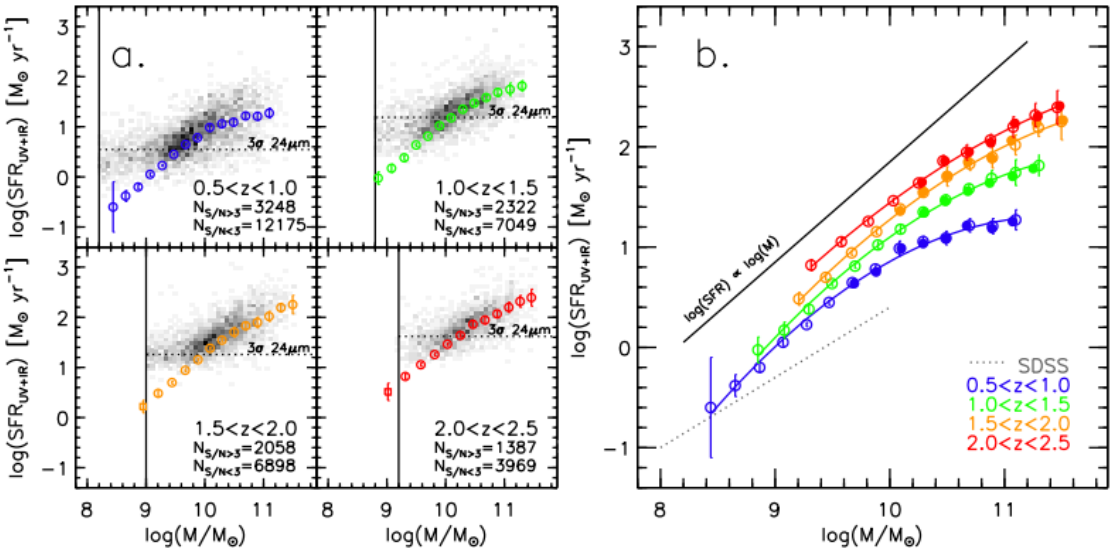

Figure 1.8: Figure 1 by Whitaker et al. (2014). The star formation rate as a function of stellar mass for star-forming galaxies. Open circles indicate the UV+IR SFRs from a stacking analysis, with a second-order polynomial fit above the mass completeness limits (solid vertical lines). The SDSS curve (grey dotted line in the right panel) by Brinchmann et al. (2004) is also given for comparison.

to $\sim 10^7$ $M_\odot$ at lower redshifts (e.g., Tremonti et al., 2004; Savaglio et al., 2005; Erb et al., 2006; Lee et al., 2006; Maiolino et al., 2008; Mannucci et al., 2009; Moustakas et al., 2011; Zahid et al., 2011; Foster et al., 2012; Zahid et al., 2012a; Berg et al., 2012; Henry et al., 2013b; Zahid et al., 2013; Pérez-Montero et al., 2013; Yuan et al., 2013; Yabe et al., 2014). Numerous studies have unveiled an evolution of MZ shifting towards lower metallicities for encreasing redshifts in a way that low-mass end evolves more dramatically than the high stellar mass range (Figure 1.7; Savaglio et al. 2005; Erb et al. 2006; Lee et al. 2006; Maiolino et al. 2008; Mannucci et al. 2009; Moustakas et al. 2011; Zahid et al. 2011; Foster et al. 2012; Zahid et al. 2013; Pérez-Montero et al. 2013; Yuan et al. 2013; Yabe et al. 2014). This appear to be qualitatively consistent with the downsizing scenario, in which high-mass galaxies assemble first most of their stars, and also most of the metals that they will ever produce. As a result, higher-mass galaxies are less capable of changing their metallicities after they have assembled most of their stars.

Extending observations to lower masses at all redshifts is then expected to provide essential insights into the physics of galaxy assembly and metal production as a whole, and in particular into the evolutionary path this population follow along cosmic times. In this sense, Henry et al. (2013b) for the first time provided measurements of intermediate-redshift ($z\sim$0.6-0.7) mass-metallicity relation for galaxies less massive than 10^9 $M_\odot$. More precisely, their sample contained 26 emission-line-selected galaxies with stellar masses in the range 8.0 $<\log M_*/M_\odot<$ 10.0 (including only a handfull below $10^{8.5}$ $M_\odot$). Amorín et al. (2014c) extended the results to stellar masses below 10^8 $M_\odot$ with a sample of extreme emission line galaxies (EELGs) between redshifts $0.2<z<0.9$. Still, the samples included in these studies are not numerous and are preferentially selected by extreme emission features that can somewhat bias our perception of the intermediate redshift dwarfs population.

1.3.1.2 Main Sequence of Star Formation

In the last decade, a number of works have revealed a close correlation between the SFR and the stellar mass of star-forming galaxies. This correlation has been found to be described by a power law (SFR $\propto M_*^{\alpha}$), with an intrinsic scatter of $\sim$0.2 –0.3 dex. This suggests the existence of a main sequence (MS; Noeske et al., 2007) populated by the vast majority of star-forming galaxies (Renzini and Peng, 2015). Thanks to the large variety of SFR indicators accessible through the exploitation of multiwavelength imaging and spectroscopic surveys, and the improved techniques to estimate stellar masses, the MS has been identified throughout a wide range of redshifts $(0-3)$ and stellar masses ($\log M_* \sim 8-11$; Brinchmann et al. 2004; Salim et al. 2007; Elbaz et al. 2007; Daddi et al. 2007; Magdis et al. 2010; González et al. 2010; Karim et al. 2011; Rodighiero et al. 2011; Zahid et al. 2012b; Whitaker et al. 2012; Huang et al. 2012; Whitaker et al. 2014). There have been already attempts to explore such sequence at even higher redshifts only recently reached. In Figure 1.8 we show the summary of the study performed by Whitaker et al. (2014) on the MS, and in particular on the low-mass end of such relation.

The MS appears to hide important information about how most of the stars in the Universe have been formed. The general interpretation of the simple fact that such correlation exists has been that SF processes are driven by "ordered" mechanisms, rather than stochastic processes such as mergers or starbursts (see Kelson, 2014, for an alternative interpretation of the MS). Furthermore, the slope of this relation is linked to star formation efficiency, and its tightness has been interpreted alternatively as a consequence of the steadiness of the SFHs or the rapid ignition and quenching of he SF processes, as well as the level of stochasticity in the gas accretion history.

However, the MS slope and dispersion differ appreciably from one study to another, likely due to sample selection, adopted SFR indicator, extinction law, and the method used to measure stellar masses. Renzini and Peng (2015) try to homogenize the definition of the MS to avoid misinterpretations.

1.4 Dwarf Galaxies Formation and Evolution

A cohesive picture of the formation and evolution of DGs remains nowadays elusive. In the following sections we describe some of the

1.4.1 Formation Scenarios

The epoch when DGs form the bulk of their stellar mass is still a matter of debate. Despite Λ-CDM predicts the early collapse of a vast number of low-mass halos (over a certain halo mass threshold, White and Rees 1978), this large amount of dwarfs have not been found. Actually, such number count discrepancy is frequently known as *the missing satellite problem* (Klypin et al., 1999). Furthermore, CDM models do not dismiss the possibility that low-mass galaxies could still be forming at the present epoch because they originate from density fluctuations much smaller than those giving rise to giant galaxies. On the other hand, the properties of late-type star-forming dwarfs (e.g., large gas content, lack of dust, blue colors, low metallicities) makes them appear as candidates to truly young objects that suffered a delay in their formation.

In practice, three scenarios have been considered from a theoretical point of view for the stellar mass assembly of DGs:

- Early formation models (e.g., White and Rees, 1978; Dekel and Silk, 1986) that predict that low-mass galaxies should experience the bulk of their SF before the end of reionization, z$\sim$6 (Zaroubi, 2013). Under this assumption, the dwarfs population is divided into those galaxies that consume most of their gas in such first SF process and those that preserve a gas reservoir until later times. The former are identified with old early-type dwarfs, and the later with late-type dwarfs. This scheme implies that we should be able to find a large fraction of the stellar mass of dwarfs in the shape of old stellar populations.

- Delayed formation models (Kepner et al., 1997) that propose a scenario for these systems where the SF is delayed until z$\sim$1. Some authors have searched for a mechanism that could either prevent these galaxies from forming until later ages, or at least reduce the SF efficiency. Cosmic reionization, powered by energetic photons from primitive galaxies (possibly from Population III stars) and AGNs, has been postulated as a very likely cause (e.g., Babul and Rees, 1992; Benítez-Llambay et al., 2015).

- Combined formation models, such as the one developed by Mamon et al. (2012), that propose a mass-dependent theoretical scheme, in which only galaxies with $\log M_*/M_\odot < 7$ form before the end of reionization.

The two later models predict a wider range of ages for the dwarfs population. Actually, they are compatible with the existence of intrinsically young dwarf galaxies at low redshift. However, most studies on the nearby dwarf galaxy population have revealed the existence of underlying SPs as old as the Universe itself. However, the uncertainties in the determination of the ages of the oldest SPs prevents dismissing the late formation of certain dwarfs (e.g. Gil de Paz and Madore, 2002). A clear example within this controversy is I Zw 18. Some works have claimed that it is a relatively young system (Izotov and Thuan, 2004; Jamet et al., 2010; Papaderos and Östlin, 2012) with SPs maximum $\sim$1.5 Gyr old (Östlin, 2000). Recently, even some authors have suggested that this galaxy could present features characteristic of Population III stars (Heap et al., 2015), such as nebular HeII emission (Kehrig et al., 2015). On the contrary, some other works (e.g., Annibali et al., 2013) have claimed that this galaxy could start "forming stars earlier than $\sim$1 Gyr ago, and possibly at epochs as old as a Hubble time".

Indeed, the observational studies have not agreed about when dwarfs undergo the dominant star forming activity (Mateo, 1998). For instance, Weisz et al. (2011a) found that the majority of the sample of the 60 Local Group dwarfs they target formed the bulk of their stellar mass (60%) prior to $z \sim 1$, independently on the morphological type (see Figure1.5 for a summary of the ages found for isolated Local Group Glaxies). Contrarily, for instance, Leitner 2012 inferred a late ($z \lesssim 1$) assembly of 70% of the stellar mass for low-mass star forming galaxies (LMSFGs) with masses $8.0 < \log M_*/M_\odot < 8.5$ using two alternative approaches: main sequence integration (MSI), and the spectral energy distribution (SED) fitting of a sample of star forming galaxies from the Sloan Digital Sky Survey (SDSS; Strauss et al. 2002).

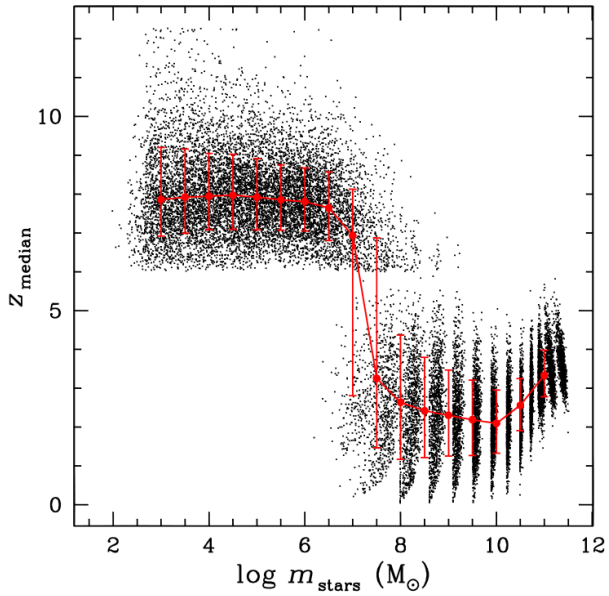

Figure 1.9: Left panel in Figure 5 from Mamon et al. (2012). Median (mass-weighted) stellar mass formation redshift as a function of the stellar mass at z=0. The black points are points represent individual galaxies, while the red symbols show medians (error bars extend from 16th to 84th percentiles).

1.4.2 Evolution Scenarios

Besides our doubts on when these galaxies undergo their main SF processes, we neither have a clear prescription for typical dwarfs SFHs. The picture of evolution of low-mass galaxies is generally presented as a continuous confrontation of processes with antagonistic effects (triggering/quenching) on the SF in low-mass DM halos: (1) the temperature reached by the Inter-Galactic Medium (IGM) after the reionization (e.g. Bullock et al., 2000; Susa and Umemura, 2004), (2) SF results such as gas depletion and feedback (e.g. Mac Low and Ferrara, 1999; Ferrara and Tolstoy, 2000; Tassis et al., 2003; Dong et al., 2003), and (3) phenomena related to high density regions (groups and clusters) and galaxy-galaxy interactions (e.g. Mayer et al., 2001b,a, 2006).

It is widely accepted that SFHs of dwarfs need to be less efficient than those followed by giants in order to preserve low values of stellar mass and metallicity, and high fractions of gas right to the nearby universe. More precisely, there have been identified three basic possible evolutionary theoretical scenarios for dwarfs, as mentioned by Kunth and Östlin (2000) and Martín-Manjón et al. (2012):

- Bursting SFH, which corresponds to a series of short and intense SF episodes separated by long quiescent periods (Davies and Phillipps, 1988). This type of SFH is favored by the low metallicities and dust content found in dwarf galaxies, as well as by their colors.
- Gasping/breathing SFH, which are characterized by long SF episodes separated by short low activity intermissions Tosi et al. (1991); Stinson et al. (2007). The gasping stands between the bursting mode and continuous SF scenario. With respect the former, gasping SFHs produce slower enrichment and older ages in their SP.
- Continuous SFH (Legrand et al., 2000), in which most of the stellar mass is assembled in a continuous low intensity SF process sprinkled with interspersed bursts. This type of SFH

implies that most of the stars in these systems are formed in the continuous low level state of SF, during the inter-burst periods, and it has been claimed to be more realistic by some authors (Lee et al., 2004).

From the observational perspective, some works have also suggested that the most probable dwarfs SFH is sporadic (e.g., Barazza et al., 2006, using color-color diagrams). Even the mere large diversity of physical conditions identified for low-mass galaxies has been argued to be incompatible with a generalized constant SFH. For instance, Sánchez Almeida et al. (2008), obtained a relationship between the duration time of the starburst phase and the quiescent periods, based on the number of objects of each type within their sample. The sporadic or cyclic SF process can be due to both interactions or/and irregular gas inflow rate. Lee et al. (2000) found that dwarfs with stronger emission lines and SF processes are found preferentially in underdense regions, which appear to be inconsistent with the view that interaction-induced starbursts dominating dwarfs SFHs. This would otherwise be expected if inflows drove preferentially SF. Besides, for instance, Lee et al. (2009) found a small percentage of starburst dwarf galaxies in whole population of the Local Volume dwarfs, which could indicate that these galaxies form stars preferentially through smoother processes.Another SFH mode has also been found observationally (e.g., Grebel, 2001), characterized by a decreasing trend since the early times.

1.5 Objectives

The main objective of this *Thesis* is to **shed light on the formation and evolution of dwarf galaxies**. In particular, we aim at reducing the uncertainties in the formation redshift of dwarf galaxies and constraining their SFHs.

We address this aim through two alternative and complementary observational approaches: (1) direct observations of galaxies at different redshifts, and (2) reconstruction of the previous galaxy history from fossil records hidden within their spectral energy distribution (SED).

To achieve this goal we carry out the following steps explained in detail in each of the chapters of this manuscript:

- Selection of a sample of candidates to dwarfs in the field at intermediate redshifts. Chapter 2.
- Spectroscopic observation with the aim of confirming spectroscopically the sample of dwarfs at intermediate redshifts. Chapter 3.
- Data set gathering: Optimization of the photometry available, and redshift and emission lines measurements. Chapter 4.
- Estimation of the physical properties of the final spectroscopic sample and their SFHs using the spectral energy distribution (SED) fitting technique recently developed by Pacifici et al. (2012). This approach presents the peculiarity and novelty of considering physical motivated SF and chemical enriching histories instead of typical idealized functions. Moreover, it allows the use of both photometric and spectroscopic data in order to study simultaneously the stellar and nebular emission. Chapter 5.

- Analysis of the global properties of the final sample: colors, structural parameters, morphology. Chapter 6.
- Analysis of the physical properties of the spectroscopically confirmed galaxies. On the one hand those derived though the SED-fitting approach: stellar mass, SFR, specific star formation rate (sSFR; sSFR=SFR$/M_*$). On the other hand those derived from the measurements of spectral features: metallicity and extinction. Chapter 7.
- Analysis of the SFHs obtained. Chapter 8.

Throughout this *Thesis* we adopt a standard Λ-CDM cosmology with $h = 0.7$, $\Omega_m = 0.3$ and $\Omega_\Lambda = 0.7$. Furthermore, magnitudes in this work are expressed in the AB system (Oke, 1974).

2

Sample Selection

In this Chapter we describe the selection of our sample of candidates to DGs at intermediate redshifts.

2.1 Our Definition of Dwarf Galaxy

This *Thesis* focuses on the cosmological field Extended Chandra Deep Field South (E-CDF-S; Lehmer et al., 2005) due mainly to the following reasons:

- Its excellent multi-wavelength photometric coverage, from UV to far-IR, maximizes the high quality of the estimations of redshift and stellar masses on which we base our selection criteria.
- Its available morphological catalogs, such as the developed by Griffith et al. (2012), which provide structural parameters on the GOODS and Galaxy Evolution from Morphology and SEDs (GEMS, Rix et al., 2004) areas. The mentioned work uses the Galaxy Analysis over Large Areas: Parameter Assessment by Galfitting Objects from SExtractor (Galapagos) code (Häußler et al., 2011), which incorporates both Galfit (Peng et al., 2002) and SExtractor (Bertin and Arnouts, 1996) to construct photometric morphological catalogs derived from the HST ACS imaging.
- Its location guaranties the possibility of performing spectroscopy of the selected sample using multi-object spectrographs available in southern hemisphere observatories[1].

We decide to build a sample of candidates to low-mass galaxies at intermediate redshift on a deep Subaru NB816 (Ajiki et al., 2006) image of the E-CDF-S using the RAINBOW database[2] (Pérez-González et al., 2008; Barro et al., 2011a,b). This catalog is the deepest available in the database at the time the selection is carried out, and appears to be ideal to search for low-mass field galaxies, presumably blue and star-forming. RAINBOW database provides estimations of physical parameters of galaxies obtained using a template fitting code based on χ^2 minimization between observed photometry and a set of $\sim$1500 semi-empirical template SEDs built from spectroscopically confirmed galaxies modeled with PEGASE stellar population synthesis models (see Appendix A in Pérez-González et al., 2008).

[1] http://www.eso.org/public/teles-instr/

[2] http://rainbowx.fis.ucm.es

As we already mentioned, there is not a unique definition of what a DG is in the literature. The selection of low-mass galaxies at intermediate redshifts has been mainly carried out using the properties of particular types of galaxies. For instance, strong emission line selections have been probed to be efficient to select DGs with stellar masses down to log $M_*/M_\odot \sim 8$ up to redshift ~ 2 (Atek et al., 2014; van der Wel et al., 2011). However, these type of selections favor extreme systems to the detriment of a more quiescent population. Nowadays, that high quality SED-fitting is applied over multiwavelength surveys extensively, DGs at intermediate redshifts can be selected using mass criteria. One of the advantages of this approach is that it avoids biasing automaticaly the selected samples toward specific extreme evolutionary stages (e.g., starbursts), and therefore, enables the study of more representative samples of the whole dwarfs population. In particular, we define DGs as those systems qualifying the following stellar-mass criterion:

$$log\, M_*/M_\odot < 8 \tag{2.1}$$

We choose this upper mass value in order to be able to identify a hypothetical bimodal behavior of the formation redshifts of low mass galaxies, as found by Mamon et al. (2012, see Figure 1.9). Such value corresponds also to the range of halo galaxy masses expected to dominate the reionization of cosmic hydrogen (Wyithe and Loeb, 2006).

As an alternative, and with the aim of increasing the surface density of targets, we also select a sample of candidates using blue compact dwarf galaxies (BCDs; Thuan and Martin 1981) as tracers of low-mass galaxies. As we already mentioned, BCDs were first identified by Zwicky (1965) as star-like field galaxies on his Palomar Sky Survey Plates. Since then, they have been studied and found to be characterized by a compact structure, abundant gas content, luminosity dominant star-forming regions (e.g., Papaderos et al., 2002), and an older stellar population of larger spatial extent containing a significant mass fraction of the system. BCD is an heterogeneous galaxy class that covers a wide range in most physical parameters (e.g., absolute magnitude, mass, SFR). For this reason, BCDs have been subclassified by size or luminosity (Cardamone et al., 2009, and references therein). Among dwarfs, BCDs present observational advantages for intermediate redshift surveys such as strong emission lines, resulting from the star-formation process they undergo, and high surface brightness (μ). Our BCDs selection criteria are based on those used by Gil de Paz et al (2003), where the physical compactness criterion used by Thuan and Martin (1981) is exchanged by a surface brightness criterion. This modification is considered in order to relate the term *compact* to the high-surface-brightness component of the galaxies and not to the total optical size that could include an extended low-surface-brightness component.

$$M_{\mathrm{B,0,AB}} > -18.5\, mag \tag{2.2}$$

$$(B-V)_0 < 0.6\, mag \tag{2.3}$$

$$\mu_{\mathrm{Reff,B,0}} < 23\, mag\, arcsec^{-2} \tag{2.4}$$

The restframe absolute magnitude and color provided by Rainbow are the synthetic values obtained from the fitted template considering the photometric redshift in each case. In order to calculate the surface brightness we used the morphological catalogs published by Griffith et al. (2012). Among other structural parameters, this catalog provides effective radius in F850W (z) and F606W (V) ACS/WFC bands on GOODS-S and GEMS. As we do not identify significant differences between

the effective radius in both band, we decide to use the values obtained for V band as a good tracer for B band at intermediate redshifts. We include in the final BCDs candidates sample only galaxies within the catalogs by Griffith et al. (2012).

As we intend to study intermediate redshift DGs, we decide to limit our study within the following redshift range:

$$0.3 < z_{\rm phot} < 1.0 \tag{2.5}$$

The lower limit was set mainly in order to avoid overlapping with previous low-redshift dwarfs studies such as the carried out by Barazza et al. (2006) on GEMS and SDSS below redshift 0.25.

The sample selection is also tuned in order to build a sample of targets observable by the Very Large Telescope (VLT; European Southern Observatory, ESO, Paranal, Chile) multi-object spectrograph VIMOS (VIsible Multi-Object Spectrograph; Le Fèvre et al., 2003). We include two criteria to account for the observational limitations. The first one, an apparent magnitude upper limit in the photometry of the band where we select the galaxies:

$$\text{Subaru NB816} < 26\ \text{AB mag} \tag{2.6}$$

The second, the upper redshift limit aforementioned, found to be the highest redshift for which VIMOS would be able to detect such faint galaxies using reasonable exposure times and atmospheric conditions (see Chapter 3).

We find 674 galaxies with $\log M_*/\mathrm{M}_\odot < 8$, and 869 BCDs. With the intention of building a more representative sample of dwarfs, we include every galaxy with stellar masses $\log M_*/\mathrm{M}_\odot < 8$ in the mass selected sample, even those that are also classified as BCDs (190 out of 674 objects). This means that the sample of candidates to BCDs only includes galaxies with stellar-masses beyond our dwarf definition limit (Figure 2.1, top left panel).

2.2 Initial Sample

Our initial sample of candidates is conformed of the combination of the samples built using the criteria aforementioned (674 mass-selected candidates to dwarfs and 869 candidates to BCDs). In Figure 2.1 we show an overview of the properties of these galaxies (we use red for the low-mass candidates and blue for the BCD candidates). With vertical lines we mark the selection criteria. In particular, we see how the mass criteria selects on average galaxies with slightly fainter, redder, and with a smaller surface brightness, than the BCDs properties, as expected. Still, we can say that the criterion based on stellar mass ($\log M_*/M_\odot < 8$) applied at intermediate redshifts selects mainly galaxies that generally match the rest-frame B band absolute magnitude and rest-frame $B-V$ color criteria of BCDs. More than half of the mass selected sample do not qualify the BCDs criterion on surface brightness.

2.2.1 Summary of Samples

For clarity, we decide to include here a summary of the different samples used along this *Thesis*.

1. The *initial sample* ($\sim$1.600 galaxies; Section 2.2) is the result of the selection criteria applied to the Subaru NB816 catalog on E-CDF-S.

2. The *observed sample* (327 galaxies) corresponds to the representative subsample gathered from the initial sample that is observed spectroscopically (Section 3.1.2).

3. The *spectroscopically confirmed sample* contains all the galaxies (94) for which a reliable spectroscopic redshift (flag 2, 3 or 4) was able to be measured (Section 4.2.1).

4. The *fitted sample* is conformed of 91 galaxies for which we can perform a proper fit of the SED (using the measured spectroscopic redshift). From this point on, the properties and selection criteria are based on spectroscopic properties (Chapter 5).

5. The *morphological sample* contains the 85 objects out of the 91 of the *fitted sample* for which the morphological catalog by Griffith et al. 2012 contains structural parameters.

6. The *final sample* (74 galaxies). For certain sections in this work, we restrict our spectroscopically confirmed sample to the redshift range between 0.3 and 0.9. Within these limits the redshift is covered by an approximately uniform mass distribution. We also defined two subsamples:

    - The low-mass star-forming galaxies (LMSFGs) sample contains only those galaxies in the *final sample* with stellar mass $\log M_*/M_\odot<8$.
    - The secondary sample includes only those galaxies with $\log M_*/M_\odot>8$.

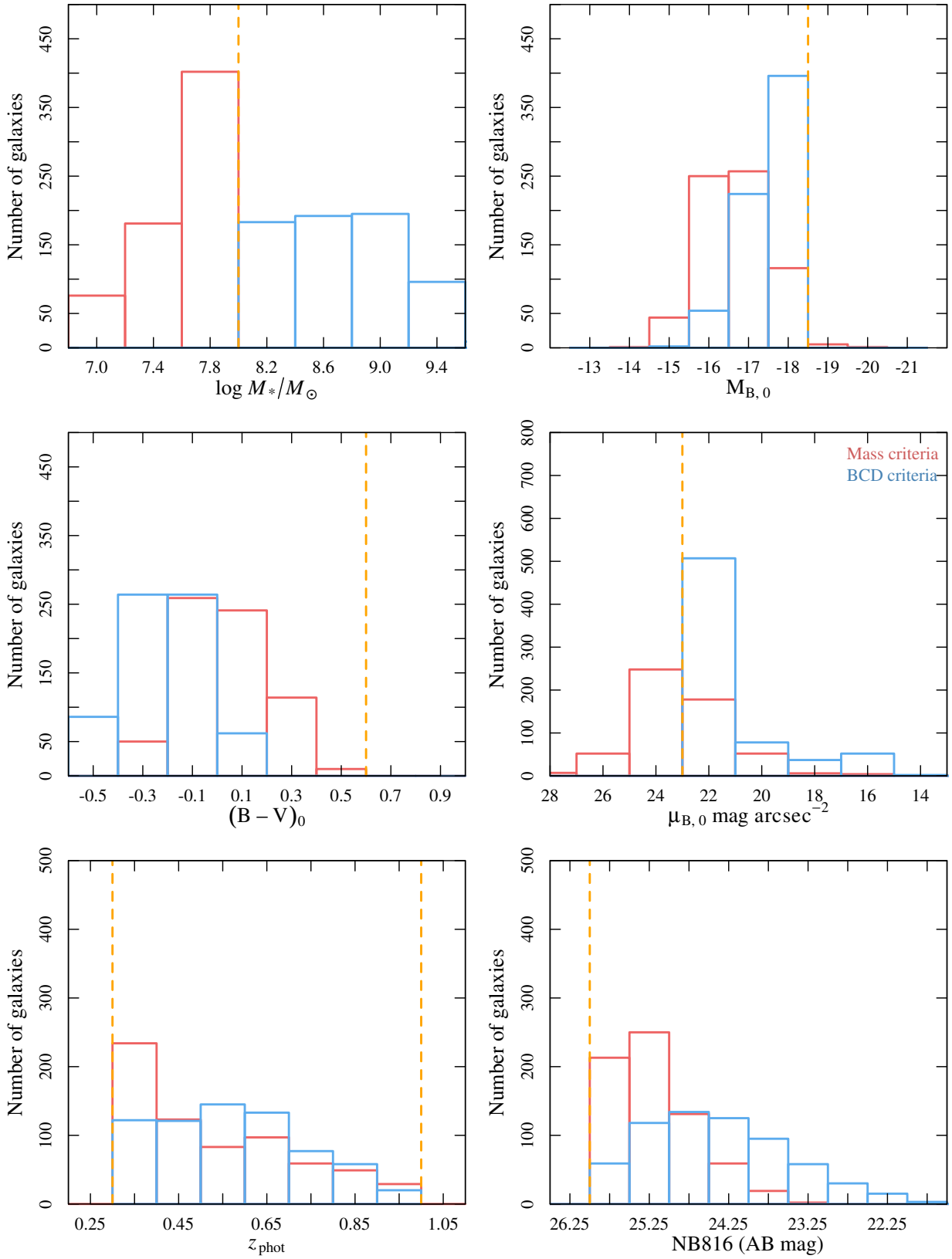

Figure 2.1: From top to bottom and right to left we show the distribution of $\log M_*/\mathrm{M}_\odot$, $M_{\mathrm{B,0,AB}}$, $(B-V)_0$, $S_{\mathrm{Reff,B,0}}/$ mag arcsec^{-2}, z_{phot}, and apparent magnitude in the seleccion band Subaru NB816 for the samples built using the two selection criteria used in this work: a stellar mass criterion (red), and a set of criteria based on the properties of BCDs (blue).

3

Spectroscopy Campaigns

One of the most important steps in the development of this work is the spectroscopic confirmation of the candidates to low-mass galaxies. Along the whole research period this work, we have applied for spectroscopic observations in 6 different occasions, trying to cover different cosmological fields and to exploit the capabilities of several instruments and astronomical facilities located on both hemispheres: At the Very Large Telescope (VLT; European Southern Observatory, ESO, Paranal, Chile), the multi-object spectrograph VIMOS (VIsible Multi-Object Spectrograph; Le Fèvre et al., 2003), and KMOS spectrograph (K-band Multi-Object Spectrograph; Sharples et al., 2010); at the Gran Telescopio de Canarias (GTC), the OSIRIS spectrograph (Optical System for Imaging and low Resolution Integrated Spectroscopy; Cepa et al., 2000); at the William Herschel Telescope (WHT), the ACAM (Benn et al., 2008) long-slit spectroscopy mode. Table 3.1 shows the observing time we were fianlly granted with.

The results of this *Thesis* are based on the observations carried out on E-CDF-S field using VLT/VIMOS.

3.1 Observing with VIMOS

VIMOS is an imager, multi-object spectrograph (MOS) and integral field spectrograph mounted on the 8 m VLT Melipal Telescope (Unit Telescope #3, UT3). It was designed to be an optimal instrument for surveys, thus, it provides a combination of large field of view (FoV; ~ 224 arcmin^2), moderate spectral resolutions ($R \sim 180 - 2500$), and a extraordinary multiplex capability in multi-slit spectroscopy mode. These properties make it also ideal for our study. Among VIMOS most important achievements we mention the VLT VIMOS Deep Survey (VVDS; Le Fèvre et al., 2013) that obtained spectroscopic redshifts for ~ 35000 galaxies and type–I AGNs.

The detector of VIMOS is divided into four not perfectly aligned quadrants separated by wide gaps. Each quadrant covers ~ 56 arcmin^2, and it is equipped with a 2048$\times$4096 pixels CCD (15 μm/pixel Deep-depletion E2V 44-82). The quadrants are arranged in a squared configuration that can be orientated following two possible Position Angles (PAs; see Figure 3.1 for a representation of the VIMOS FoV and PAs). A single exposure taken with VIMOS produces four images (one for each VIMOS quadrant).

VIMOS-MOS observations are carried out using masks (one per quadrant) prepared using a laser cutting Mask Manufacturing Unit. In order to build correctly the masks it is useful (even necessary) to have an image of the area covered by the MOS pointings taken by the same instrument.

Table 3.1: Description of the observations

Program	Year	Observatory/Instrument	Mode	Type	Field	Granted
088.A-0321	2011	VLT/VIMOS	Visitor	MOS	E-CDF-S	8h
090.A-0858	2012	VLT/VIMOS	Service	MOS	E-CDF-S	8h
127-GTC54/13A	2013	GTC/OSIRIS	Service	Long-slit	HDFN	10h
164-GTC78/14B	2014	GTC/OSIRIS	Service	MOS	UDS	12h

In this image all the possible impacts of the instrumentation (mechanical flexures, distortions, vignetting, etc) are already taken into account. This image is known as *pre-imaging*, and it is mandatory for all VIMOS-MOS observations. In Section 3.1.1 we describe the pre-imaging runs and in Section 3.1.2 we describe the mask designing process.

VIMOS MOS-mode offers a variety of grisms which provide resolutions from 180 to 2500. The associated order sorting filters available for each grism limit the wavelength range in each case, leading to necessarily narrower spectral ranges ($\sim$ 300 Å) in the highest resolution configurations, and narrow ($\sim$ 2000 Å) to wide ($\sim$ 5000 Å) ranges in the lowest resolution cases. The multiplex capability changes for each case due to fact that for narrower wavelength ranges, more than one spectrum can be included in a raw on the detector (i.e. the slits can overlap in the spatial direction).

In order to plan our observations we first identify the most suitable mode and configuration for our desired observations. We opt for the medium resolution grism (MR; R =580 for 1" wide slits) and the default filter (GG475). Both of them together provide a wavelength range that covers 4800-10000 Å and a 2.5 Å/pixel dispersion, with spatial resolution of 0.2"/pix. This wavelength regime allows to detect simultaneously the most prominent emission lines as [OII]$\lambda\lambda$3727, Hβ or [OIII]$\lambda\lambda$4959,5007 along the whole redshift range of the sample ($0.3 < z_{phot} < 1$). The apparent surface density of our initial sample of galaxies in the the E-CDF-S field is 1.6 arcmin^{-2}. Despite the fact that with this number we could take advantage of the maximum multiplexing allowed by shortest wavelength ranges, we prioritize the wide spectral range over the number of targets observed.

VIMOS Exposure Time Calculator[1] (ETC; version 3.2.9.) estimates how SNR changes with observing considerations such as the Moon age, seeing, etc, and with the properties of our targets. We use the ETC to identify the optimal exposure times and atmospheric conditions for the pre-imaging and MOS observations that allow us to perform the desire science. As spectral reference we use the *Starburst 1* spectrum from Kinney et al. (1996). Considering the worst case of the sample, we use a galaxy with i=26.0 AB mag located at z=1. Furthermore, we select seeings between 1-1.2", an airmass of 1.2, and slit widths varying between 1.2-1.4". Exposure times of 4 h return for dark nights (*three days from New Moon*) SNR=2.5 Å^{-1} for the peak of the [OII]λ3727 emission line (with an expected flux of $\sim$10^{17} erg s^{-1} cm^{-2}) and SNR=1 Å^{-1} for the continuum. *Seven days from New Moon* produces only slightly lower SNR values. *Ten days from New Moon* means SNR=2 Å^{-1} for the peak of the [OII]λ3727 line and SNR=0.8 Å^{-1} for the continuum. As an acceptable option and, with the aim of increasing the probability of our program to be observed, we accept gray nights (*seven days from New Moon*).

[1] http://www.eso.org/observing/etc/

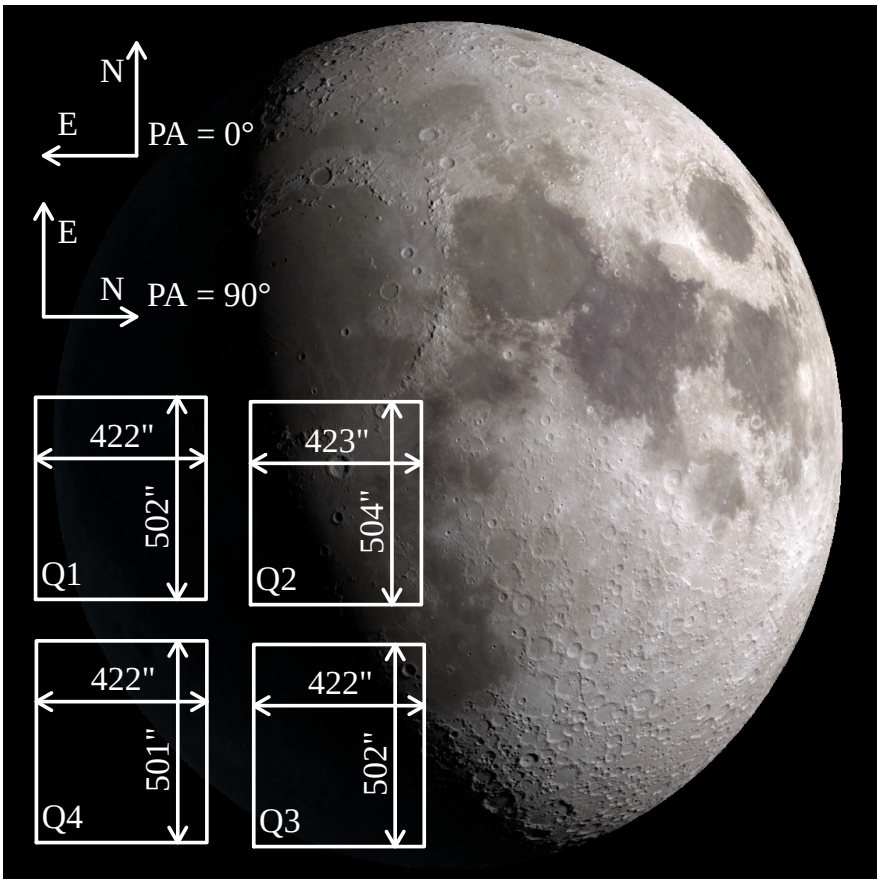

Figure 3.1: VIMOS FoV and possible PAs. Approximate comparison with the size of the Moon (Image from NASA/Goddard Space Flight Center Scientific Visualization Studio; http://svs.gsfc.nasa.gov/).

VLT allows observations carried out under *visitor* or *service modes*[2]. In the former case, the dates of the observation are fixed, and the observers can attend them at the observatory. In the later, the observations are observed when the observing conditions match those requested and there is no other program in the queue with higher priority. The mode remarkably affects the design of the observations due to the fact that for *service mode* the observations have to be divided into blocks (observing blocks, OBs) with a length limitation (1 h). As overheads need to be included as part of each 1 h long OB, the length limitation implies that getting the same amount of time for science exposures requires a larger total amount of granted time.

We carry out 2 VIMOS spectroscopy programs (Table 3.2). The first one (088.A-0321) is performed under *visitor mode*, and it is divided into two pointings (1 & 2). Observations are attended by Jesús Gallego and Lucía Rodríguez Muñoz. The second one (090.A-0858) is performed under *service mode*, and consists on a single pointing (3). The FoV covered by Pointings 1 & 3 is the same.

We use slit widths of 1.2" and 1.4" in the first and second program, respectively. The difference was motivated by the fact that we relaxed our atmospheric specifications in the second run. Given the small sizes of the galaxies in our sample, their size is expected to be dominated by the seeing during the observations. Therefore, unless the observations are carried out under extremely good seeing conditions, in which we would include a larger fraction of sky within the slits, these

[2] *Pre-imaging* runs are always carried out under *service mode*.

Table 3.2: VIMOS observations

Run-Pointing BCDs[c]	α [J2000]	δ [J2000]	T_{exp}	# [s]	# Slits	# Dwarfs
1[a]-1	03h32m33.5s	-27°45' 26.3"	14400	119	94	25
1[a]-2	03h32m22.8s	-27°51' 09.5"	14400	119	99	20
2[b]-3	03h32m33.5s	-27°45' 26.3"	13680	92	60	32

[a] Program 088.A-0321. Visitor Mode Observations.

[b] Program 090.A-0858. Service Mode Observations.

[c] None of these BCDs are dwarfs, following our mass criterion. The galaxy 2010 was observed in the three pointings in order to use it as a check for the flux calibration. Also, the galaxy 1344 was observed in the pointings 2 and 3.

width values are a conservative choice made in order, once again, to maximize the probability of the program to be carried out.

In the following sections we describe the steps of the observational procedure including the pre-imaging (Section 3.1.1), and the mask design (Section 3.1.2).

3.1.1 Pre-imaging

As it has been mentioned before, the objective of the *pre-imaging* is to have an image of the FoV of the pointings that are planned to be covered by the science OBs. The *pre-imaging* can be used in two possible ways depending on whether the targets are visible on it or not. When the targets are bright enough, or the image is deep enough, then x-y coordinates of the targets on the image are used directly to place the slits on the masks. If the targets are so faint that the *pre-imaging* would need too much exposure time to detect them, then, visible objects on the field (preferably stars), that are also included in the catalog where the sample selection is made, are used as references to convert the coordinates of the catalog to the reference system of the instrument.

The *pre-imaging* is observed using *service mode* weeks or months in advance the spectroscopic observations, so that there is enough time to design the masks and the final specifications of the observing plan or OBs sequence.

It is mandatory to obtain the *pre-imaging* in R band. We run 3×365 s exposures per pointing. VIMOS ETC version 3.2.9 returns SNR ~ 5 for a 1800 s exposure time image on a target as faint as the faintest galaxy in our sample (i=26.0 AB mag), which is enough to compute centroids.

The guide star for MOS is selected at the time the *pre-imaging* is designed, and then, the guide star coordinates and position of the guide probe is stored in the pre-image headers, and subsequently propagated to the masks and science observations.

Figure 3.2 and 3.3 show single exposure images of the *pre-imaging* of the four quadrants of the Pointins 1 & 3 and Pointing 2, respectively. Irregular dark areas (Q3 and Q4 in Pointing 1 & 3 and Q3 in Pointing 2) are caused by the vignetting due to the guide star arm probe. The clear, extended, and diffuse patterns in Q3 and Q4 are caused by variations in the sensitivity of the detector and/or by distortions in the optical path.

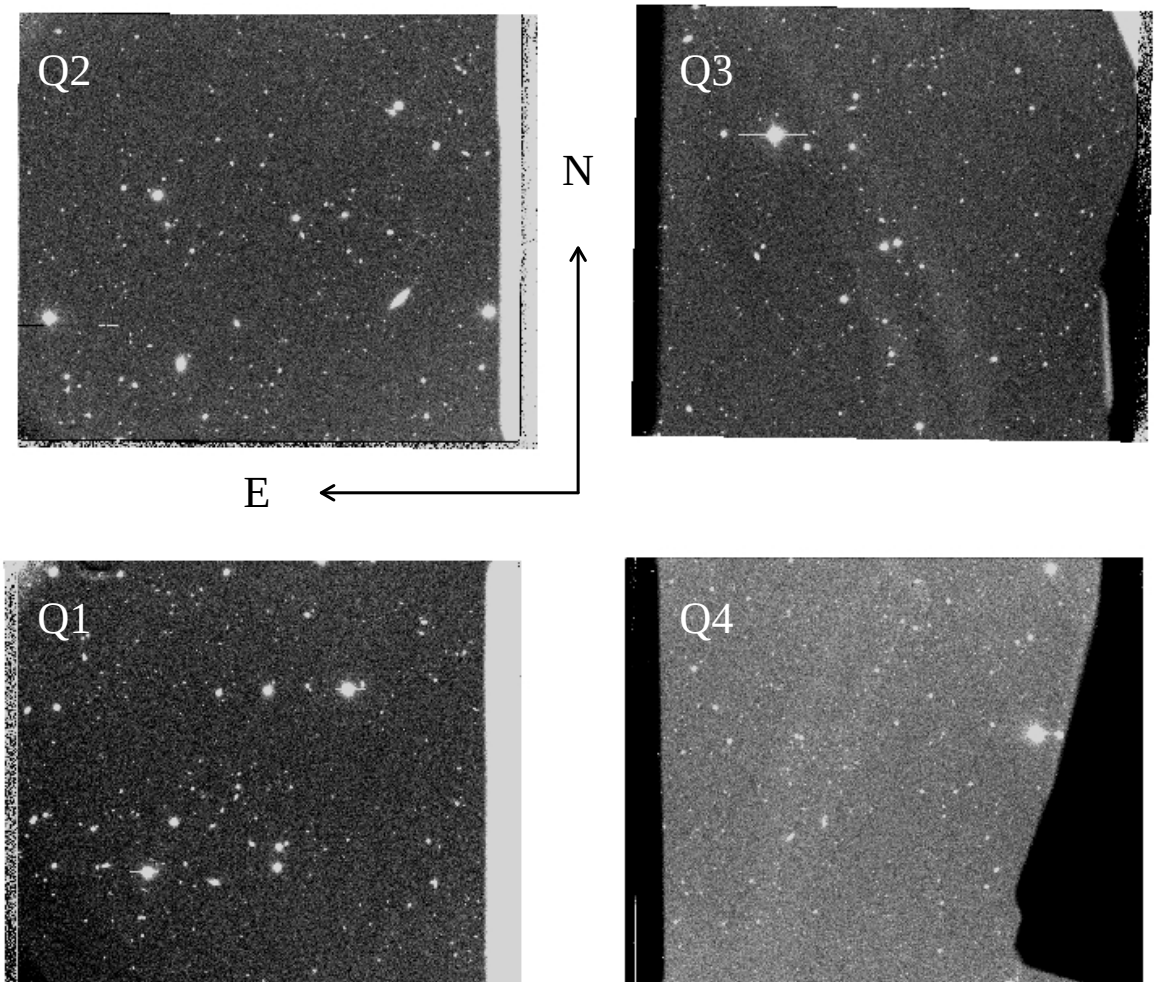

Figure 3.2: Raw single exposure images of the four quadrants of Pointing 1 and Pointing 3 pre-imaging. The dark regions on the right in Q3 and Q4 are due to vignetting.

3.1.2 Mask Design

The slit masks are prepared for the four quadrants of VIMOS and all the pointings using the VMMPS software (Bottini et al., 2005). Given the faintness of the targets of our study, and despite the exposure time used (Section 3.1.1), they are not detected on the *pre-images*. In this case, VMMPS provides a task for a correct design of the masks, that converts our catalog of coordinates to a catalog of VIMOS x-y *pre-images* coordinates. We use as input two catalogs that contain:

1. The *pre-imaging* x-y coordinates of ∼40–50 reference objects (per VIMOS quadrant) which are also visible in the selection image. This number of reference objects are enough for the reliable cross-correlation between coordinates of the input catalog and the VIMOS *pre-images* coordinate system. In particular, we obtain values of RMS of ~ 0.1" for all quadrants and the three pointings. To build this catalog we need to run SExtractor on the *pre-imaging* and match the position of the sources found with a subselecton of relatively bright point-like sources included in the selection catalog. We check carefully the objects matching and delete manually and individually problematic cases, such as irregular sources, or saturated stars.

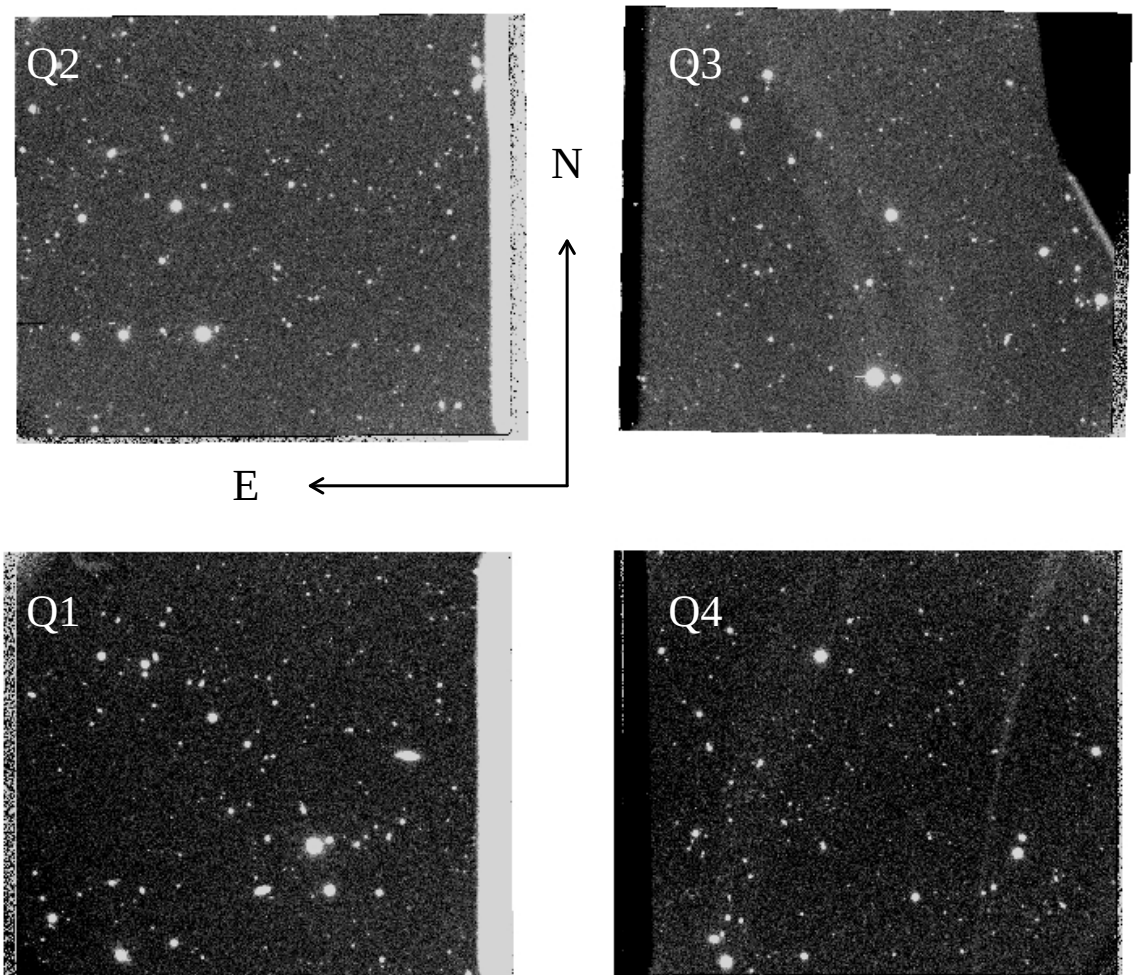

Figure 3.3: Raw single exposure images of the four quadrants of Pointing 2 pre-imaging. Here, vignetting only affects the top-right corner of Q3.

2. The *full catalog* of sources on the selection band that includes:

   - Our catalog of targets described in Chapter 2: mass selected candidates to dwarfs and BCDs.
   - The coordinates of the already mentioned reference objects.
   - For the correct alignment of the masks it is required also to include a minimum of 3 pseudo-slits per quadrant where reference stars are centered. We need to take into account that these stars should be bright enough to appear in short exposures. Then, we identify a sample of possible reference stars on the *pre-imaging*, with R $\sim$ 17–19 AB mag, and we add them to the final catalog.

It is in this catalog when we assign an ID to the objects in the catalog. For an easier identification of the galaxies selected by the different sample selections, we use IDs smaller that 1000 for mass selected galaxies, while we use IDs larger than 1000 with those systems selected as BCDs.

For the design of the masks from the *full catalog*, some objects may be assigned with different priorities: *compulsory*, *optional*, and *forbidden*. In particular, those designated as *compulsory*,

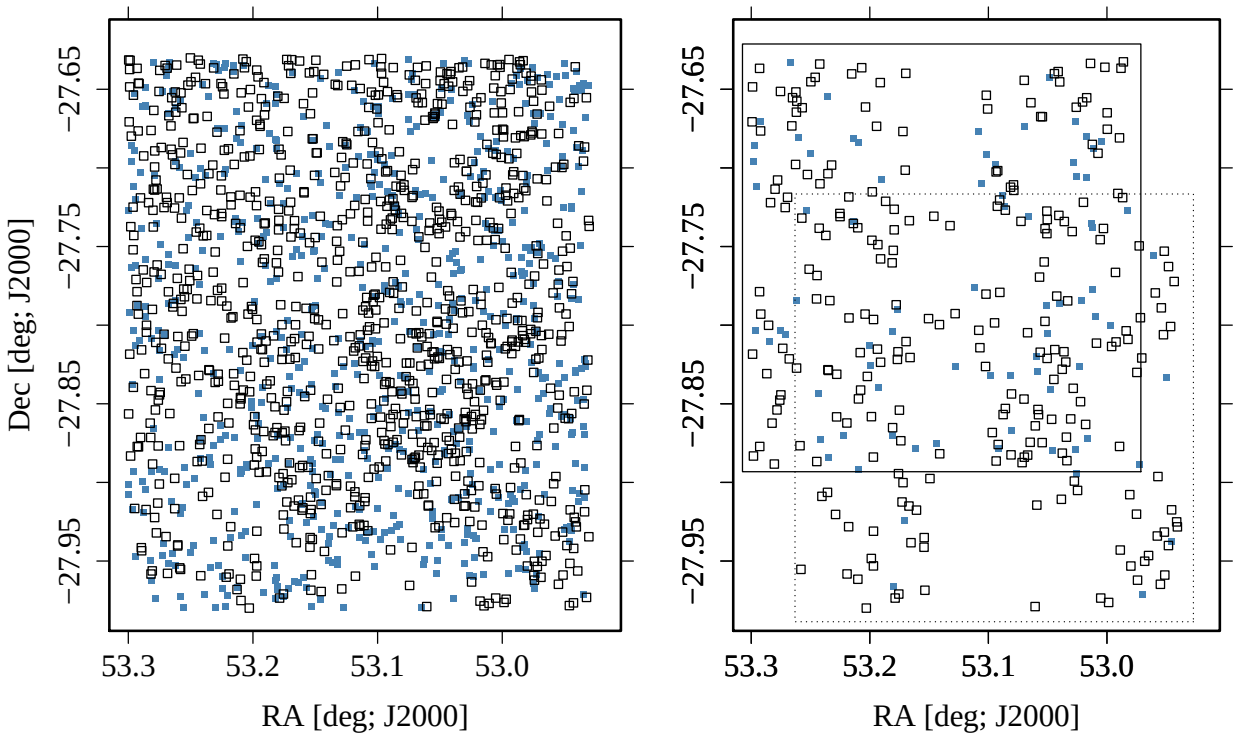

Figure 3.4: Spatial distribution of our total sample of galaxies (left panel) and those finally observed (right panel). Empty squares represent low-mass galaxies and blue squares represent BCDs. Solid black line outlines the area target in the Pointings 1 and 3. Dotted line marks the border of the area covered by Pointing 2.

are included in the mask design if at all possible. We set as *compulsory* the candidates to dwarfs selected by mass. We set as *optional* the reference sample of galaxies selected as BCDs. Galaxies located too near the edges of the detector or within the vignetting area are set as *forbidden*. The minimum slit length is set at 12" as a compromise between maximizing the number of slits on the mask and the correct sampling of the sky at both sides of the object (our dwarfs have an average half light radius 0.21±0.14" as measured in HST/ACS F606W and F850W images). Smaller sizes do not increase significantly the number of slits that could be allocated in each mask. VMMPS works across the field, placing a slit over the next available object. The majority of slits are then assigned to "random" targets in the catalog (taking into account the priorities) in a way that the number of slits in each mask is maximized. We verify that the final set of slits include at least the 3 pseudo-slits per quadrant in a triangular pattern, needed for the correct alignment of the masks. In some cases, this implies a manual modification of the masks or/and tuning of the initial catalog before running VMMPS.

The slits are aligned N-S (default VIMOS MOS mode rotator angle) to minimize slit losses from atmospheric differential refraction. For the same reason, the observations in service mode are limited to an Hour Angle of $H \leq |2h|$.

With the current input catalogs and methodology, 119 slits are placed in each of the first two runs, and 92 slits in the third one. The decrease in the number of slits allocated in the last run is due to the fact that the number of available targets is lower, given that the first and third pointings are centered on the same coordinates. We forced VMMPS to repeat at least one galaxy in the different runs, so that we had compatibility tests of the results derived from the different pointings. Thus, a total of 330 slits were defined for a total of 327 targets: 253 candidates to dwarfs ($\log \mathrm{M}_*/\mathrm{M}_\odot < 8$)

Table 3.3: VIMOS observations (cont.)

Run-Pointing	α [J2000]	δ [J2000]	Dates	T_{exp} [s]	Slit width	Air mass	Seeing
1[a]-1	03h32m33.5s	-27°45' 26.3"	2011-Nov-17	12000	1.2"	∼1.2	∼0.6"
1[a]-2	03h32m22.8s	-27°51' 09.5"	2011-Nov-18	9600	1.2"	∼1.2	∼0.6"
2[b]-3	03h32m33.5s	-27°45' 26.3"	2012-Dic-8, 9, 17 & 21	13680	1.4"	∼1.2	∼0.9-1.7"

[a] Program 088.A-0321. Visitor Mode Observations.

[b] Program 090.A-0858. Service Mode Observations.

and 74 candidates to BCDs. Figure 3.4 shows the spatial distribution of the 327 targets.

The position of the slits on the mask allow the vast majority of spectra extend over the full wavelength range. However, the end of some spectra are permitted to be lost due to the ends of the spectra falling off the detector area.

The results of a Kosmogorov-Smirnov Test for photometric redshift, stellar mass and color of the subsample observed with respect the initial sample suggests that the subsample of galaxies observed are representative of the whole sample selected: z_{phot} D=0.1429, p-value=0.9988, M_* D=0.25, p-value=0.9105, $(B-V)_0$ D=0.222, p-value=0.9794. Figure 3.5 shows a comparison between the properties of the initial sample and the observed one.

3.1.3 Observations

First program (088.A-0321) was design as 2 different pointings, each of them divided into $6 \times 2400\,\mathrm{s}$ exposures, between which the telescope was offset in a pattern of positions separated by 0.6" along the slit. Due to technical problems within the time scheduled for the run, the final exposure time was $12000\mathrm{s}$ and $9600\mathrm{s}$ for Pointing 1 and 2, respectively. Observations for first program were executed in two consecutive nights with a mean air mass of ∼1.2 and excellent atmospheric conditions with a steady seeing of ∼0.6". Second program (090.A-0858) consisted of 1 pointing (Pointing 3), with the same coordinates as Pointing 1, of 8×1710 s. Because of the lack of an atmospheric dispersion corrector on VIMOS, observations carried out in Service Mode are limited to ±2 hr of hour-angle. Observations for second program were executed with a mean air mass of ∼1.2 and variable seeing between 0.9" and 1.7". In Table 3.3 we summarize the atmospheric conditions and final exposure times of the observations.

3.1.4 Reduction

Data reduction is a crucial process that allows to obtain scientific results from observational data. Therefore, it is a delicate task characterized in general by a high level of complexity. With the observational optimization achieved by the new generations of instruments (i.e. MOS and IFU capabilities) the sophistication of the observational data has dramatically increased, adding to the standard and basic reduction process additional difficulties to overcome. For this reason, the development of specific pipelines designed with the purpose of reducing data taken by a given instruments is extremely valuable.

Table 3.4: Missing keywords in the original FITS files.

HIERARCH ESO INS ADF TYPE	HIERARCH ESO INS SLIT1 ID
HIERARCH ESO INS ADF VERSION	HIERARCH ESO INS SLIT1 OBJ RA
HIERARCH ESO INS ADF UNIT	HIERARCH ESO INS SLIT1 OBJ DEC
HIERARCH ESO INS ADF ID	HIERARCH ESO INS SLIT1 X
HIERARCH ESO INS ADF ADMID	HIERARCH ESO INS SLIT1 Y
HIERARCH ESO INS ADF COMMENT	HIERARCH ESO INS SLIT1 DIMX
HIERARCH ESO INS MASK2 ID	HIERARCH ESO INS SLIT1 DIMY
HIERARCH ESO INS ADF GRISM NAME	...
HIERARCH ESO INS ADF GRISM SPECTLEN	...
HIERARCH ESO INS ADF SKYREG	HIERARCH ESO INS SLITN TYPE
HIERARCH ESO INS REF NO	HIERARCH ESO INS SLITN ID
HIERARCH ESO INS ARC NO	HIERARCH ESO INS SLITN OBJ RA
HIERARCH ESO INS SLIT NO	HIERARCH ESO INS SLITN OBJ DEC
HIERARCH ESO INS SHU NO	HIERARCH ESO INS SLITN X
HIERARCH ESO INS SLIT1 TYPE	HIERARCH ESO INS SLITN Y

The VIMOS Pipeline and Graphical Interface (VIPGI; Scodeggio et al. 2005) was developed specifically for the reduction of the VVDS data. It undertakes standard processing of bias subtraction and flux and wavelength calibration of the spectra, identification of objects in the slit profile, and extraction of the one-dimensional spectra. VIPGI performs a rather automatic reduction procedure with some points of possible intervention, which allow tuning the process to make it more appropriate for precise types of observations and targets. Moreover, it greatly facilitates the management of the large amount of data produced by VIMOS. Given the efficacy proved by VIPGI for the optimal reduction of large amounts of spectra, we decided to use this software for the reduction of our VIMOS MOS data.

Alternatively, we decide to use R$_{\rm E}$D$^{\rm uc}_{\rm m}$E (Cardiel, 1999) for certain steps of the reduction and only some data sets, that we will explain in due time. This software is an astronomical data reduction package, specifically designed for the analysis of long-slit spectroscopy. R$_{\rm E}$D$^{\rm uc}_{\rm m}$E is flexible and compatible with data from different instruments.

First, VIPGI carries out an exploration of the FITS files to work with during the reduction process: bias, flat-fields, arc-lamps, science (Figure 3.8, Figure 3.7, Figure 3.6) and calibration frames (Figures 3.11, Figure 3.10, Figure 3.9). The software reads the header of the FITS and identifies each type of frame. Then, it classifies them by type and detector quadrant. This apparently simple task is a useful feature of VIPGI because the original names of the files do not give much information about the data they contain, but only the date and time of the observation. In this process, VIPGI also check whether the information needed in the whole reduction process is available in the header (e.g., grism and mask description). Furthermore, in the case of the calibration frames it adds an extension that contains the tabular spectrum of the standard star.

In our case, we initially received the data with a defective header that did not include certain keywords regarding the position of the slits on the masks. This situation was solved by Fernando Selman (ESO) with the help of, Caroline Foster, Dieter Nürnberger, and Willem-Jan de Wit (ESO), who added the missing keywords (Table 3.4) to the FITS headers.

At the same time the FITS are checked, VIPGI appends to the headers of flat-fields, arc-lamps, science and calibration frames some *first guesses* about where the spectra are expected to be located on the images. These *first guesses* may be spurious due to incorrect default suppositions or/and instrument flexures during the observations. For this reason, the first step of the reduction is to check the expected position of the spectra on the detector. To this aim, we compare the HeNeAr *Arc-Lamp* frame obtained immediately following the science exposures with the position of a line catalog set where the *first guesses* predict they should fall. We tailor the actual line catalog to be used to avoid not reliable lines. Then, we move the line catalog superimposed to the arc-lamp until the lines and their edges overlap with the spectra on the image, and we replace with these new guesses the previous ones. This process takes into account possible shifts (in the spectral and spatial directions) and tilt of the spectra, which is not very important on our case.

Afterwards, we create a *Master Bias* as a combination of tens of individual bias frames. Among the different options for the combination of the bias, we combine them using a κ-σ clipping method with a κ=3. This means that each pixel with a value over 3σ is rejected. The mean of the remaining pixels in the stack is computed for each pixel.

Once the approximate position of the spectra is known, we can proceed to actually trace the spectra on the CCD. VIPGI carries out this task searching the spectra edges at the grism central wavelength for each slit around the expected location detailed by the *new first guesses*. At the same time, VIPGI creates a Master Flat-field combining the different flat-fields. In our case, no flat-fielding correction was finally carried out on any of the images as it implied a decrease in the quality of the two-dimensional spectra. Then, we created a mock *Master Flat-Field* with a value 1 in every pixel. The location of the spectra are stored as an extension of the *Master Flat-Field* FITS.

VIPGI wavelength calibration consists on the creation of a so-called *Master Lamp* that contains the actual calibration. VIPGI uses the information about the position of the spectra obtained to locate the spectra of the *Arc-Lamp* frames. Then, it searches the emission lines in the catalog tailored previously around the expected positions. For each slit, it fits all the emission lines peaks with a 3^{rd} polynomial, and stores the result as another extension of the FITS file under analysis.

The wavelength calibration is recommended to be checked and re-fined for each slit in each science and calibration frame. VIPGI provides a task to this aim that displays the deviations of the positions of the arc-lamp emission lines with respect the polynomial fit. We exclude some lines that are systematically outliers in all slits, we also dismiss others that do not behave correctly in particular cases, and we finally re-compute the fit. We reach levels of RMS < 0.1 pixels in all the cases.

Once we reach this point, the science and calibration frames need to go through a preliminary reduction process which substracts the *Master Bias* frame, trims the over-scan and appends the extension stored in the *Master Flat* FITS with the location of the spectra to the FITS file.

Once we apply this preliminary reduction to the frames of the standard, we compute the spectrophotometric calibration. In practice, VIPGI compares the observed spectrum of the standard star with the tabular one, and derives an instrument response function. For Pointing 1 and Pointing 2 we use the spectrum of the standard-star LTT-3864 observed the same first night. The FITS file of the standard-star observed the second night presented some not-identified defect that made impossible its use. Then, it interpolates the instrument response function below 7500Åand

performs a smoothing above such wavelength, where fringing component is dominant. Then, we can check and modify the instrument response function obtained automatically. This can be done using the task *Check spectrophotom. Calibration*. We need to bear in mind two problems that we need to correct. First, atmospheric features that are included in the calculation of the sensitivity function and that can produce a spurious deviation as they change depending on spatial location, time and atmospheric conditions. As the tabular spectrum and the observations contain this features, this regions should not be considered for the calculation of the sensitivity. What we do is editing manually the sensitivity function so that it does not follow the atmospheric features. Second, the filter we select for our observations cuts the range of wavelength at 10000Å. But, below such wavelength there is an overlap of the second order over the first one. So, in that area there is more flux than there should be, and therefore, the correction of the sensitivity is underestimated (the sensitivity is thought to be larger there). This can produce a decreasing trend in the spectra towards the reddest wavelengths after correcting from detector sensitivity. Solving this problem is difficult also because of the presence of a wide atmospheric absorption over 9600Å, which hampers an accurate evaluation of this impact on the curve. We edit the sensitivity function so that it does not follow such atmospheric perturbation and dragging down in the red part of the spectra so that the excess of flux is corrected. In Figure 3.12 and 3.13 we show the instrument sensitivity curve (bottom panels) as it is derived automatically, and as it looks finally after adjusting it, respectively.

Once the preliminary reduction is done, and the spectrophotometric calibration is computed, we can perform the reduction of each single science frame. The procedure followed by VIPGI goes through the following steps:

1. Detection of the objects. To this aim, VIPGI obtains a profile of each slit by collapsing them along the dispersion axis. To avoid the impact of cosmic rays, we decrease the percentages of spectrum (pixels) to be collapsed to 60-80%, depending on the quality of the results. This means that the brightest 40-20% is excluded. We set the detection threshold between 0.5 and 2σ above the mean profile level, and the minimum number of pixels over such value that are considered objects to 3. This three numbers are crucial for the correct extraction of the 1D spectra of the objects in the slits, specially for faint objects. The object or objects within each slits are located.

2. The background is determined and subtracted. We use two different approaches provided by VIPGI and in each case we opt to continue the analysis on the one that produces best results. The first determination method uses the median value of the profile outside the object region. The second fits the profile outside the object(s) regions to a 2^{nd} degree polynomial.

3. 2D spectra are extracted and re-sampled on a linear wavelength scale and saved as another extension of the FITS file.

4. 1D spectra are extracted for all the objects identified by summing up the flux within the pixels of each object region collapsed in the direction of the slit.

5. The sensitivity function is used to flux calibrate each spectrum.

Then, we need to check carefully whether all the objects are extracted correctly. We can do this by checking the slit profile and 2D spectra. In certain slits it can occur that an object remains undetected. Sometimes, when there is not continuum but only a faint emission line, the slit profile

only exhibits a very weak signal of the presence of the object. It can also be frequent that part of the objects, mainly the faint "wings", are not taken into account. In such cases we perform the *Add Manual Detections* task, which allows to specify the pixels to be collapse. Only one object can be added manually per slit and task run. We repeat the process until all the objects are detected correctly.

Atmospheric absorption correction can also be performed. To this aim we select different slit within the mask we are working on in which the atmospheric features are clear. This normally occurs in high SNR spectra. In our case, we only have a handful of them in each mask. The features included in the recipe are 6800Å, 7100Å, 7620Å, and > 9300Å. When the number of reference objects is too low (which is the case of the first quadrant in the first pointing) the atmospheric absorption produces strange features in the spectra. Only in these cases we decide to not to apply it and be careful when we measure the emission lines.

Finally, we run the task that align and combine the different science frames.

Data from the second run (Pointing 3) presents an incompatibility with VIPGI that raises problems along the reduction process. Although we can finally apply the preliminary reduction to all the frames, as well as part of the final reduction, the objects are not able to be extracted. We actually could not find the precise reasons for such a problem. Then, we decide to work with $\mathrm{R_ED^{uc}_mE}$ (Cardiel, 1999) and our own dedicated scripts from that point.

Another peculiarity of this run is the difference of seeing (0.9-1.7 arcsec) among the different exposures, which were taken in different nights. We check the different results we obtain considering all the exposures or only those with seeing $<$1.4 arcsec (which is the width of the slits) and we do not identify significant variations. As we get slightly larger SNRs when we combine all of them, we opt for this approach.

We extract the individual reduced 2D spectra (which are wavelength-calibrated and background-extracted) from the corresponding FITS extension (Figure 3.14, 3.15, 3.16, 3.17). Then, we collapse the spectra to obtain a slit profile where to identify the objects in the slit. We initially try to collapse different parts of the spectra in order to optimize the extraction of faint continuum and emission lines separately. As we do not identify significant differences ($\sim$1 pixel) between both approaches, we decide to perform a unique collapse of the whole spectra. In each slit profile we identify the objects and extract their 1D spectra simply summing up the flux of the pixels within them in the direction of the slit, as VIPGI does.

Then, we perform the flux calibration. In this case, the standard star observed is G158-100 (Oke 1990). We extract the observed spectrum from the frame that has been preliminary reduced through VIPGI. Then, we search for a tabulated spectrum of the standard that covers the same wavelength range. Nevertheless, the wavelength range $>$9.000Å appears to be not available. We try to extend the missing wavelength range fitting a *Black Body* emission with the temperature of the standard star, but we are not satisfied with the curve obtained. As a final option, we decide to use the average response curve provided by the ESO VIMOS quality control[3]. These curves R_{mst} can be applied by hand to the 1D spectra following the expression

$$F_{obs} = R_{mst} \times f_{raw} \times 10^{0.4 \times airmass \times extinction} \tag{3.1}$$

[3]http://www.eso.org/observing/dfo/quality/VIMOS/qc/response.html

where f_{raw} is the spectrum observed in electrons/s/Å, and the airmass is the mean value during the observations. We consider the optical extinction curve by Patat et al. (2011) for Cerro Paranal under typical clear-sky observing conditions.

After all these steps we are able to gather 327 reduced VIMOS spectra ready for the analysis. In the Appendix B we show the spectra of the final sample of our study.

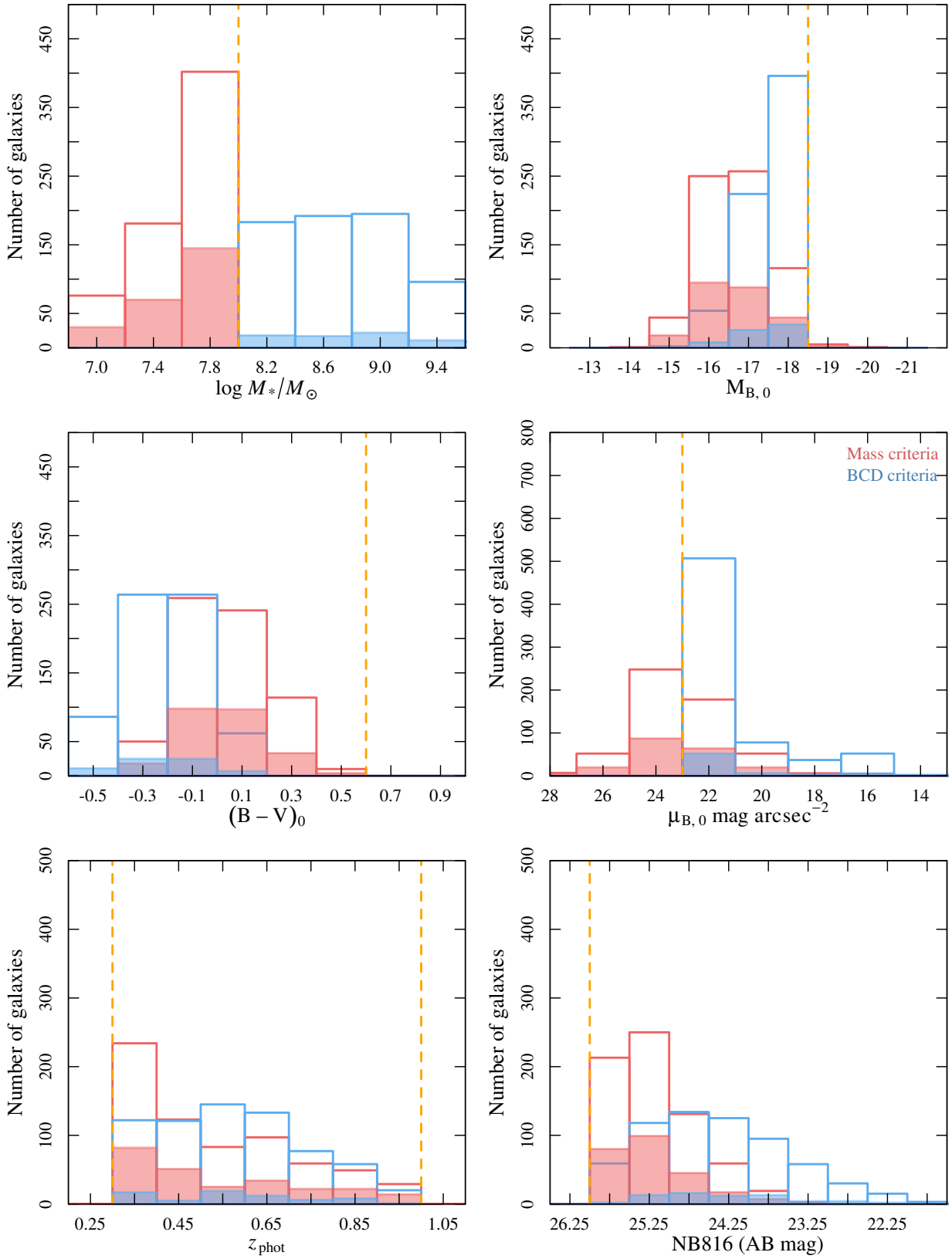

Figure 3.5: From top to bottom and right to left we show the distribution of $\log M_*/\mathrm{M}_\odot$, $M_{\mathrm{B,0,AB}}$, $(B-V)_0$, $S_{\mathrm{Reff,B,0}}/$ mag arcsec^{-2}, z_{phot}, and apparent magnitude in the seleccion band Subaru NB816 for the sample observed (filled histograms), and the initial sample (open histogram). We separate the sample into the two subsamples of galaxies selected using the two selection criteria: a stellar mass criterion (red), and a set of criteria based on the properties of BCDs (blue).

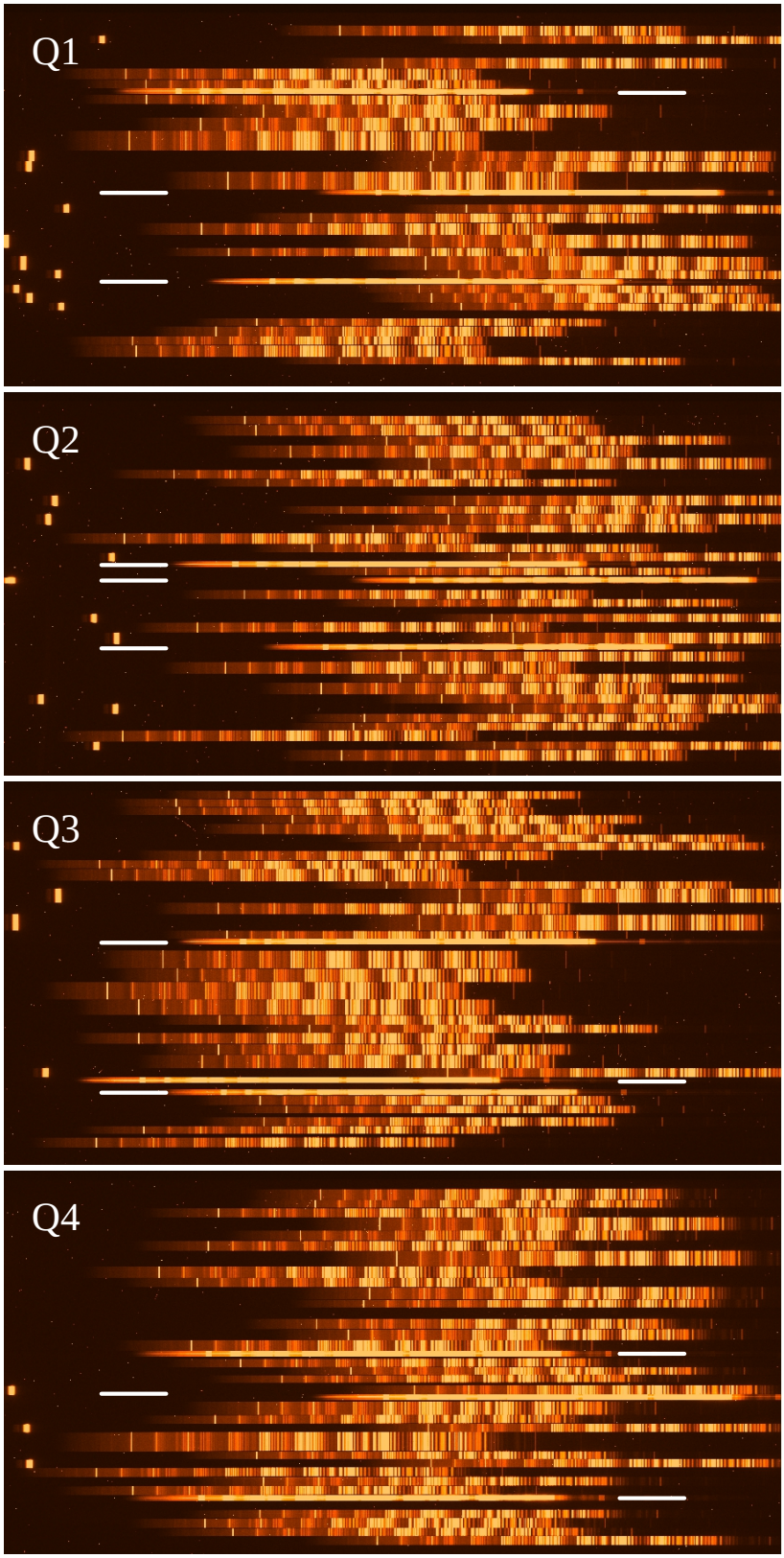

Figure 3.6: Raw science exposures (24000 s) of the four quadrants of Pointing 1. Short white horizontal lines mark where the fiducial stars are located. Wavelength increases to the right. The presence of sky emission lines dominates the spectra towards redder wavelength ranges. The long exposure time explains the amount of cosmic rays visible in the images.

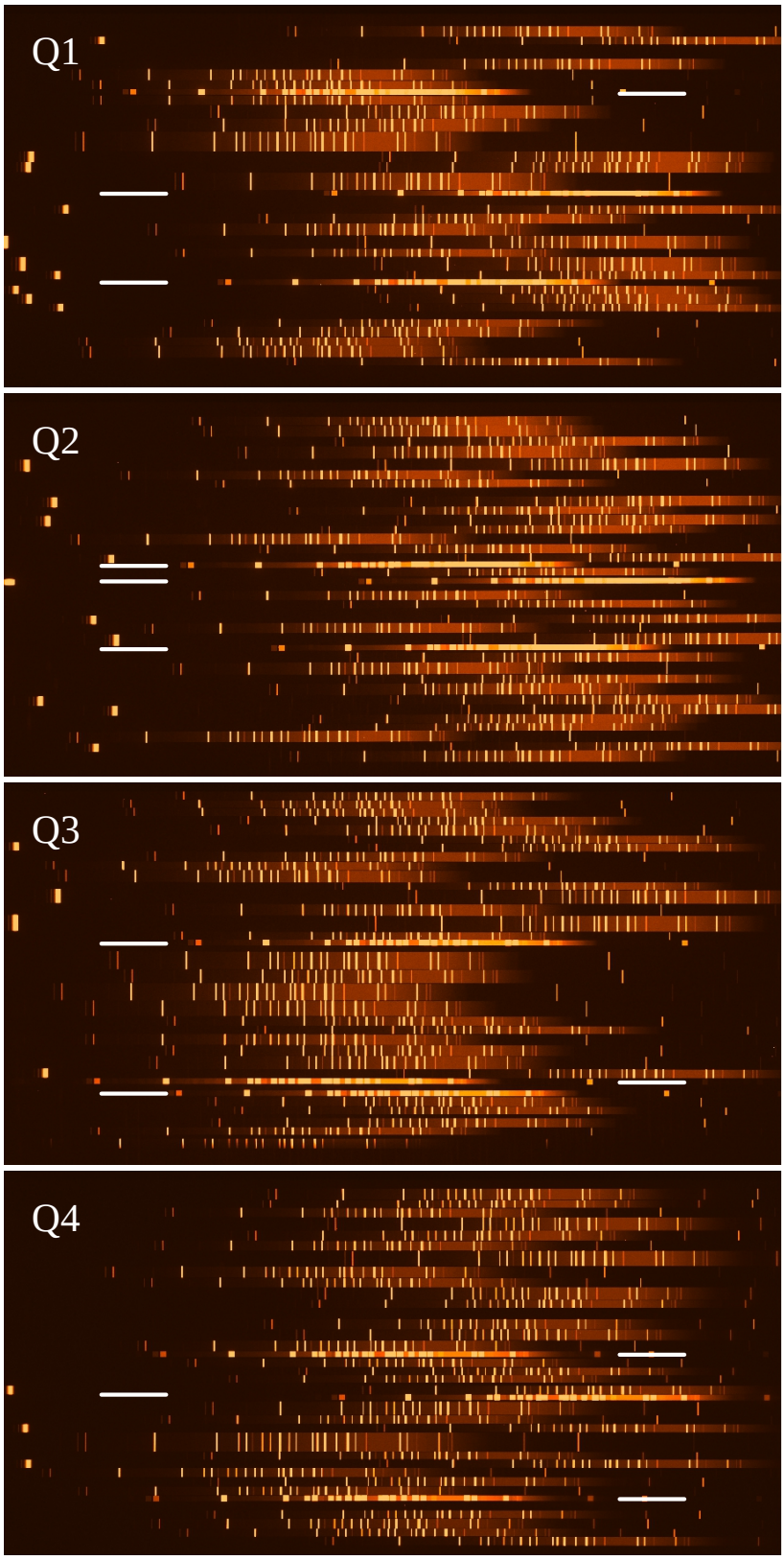

Figure 3.7: Raw arc-lamp exposures (HeNeAr) corresponding to the four quadrants of Pointing 1. Short white horizontal lines mark the locations of the squared slits for the fiducial stars. Wavelength increases to the right.

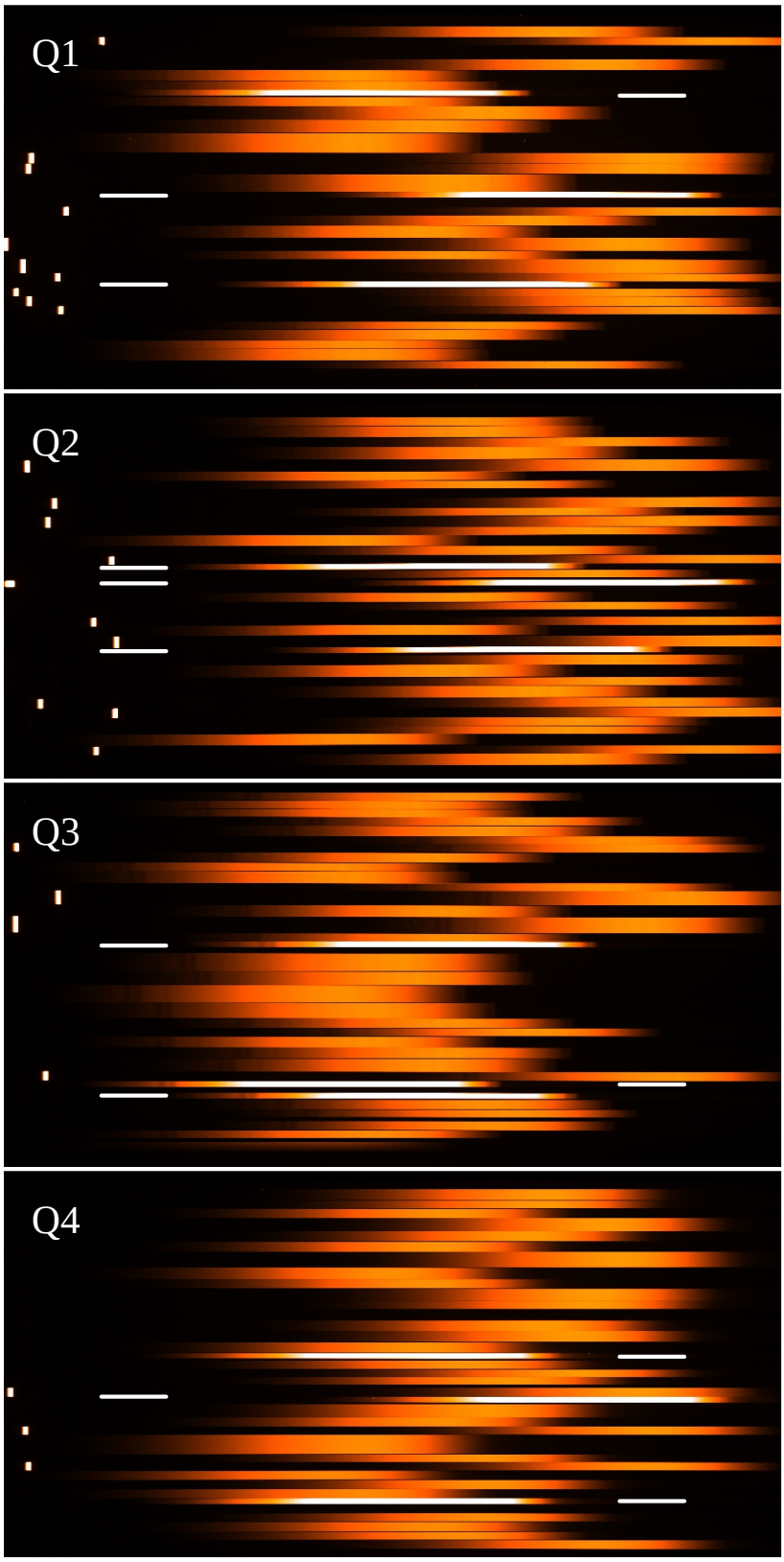

Figure 3.8: Raw flat-field exposures corresponding to the four quadrants of Pointing 1. Short white horizontal lines mark the locations of the squared slits for the fiducial stars. Wavelength increases to the right.

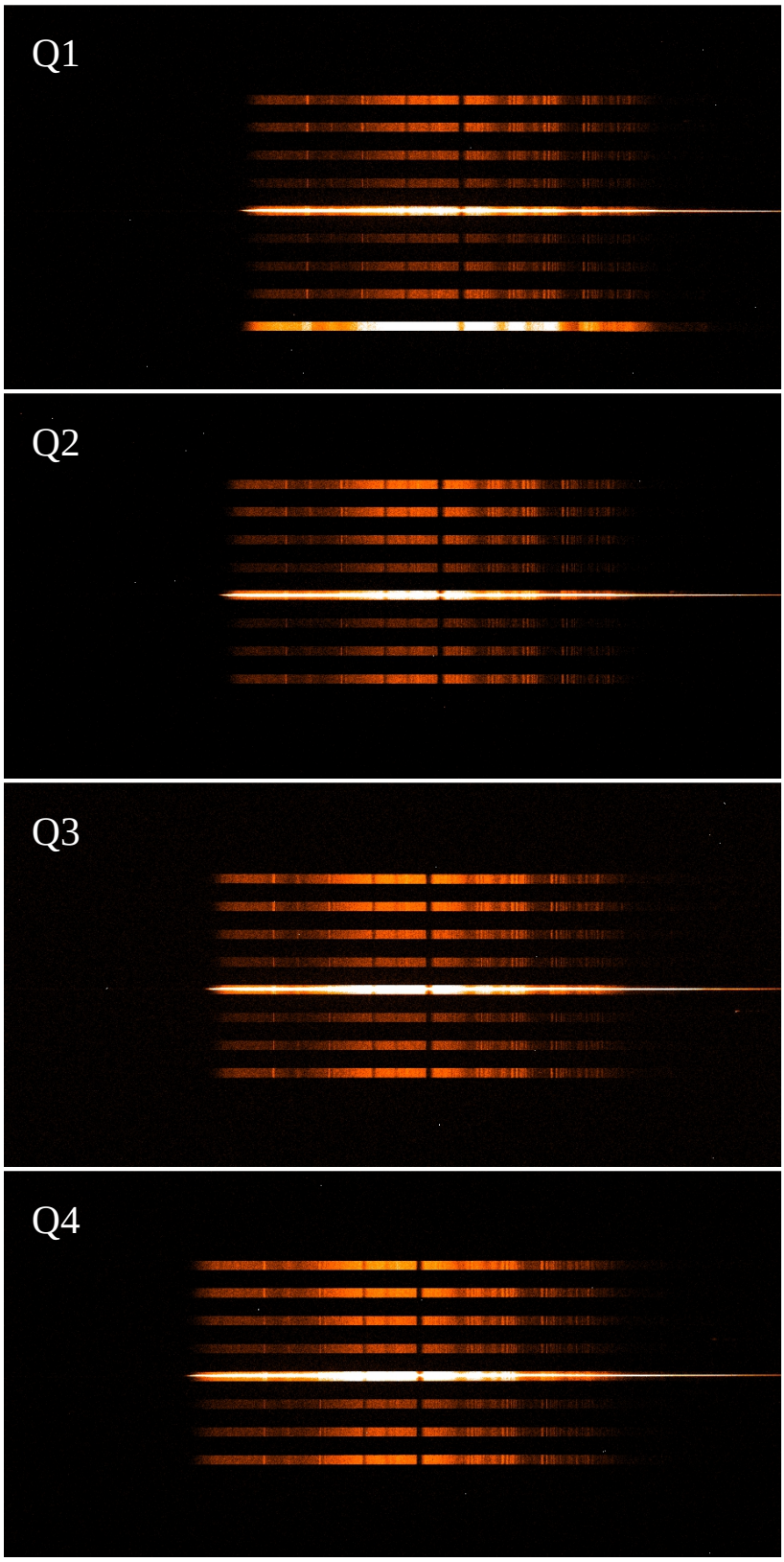

Figure 3.9: Raw exposures (14 s) of the standard star LTT-3864 for the four quadrants of Pointing 1. Wavelength increases to the right.

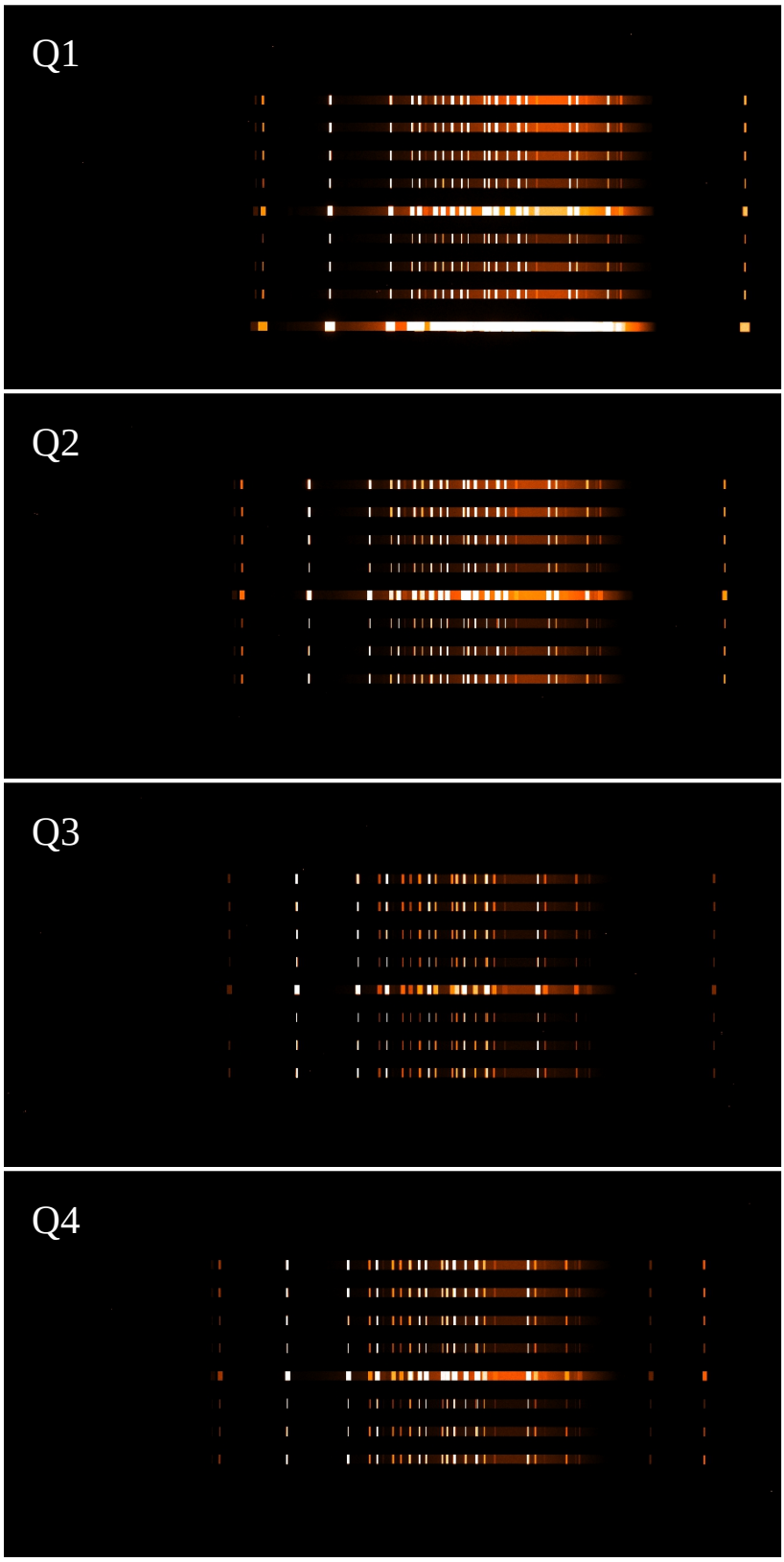

Figure 3.10: Raw exposures (14 s) of the arc (HeNeAr) for the standard star frame. The panels show the four quadrants of Pointing 1. Wavelength increases to the right.

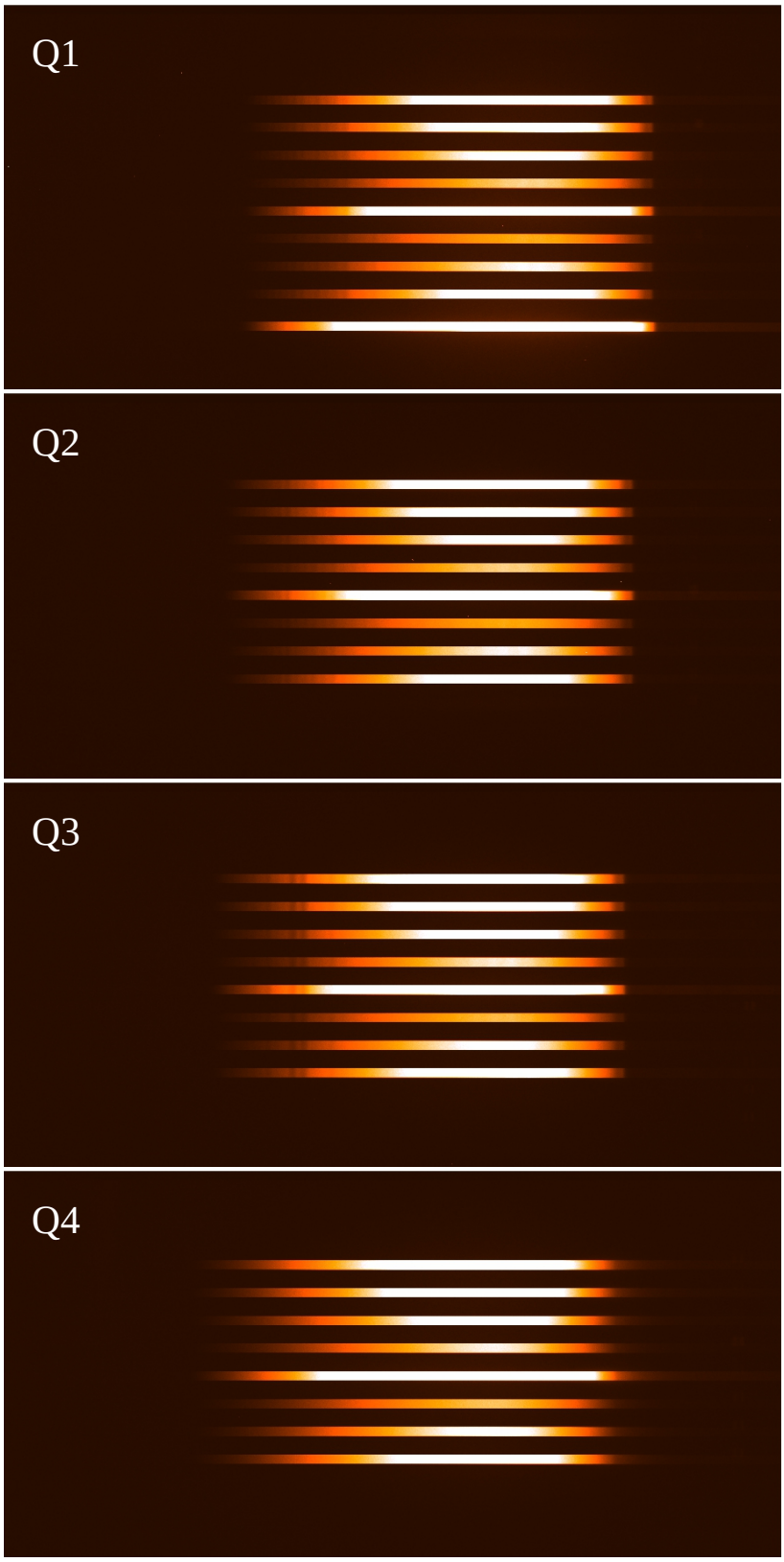

Figure 3.11: Raw exposures (14 s) of the flat fields for the standard star frame. The panels show the four quadrants of Pointing 1. Wavelength increases to the right.

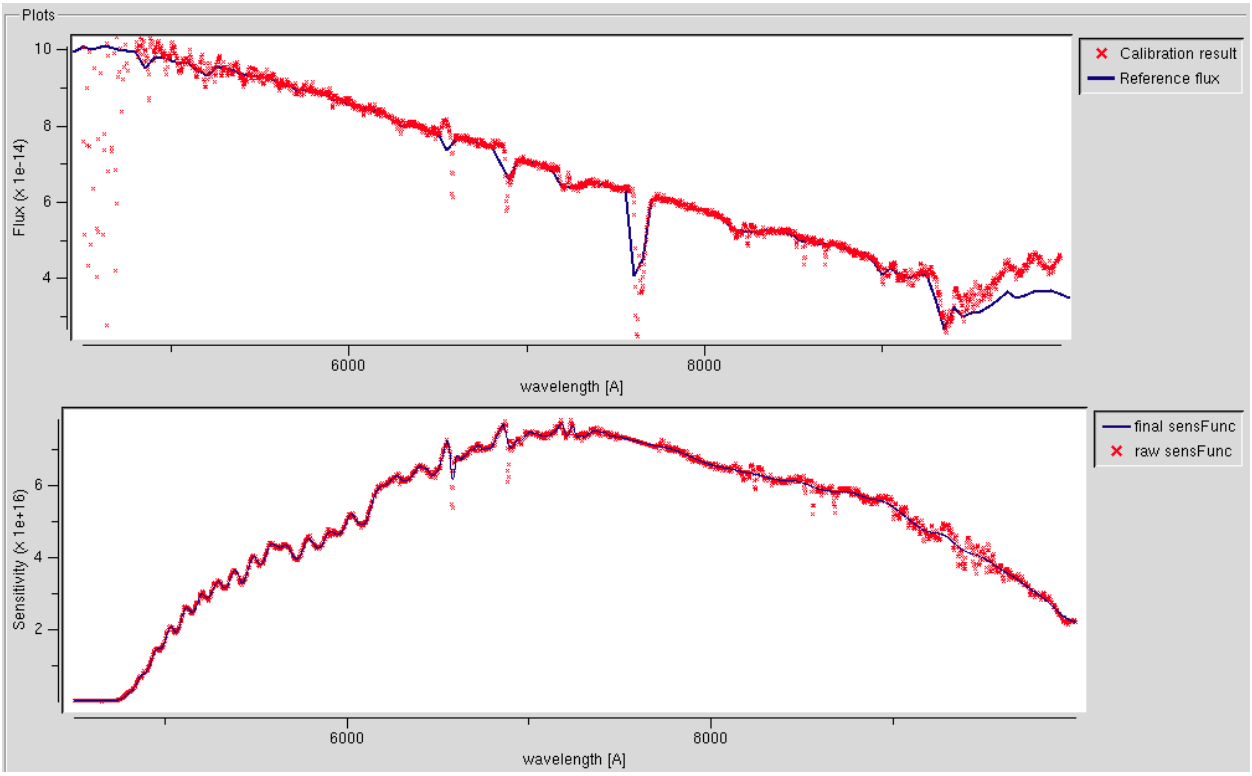

Figure 3.12: Automatically generated instrument sensitivity curve. Top panel shows the tabular spectrum of the standard (blue line) and its reconstruction (red crosses) when the sensitivity curve obtained is applied to the observations. Bottom panel shows the final interpolation (blue line) of the raw sensitivity curve (red crosses). We show the *Check Spectrophotom. Calibration* task display.

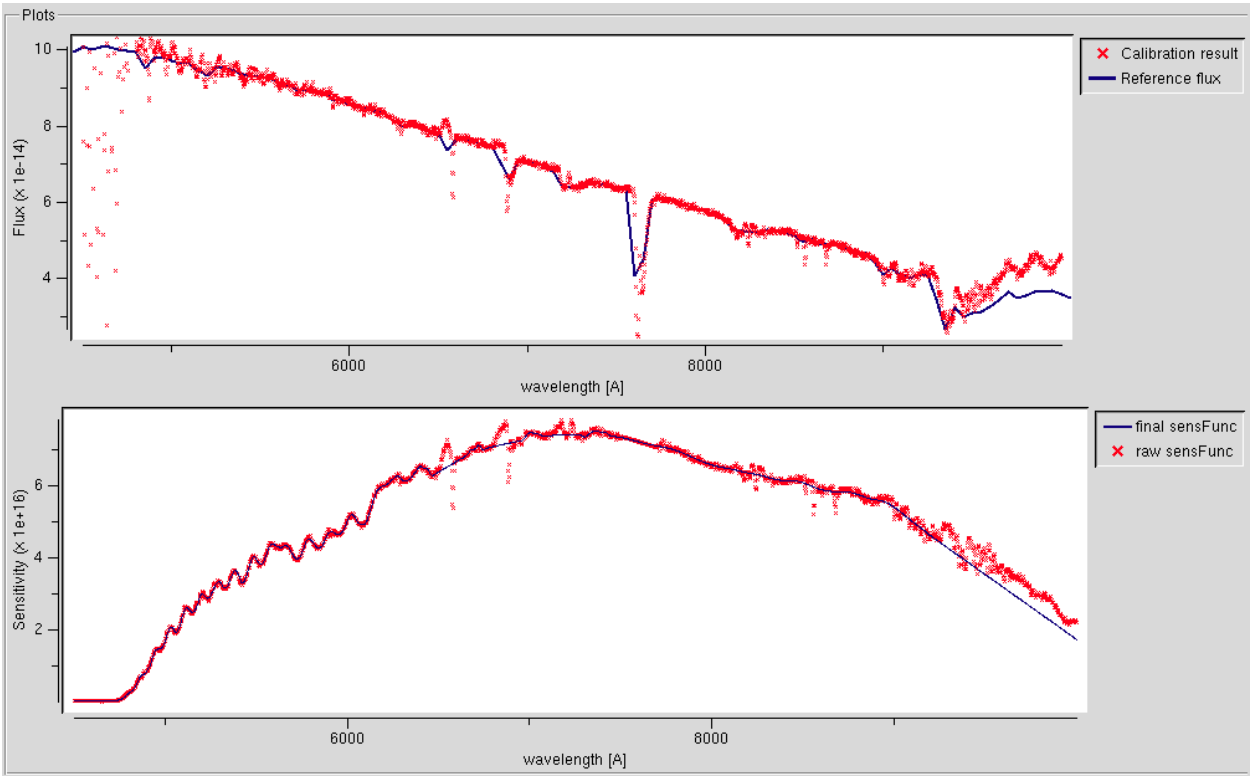

Figure 3.13: Manually modified instrument sensitivity curve. Top panel shows the tabular spectrum of the standard (blue line) and its reconstruction (red crosses) when the sensitivity curve obtained is applied to the observations. Bottom panel shows the final interpolation (blue line) of the raw sensitivity curve (red crosses). We show the *Check Spectrophotom. Calibration* task display.

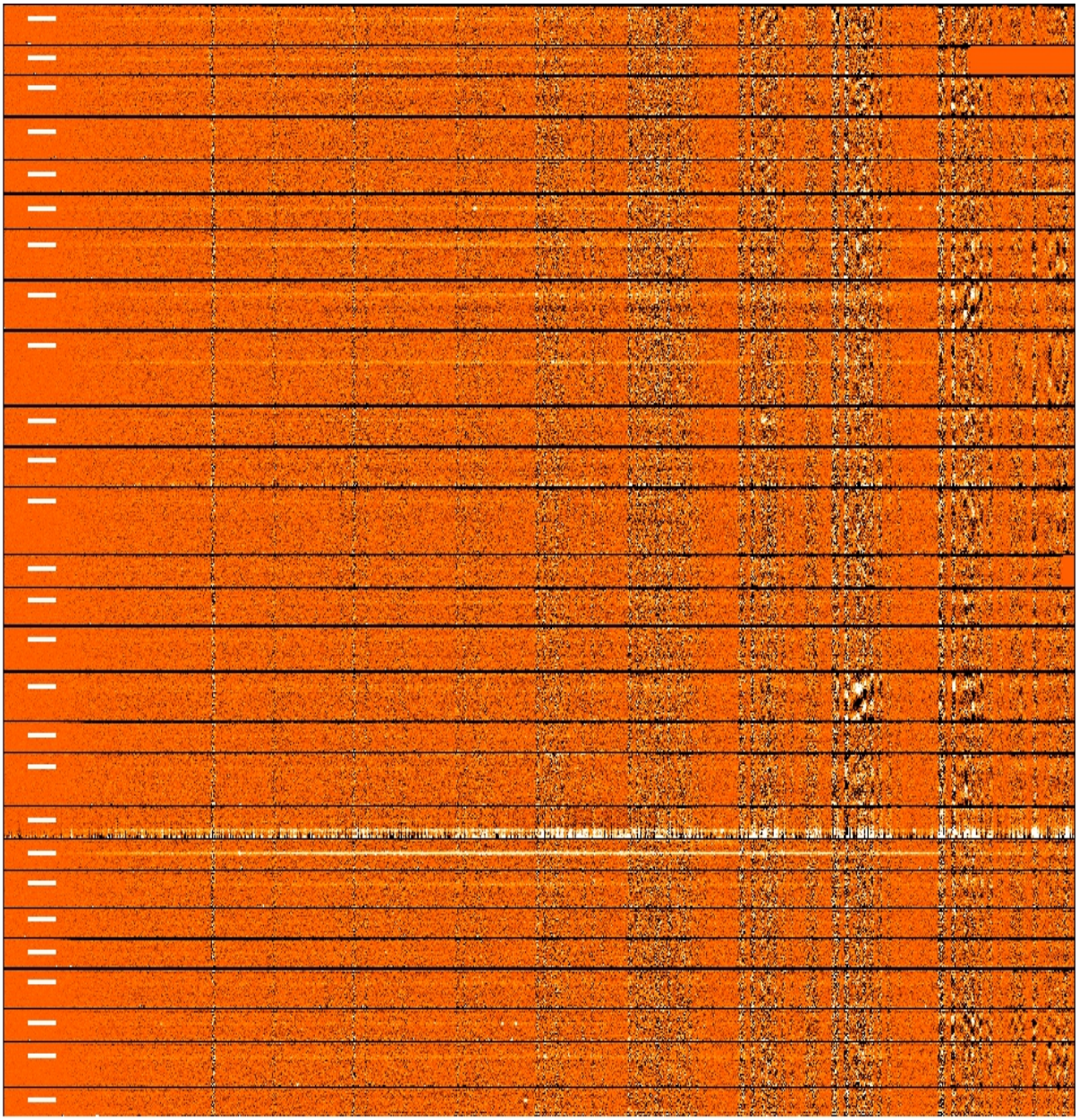

Figure 3.14: Final 2D spectra extracted from each slit in the quadrant 1 of the first pointing. The white lines represent where the target is located in the slit.

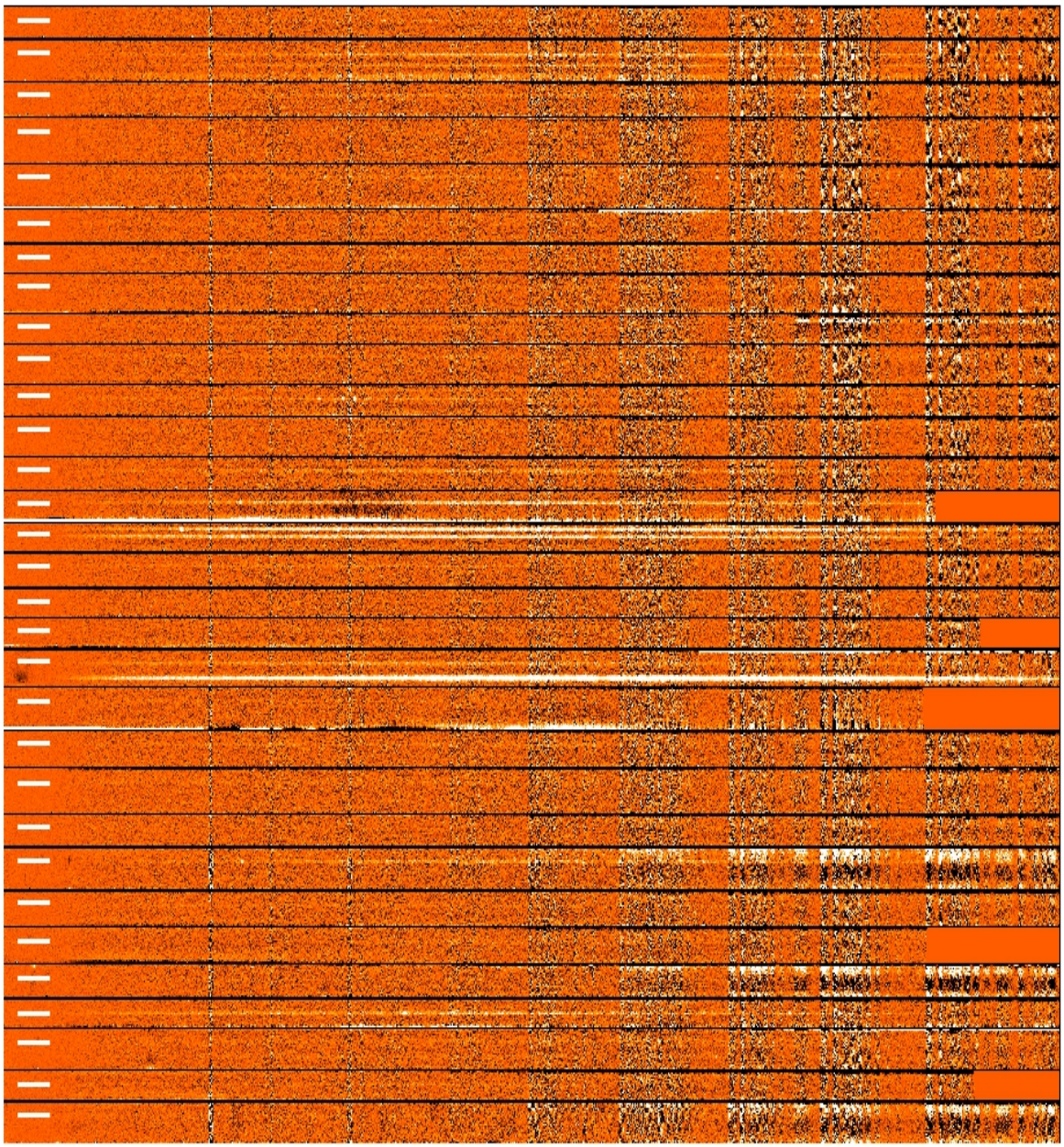

Figure 3.15: Final 2D spectra extracted from each slit in the quadrant 2 of the first pointing. The white lines represent where the target is located in the slit.

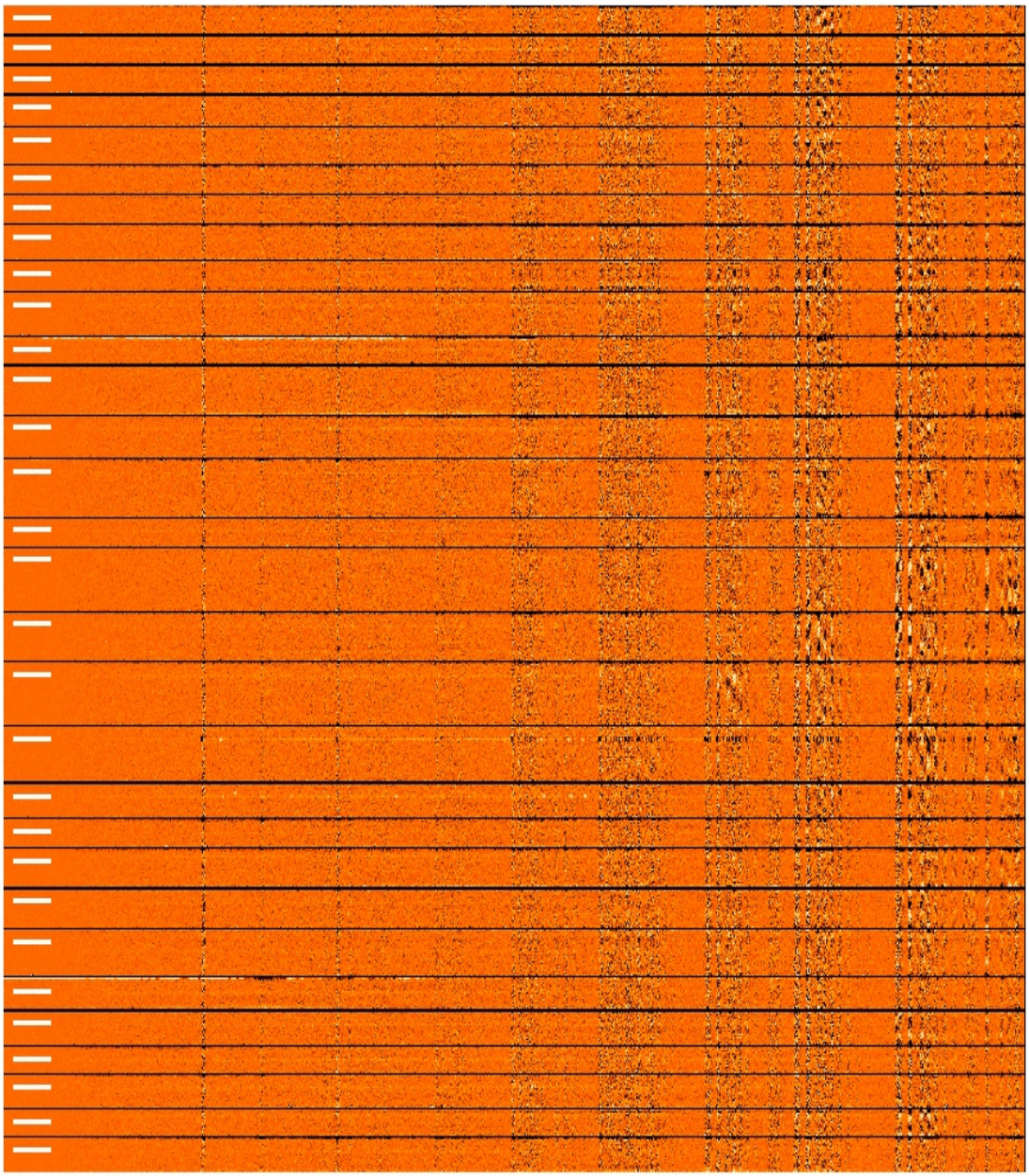

Figure 3.16: Final 2D spectra extracted from each slit in the quadrant 3 of the first pointing. The white lines represent where the target is located in the slit.

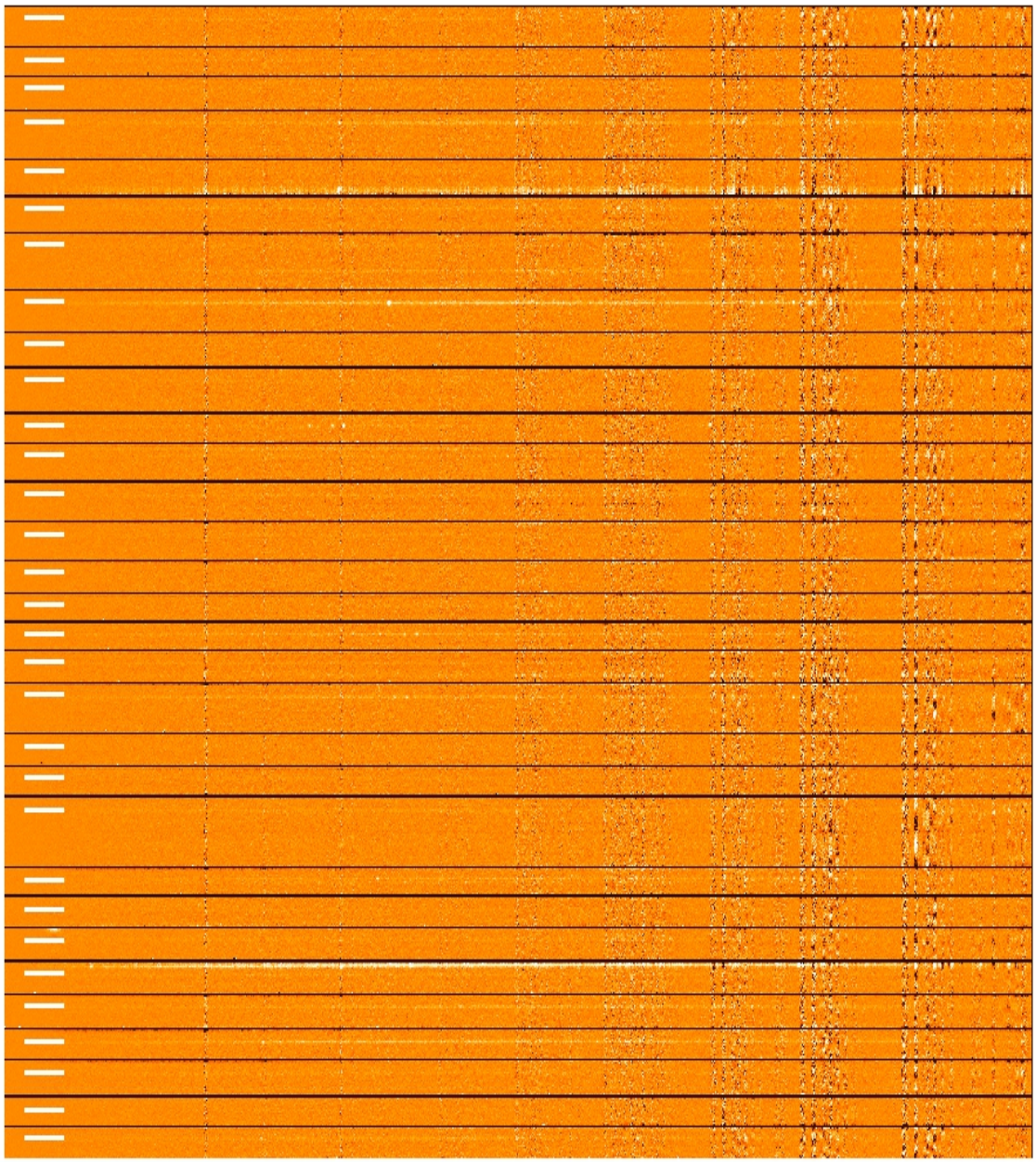

Figure 3.17: Final 2D spectra extracted from each slit in the quadrant 4 of the first pointing. The white lines represent where the target is located in the slit.

4

Observational Data

4.1 Ancillary Multi-wavelength Photometry

We aim to assemble a full and reliable multi-wavelength photometry data-set for our sample of candidates on the E-CDF-S field. The primary selection performed with Rainbow uses photometry obtained using an approach adapted to the average ordinary galaxy population. In our case, given the faintness and compactness of the galaxies in our sample a more careful photometric extraction is needed. Hence, we needed to gather a reliable homogeneous multiwavelength (UV-IR) photometry catalog across the E-CDF-S field.

Great efforts have been carried out to build homogeneous composite catalogs using images coming from different sources, and thus, presenting different depths and resolutions. Such is the case of the works by Cardamone et al. (2010, C10) on the E-CDFS field, and Guo et al. (2013, G13) that uses TFIT (a software package specifically designed for measuring photometry on data sets with different angular resolutions by Laidler et al. 2007) on the GOODS-S. Nevertheless, these multi-wavelength catalogs present significant systematics for faint objects right on the limiting magnitude of most of the bands they include (i.e. see Figure 11 in Guo et al. 2013). Furthermore, the former one, built on a ground-based BVR image with a point spread function of ~ 0.8", is affected by the fact that does not separate correctly the galaxies with nearby neighbors. For these reasons, we opted for performing our own reliable aperture photometry in different optical and near to medium IR bands across the E-CDF-S field.

To this aim we use the Rainbow software package (see Pérez-González et al. 2008; Barro et al. 2011a,b, for a detailed explanation on the performance of this code), that allows performing aperture photometry in multiple bands simoultaneously using prior based positions (determined using SExtractor, Bertin and Arnouts 1996), and deconvolution algorithms for those lower resolution images. More precisely, we use the following strategy:

- Rainbow code needs to start from a primary selection catalog for the deconvolution procedure to be applied. Given our selection sample is based on the Subaru NB816, we first identify the counterparts (within a 2" search radius) of these sources in IRAC 3.6+4.5μm catalogs built with SExtractor. Then, this new catalog is cross-correlated to all those from the rest of the bands (optical/NIR), for which also SExtractor has been used for the identification of the sources, using again a 2" search radius. To avoid possible problems due to small misalignment of the images, the cross-matching is preceeded by their re-alignment, which is carried out using the position of several sources. In the case multiple counterparts

are found in the optical/NIR images during the cross-matching, the photometry is obtained for all of them.

- Optical and n-IR bands: We only consider HST bands and ground-based images with a seeing $\lesssim$1" (except in the case of the JHK bands). In particular we use HST/ACS b, v, i, z bands, and deep VIMOS U and R images from GOODS (Giavalisco et al., 2004; Nonino et al., 2009), the MUSYC 18 medium-band and J and K imaging (Cardamone et al., 2010; Taylor et al., 2009), ESO Wide Field Imager (WFI) $U38$, U, B, V, and R images reduced by the Garching-Bonn Deep Survey (GaBoDS) consortium (Hildebrandt et al., 2006), H imaging from ESO SofI (Moy et al., 2003), and HST/WFC3 F105W, F145W, and F160W from CANDELS (Grogin et al., 2011; Koekemoer et al., 2011). The fluxes considered are those measured directly on the images using a unique appropriate aperture (based on Kron 1980, apertures for an intergrated photometry) for each object. The apertures are obtained as the mean of those found for each band and each galaxy. Then they are checked individualy. For those cases, where they are found to be too big they are modified in order to avoid both contamination from close-by galaxies and adding too much noise to the measurements. Furthermore, a minimum value is set to 1.2" in order to obtain compatible photometry for all the bands.

- IRAC 3.6, 4.5, 5.8 and 8.0 μm bands (Damen et al., 2011; Ashby et al., 2013): We obtain the fluxes applying, when needed, a deblending procedure on the images using the information of the other bands available for each object. In practise, Rainbow software normally measures the photometry within circular apertures of 2.0" of radius. The software looks for nearby objects closer than 4" in another band, typically an optical band representative of the whole dataset, and in our case, the selection band. In such cases, it is considered that they could be contaminating the flux of the target, and to avoid so, the IRAC photometry is measured in a smaller apperture (0.9"). Finally, the apperture corrections for point sources (such as those in the case of our compact and distant targets) is calculated analyzing the Point Spread Funtion, and applied. The final values used are calculated as the mean of the values measured and the values from the C10 and G13 catalogs, all weighted by their errors. Those values that presented some evidences of dust contamination (a clear sudden increase in the longer wavelength bands, typically 5.8 and 8.0μm) were also dismissed.

- Finally, we check individually all the cases for which multiple counterparts were found to identify those that are our real targets.

As a result of our methodology, the final photometry obtained is significatly less noisy than the initial photometric dataset. This is crucial for our subsequent following SED-fitting approach, as the quality of our photometry is a limiting factor of the quality of our final results.

Table 4.1 summarizes the main characteristics of the data set considered. It shows the depth in terms of limiting magnitude (5σ), and the image quality in terms of FWHM (") of the point spread function. Finally, we specify in each case if the photometry finally used in the analysis (see Chapter 5) is measured (M) or taken from a catalog (C), along with the corresponding sources. The typical uncertainties in the absolute photometric calibrations are lower than 0.05 mag in all bands, as determined in C10 for the MUSYC data (including small zero point offsets based on the comparison with templates used in the photometric redshift determination), Reach et al. (2005) for the IRAC data, and Sirianni et al. (2005) and Kalirai et al. (2009) for the ACS/WFC3 data.

Table 4.1: Photometric Data Set

Band	$m_{lim,AB}$	FWHM (")	Source	Measured (M) / Catalog (C)
NB816^{+}	25.40	0.90	Suprime-Cam	M
R	29.00 (1σ)	0.75	VIMOS - GOODS	M
U	27.97	0.80	VIMOS - GOODS	M
$U38$	25.33	0.98	WFI - GaBoDS[f]	M
U	25.86	1.05	WFI - GaBoDS[f]	M
B	26.45	1.01	WFI - GaBoDS[f]	M
V	26.27	0.94	WFI - GaBoDS[f]	M
R	26.37	0.83	WFI - GaBoDS[f]	M
J	22.44	1.48	ISPI - MUSYC[h]	M
H	22.46	1.49	SofI - ESO[g]	M
K	21.98	0.94	ISPI - MUSYC[h]	M
IA427	25.01	1.01	Suprime-Cam - MUSYC	M
IA445	25.18	1.23	Suprime-Cam - MUSYC	M
IA464	24.38	1.79	Suprime-Cam - MUSYC	M
IA484	26.22	0.76	Suprime-Cam - MUSYC	M
IA505	25.29	0.94	Suprime-Cam - MUSYC	M
IA527	26.18	0.83	Suprime-Cam - MUSYC	M
IA550	25.45	1.13	Suprime-Cam - MUSYC	M
IA574	25.16	0.95	Suprime-Cam - MUSYC	M
IA598	26.05	0.63	Suprime-Cam - MUSYC	M
IA624	25.91	0.61	Suprime-Cam - MUSYC	M
IA651	26.14	0.60	Suprime-Cam - MUSYC	M
IA679	26.02	0.80	Suprime-Cam - MUSYC	M
IA709	24.52	1.60	Suprime-Cam - MUSYC	M
IA738	25.93	0.77	Suprime-Cam - MUSYC	M
IA767	24.92	0.70	Suprime-Cam - MUSYC	M
IA797	24.69	0.68	Suprime-Cam - MUSYC	M
IA856	24.41	0.67	Suprime-Cam - MUSYC	M
b	28.95	0.08	*HST*/ACS - GOODS	M
v	29.35	0.08	*HST*/ACS - GOODS	M
i	28.55	0.08	*HST*/ACS - GOODS	M
z	28.55	0.09	*HST*/ACS - GOODS	M
F814W	28.77	0.09	*HST*/ACS - GOODS	M
F105W	27.45	0.15	*HST*/WFC3 - CANDELS	M
F125W	27.66	0.16	*HST*/WFC3 - CANDELS	M
F160W	27.36	0.17	*HST*/WFC3 - CANDELS	M
IRAC 3.6 μm	23.89[e]/26.52[d]	1.66	*Spitzer* - GOODS - SEDS	C[a]/C[b]/M
IRAC 4.5 μm	23.75[e]/26.25[d]	1.72	*Spitzer* - GOODS - SEDS	C[a]/C[b]/M
IRAC 5.8 μm	22.44[e]/23.75[c]	1.88	*Spitzer* - GOODS - SIMPLE	C[a]/C[b]/M
IRAC 8.0 μm	22.50[e]/23.72[c]	1.98	*Spitzer* - GOODS - SIMPLE	C[a]/C[b]/M

[+] Selection band.
[a] Cardamone et al. (2010).
[b] Guo et al. (2013).
[c] This is the average depth of the two GOODS Spitzer epochs.
[d] Spitzer Extended Deep Survey (SEDS Ashby et al., 2013).
[e] Spitzer IRAC/MUSYC Public Legacy Survey in the E-CDF-S (SIMPLE Damen et al., 2011).

In the Appendix B we show the photometry finally considered for each of the galaxies in the sample. We use open and filled circles for photometric points from broad and narrow bands, respectively. Yellow points represent ground based photometric values. We use pink to mark

MUSYC survey photometric bands. HST and IRAC observations are shown in blue and green color, respectively. The dismissed IRAC bands due to possible dust emission contamination are represented by grey color.

Table 4.2: Photometry. Table 1

Galaxy	$NB816_{SUBARU}$		R_{VIMOS}		U_{VIMOS}		B_{MUSYC}		V_{MUSYC}	
	mag	$\pm\Delta$	mag	$\pm\Delta$	mag	$\pm\Delta$	mag	$\pm\Delta$	mag	$\pm\Delta$
17	24.80	0.11	–	–	25.80	0.08	25.73	0.08	25.62	0.09
26	25.04	0.15	–	–	25.87	0.14	26.35	0.31	26.07	0.28
35	24.04	0.10	–	–	–	–	25.31	0.06	25.00	0.07
43	24.24	0.10	26.09	0.09	24.81	0.05	24.81	0.04	24.71	0.04
53	25.80	0.16	26.45	0.40	26.59	0.15	26.54	0.13	26.37	0.15
88	23.20	0.10	23.10	0.05	23.37	0.05	23.24	0.02	23.17	0.02
101	23.85	0.10	23.97	0.05	25.01	0.05	23.97	0.02	23.91	0.02
121	23.98	0.10	25.05	0.07	25.38	0.05	25.36	0.05	25.22	0.05
145	23.55	0.10	24.01	0.07	25.00	0.05	24.75	0.05	24.44	0.06
156	24.94	0.11	–	–	26.18	0.09	26.16	0.10	25.77	0.12
164	25.13	0.12	25.04	0.05	25.23	0.05	25.27	0.07	25.21	0.07
173	24.75	0.17	25.50	0.30	27.19	0.27	26.20	0.24	25.54	0.18
181	23.56	0.10	24.03	0.05	24.45	0.05	24.40	0.02	24.34	0.03
183	25.85	0.17	25.80	0.09	26.67	0.08	26.68	0.15	26.35	0.15
193	24.63	0.11	25.18	0.07	25.96	0.08	25.90	0.13	25.50	0.11
195	25.98	0.20	25.69	0.07	26.37	0.07	26.36	0.14	26.14	0.14
205	24.29	0.10	25.04	0.06	–	–	–	–	–	–
210	26.04	0.21	26.12	0.10	26.96	0.09	26.96	0.19	26.43	0.22
220	25.01	0.12	24.91	0.07	25.73	0.09	25.17	0.04	24.89	0.05
227	26.04	0.18	25.95	0.08	26.48	0.08	26.67	0.17	26.73	0.22
235	25.93	0.18	26.00	0.06	26.14	0.06	26.12	0.09	26.38	0.19
236	24.86	0.12	24.77	0.05	25.73	0.06	25.42	0.07	25.04	0.05
237	25.30	0.14	25.46	0.06	26.61	0.09	26.74	0.18	26.26	0.13
241	25.36	0.14	25.40	0.06	26.25	0.06	26.14	0.14	26.06	0.13
253	25.86	0.22	26.37	0.08	27.22	0.18	27.56	0.35	27.04	0.36
259	23.89	0.10	24.19	0.05	24.75	0.05	24.78	0.03	24.62	0.03
277	25.57	0.14	25.35	0.06	26.05	0.06	25.67	0.09	25.73	0.12
293	24.93	0.11	24.96	0.05	26.00	0.06	25.84	0.08	25.45	0.07
296	25.23	0.12	24.91	0.05	25.44	0.05	25.38	0.05	25.36	0.08
297	25.69	0.14	25.97	0.06	26.85	0.10	26.76	0.13	26.48	0.12
306	24.71	0.11	24.76	0.05	25.43	0.05	25.63	0.05	25.43	0.06
312	24.73	0.11	24.78	0.05	25.16	0.05	24.95	0.03	24.84	0.04
315	26.05	0.19	26.48	0.08	26.61	0.08	26.78	0.17	26.77	0.21
317	24.34	0.10	24.90	0.05	25.81	0.06	25.86	0.07	25.58	0.11
386	24.25	0.11	24.53	0.05	25.73	0.06	25.60	0.06	25.04	0.05
396	24.71	0.12	24.77	0.05	25.57	0.06	25.44	0.05	24.84	0.04
440	26.20	0.19	26.03	0.07	26.56	0.08	26.84	0.19	26.87	0.23
454	25.29	0.12	25.22	0.06	26.08	0.06	25.79	0.06	25.56	0.07
455	24.64	0.11	25.32	0.06	26.43	0.07	26.07	0.08	25.77	0.12
464	25.00	0.14	25.30	0.05	25.75	0.05	25.74	0.06	25.70	0.08
474	25.04	0.15	–	–	26.14	0.08	25.74	0.07	25.47	0.08
481	24.84	0.11	25.32	0.07	25.34	0.05	25.25	0.05	25.28	0.06
488	24.61	0.11	24.88	0.06	26.09	0.07	26.07	0.11	25.58	0.07
490	24.43	0.10	24.84	0.05	25.03	0.05	25.06	0.03	25.08	0.06
510	24.31	0.10	24.33	0.05	24.42	0.05	24.44	0.02	24.36	0.03

Continues on next page

Table 4.2: Photometry. Table 1. Cont.

Galaxy	SUBARU$_{NB816}$		B_{VIMOS}		U_{VIMOS}		B_{MUSYC}		V_{MUSYC}	
	mag	$\pm\Delta$	mag	$\pm\Delta$	mag	$\pm\Delta$	mag	$\pm\Delta$	mag	$\pm\Delta$
518	25.29	0.12	25.69	0.09	26.53	0.08	26.77	0.19	26.26	0.16
519	24.68	0.11	24.93	0.08	25.10	0.06	25.10	0.04	25.01	0.04
520	24.54	0.11	24.84	0.05	25.82	0.06	25.76	0.08	25.36	0.06
524	24.61	0.13	–	–	24.55	0.06	24.70	0.04	24.68	0.07
536	25.74	0.14	26.02	0.07	26.76	0.08	26.99	0.18	26.54	0.16
539	25.80	0.22	25.88	0.09	26.04	0.07	26.57	0.16	26.42	0.14
543	23.59	0.10	24.35	0.05	26.38	0.07	25.68	0.06	25.09	0.05
544	25.35	0.12	25.26	0.06	26.04	0.07	25.86	0.06	25.52	0.07
551	23.89	0.10	24.22	0.05	25.43	0.06	24.75	0.03	24.39	0.03
565	24.78	0.12	24.84	0.06	25.80	0.06	25.86	0.07	25.61	0.08
571	24.80	0.11	25.83	0.06	27.20	0.15	26.67	0.19	26.58	0.17
584	23.91	0.10	24.20	0.05	24.54	0.05	24.45	0.03	24.47	0.04
594	25.03	0.14	24.70	0.05	25.75	0.06	25.32	0.04	25.13	0.05
601	25.32	0.15	25.36	0.07	26.44	0.09	26.69	0.20	26.25	0.18
612	25.63	0.15	26.01	0.08	26.34	0.07	26.21	0.12	26.83	0.26
626	25.14	0.14	25.47	0.07	25.60	0.06	25.64	0.06	25.84	0.11
634	25.12	0.12	25.35	0.05	25.54	0.06	25.50	0.06	25.49	0.08
642	25.70	0.20	26.08	0.10	26.18	0.07	26.26	0.10	26.37	0.15
1017	24.28	0.12	–	–	–	–	25.57	0.10	25.19	0.08
1032	21.93	0.10	–	–	23.88	0.05	23.39	0.02	22.78	0.02
1056	22.82	0.10	23.39	0.05	24.52	0.05	24.09	0.03	23.80	0.03
1090	24.99	0.13	25.87	0.20	26.58	0.10	26.23	0.13	25.96	0.10
1126	24.39	0.11	25.40	0.07	25.85	0.06	25.76	0.06	25.55	0.07
1202	24.32	0.10	24.98	0.05	26.20	0.07	26.06	0.13	25.80	0.09
1210	24.72	0.11	25.43	0.06	26.06	0.06	25.88	0.09	25.89	0.09
1220	24.49	0.12	24.76	0.07	25.52	0.06	25.46	0.05	25.16	0.08
1234	24.39	0.10	24.64	0.05	25.66	0.06	25.42	0.05	24.90	0.04
1245	24.61	0.11	25.13	0.06	25.37	0.06	25.53	0.05	25.52	0.08
1247	25.05	0.12	24.75	0.07	25.30	0.06	25.13	0.05	24.92	0.04
1251	24.29	0.10	24.78	0.06	26.26	0.09	25.82	0.09	25.14	0.05
1309	24.39	0.10	24.72	0.05	25.62	0.05	25.58	0.07	25.20	0.09
1313	23.64	0.10	24.03	0.05	25.05	0.05	24.78	0.07	24.59	0.06
1332	24.61	0.11	24.88	0.06	26.13	0.06	–	–	–	–
1344	24.53	0.10	23.79	0.05	24.72	0.05	24.76	0.03	24.50	0.04
1378	23.82	0.10	24.16	0.05	25.53	0.05	25.20	0.04	24.57	0.03
1403	23.89	0.10	24.47	0.05	25.38	0.05	25.27	0.05	25.19	0.07
1454	26.00	0.16	26.53	0.09	27.38	0.16	27.25	0.29	27.13	0.36
1514	24.92	0.11	25.25	0.06	25.63	0.05	25.64	0.07	25.63	0.12
1565	24.69	0.11	25.10	0.05	–	–	25.91	0.07	25.55	0.07
1585	24.01	0.10	24.38	0.05	25.09	0.05	25.08	0.03	24.97	0.05
1605	25.40	0.13	26.22	0.07	26.51	0.07	26.93	0.17	26.78	0.19
1656	25.00	0.11	25.84	0.08	25.94	0.06	25.93	0.10	26.11	0.13
1723	24.73	0.11	25.49	0.06	25.97	0.06	26.17	0.09	25.98	0.09
1727	24.24	0.10	24.70	0.05	25.85	0.08	25.59	0.08	25.29	0.06
1752	22.69	0.10	23.02	0.05	24.06	0.05	23.44	0.01	23.11	0.01
1765	26.17	0.20	26.41	0.10	26.45	0.08	26.45	0.13	26.71	0.27

Continues on next page

Table 4.2: Photometry. Table 1. Cont.

Galaxy	SUBARU$_{NB816}$		B_{VIMOS}		U_{VIMOS}		B_{MUSYC}		V_{MUSYC}	
	mag	$\pm\Delta$	mag	$\pm\Delta$	mag	$\pm\Delta$	mag	$\pm\Delta$	mag	$\pm\Delta$
1796	22.45	0.10	22.96	0.05	24.24	0.05	23.90	0.02	23.59	0.02
1804	24.62	0.11	25.02	0.06	26.25	0.07	26.01	0.08	25.79	0.09
1860	24.25	0.10	24.85	0.05	25.19	0.06	25.16	0.04	25.13	0.07
1861	23.25	0.10	23.66	0.05	24.91	0.06	24.72	0.03	24.44	0.04
2010	25.92	0.15	25.42	0.06	26.25	0.06	26.45	0.11	25.88	0.11

Table 4.3: Photometry. Table 2

Galaxy	R_{MUSYC}		U_{MUSYC}		$U_{MUSYC}38$		b_{ACS}		v_{ACS}	
	mag	$\pm\Delta$	mag	$\pm\Delta$	mag	$\pm\Delta$	mag	$\pm\Delta$	mag	$\pm\Delta$
17	25.39	0.09	26.04	0.20	26.15	0.30	–	–	–	–
26	25.17	0.13	26.36	0.38	–	–	–	–	–	–
35	24.63	0.04	25.66	0.13	25.15	0.15	–	–	–	–
43	24.47	0.04	25.04	0.09	24.92	0.12	–	–	–	–
53	25.96	0.11	27.05	0.44	26.93	0.69	–	–	–	–
88	22.98	0.03	23.53	0.04	23.44	0.05	–	–	–	–
101	23.87	0.02	25.65	0.14	25.04	0.12	–	–	–	–
121	24.96	0.05	25.82	0.13	25.56	0.19	–	–	–	–
145	23.85	0.04	25.60	0.15	25.00	0.20	–	–	–	–
156	25.00	0.05	26.50	0.25	26.71	0.52	–	–	–	–
164	25.10	0.06	25.76	0.18	25.59	0.24	–	–	–	–
173	25.74	0.25	27.72	1.04	27.67	1.45	–	–	–	–
181	23.92	0.02	24.80	0.05	24.72	0.08	–	–	–	–
183	25.90	0.14	27.92	0.64	27.43	0.77	25.99	0.14	25.70	0.10
193	25.09	0.09	26.91	0.44	26.36	0.49	–	–	–	–
195	25.70	0.14	26.58	0.30	26.30	0.49	26.49	0.19	25.63	0.10
205	–	–	–	–	–	–	–	–	–	–
210	26.04	0.15	30.15	2.17	26.51	0.39	26.56	0.18	26.00	0.10
220	24.83	0.05	25.72	0.12	25.82	0.26	–	–	–	–
227	26.24	0.14	27.22	0.39	26.62	0.47	26.02	0.12	26.05	0.11
235	26.03	0.11	26.31	0.19	26.66	0.47	25.82	0.07	25.94	0.08
236	24.75	0.06	26.00	0.17	25.70	0.22	25.39	0.07	24.71	0.04
237	25.34	0.07	26.74	0.32	26.71	0.41	26.59	0.20	25.37	0.08
241	25.49	0.11	26.54	0.27	26.18	0.26	25.69	0.07	25.66	0.08
253	27.36	0.36	27.20	0.43	27.60	0.86	26.37	0.17	26.26	0.10
259	24.06	0.03	25.06	0.09	24.87	0.11	24.50	0.02	24.07	0.02
277	25.23	0.08	26.30	0.23	26.56	0.41	26.07	0.11	25.50	0.07
293	25.00	0.05	26.33	0.18	26.24	0.30	25.58	0.09	24.93	0.04
296	24.87	0.04	25.74	0.10	25.57	0.18	25.10	0.03	24.78	0.03
297	25.93	0.08	27.53	0.47	26.86	0.41	26.22	0.09	25.75	0.06
306	24.77	0.05	25.81	0.12	25.55	0.15	25.13	0.04	24.78	0.03
312	24.69	0.04	25.37	0.11	25.46	0.15	25.26	0.05	24.85	0.04
315	26.70	0.30	27.58	0.52	26.44	0.39	26.52	0.15	26.46	0.17

Continues on next page

Table 4.3: Photometry. Table 2. Cont.

Galaxy	R_{MUSYC}		U_{MUSYC}		$U_{MUSYC}38$		b_{ACS}		v_{ACS}	
	mag	$\pm\Delta$	mag	$\pm\Delta$	mag	$\pm\Delta$	mag	$\pm\Delta$	mag	$\pm\Delta$
317	24.88	0.05	26.46	0.25	26.32	0.33	–	–	24.61	0.06
386	24.53	0.03	26.04	0.14	26.12	0.33	25.41	0.05	24.58	0.02
396	24.66	0.04	26.06	0.16	26.02	0.25	25.45	0.06	24.75	0.03
440	25.88	0.11	26.88	0.36	26.64	0.58	26.35	0.19	25.90	0.10
454	25.12	0.08	26.46	0.27	26.07	0.25	25.79	0.08	25.19	0.05
455	25.27	0.07	27.31	0.55	25.97	0.26	26.08	0.13	25.57	0.08
464	25.27	0.06	26.63	0.22	26.06	0.25	25.83	0.08	25.31	0.08
474	25.40	0.09	26.55	0.22	26.20	0.31	–	–	–	–
481	25.14	0.05	25.83	0.13	25.61	0.17	25.11	0.06	25.11	0.07
488	24.80	0.04	26.76	0.28	27.66	0.78	25.73	0.07	25.00	0.05
490	24.83	0.04	25.39	0.09	25.13	0.11	24.85	0.04	24.80	0.03
510	24.34	0.03	24.75	0.07	24.57	0.12	–	–	–	–
518	25.72	0.08	26.74	0.25	26.97	0.69	26.90	0.27	25.59	0.09
519	24.81	0.04	25.44	0.12	25.18	0.13	–	–	–	–
520	24.77	0.03	25.96	0.13	26.16	0.30	25.54	0.06	24.87	0.03
524	24.60	0.05	24.74	0.10	25.07	0.17	–	–	–	–
536	26.06	0.10	26.43	0.25	26.61	0.40	26.40	0.17	26.05	0.11
539	26.02	0.11	27.40	0.44	26.34	0.37	–	–	–	–
543	24.21	0.02	26.47	0.28	27.27	0.64	–	–	–	–
544	25.11	0.05	26.34	0.21	25.89	0.30	–	–	25.15	0.08
551	24.15	0.03	25.54	0.11	26.01	0.34	24.82	0.03	24.07	0.02
565	24.88	0.04	26.79	0.34	25.82	0.20	–	–	–	–
571	25.71	0.08	27.17	0.38	27.09	0.60	26.41	0.14	25.87	0.11
584	24.08	0.03	24.82	0.06	24.47	0.08	–	–	–	–
594	24.71	0.05	26.44	0.20	25.91	0.29	–	–	–	–
601	25.34	0.10	27.25	0.46	27.76	1.01	–	–	–	–
612	25.93	0.13	27.02	0.34	26.99	0.51	–	–	–	–
626	25.38	0.08	25.97	0.15	26.15	0.29	–	–	–	–
634	25.32	0.08	26.05	0.22	25.54	0.27	–	–	–	–
642	26.06	0.15	27.03	0.34	27.28	0.79	–	–	–	–
1017	24.76	0.06	25.89	0.18	25.74	0.33	–	–	–	–
1032	22.31	0.01	24.29	0.06	24.02	0.12	–	–	–	–
1056	23.16	0.03	24.59	0.09	24.45	0.13	–	–	–	–
1090	25.61	0.07	26.50	0.22	26.85	0.48	–	–	–	–
1126	25.29	0.08	26.08	0.15	25.94	0.22	–	–	–	–
1202	25.03	0.05	26.66	0.25	25.85	0.23	–	–	–	–
1210	25.46	0.09	26.60	0.22	25.94	0.23	25.62	0.06	25.44	0.07
1220	24.62	0.04	25.86	0.13	25.47	0.14	–	–	–	–
1234	24.55	0.03	25.90	0.19	25.74	0.27	–	–	24.60	0.04
1245	25.14	0.06	25.44	0.08	25.63	0.19	25.32	0.06	25.01	0.05
1247	24.68	0.03	25.45	0.08	25.24	0.12	–	–	–	–
1251	24.63	0.04	26.58	0.36	27.66	0.85	–	–	–	–
1309	24.67	0.05	26.20	0.18	26.07	0.25	25.19	0.07	24.72	0.04
1313	23.99	0.05	25.33	0.23	25.94	0.41	24.69	0.07	24.13	0.03
1332	–	–	–	–	–	–	25.87	0.07	24.85	0.03
1344	23.87	0.02	25.08	0.07	24.96	0.09	24.53	0.03	23.84	0.02

Continues on next page

Table 4.3: Photometry. Table 2. Cont.

Galaxy	R_{MUSYC}		U_{MUSYC}		$U_{MUSYC}38$		b_{ACS}		v_{ACS}	
	mag	$\pm\Delta$	mag	$\pm\Delta$	mag	$\pm\Delta$	mag	$\pm\Delta$	mag	$\pm\Delta$
1378	24.15	0.03	26.05	0.17	25.92	0.28	25.22	0.05	24.18	0.02
1403	24.40	0.04	25.88	0.16	26.06	0.34	25.25	0.07	24.60	0.04
1454	26.72	0.22	28.51	1.26	27.80	0.95	26.00	0.10	26.68	0.16
1514	25.13	0.07	26.31	0.28	26.27	0.33	25.88	0.08	25.25	0.05
1565	25.02	0.05	–	–	26.43	0.36	26.34	0.12	25.16	0.04
1585	24.31	0.03	25.68	0.15	25.18	0.12	24.69	0.04	24.41	0.03
1605	26.60	0.18	26.98	0.32	26.95	0.54	26.29	0.10	25.81	0.08
1656	25.57	0.08	26.26	0.21	26.15	0.31	26.00	0.12	25.83	0.09
1723	25.39	0.06	25.96	0.13	26.07	0.26	25.52	0.06	25.60	0.07
1727	24.67	0.04	26.38	0.20	25.73	0.19	–	–	–	–
1752	22.94	0.01	24.39	0.04	24.24	0.05	–	–	–	–
1765	26.39	0.18	26.43	0.20	28.31	1.46	–	–	–	–
1796	22.90	0.01	24.65	0.05	24.62	0.12	–	–	–	–
1804	25.00	0.07	26.33	0.29	27.62	1.13	–	–	–	–
1860	24.82	0.04	25.46	0.10	25.17	0.12	–	–	–	–
1861	23.64	0.02	25.29	0.11	25.36	0.13	–	–	–	–
2010	25.30	0.06	26.59	0.27	26.16	0.33	25.74	0.08	25.57	0.07

Table 4.4: Photometry. Table 3

Galaxy	i_{ACS}		z_{ACS}		$F814W_{ACS}$		$F105W_{WFC3}$		$F125W_{WFC3}$	
	mag	$\pm\Delta$	mag	$\pm\Delta$	mag	$\pm\Delta$	mag	$\pm\Delta$	mag	$\pm\Delta$
17	–	–	–	–	–	–	–	–	–	–
26	–	–	–	–	–	–	–	–	–	–
35	–	–	–	–	–	–	–	–	–	–
43	–	–	–	–	–	–	–	–	–	–
53	–	–	–	–	–	–	–	–	–	–
88	–	–	–	–	–	–	–	–	–	–
101	–	–	–	–	–	–	–	–	–	–
121	–	–	–	–	–	–	–	–	–	–
145	–	–	–	–	–	–	–	–	–	–
156	–	–	–	–	–	–	–	–	–	–
164	–	–	–	–	–	–	–	–	–	–
173	–	–	–	–	–	–	–	–	–	–
181	–	–	–	–	23.39	0.02	–	–	–	–
183	25.18	0.07	25.43	0.11	–	–	–	–	25.66	0.07
193	–	–	–	–	24.38	0.06	–	–	–	–
195	25.47	0.12	27.01	0.51	–	–	–	–	25.91	0.12
205	–	–	–	–	24.41	0.04	–	–	–	–
210	25.36	0.10	25.47	0.15	–	–	–	–	25.84	0.10
220	–	–	–	–	–	–	–	–	–	–
227	25.61	0.11	25.48	0.13	–	–	25.50	0.09	25.39	0.06
235	25.59	0.11	25.01	0.08	–	–	–	–	25.57	0.06

Continues on next page

Table 4.4: Photometry. Table 3. Cont.

Galaxy	i_{ACS}		z_{ACS}		$F814W_{ACS}$		$F105W_{WFC3}$		$F125W_{WFC3}$	
	mag	$\pm\Delta$	mag	$\pm\Delta$	mag	$\pm\Delta$	mag	$\pm\Delta$	mag	$\pm\Delta$
236	24.60	0.05	24.35	0.05	–	–	24.51	0.03	24.45	0.03
237	25.28	0.07	25.23	0.09	–	–	–	–	25.00	0.04
241	25.10	0.06	25.34	0.16	–	–	–	–	25.02	0.04
253	26.28	0.15	25.36	0.08	25.83	0.24	26.31	0.14	25.92	0.09
259	23.70	0.02	23.71	0.02	23.67	0.03	23.60	0.01	23.64	0.02
277	24.98	0.07	25.01	0.08	25.37	0.11	24.95	0.05	25.18	0.04
293	24.42	0.04	24.42	0.05	–	–	–	–	24.37	0.03
296	24.77	0.05	24.70	0.06	25.10	0.10	24.78	0.03	24.87	0.03
297	25.25	0.07	25.26	0.07	25.35	0.10	–	–	25.43	0.04
306	24.27	0.04	24.39	0.04	24.38	0.05	24.39	0.03	24.48	0.02
312	24.49	0.05	24.19	0.03	–	–	–	–	23.73	0.02
315	25.65	0.12	25.85	0.17	26.53	0.30	25.81	0.07	25.43	0.07
317	23.61	0.03	23.68	0.04	–	–	–	–	–	–
386	24.11	0.03	24.07	0.03	–	–	–	–	24.03	0.02
396	24.66	0.07	24.85	0.07	24.51	0.04	24.71	0.07	24.75	0.04
440	25.46	0.08	25.29	0.14	26.34	0.21	26.47	0.33	25.61	0.11
454	24.88	0.05	24.75	0.11	–	–	24.83	0.03	24.86	0.04
455	24.75	0.04	24.52	0.07	24.68	0.04	24.43	0.05	24.26	0.04
464	24.83	0.13	24.81	0.12	–	–	–	–	24.59	0.03
474	–	–	–	–	–	–	–	–	–	–
481	24.65	0.05	24.42	0.04	–	–	24.40	0.01	24.30	0.01
488	24.37	0.06	24.36	0.04	–	–	24.11	0.02	24.09	0.02
490	24.34	0.03	24.10	0.03	24.29	0.04	23.97	0.03	24.02	0.04
510	–	–	–	–	–	–	–	–	–	–
518	25.19	0.09	25.34	0.12	–	–	25.24	0.04	25.25	0.05
519	–	–	–	–	24.31	0.05	–	–	–	–
520	24.39	0.04	24.35	0.05	24.19	0.05	24.29	0.05	24.18	0.03
524	–	–	–	–	–	–	–	–	–	–
536	25.56	0.13	25.58	0.15	25.92	0.26	26.15	0.18	25.89	0.09
539	–	–	–	–	–	–	–	–	26.38	0.31
543	–	–	–	–	–	–	–	–	–	–
544	24.96	0.08	24.75	0.11	25.04	0.13	–	–	–	–
551	23.89	0.03	23.85	0.03	23.65	0.04	23.75	0.03	23.75	0.02
565	–	–	–	–	–	–	–	–	–	–
571	25.01	0.08	24.98	0.08	–	–	24.58	0.05	24.35	0.06
584	–	–	–	–	–	–	–	–	–	–
594	–	–	–	–	–	–	–	–	–	–
601	–	–	–	–	–	–	–	–	–	–
612	–	–	–	–	–	–	–	–	–	–
626	–	–	–	–	–	–	–	–	–	–
634	–	–	–	–	–	–	–	–	–	–
642	–	–	–	–	–	–	–	–	–	–
1017	–	–	–	–	–	–	–	–	–	–
1032	–	–	–	–	–	–	–	–	–	–
1056	–	–	–	–	–	–	–	–	–	–
1090	–	–	–	–	–	–	–	–	–	–

Continues on next page

Table 4.4: Photometry. Table 3. Cont.

Galaxy	i_{ACS}		z_{ACS}		$F814W_{ACS}$		$F105W_{WFC3}$		$F125W_{WFC3}$	
	mag	$\pm\Delta$	mag	$\pm\Delta$	mag	$\pm\Delta$	mag	$\pm\Delta$	mag	$\pm\Delta$
1126	–	–	–	–	–	–	–	–	–	–
1202	–	–	–	–	–	–	–	–	–	–
1210	24.60	0.06	24.34	0.04	–	–	–	–	24.20	0.03
1220	–	–	–	–	–	–	–	–	–	–
1234	24.17	0.04	24.17	0.05	–	–	–	–	–	–
1245	24.64	0.06	24.82	0.07	–	–	–	–	24.67	0.04
1247	–	–	–	–	–	–	–	–	–	–
1251	–	–	–	–	24.20	0.03	–	–	–	–
1309	24.27	0.03	24.06	0.04	–	–	23.95	0.02	23.79	0.02
1313	23.73	0.04	23.52	0.06	–	–	23.34	0.02	23.36	0.02
1332	24.76	0.04	24.53	0.05	–	–	24.20	0.03	24.22	0.02
1344	24.41	0.04	23.92	0.03	–	–	–	–	24.43	0.03
1378	23.81	0.02	23.61	0.03	23.79	0.03	23.57	0.01	23.46	0.01
1403	23.94	0.04	23.73	0.03	23.96	0.03	–	–	23.45	0.02
1454	25.94	0.17	25.60	0.12	25.11	0.10	25.65	0.07	25.29	0.06
1514	24.67	0.04	24.31	0.04	24.50	0.05	24.34	0.05	24.26	0.02
1565	24.92	0.09	24.77	0.06	25.25	0.07	25.23	0.14	24.76	0.04
1585	23.88	0.03	23.81	0.03	23.78	0.02	23.65	0.03	23.69	0.03
1605	25.21	0.07	24.97	0.09	25.51	0.08	24.95	0.07	25.41	0.09
1656	25.29	0.07	25.08	0.07	–	–	24.90	0.03	24.61	0.03
1723	24.82	0.08	24.60	0.05	–	–	24.68	0.05	24.57	0.05
1727	–	–	–	–	–	–	–	–	–	–
1752	–	–	–	–	–	–	–	–	–	–
1765	–	–	–	–	–	–	–	–	–	–
1796	–	–	–	–	–	–	–	–	–	–
1804	–	–	–	–	–	–	–	–	–	–
1860	–	–	–	–	–	–	–	–	–	–
1861	–	–	–	–	–	–	–	–	–	–
2010	24.81	0.05	25.17	0.08	–	–	24.87	0.02	24.96	0.01

Table 4.5: Photometry. Table 4

Galaxy	$F160W_{WFC3}$		IRAC 3.6		IRAC 4.5		IRAC 5.8		IRAC 8.0	
	mag	$\pm\Delta$	mag	$\pm\Delta$	mag	$\pm\Delta$	mag	$\pm\Delta$	mag	$\pm\Delta$
17	–	–	23.30	0.09	23.71	0.14	23.90	0.52	24.37	0.67
26	–	–	25.14	0.41	25.94	0.80	–	–	–	–
35	–	–	24.31	0.24	24.92	0.35	24.17	0.65	24.89	0.80
43	–	–	24.34	0.20	25.30	0.48	24.24	0.59	–	–
53	–	–	24.49	0.21	25.18	0.41	–	–	–	–
88	–	–	23.33	0.09	23.18	0.09	23.81	0.44	22.86	0.23
101	–	–	23.95	0.15	23.74	0.14	23.19	0.28	23.46	0.33
121	–	–	23.02	0.08	23.48	0.13	24.07	0.49	25.70	1.44
145	–	–	23.23	0.08	23.55	0.12	–	–	24.52	0.73

Continues on next page

Table 4.5: Photometry. Table 4. Cont.

Galaxy	$F160W_{WFC3}$		IRAC 3.6		IRAC 4.5		IRAC 5.8		IRAC 8.0	
	mag	$\pm\Delta$	mag	$\pm\Delta$	mag	$\pm\Delta$	mag	$\pm\Delta$	mag	$\pm\Delta$
156	–	–	24.73	0.26	24.83	0.30	24.33	0.57	28.11	3.35
164	–	–	23.59	0.10	24.01	0.15	23.84	0.41	23.54	0.30
173	–	–	25.07	0.35	25.51	0.53	24.84	0.84	24.20	0.64
181	–	–	22.87	0.06	23.28	0.10	23.64	0.43	23.93	0.55
183	25.39	0.07	25.60	0.33	25.80	0.38	24.81	0.71	25.65	1.19
193	–	–	24.11	0.15	25.52	0.51	23.94	0.41	24.28	0.67
195	25.58	0.10	25.36	0.32	25.86	0.38	24.41	0.62	24.26	0.61
205	–	–	–	–	–	–	–	–	–	–
210	25.59	0.10	26.12	0.57	25.96	0.39	24.56	0.67	–	–
220	–	–	25.23	0.43	25.58	0.60	24.27	0.80	23.61	0.36
227	25.44	0.08	25.14	0.36	25.75	0.53	24.32	0.53	25.15	0.91
235	25.38	0.07	25.62	0.39	26.40	0.55	24.69	0.65	–	–
236	24.33	0.03	24.74	0.20	25.07	0.27	24.75	0.65	–	–
237	25.14	0.07	24.96	0.24	25.81	0.40	24.97	0.84	24.81	0.74
241	24.88	0.04	25.02	0.26	25.34	0.27	24.49	0.64	26.01	1.66
253	26.15	0.14	25.48	0.48	26.93	1.20	25.04	1.15	–	–
259	23.57	0.01	23.84	0.12	24.33	0.18	24.25	0.44	24.61	0.71
277	25.26	0.06	25.65	0.40	25.52	0.42	26.34	1.89	25.47	1.06
293	24.41	0.03	24.55	0.19	24.91	0.20	26.12	1.44	24.68	0.68
296	25.03	0.04	25.41	0.43	25.41	0.46	–	–	–	–
297	25.50	0.06	25.68	0.38	25.75	0.50	27.02	2.09	25.41	1.06
306	24.38	0.02	24.70	0.22	25.12	0.30	24.91	0.61	–	–
312	23.58	0.02	23.27	0.05	23.45	0.04	24.03	0.37	23.60	0.27
315	25.50	0.09	25.37	0.33	25.79	0.53	25.29	0.91	25.48	1.06
317	–	–	24.48	0.22	24.97	0.36	23.64	0.37	–	–
386	24.02	0.02	24.36	0.22	24.60	0.23	26.18	1.52	23.50	0.34
396	24.68	0.05	24.31	0.16	24.57	0.19	24.65	0.64	25.20	0.90
440	25.79	0.16	25.64	0.44	25.41	0.35	–	–	–	–
454	24.61	0.03	24.98	0.30	25.20	0.31	24.19	0.45	24.96	0.77
455	24.24	0.04	23.66	0.12	23.61	0.11	23.52	0.27	24.03	0.41
464	24.46	0.05	24.21	0.16	24.66	0.21	25.47	0.93	25.14	0.91
474	–	–	24.41	0.25	24.33	0.23	–	–	24.86	0.72
481	24.31	0.01	24.05	0.12	24.46	0.16	24.83	0.64	24.93	0.71
488	23.96	0.02	24.08	0.16	24.38	0.17	24.17	0.52	25.83	1.51
490	24.30	0.05	23.58	0.10	23.82	0.11	24.85	0.52	23.57	0.26
510	–	–	22.66	0.04	23.43	0.10	22.45	0.13	22.63	0.13
518	25.32	0.06	25.37	0.39	25.46	0.39	24.45	0.55	–	–
519	–	–	23.43	0.09	23.74	0.12	26.63	2.10	23.70	0.34
520	24.02	0.03	24.56	0.21	25.10	0.35	24.72	0.68	24.92	0.72
524	–	–	24.62	0.22	23.97	0.14	24.52	0.76	–	–
536	25.74	0.10	25.33	0.38	25.90	0.62	–	–	25.77	1.09
539	25.68	0.23	25.69	0.58	25.54	0.47	24.46	0.73	26.13	1.93
543	–	–	22.75	0.05	23.12	0.07	22.86	0.22	24.16	0.63
544	–	–	24.48	0.22	24.66	0.28	24.13	0.52	25.17	0.97
551	23.74	0.04	23.91	0.16	24.19	0.23	25.19	1.09	25.01	1.00
565	–	–	24.81	0.29	25.11	0.39	23.96	0.47	–	–

Continues on next page

Table 4.5: Photometry. Table 4. Cont.

Galaxy	$F160W_{WFC3}$		IRAC 3.6		IRAC 4.5		IRAC 5.8		IRAC 8.0	
	mag	$\pm\Delta$	mag	$\pm\Delta$	mag	$\pm\Delta$	mag	$\pm\Delta$	mag	$\pm\Delta$
571	23.96	0.04	24.21	0.12	24.41	0.17	25.62	0.97	25.86	1.29
584	–	–	23.85	0.14	24.78	0.30	23.65	0.39	–	–
594	–	–	25.37	0.43	25.12	0.39	–	–	–	–
601	–	–	25.60	0.59	25.82	0.71	–	–	–	–
612	–	–	25.30	0.39	–	–	–	–	24.31	0.48
626	–	–	25.08	0.25	25.66	0.45	–	–	24.65	0.62
634	–	–	23.95	0.14	24.40	0.23	24.77	1.17	23.67	0.33
642	–	–	24.84	0.21	25.58	0.43	23.74	0.27	–	–
1017	–	–	23.94	0.15	25.26	0.51	24.39	0.61	–	–
1032	–	–	22.01	0.04	22.26	0.05	23.47	0.41	22.83	0.21
1056	–	–	22.28	0.04	22.51	0.05	22.12	0.11	22.81	0.19
1090	–	–	24.35	0.19	24.45	0.23	30.34	1.86	24.63	0.69
1126	–	–	24.22	0.15	24.74	0.26	–	–	–	–
1202	–	–	24.12	0.20	24.79	0.35	–	–	26.17	1.82
1210	24.10	0.04	24.00	0.16	24.68	0.22	23.84	0.39	–	–
1220	–	–	24.53	0.24	25.18	0.41	24.82	0.77	25.29	1.02
1234	–	–	24.85	0.29	25.02	0.38	25.56	1.09	–	–
1245	24.59	0.03	24.63	0.16	25.13	0.20	–	–	24.14	0.46
1247	–	–	24.63	0.27	25.25	0.47	23.16	0.26	25.24	0.93
1251	–	–	22.55	0.04	22.66	0.05	22.66	0.17	24.74	0.79
1309	23.65	0.02	23.38	0.07	23.87	0.11	23.82	0.35	24.28	0.56
1313	23.27	0.02	23.23	0.06	23.53	0.07	24.49	0.54	24.79	0.69
1332	24.17	0.02	23.34	0.07	23.57	0.08	23.18	0.25	23.26	0.28
1344	24.48	0.03	24.52	0.15	24.79	0.14	24.55	0.64	24.25	0.53
1378	23.36	0.01	23.95	0.11	24.21	0.15	26.05	1.29	23.63	0.33
1403	23.32	0.02	23.18	0.05	23.48	0.07	23.58	0.28	24.18	0.44
1454	25.43	0.07	25.33	0.28	26.06	0.54	25.17	0.83	29.14	3.98
1514	24.31	0.03	24.08	0.13	24.68	0.20	24.10	0.41	24.89	0.71
1565	24.55	0.04	23.73	0.09	23.92	0.10	24.05	0.36	23.83	0.29
1585	23.53	0.02	23.59	0.09	24.09	0.13	23.53	0.29	24.90	0.95
1605	25.20	0.11	24.97	0.38	25.50	0.50	–	–	26.68	1.84
1656	24.57	0.03	23.16	0.05	23.78	0.15	23.79	0.28	24.28	0.37
1723	24.79	0.09	24.81	0.27	25.48	0.54	26.13	1.46	24.76	0.66
1727	–	–	23.70	0.11	24.31	0.22	25.23	0.98	24.52	0.57
1752	–	–	22.87	0.05	23.22	0.08	22.99	0.21	25.08	0.91
1765	–	–	24.19	0.16	24.52	0.23	26.07	1.65	24.27	0.53
1796	–	–	21.96	0.03	22.22	0.04	22.47	0.15	22.10	0.10
1804	–	–	24.86	0.29	24.82	0.31	–	–	–	–
1860	–	–	24.61	0.28	24.86	0.34	24.27	0.59	–	–
1861	–	–	23.02	0.08	23.15	0.09	22.95	0.25	23.90	0.65
2010	24.84	0.01	25.54	0.45	25.86	0.49	24.83	0.64	–	–

Table 4.6: Photometry. Table 5

Galaxy	IA427		IA445		IA464		IA484		IA505	
	mag	$\pm\Delta$	mag	$\pm\Delta$	mag	$\pm\Delta$	mag	$\pm\Delta$	mag	$\pm\Delta$
17	26.15	0.30	26.25	0.28	26.57	0.39	25.69	0.13	25.84	0.17
26	25.62	0.34	27.28	0.88	–	–	25.82	0.18	25.98	0.39
35	25.10	0.12	25.55	0.13	26.02	0.24	25.12	0.06	25.21	0.13
43	24.77	0.10	25.16	0.08	25.69	0.20	24.67	0.05	24.95	0.11
53	27.59	1.02	27.38	0.50	26.97	0.39	26.04	0.12	27.33	0.55
88	23.13	0.05	23.17	0.02	23.71	0.06	23.16	0.02	23.27	0.05
101	24.45	0.06	24.43	0.04	24.14	0.03	23.77	0.02	23.90	0.04
121	25.57	0.17	25.60	0.10	27.31	0.54	25.15	0.07	25.53	0.13
145	24.85	0.14	24.67	0.08	25.50	0.21	24.80	0.06	24.51	0.09
156	25.78	0.26	26.50	0.28	27.62	0.77	25.84	0.13	25.61	0.19
164	25.29	0.12	25.53	0.11	25.96	0.19	25.15	0.05	25.35	0.12
173	28.22	1.95	26.47	0.61	25.35	0.23	25.75	0.19	26.72	0.81
181	24.55	0.07	24.50	0.04	25.37	0.13	24.37	0.03	24.42	0.07
183	26.26	0.31	26.77	0.28	27.59	0.61	26.07	0.12	27.74	0.79
193	26.20	0.35	26.45	0.30	27.19	0.54	25.63	0.12	25.80	0.21
195	29.18	2.01	27.23	0.44	29.17	1.93	26.18	0.15	27.15	0.65
205	–	–	–	–	–	–	–	–	–	–
210	–	–	27.78	0.72	–	–	28.07	0.68	26.47	0.34
220	25.21	0.14	25.24	0.08	25.83	0.18	24.95	0.05	24.99	0.09
227	26.20	0.32	26.74	0.30	26.62	0.31	26.54	0.17	27.45	0.61
235	25.74	0.30	26.90	0.37	26.67	0.45	25.85	0.11	26.52	0.40
236	25.46	0.15	25.77	0.18	26.56	0.41	25.17	0.06	25.08	0.13
237	26.04	0.23	27.51	0.63	26.77	0.49	26.35	0.19	25.48	0.14
241	26.19	0.27	26.51	0.24	30.70	3.51	26.09	0.15	26.25	0.35
253	27.47	0.76	27.76	0.72	–	–	27.02	0.38	26.90	0.59
259	24.66	0.08	24.81	0.05	25.48	0.15	24.61	0.04	24.61	0.07
277	26.02	0.25	25.99	0.23	26.17	0.23	25.71	0.10	26.43	0.35
293	26.21	0.28	25.89	0.17	26.53	0.26	25.86	0.09	26.16	0.22
296	25.60	0.19	25.50	0.09	26.15	0.30	25.20	0.06	25.11	0.11
297	26.56	0.31	28.35	0.76	–	–	26.78	0.26	–	–
306	25.33	0.13	25.75	0.11	26.70	0.32	25.45	0.08	25.73	0.22
312	25.03	0.12	24.89	0.05	25.55	0.18	24.84	0.04	25.00	0.09
315	26.49	0.45	27.82	0.70	26.93	0.43	26.26	0.15	26.16	0.26
317	26.21	0.28	25.90	0.22	26.62	0.38	25.61	0.08	26.01	0.21
386	25.91	0.40	25.79	0.13	26.99	0.47	25.50	0.09	25.74	0.18
396	25.22	0.15	25.60	0.12	26.32	0.30	25.10	0.07	25.14	0.10
440	26.22	0.39	28.80	1.17	–	–	26.84	0.24	27.07	0.55
454	25.67	0.29	26.16	0.17	26.44	0.33	25.78	0.14	25.37	0.14
455	25.88	0.20	25.96	0.15	26.51	0.34	26.04	0.12	25.93	0.18
464	26.02	0.24	25.77	0.17	26.79	0.42	25.91	0.10	25.88	0.19
474	25.96	0.25	25.83	0.15	26.70	0.35	25.63	0.09	25.79	0.22
481	25.20	0.15	25.37	0.08	26.07	0.24	25.05	0.05	25.57	0.20
488	26.49	0.39	26.48	0.27	27.26	0.65	25.98	0.11	25.76	0.18
490	24.87	0.10	25.11	0.08	26.38	0.28	24.99	0.06	25.41	0.17
510	24.27	0.07	24.50	0.07	25.24	0.16	24.31	0.04	24.35	0.06

Continues on next page

Table 4.6: Photometry. Table 5. Cont.

Galaxy	IA427		IA445		IA464		IA484		IA505	
	mag	±Δ	mag	±Δ	mag	±Δ	mag	±Δ	mag	±Δ
518	26.69	0.49	26.61	0.25	28.90	1.49	27.32	0.52	29.60	2.25
519	24.88	0.10	25.23	0.07	25.86	0.23	24.98	0.05	25.00	0.11
520	27.65	0.87	25.92	0.13	27.02	0.53	25.57	0.07	25.81	0.18
524	24.58	0.14	25.07	0.11	25.51	0.30	24.75	0.08	25.28	0.18
536	26.80	0.44	26.53	0.35	27.96	1.08	26.42	0.19	26.60	0.42
539	26.78	0.63	27.26	0.61	–	–	26.15	0.16	26.68	0.57
543	26.66	0.52	25.88	0.19	26.68	0.42	25.54	0.08	25.51	0.15
544	25.84	0.28	26.02	0.24	26.78	0.34	25.73	0.10	25.98	0.19
551	25.13	0.14	25.18	0.08	25.41	0.18	24.39	0.03	24.45	0.06
565	25.97	0.28	26.81	0.41	26.57	0.31	25.76	0.09	26.22	0.25
571	27.21	0.64	27.12	0.46	27.43	0.75	26.03	0.13	26.72	0.36
584	24.57	0.09	24.68	0.06	24.99	0.13	24.29	0.04	24.66	0.10
594	25.87	0.25	26.04	0.18	26.20	0.24	25.26	0.06	25.73	0.16
601	30.22	3.48	–	–	–	–	26.93	0.34	27.93	1.05
612	25.86	0.21	26.28	0.22	26.53	0.35	26.24	0.19	26.56	0.33
626	25.61	0.19	26.19	0.17	26.20	0.27	25.58	0.11	26.03	0.27
634	25.49	0.17	25.44	0.09	26.40	0.31	25.24	0.06	25.93	0.21
642	26.60	0.40	26.41	0.24	27.41	0.64	26.20	0.14	26.94	0.55
1017	25.35	0.19	25.62	0.15	25.87	0.22	25.56	0.12	25.90	0.33
1032	23.60	0.06	23.47	0.03	23.99	0.06	23.09	0.02	23.12	0.03
1056	24.24	0.09	24.11	0.05	23.96	0.07	24.00	0.03	24.00	0.06
1090	27.44	0.68	27.93	1.00	26.53	0.27	26.14	0.16	26.77	0.38
1126	25.73	0.18	25.71	0.14	27.40	0.54	25.55	0.09	25.84	0.21
1202	26.34	0.44	26.10	0.15	–	–	25.79	0.09	26.10	0.24
1210	27.06	0.53	26.98	0.45	32.47	4.65	25.77	0.12	26.08	0.25
1220	25.43	0.14	25.75	0.11	27.38	0.86	25.30	0.08	25.69	0.16
1234	26.06	0.28	25.69	0.13	26.22	0.23	25.31	0.06	25.01	0.12
1245	25.57	0.16	25.78	0.13	26.52	0.26	25.43	0.09	25.39	0.17
1247	25.50	0.20	25.52	0.09	26.37	0.23	25.01	0.07	25.14	0.12
1251	26.22	0.28	26.07	0.23	26.39	0.40	25.55	0.08	25.38	0.13
1309	25.57	0.15	25.63	0.12	26.78	0.39	25.24	0.08	25.54	0.14
1313	25.01	0.19	25.22	0.14	25.67	0.31	24.58	0.07	24.77	0.14
1332	–	–	–	–	–	–	–	–	–	–
1344	24.86	0.14	24.98	0.07	25.74	0.23	24.67	0.05	24.42	0.08
1378	25.41	0.16	25.46	0.15	27.03	0.54	25.11	0.05	24.81	0.08
1403	25.30	0.17	25.37	0.13	26.11	0.20	25.04	0.06	25.25	0.15
1454	29.97	2.69	28.64	1.12	28.93	1.84	27.60	0.61	–	–
1514	25.66	0.21	25.81	0.15	26.58	0.48	25.65	0.09	25.54	0.15
1565	25.81	0.26	25.95	0.24	26.02	0.25	25.40	0.06	25.84	0.21
1585	24.99	0.15	25.21	0.11	25.94	0.20	24.95	0.08	24.93	0.08
1605	27.06	0.59	27.13	0.36	26.62	0.29	27.26	0.32	26.27	0.28
1656	25.94	0.23	26.36	0.20	27.36	0.49	25.98	0.10	26.63	0.44
1723	25.59	0.24	25.88	0.14	26.85	0.47	25.65	0.08	25.98	0.22
1727	25.71	0.27	25.95	0.15	26.68	0.34	25.45	0.07	25.91	0.19
1752	23.55	0.04	23.60	0.02	23.99	0.04	23.13	0.01	23.20	0.02
1765	27.32	0.66	26.96	0.39	28.28	1.03	26.03	0.20	27.96	1.05

Continues on next page

Table 4.6: Photometry. Table 5. Cont.

Galaxy	IA427		IA445		IA464		IA484		IA505	
	mag	±Δ	mag	±Δ	mag	±Δ	mag	±Δ	mag	±Δ
1796	23.92	0.04	24.01	0.03	24.57	0.07	23.69	0.02	23.69	0.03
1804	25.98	0.24	26.70	0.27	26.77	0.38	25.67	0.11	25.72	0.20
1860	25.48	0.17	25.55	0.10	25.67	0.15	24.98	0.05	25.30	0.11
1861	24.76	0.10	24.92	0.07	26.41	0.27	24.55	0.04	24.56	0.06
2010	27.00	0.48	26.65	0.25	–	–	26.26	0.12	25.91	0.21

Table 4.7: Photometry. Table 6

Galaxy	IA527		IA550		IA574		IA598		IA624	
	mag	±Δ	mag	±Δ	mag	±Δ	mag	±Δ	mag	±Δ
17	25.79	0.09	25.70	0.10	25.86	0.25	25.54	0.09	25.28	0.09
26	26.01	0.37	26.83	0.54	–	–	25.16	0.12	25.12	0.14
35	25.07	0.05	25.24	0.08	25.17	0.14	24.80	0.08	24.48	0.07
43	24.79	0.04	24.80	0.04	24.99	0.10	24.60	0.05	24.35	0.05
53	26.52	0.18	26.41	0.23	26.67	0.36	26.52	0.20	26.32	0.26
88	23.30	0.02	23.19	0.04	22.81	0.03	22.86	0.02	22.89	0.02
101	23.95	0.02	23.94	0.02	24.02	0.04	23.81	0.02	23.67	0.03
121	25.40	0.09	25.34	0.07	25.49	0.23	25.09	0.07	24.87	0.08
145	24.61	0.06	24.70	0.09	24.13	0.07	24.05	0.04	23.81	0.04
156	25.97	0.14	25.99	0.14	25.25	0.12	25.22	0.07	25.05	0.08
164	25.15	0.06	25.29	0.09	25.80	0.23	25.02	0.07	25.24	0.11
173	25.61	0.18	25.39	0.20	25.54	0.33	25.58	0.20	25.05	0.14
181	24.30	0.03	24.42	0.04	24.41	0.06	24.18	0.03	24.04	0.03
183	26.91	0.23	26.26	0.17	25.68	0.24	25.78	0.11	25.76	0.15
193	25.79	0.14	25.64	0.13	25.40	0.16	25.06	0.07	24.93	0.08
195	26.36	0.24	26.49	0.29	26.39	0.37	25.79	0.16	25.86	0.16
205	–	–	–	–	–	–	–	–	–	–
210	26.63	0.29	26.93	0.44	–	–	26.54	0.28	26.00	0.18
220	25.01	0.05	24.99	0.08	25.08	0.17	24.85	0.06	24.78	0.07
227	26.71	0.27	26.50	0.19	27.00	0.48	26.83	0.35	25.76	0.18
235	26.10	0.17	25.83	0.16	26.01	0.28	26.08	0.18	26.10	0.23
236	24.89	0.07	25.02	0.07	24.99	0.10	24.69	0.05	24.65	0.06
237	25.75	0.11	25.97	0.20	25.76	0.18	25.31	0.08	25.18	0.13
241	25.74	0.09	26.50	0.26	25.69	0.17	25.16	0.07	25.15	0.08
253	27.00	0.27	26.43	0.29	–	–	26.83	0.39	26.38	0.23
259	24.73	0.06	24.67	0.04	24.46	0.07	23.94	0.02	24.01	0.04
277	25.68	0.12	25.56	0.09	25.56	0.18	25.17	0.08	25.22	0.10
293	25.48	0.09	26.00	0.13	25.12	0.13	25.05	0.07	24.83	0.06
296	25.12	0.05	25.31	0.06	25.62	0.19	24.90	0.06	23.92	0.02
297	26.67	0.20	26.43	0.15	27.11	0.47	25.95	0.11	25.69	0.10
306	25.40	0.06	25.73	0.14	25.44	0.15	24.78	0.05	24.60	0.05
312	24.94	0.04	24.88	0.06	25.03	0.09	24.65	0.04	24.69	0.07
315	26.81	0.23	27.01	0.36	27.81	1.08	26.96	0.35	26.52	0.33

Continues on next page

Table 4.7: Photometry. Table 6. Cont.

Galaxy	IA527		IA550		IA574		IA598		IA624	
	mag	±Δ	mag	±Δ	mag	±Δ	mag	±Δ	mag	±Δ
317	25.54	0.07	25.72	0.11	26.13	0.26	25.26	0.08	24.86	0.07
386	25.10	0.06	25.03	0.06	24.86	0.12	24.57	0.06	24.44	0.04
396	24.76	0.05	24.95	0.06	25.07	0.12	24.68	0.05	24.56	0.05
440	26.81	0.25	26.66	0.30	26.91	0.48	26.21	0.16	25.73	0.13
454	25.79	0.09	26.04	0.13	25.35	0.16	25.40	0.08	24.90	0.06
455	25.70	0.10	25.80	0.12	25.75	0.25	25.58	0.08	25.27	0.08
464	25.64	0.08	25.68	0.10	25.87	0.22	25.67	0.13	25.50	0.09
474	25.56	0.08	25.35	0.10	25.45	0.16	25.15	0.07	25.32	0.11
481	25.36	0.07	25.31	0.10	25.30	0.13	25.14	0.06	25.07	0.06
488	25.91	0.10	26.11	0.17	25.29	0.16	24.84	0.05	24.86	0.08
490	25.03	0.07	25.07	0.06	25.22	0.12	24.86	0.07	24.88	0.06
510	24.27	0.03	24.39	0.03	24.48	0.08	24.18	0.03	24.10	0.04
518	26.34	0.15	26.01	0.14	25.71	0.20	25.66	0.11	25.47	0.13
519	24.97	0.04	25.13	0.08	25.33	0.15	24.86	0.05	24.70	0.07
520	25.42	0.07	25.13	0.07	25.78	0.19	24.81	0.06	24.65	0.05
524	24.79	0.06	24.92	0.08	25.14	0.22	24.77	0.07	24.55	0.07
536	26.78	0.22	27.12	0.38	26.23	0.30	26.07	0.14	26.06	0.22
539	26.59	0.23	26.29	0.19	29.92	3.01	26.37	0.21	25.97	0.17
543	25.16	0.09	25.09	0.06	24.98	0.11	24.51	0.04	24.17	0.03
544	25.70	0.08	25.70	0.09	25.28	0.14	25.34	0.08	25.27	0.10
551	24.36	0.04	24.36	0.04	24.61	0.11	24.09	0.04	23.95	0.03
565	25.79	0.10	25.80	0.11	25.42	0.14	24.93	0.07	24.84	0.05
571	26.33	0.14	26.10	0.17	26.91	0.60	25.95	0.13	25.65	0.11
584	24.46	0.04	24.41	0.04	24.40	0.08	24.36	0.05	24.30	0.05
594	25.34	0.07	25.27	0.11	25.16	0.11	25.01	0.06	23.90	0.03
601	27.21	0.41	26.59	0.30	25.51	0.21	25.83	0.21	25.40	0.15
612	26.75	0.21	26.68	0.23	26.79	0.44	26.02	0.19	25.93	0.16
626	25.70	0.10	25.84	0.18	25.80	0.20	25.42	0.09	25.21	0.12
634	25.25	0.08	25.86	0.12	26.26	0.33	25.15	0.08	25.47	0.12
642	26.18	0.13	26.45	0.20	25.68	0.23	26.09	0.15	26.81	0.41
1017	25.36	0.08	25.74	0.16	25.62	0.29	25.45	0.11	24.79	0.07
1032	22.85	0.02	22.61	0.01	22.72	0.03	22.35	0.02	22.24	0.02
1056	23.82	0.03	23.88	0.04	23.70	0.06	23.35	0.03	23.18	0.02
1090	26.19	0.13	25.89	0.12	26.95	0.46	25.53	0.08	25.56	0.12
1126	25.81	0.09	25.43	0.09	26.36	0.30	25.41	0.09	25.26	0.09
1202	25.93	0.12	25.78	0.11	25.77	0.17	25.39	0.08	25.08	0.08
1210	25.96	0.13	26.24	0.16	25.56	0.18	25.68	0.15	25.84	0.14
1220	25.54	0.07	25.07	0.06	25.28	0.12	24.75	0.05	24.60	0.05
1234	24.79	0.04	24.88	0.04	24.80	0.09	24.49	0.04	24.37	0.05
1245	25.61	0.10	25.60	0.08	25.35	0.14	25.45	0.08	25.07	0.08
1247	25.31	0.06	25.28	0.06	24.81	0.09	24.54	0.04	24.57	0.04
1251	25.18	0.08	25.05	0.07	24.90	0.12	24.60	0.06	24.55	0.07
1309	25.15	0.07	25.21	0.08	25.04	0.14	24.89	0.07	24.74	0.05
1313	24.64	0.09	24.63	0.09	24.61	0.13	23.94	0.05	24.00	0.05
1332	–	–	–	–	–	–	–	–	–	–
1344	24.30	0.03	24.65	0.04	24.75	0.09	24.23	0.03	24.53	0.06

Continues on next page

Table 4.7: Photometry. Table 6. Cont.

Galaxy	IA527		IA550		IA574		IA598		IA624	
	mag	±Δ	mag	±Δ	mag	±Δ	mag	±Δ	mag	±Δ
1378	24.58	0.04	24.49	0.05	24.67	0.08	24.11	0.03	24.00	0.03
1403	25.22	0.09	25.19	0.07	25.54	0.16	24.92	0.06	24.41	0.05
1454	28.72	1.28	–	–	27.31	0.87	26.81	0.31	26.82	0.39
1514	25.50	0.09	25.24	0.12	25.16	0.15	25.27	0.11	25.23	0.11
1565	25.86	0.10	25.41	0.12	25.00	0.10	25.04	0.08	24.88	0.07
1585	24.92	0.04	24.89	0.07	24.81	0.09	24.70	0.05	24.25	0.03
1605	28.42	0.79	26.86	0.28	27.72	0.94	26.73	0.27	26.53	0.33
1656	25.88	0.11	25.89	0.11	25.94	0.25	25.85	0.12	25.53	0.10
1723	25.94	0.11	26.06	0.13	25.82	0.28	25.65	0.11	25.41	0.15
1727	25.60	0.13	25.49	0.09	25.28	0.13	24.89	0.09	24.73	0.07
1752	23.11	0.01	23.09	0.01	22.99	0.02	22.94	0.01	22.85	0.01
1765	26.67	0.24	26.68	0.28	28.39	1.33	26.03	0.22	26.42	0.21
1796	23.63	0.02	23.64	0.02	23.25	0.02	22.97	0.01	22.76	0.01
1804	25.64	0.11	25.98	0.14	25.66	0.23	25.10	0.06	24.89	0.06
1860	25.12	0.05	25.20	0.09	25.15	0.11	25.05	0.06	24.78	0.08
1861	24.61	0.04	24.59	0.04	24.19	0.05	23.78	0.02	23.55	0.02
2010	25.72	0.07	25.81	0.12	25.91	0.18	25.58	0.08	25.43	0.11

Table 4.8: Photometry. Table 7

Galaxy	IA651		IA679		IA738		IA767		IA797	
	mag	±Δ	mag	±Δ	mag	±Δ	mag	±Δ	mag	±Δ
17	25.39	0.08	25.53	0.09	25.27	0.10	25.55	0.25	25.35	0.29
26	24.88	0.09	25.12	0.15	24.94	0.14	24.22	0.20	25.16	0.51
35	24.30	0.04	24.47	0.04	24.21	0.04	24.30	0.10	24.07	0.10
43	24.31	0.03	24.42	0.04	24.27	0.04	24.20	0.09	24.08	0.09
53	25.88	0.20	25.86	0.10	25.50	0.12	25.56	0.26	25.45	0.45
88	23.08	0.02	23.03	0.02	23.01	0.02	21.05	0.02	21.98	0.04
101	23.78	0.03	23.91	0.02	23.84	0.03	24.00	0.08	23.99	0.10
121	24.73	0.04	24.96	0.05	24.62	0.06	24.30	0.15	24.25	0.10
145	23.97	0.03	23.89	0.05	23.58	0.03	23.64	0.07	23.83	0.11
156	25.14	0.06	25.16	0.08	24.73	0.06	24.95	0.22	25.44	0.34
164	25.03	0.05	25.26	0.06	24.99	0.06	24.88	0.13	25.05	0.18
173	25.25	0.13	25.31	0.19	24.96	0.13	24.75	0.30	25.19	0.52
181	23.68	0.02	23.83	0.02	23.60	0.02	23.65	0.06	23.52	0.06
183	25.79	0.10	25.83	0.12	25.35	0.12	24.41	0.09	26.55	0.71
193	24.91	0.08	25.08	0.07	24.60	0.05	25.57	0.39	24.47	0.15
195	25.66	0.11	25.82	0.15	25.72	0.14	24.72	0.16	25.48	0.33
205	–	–	–	–	–	–	–	–	–	–
210	26.46	0.21	26.39	0.22	26.23	0.23	26.74	0.71	26.92	0.94
220	24.78	0.05	25.00	0.06	24.46	0.04	24.84	0.21	25.24	0.23
227	25.74	0.11	25.91	0.15	25.73	0.12	26.62	0.54	–	–
235	25.87	0.11	26.17	0.13	25.66	0.16	25.90	0.35	27.26	1.23

Continues on next page

Table 4.8: Photometry. Table 7. Cont.

Galaxy	IA651		IA679		IA738		IA767		IA797	
	mag	±Δ	mag	±Δ	mag	±Δ	mag	±Δ	mag	±Δ
236	24.47	0.05	24.60	0.03	24.67	0.05	24.79	0.12	24.70	0.17
237	25.39	0.08	25.27	0.07	25.39	0.12	25.28	0.24	25.46	0.31
241	25.21	0.07	25.40	0.08	25.26	0.08	24.98	0.17	25.75	0.35
253	26.33	0.20	26.36	0.17	26.22	0.24	–	–	26.86	0.91
259	23.90	0.03	24.04	0.02	23.81	0.03	23.87	0.09	23.51	0.06
277	25.36	0.07	25.54	0.10	25.13	0.10	25.68	0.33	25.92	0.39
293	24.90	0.04	24.90	0.05	24.74	0.06	24.55	0.11	24.58	0.15
296	24.75	0.05	25.27	0.06	25.16	0.08	25.39	0.19	24.93	0.15
297	25.77	0.08	26.46	0.14	25.33	0.08	26.32	0.40	25.88	0.36
306	24.63	0.04	24.89	0.06	24.67	0.05	24.51	0.12	24.19	0.16
312	24.65	0.04	24.62	0.04	24.52	0.04	24.76	0.13	24.49	0.15
315	26.93	0.39	26.75	0.29	25.95	0.16	25.67	0.29	25.72	0.45
317	24.67	0.04	24.80	0.05	24.63	0.05	24.87	0.23	24.48	0.15
386	24.48	0.05	24.63	0.04	24.44	0.04	24.50	0.11	24.46	0.21
396	24.51	0.04	24.69	0.04	24.63	0.07	24.56	0.12	24.80	0.26
440	26.01	0.19	25.89	0.11	25.49	0.12	25.81	0.33	25.52	0.33
454	25.05	0.05	25.22	0.06	24.91	0.06	24.59	0.12	25.03	0.25
455	25.22	0.06	25.10	0.05	24.78	0.05	24.86	0.14	24.86	0.16
464	25.11	0.06	25.14	0.05	24.82	0.08	24.66	0.12	24.75	0.16
474	25.12	0.07	25.29	0.07	24.95	0.07	24.80	0.14	24.67	0.20
481	25.13	0.05	25.30	0.08	24.62	0.04	24.81	0.19	24.89	0.20
488	24.79	0.04	24.88	0.05	24.57	0.06	24.27	0.13	24.92	0.28
490	24.78	0.05	24.59	0.04	24.33	0.04	24.36	0.11	24.53	0.14
510	24.16	0.03	24.38	0.03	24.25	0.04	24.31	0.11	24.33	0.13
518	25.71	0.10	25.86	0.11	25.33	0.09	25.09	0.21	25.10	0.31
519	24.85	0.04	24.81	0.05	24.50	0.04	24.48	0.12	24.50	0.12
520	24.69	0.04	24.80	0.07	24.53	0.05	24.58	0.13	24.78	0.17
524	24.74	0.06	24.92	0.07	24.65	0.07	25.11	0.46	25.41	0.45
536	25.83	0.13	25.92	0.10	25.67	0.11	25.40	0.23	24.78	0.18
539	25.66	0.12	25.69	0.10	25.56	0.12	25.81	0.43	25.67	0.36
543	24.14	0.03	24.15	0.03	23.73	0.03	23.68	0.08	23.56	0.06
544	25.23	0.08	25.18	0.05	24.91	0.05	24.81	0.15	25.42	0.25
551	24.12	0.03	24.16	0.04	24.02	0.03	23.94	0.10	23.96	0.09
565	24.75	0.04	25.01	0.05	24.70	0.05	24.62	0.15	24.70	0.19
571	25.47	0.08	25.38	0.09	25.09	0.10	25.13	0.18	25.09	0.21
584	23.92	0.03	23.96	0.03	23.88	0.04	23.79	0.09	23.80	0.08
594	24.52	0.06	25.23	0.06	24.98	0.07	25.35	0.21	24.83	0.26
601	25.47	0.11	25.69	0.14	25.15	0.10	25.86	0.39	25.78	0.45
612	25.87	0.14	25.80	0.10	25.64	0.13	25.76	0.30	25.82	0.40
626	25.20	0.07	25.31	0.07	25.30	0.11	25.77	0.34	25.10	0.29
634	25.25	0.06	25.40	0.07	25.26	0.08	26.07	0.38	25.31	0.30
642	26.28	0.20	25.91	0.13	26.43	0.29	25.91	0.39	25.41	0.40
1017	24.62	0.07	24.66	0.07	24.47	0.05	24.14	0.11	24.24	0.14
1032	22.23	0.01	22.27	0.01	22.03	0.01	22.06	0.02	22.09	0.03
1056	23.18	0.02	23.09	0.02	22.92	0.02	23.05	0.05	22.96	0.08
1090	25.19	0.06	25.40	0.07	25.17	0.11	25.04	0.26	25.52	0.33

Continues on next page

Table 4.8: Photometry. Table 7. Cont.

Galaxy	IA651		IA679		IA738		IA767		IA797	
	mag	±Δ	mag	±Δ	mag	±Δ	mag	±Δ	mag	±Δ
1126	25.26	0.06	25.22	0.06	24.66	0.05	24.60	0.14	24.61	0.17
1202	24.88	0.06	24.75	0.05	24.42	0.05	24.62	0.11	24.45	0.11
1210	25.45	0.08	25.44	0.08	24.79	0.05	25.10	0.19	24.88	0.20
1220	24.61	0.05	24.62	0.04	24.14	0.04	24.40	0.11	24.65	0.17
1234	24.39	0.03	24.50	0.03	24.34	0.04	24.37	0.10	24.56	0.12
1245	24.93	0.04	24.95	0.05	24.82	0.05	24.88	0.13	24.91	0.16
1247	24.57	0.03	24.82	0.07	24.38	0.03	23.87	0.06	24.69	0.15
1251	24.45	0.05	24.66	0.04	24.34	0.04	24.52	0.11	24.31	0.11
1309	24.38	0.04	24.57	0.04	24.37	0.04	24.40	0.12	24.55	0.15
1313	23.93	0.05	23.90	0.04	23.73	0.04	23.67	0.13	23.65	0.12
1332	–	–	–	–	–	–	–	–	–	–
1344	24.27	0.03	22.65	0.01	24.53	0.04	24.70	0.14	24.98	0.23
1378	23.98	0.02	24.04	0.03	23.96	0.03	24.04	0.07	23.85	0.10
1403	24.25	0.04	24.23	0.04	24.02	0.03	23.79	0.09	23.74	0.06
1454	26.31	0.26	26.81	0.30	26.12	0.18	25.95	0.37	27.43	1.45
1514	24.78	0.04	24.72	0.05	24.86	0.07	24.62	0.13	24.81	0.19
1565	24.84	0.05	25.05	0.06	24.79	0.05	24.45	0.11	25.00	0.18
1585	24.17	0.02	24.20	0.04	24.06	0.04	23.86	0.06	24.03	0.11
1605	26.52	0.19	26.80	0.33	25.72	0.13	25.88	0.39	26.34	0.64
1656	25.79	0.11	25.51	0.07	25.17	0.07	25.09	0.19	25.28	0.25
1723	25.15	0.06	25.27	0.07	25.12	0.07	25.19	0.21	24.82	0.16
1727	24.54	0.05	24.62	0.04	24.28	0.04	24.16	0.08	24.23	0.14
1752	22.88	0.01	22.93	0.01	22.74	0.01	22.58	0.02	22.68	0.03
1765	26.53	0.22	26.39	0.17	26.16	0.22	26.66	0.63	26.87	0.86
1796	22.79	0.01	22.82	0.01	22.60	0.01	22.49	0.02	22.54	0.02
1804	24.75	0.04	24.96	0.05	24.77	0.05	24.93	0.20	24.72	0.17
1860	24.88	0.05	24.85	0.04	24.32	0.03	24.48	0.10	24.01	0.08
1861	23.55	0.02	23.63	0.02	23.38	0.02	23.27	0.07	23.27	0.05
2010	25.46	0.07	25.58	0.08	25.38	0.08	25.19	0.19	25.20	0.26

Table 4.9: Photometry. Table 8

Galaxy	IA856		J_{MUSYC}		H_{MUSYC}		K_{MUSYC}	
	mag	±Δ	mag	±Δ	mag	±Δ	mag	±Δ
17	24.81	0.25	24.44	0.42	24.95	0.48	24.56	0.65
26	24.72	0.34	–	–	–	–	23.66	0.56
35	24.30	0.15	23.83	0.30	–	–	22.85	0.26
43	24.07	0.12	23.91	0.18	23.51	0.10	–	–
53	24.81	0.21	25.68	0.91	25.68	0.56	–	–
88	23.23	0.09	23.56	0.28	23.00	0.08	–	–
101	23.86	0.11	24.30	0.36	–	–	24.22	0.53
121	23.96	0.13	23.95	0.12	23.87	0.10	22.73	0.20
145	23.38	0.09	23.17	0.07	23.56	0.15	22.66	0.26

Continues on next page

Table 4.9: Photometry. Table 8. Cont.

Galaxy	IA856		J_{MUSYC}		H_{MUSYC}		K_{MUSYC}	
	mag	$\pm\Delta$	mag	$\pm\Delta$	mag	$\pm\Delta$	mag	$\pm\Delta$
156	25.00	0.29	24.57	0.54	–	–	–	–
164	24.45	0.18	24.57	0.39	25.32	0.28	24.47	0.68
173	24.30	0.34	23.67	0.12	–	–	23.32	0.49
181	23.38	0.05	23.68	0.15	23.24	0.07	23.58	0.46
183	–	–	25.33	0.34	22.80	0.05	–	–
193	26.02	0.62	24.08	0.35	25.26	0.40	27.49	3.02
195	26.43	0.91	24.87	0.41	26.45	0.54	23.38	0.28
205	–	–	–	–	–	–	–	–
210	25.56	0.44	26.27	0.94	25.39	0.17	25.99	1.44
220	24.35	0.15	–	–	–	–	24.33	0.59
227	25.29	0.32	–	–	–	–	25.82	1.32
235	26.90	1.06	26.58	1.23	27.34	0.90	22.92	0.15
236	24.83	0.24	25.33	0.66	24.10	0.16	24.00	0.47
237	25.24	0.33	26.38	0.80	24.53	0.19	25.24	0.91
241	27.46	1.57	26.74	1.37	26.13	0.43	–	–
253	24.77	0.23	24.07	0.23	24.61	0.16	–	–
259	24.26	0.12	24.36	0.27	23.78	0.06	23.69	0.31
277	26.39	0.73	–	–	24.14	0.11	–	–
293	24.84	0.25	–	–	24.43	0.16	23.37	0.44
296	24.87	0.21	24.80	0.27	25.12	0.14	25.28	1.21
297	–	–	25.36	0.31	–	–	–	–
306	24.74	0.19	–	–	25.95	0.29	–	–
312	24.39	0.14	23.78	0.09	23.73	0.09	–	–
315	24.87	0.26	–	–	26.67	0.60	–	–
317	24.72	0.22	25.34	0.35	25.79	0.51	26.66	2.40
386	23.96	0.10	24.07	0.22	23.98	0.10	22.98	0.20
396	25.05	0.31	24.17	0.14	–	–	23.79	0.41
440	26.53	0.75	–	–	25.44	0.48	25.29	1.30
454	25.47	0.49	25.21	0.36	24.69	0.13	24.14	0.61
455	24.50	0.14	24.92	0.24	23.74	0.11	26.16	1.99
464	24.48	0.17	25.17	0.35	–	–	25.92	1.70
474	25.16	0.31	24.77	0.24	–	–	–	–
481	24.47	0.17	23.73	0.15	24.57	0.10	24.25	0.56
488	24.29	0.15	–	–	25.76	0.26	23.24	0.23
490	24.55	0.21	24.94	0.28	25.08	0.22	–	–
510	24.04	0.15	24.59	0.21	23.43	0.08	23.25	0.30
518	24.56	0.16	–	–	–	–	–	–
519	24.37	0.16	24.37	0.20	24.69	0.30	26.39	2.13
520	24.46	0.14	–	–	26.46	0.62	23.05	0.22
524	24.81	0.32	24.30	0.22	–	–	24.04	1.04
536	26.03	0.52	26.96	1.15	25.02	0.18	–	–
539	24.71	0.26	25.17	0.46	–	–	–	–
543	23.23	0.06	23.30	0.08	23.68	0.09	22.41	0.11
544	24.81	0.28	24.06	0.16	–	–	–	–
551	23.80	0.10	25.21	0.39	23.98	0.09	23.21	0.33
565	25.07	0.31	–	–	24.62	0.15	23.69	0.35

Continues on next page

Table 4.9: Photometry. Table 8. Cont.

Galaxy	IA856		J_{MUSYC}		H_{MUSYC}		K_{MUSYC}	
	mag	$\pm\Delta$	mag	$\pm\Delta$	mag	$\pm\Delta$	mag	$\pm\Delta$
571	24.83	0.25	24.77	0.19	24.82	0.22	–	–
584	23.93	0.14	24.12	0.19	–	–	24.39	0.78
594	26.34	0.80	24.24	0.18	26.18	0.62	–	–
601	25.73	0.55	25.17	0.52	–	–	–	–
612	25.18	0.27	25.11	0.50	26.93	0.97	22.91	0.28
626	25.83	0.53	25.57	0.46	25.53	0.45	–	–
634	24.41	0.14	26.72	1.09	25.51	0.42	–	–
642	25.60	0.48	28.39	2.11	–	–	30.19	5.84
1017	24.37	0.19	–	–	–	–	–	–
1032	21.90	0.03	21.89	0.05	22.03	0.05	21.66	0.14
1056	22.95	0.08	23.03	0.14	22.33	0.05	22.00	0.23
1090	28.56	2.50	–	–	24.34	0.20	–	–
1126	24.46	0.15	23.97	0.13	25.29	0.25	23.92	0.38
1202	24.33	0.17	25.77	0.86	27.00	1.41	23.95	0.60
1210	24.67	0.19	24.82	0.49	24.12	0.11	24.34	0.73
1220	24.41	0.18	24.77	0.24	25.25	0.32	–	–
1234	24.55	0.16	23.93	0.20	–	–	24.78	0.86
1245	24.74	0.17	25.46	0.39	–	–	23.35	0.28
1247	24.68	0.17	23.95	0.12	26.24	0.64	–	–
1251	24.73	0.26	23.35	0.16	23.32	0.08	24.82	0.91
1309	23.95	0.10	25.42	0.54	24.05	0.14	25.53	1.09
1313	23.52	0.14	24.08	0.41	23.71	0.09	–	–
1332	–	–	–	–	–	–	–	–
1344	24.01	0.11	25.28	0.43	–	–	23.71	0.42
1378	23.63	0.08	23.41	0.08	23.74	0.07	22.82	0.20
1403	24.47	0.21	23.97	0.15	23.96	0.08	23.82	0.53
1454	26.98	1.16	–	–	25.26	0.19	24.89	0.81
1514	24.55	0.20	24.43	0.24	25.66	0.38	24.34	0.62
1565	25.00	0.29	27.49	1.58	25.00	0.27	29.60	4.96
1585	23.92	0.09	26.98	1.08	24.05	0.10	22.57	0.16
1605	25.74	0.51	24.39	0.19	25.75	0.31	25.12	1.10
1656	24.54	0.14	24.88	0.36	24.08	0.08	–	–
1723	24.41	0.14	24.98	0.27	–	–	23.37	0.27
1727	23.91	0.12	23.83	0.11	–	–	23.80	0.44
1752	22.76	0.05	23.07	0.06	23.04	0.06	23.13	0.31
1765	27.04	1.01	25.81	0.69	23.80	0.09	–	–
1796	22.42	0.03	22.47	0.03	22.54	0.05	21.71	0.15
1804	24.58	0.18	24.71	0.24	24.18	0.17	–	–
1860	24.41	0.16	24.77	0.27	25.41	0.46	22.94	0.26
1861	23.19	0.06	23.10	0.08	23.47	0.07	23.58	0.47
2010	25.50	0.32	–	–	25.92	0.25	26.72	2.13

4.2 Data from VIMOS Spectroscopy

4.2.1 Redshift Measurements

Redshift measurements are carried out individually for each galaxy. In each case, after a thorough inspection of the spectrum we identify the obvious spectral features, including emission and absorption lines, and breaks. Comparing their relative positions we computationally identify the value of the most likely redshift. VIPGI interface provides a direct access to EZ software (Scaramella et al. 2013, in preparation) that facilitates the task. In partícular, the software computes the most likely redshift given the observed wavelength of the different features identified. The spectra obtained in the third observing program are inspected using $\mathrm{R_ED^{uc}_mE}$ (Cardiel, 1999) software. In this case, the redshifts are calculated using our own scripts. The final redshifts are derived independently of the photometric redshifts assigned for the galaxies. The typical uncertainties we get are $\sim$0.1%.

We assign each estimation with a confidence class (*flag*) that captures the subjectively estimated reliability of the spectroscopic redshift measurement, following the description in Lilly et al. (2007). The basic scheme used consists on an integer from 0 (no redshift) to a maximum of 4 (most reliable) with an additional class 9 for those cases in which a single but clear emission line is identified. Normally, the line observed in the cases is expected to be either Lyα, [OII]$\lambda\lambda$3727, [OIII]λ5007 or Hα, and the identification of Hβ or [OIII]λ4959 can be rejected. We are able to measure spectroscopic redshifts (independently of their quality) for 165 galaxies, out of 327 spectra observed. Table 4.10 shows the number of redshifts measured and the frequency of the different quality flag assigned within the different pointings. For the rest of the work we consider *reliable* the redshifts measurements based on a minimum of two spectral features (e.g., emission/absorption lines, breaks) independently of their signal to noise ratio. This includes flags 2, 3, and 4. Although, flag 2 redshifts are normally not included as reliable in the literature we decide to consider them given we are conservative in our flag assignation. As we can see, although the fraction of spectra on which we can not measure the redshift is similar for all the pointings (44-55%), the fraction of flag 9 redshifts increase by a factor of 6 for the last one, leading to the lowest success ratio (16%), defined as the fraction of redshifts with flags 2, 3, or 4. The main reason for this is the worse atmospheric conditions under which the observations of the Pointing 3 were carried out. Probably, in these cases, only [OII]$\lambda\lambda$3727, or [OIII]λ5007 can be identified.

In Figure 4.1 we show the differences between the photometric redshifts and spectroscopic redshifts of our targets. The large dispersion in the comparison reinforce the importance of specroscopic surveys of these kind of systems for a correct derivation of their physical properties. We use different colors to represent galaxies that in the end of our analysis present masses larger or smaller than $\log M_*/M_\odot$ =8.

Figure 4.2 depicts the comparison between the spectroscopic redshifts measured and the photometric redshifts calculated by the 3D-HST team (Skelton et al., 2014) in order to compare their values to their spectroscopic redshift measurements. These authors make use of a similar photometric dataset to the one we use in this work. They include ACS, CANDELS, U and R-band images from VIMOS, GaBoDS, and 14 Subaru medium bands from MUSYC. As we can see, except in 4 rare cases, the $z_{\rm phot}$'s are extremely in agreement with our reliable $z_{\rm spec}$'s, exhibing a dispersion $\lesssim$0.05. This shows the importance of the election of the right photometric dataset

Table 4.10: Summary of redshift measurements.

Program	Galaxies observed	Total measured	flag 1	flag 2	flag 3	flag 4	flag 9	Not measured	Success rate
088.A-0321	119	59	12	9	17	18	3	60	31%
088.A-0321	118	65	24	10	18	8	5	53	31%
090.A-0858	91	41	5	3	9	3	21	50	16%

to perform the SED-fitting procedure. The difference in dispersion between Figure 4.1 and this one is probably mostly due to the inclusion of noisy photometry in the dataset used to derive the photometric redshifts used for the selection. This could imply that our approach can be more generally applicable to larger samples of not spectroscopically confirmed dwarfs. However, we cannot assure that the quality of the photometric redshifts is as good as it is for the reliable redshift cases, for those galaxies for which we are not able to measure a redshifts.

Our analysis is limited to the galaxies for which we are able to measure a reliable spectroscopic redshift (flags 2, 3, and 4). In order to check whether the properties (based on photometric redshifts) of these galaxies follow the distribution of those observed, we again plot a set of histograms (Figures 4.3; analogous to Figures 2.1, 3.5) with the $\log M_*/\mathrm{M}_\odot$, $M_{\mathrm{B,0,AB}}$, $(B-V)_0$, $S_{\mathrm{Reff,B,0}}/$ mag arcsec^{-2}, z_{phot}, and apparent magnitude in the seleccion band $\mathrm{Subaru\ NB816}$ for the sample of galaxies for which we are able to measure a spectroscopic redshifts (filled histograms), and the observed sample (open histogram). Again, we can see straight away that the representativity is significant.

4.2.2 Emission Lines Measurements

All the galaxies for which we can measure a redshift are emission line galaxies. Table 4.11 shows the list of emission lines found for at least one of the galaxies without any restriction in the significance of the detection. Within this list we find the classical strong emission lines [OII]$\lambda\lambda$3727, Hβ, [OIII]$\lambda\lambda$4959,5007, and Hα, but also others such as HeIλ3531, H10, H9, [NeIII]λ3868, HeI+H8, [NeIII]+H7, Hδ, Hγ, [OIII]λ4363, HeIλ4471, HeIλ4921, HeIλ5876, [NII]λ6584, HeIλ6678, and [SII]$\lambda\lambda$6717,6731. For each galaxy we measure the emission lines we can identify in the spectrum, except in those cases in which the lines are obviously dramatically affected by sky emission lines. There are 7 galaxies for which we cannot measure any emission lines due to this problem.

We measure emission line fluxes from the individual spectra using $\mathrm{R_E D_m^{uc} E}$ (Cardiel, 1999). $\mathrm{R_E D_m^{uc} E}$ provides several programs for specific analysis tasks (e.g., graphics, statistics, arithmetic, measurements). In particular, *midelines* displays an interactive interface in which each 1D-spectra can be visualized, explored, and measured. We apply the following technique to all the lines identified in the VIMOS spectra manually in order to avoid contamination of sky residuals in both continuum fit or emission measurement:

1. For each emission line, we first define two adjacent wavelength ranges where to measure the continuum level. *midelines* allows to fit the continuum with different degree polynomials. As a simplification, we use a simple linear function.

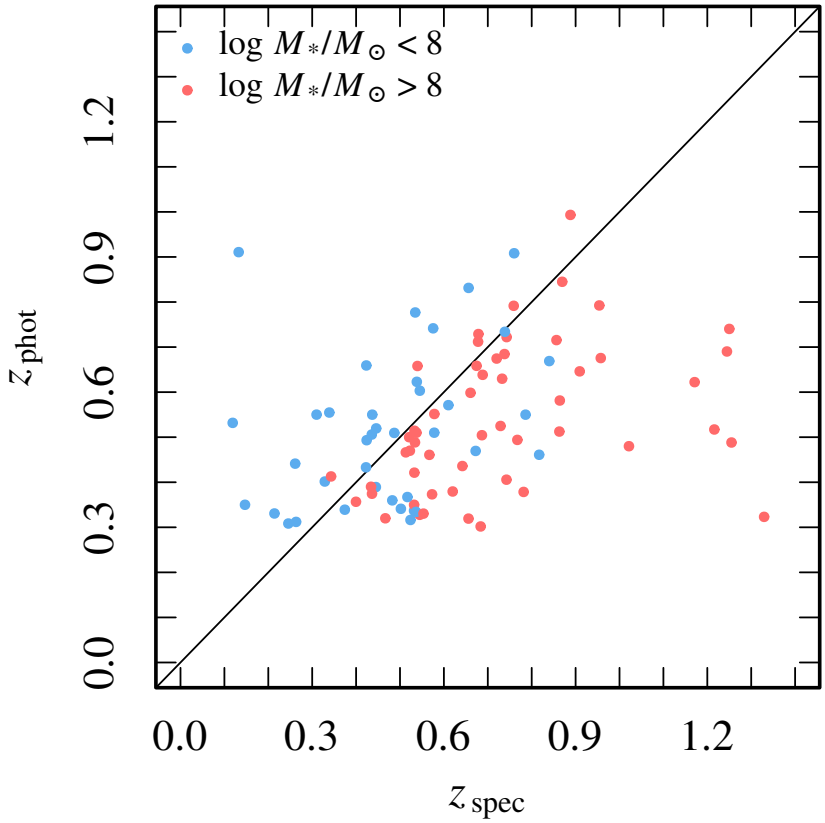

Figure 4.1: Comparison between the photometric redshifts and the spectroscopic redshifts for those reliable cases ($2 \leq$ Confidence Class < 9). We divide our sample by stellar mass (Chapters 5, Chapters 7): red points are used for more massive galaxies (log $M_*/M_\odot$>8), and blue points represent lower mass galaxies (log $M_*/M_\odot$<8).

2. We fit the corresponding emission line with a Gaussian. *midelines* performs the fit using as input the wavelength range corresponding to the emission line.

3. We record the wavelength ranges used to measure, the continuum level, the parameters of the Gaussian curve fitted, and the value of the fluxes of the emission line under the best Gaussian profile fit and under the spectrum.

midelines itself does not return an estimation of the uncertainties of the measurements. Therefore, we are obliged to perform our own. We consider that the two main sources of uncertainties are (1) the noise and (2) the uncertainties in the placement of the level of continuum, that can be affected by both the noise and the wavelength ranges we use to fit it. To account for these contributions we decide to repeat the measurements of the emission lines 500 times, modifying each time the spectra and the measurement in the following ways:

1. For each iteration we modify the initial spectrum by varying randomly the value of the flux in each pixel within the noise distribution. As a simplification, we assume the noise distribution is the same for every pixel of the spectrum (including emission lines and continuum). As an estimation, we consider the noise (RMS) of the continuum in the ranges we use to calculate the continuum level. In practice, we use *istat*, which is another program included in the $\mathrm{RED}^{\mathrm{uc}}_{\mathrm{m}}\mathrm{E}$ package, to measure the RMS in the mentioned wavelength ranges. Then, we build

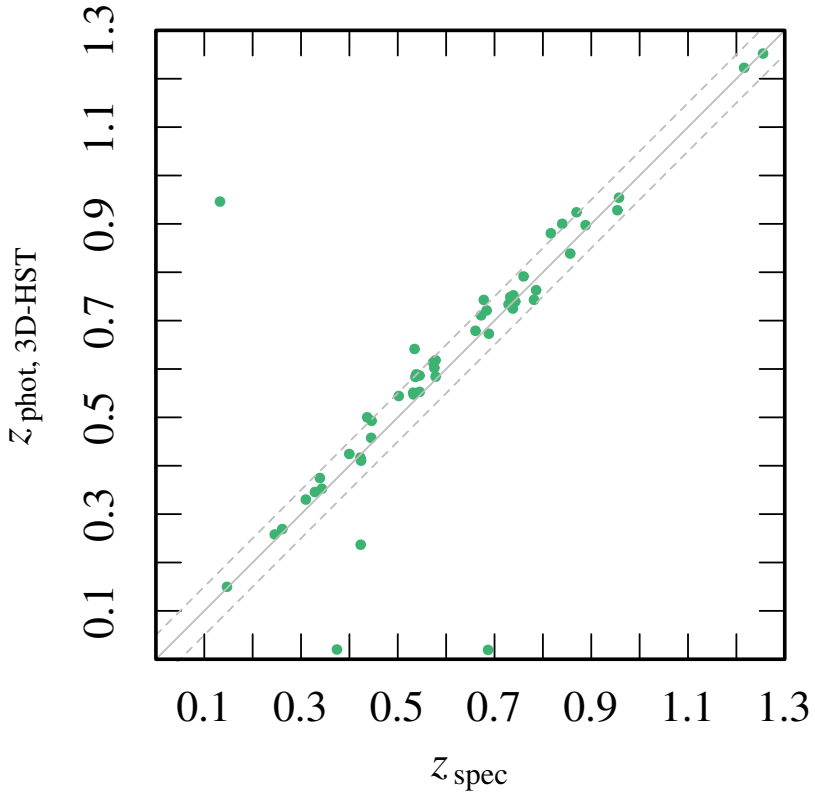

Figure 4.2: Comparison between the spectroscopic redshifts measured and the photometric redshifts obtained by Skelton et al. 2014. The grey lines represent a dispersion of ± 0.05.

a noise spectrum with the same size (number of pixels) than the initial one, by giving to each pixel a random value within a normal distribution with a σ equal to the RMS measured. The final spectrum used in each iteration is the sum of the the initial spectrum and the iteration noise spectrum.

2. We randomly modify the wavelength windows used to fit the continuum and the emission lines. We limit the new ranges within the limits of the original windows and consider a minimum width of 10 pixels. We allow for 10% variations in the width of the range defined to fit the emission line.

The median uncertainty obtained using this approach for the measurements of the emission lines fluxes is $\sim 10\%$ of both the flux measured under the gaussian, and the flux directly measured on the spectra. In our case we opt for using the later.

Table 4.12, 4.13, 4.14, and 4.15 show the measurements of the emission lines. For each galaxy, we report the flux (F; 10^{17} erg s^{-1} cm^{-2}) and the rest frame equivalent width (EW$_{\text{rf}}$; Å). The reported equivalent widths are corrected from the observed to the rest frame using

$$\text{EW}_{\text{rf}} = \frac{\text{EW}_{\text{obs}}}{(1 - z_{\text{spec}})} \tag{4.1}$$

We check the values of the emission line fluxes measured for the galaxies included in both

Table 4.11: Summary of emission line detections in the VIMOS spectra

λ (Å)	Line	Detection rate (%)
3531	HeI	1
3727	[OII]	88
3798	H10	2
3835	H9	3
3868	[NeIII]	19
3889	HeI+H8	7
3968	[NeIII]+H7	9
4102	Hδ	13
4340	Hγ	29
4363	[OIII]	5
4471	HeI	1
4861	Hβ	59
4921	HeI	2
4959	[OIII]	56
5007	[OIII]	71
5876	HeI	3
6563	Hα	21
6584	[NII]	9
6678	HeI	1
6717	[SII]	1
6731	[SII]	1

observing programs. The impact of the different reduction processes carried out for the two first pointings and the third (Section 3.1.4) appears to remain below the 20% in terms of emission lines fluxes. For these galaxies we report the average value of their fluxes and EWs in Table 4.12, 4.13, 4.14, and 4.15.

At first glance, the data clearly suggest that the galaxies in our sample are not predominantly extreme emission line galaxies (EWs$\sim$1000Å), such as those observed by van der Wel et al. (2011). In particular, only 3 out of 64 galaxies with detected [OIII]λ5007 emission line present EWs consistent with such study. Only 29 (45%) present values compatible with EWs $\geq$100Å (definition of extreme emission line galaxies used by Amorín et al. 2014c). We think that the fact that we include both *booming* and less extreme systems in our sample is due to our mass selection criterion.

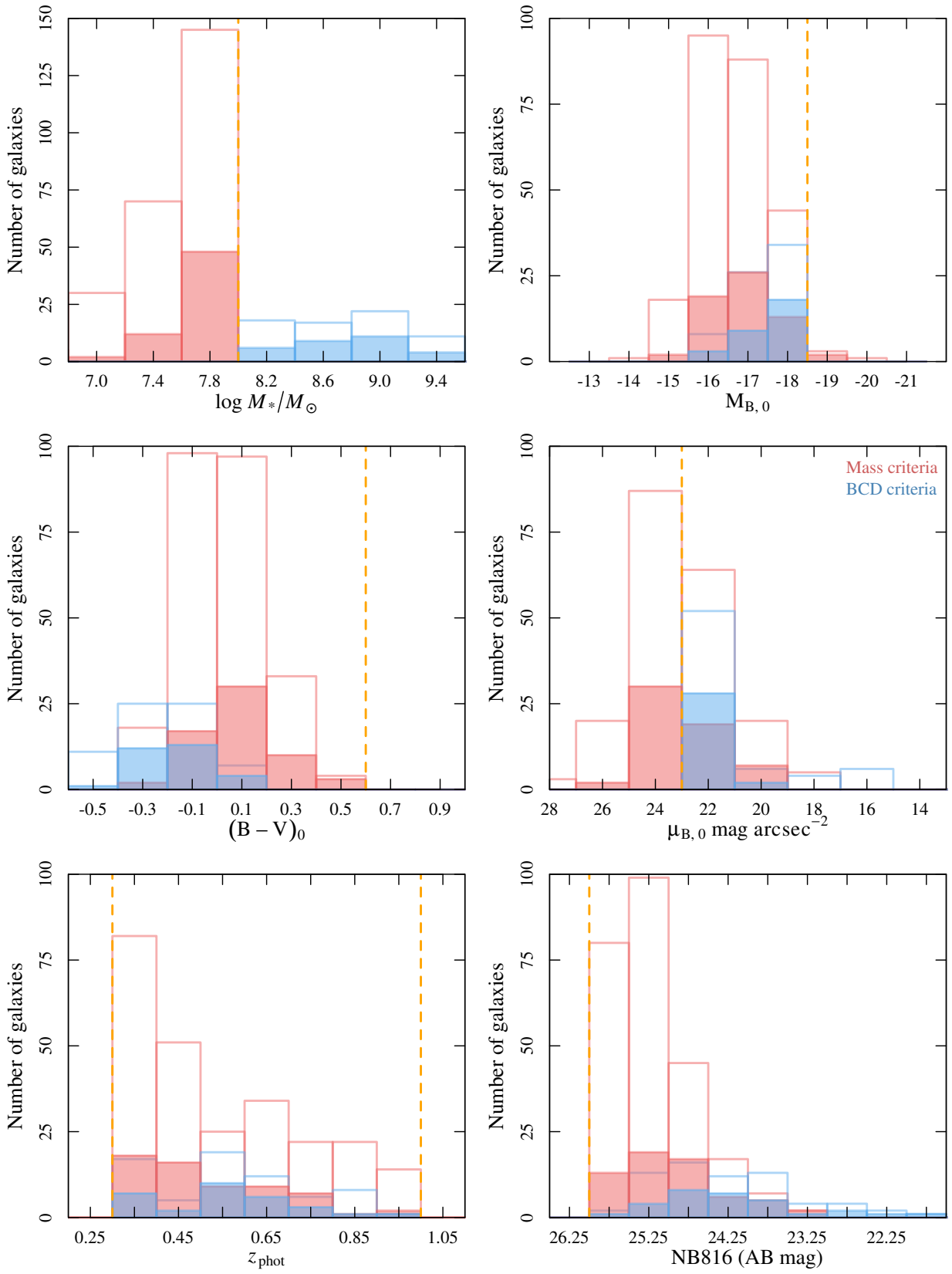

Figure 4.3: From top to bottom and right to left we show the distribution of $\log M_*/\mathrm{M}_\odot$, $M_{\mathrm{B,0,AB}}$, $(B-V)_0$, $S_{\mathrm{Reff,B,0}}/$ mag arcsec^{-2}, z_{phot}, and apparent magnitude in the seleccion band Subaru NB816 for the sample of galaxies for which we are able to measure a spectroscopic redshifts (filled histograms), and the initial sample (open histogram). We separate the sample into the two subsamples of galaxies selected using the two selection criteria: a stellar mass criterion (red), and a set of criteria based on the properties of BCDs (blue).

Table 4.12: Redshifts and emission lines measurements. Table 1.

ID	z_{spec}	HeIλ3531		[OII]λ3727		H10		H9		[NeIII]λ3868	
		F	EW$_{rf}$	F	EW$_{rf}$	F	EW$_{rf}$	F	EW$_{rf}$	F	EW$_{rf}$
(1)	(2)	(3)	(4)	(5)	(6)	(7)	(8)	(9)	(10)	(11)	(12)
17	0.642	–	–	$0.3^{0.5}_{0.1}$	14^{29}_{6}	–	–	–	–	–	–
26	0.517	–	–	$0.3^{0.3}_{0.2}$	32^{45}_{24}	–	–	–	–	–	–
35	0.656	–	–	$1.9^{2.1}_{1.6}$	51^{70}_{37}	–	–	–	–	$0.9^{1.1}_{0.5}$	16^{24}_{9}
53	0.742	–	–	$0.5^{0.6}_{0.5}$	63^{93}_{46}	–	–	–	–	–	–
88	0.553	–	–	$19.7^{21.2}_{18.3}$	106^{139}_{85}	$0.7^{1.5}_{0.2}$	4^{10}_{1}	$0.7^{1.4}_{0.1}$	4^{10}_{1}	$8.2^{9.3}_{7.1}$	49^{66}_{37}
145	0.521	–	–	$2.1^{2.2}_{1.9}$	97^{128}_{79}	–	–	–	–	–	–
156	0.513	–	–	$0.8^{0.9}_{0.7}$	47^{63}_{37}	–	–	–	–	–	–
173	0.214	–	–	–	–	–	–	–	–	–	–
181	0.759	–	–	$6.9^{7.6}_{6.3}$	70^{94}_{57}	–	–	–	–	$0.7^{1.2}_{0.1}$	6^{12}_{1}
183	0.532	–	–	$0.4^{0.4}_{0.3}$	37^{62}_{23}	–	–	–	–	$0.2^{0.2}_{0.1}$	14^{23}_{9}
193	0.482	–	–	$0.6^{0.7}_{0.5}$	34^{55}_{21}	–	–	–	–	–	–
195	0.538	–	–	$0.7^{0.7}_{0.6}$	71^{94}_{57}	–	–	–	–	$0.1^{0.2}_{0.1}$	10^{17}_{6}
220	0.119	–	–	–	–	–	–	–	–	–	–
227	0.672	–	–	$0.4^{0.4}_{0.3}$	50^{69}_{36}	–	–	–	–	–	–
235	0.840	–	–	–	–	–	–	–	–	–	–
236	0.329	–	–	$0.4^{0.6}_{0.2}$	9^{15}_{4}	–	–	–	–	–	–
237	0.423	–	–	–	–	–	–	–	–	–	–
241	0.545	–	–	$0.3^{0.4}_{0.3}$	26^{139}_{134}	–	–	–	–	–	–
253	0.760	–	–	$0.2^{0.2}_{0.2}$	64^{39}_{143}	–	–	–	–	–	–
259	0.573	–	–	$5.3^{6.0}_{4.6}$	47^{63}_{36}	–	–	–	–	$0.8^{1.4}_{0.1}$	6^{13}_{1}
277	0.437	–	–	$0.3^{0.4}_{0.2}$	18^{32}_{9}	–	–	–	–	–	–
293	0.545	–	–	$0.4^{0.5}_{0.3}$	40^{70}_{27}	–	–	–	–	–	–
296	0.261	–	–	–	–	–	–	–	–	$0.4^{0.6}_{0.2}$	11^{21}_{5}
297	0.446	–	–	–	–	–	–	–	–	–	–
306	0.576	–	–	$1.2^{1.3}_{1.0}$	46^{61}_{35}	–	–	–	–	–	–
312	1.216	–	–	$2.7^{2.9}_{2.6}$	77^{101}_{60}	–	–	–	–	$0.5^{0.7}_{0.4}$	13^{20}_{8}
315	0.132	–	–	–	–	–	–	–	–	–	–
317	0.620	–	–	$1.0^{1.2}_{0.8}$	45^{71}_{29}	–	–	–	–	–	–
386	0.400	–	–	$0.7^{0.8}_{0.5}$	24^{35}_{16}	–	–	–	–	–	–
396	0.310	–	–	–	–	–	–	–	–	–	–
440	0.535	–	–	$0.5^{0.6}_{0.4}$	35^{66}_{21}	–	–	–	–	–	–
454	0.536	–	–	$1.1^{1.2}_{0.9}$	50^{71}_{37}	$0.2^{0.3}_{0.0}$	7^{15}_{2}	–	–	–	–
455	0.687	–	–	$0.6^{0.6}_{0.5}$	48^{62}_{36}	–	–	–	–	–	–
464	0.729	–	–	$1.0^{1.1}_{0.9}$	65^{109}_{47}	–	–	–	–	–	–
481	0.954	–	–	$2.1^{2.3}_{1.9}$	63^{81}_{50}	–	–	–	–	–	–
488	0.533	–	–	$1.5^{1.7}_{1.4}$	59^{77}_{45}	–	–	–	–	–	–
490	0.856	–	–	$3.5^{3.8}_{3.3}$	81^{101}_{66}	–	–	–	–	$0.5^{0.7}_{0.3}$	10^{17}_{5}
510	1.329	–	–	$1.2^{1.4}_{1.1}$	33^{46}_{24}	–	–	–	–	–	–
519	0.909	–	–	$3.9^{4.1}_{3.8}$	146^{188}_{119}	–	–	–	–	$0.9^{1.0}_{0.7}$	26^{36}_{18}
520	0.445	–	–	$1.1^{1.4}_{0.9}$	31^{45}_{20}	–	–	$0.3^{0.5}_{0.1}$	8^{18}_{2}	–	–
524	1.250	–	–	–	–	–	–	–	–	$1.2^{1.3}_{1.1}$	50^{71}_{39}
536	0.578	–	–	–	–	–	–	–	–	–	–
539	0.739	–	–	$0.7^{0.8}_{0.6}$	90^{150}_{59}	–	–	–	–	$0.3^{0.3}_{0.2}$	15^{23}_{10}
543	0.720	–	–	$0.3^{0.6}_{0.0}$	7^{14}_{1}	–	–	–	–	–	–
544	0.436	–	–	$0.8^{1.0}_{0.7}$	56^{80}_{39}	–	–	–	–	–	–
551	0.246	–	–	–	–	–	–	–	–	–	–
565	0.567	–	–	$1.1^{1.3}_{1.0}$	44^{62}_{32}	–	–	–	–	–	–
571	0.684	–	–	$0.4^{0.5}_{0.4}$	40^{56}_{30}	–	–	–	–	–	–
584	0.767	–	–	$4.3^{4.8}_{4.0}$	74^{100}_{60}	–	–	–	–	–	–
594	0.263	–	–	–	–	–	–	–	–	–	–
601	0.534	–	–	$0.3^{0.4}_{0.2}$	20^{31}_{13}	–	–	–	–	–	–
612	0.786	–	–	$0.7^{0.8}_{0.7}$	97^{139}_{78}	–	–	–	–	–	–
626	0.656	–	–	$0.8^{0.9}_{0.7}$	48^{73}_{35}	–	–	–	–	–	–
634	1.255	–	–	$4.6^{4.7}_{4.4}$	154^{192}_{127}	–	–	–	–	$0.2^{0.3}_{0.1}$	5^{9}_{2}
642	0.817	–	–	$0.4^{0.5}_{0.2}$	13^{26}_{7}	–	–	–	–	–	–
1017	0.674	–	–	$0.3^{0.5}_{0.1}$	14^{26}_{5}	–	–	–	–	–	–
1032	0.467	–	–	$3.7^{5.7}_{1.9}$	14^{25}_{7}	–	–	–	–	–	–
1056	0.522	–	–	$3.0^{3.5}_{2.4}$	40^{55}_{29}	–	–	–	–	–	–
1090	0.610	–	–	$0.6^{0.6}_{0.5}$	70^{103}_{52}	–	–	–	–	–	–
1126	0.864	–	–	$1.8^{2.0}_{1.7}$	156^{408}_{79}	–	–	–	–	–	–
1202	0.679	–	–	$0.8^{1.0}_{0.5}$	22^{34}_{13}	–	–	–	–	–	–
1220	0.487	–	–	$1.9^{2.2}_{1.7}$	60^{88}_{46}	–	–	–	–	–	–
1234	0.436	–	–	$1.9^{2.2}_{1.6}$	62^{91}_{41}	–	–	–	–	–	–
1245	0.678	–	–	$1.1^{1.4}_{0.9}$	34^{49}_{26}	–	–	–	–	–	–

Continues on next page

Table 4.12: Redshifts and emission lines measurements. Table 1. Cont.

ID	z_{spec}	HeIλ3531		[OII]λ3727		H10		H9		[NeIII]λ3868	
		F	EW$_{rf}$	F	EW$_{rf}$	F	EW$_{rf}$	F	EW$_{rf}$	F	EW$_{rf}$
(1)	(2)	(3)	(4)	(5)	(6)	(7)	(8)	(9)	(10)	(11)	(12)
1247	0.524	–	–	$1.0^{1.2}_{0.8}$	28^{41}_{20}	–	–	$0.1^{0.2}_{0.1}$	2^{8}_{2}	–	–
1251	0.434	–	–	–	–	–	–	–	–	–	–
1309	0.743	–	–	$1.0^{1.1}_{0.9}$	75^{99}_{60}	–	–	–	–	–	–
1313	0.578	–	–	$2.4^{2.8}_{2.1}$	43^{59}_{31}	–	–	–	–	–	–
1332	0.339	–	–	$1.4^{1.6}_{1.2}$	54^{75}_{41}	–	–	–	–	–	–
1344	0.374	–	–	$1.7^{2.0}_{1.4}$	47^{64}_{32}	–	–	–	–	$1.2^{1.5}_{1.0}$	28^{41}_{20}
1378	0.343	–	–	$1.5^{1.8}_{1.2}$	31^{46}_{21}	–	–	–	–	$0.4^{0.6}_{0.1}$	6^{13}_{1}
1403	0.688	–	–	$2.6^{3.1}_{2.1}$	44^{63}_{31}	–	–	–	–	–	–
1454	0.738	–	–	$0.7^{0.8}_{0.7}$	114^{707}_{557}	–	–	–	–	–	–
1514	0.782	–	–	$0.1^{0.1}_{0.0}$	3^{8}_{0}	–	–	–	–	–	–
1585	0.661	–	–	$1.7^{2.1}_{1.3}$	37^{54}_{25}	–	–	–	–	–	–
1605	0.888	–	–	$0.3^{0.4}_{0.2}$	46^{85}_{26}	–	–	–	–	–	–
1656	0.870	–	–	$0.8^{0.9}_{0.7}$	62^{88}_{46}	–	–	–	–	–	–
1723	0.733	–	–	$0.5^{0.6}_{0.4}$	29^{47}_{19}	–	–	–	–	–	–
1727	0.540	–	–	$1.2^{1.4}_{1.0}$	47^{66}_{34}	–	–	–	–	–	–
1752	0.147	–	–	–	–	–	–	–	–	–	–
1765	0.957	–	–	$0.5^{0.5}_{0.5}$	74^{111}_{58}	–	–	–	–	–	–
1796	0.532	–	–	$6.3^{7.4}_{5.1}$	35^{50}_{26}	–	–	–	–	–	–
1804	0.533	$0.2^{0.3}_{0.1}$	8^{14}_{3}	$0.7^{0.9}_{0.5}$	36^{54}_{24}	–	–	–	–	–	–
1860	0.863	–	–	$1.3^{1.6}_{1.0}$	19^{27}_{14}	–	–	–	–	$0.3^{0.6}_{0.1}$	4^{8}_{1}
1861	0.538	–	–	$2.3^{2.7}_{1.9}$	30^{42}_{23}	–	–	–	–	–	–
2010	0.424	–	–	$1.3^{1.4}_{1.1}$	72^{99}_{54}	–	–	–	–	–	–

Table 4.13: Redshifts and emission lines measurements. Table 2.

ID	z_{spec}	HeIλ3889+H8		[NeIII]λ3968+H7		Hδ		Hγ		[OIII]λ4363		HeIλ4471	
		F	EW$_{rf}$	F	EW$_{rf}$	F	EW$_{rf}$	F	EW$_{rf}$	F	EW$_{rf}$	F	EW$_{rf}$
(1)	(2)	(3)	(4)	(5)	(6)	(7)	(8)	(9)	(10)	(11)	(12)	(13)	(14)
17	0.642	–	–	–	–	–	–	–	–	–	–	–	–
26	0.517	–	–	–	–	–	–	–	–	–	–	–	–
35	0.656	–	–	–	–	–	–	$0.3^{0.6}_{0.1}$	7^{13}_{1}	–	–	–	–
53	0.742	–	–	–	–	–	–	–	–	–	–	–	–
88	0.553	$2.8^{3.6}_{2.0}$	17^{25}_{11}	$4.9^{5.9}_{3.8}$	29^{42}_{20}	$4.2^{5.2}_{3.1}$	27^{39}_{17}	$7.9^{8.9}_{7.0}$	57^{73}_{44}	$1.6^{2.5}_{0.9}$	11^{18}_{5}	$0.7^{1.3}_{0.1}$	5^{11}_{1}
145	0.521	–	–	–	–	$0.2^{0.3}_{0.1}$	8^{17}_{3}	$0.2^{0.3}_{0.0}$	7^{15}_{1}	–	–	–	–
156	0.513	–	–	–	–	–	–	–	–	–	–	–	–
173	0.214	–	–	–	–	–	–	–	–	–	–	–	–
181	0.759	–	–	$0.1^{0.6}_{0.4}$	1^{5}_{3}	$0.2^{0.8}_{0.3}$	2^{7}_{2}	$0.2^{0.9}_{0.5}$	2^{10}_{3}	–	–	–	–
183	0.532	–	–	–	–	–	–	$0.2^{0.3}_{0.2}$	25^{39}_{14}	–	–	–	–
193	0.482	–	–	–	–	–	–	–	–	–	–	–	–
195	0.538	–	–	–	–	–	–	$0.2^{0.2}_{0.2}$	22^{35}_{16}	–	–	–	–
220	0.119	–	–	–	–	–	–	–	–	–	–	–	–
227	0.672	–	–	–	–	–	–	–	–	–	–	–	–
235	0.840	–	–	–	–	–	–	–	–	–	–	–	–
236	0.329	–	–	–	–	–	–	–	–	–	–	–	–
237	0.423	–	–	–	–	–	–	–	–	–	–	–	–
241	0.545	–	–	–	–	–	–	–	–	–	–	–	–
253	0.760	–	–	–	–	–	–	–	–	–	–	–	–
259	0.573	–	–	–	–	–	–	$0.6^{1.4}_{0.1}$	5^{12}_{0}	$0.4^{0.9}_{0.2}$	3^{8}_{2}	–	–
277	0.437	–	–	–	–	–	–	–	–	–	–	–	–
293	0.545	–	–	–	–	–	–	–	–	–	–	–	–
296	0.261	–	–	$0.4^{0.5}_{0.2}$	18^{31}_{9}	$0.3^{0.5}_{0.2}$	15^{26}_{8}	$0.6^{0.7}_{0.5}$	36^{53}_{25}	–	–	–	–
297	0.446	–	–	–	–	–	–	–	–	–	–	–	–
306	0.576	–	–	–	–	–	–	–	–	–	–	–	–
312	1.216	–	–	–	–	–	–	–	–	–	–	–	–
315	0.132	–	–	–	–	–	–	–	–	–	–	–	–
317	0.620	–	–	–	–	–	–	–	–	–	–	–	–
386	0.400	–	–	–	–	–	–	$0.1^{0.2}_{0.1}$	1^{7}_{3}	–	–	–	–
396	0.310	–	–	–	–	–	–	–	–	–	–	–	–
440	0.535	–	–	–	–	–	–	–	–	–	–	–	–
454	0.536	–	–	–	–	–	–	$0.1^{0.2}_{0.0}$	4^{9}_{1}	–	–	–	–

Continues on next page

Table 4.13: Redshifts and emission lines measurements. Table 2. Cont.

ID	z_{spec}	HeIλ3889+H8		[NeIII]λ3968+H7		Hδ		Hγ		[OIII]λ4363		HeIλ4471	
		F	EW$_{rf}$	F	EW$_{rf}$	F	EW$_{rf}$	F	EW$_{rf}$	F	EW$_{rf}$	F	EW$_{rf}$
(1)	(2)	(3)	(4)	(5)	(6)	(7)	(8)	(9)	(10)	(11)	(12)	(13)	(14)
455	0.687	–	–	–	–	–	–	–	–	–	–	–	–
464	0.729	–	–	–	–	–	–	–	–	–	–	–	–
481	0.954	–	–	–	–	–	–	–	–	–	–	–	–
488	0.533	–	–	–	–	–	–	–	–	–	–	–	–
490	0.856	$0.2^{0.3}_{0.0}$	4^{11}_{1}	–	–	–	–	$0.4^{0.6}_{0.3}$	11^{20}_{6}	–	–	–	–
510	1.329	–	–	–	–	–	–	–	–	–	–	–	–
519	0.909	$0.3^{0.5}_{0.2}$	10^{18}_{5}	$0.5^{0.8}_{0.3}$	17^{28}_{9}	$0.5^{0.6}_{0.3}$	14^{23}_{7}	–	–	–	–	–	–
520	0.445	–	–	–	–	–	–	–	–	–	–	–	–
524	1.250	–	–	–	–	$0.9^{0.9}_{0.7}$	69^{147}_{184}	$1.2^{1.5}_{0.8}$	30^{64}_{87}	–	–	–	–
536	0.578	–	–	–	–	–	–	–	–	–	–	–	–
539	0.739	–	–	–	–	$0.1^{0.1}_{0.0}$	5^{12}_{0}	$0.3^{0.4}_{0.2}$	31^{59}_{16}	–	–	–	–
543	0.720	–	–	–	–	–	–	–	–	–	–	–	–
544	0.436	–	–	–	–	–	–	–	–	–	–	–	–
551	0.246	–	–	–	–	–	–	–	–	–	–	–	–
565	0.567	–	–	–	–	–	–	–	–	–	–	–	–
571	0.684	–	–	–	–	–	–	–	–	–	–	–	–
584	0.767	–	–	$0.3^{0.6}_{0.1}$	4^{10}_{1}	–	–	$0.8^{1.1}_{0.5}$	13^{22}_{8}	–	–	–	–
594	0.263	–	–	–	–	$0.1^{0.3}_{0.0}$	5^{12}_{0}	$0.3^{0.5}_{0.2}$	16^{27}_{8}	–	–	–	–
601	0.534	–	–	–	–	–	–	–	–	–	–	–	–
612	0.786	–	–	–	–	–	–	–	–	–	–	–	–
626	0.656	–	–	–	–	–	–	$0.3^{0.3}_{0.2}$	19^{28}_{12}	–	–	–	–
634	1.255	–	–	–	–	–	–	–	–	–	–	–	–
642	0.817	–	–	–	–	–	–	–	–	–	–	–	–
1017	0.674	–	–	–	–	–	–	–	–	–	–	–	–
1032	0.467	–	–	–	–	–	–	–	–	–	–	–	–
1056	0.522	–	–	–	–	–	–	$0.0^{0.6}_{0.4}$	0^{7}_{4}	–	–	–	–
1090	0.610	–	–	–	–	–	–	–	–	–	–	–	–
1126	0.864	–	–	–	–	–	–	–	–	–	–	–	–
1202	0.679	–	–	–	–	–	–	–	–	–	–	–	–
1220	0.487	–	–	–	–	–	–	–	–	–	–	–	–
1234	0.436	–	–	–	–	–	–	–	–	–	–	–	–
1245	0.678	–	–	–	–	–	–	–	–	–	–	–	–
1247	0.524	$0.5^{0.7}_{0.3}$	17^{31}_{10}	$0.5^{0.7}_{0.3}$	12^{21}_{6}	$0.4^{0.5}_{0.2}$	9^{15}_{5}	$0.8^{1.0}_{0.5}$	27^{38}_{17}	$0.2^{0.4}_{0.0}$	8^{16}_{2}	–	–
1251	0.434	–	–	–	–	–	–	–	–	–	–	–	–
1309	0.743	–	–	–	–	–	–	–	–	–	–	–	–
1313	0.578	–	–	–	–	–	–	–	–	–	–	–	–
1332	0.339	–	–	–	–	–	–	–	–	–	–	–	–
1344	0.374	$0.6^{0.8}_{0.3}$	14^{23}_{8}	$1.2^{1.5}_{0.9}$	30^{43}_{19}	$1.0^{1.2}_{0.7}$	25^{36}_{17}	$2.2^{2.5}_{1.8}$	43^{58}_{33}	$0.4^{0.7}_{0.1}$	8^{15}_{3}	–	–
1378	0.343	–	–	–	–	–	–	–	–	–	–	–	–
1403	0.688	–	–	–	–	–	–	–	–	–	–	–	–
1454	0.738	–	–	–	–	–	–	–	–	–	–	–	–
1514	0.782	–	–	–	–	–	–	–	–	–	–	–	–
1585	0.661	–	–	–	–	–	–	–	–	–	–	–	–
1605	0.888	–	–	–	–	–	–	$0.1^{0.1}_{0.0}$	10^{21}_{3}	–	–	–	–
1656	0.870	–	–	–	–	–	–	$0.1^{0.2}_{0.1}$	9^{17}_{4}	–	–	–	–
1723	0.733	–	–	–	–	–	–	$0.1^{0.2}_{0.1}$	9^{14}_{5}	–	–	–	–
1727	0.540	–	–	–	–	–	–	–	–	–	–	–	–
1752	0.147	–	–	–	–	–	–	–	–	–	–	–	–
1765	0.957	–	–	–	–	–	–	–	–	–	–	–	–
1796	0.532	–	–	–	–	–	–	$0.3^{1.6}_{0.9}$	1^{8}_{4}	–	–	–	–
1804	0.533	–	–	–	–	–	–	–	–	–	–	–	–
1860	0.863	–	–	–	–	$0.7^{0.8}_{0.5}$	27^{43}_{17}	–	–	–	–	–	–
1861	0.538	–	–	–	–	–	–	–	–	–	–	–	–
2010	0.424	$0.2^{0.3}_{0.1}$	9^{16}_{3}	–	–	–	–	$0.0^{0.2}_{0.1}$	2^{8}_{3}	–	–	–	–

Table 4.14: Redshifts and emission lines measurements. Table 3.

ID	z_{spec}	Hβ		HeIλ4921		[OIII]λ4959		[OIII]λ5007		HeIλ5876	
		F	EW$_{rf}$	F	EW$_{rf}$	F	EW$_{rf}$	F	EW$_{rf}$	F	EW$_{rf}$
(1)	(2)	(3)	(4)	(5)	(6)	(7)	(8)	(9)	(10)	(11)	(12)
17	0.642	–	–	–	–	–	–	$0.8^{0.9}_{0.8}$	56^{77}_{43}	–	–

Continues on next page

Table 4.14: Redshifts and emission lines measurements. Table 3. Cont.

ID	z_{spec}	Hβ		HeIλ4921		[OIII]λ4959		[OIII]λ5007		HeIλ5876	
		F	EW$_{rf}$	F	EW$_{rf}$	F	EW$_{rf}$	F	EW$_{rf}$	F	EW$_{rf}$
(1)	(2)	(3)	(4)	(5)	(6)	(7)	(8)	(9)	(10)	(11)	(12)
26	0.517	–	–	–	–	–	–	–	–	–	–
35	0.656	$1.1^{1.3}_{0.8}$	26^{38}_{18}	–	–	$2.4^{2.6}_{2.1}$	52^{68}_{40}	–	–	–	–
53	0.742	–	–	–	–	–	–	$1.3^{1.3}_{1.2}$	146^{201}_{115}	–	–
88	0.553	$16.3^{17.3}_{15.4}$	139^{173}_{112}	–	–	$41.5^{42.3}_{40.5}$	377^{455}_{314}	$108.1^{109.0}_{107.0}$	978^{1205}_{823}	$1.4^{2.0}_{0.8}$	25^{48}_{11}
145	0.521	$0.5^{0.6}_{0.3}$	17^{24}_{10}	–	–	$0.6^{0.7}_{0.4}$	21^{28}_{15}	$0.7^{0.9}_{0.6}$	26^{36}_{19}	–	–
156	0.513	–	–	–	–	$0.2^{0.4}_{0.1}$	11^{19}_{5}	$1.2^{1.3}_{1.0}$	82^{128}_{58}	–	–
173	0.214	–	–	–	–	–	–	$0.7^{0.8}_{0.6}$	99^{193}_{60}	–	–
181	0.759	$2.2^{2.7}_{1.6}$	26^{41}_{16}	–	–	$2.5^{3.0}_{2.0}$	30^{42}_{22}	$7.8^{8.5}_{7.3}$	100^{127}_{81}	–	–
183	0.532	$0.6^{0.6}_{0.6}$	64^{92}_{50}	–	–	$1.2^{1.2}_{1.1}$	127^{159}_{104}	$3.1^{3.1}_{3.0}$	322^{406}_{262}	–	–
193	0.482	$0.3^{0.4}_{0.1}$	11^{20}_{5}	–	–	–	–	$1.0^{1.2}_{0.9}$	44^{66}_{32}	–	–
195	0.538	$0.5^{0.5}_{0.4}$	96^{157}_{69}	–	–	$0.4^{0.4}_{0.3}$	53^{88}_{38}	$2.3^{2.3}_{2.2}$	265^{366}_{214}	–	–
220	0.119	$0.3^{0.3}_{0.2}$	14^{22}_{8}	–	–	–	–	$0.4^{0.5}_{0.2}$	20^{30}_{12}	–	–
227	0.672	–	–	–	–	–	–	–	–	–	–
235	0.840	–	–	–	–	$0.3^{0.3}_{0.3}$	59^{84}_{44}	$1.1^{1.1}_{1.1}$	417^{828}_{266}	–	–
236	0.329	$0.4^{0.6}_{0.1}$	10^{18}_{3}	–	–	$0.5^{0.7}_{0.3}$	14^{22}_{7}	$1.6^{1.8}_{1.4}$	44^{58}_{34}	–	–
237	0.423	–	–	–	–	–	–	$0.3^{0.4}_{0.2}$	25^{39}_{15}	–	–
241	0.545	$0.2^{0.3}_{0.2}$	14^{25}_{8}	–	–	$0.2^{0.3}_{0.1}$	14^{24}_{6}	$0.4^{0.5}_{0.4}$	29^{40}_{21}	–	–
253	0.760	$0.2^{0.3}_{0.2}$	12^{17}_{9}	–	–	$0.6^{0.7}_{0.6}$	42^{51}_{35}	$2.0^{2.0}_{1.9}$	160^{207}_{137}	–	–
259	0.573	$1.1^{2.0}_{0.4}$	11^{23}_{3}	–	–	$2.1^{3.1}_{1.1}$	11^{19}_{5}	$7.8^{8.9}_{6.8}$	47^{63}_{36}	–	–
277	0.437	–	–	–	–	$0.3^{0.4}_{0.2}$	21^{34}_{12}	$0.8^{0.9}_{0.7}$	51^{74}_{37}	–	–
293	0.545	$0.2^{0.3}_{0.1}$	14^{21}_{8}	–	–	–	–	$0.2^{0.3}_{0.1}$	13^{20}_{8}	–	–
296	0.261	$1.5^{1.5}_{1.4}$	125^{152}_{103}	–	–	$1.6^{1.7}_{1.5}$	145^{211}_{110}	$4.8^{5.0}_{4.7}$	419^{568}_{327}	–	–
297	0.446	$0.3^{0.4}_{0.3}$	69^{105}_{49}	–	–	$0.4^{0.5}_{0.4}$	53^{68}_{43}	–	–	–	–
306	0.576	$0.6^{0.8}_{0.5}$	25^{47}_{17}	–	–	$0.5^{0.6}_{0.4}$	21^{28}_{14}	$2.1^{2.3}_{1.9}$	111^{158}_{85}	–	–
312	1.216	–	–	–	–	–	–	–	–	–	–
315	0.132	–	–	–	–	–	–	$0.3^{0.4}_{0.2}$	29^{48}_{18}	–	–
317	0.620	–	–	–	–	–	–	$1.0^{1.2}_{0.9}$	32^{46}_{21}	–	–
386	0.400	$0.3^{0.5}_{0.0}$	6^{13}_{1}	–	–	$0.3^{0.5}_{0.1}$	8^{13}_{2}	$1.2^{1.4}_{0.9}$	31^{43}_{22}	–	–
396	0.310	–	–	–	–	–	–	$0.3^{0.4}_{0.1}$	11^{19}_{4}	–	–
440	0.535	$0.1^{0.2}_{0.1}$	13^{20}_{9}	–	–	$0.1^{0.2}_{0.1}$	15^{22}_{11}	$0.7^{0.7}_{0.7}$	69^{89}_{55}	–	–
454	0.536	$0.6^{0.8}_{0.5}$	31^{44}_{20}	–	–	$0.6^{0.7}_{0.5}$	31^{43}_{21}	$1.8^{1.9}_{1.6}$	86^{110}_{71}	–	–
455	0.687	$0.1^{0.2}_{0.0}$	6^{17}_{1}	–	–	$0.2^{0.3}_{0.2}$	19^{32}_{10}	$0.7^{0.8}_{0.7}$	69^{96}_{52}	–	–
464	0.729	$0.3^{0.4}_{0.3}$	19^{31}_{14}	–	–	–	–	$1.4^{1.5}_{1.4}$	86^{116}_{70}	–	–
481	0.954	–	–	–	–	–	–	–	–	–	–
488	0.533	$0.2^{0.4}_{0.1}$	5^{12}_{2}	–	–	–	–	$0.8^{1.0}_{0.6}$	25^{36}_{17}	–	–
490	0.856	$1.1^{1.2}_{0.9}$	32^{43}_{24}	–	–	$1.9^{2.1}_{1.7}$	69^{97}_{52}	$5.3^{5.4}_{5.2}$	254^{340}_{197}	–	–
510	1.329	–	–	–	–	–	–	–	–	–	–
519	0.909	$2.2^{2.3}_{2.1}$	148^{212}_{107}	–	–	$1.8^{1.9}_{1.7}$	84^{105}_{65}	$8.5^{8.6}_{8.4}$	321^{414}_{259}	–	–
520	0.445	$0.4^{0.6}_{0.2}$	10^{18}_{4}	–	–	$0.5^{0.7}_{0.2}$	11^{19}_{4}	$2.2^{2.5}_{1.9}$	53^{74}_{38}	–	–
524	1.250	–	–	–	–	–	–	–	–	–	–
536	0.578	$0.3^{0.3}_{0.3}$	45^{61}_{35}	–	–	$0.7^{0.8}_{0.7}$	111^{142}_{88}	$1.7^{1.7}_{1.7}$	267^{384}_{208}	–	–
539	0.739	–	–	–	–	–	–	$2.3^{2.4}_{2.2}$	166^{238}_{127}	–	–
543	0.720	–	–	–	–	$0.4^{0.6}_{0.1}$	7^{14}_{2}	$0.4^{0.7}_{0.2}$	9^{16}_{3}	–	–
544	0.436	$0.3^{0.4}_{0.3}$	38^{58}_{23}	–	–	$0.4^{0.5}_{0.4}$	42^{58}_{31}	$1.1^{1.2}_{1.0}$	71^{96}_{54}	–	–
551	0.246	$0.1^{0.4}_{0.2}$	2^{8}_{3}	–	–	–	–	$0.5^{0.8}_{0.2}$	12^{21}_{3}	–	–
565	0.567	–	–	–	–	–	–	–	–	–	–
571	0.684	$0.1^{0.2}_{0.0}$	6^{11}_{1}	–	–	–	–	–	–	–	–
584	0.767	$1.6^{1.8}_{1.4}$	36^{49}_{28}	–	–	–	–	$7.6^{7.9}_{7.4}$	206^{256}_{171}	–	–
594	0.263	$1.2^{1.3}_{1.1}$	54^{69}_{43}	–	–	$2.4^{2.6}_{2.2}$	115^{146}_{94}	$6.8^{7.0}_{6.6}$	310^{376}_{262}	–	–
601	0.534	–	–	–	–	–	–	$0.6^{0.8}_{0.5}$	31^{54}_{18}	–	–
612	0.786	–	–	–	–	$1.0^{1.1}_{1.0}$	176^{442}_{93}	$3.9^{4.0}_{3.8}$	556^{1209}_{270}	–	–
626	0.656	$0.7^{0.7}_{0.6}$	119^{182}_{86}	–	–	$1.2^{1.3}_{1.2}$	225^{382}_{160}	–	–	–	–
634	1.255	–	–	–	–	–	–	–	–	–	–
642	0.817	–	–	–	–	–	–	$1.9^{2.1}_{1.8}$	149^{219}_{383}	–	–
1017	0.674	–	–	–	–	–	–	–	–	–	–
1032	0.467	$1.1^{2.6}_{0.6}$	4^{13}_{2}	–	–	$1.2^{2.6}_{0.3}$	5^{11}_{1}	$3.3^{5.2}_{1.5}$	13^{24}_{5}	–	–
1056	0.522	$0.6^{0.9}_{0.2}$	6^{11}_{2}	–	–	$0.4^{0.9}_{0.1}$	4^{11}_{1}	$0.3^{0.8}_{0.1}$	3^{10}_{1}	–	–
1090	0.610	–	–	–	–	–	–	–	–	–	–
1126	0.864	$1.2^{1.3}_{1.1}$	94^{164}_{62}	–	–	$1.2^{1.3}_{1.1}$	124^{266}_{65}	$1.8^{1.8}_{1.7}$	262^{654}_{118}	–	–
1202	0.679	$0.2^{0.4}_{0.0}$	4^{10}_{0}	–	–	–	–	–	–	–	–
1220	0.487	$0.2^{0.3}_{0.1}$	7^{11}_{3}	–	–	$0.8^{1.0}_{0.6}$	29^{44}_{19}	$2.9^{3.1}_{2.7}$	119^{169}_{84}	–	–
1234	0.436	$0.4^{0.7}_{0.1}$	11^{20}_{3}	–	–	$0.3^{0.6}_{0.0}$	7^{13}_{1}	$1.4^{1.7}_{1.1}$	34^{49}_{23}	–	–
1245	0.678	$0.3^{0.5}_{0.1}$	10^{20}_{3}	–	–	$0.8^{1.0}_{0.7}$	24^{34}_{18}	$2.0^{2.1}_{1.8}$	59^{78}_{48}	–	–
1247	0.524	$1.8^{2.0}_{1.7}$	79^{105}_{64}	–	–	$3.0^{3.1}_{2.8}$	140^{178}_{115}	$4.7^{4.9}_{4.5}$	220^{284}_{181}	–	–
1251	0.434	$0.2^{0.3}_{0.1}$	11^{17}_{6}	–	–	$0.6^{0.7}_{0.4}$	27^{38}_{19}	$0.2^{0.3}_{0.0}$	12^{7}_{17}	–	–
1309	0.743	–	–	–	–	–	–	$0.8^{0.9}_{0.7}$	52^{74}_{36}	–	–

Continues on next page

Table 4.14: Redshifts and emission lines measurements. Table 3. Cont.

ID	z_{spec}	Hβ		HeIλ4921		[OIII]λ4959		[OIII]λ5007		HeIλ5876	
		F	EW$_{rf}$	F	EW$_{rf}$	F	EW$_{rf}$	F	EW$_{rf}$	F	EW$_{rf}$
(1)	(2)	(3)	(4)	(5)	(6)	(7)	(8)	(9)	(10)	(11)	(12)
1313	0.578	$0.8^{1.2}_{0.4}$	11^{20}_{4}	–	–	$1.0^{1.4}_{0.6}$	14^{23}_{8}	$2.3^{2.7}_{1.9}$	33^{44}_{25}	–	–
1332	0.339	$0.7^{0.9}_{0.4}$	19^{31}_{12}	–	–	$0.9^{1.1}_{0.7}$	27^{40}_{17}	$3.1^{3.4}_{2.9}$	94^{120}_{76}	–	–
1344	0.374	$5.8^{6.2}_{5.5}$	135^{169}_{110}	–	–	$11.9^{12.3}_{11.5}$	271^{331}_{221}	$38.1^{38.5}_{37.8}$	908^{1108}_{774}	$0.6^{0.8}_{0.4}$	25^{41}_{16}
1378	0.343	$0.1^{0.4}_{0.2}$	2^{7}_{2}	–	–	$0.5^{1.0}_{0.1}$	8^{16}_{1}	$1.5^{1.9}_{1.1}$	24^{34}_{15}	–	–
1403	0.688	$0.7^{1.0}_{0.3}$	11^{19}_{4}	–	–	–	–	–	–	–	–
1454	0.738	–	–	–	–	–	–	$0.4^{0.5}_{0.4}$	105^{369}_{417}	–	–
1514	0.782	–	–	–	–	–	–	–	–	–	–
1585	0.661	–	–	–	–	$0.3^{0.6}_{0.1}$	6^{12}_{1}	$1.0^{1.3}_{0.8}$	20^{32}_{12}	–	–
1605	0.888	$0.1^{0.1}_{0.1}$	40^{76}_{26}	–	–	–	–	–	–	–	–
1656	0.870	–	–	–	–	$0.4^{0.4}_{0.3}$	83^{157}_{51}	–	–	–	–
1723	0.733	–	–	–	–	$0.2^{0.3}_{0.1}$	15^{25}_{7}	–	–	–	–
1727	0.540	–	–	–	–	–	–	–	–	–	–
1752	0.147	$0.5^{1.1}_{0.0}$	4^{9}_{0}	$0.4^{1.2}_{0.4}$	3^{10}_{3}	$0.8^{1.7}_{0.2}$	6^{15}_{1}	$3.8^{5.2}_{2.7}$	29^{47}_{18}	–	–
1765	0.957	–	–	–	–	$0.5^{0.5}_{0.5}$	84^{134}_{57}	$2.7^{2.8}_{2.6}$	154^{126}_{296}	–	–
1796	0.532	$2.3^{3.5}_{0.9}$	10^{17}_{4}	–	–	–	–	$1.9^{3.4}_{0.6}$	9^{18}_{3}	–	–
1804	0.533	–	–	$0.1^{0.3}_{0.0}$	6^{13}_{0}	–	–	–	–	–	–
1860	0.863	$1.1^{1.3}_{1.0}$	40^{62}_{29}	–	–	$1.3^{1.4}_{1.2}$	36^{52}_{28}	$4.1^{4.2}_{3.9}$	62^{73}_{54}	–	–
1861	0.538	$0.8^{1.4}_{0.4}$	9^{17}_{4}	–	–	$1.2^{2.0}_{0.5}$	14^{24}_{5}	$1.6^{2.1}_{1.1}$	18^{27}_{11}	–	–
2010	0.424	$0.6^{0.7}_{0.4}$	30^{44}_{20}	–	–	$1.1^{1.3}_{0.9}$	58^{83}_{43}	$3.4^{3.6}_{3.3}$	181^{232}_{146}	–	–

Table 4.15: Redshifts and emission lines measurements. Table 4.

ID	z_{spec}	Hα		[NII]λ6584		HeIλ6678		[NII]λ6717		[SII]λ6731	
		F	EW$_{rf}$	F	EW$_{rf}$	F	EW$_{rf}$	F	EW$_{rf}$	F	EW$_{rf}$
(1)	(2)	(3)	(4)	(5)	(6)	(7)	(8)	(9)	(10)	(11)	(12)
17	0.642	–	–	–	–	–	–	–	–	–	–
26	0.517	–	–	–	–	–	–	–	–	–	–
35	0.656	–	–	–	–	–	–	–	–	–	–
53	0.742	–	–	–	–	–	–	–	–	–	–
88	0.553	–	–	–	–	–	–	–	–	–	–
145	0.521	$1.9^{4.8}_{0.4}$	16^{13}_{38}	–	–	–	–	–	–	–	–
156	0.513	–	–	–	–	–	–	–	–	–	–
173	0.214	$0.8^{0.9}_{0.8}$	85^{126}_{65}	–	–	–	–	–	–	–	–
181	0.759	–	–	–	–	–	–	–	–	–	–
183	0.532	–	–	–	–	–	–	–	–	–	–
193	0.482	–	–	–	–	–	–	–	–	–	–
195	0.538	–	–	–	–	–	–	–	–	–	–
220	0.119	$1.4^{1.6}_{1.3}$	108^{139}_{87}	$0.1^{0.2}_{0.1}$	7^{13}_{3}	–	–	–	–	–	–
227	0.672	–	–	–	–	–	–	–	–	–	–
235	0.840	–	–	–	–	–	–	–	–	–	–
236	0.329	$1.8^{2.0}_{1.6}$	78^{104}_{61}	$1.6^{2.1}_{1.3}$	57^{94}_{36}	–	–	–	–	–	–
237	0.423	–	–	–	–	–	–	–	–	–	–
241	0.545	–	–	–	–	–	–	–	–	–	–
253	0.760	–	–	–	–	–	–	–	–	–	–
259	0.573	–	–	–	–	–	–	–	–	–	–
277	0.437	–	–	–	–	–	–	–	–	–	–
293	0.545	–	–	–	–	–	–	–	–	–	–
296	0.261	$3.5^{3.6}_{3.5}$	434^{583}_{347}	$0.2^{0.3}_{0.2}$	25^{37}_{17}	–	–	–	–	–	–
297	0.446	–	–	–	–	–	–	–	–	–	–
306	0.576	–	–	–	–	–	–	–	–	–	–
312	1.216	–	–	–	–	–	–	–	–	–	–
315	0.132	$0.4^{0.5}_{0.3}$	41^{177}_{17}	–	–	–	–	–	–	–	–
317	0.620	–	–	–	–	–	–	–	–	–	–
386	0.400	$1.0^{1.1}_{0.8}$	62^{102}_{40}	$0.1^{0.2}_{0.1}$	4^{16}_{3}	–	–	–	–	–	–
396	0.310	$0.7^{0.8}_{0.5}$	39^{54}_{27}	–	–	–	–	–	–	–	–
440	0.535	–	–	–	–	–	–	–	–	–	–
454	0.536	–	–	–	–	–	–	–	–	–	–
455	0.687	–	–	–	–	–	–	–	–	–	–
464	0.729	–	–	–	–	–	–	–	–	–	–
481	0.954	–	–	–	–	–	–	–	–	–	–

Continues on next page

Table 4.15: Redshifts and emission lines measurements. Table 4. Cont.

ID	z_{spec}	Hα		[NII]λ6584		HeIλ6678		[SII]λ6717		[SII]λ6731	
		F	EW$_{rf}$	F	EW$_{rf}$	F	EW$_{rf}$	F	EW$_{rf}$	F	EW$_{rf}$
(1)	(2)	(3)	(4)	(5)	(6)	(7)	(8)	(9)	(10)	(11)	(12)
488	0.533	–	–	–	–	–	–	–	–	–	–
490	0.856	–	–	–	–	–	–	–	–	–	–
510	1.329	–	–	–	–	–	–	–	–	–	–
519	0.909	–	–	–	–	–	–	–	–	–	–
520	0.445	–	–	–	–	–	–	–	–	–	–
524	1.250	–	–	–	–	–	–	–	–	–	–
536	0.578	–	–	–	–	–	–	–	–	–	–
539	0.739	–	–	–	–	–	–	–	–	–	–
543	0.720	–	–	–	–	–	–	–	–	–	–
544	0.436	–	–	–	–	–	–	–	–	–	–
551	0.246	$0.5^{0.8}_{0.2}$	16^{29}_{7}	$0.2^{0.4}_{0.1}$	5^{18}_{4}	–	–	–	–	–	–
565	0.567	–	–	–	–	–	–	–	–	–	–
571	0.684	–	–	–	–	–	–	–	–	–	–
584	0.767	–	–	–	–	–	–	–	–	–	–
594	0.263	$4.2^{4.3}_{4.1}$	328^{469}_{264}	–	–	–	–	–	–	–	–
601	0.534	–	–	–	–	–	–	–	–	–	–
612	0.786	–	–	–	–	–	–	–	–	–	–
626	0.656	–	–	–	–	–	–	–	–	–	–
634	1.255	–	–	–	–	–	–	–	–	–	–
642	0.817	–	–	–	–	–	–	–	–	–	–
1017	0.674	–	–	–	–	–	–	–	–	–	–
1032	0.467	$2.7^{4.0}_{1.5}$	17^{35}_{8}	–	–	–	–	–	–	–	–
1056	0.522	–	–	–	–	–	–	–	–	–	–
1090	0.610	–	–	–	–	–	–	–	–	–	–
1126	0.864	–	–	–	–	–	–	–	–	–	–
1202	0.679	–	–	–	–	–	–	–	–	–	–
1220	0.487	$1.5^{1.6}_{1.4}$	89^{72}_{119}	–	–	–	–	–	–	–	–
1234	0.436	–	–	–	–	–	–	–	–	–	–
1245	0.678	–	–	–	–	–	–	–	–	–	–
1247	0.524	–	–	–	–	–	–	–	–	–	–
1251	0.434	$0.4^{0.4}_{0.3}$	34^{51}_{24}	–	–	–	–	–	–	–	–
1309	0.743	–	–	–	–	–	–	–	–	–	–
1313	0.578	–	–	–	–	–	–	–	–	–	–
1332	0.339	–	–	–	–	–	–	–	–	–	–
1344	0.374	$14.0^{14.2}_{13.8}$	1047^{1451}_{785}	$0.3^{0.3}_{0.2}$	26^{69}_{12}	$0.2^{0.3}_{0.2}$	40^{68}_{25}	$0.2^{0.2}_{0.1}$	19^{30}_{12}	$0.2^{0.2}_{0.1}$	18^{27}_{12}
1378	0.343	$2.3^{2.6}_{1.9}$	46^{60}_{35}	–	–	–	–	–	–	–	–
1403	0.688	–	–	–	–	–	–	–	–	–	–
1454	0.738	–	–	–	–	–	–	–	–	–	–
1514	0.782	–	–	–	–	–	–	–	–	–	–
1585	0.661	–	–	–	–	–	–	–	–	–	–
1605	0.888	–	–	–	–	–	–	–	–	–	–
1656	0.870	–	–	–	–	–	–	–	–	–	–
1723	0.733	–	–	–	–	–	–	–	–	–	–
1727	0.540	–	–	–	–	–	–	–	–	–	–
1752	0.147	$4.9^{5.7}_{4.2}$	44^{60}_{35}	$0.3^{1.0}_{0.5}$	3^{11}_{4}	–	–	–	–	–	–
1765	0.957	–	–	–	–	–	–	–	–	–	–
1796	0.532	–	–	–	–	–	–	–	–	–	–
1804	0.533	–	–	–	–	–	–	–	–	–	–
1860	0.863	–	–	–	–	–	–	–	–	–	–
1861	0.538	–	–	–	–	–	–	–	–	–	–
2010	0.424	$1.5^{1.6}_{1.3}$	170^{322}_{107}	–	–	–	–	–	–	–	–

For each galaxy we report the spectroscopic redshift and emission line measurements. In particular, we show the median and 16th and 84th percentiles of the flux (F; 10^{17} erg s^{-1} cm^{-2}) and the equivalent width (EW; Å)

5

SED-fitting

The spectral energy distribution (SED) of an unresolved galaxy is the superposition of the light either emitted or reprocessed by its different components: stellar populations and inter-stellar medium (ISM), including gas and dust. Thus, a SED hides superposed traces of the properties of those components, and therefore, a detailed analysis of the SED of a galaxy should in theory allow us to fully understand the properties of such galaxy, and the evolutionary path the galaxy has undergone along cosmic times. Nevertheless, in practice, disentangling these properties is a difficult task due to the heterogeneous and complex nature of galaxies.

SED-fitting[1] methodology attempts to derive physical properties of galaxies by basically comparing their observed SEDs (multi-wavelength photometry, emission lines) to models. This technique is nowadays extensively applied to large cosmological surveys with the aim of better understanding the growth and aging of galaxies over cosmic times by deriving reliable estimates of mass, metallicity, SFR, formation epoch and SFHs (e.g., Kauffmann et al., 2003b; Pérez-González et al., 2008; Barro et al., 2011b; Skelton et al., 2014).

The approach we use in this work was developed by Pacifici et al. (2012). Summarizing, it consists on a Bayesian analysis that combines a large library of physically motivated SF and chemical enrichment histories from cosmological simulations with state-of-the-art models of stellar population synthesis, nebular emission, and attenuation by dust.

- Bayesian inference for SED-fitting is basically based on libraries of SED models and prior assumptions for the physical parameters, and it implies certain advantages with respect other approaches. Among them it is specially interesting the fact that uncertainties on the derived parameters include measurement uncertainties as well as intrinsic degeneracies.
- An important advantage of this approach by Pacifici et al. (2012) is that it allows to consider both photometric and spectroscopic information at the same time, what can improve the retrieved estimations of sSFR and oxygen abundance, and therefore, better constrain the properties of the ongoing SF process in star-forming galaxies.
- The use of physically motivated SF and chemical enrichment histories is also a key reason to use this approach. Specific simplified parametric SFHs have been found to be useful to reproduce properties of large samples of galaxies. Nevertheless, we believe that this singular approach can help us to better characterize the SFHs of our atypical sample of low-mass galaxies.

The application of this methodology to our sample of targets provides us with best estimates and confidence ranges of stellar mass ($M_*/M_\odot$), star formation rate (SFR$/M_\odot$yr^{-1}), specific star formation rate (sSFR$= SFR/M_*/$Gyr^{-1}), oxygen abundances ($12 + \log(\mathrm{O/H})$), and dust attenuation ($\hat{\tau}_V$), along with a best-estimate SFH for each galaxy.

[1] http://sedfitting.org/SED08/Welcome.html for a review on the technique and a summary of SED-fitting approaches.

In this Chapter we briefly describe the SED-fitting technique developed by Pacifici et al. (2012), and explain how we apply it to our novel observational data. In Chapters 7 and 8 we analyze and explain some of the results of this approach.

5.1 Modeling SEDs

By definition, the Bayesian approaches rely on our capability to synthesize realistic SED libraries, and synthetic observables comparable to observational data. Indeed, the build of a library of SED models is the key and most challenging step in this SED-fitting methodology. Actually, its biggest caveats are precisely the sensitivity to the prior distribution of parameters (that could bias the results) and, connected to this, the dependence on realistic input physics in the modeling. Building a library of models requires a detailed knowledge of the constituents of galaxies, their physical properties and processes, interactions, and evolution. Its complexity leads generally to the consideration of inevitable simplifications and assumptions.

In this approach we use (Pacifici et al., 2012), the luminosity as a function of wavelength produced by a galaxy at a time t is expressed as $T_\lambda^+(t, t')$

$$L_\lambda(t) = \int_0^t dt'\, L_{\lambda,\, stars}(t, t')\, T_{\lambda,\, ISM}(t, t') \tag{5.1}$$

where $L_{\lambda,\,\mathrm{stars}}$ is the contribution of the stars to the total luminosity of the galaxy, and $T_{\lambda,\,\mathrm{ISM}}(t, t')$ is the transmission function of the IGM. We divide $T_{\lambda,\,\mathrm{ISM}}(t, t')$ into the nebular continuum and emission lines contributions, $T_\lambda^+(t, t')$, and the neutral ISM transmission funcion, $T_\lambda^0(t, t')$.

$$T_{\lambda,\,\mathrm{ISM}}(t, t') = T_\lambda^+(t, t')\; T_\lambda^0(t, t') \tag{5.2}$$

In the following subsections we describe how each contribution is modeled.

5.1.1 Stellar Component

The emission of the stellar constituent of a galaxy is basically the superposition of the spectra emitted at a certain moment by the stellar populations (SPs) formed within the galaxy along its life. Therefore, it combines the emission of stars of different masses and metallicities (i.e. following different evolutionary paths) that belong to stellar populations of different ages.

The main ingredients required to perform the modeling of this galactic component are:

- The evolution of the SFR and the metallicity within the galaxy along the time, or star formation history (SFH) and enrichment evolution. Subsection 5.1.1.1.
- A prescription for the mass distribution of the stars formed by those SF processes, also referred to as initial mass function (IMF). Subsection 5.1.1.2.
- A theory for the evolution of stars of given initial mass and chemical composition.
- A library of stellar spectral energy distributions to describe the emission from any single star with a given mass, metallicity and age. In our case we use the state-of-the-art models of stellar population synthesis of Bruzual and Charlot (2003).

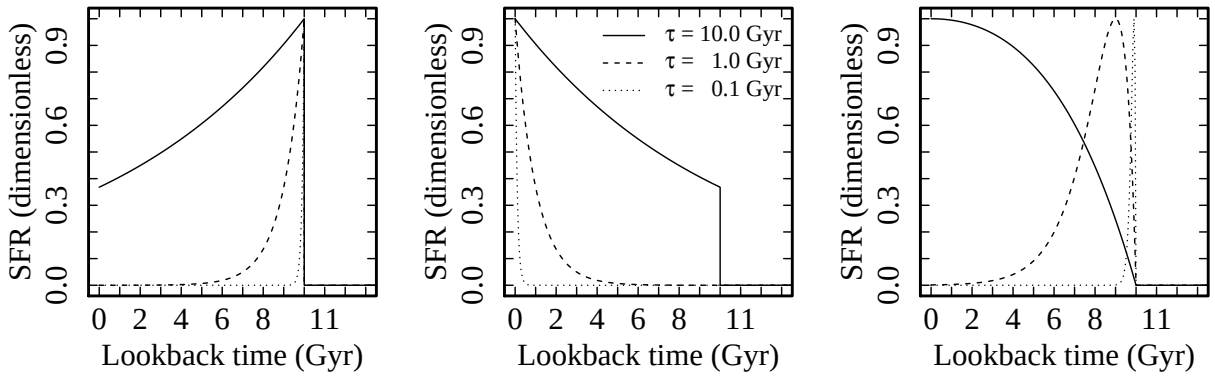

Figure 5.1: Left: τ-models. Central: Reversed exponential models. Right: Delayed τ-models. In each case we represent those curves for ages of 10 Gyr and $\tau = 0.1, 1, 10$ Gyr with dotted, dashed and solid lines, respectively. All the models shown are normalized by the higher value of SFR reached by the SFH.

Then, the stellar emission of a galaxy can be expressed as the

$$L_{\lambda,\,stars}(t) = \int_0^t dt'\,\psi(t-t')\,S_\lambda[t', Z(t-t')] \tag{5.3}$$

where $\psi(t-t')$ is the SFR at time $t-t'$, and $S_\lambda[t', Z(t-t')]$ is the luminosity per unit of wavelength and per unit of mass of a stellar population of age t' and metallicity $Z(t-t')$.

5.1.1.1 Star Formation and Chemical Enrichment Histories

Hence, first of all, we build a library of SF and chemical enrichment histories to be able to populate the model galaxies with SPs. In order to simplify the approaches, SFHs of stellar populations have been traditionally simplified by simple mathematical functions:

- *Instantaneous burst* of star formation, which forms a single stellar population of a common age.
- *Exponentially declining* or τ-models (Figure 5.1, left panel) following SFR$\propto\ e^{-t/\tau}$. When the timescale, τ, is comparable to or larger than the age of the stellar population, accounting from the moment the SF activity is ignited, these models are in practice equivalent to constant SFHs.
- *Constant SFR*. As we already mentioned, constant SFHs can be represented by a τ-model with a large timescale.
- *Reversed exponential* (Figure 5.1, central panel): SFR$\propto e^{t/\tau}$
- *Delayed*: SFR$\propto t\,e^{-t/\tau}$ (Figure 5.1, right panel). Also SFR$\propto t^2/\tau\,e^{-t/\tau}$.

Despite the fact that these descriptions have been proven to be successful to reproduce certain properties in specific types of galaxies, an increasing number of analyses have pointed out the limitations of simplified functions. One of the novelties and advantages of the approach by Pacifici et al. (2012) is that it uses a library of more sophisticated, physically motivated SF and chemical enrichment histories derived applying semi-analytic recipes (De Lucia and Blaizot, 2007) to the output of the Millennium cosmological simulation (Springel et al., 2005). This simulation follows the growth, interaction and merging history of dark matter haloes from redshift $z = 127$ to the present.

To characterize the SFHs in our libraries we define the following milestones of stellar mass assembly:

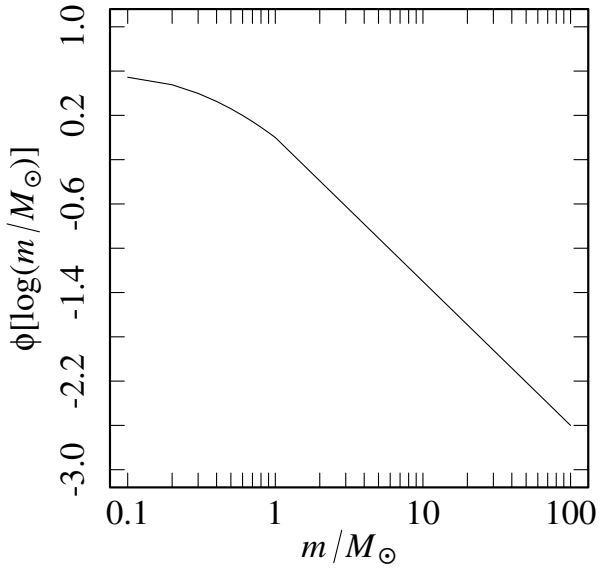

Figure 5.2: Chabrier IMF normalized to solar units.

- t_0: Lookback time at the onset of SF.
- t_{10}: Lookback time when a galaxy forms the 10% of the final stellar mass.
- t_{50}: Lookback time when a galaxy forms the 50% of the final stellar mass.

The library is tuned to avoid possible biases in the statistics and in the subsequent fitting process by randomly drawing the evolutionary stages at which a galaxy is looked at in the library linearly in lookback time, allowing for a uniform distribution of timescales (t_0) at each redshift (Figure A.1). A uniform distribution in t_0 gives to the fit all possible lengths of SFHs with no bias. The distributions of t_{10} and t_{50} (Figure A.2 and Figure A.3 respectively) are a consequence of both the t_0 distribution (for instance, if t_0 is short then t_{10} and t_{50} can only be short) and the shapes of the SFHs included in the library (for example, rising SFHs have shorter t_{50} than constant ones).

5.1.1.2 Initial Mass Function

The IMF allows to calculate the number of stars per unit of mass formed along the SFH. Among its different parametrizations most commonly used in the literature (e.g., Salpeter, 1955; Miller and Scalo, 1979; Kroupa, 2001) we use Chabrier (2003) IMF (Figure 5.2) defined by

$$\phi\left[\log(m)\right] \propto \begin{cases} exp\left[-\dfrac{(\log m - log\, m_c)^2}{2\sigma^2}\right] & \text{for } 0.1 \leq m/M_\odot < 1.0, \\ m^{1.3} & \text{for } 1.0 \leq m/M_\odot \end{cases} \tag{5.4}$$

where m is the mass, and $m_c = 0.079^{-0.016}_{+0.021}$ and $\sigma = 0.69^{-0.01}_{+0.05}$.

Theoretically, the IMF should change with star-forming conditions (Elmegreen 2004; Bate & Bonnell 2005; Larson 2005; Hennebelle & Chabrier 2008; Krumholz et al. 2011; Hopkins 2012). In this sence, further studies are still needed to fully characterize the shape of the appropriate IMF to the physical conditions of star formation in our type of galaxies. Yet the observed IMF does not vary significantly in different

regions of the Milky Way and Magellanic Clouds. The deviations observed remain within the limits of statistical uncertainties (Bastian et al. 2010), leading to the assumption of a universal IMF.

5.1.2 Nebular Emission

Being able to account for the nebular emission in a SED-fitting process is really important, as it increases our capability of constraining the more recent SF processes. This is even of greater importance when the young stellar population can outshine the older, what could lead to biased results.

Nebular emission, or transmission function $T_\lambda^+(t, t')$ of gas ionized by the stars with age t' at time t, is modeled based on the photoionization code CLOUDY (Ferland, 1996) as in Charlot and Longhetti (2001). The ionization by stars older than 10 Myr is neglected (Charlot and Longhetti, 2001), so that

$$T_\lambda^+(t, t') = 1 \ \text{ for } \ t' > 10\, Myr \tag{5.5}$$

Furthermore $T_\lambda^+(t, t')$ is close to zero at wavelengths smaller than Lyα emission.

The main adjustable parameters for the modeling of nebular emission are the interstellar metallicity, the ionization parameter and dust-to-metal ratio. For further details we recommend the reader to check Pacifici et al. (2012).

5.1.3 Attenuation by Dust

The impact of the dust attenuation on the emission of a galaxy depends on several factors , such as the amount and distribution of the interstellar material, the gas metallicity and physical conditions, and the orientation of the galaxy with respect our line of sight.

We use an attenuation by dust model à la Charlot and Fall (2000), as in Pacifici et al. (2013), (see also Chevallard et al., 2013). In this approach, and for simplicity, the dust attenuation optical depth of a galaxy is assumed to not depend on global galaxy parameters, such as the age, the specific star formation rate, and the gas-phase metallicity. Under these assumptions, we can express transmission function of the neutral ISM simply as a function of stellar age, t',

$$T_\lambda^0(t, t') = T_\lambda^0(t') \tag{5.6}$$

Indeed, stars younger than 10 Myr (time-scale of the giant molecular clouds dissipation; e.g., Blitz & Shu 1980; Kawamura et al. 2009) are more attenuated than older stars. This effect is modeled following the expression

$$T_\lambda^0(t') = \exp\left[-\hat{\tau}_\lambda(t')\right] \tag{5.7}$$

where $\hat{\tau}_\lambda(t')$ in the attenuation optical depth of the dust seen by stars of age t'. Furthermore, different attenuations are consider for the molecular clouds where the SF take place and the more diffuse ISM. The dependence of the different attenuations with wavelength is also taken into account. Furthermore, different slopes of the attenuation curve are considered to account for the fact that the curve should flatten when the optical depth increases (Pierini et al. 2004; Tuffs et al. 2004; Rocha et al. 2008). The $\hat{\tau}_\lambda(t')$ is expressed as a function of $\hat{\tau}_V(t')$, the total effective V-band absorption optical depth of the dust.

Table 5.1: Prior distribution of the physical properties of the galaxies in the library of SF and chemical enrichment histories averaged over the last 10 Myr.

Parameter	Range
sSFR/Gyr^{-1}	-2 – 2
12+log(O/H)	7.0 –9.4
$\hat{\tau}_V$	0.0 – 1.5

5.2 SED-fitting Approach

We obtain a library of approximately 1.5 million spectral models by combining the modeling procedure described in the previous subsections and considering the priors shown in Table 5.1. The main difference with respect the values used in Pacifici et al. (2013), is that in our case we vary $\hat{\tau}_V$ in the range $0.0 < \hat{\tau}_V < 1.5$ (instead of $0 < \hat{\tau}_V < 3$, as this is more suitable to fit our sample of blue low-mass candidates with emission lines. Recent measurements of the dust-to-gas ratio in nearby, metal-poor and low mass galaxies indicate that such galaxies have much less dust than expected based on the linear metallicity scaling (e.g., Rémy-Ruyer et al., 2014; Shi et al., 2014).

Once this is done, we infer the observational data of our sample of galaxies for each of the models in the library (i.e. photometry and emission line measurements). Regarding the photometry, we obtain the synthetic fluxes by convolving each model with the transmission curves of all the filters in our photometry (Table 4.1). Then, in order to obtain the fluxes and EWs of the emission lines identified in the spectra (Table 4.11), we consider the same wavelength ranges used to obtain manually (before the iterative process) the level of the continuum and the fluxes of the emission lines for our VIMOS spectra.

We fit the photometry and EWs of the sample of 94 galaxies (Section 4) to the synthetic photometry and EWs inferred for those models with redshifts equal to the spectroscopic redshift of the target ± 0.02. In practice, this means that each target is compared to approximately about 50000 models. In the left panel of Figure 5.3 we show the distribution of the number of models fitted in each case. We opt for fitting the EWs instead of the emission line fluxes as a conservative approach to avoid the impact of possible not detected inconsistencies in the flux calibration.

We calculate a likelihood of the fit for each model as described in Pacifici et al. (2012):

$$\ln P(\mathcal{M}_j \mid \{\mathcal{O}_i\}) = -\frac{1}{2}\sum_i \left(\frac{\mathcal{O}_i - w_j \mathcal{M}_{j,i}}{\sigma_i}\right) \tag{5.8}$$

where $\mathcal{O}_i$ and $\mathcal{O}_i$ are the spectral energy distributions of the observations ans the model, respectively, and σ_i is the uncertainty[2] corresponding the observational data $\mathcal{O}_i$, and w_i is the scaling factor that maximizes $P(\mathcal{M}_j \mid \{\mathcal{O}_i\})$ with the following expression:

$$w_j = \left(\sum_i \frac{\mathcal{O}_i \mathcal{M}_{j,i}}{\sigma_i^2}\right) \left[\sum_i \left(\frac{\mathcal{M}_{j,i}}{\sigma_i}\right)^2\right]^{-1} \tag{5.9}$$

[2]To enlarge the number of models contributing to each fit, we consider a minimum value of 0.05 mag for the photometry.

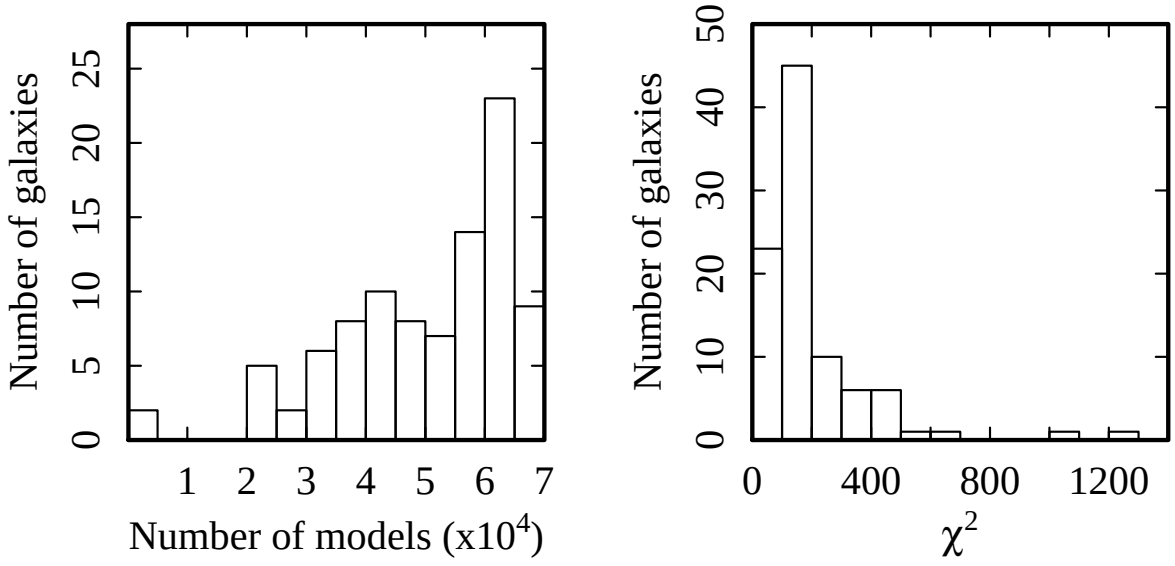

Figure 5.3: Left: Number of models with over near-zero probability. Right: Distribution of χ^2.

In the right panel of Figure 5.3 we show the distribution of the χ^2 obtained for the fits. Also, for a more detailed idea on how the photometry is fitted we show in Appendix A the photometry residuals obtained.

Then, we build a probability density function (PDF) for the value of each parameter based on the likelihood of the fits (see Appendix B). Median values of such probability distributions are recorded as the best-estimates of the physical parameters. The typical uncertainties (median half the 16th–84th percentile range) are $\sim$0.1 dex for the stellar mass, $\sim$0.1 dex for the SFR, $\sim$0.2 dex for the sSFR, $\sim$0.2 for $12 + \log(\mathrm{O/H})$, and $\sim$0.1 for $\hat{\tau}_V$. One of the advantages of Bayesian approach is that degeneracies are imprinted in the PDFs. The classical degenerations stellar metallicity-age and age-dust should not have a big impact on the results since the oxygen abundance we obtain applies only to the current young stars (10 Myr old), and not large amounts of dust are expected given the blue colors of the sample. Nevertheless, some PDFs present multiple picks and others broad shapes. This probably means that the uncertainties on the photometry or on the emission lines are large. In Appendix A we show for each galaxy the models χ^2 distributions that contribute to the probability density functions (i.e. those for which a probability larger than 0 is obtained).

Furthermore, a best-estimate SFH is derived as the average of the first 10 best-fit model SFHs weighted by their likelihood (see Appendix B).

We obtain fits for 91 galaxies. We exclude one galaxy (205) with less than 12 photometric points and other 2 (43 and 1210) for which the fitting process returns near-zero probability for more than 95% of the models in the library (Figure 5.3).

5.3 Output: Physical Parameters and SFHs

Table 5.2 lists the values of the physical parameters obtained for the 91 galaxies. For each galaxy we show: (1) ID; (2) z_{spec}; (3) $\log M_*/M_\odot$; $\log \mathrm{SFR}/M_\odot \mathrm{yr}^{-1}$; $\log \mathrm{sSFR}/\mathrm{Gyr}^{-1}$; 12+log(O/H); $\hat{\tau_V}$. The analysis of the physical parameters is included in Chapter 7. We show the best-estimate SFHs obtained for each galaxy in Appendix B. We discuss the properties of these SFHs in Chapter 8.

It is worth mentioning that results corresponding to the galaxies observed in different nights and observing runs (1344 and 2010) are consistent within the error bars. Table 5.2 shows the average values for them. There are two reasons for such agreement:

1. Emission lines measurements appear to be consistent for the different spectra taken for each of these galaxies (within a 20%).
2. The fact that photometric data do not change. As individual photometric and spectroscopic data are weighted equally (only by the uncertainties), more than half of the data points fitted are exactly the same in both cases.

Pacifici et al. (2012) show in their Table 2 a summary of the constrains on galaxy physical parameters retrieved using their approach and different observational datasets. On the one hand, in the case of stellar mass, they reach a high level of accuracy (0.04) and uncertainties of $\sim$0.2 dex using rest-frame $ugriz$ photometry. They also explore the impact of the σ of the detection on these results. They note that reducing the SNR from 20 to 5 can increase the uncertainties by about 30 to 90%. The number of photometric bands we include in the SED-fitting, combined with the average 10σ detections of our galaxies guarantee that we achieve high quality stellar mass estimations. Nevertheless, it has been probed that star-forming galaxies mass estimations can be affected by a systematic bias produced by the young stars outshining the underlying older stellar populations (Sawicki and Yee, 1998; Papovich et al., 2001). This effect increases in studies of spatially unresolved systems, such as ours, for which masses can be underestimated by 0.12 dex (Sorba and Sawicki, 2015). Considering not simplified SFHs in the SED-fitting can ease the impact of the oushining systematic bias, as the stellar content of the galaxy is less simplified. The results of Pacifici et al. (2012) show also that the impact of including EWs of emission lines in their analysis can improve notably the estimations of SFR, sSFR, metallicity, and extinction. Nevertheless, the dependence of these results on the different emission lines included in the analysis and their detection significance makes it difficult to evaluate the expected general quality of our estimations. In general, SFR and sSFR can be more reliably constrained than metallicities and dust extinction through our approach. For this reason, we do not include individual sections to analyze the estimations of these last two physical parameters. Alternatively, we analyze the metallicities and dust extinctions obtained from direct measurements on the VIMOS spectra.

Table 5.2: Physical Parameters. SED-fitting output.

ID	z_{spec}	$\log M_*/M_\odot$	$\log \mathrm{SFR}/M_\odot yr^{-1}$	$\log \mathrm{sSFR}/Gyr^{-1}$	12+log(O/H)	$\hat{\tau}_V$
(1)	(2)	(3)	(4)	(5)	(6)	(7)
17	0.642	$8.8^{8.8}_{8.8}$	$-0.3^{-0.2}_{-0.4}$	$-0.1^{-0.1}_{-0.2}$	$7.4^{7.4}_{7.1}$	$0.3^{0.3}_{0.2}$
26	0.517	$7.9^{8.1}_{7.8}$	$-0.9^{-0.6}_{-1.3}$	$0.1^{0.6}_{-0.3}$	$8.0^{8.3}_{7.7}$	$0.4^{0.8}_{0.1}$
35	0.656	$8.3^{8.5}_{8.3}$	$-0.2^{0.2}_{-0.3}$	$0.4^{0.8}_{0.4}$	$8.1^{8.4}_{7.6}$	$0.5^{0.8}_{0.5}$
53	0.742	$8.3^{8.4}_{8.1}$	$-0.7^{-0.5}_{-0.9}$	$0.0^{0.3}_{-0.2}$	$7.9^{8.3}_{7.6}$	$0.3^{0.5}_{0.1}$
88	0.553	$9.0^{9.0}_{9.0}$	$0.6^{0.6}_{0.6}$	$0.6^{0.6}_{0.5}$	$7.7^{7.7}_{7.7}$	$0.3^{0.3}_{0.3}$
121	1.022	$9.1^{9.2}_{9.0}$	$0.2^{0.4}_{0.0}$	$0.1^{0.3}_{-0.1}$	$7.9^{8.6}_{7.5}$	$0.5^{0.9}_{0.4}$
145	0.521	$8.7^{8.8}_{8.7}$	$-0.2^{-0.1}_{-0.3}$	$0.1^{0.2}_{-0.1}$	$7.5^{7.6}_{7.3}$	$0.6^{0.6}_{0.3}$
156	0.513	$8.0^{8.1}_{7.9}$	$-1.0^{-0.6}_{-1.3}$	$-0.1^{0.3}_{-0.3}$	$8.0^{8.5}_{7.7}$	$0.5^{1.0}_{0.2}$
164	1.245	$9.0^{9.1}_{8.8}$	$0.5^{0.6}_{0.4}$	$0.5^{0.6}_{0.4}$	$7.4^{7.7}_{7.2}$	$0.3^{0.4}_{0.2}$
173	0.214	$7.9^{8.0}_{7.7}$	$-2.0^{-1.7}_{-2.4}$	$-0.9^{-0.6}_{-1.2}$	$8.2^{8.5}_{7.6}$	$0.8^{1.1}_{0.4}$
181	0.759	$9.0^{9.1}_{9.0}$	$0.2^{0.4}_{0.1}$	$0.2^{0.3}_{0.1}$	$7.8^{8.5}_{7.6}$	$0.3^{0.4}_{0.3}$
183	0.532	$7.7^{7.7}_{7.5}$	$-0.6^{-0.3}_{-0.7}$	$0.7^{1.1}_{0.6}$	$7.8^{7.8}_{7.5}$	$0.6^{0.9}_{0.6}$
193	0.482	$7.8^{7.8}_{7.7}$	$-0.5^{-0.5}_{-0.8}$	$0.7^{0.8}_{0.4}$	$7.9^{7.9}_{7.9}$	$1.4^{1.4}_{0.8}$
195	0.538	$7.5^{7.6}_{7.4}$	$-1.0^{-1.0}_{-1.1}$	$0.4^{0.4}_{0.4}$	$7.9^{7.9}_{7.9}$	$0.1^{0.1}_{0.1}$
210	0.423	$7.7^{7.8}_{7.4}$	$-0.6^{-0.4}_{-0.9}$	$0.6^{1.1}_{0.4}$	$7.5^{7.7}_{7.3}$	$0.9^{1.2}_{0.7}$
220	0.119	$6.8^{7.0}_{6.7}$	$-2.5^{-2.3}_{-2.6}$	$-0.3^{-0.2}_{-0.4}$	$7.9^{8.0}_{7.6}$	$0.1^{0.2}_{0.1}$
227	0.672	$7.9^{8.0}_{7.9}$	$-0.9^{-0.8}_{-1.2}$	$0.1^{0.2}_{-0.2}$	$7.8^{8.3}_{7.8}$	$0.1^{0.2}_{0.0}$
235	0.840	$7.9^{8.0}_{7.6}$	$-0.4^{-0.3}_{-0.4}$	$0.8^{1.0}_{0.7}$	$7.4^{7.6}_{7.2}$	$0.2^{0.3}_{0.1}$
236	0.329	$7.7^{7.7}_{7.6}$	$-1.6^{-1.3}_{-1.6}$	$-0.3^{-0.1}_{-0.3}$	$8.2^{8.7}_{7.8}$	$0.2^{0.4}_{0.2}$
237	0.423	$7.6^{7.7}_{7.6}$	$-1.3^{-1.2}_{-1.8}$	$0.0^{0.2}_{-0.5}$	$8.4^{8.7}_{7.8}$	$0.7^{0.9}_{0.2}$
241	0.545	$7.8^{7.9}_{7.7}$	$-0.9^{-0.8}_{-1.2}$	$0.3^{0.4}_{-0.1}$	$8.0^{8.0}_{7.9}$	$0.8^{0.8}_{0.4}$
253	0.760	$7.7^{7.8}_{7.7}$	$-0.9^{-0.8}_{-1.0}$	$0.4^{0.5}_{0.2}$	$8.1^{8.2}_{7.9}$	$0.4^{0.7}_{0.2}$
259	0.573	$8.3^{8.5}_{8.2}$	$0.1^{0.1}_{-0.4}$	$0.8^{0.8}_{0.2}$	$8.2^{8.2}_{7.9}$	$1.3^{1.3}_{0.4}$
277	0.437	$7.4^{7.5}_{7.3}$	$-0.4^{-0.4}_{-0.7}$	$1.2^{1.2}_{0.8}$	$7.1^{7.2}_{7.1}$	$1.0^{1.0}_{0.5}$
293	0.545	$8.2^{8.3}_{8.1}$	$-0.7^{-0.4}_{-1.0}$	$0.0^{0.3}_{-0.2}$	$7.7^{8.2}_{7.6}$	$0.6^{0.9}_{0.3}$
296	0.261	$7.6^{7.6}_{7.6}$	$-1.1^{-1.1}_{-1.2}$	$0.3^{0.3}_{0.2}$	$7.6^{7.6}_{7.6}$	$0.1^{0.1}_{0.0}$
297	0.446	$7.7^{7.8}_{7.6}$	$-0.8^{-0.7}_{-0.9}$	$0.5^{0.6}_{0.4}$	$7.1^{7.2}_{7.1}$	$0.5^{0.6}_{0.4}$
306	0.576	$7.9^{7.9}_{7.9}$	$-0.4^{-0.3}_{-0.4}$	$0.7^{0.7}_{0.6}$	$8.2^{8.3}_{8.2}$	$0.8^{0.8}_{0.8}$
312	1.216	$9.4^{9.4}_{9.2}$	$0.7^{0.8}_{0.6}$	$0.3^{0.4}_{0.3}$	$8.7^{8.7}_{8.7}$	$0.3^{0.3}_{0.3}$
315	0.132	$6.9^{7.0}_{6.9}$	$-2.7^{-2.7}_{-2.8}$	$-0.7^{-0.6}_{-0.7}$	$8.6^{8.6}_{8.6}$	$0.2^{0.2}_{0.2}$
317	0.620	$8.2^{8.3}_{8.1}$	$-0.7^{-0.6}_{-1.1}$	$0.0^{0.2}_{-0.2}$	$7.8^{8.4}_{7.6}$	$0.5^{0.7}_{0.5}$
386	0.400	$8.1^{8.2}_{8.1}$	$-0.9^{-0.8}_{-1.2}$	$0.0^{0.0}_{-0.4}$	$8.3^{8.5}_{8.3}$	$0.9^{1.1}_{0.4}$
396	0.310	$7.3^{7.4}_{7.3}$	$-1.8^{-1.7}_{-2.0}$	$-0.1^{-0.1}_{-0.3}$	$7.7^{7.9}_{7.7}$	$0.4^{0.5}_{0.0}$
440	0.535	$7.5^{7.6}_{7.5}$	$-1.4^{-1.2}_{-1.5}$	$0.1^{0.2}_{0.0}$	$7.6^{8.1}_{7.4}$	$0.1^{0.3}_{0.1}$
454	0.536	$8.0^{8.0}_{7.9}$	$-0.8^{-0.7}_{-0.9}$	$0.2^{0.3}_{0.0}$	$7.6^{8.6}_{7.5}$	$0.2^{0.3}_{0.1}$
455	0.687	$8.7^{8.8}_{8.6}$	$-0.2^{0.0}_{-0.4}$	$0.1^{0.2}_{-0.1}$	$7.5^{8.6}_{7.3}$	$1.0^{1.2}_{0.8}$
464	0.729	$8.4^{8.5}_{8.4}$	$-0.6^{-0.5}_{-0.7}$	$0.0^{0.1}_{-0.2}$	$8.6^{8.7}_{7.8}$	$0.2^{0.5}_{0.1}$
474	1.171	$8.7^{8.9}_{8.6}$	$0.9^{1.1}_{0.8}$	$1.1^{1.3}_{1.0}$	$7.4^{7.6}_{7.2}$	$0.9^{1.1}_{0.7}$
481	0.954	$8.9^{8.9}_{8.9}$	$0.2^{0.3}_{0.2}$	$0.3^{0.4}_{0.3}$	$8.7^{8.7}_{8.7}$	$0.2^{0.2}_{0.2}$
488	0.533	$8.2^{8.2}_{8.1}$	$-0.7^{-0.4}_{-0.8}$	$0.1^{0.4}_{0.1}$	$8.4^{8.4}_{7.7}$	$0.7^{1.1}_{0.7}$
490	0.856	$8.6^{8.6}_{8.5}$	$0.0^{0.0}_{-0.1}$	$0.5^{0.5}_{0.5}$	$7.8^{7.8}_{7.8}$	$0.2^{0.2}_{0.2}$
510	1.329	$9.5^{9.6}_{9.4}$	$0.8^{0.9}_{0.8}$	$0.2^{0.4}_{0.1}$	$7.2^{7.3}_{7.2}$	$0.2^{0.4}_{0.2}$
518	0.502	$7.7^{7.8}_{7.6}$	$-1.1^{-0.8}_{-1.4}$	$0.1^{0.5}_{-0.2}$	$8.0^{8.3}_{7.8}$	$0.8^{1.0}_{0.4}$
519	0.909	$8.7^{8.8}_{8.7}$	$0.8^{0.9}_{0.8}$	$1.1^{1.1}_{1.0}$	$7.3^{7.3}_{7.3}$	$1.3^{1.3}_{1.3}$
520	0.445	$7.9^{8.0}_{7.8}$	$-0.4^{-0.4}_{-0.6}$	$0.6^{0.7}_{0.4}$	$8.7^{8.7}_{8.7}$	$1.1^{1.1}_{1.0}$
524	1.250	$8.9^{9.0}_{8.8}$	$0.5^{0.6}_{0.4}$	$0.6^{0.8}_{0.5}$	$8.0^{8.1}_{7.7}$	$0.1^{0.2}_{0.1}$
536	0.578	$7.6^{7.7}_{7.5}$	$-1.0^{-0.8}_{-1.1}$	$0.4^{0.6}_{0.3}$	$7.9^{8.0}_{7.8}$	$0.2^{0.5}_{0.1}$
539	0.739	$7.8^{7.9}_{7.7}$	$-0.9^{-0.8}_{-0.9}$	$0.4^{0.4}_{0.3}$	$7.8^{8.0}_{7.8}$	$0.0^{0.1}_{0.0}$
543	0.720	$9.1^{9.1}_{9.0}$	$1.0^{1.0}_{0.9}$	$0.9^{0.9}_{0.9}$	$7.1^{7.2}_{7.1}$	$1.4^{1.4}_{1.4}$
544	0.436	$8.3^{8.4}_{8.2}$	$-1.0^{-0.9}_{-1.0}$	$-0.3^{-0.2}_{-0.3}$	$7.3^{7.3}_{7.2}$	$0.1^{0.2}_{0.1}$
551	0.246	$7.8^{7.8}_{7.7}$	$-1.6^{-1.6}_{-1.7}$	$-0.3^{-0.3}_{-0.4}$	$8.4^{8.4}_{8.4}$	$0.6^{0.6}_{0.6}$
565	0.567	$8.1^{8.1}_{8.0}$	$-1.4^{-1.2}_{-2.0}$	$-0.5^{-0.3}_{-1.1}$	$8.4^{8.5}_{8.0}$	$0.3^{0.5}_{0.1}$
571	0.684	$8.8^{8.9}_{8.7}$	$-0.7^{-0.4}_{-0.9}$	$-0.6^{-0.3}_{-0.8}$	$8.4^{8.7}_{7.7}$	$0.6^{1.1}_{0.4}$
584	0.767	$8.3^{8.4}_{8.3}$	$0.3^{0.4}_{0.2}$	$1.1^{1.1}_{0.6}$	$7.8^{7.8}_{7.8}$	$0.7^{0.7}_{0.3}$
594	0.263	$7.5^{7.7}_{7.4}$	$-1.2^{-1.1}_{-1.3}$	$0.4^{0.4}_{0.1}$	$7.6^{7.8}_{7.5}$	$0.3^{0.3}_{0.2}$
601	0.534	$8.0^{8.1}_{7.9}$	$-1.4^{-1.1}_{-1.8}$	$-0.5^{-0.1}_{-0.9}$	$8.2^{8.5}_{7.7}$	$0.7^{1.0}_{0.2}$
612	0.786	$7.8^{8.0}_{7.6}$	$-0.4^{-0.3}_{-0.6}$	$0.7^{0.9}_{0.5}$	$7.9^{8.1}_{7.7}$	$0.2^{0.3}_{0.2}$
626	0.656	$7.6^{7.9}_{7.5}$	$-0.5^{-0.4}_{-0.6}$	$0.9^{0.9}_{0.5}$	$7.7^{7.8}_{7.4}$	$0.1^{0.2}_{0.0}$
634	1.255	$8.8^{8.9}_{8.7}$	$0.3^{0.4}_{0.2}$	$0.6^{0.6}_{0.4}$	$7.7^{7.9}_{7.7}$	$0.2^{0.2}_{0.2}$

Continues on next page

Table 5.2: Physical Parameters. SED-fitting output. Cont.

ID	z_{spec}	$\log M_*/M_\odot$	$\log \mathrm{SFR}/M_\odot yr^-1$	$\log \mathrm{sSFR}/Gyr^-1$	12+log(O/H)	$\hat{\tau}_\mathrm{V}$
(1)	(2)	(3)	(4)	(5)	(6)	(7)
642	0.817	$7.5^{7.6}_{7.5}$	$0.0^{0.0}_{-0.4}$	$1.4^{1.4}_{1.1}$	$7.1^{7.8}_{7.1}$	$0.6^{0.6}_{0.1}$
1017	0.674	$8.4^{8.5}_{8.3}$	$-0.6^{-0.4}_{-1.0}$	$-0.1^{0.2}_{-0.5}$	$8.1^{8.4}_{7.7}$	$0.6^{0.9}_{0.2}$
1032	0.467	$9.1^{9.2}_{9.1}$	$-1.1^{-1.1}_{-1.2}$	$-1.3^{-1.3}_{-1.3}$	$7.5^{7.5}_{7.5}$	$0.2^{0.2}_{0.2}$
1056	0.522	$9.2^{9.3}_{9.2}$	$0.1^{0.1}_{0.1}$	$-0.2^{-0.1}_{-0.2}$	$7.2^{7.2}_{7.2}$	$0.8^{0.8}_{0.7}$
1090	0.610	$7.6^{7.6}_{7.6}$	$-1.2^{-1.2}_{-1.3}$	$0.2^{0.3}_{0.2}$	$7.2^{7.2}_{7.2}$	$0.9^{0.9}_{0.9}$
1126	0.864	$8.3^{8.4}_{8.3}$	$0.4^{0.4}_{0.3}$	$1.0^{1.1}_{0.9}$	$7.8^{8.0}_{7.4}$	$0.7^{0.8}_{0.6}$
1202	0.679	$8.2^{8.3}_{8.2}$	$-0.7^{-0.4}_{-0.8}$	$0.1^{0.4}_{0.1}$	$8.7^{8.7}_{8.2}$	$0.6^{0.8}_{0.6}$
1220	0.487	$7.9^{8.0}_{7.8}$	$-1.0^{-0.8}_{-1.1}$	$0.1^{0.2}_{-0.1}$	$8.4^{8.4}_{8.1}$	$0.2^{0.6}_{0.1}$
1234	0.436	$8.0^{8.0}_{8.0}$	$-0.5^{-0.5}_{-0.6}$	$0.5^{0.5}_{0.3}$	$8.6^{8.7}_{8.1}$	$0.9^{0.9}_{0.8}$
1245	0.678	$8.1^{8.3}_{8.1}$	$-0.8^{-0.6}_{-1.0}$	$0.0^{0.1}_{-0.1}$	$8.1^{8.2}_{7.5}$	$0.0^{0.1}_{0.0}$
1247	0.524	$7.8^{7.9}_{7.7}$	$-0.4^{-0.3}_{-0.4}$	$0.8^{0.9}_{0.8}$	$7.4^{7.7}_{7.4}$	$0.3^{0.3}_{0.3}$
1251	0.434	$8.7^{8.7}_{8.6}$	$-0.9^{-0.8}_{-0.9}$	$-0.6^{-0.5}_{-0.6}$	$8.2^{8.2}_{8.2}$	$1.4^{1.4}_{1.4}$
1309	0.743	$8.8^{8.8}_{8.7}$	$0.1^{0.3}_{0.0}$	$0.3^{0.5}_{0.2}$	$7.7^{8.6}_{7.7}$	$0.7^{0.8}_{0.7}$
1313	0.578	$8.6^{8.7}_{8.6}$	$0.0^{0.0}_{-0.1}$	$0.3^{0.4}_{0.2}$	$7.8^{7.8}_{7.7}$	$1.1^{1.1}_{0.8}$
1332	0.339	$8.0^{8.1}_{7.9}$	$-0.9^{-0.9}_{-1.1}$	$0.0^{0.1}_{-0.1}$	$7.7^{8.5}_{7.3}$	$1.0^{1.2}_{1.0}$
1344	0.374	$8.0^{8.0}_{8.0}$	$-0.3^{-0.2}_{-0.3}$	$0.7^{0.7}_{0.6}$	$7.8^{7.8}_{7.8}$	$0.4^{0.4}_{0.3}$
1378	0.343	$8.5^{8.5}_{8.5}$	$-1.1^{-1.1}_{-1.2}$	$-0.7^{-0.6}_{-0.7}$	$7.6^{7.6}_{7.5}$	$0.5^{0.5}_{0.5}$
1403	0.688	$8.8^{8.8}_{8.7}$	$-0.1^{-0.1}_{-0.2}$	$0.1^{0.1}_{0.0}$	$8.4^{8.5}_{8.0}$	$0.9^{1.2}_{0.9}$
1454	0.738	$8.3^{8.4}_{8.1}$	$-0.7^{-0.4}_{-1.0}$	$0.0^{0.4}_{-0.4}$	$8.1^{8.4}_{7.6}$	$0.5^{1.0}_{0.3}$
1514	0.782	$8.7^{8.7}_{8.6}$	$0.0^{0.0}_{-0.1}$	$0.3^{0.3}_{0.2}$	$7.8^{7.9}_{7.8}$	$0.5^{0.5}_{0.5}$
1585	0.661	$8.5^{8.6}_{8.5}$	$-0.3^{-0.2}_{-0.5}$	$0.2^{0.3}_{-0.2}$	$8.4^{8.4}_{7.8}$	$0.8^{0.8}_{0.1}$
1605	0.888	$8.3^{8.4}_{8.3}$	$-0.4^{-0.3}_{-0.4}$	$0.3^{0.4}_{0.3}$	$8.0^{8.1}_{8.0}$	$0.4^{0.4}_{0.4}$
1656	0.870	$9.0^{9.0}_{9.0}$	$-0.4^{-0.3}_{-0.4}$	$-0.4^{-0.4}_{-0.4}$	$7.3^{7.4}_{7.3}$	$0.1^{0.1}_{0.1}$
1723	0.733	$8.4^{8.5}_{8.4}$	$-0.8^{-0.5}_{-0.9}$	$-0.2^{0.1}_{-0.3}$	$7.9^{8.0}_{7.6}$	$0.1^{0.3}_{0.0}$
1727	0.540	$8.8^{8.9}_{8.7}$	$-1.1^{-0.9}_{-1.3}$	$-0.9^{-0.7}_{-1.0}$	$8.0^{8.5}_{7.5}$	$0.1^{0.3}_{0.0}$
1752	0.147	$7.6^{7.7}_{7.4}$	$-0.9^{-0.8}_{-0.9}$	$0.5^{0.6}_{0.5}$	$8.4^{8.5}_{8.4}$	$1.4^{1.4}_{1.3}$
1765	0.957	$9.0^{9.2}_{9.0}$	$-0.5^{-0.3}_{-0.6}$	$-0.6^{-0.5}_{-0.7}$	$7.3^{7.6}_{7.2}$	$0.1^{0.2}_{0.0}$
1796	0.532	$9.1^{9.1}_{9.0}$	$0.2^{0.4}_{0.2}$	$0.1^{0.3}_{0.1}$	$8.2^{8.2}_{7.6}$	$1.3^{1.4}_{1.3}$
1804	0.533	$8.2^{8.2}_{8.1}$	$-1.5^{-1.1}_{-2.0}$	$-0.7^{-0.3}_{-1.2}$	$8.1^{8.6}_{7.5}$	$0.4^{0.9}_{0.1}$
1860	0.863	$8.4^{8.4}_{8.4}$	$0.1^{0.1}_{0.1}$	$0.7^{0.8}_{0.7}$	$7.5^{7.5}_{7.5}$	$0.4^{0.4}_{0.4}$
1861	0.538	$8.7^{8.8}_{8.6}$	$-0.1^{0.0}_{-0.5}$	$0.2^{0.2}_{-0.1}$	$8.0^{8.1}_{7.1}$	$1.3^{1.3}_{0.9}$
2010	0.424	$7.9^{7.9}_{7.8}$	$-0.9^{-0.9}_{-1.0}$	$0.2^{0.2}_{0.1}$	$8.6^{8.6}_{8.6}$	$0.2^{0.2}_{0.2}$

For each galaxy we show: (1) ID; (2) z_{spec}; (3) $\log M_*/M_\odot$; (4) $\log \mathrm{SFR}/M_\odot \mathrm{yr}^{-1}$; (5) $\log \mathrm{sSFR}/\mathrm{Gyr}^{-1}$; (6) 12+log(O/H); (7)$\hat{\tau}_\mathrm{V}$. In each case, we give the median, and 16th and 84th percentiles of the PDF.

6

Global Properties

In this section we describe the global properties of our sample of spectroscopically confirmed galaxies. By analyzing their morphological type, colors, and structural parameters we try to provide insight into their nature, and to place them within the whole galaxy population scheme.

6.1 Visual Morphological Classification

As the review *Classification and Stellar Content of Galaxies Obtained from Direct Photography* by Sanders et al. (2003) points out: "the first step in the development of most sciences is a classification of the objects under study". In this way, taxonomy is the tool to move from the mere*observation* to the *understanding* by identifying differences among the similar and similarities among the different.

The importance of morphological classifications resides in the fact that beyond the mere appearance differences, the various morphological/structural types are related to different physical properties (Roberts and Haynes, 1994).

Due to historical reasons, visual classifications are the most frequent in literature. Large surveys such as the Sloan Digital Sky Survey (SDSS; York et al. 2000) have enabled the visual classification of thousands of galaxies in the nearby Universe. The citizen science project Galaxy Zoo (Lintott et al. 2008) has extended morphological classifications to the general public and has produced catalogs of nearly one million galaxies from the SDSS.

Thanks to the various HST deep field surveys, we have been able to probe galaxy morphology to ever increasing redshifts. Nevertheless, the fact that different wavelengths trace different constituents of galaxies complicates the homogenization of morphological studies when performed at different redshifts. Recently, some works have focused on the structure of high redshift galaxies enabled by near-infrared imaging from WFC3. In particular, the work by Kartaltepe et al. (2014) attempts to extend the same morphological classification used in the local universe beyond such limit using the infrared imaging surveys performed with the WFC3.

The classification scheme we use is based on the one defined by Kartaltepe et al. (2014) and considers the typical broad Hubble Sequence (Hubble, 1936) types. It is divided into two sections: the first one related to the morphology itself, and the second one related to the possible interactions between close neighbors. Also, a set of flags are included to specify more particular features such as the possible mismatch of the target with nearby companions or the possible contamination of

the photometry of the target by the emission of close neighbors. Our classification is applied to all the ACS bands available to take into account the fact that different wavelengths trace different structures and also the fact that the sample spreads over a wide range of redshifts, in a way that not always the same band traces the same features.

- Morphology Class
  - *Disk-like* galaxies present a disky structure that may or may not show clear spiral arms. In our case, given the low-mass nature of our sample, the presence of spiral arms is barely expected.
  - *Spheroid* galaxies show an inner concentration of the surface brightness, and an extended, smoother, and roughly round region.
  - *Irregular* (*Irr*) galaxies display an irregular structure, regardless of surface brightness. This includes either strongly or slightly disturbed objects.
  - *Compact* systems are either clear point sources, or unresolved compact galaxies so small that the internal structure cannot be discerned. Normally, they appear as the inner concentration of a spheroid without the extended low surface brightness component.
  - *Unclassifiable* objects are problematic and cannot be classified either because of a problem with the image (e.g., there is no ACS image available for the coordinates of the galaxy), or because it is too faint for any structure to be identified.
- Interaction Class
  - *Merger*. These galaxies are single objects (including sources with double nuclei) that appear to have undergone a merger by ,e.g., evidence of tidal features/structures. Mergers are by definition irregular systems.
  - *Interaction*. The galaxy appears to be interacting with a companion galaxy (even if it is not included in the 5"$\times$5" postage stamps explored to perform the classification) and show tidal interaction or disturbed morphology.
  - *Close neighbor*. The primary galaxy could be interacting with a nearby galaxy (projected) within a 2.5" radii but does not show tidal interaction or disturbed morphology.
- Flag
  - Blending: Due to the fact that the sample selection was performed on a Subaru NB816 image, and consequently with a lower resolution than the HST bands. We consider important to add a flag for those cases where a possible blending problem could occur. As we have optimized the apertures for each case using Rainbow software package, the photometry should not be affected by this problem in most cases. In any case, this information is important when analyzing the properties inferred from the photometry, such as stellar masses and all the resultant parameters in the SEDs fitting process.

In Figures 6.3, 6.4, and 6.5 we show ACS RGBs of our sample of spectroscopically confirmed galaxies ordered by redshift. We use v, and z bands images for those galaxies within the GEMS area, and b, v, and z bands for those that fall in GOODS.

In Table 6.1 we show the morphologies (Column 3), interaction class (Column 4) and flag (Column 5) assigned to each of the galaxies in our sample. We find 39 (42%) disk-like, 34 (36%) Irr, 16 (17%) compact, and 5 (5%) unclassifiable (Table 6.1 [a]). We do not identify any Sph galaxy within our sample. Although we do not expect to find "classical" spheroidals within our sample, blue spheroidals have been identified (for instance) by Mahajan et al. (2015), within the Galaxy and Mass Assembly survey (GAMA; Driver et al. 2011). This could mean that we are including them into another type such as compact or even disk-like. Actually, Mahajan et al. (2015) assert that colour plays a key role in successfully identifying these galaxies. As we are basing our classification in monocromatic images it is likely that we are failing to segregate them.

It is interesting to point out that in spite of the *a priori* compactness of the whole sample, compact class turns out to be one of the less populated types. Most of the galaxies classified as compact (in particular 156, 297, 594, 1202) present an appearance very similar to the Green Peas (Cardamone et al., 2009) identified in the SDSS. The distinctive quasi-stellar shape and green color of the GPs is a consequence of the excess of flux in the band used as green light image for the RGB stamps due to the main contribution of the emission line [OIII]λ5007. It is also interesting to notice the difference between the morphological type *compact*, and the galaxy type *BCD*, which gathers morphologically heterogeneous galaxies. Indeed, GP can be classified as extreme cases within the BCDs.

We remind the reader that galaxies selected by mass ($\log M_*/M_\odot$ <8) have an ID below 1000, while objects selected by BCDs properties were named with IDs over such value. Said that, we can explore the type of objects selected preferentially by each criterion (Table 6.1 [b]). In particular, our sample contains 94 galaxies, out of which 62 were selected by mass, and 32 were selected as BCDs. Among the first 62, 17 (27%) are disk-like, 29 (47%) are Irr, 12 (20%) are compacts, and 4 (6%) are unclassifiable. Among those selected as BCDs, 22 (69%) are disk-likes, 5 (16%) are Irr, 4 (12%) are compacts, and 1 (3%) is unclassifiable. Considering these values we can affirm that BCD criteria mainly select disk-like galaxies, while the mass criterion is more inclusive in terms of morphology and favors Irr galaxies. 85% and 75% of Irr and compact galaxies in our sample, respectively, were selected as low mass galaxies. On the other hand, the fraction of interacting systems remain similar for both samples.

It is important to bear in mind the fact that our initial samples were selected using not significantly accurate photometric redshifts. For this reason, we repeat the analysis for the final spectroscopically confirmed sample of 91 galaxies for which we apply the SED-fitting approach and obtain best estimate physical parameters and SFHs. Then, we identify low-mass and BCDs systems following the same definitions used in the selection (Chapter 2), but now, considering the synthetic absolute magnitude and colors derived from the best-fit spectral template, and the stellar mass returned by the SED-fitting. Furthermore, we limit this part of the analysis to the 85 galaxies for which we have estimations of physical parameters and structural parameters in the catalog published by Griffith et al. (2012). Only in these cases we have the information necessary to classify a galaxy as BCD.

A summary of the morphological characteristics of the samples can be found in Table 6.1 [c]. Among the 85, there are 33 BCDs (following the definition in Chapter 2) and 35 low-mass galaxies ($\log M_*/M_\odot$). The morphological classification and fraction of interaction classes of the later are overall consistent wth those obtained for the initial sample. We can interpret this result as a probe that our mass selection works despite the problems shown with the photometric redshifts. Never-

Table 6.1: Morphology

Sample	Morphology Class				Interaction Class			Flag
	disk-like	Irr	Compact	U	Merger	Interaction	Neighbor	Blending
Total [a]	39 (42%)	34 (36%)	16 (17%)	5 (5%)	5 (5%)	31 (32%)	45 (47%)	13 (14%)
Mass selected [b]	17 (27%)	29 (47%)	12 (20%)	4 (6%)	4 (6%)	21 (34%)	31 (50%)	6 (10%)
Selected as BCDs [b]	22 (69%)	5 (16%)	4 (12%)	1 (3%)	1 (3%)	10 (31%)	14 (44%)	7 (22%)
Total [c]	36 (42%)	31 (36%)	13 (15%)	5 (6%)	5 (6%)	26 (31%)	41 (48%)	11 (13%)
Low mass [c]	13 (31%)	15 (43%)	6 (17%)	1 (3%)	1 (3%)	13 (37%)	17 (49%)	3 (9%)
BCDs [c]	15 (45%)	7 (21%)	9 (27%)	2 (6%)	2 (6%)	9 (27%)	17 (52%)	5 (15%)
Only BCDs [c]	9 (50%)	3 (17%)	4 (22%)	2 (11%)	2 (11%)	5 (28%)	8 (44%)	5 (28%)
BCD and low-mass [c]	6 (40%)	4 (27%)	5 (33%)	0 (0%)	0 (0%)	4 (27%)	9 (60%)	0 (0%)
Only low-mass [c]	7 (35%)	11 (55%)	1 (5%)	1 (5%)	0 (0%)	9 (45%)	8 (40%)	3 (15%)
Not BCD not low-mass [c]	14 (44%)	13 (40%)	3 (9%)	2 (6%)	2 (6%)	8 (25%)	16 (50%)	3 (9%)

[a] Total sample of galaxies (94) for which a reliable redshift was measured on the VIMOS spectroscopy.
[b] The galaxies in the total sample are divided considering their initial selection performed using the stellar ass and photometric information derived with the photometric redshifts. The highest priority sample was the mass selected. This means that low-mass includes any type of dwarf, including BCDs (in particular, there are 5 low mass galaxies that qualify as BCDs). Contrarily, no low-mass galaxies are included in the BCDs sample.
[c] Final samples. In this case, the division of the total sample is performed using the final values of spectroscopic redshift and the physical parameters returned by the SED-fitting approach. The total number of galaxies considered here is 91 and not 94 because we had to exclude one galaxy with less than 12 photometric points and two others for which the fitting process returned near-zero probability for more than 95% of the models in the library.

theless, BCDs present now larger fraction of compacts than the initial sample of BCDs, which is reasonable given the definition of BCD itself. If we compare now the sample that includes only BCDs with the sample that includes only low-mass galaxies, we can see that the main difference between them is the enhanced fraction of Irr systems included in he later. Therefore, it appears that Irr galaxies are targeted more efficiently using a mass selection criteria than a BCD criteria, which is consistent with the definition of BCDs. The sample that includes galaxies that qualify both as low-mass and BCDs present a similar fraction of disk-like, Irr, and Compact. Finally, the sample of galaxies that contain galaxies that do not qualify as neither low-mass or BCDs is dominated by disk-like and Irr objects.

The fraction of possible mergers in the total samples is small ($\sim$5%). Nevertheless, $\sim$30% of the sample present morphologies that resemble some kind of interaction with neighbors within or outside the field of view explored around each galaxy. A further study on the environment of these galaxies would be extremely valuable.

In Figure 6.1 we show the dependence of the stellar mass, SFR and sSFR (left, central, and right panels in the Figure 6.1; the three of them obtained through the SED-fitting described in Chapter 5) with the morphology type. As we can see, the distribution of the three parameters overlap generally throughout the whole ranges covered by the sample. Regarding the dependence with stellar mass ($\log M_*/M_\odot$), the median and percentiles values for disk-like, Irr, compact, and unclassifiable types are respectively $8.3^{8.8}_{7.6}$, $8.0^{8.8}_{7.7}$, $8.0^{8.8}_{7.7}$, $9.0^{9.5}_{7.8}$. Despite the dispersion we discern that disk-like systems are slightly biased toward higher masses. The mass distribution of disk-like type looks bimodal, with the lower mass maximum coincident with compacts and Irrs distributions maximums. This could mean that we are classifying compacts as disk-like galaxies in some cases. Given the more obvious morphological difference between disk-like and Irr types, we dismiss the contamination by the later in the disk-like mass distribution. Removing the hypothetical contamination by compacts, the difference in mass would be more clear. The same bimodality appears in the SFR distribution with the same consequences. Actually, once again, the lowest SFR maximum of the disk-like distribution lies on the same bin than the maximum of the distribution of compacts. The median and percentiles are in this case ($\log \mathrm{SFR}/M_\odot \mathrm{yr}^{-1}$) $-0.6^{+0.1}_{-1.0}$, $-0.5^{+0.2}_{-1.4}$, $-0.8^{0.0}_{-1.1}$, $0.6^{+0.9}_{-1.6}$ for disk-like, Irr, compact and unclassifiable, respectively. Probably, correcting from the compacts contamination in disk-like distribution would shift the average value of SFR for disk-likes to $\sim$0.0. The distributions of sSFR are even more indistinguishable, with median and percentiles ($\log \mathrm{sSFR/Gyr}^{-1}$) $0.1^{+0.5}_{-0.2}$, $0.2^{+0.8}_{-0.3}$, $0.3^{+0.5}_{-0.1}$, $0.2^{+1.1}_{-1.3}$ for disk-like, Irr, compact and unclassifiable systems, respectively.

Figure 6.2 represents the distributions of the properties used in the selection criteria applied to build the initial samples (stellar mass, $M_{B,0}$, $(B-V)_0$ and $\mu_{B,0,reff}$) for the different morphological types. We can see how all the distributions overlap along the whole range of values of each parameter. The clearest trends are found in stellar mass (as in Figure 6.1) and surface brightness (although the confusion between disk-like and compact may smooth the trend), in which compact present the highest values, as expected.

Regarding the blending flag, we find only a 13% of galaxies (in the sample of 85 galaxies) that could be affected by such problem.

In Figures 6.3, 6.4, and 6.5 we show for each of the 94 galaxies for which we measure a reliable redshift (sorted by z_{spec}), the 5'$\times$5' RGB images built using ACS v, i, and z bands on GOODS-S and v and z bands for those galaxies on GEMS. In each panel we show the ID, the spectroscopic redshift, the morphological type, and the apparent magnitude in the selection band (Subaru NB816).

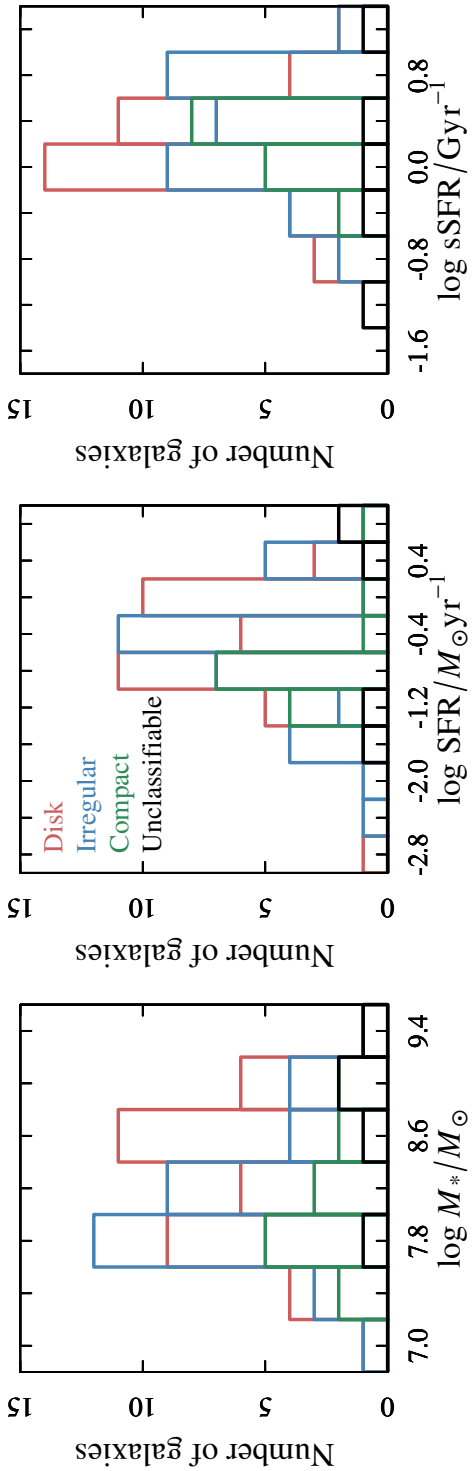

Figure 6.1: Dependence of the distribution of the physical parameters obtained through the SED-fitting (log $M_*/M_\odot$, log SFR/$M_\odot$yr^{-1}, log sSFR/Gyr^{-1}) for the different morphological types.

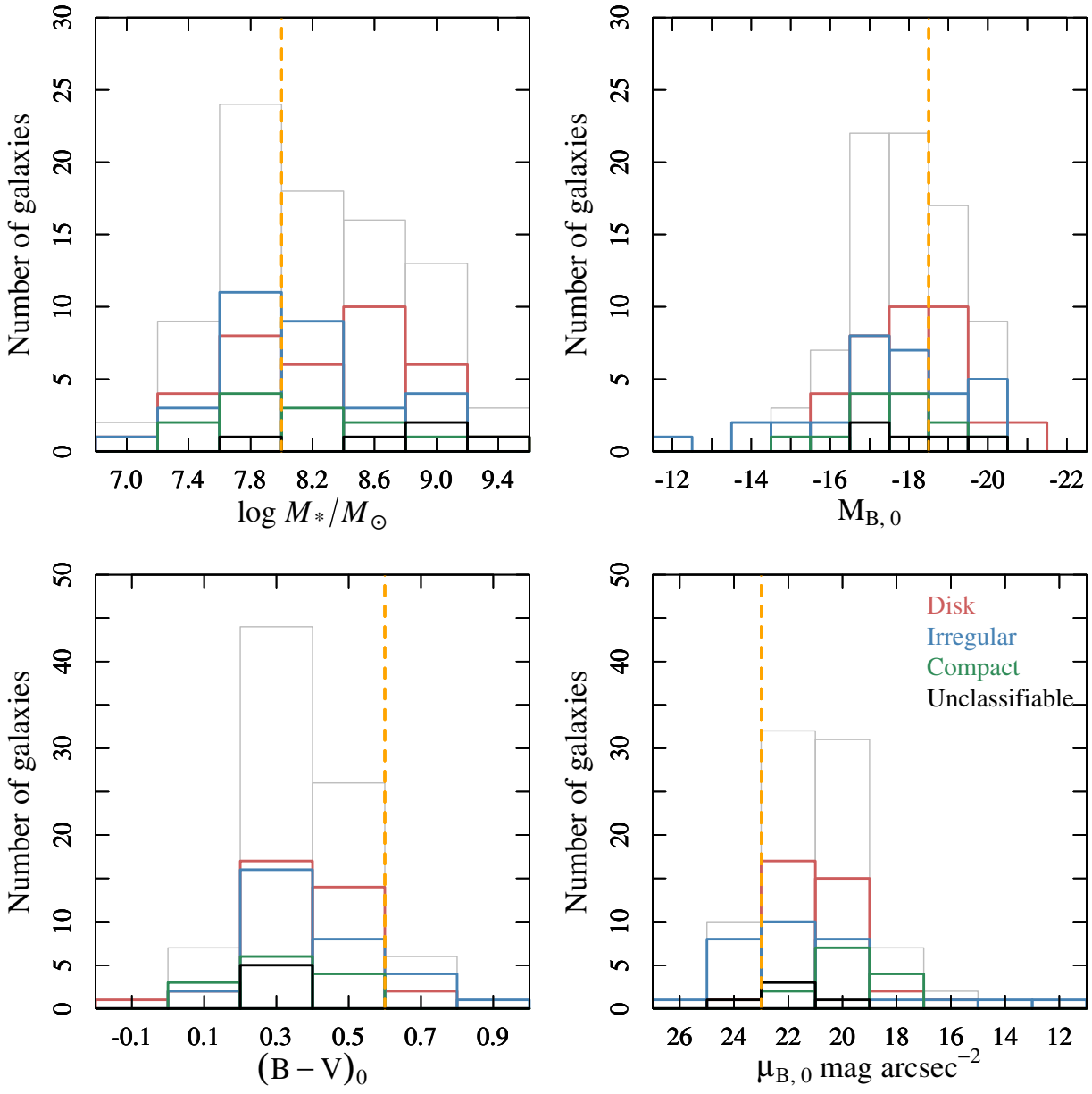

Figure 6.2: Stellar mass, $M_{B,0}$, $(B-V)_0$ and $\mu_{B,0,reff}$ dependence with morphology. The restframe magnitudes used in this plot are obtained from the spectral template best fitted to each galaxy observed photometry. Vertical dashed lines represent the selection criteria applied to built our initial samples of low-mass galaxies and BCDs. The gray histogram shows the distribution of the total sample of 85 galaxies for which the morphological catalog by Griffith et al. (2012) has a counterpart.

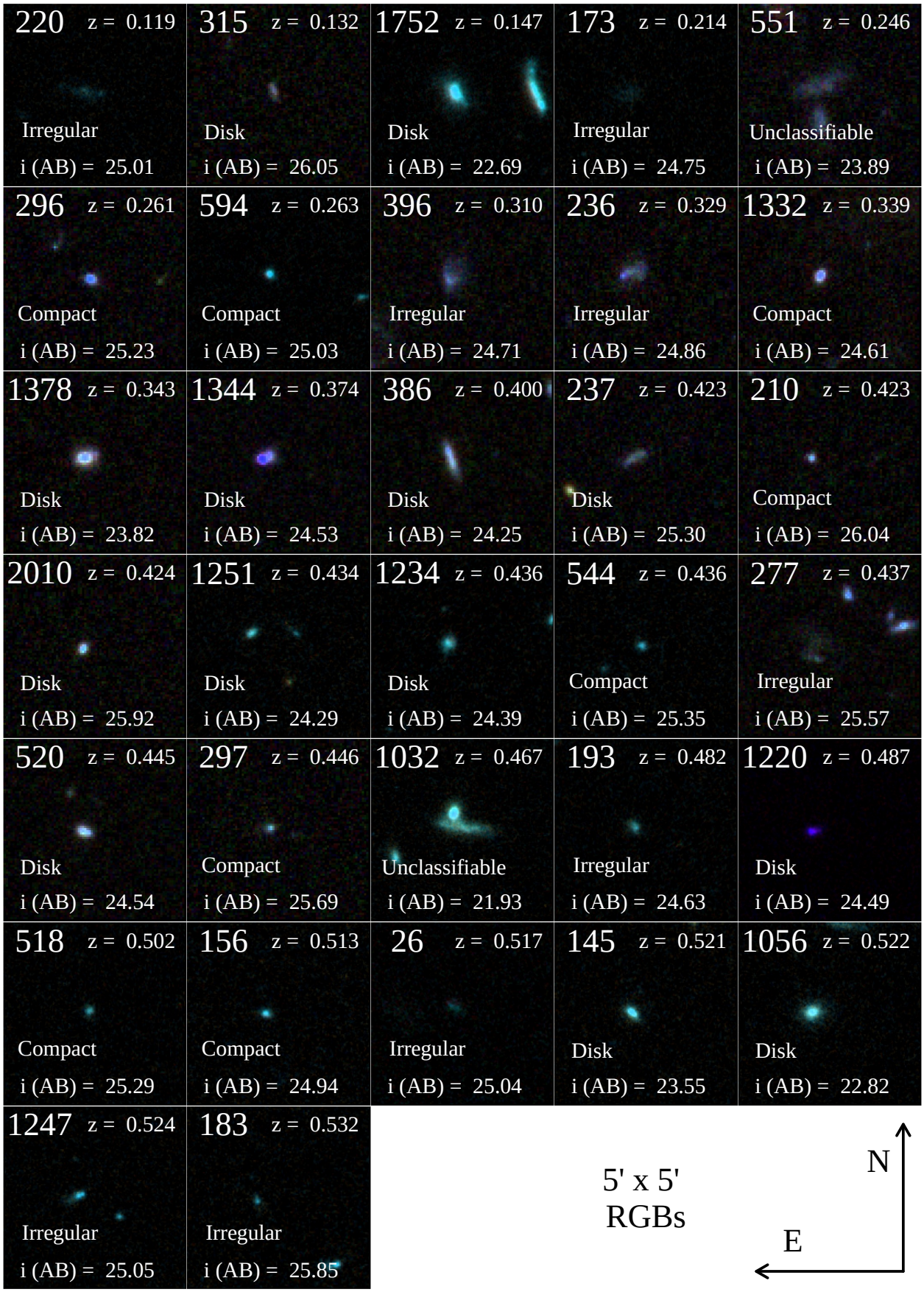

Figure 6.3: RGB images built using ACS v, i, and z bands on GOODS-S and v and z bands for those galaxies on GEMS.

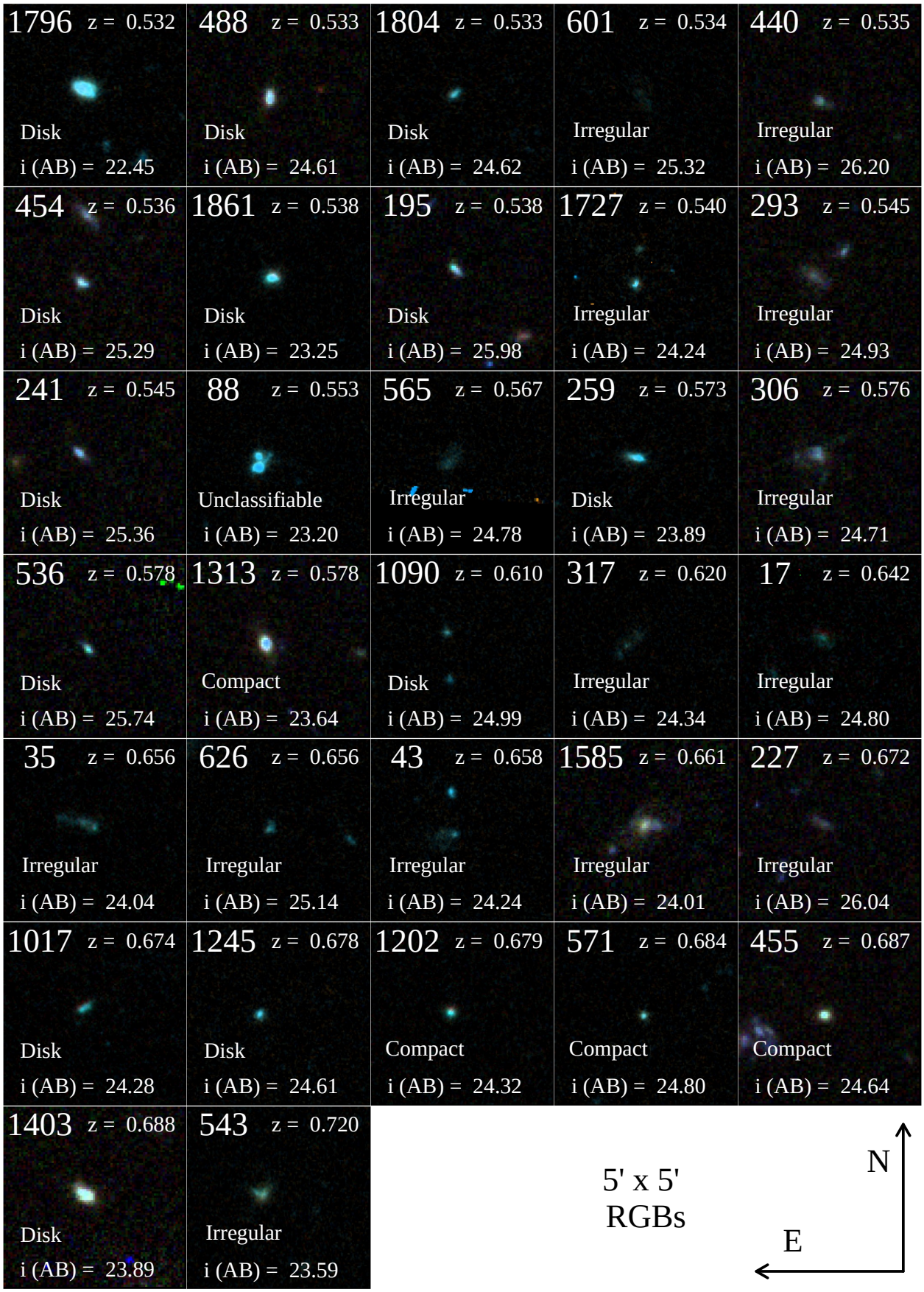

Figure 6.4: RGB images built using ACS v, i, and z bands on GOODS-S and v and z bands for those galaxies on GEMS.

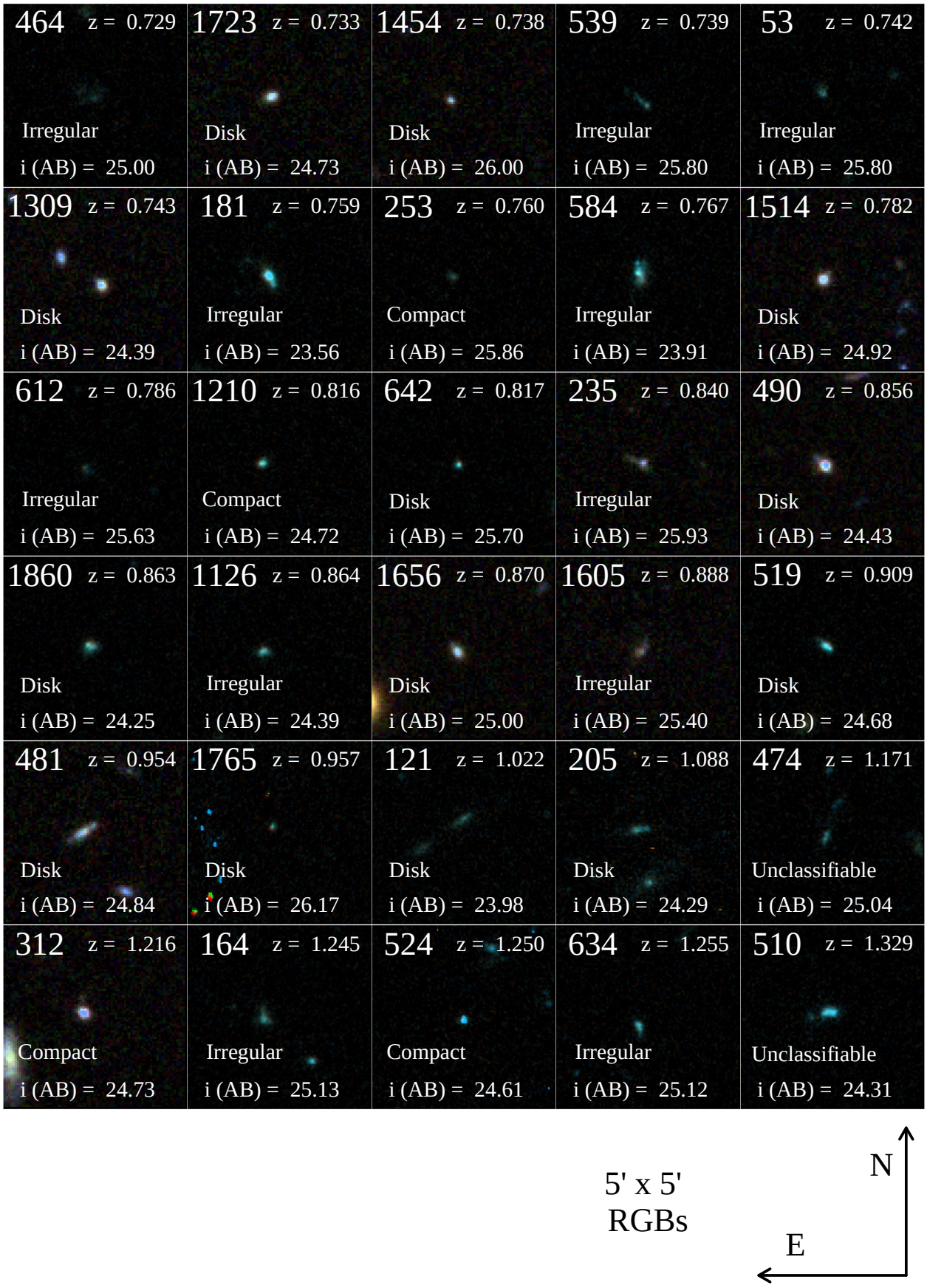

Figure 6.5: RGB images built using ACS v, i, and z bands on GOODS-S and v and z bands for those galaxies on GEMS.

6.2 Colors and Luminosities

Our sample of galaxies span a range in observed color -0.5 $\lesssim v-z \lesssim$ 1.2. In Figure 6.6 we show the distribution of observed $v-z$, $B-v$ and $B-z$ colors (left, central, and right panel) of our galaxies with redshift, and the tracks described by some of the templates published by Fukugita et al. (1995). First of all, we observe that our $B-v$ color (central panel in Figure 6.6) does not seem to be useful to discriminate between different templates along the whole redshift range as the distances between the tracks decrease with increasing z. Most of our galaxies lie in the area populated by star-forming galaxies (between Sab and Sbc) in the three panels of Figure 6.6. Only a few of them go below the track traced by Scd galaxies, into the area populated by Im galaxies. This could indicate that our sample is not made of extremely blue and irregular objects. This assessment could be reinforced by the not-numerous subsample of BCDs found within our final sample (only $\sim$30%). Furthermore, the morphological classification performed in Section 6.1 returned 42% of disk-likes for our sample rather than compact or Irr objects (36% and 15% respectively). Nevertheless, it is worth mentioning that no morphological segregation appears with color.

Redshift allows us to estimate blue rest-frame luminosities. Instead of using the observed photometry and assuming a k-correction based on measured colors and prototype templates (i.e., Fukugita et al. 1995; Kinney et al. 1996), we decide to calculate the synthetic rest-frame photometry using the templates fitted to the photometry and emission lines in the SED-fitting. The reason for this decision is that the templates fitted represent more accurately, by definition, the photometric properties of the targets than simplified prototypes. As always in this case, we rely on the realism of the spectral models.

In Table 6.2 we list: spectroscopic redshifts (Column 2), observed v apparent magnitude (Column 6), $v-z$ observed color (Column 7), k-correction (Column 12), and rest-frame synthetic blue luminosity (Column 13).

6.2.1 UVJ Diagram

The color-color diagram that shows rest-frame $U-V$ vs. $V-J$, also referred to as UVJ diagram (Figure 6.7), is known for being a useful tool to distinguish between quiescent galaxies from star-forming galaxies, as they populate different regions in this plane (a diagonal and a cluster in the upper left-hand region, respectively). $U-V$ color provides information on the blue part of the spectra, in particular on the Balmer break at 4000Å, which is influenced by the presence of a young stellar population (i.e., recent or ongoing SF) and the dust extinction. More precisely, (in absence of dust) this color gives information on the sSFR. Then, not-dusty star-forming galaxies should present bluer values than quiescent galaxies or dusty star-forming galaxies, and therefore, they should appear below them in the diagram. At the same time, $V-J$ color provides information about the older stellar population and also the dust extinction. Therefore, in absence of dust, the horizontal position of the galaxies depend on the mass of the underlying stellar population of the galaxies. A hypothetical paucity of an older underlying stellar population would move the galaxies to the left. The dust extinction produce a reddening in both colors that would move the galaxies both up and to the right. The UVJ diagram breaks the degeneracy between red star-forming and red quiescent galaxies. While galaxies with blue $U-V$ colors in general exhibit relatively unobscured star formation activity, red galaxies could be either quiescent galaxies with evolved

stellar populations or dust-obscured starbursts. But since dust-free quiescent galaxies are blue in $V - J$, they occupy an area in the UVJ plane that is distinct from the star-forming galaxies, allowing the two populations to be empirically separated. UVJ has been used in a number of works recently (e.g., Labbé et al. 2005; Wuyts et al. 2007; Williams et al. 2009; Patel et al. 2012).

In Figure 6.7 we show three UVJ diagrams plotted using the photometry obtained from the templates as mentioned before. Left, central and right panels show the dependence with stellar mass, SFR, and sSFR respectively using the size of the points (i.e., increasing values correspond to larger circles). The targets appear on a sequence that goes from bluer to redder in both colors. Nevertheless, they are not located on the sequence of star-forming galaxies found by the other works mentioned, but parallel over it. This means that $U-V$ colors are redder for a given sequence $V-J$ color, or/and that the $V-J$ colors are bluer for a given sequence $U-V$ color. Interestingly, the area populated by our sample of dwarfs is only found to be populated by galaxies at high redshift ($z \gtrsim 3$; Kriek et al. 2014; Skelton et al. 2014). We consider two possible reasons for this offset in the SF sequence of our sample. The first would be that our sample is not conformed by "booming" star-forming galaxies. This is actually something we have already been observing. The second would be the paucity of stellar mass in older stellar populations.

In the left panel in Figure 6.7, the symbol sizes increase with increasing stellar mass. We see that galaxies with higher mass tend to present the redder values in both colors. In the central panel, the symbols sizes increase with increasing SFR. In theory, considering the existence of the main sequence of SF we should see the same trend in this case, but it is not strikingly clear. In the right panel, the symbols sizes increase with increasing sSFR. As we can see, the galaxies with lower sSFR tend to be redder in both colors. Actually, some of the galaxies with lowest sSFR fall already within the quiescent region.

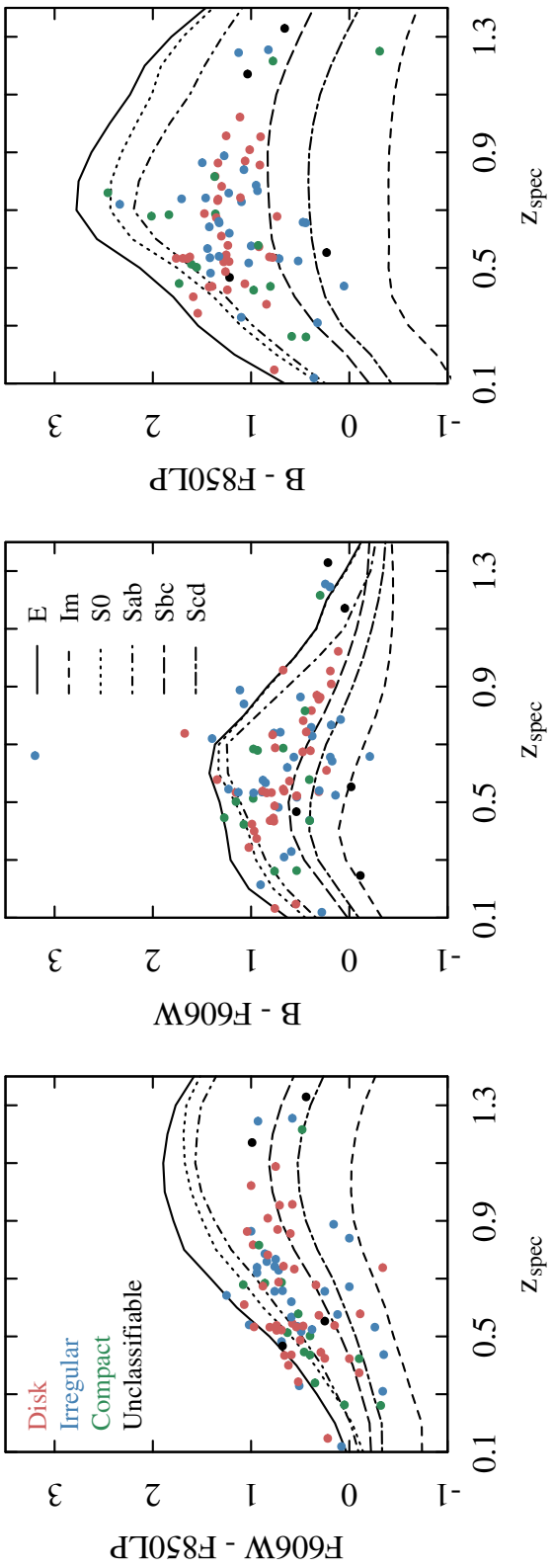

Figure 6.6: Observed colors as a function of redshift: $v - z$, MUSYC $B - v$, and MUSYC $B - z$, left, central, and right panels, respectively. The tracks represent colors variations of the templates by Fukugita et al. (1995).

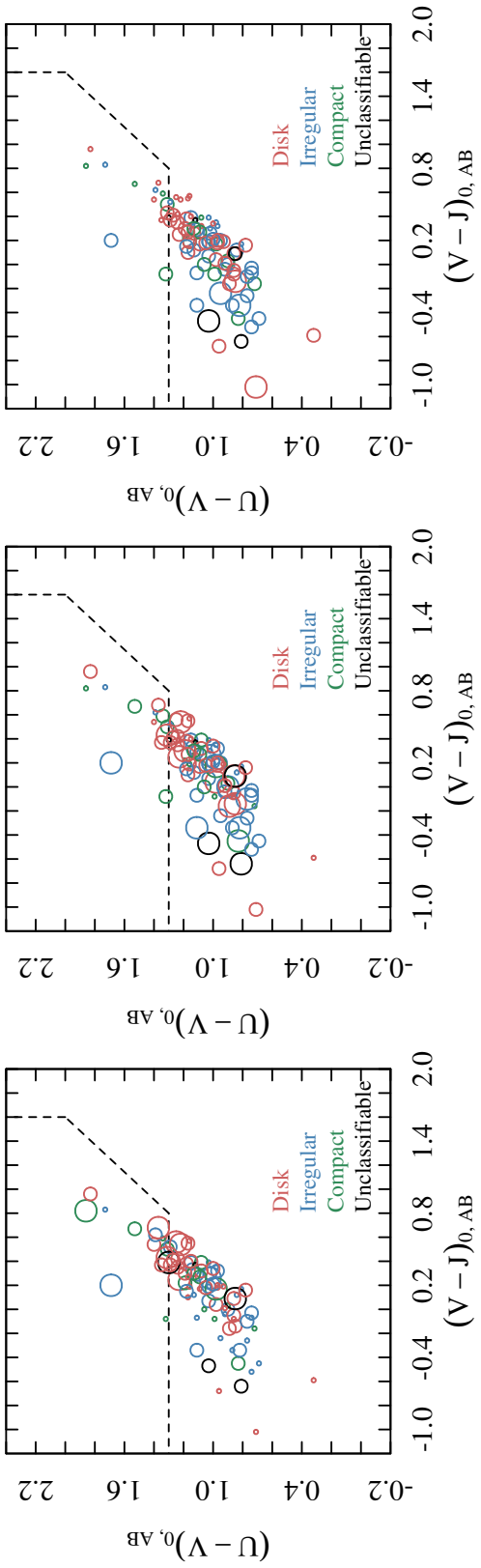

Figure 6.7: Rest-frame $U - V$ vs. $V - J$ colors for our sample. Dashed lines mark the boundaries that separate star-forming galaxies (bottom right) and quiescent (top left) galaxies, as defined by Williams et al. (2009). Left: Symbol size increase with stellar mass. Center: Symbol size increase with SFR. Center: Symbol size increase with SSFR.

6.3 Structural Parameters

The qualitative classification of galaxies based on their appearance has been proven to be somewhat problematic due to its subjective nature, which leads to discrepancies between classifications performed by different individuals. An approach to quantify the structural properties of galaxies is the analysis of their 1D or 2D light distribution and decomposition. Generally, the galaxy light profile is fitted with analytical profiles for the different components (e.g., disk-likes, bulges, and bars). The most commonly used profile is the so called Sersic (1968) profile, defined as

$$\Sigma(r) = \Sigma_{eff}\, e^{-k\left[(r/R_{eff})^{1/n}-1\right]} \tag{6.1}$$

where R_{eff} is the effective radius of the galaxy, defined as the radius within which half the luminosity of the galaxy is enclosed, Σ_{eff} is the surface brightness at R_{eff}, n is the Sèrsic index that controls the shape of the intensity profile, and k is coupled to n such that half of the total flux is always within R_{eff}. In Figure 6.8 we show the shape of Sèrsic profile for different values of n (Figure 1 by Graham and Driver 2005). Typically, n presents values smaller than 1.5 for late-type galaxies, and larger than 1.5 for early-type galaxies.

The Advanced Camera for Surveys General Catalog (ACS-GC), presented by Griffith et al. (2012), provides structural information of the galaxies in the HST/ACS surveys on GOODS-S and GEMS areas (among others). To obtain the quantitative morphology they use the Galaxy Analysis over Large Areas: Parameter Assessment by Galfitting Objects from SExtractor (GALAPAGOS; Häußler et al., 2011), which incorporates both GALFIT (Peng et al., 2002) and SExtractor (Bertin and Arnouts, 1996) on HST/ACS F606W and F850LP (v and z-bands, respectively) imaging. GALFIT is designed to measure structural parameters from galaxy images. Griffith et al. (2012) model each source in the catalog with a single Sèrsic profile. Each galaxy in the catalog is assigned a set of structural parameters derived from the fit and a quality flag (0 for the good fits and 1 for the bad fits, as defined in Griffith et al. 2012).

Among the different free parameters of the Sèrsic profile available in the catalog, we mainly focus on R_{eff} and n, all of them derived using GALFIT on the ACS v-band. Furthermore, we make use of the surface brightness within the R_{eff}, $\mu_{R_{eff}}$, in the same band. It is worth noting that the radii values derived from both images are very similar in most cases (i.e., $R_{eff,\,v}/R_{eff,\,z}$ median and percentiles are $0.9^{1.1}_{0.6}$). We appreciate slight differences between the values of these parameters for the diverse morphological classes. Regarding the half-light radius we see that, as expected, compacts present the lowest values ($0.5^{0.7}_{0.3}$), followed by disk-likes ($0.8^{1.4}_{0.6}$), irregulars ($1.2^{2.2}_{0.9}$) and unclassifiable ($1.6^{1.9}_{1.1}$). The extremely small sizes of some of the galaxies in our sample, in particular compacts, and a small percentage of disk-likes (possibly misclassified), are in the range of those characteristic of ultra compact blue dwarf galaxies, as defined by Corbin et al. (2006), and Green Peas (Cardamone et al., 2009). Median surface brightness is maximum for compact galaxies ($20.9^{22.1}_{20.0}$), followed by disk-likes and unclassifiable systems with very similar values ($21.9^{21.1}_{22.6}$ and $21.9^{24.0}_{20.1}$, respectively), and finally, irregulars ($23.5^{23.9}_{21.3}$). All these results are consistent with what is expected from the different morphologies.

In Table 6.2 we show the values of $R_{eff,\,v}$ in kpc (Column 8), surface brightness within the $R_{eff,\,v}$ or $\mu_{R_{eff},\,v}$ (Column 9), n_v (Column 10), GALFIT fit quality flag (Column 11), for each of the galaxies in our sample ordered by identification. We do not find counterparts for four of our

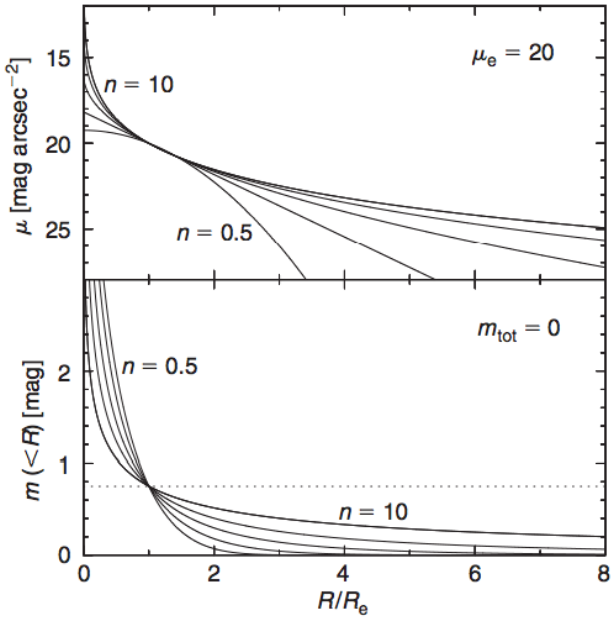

Figure 6.8: Top panel: Sèrsic surface brightness (μ in the plot) profiles for n = 0.5,1,2,4, and 10. The curves are normalized at $\mu_e = 20$, which means that they are forced to match such value of the surface brightness at the R_{eff} (R_e in the plot). Bottom panel: Sèrsic aperture magnitude profiles normalized such that the total magnitude (m_{tot}) equals zero. Figure 1 by Graham and Driver 2005.

systems (IDs 227, 237, 253, and 524) within the ACS-GC. In some cases the counterpart is not found only in z-band (IDs 173, 293, 315, 551, and 601).

The structural properties of galaxies tend to follow certain scaling relationships, that can be used to probe their nature (Binggeli, 1994; Phillips et al., 1997). In Figure 6.9 (left panel) we plot the distribution of blue luminosities with redshift. The galaxies span a range of approximately 10 mag following a strong correlation due to the observational bias. B rest-frame luminosity against the $R_{eff,v}$ (kpc) is shown in the right panel of Figure 6.9. Despite the difference in wavelength, we consider that the rest-frame blue band R_{eff} is well traced by the $R_{eff,v}$. As we have already mentioned, the difference between the R_{eff} measured on the v and z-bands are small. Except for the brightest systems, the sample falls well off the sequence defined by giant spirals and ellipticals. In the central panel of the same figure we represent the luminosity against the surface brightness. We also represent the regions populated mainly by ellipticals, spirals, irregulars and spheroidals (Phillips et al., 1997). Interestingly, our irregulars populate mainly the irregulars region and partially the spheroidal area, while compacts and disk-likes appear spread mainly over the spheroidal region (due to their compactness). The galaxies that appear on elliptical galaxies sector would move to the region populated by the rest of the sample if they suffered simple fading (arrow).

In order to test if the visual morphology of the galaxies in our sample is associated with their light profile, in Figure 6.10 we show the distribution of the different morphological types in surface brightness, effective radius, absolute magnitude and Sersic index. In order to be as consistent as possible we use the surface brightness, effective radius and Sèrsic index derived by Griffith et al. (2012) for ACS F606W band. The the rest frame B band absolute magnitude is derived using the best-fitting template. In the left panel we do not apreciate any trend between n and the luminosity of the galaxies in our sample. However, we can see that the central and right panles show a slight

trend in which galaxies characterized byless surface brightness and larger effective radii present lower values of n. Although Irr galaxies appear to dominate the lowest Sèrsic indexes, the overlap of the different morphological types in this plots question the efficiency of n to separate different dwarf morphological populations. Actually, Mahajan et al. (2015) also claim that while Sèrsic index appears to be a good quantitative representation of the morphology for luminous galaxies, it is not an effective classifying index for dwarfs, even at the low redshift they explore ($z \leq 0.02$). Average values present clearer and expected differences between the types. Sèrsic indexes for disk-like and Irr are $1.1^{3.2}_{0.6}$ and $0.9^{1.7}_{0.4}$ respectively, what would correspond to late-type galaxies ($n<1.5$), while compact and unclassifiable galaxies present higher values ($1.8^{3.2}_{1.2}$ and $2.0^{5.6}_{0.1}$). Nevertheless, n distribution for disk-likes present an extended tail reaching a maximum at values of about 4, which could mean that we are including an heterogeneous sample of galaxies in this type, or a contamination by compacts. Number counts are too small to be able to assert such hypothesis.

In their work, Mahajan et al. (2015) also perform a multi-dimensional approach to identify possible clustering of the different dwarf population, combining structural properties with physical parameters such as SFR, sSFR or stellar mass. In this way, they try to explore hypothetical differences hidden within the 2-dimensional plots. The SFR and sSFR distribution of passively evolving DGs statistically distinguish them from other galaxies with similar luminosity, but they do not find any other difference between them and/or star-forming populations. Their interpretation for this is that "the morphology classification scheme(s) used in literature for dwarf galaxies only reflect the observational differences based on luminosity and surface brightness among the apparent distinct classes, rather than any physical differences between them".

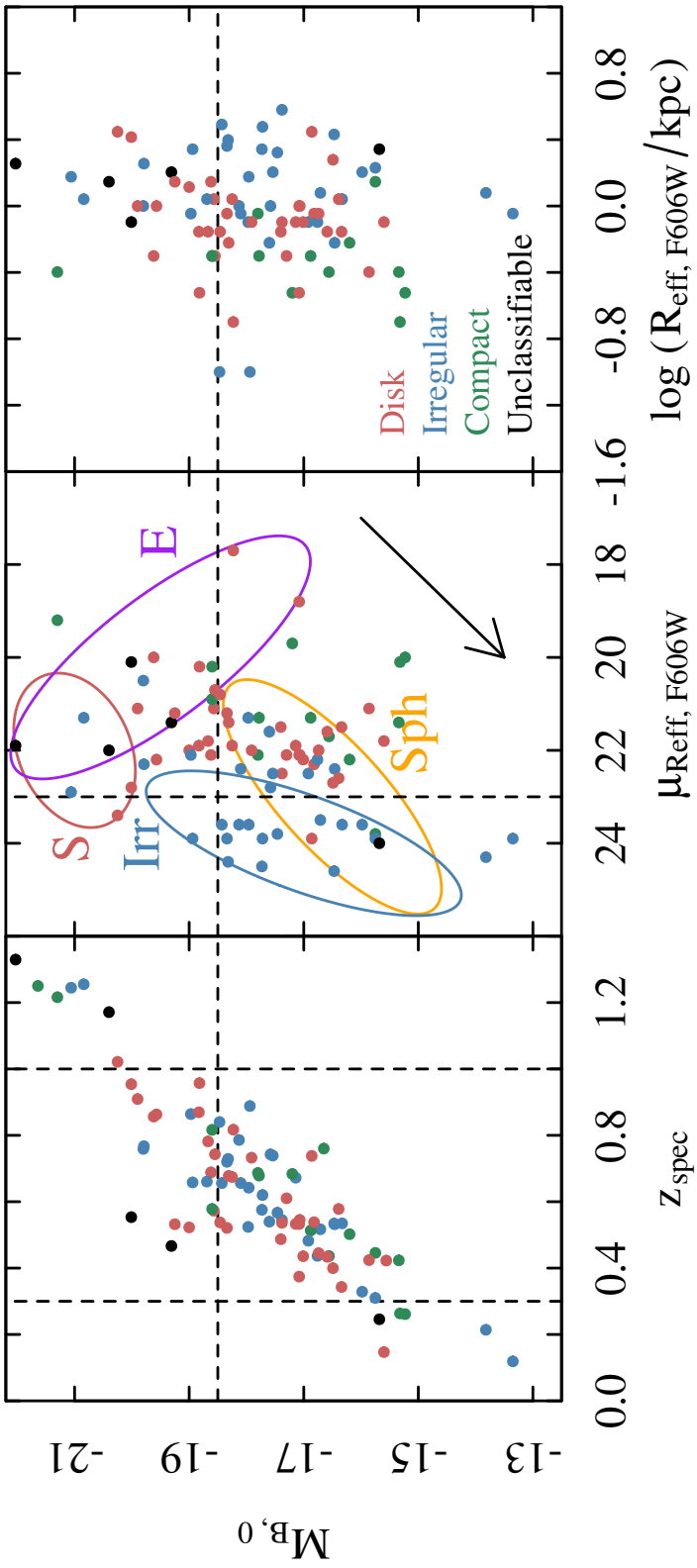

Figure 6.9: Left: the distribution of derived absolute rest-frame B magnitude with redshift. Our sample of galaxies spans a wide range in luminosity, indicating its level of heterogeneity. Center: absolute rest-frame B magnitude against the ACS F606W band surface brightness within the effective radius (uncertainties of 0.2 mag arcsec^{-2}). The arrow shows the direction of simple fading. Right: relation between rest-frame blue luminosities and effective radius measured on the ACS F606W band. The effective radius and surface brightness are taken from the catalog presented by Griffith et al. (2012).

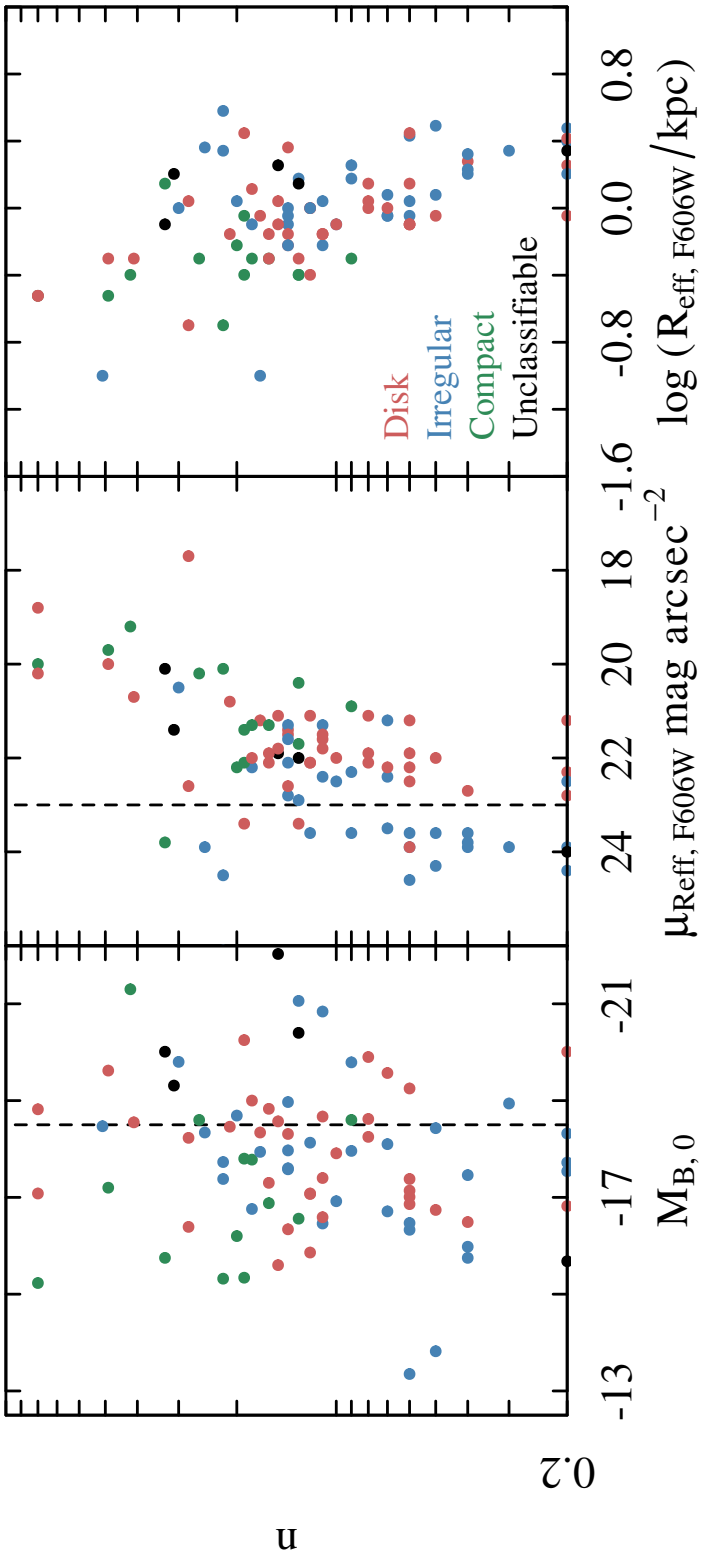

Figure 6.10: Left: the distribution of Sèrsic index with the derived absolute rest-frame B magnitude (obtained from the best-fit template). Our sample of galaxies spans a wide range in luminosity, indicating its level of heterogeneity. Center: Sèrsic index against the ACS F606W band surface brightness within the effective radius. Right: relation between the Sèrsic index and effective radius measured on the ACS F606W band. Effective radii, surface brightness, and Sèrsic indexes are taken from the catalog published by Griffith et al. (2012) and present uncertainties of 0.1 kpc, 0.2 mag arcsec^{-2}, and 0.2, respectively. Uncertainties are small in all plots.

Table 6.2: Morphology

ID	z_{spec}	Morph. Class	Interact. Class	Flag	v	$v-z$	R_{eff} (kpc)	$\mu_{Reff,v}$ mag arcsec^{-2}	n	Flag Galfit	$k-$corr.	$M_{B,0}$
(1)	(2)	(3)	(4)	(5)	(6)	(7)	(8)	(9)	(10)	(11)	(12)	(13)
17	0.642	3	2	0	25.55 ± 0.03	1.25 ± 0.05	2.0 ± 0.1	23.6 ± 0.1	0.9 ± 0.1	0	0.51	-17.88
26	0.517	3	3	0	25.82 ± 0.03	0.49 ± 0.07	1.3 ± 0.1	23.5 ± 0.1	0.7 ± 0.1	0	0.28	-16.81
35	0.656	3	1	0	24.75 ± 0.02	0.76 ± 0.04	4.2 ± 0.1	23.6 ± 0.1	0.5 ± 0.0	0	0.53	-18.76
43	0.658	3	2	1	25.02 ± 0.02	0.68 ± 0.05	3.0 ± 0.1	23.9 ± 0.0	0.3 ± 0.0	0	0.54	-18.50
53	0.742	3	0	0	25.84 ± 0.03	0.76 ± 0.04	1.4 ± 0.1	22.8 ± 0.1	1.4 ± 0.2	0	0.71	-18.17
88	0.553	5	1	1	23.26 ± 0.01	0.25 ± 0.08	0.9 ± 0.0	20.1 ± 0.0	3.3 ± 0.2	0	0.35	-19.62
121	1.022	1	3	1	25.25 ± 0.04	1.00 ± 0.06	5.6 ± 0.4	23.4 ± 0.2	1.9 ± 0.2	0	1.04	-19.95
145	0.521	1	-1	0	24.21 ± 0.01	0.74 ± 0.01	1.0 ± 0.0	21.2 ± 0.0	1.7 ± 0.1	0	0.28	-18.44
156	0.513	4	3	0	25.18 ± 0.01	0.63 ± 0.06	0.6 ± 0.0	21.3 ± 0.1	1.6 ± 0.2	0	0.27	-17.42
164	1.245	3	2	0	25.07 ± 0.02	0.93 ± 0.04	3.8 ± 0.1	22.9 ± 0.1	1.3 ± 0.1	0	1.27	-20.89
173	0.214	3	3	0	25.30 ± 0.03	–	0.8 ± 0.0	24.3 ± 0.1	0.5 ± 0.1	0	-0.18	-14.64
181	0.759	3	3	0	24.01 ± 0.01	0.84 ± 0.02	1.5 ± 0.0	20.5 ± 0.1	3.0 ± 0.2	0	0.74	-20.10
183	0.532	3	2	0	25.71 ± 0.03	-0.26 ± 0.08	0.7 ± 0.0	22.4 ± 0.1	1.1 ± 0.2	1	0.31	-17.02
193	0.482	3	3	0	25.18 ± 0.01	0.69 ± 0.03	0.9 ± 0.0	22.5 ± 0.1	1.0 ± 0.1	0	0.21	-17.20
195	0.538	1	3	0	25.70 ± 0.04	0.15 ± 0.07	1.0 ± 0.1	22.3 ± 0.2	0.2 ± 0.1	1	0.32	-17.07
205	1.088	1	2	0	25.03 ± 0.02	0.75 ± 0.04	4.8 ± 0.2	22.6 ± 0.1	1.4 ± 0.1	0	1.09	-20.39
210	0.423	4	3	0	25.89 ± 0.03	-0.10 ± 0.08	0.4 ± 0.0	21.4 ± 0.2	1.9 ± 0.6	1	0.11	-16.05
220	0.119	3	3	0	24.89 ± 0.02	0.08 ± 0.12	0.6 ± 0.0	23.9 ± 0.1	0.6 ± 0.1	0	-0.25	-13.58
227	0.672	3	2	0	–	–	–	–	–	–	0.57	–
235	0.840	3	-1	0	25.05 ± 0.02	–	0.1 ± 7.5	$12.7 \pm$ –.–	$5.1 \pm$ –.–	1	0.85	-19.44
236	0.329	3	2	0	24.83 ± 0.02	0.51 ± 0.05	1.4 ± 0.0	23.6 ± 0.1	0.4 ± 0.0	0	-0.03	-16.33
237	0.423	1	3	0	–	–	–	–	–	–	0.11	–
241	0.545	1	3	0	25.47 ± 0.03	0.58 ± 0.06	1.2 ± 0.1	22.1 ± 0.1	1.2 ± 0.2	0	0.33	-17.35
253	0.760	4	3	0	–	–	–	–	–	1	0.75	–
259	0.573	1	3	0	24.17 ± 0.01	0.31 ± 0.17	1.3 ± 0.0	21.1 ± 0.1	1.5 ± 0.1	0	0.39	-18.84
277	0.437	3	2	0	25.27 ± 0.04	-0.35 ± 0.07	0.8 ± 0.0	22.2 ± 0.1	1.8 ± 0.2	0	0.14	-16.78
293	0.545	3	2	1	24.61 ± 0.12	–	4.4 ± 0.8	26.1 ± 0.4	2.2 ± 0.3	1	0.33	-18.21
296	0.261	4	3	0	24.62 ± 0.06	-0.32 ± 0.08	0.2 ± 0.0	20.0 ± 0.2	8.0 ± 1.9	1	-0.12	-15.87

Continues on next page

Table 6.2: Morphology. Cont.

ID	z_{spec}	Morph. Class	Interact. Class	Flag	v	$v-z$	$R_{eff,v}$ (kpc)	$\mu_{Reff,v}$ mag arcsec^{-2}	n	Flag Galfit	$k-$corr.	$M_{B,0}$
(1)	(2)	(3)	(4)	(5)	(6)	(7)	(8)	(9)	(10)	(11)	(12)	(13)
297	0.446	4	-1	0	25.49 ± 0.12	0.46 ± 0.14	1.4 ± 0.3	23.8 ± 0.5	3.3 ± 0.7	1	0.15	-16.63
306	0.576	3	2	0	24.75 ± 0.06	0.12 ± 0.13	2.7 ± 0.3	24.5 ± 0.2	2.2 ± 0.2	0	0.39	-18.28
312	1.216	4	3	0	24.65 ± 0.02	0.48 ± 0.04	0.9 ± 0.1	19.2 ± 0.2	4.2 ± 0.8	1	1.22	-21.20
315	0.132	1	2	0	26.02 ± 0.07	–	0.3 ± 0.0	23.4 ± 0.3	1.3 ± 0.2	1	-0.24	-12.70
317	0.620	3	-1	0	25.23 ± 0.02	0.59 ± 0.05	3.8 ± 0.1	23.9 ± 0.1	0.2 ± 0.0	0	0.47	-18.07
386	0.400	1	3	0	24.63 ± 0.02	0.62 ± 0.04	1.8 ± 0.0	22.7 ± 0.1	0.4 ± 0.1	0	0.08	-17.13
396	0.310	3	2	0	24.78 ± 0.02	-0.34 ± 0.07	1.4 ± 0.0	23.9 ± 0.1	0.4 ± 0.0	0	-0.05	-16.21
440	0.535	3	2	0	25.95 ± 0.04	0.53 ± 0.09	1.3 ± 0.1	23.6 ± 0.2	0.6 ± 0.1	1	0.31	-16.80
454	0.536	1	3	0	25.48 ± 0.02	0.47 ± 0.36	1.0 ± 0.0	22.5 ± 0.1	0.6 ± 0.1	1	0.31	-17.28
455	0.687	4	3	0	25.40 ± 0.04	0.69 ± 0.07	1.2 ± 0.1	22.1 ± 0.2	1.9 ± 0.3	1	0.60	-18.30
464	0.729	3	3	0	25.36 ± 0.02	0.72 ± 0.05	3.7 ± 0.1	24.4 ± 0.1	0.2 ± 0.0	0	0.68	-18.58
474	1.171	5	1	1	25.69 ± 0.02	0.99 ± 0.10	3.3 ± 0.1	22.0 ± 0.1	1.3 ± 0.2	0	1.17	-20.01
481	0.954	1	3	0	25.06 ± 0.02	0.71 ± 0.05	4.9 ± 0.1	22.8 ± 0.1	0.2 ± 0.1	1	0.98	-19.89
488	0.533	1	3	0	24.92 ± 0.02	0.54 ± 0.04	1.1 ± 0.0	22.1 ± 0.1	1.2 ± 0.1	0	0.31	-17.82
490	0.856	1	2	0	24.75 ± 0.03	0.60 ± 0.04	0.8 ± 0.0	20.0 ± 0.2	4.9 ± 0.8	1	0.87	-19.80
510	1.329	5	1	0	24.22 ± 0.01	0.44 ± 0.03	4.7 ± 0.1	21.9 ± 0.1	1.5 ± 0.1	0	1.39	-22.04
518	0.502	4	3	0	25.62 ± 0.04	0.40 ± 0.06	0.6 ± 0.0	22.2 ± 0.2	2.0 ± 0.4	1	0.25	-16.90
519	0.909	1	3	0	24.92 ± 0.01	0.83 ± 0.02	1.8 ± 0.0	21.1 ± 0.1	0.8 ± 0.1	0	0.93	-19.85
520	0.445	1	3	0	24.99 ± 0.01	0.29 ± 0.03	0.9 ± 0.0	22.0 ± 0.1	0.5 ± 0.0	0	0.15	-17.12
524	1.250	4	3	0	–	–	–	–	–	1	1.28	–
536	0.578	1	3	0	25.64 ± 0.07	-0.11 ± 0.55	1.4 ± 0.2	22.6 ± 0.3	2.8 ± 0.6	1	0.40	-17.40
539	0.739	3	2	0	25.80 ± 0.03	0.94 ± 0.08	2.4 ± 0.1	22.5 ± 0.1	0.2 ± 0.1	1	0.70	-18.19
543	0.720	3	2	0	24.28 ± 0.03	0.94 ± 0.03	3.4 ± 0.2	23.9 ± 0.1	2.5 ± 0.1	0	0.67	-19.61
544	0.436	4	3	0	25.46 ± 0.02	0.40 ± 0.05	0.4 ± 0.0	21.7 ± 0.1	1.3 ± 0.2	1	0.13	-16.58
551	0.246	5	2	1	24.86 ± 0.02	–	1.7 ± 0.0	24.0 ± 0.1	0.2 ± 0.0	0	-0.14	-15.47
565	0.567	3	3	0	25.01 ± 0.02	0.59 ± 0.04	2.5 ± 0.1	23.8 ± 0.1	0.4 ± 0.0	0	0.37	-17.96
571	0.684	4	3	0	25.69 ± 0.04	0.86 ± 0.06	0.4 ± 0.0	19.7 ± 0.3	4.9 ± 1.6	1	0.59	-17.99
584	0.767	3	-1	0	24.27 ± 0.01	0.75 ± 0.02	2.8 ± 0.0	22.3 ± 0.0	0.9 ± 0.0	0	0.76	-19.88

Continues on next page

Table 6.2: Morphology. Cont.

ID	z_{spec}	Morph. Class	Interact. Class	Flag	v	$v-z$	$R_{eff,v}$ (kpc)	$\mu_{Reff,v}$ mag arcsec^{-2}	n	Flag Galfit	$k-$corr.	$M_{B,0}$
(1)	(2)	(3)	(4)	(5)	(6)	(7)	(8)	(9)	(10)	(11)	(12)	(13)
594	0.263	4	3	0	24.78 ± 0.01	0.05 ± 0.03	0.2 ± 0.0	20.1 ± 0.1	2.2 ± 0.3	0	-0.12	-15.73
601	0.534	3	2	0	25.56 ± 0.04	–	3.2 ± 0.2	24.6 ± 0.1	0.6 ± 0.1	0	0.31	-17.18
612	0.786	3	2	0	26.12 ± 0.05	0.86 ± 0.09	1.6 ± 0.1	23.6 ± 0.2	1.2 ± 0.2	1	0.80	-18.13
626	0.656	3	2	0	25.45 ± 0.02	0.25 ± 0.04	1.2 ± 0.0	22.4 ± 0.1	0.7 ± 0.1	0	0.53	-18.06
634	1.255	3	2	0	25.26 ± 0.01	0.58 ± 0.03	2.8 ± 0.1	21.3 ± 0.1	1.1 ± 0.1	0	1.29	-20.75
642	0.817	1	3	0	25.87 ± 0.13	0.98 ± 0.13	0.4 ± 0.1	17.7 ± 3.0	2.8 ± 1.1	1	0.83	-18.52
1017	0.674	1	2	0	25.10 ± 0.01	0.88 ± 0.03	1.6 ± 0.0	21.9 ± 0.1	0.8 ± 0.1	0	0.57	-18.52
1032	0.467	5	1	1	22.85 ± 0.01	0.68 ± 0.01	1.7 ± 0.0	21.4 ± 0.1	3.1 ± 0.1	0	0.18	-19.42
1056	0.522	1	3	0	23.56 ± 0.01	0.69 ± 0.02	1.5 ± 0.0	22.0 ± 0.0	1.8 ± 0.1	0	0.29	-19.10
1090	0.610	1	3	1	26.00 ± 0.03	1.07 ± 0.15	0.6 ± 0.0	22.1 ± 0.2	1.6 ± 0.4	1	0.46	-17.24
1126	0.864	3	3	0	25.26 ± 0.02	1.00 ± 0.03	1.5 ± 0.0	22.1 ± 0.1	1.4 ± 0.2	0	0.88	-19.33
1202	0.679	4	-1	0	25.13 ± 0.02	1.08 ± 0.04	0.7 ± 0.0	21.3 ± 0.1	1.8 ± 0.2	0	0.58	-18.52
1210	0.816	4	3	0	25.43 ± 0.04	0.92 ± 0.05	0.8 ± 0.1	20.9 ± 0.3	0.9 ± 0.5	1	0.83	-18.95
1220	0.487	1	0	0	24.70 ± 0.01	0.50 ± 0.03	0.8 ± 0.0	21.5 ± 0.1	1.1 ± 0.1	0	0.22	-17.72
1234	0.436	1	3	0	24.61 ± 0.01	0.59 ± 0.02	0.8 ± 0.0	22.2 ± 0.0	0.6 ± 0.0	0	0.13	-17.43
1245	0.678	1	-1	0	25.13 ± 0.02	0.34 ± 0.04	0.8 ± 0.0	21.4 ± 0.1	1.4 ± 0.2	0	0.58	-18.51
1247	0.524	3	2	1	24.99 ± 0.01	0.38 ± 0.06	0.9 ± 0.0	21.3 ± 0.1	1.4 ± 0.1	0	0.29	-17.69
1251	0.434	1	3	1	25.05 ± 0.01	0.66 ± 0.02	0.7 ± 0.0	21.6 ± 0.1	1.1 ± 0.1	0	0.13	-16.98
1309	0.743	1	2	1	25.14 ± 0.04	0.67 ± 0.06	0.7 ± 0.0	20.7 ± 0.2	4.1 ± 0.8	1	0.71	-18.88
1313	0.578	4	3	0	24.37 ± 0.01	0.52 ± 0.02	0.6 ± 0.0	20.2 ± 0.1	2.6 ± 0.3	0	0.40	-18.67
1332	0.339	4	3	0	24.79 ± 0.01	0.35 ± 0.03	0.3 ± 0.0	20.4 ± 0.1	1.3 ± 0.2	0	-0.01	-16.46
1378	0.343	1	-1	0	24.18 ± 0.01	0.52 ± 0.03	0.6 ± 0.0	21.5 ± 0.1	1.4 ± 0.1	0	0.00	-17.11
1403	0.688	1	3	0	24.51 ± 0.01	0.72 ± 0.02	1.9 ± 0.0	22.1 ± 0.1	0.8 ± 0.1	0	0.60	-19.19
1454	0.738	1	3	0	25.57 ± 0.05	-0.34 ± 0.08	4.1 ± 0.3	23.9 ± 0.2	0.6 ± 0.1	1	0.70	-18.42
1514	0.782	1	3	0	25.17 ± 0.02	0.83 ± 0.04	1.1 ± 0.0	21.8 ± 0.1	1.1 ± 0.1	0	0.79	-19.06
1585	0.661	3	2	1	21.88 ± 1.22	-1.87 ± 1.22	1.5 ± 2.5	14.1 ± 4.0	2.0 ± 1.7	1	0.54	-21.66
1605	0.888	3	2	0	$25.82 \pm -.—$	$0.16 \pm -.—$	$0.1 \pm -.–$	$14.1 \pm -.–$	$1.7 \pm -.–$	1	0.90	-18.87
1656	0.870	1	2	0	25.60 ± 0.03	0.73 ± 0.05	1.2 ± 0.1	21.9 ± 0.2	1.6 ± 0.3	1	0.88	-19.01

Continues on next page

Table 6.2: Morphology. Cont.

ID	z_{spec}	Morph. Class	Interact. Class	Flag	v	$v-z$	$R_{eff,v}$ (kpc)	$\mu_{Reff,v}$ mag arcsec^{-2}	n	Flag Galfit	$k-$corr.	$M_{B,0}$
(1)	(2)	(3)	(4)	(5)	(6)	(7)	(8)	(9)	(10)	(11)	(12)	(13)
1723	0.733	1	-1	0	25.39 ± 0.03	0.56 ± 0.04	1.2 ± 0.1	22.0 ± 0.1	1.0 ± 0.2	1	0.69	-18.57
1727	0.540	3	2	1	25.28 ± 0.02	1.02 ± 0.04	0.7 ± 0.0	21.6 ± 0.1	1.4 ± 0.3	1	0.32	-17.51
1752	0.147	1	2	0	22.90 ± 0.01	0.22 ± 0.01	0.5 ± 0.0	21.8 ± 0.0	1.5 ± 0.0	0	-0.24	-16.08
1765	0.957	1	3	0	25.78 ± 0.09	0.58 ± 0.09	0.6 ± 0.1	20.2 ± 0.4	8.0 ± 3.5	1	0.98	-19.19
1796	0.532	1	2	0	23.06 ± 0.00	0.81 ± 0.01	1.6 ± 0.0	21.2 ± 0.0	0.6 ± 0.0	0	0.31	-19.67
1804	0.533	1	3	0	25.22 ± 0.01	0.97 ± 0.04	0.9 ± 0.0	21.9 ± 0.1	0.6 ± 0.1	0	0.31	-17.52
1860	0.863	1	3	0	24.86 ± 0.01	1.04 ± 0.02	1.7 ± 0.0	22.2 ± 0.1	0.7 ± 0.1	0	0.87	-19.72
1861	0.538	1	-1	0	23.84 ± 0.01	0.74 ± 0.01	0.8 ± 0.0	20.8 ± 0.0	2.1 ± 0.1	0	0.32	-18.93
1344	0.374	1	-1	0	23.82 ± 0.03	-0.10 ± 0.04	0.3 ± 0.0	18.8 ± 0.1	8.0 ± 1.1	0	0.04	-17.73
2010	0.424	1	-1	0	25.46 ± 0.02	0.25 ± 0.04	0.4 ± 0.0	21.1 ± 0.1	1.2 ± 0.3	1	0.11	-16.49

For each galaxy in our sample we present: (1) object ID; (2) spectroscopic redshift; (3) morphological class with 1, 2, 3, 4, and 5 as Disk-like, Spheroid, Irregular, Compact, and Unclassifiable; (4) interaction class with 1, 2, 3, and -1 as Merger, Interaction, Close neighbor, and None; (5) hypothetical blending flag with 0 and 1 for not-problematic and problematic cases; (6) observed v magnitude, (7) observed $v-z$ color, (8) half-light radius measured on the v-band image in kpc, (9) v surface brightness at the effective radius; (10) Sèrsic index derived from the fit in the v image; (11) GALFIT fit quality flag, 0 and 1 for good or bad fit; (12) k-correction obtained using the Fukugita et al. (1995) templates; (13) rest-frame blue absolute magnitude from the SED-fitting templates. Columns 8, 9, 10, 11 present values from Griffith et al. (2012) morphological catalogs. Galaxies 235 and 1605 present anomalies in the uncertainties of the structural properties. Actually, their GALFIT fit quality denotes a bad fit.

7

Physical Properties

In this section, we describe and discuss the physical properties derived from the SED-fitting analysis and the direct measurements of their spectral features.

7.1 Physical Parameters from SED-fitting

We derive the stellar masses and SFRs for 91 galaxies using the methodology described in Chapter 5. Out of 91, 60 were selected by mass (see Chapter 2) and 31 were selected for qualifying as BCDs. For clarity, we insist in the fact that none of the BCDs candidates matched the low mass selection criterion.

7.1.1 Stellar Mass

Stellar masses span over almost 3 dex, from $10^7 M_\odot$ to from $10^{9.5}$ $M_\odot$ (Figure 7.1, top panels). These values of stellar mass and spectroscopic redshift make our spectroscopically confirmed sample one of the firsts in its kind. Lee et al. (2006) study 25 galaxies in a similar range of stellar mass in the nearby universe. Recently, Henry et al. (2013a) study a sample of 26 emission-line-selected galaxies at z $\sim$0.6–0.7 with stellar masses reaching 10^8 $M_\odot$. We extend this work 1 dex towards lower masses at a similar but wider redshift range. van der Wel et al. (2011) study 69 extreme emission line galaxies (EELG) with stellar masses down to $10^8 M_\odot$ at z>1. The selection of our sample is not biased towards EELGs, nevertheless, if such population existed at z<1 we should be able to detect it. As we have seen, the targets of our study do not present predominantly booming emission lines (rest-frame log EW>3). This could be due to the low statistics we still reach at each redshift. If the starburst that produces the extreme emission is characterized by short timescales, then the probability of observing it is smaller. Besides, booming emission lines can induce an overestimation of stellar masses in a SED-fitting. This could imply that we exclude these galaxies in our mass selection. Nevertheless, we think that the large number of (narrow, medium and broad) bands used to derive stellar masses avoids this possibility. The low fraction of EELGs in our sample could be in agreement with one of the conclusion in the work by van der Wel et al. (2011): "most of the stars in present-day dwarf galaxies formed in strong short-lived bursts, mostly at $z >$ 1". Amorín et al. (2014c) study also a sample of 31 low-luminosity EELG at intermediate redshift (0.2< z <0.9).

In Figure 7.2 we represent the stellar mass estimations based on the photometric redshift

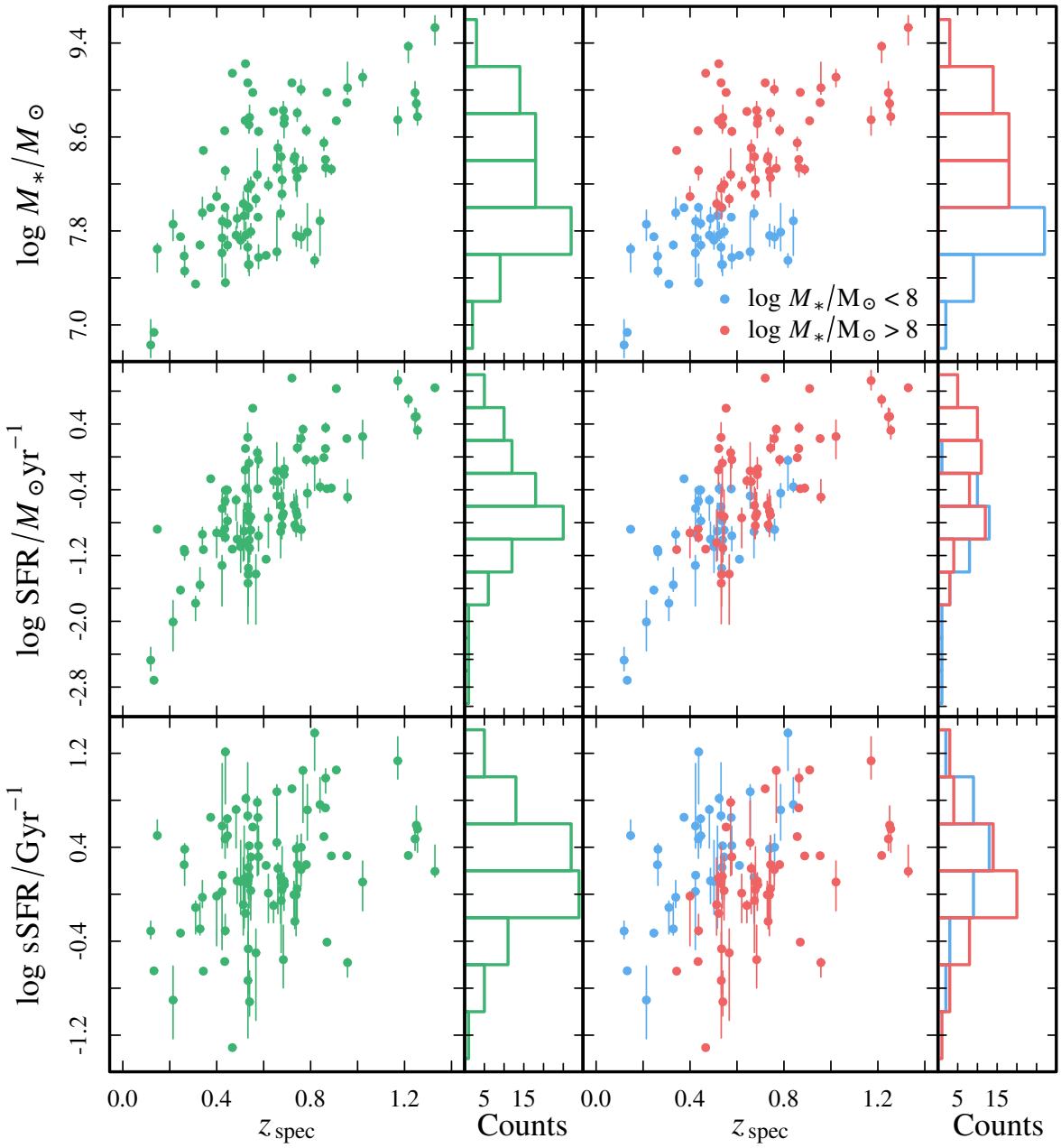

Figure 7.1: SED-fitting best-estimate stellar mass, SFR, and sSFR (top, central, and bottom panels respectively) as a function of $z_{\rm spec}$.

and Rainbow database approach and spectroscopic redshifts using the methodology explained in Chapter 5. We assume an uncertainty of 0.3dex for the former. The color code used is based on the stellar mass derived with spectroscopic redshift. We obtain masses bellow 10^8 $M_\odot$ for 38 galaxies (42%), and therefore, larger masses for 53 objects (58%). The dispersion in terms of absolute deviation is 0.0 with percentiles 16th and 84th, -0.9 and 0.4 respectively. This values slightly improves for the lowest mass subsample (blue points). Due to the fact that a significant fraction of galaxies selected for having stellar masses bellow 10^8 $M_\odot$ are assigned larger spectroscopic masses (50%), the behavior worsens for the red points. This plot is tightly linked to Figure 4.1, in which we can see the differences between the photometric and spectroscopic redshifts. When

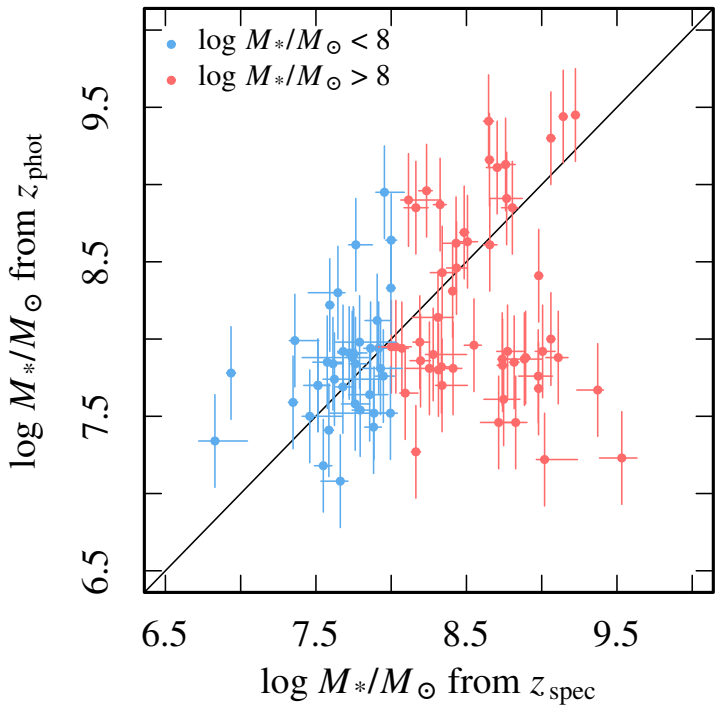

Figure 7.2: Comparison between the stellar masses used for the selection and those obtained through the SED-fitting. See Figure 4.1 in Chapter 4 for a comparison between photometric redshift and spectroscopic redshift. We use blue and red for the galaxies less and more massive than 10^8 $M_\odot$, respectively.

the photometric estimation of the redshift is far bellow the spectroscopic redshift, then the stellar mass is underestimated. Such effect can be observed if we compare both figures. Only a handful of galaxies with photometric stellar masses over the low-mass limit qualify as spectroscopic dwarfs (considering the same mass criterion), which probably means that the photometric redshifts and photometric stellar masses are less reliable in the cases of less massive systems. Despite the dispersion our whole final sample contains exclusively low-mass galaxies with values ranging log $M_*/M_\odot \sim 7 - 9.5$. For this reason no bias is introduced in the properties of the sample.

If we go back to Figure 4.2 we can see how new photometric redshift estimations (e.g., Skelton et al., 2014) are much more reliable. This important fact implies that nowadays our approach could be applied to photometric samples extensively.

7.1.2 Star Formation Rate

SFRs span a wide 3 dex range varying within log SFR/$M_[\odot]$yr^{-1}∼-2.8–0.8. In Figure 7.1 (middle panels) we can see how higher redshift galaxies are biased toward higher SFRs. Although this can be due to our limitation to observe low mass galaxies at high redshifts, we also identify a clear SFR limiting value as a function of redshift. In particular, for those 5 galaxies with log$M_*/M_\odot$<8 at $z_{\rm spec}$>0.7 we obtain SFRs typical of minimum 0.4 dex larger stellar masses. We conclude we could not detect such galaxies if they were undergoing weaker SF processes.

The galaxies in our sample present SFRs compatible with other studies such as (e.g., Brinchmann et al., 2004; Bauer et al., 2005; Salim et al., 2007; Amorín et al., 2012; Atek et al., 2014).

Nevertheless, in our case, for the same masses we include galaxies with lower SFRs and exclude extremely star-forming galaxies (e.g., GPs) or starbursts forming stars at rates $>10 M_{\odot}$ yr^{-1}.

Cosmic star formation history studies over large redshift ranges require the use of different star formation rate indicators. For instance, Hα appears as a useful SFR tracer for nearby galaxies, but it is not easily observable for more distant galaxies, because redshifts larger than $\sim$0.4 shifts the line into the IR wavelengths. As there are discrepancies among the values of SFR obtained through different tracers, we need to take them into account. In our case, we use the SFRs that the SED-fitting approach returns. Pacifici et al. (2015) find a good agreement between the main sequence built with best-estimate SFRs and M_*'s, and those by Whitaker et al. (2012) and Karim et al. (2011) which are obtained by UV+IR and radio, respectively. An individual approach to check whether there is a good correlation between these SFRs and the derived using classical tracers is still to be performed.

7.1.3 Specific Star Formation Rate

As we have already mentioned, sSFR is a very interesting parameter. It is directly linked to the strength of the SF process the galaxy undergoes. In particular, it measures the star formation rate per unit galaxy stellar mass, but it can be interpreted as the inverse of the time the galaxy would need to double its current stellar mass if it maintained the current SFR.

Our sample presents on average high values of sSFR, which means that these low-mass galaxies undergo an intense SF process. Our results (Figure 7.1 lower panels) cover the range between log sSFR$\sim$-10.2$-$-7.8 yr^{-1}. In particular, this range overlaps with the high sSFR values (10^{-7} to 10^{-9} yr^{-1}) obtained by similar studies at lower and higher redshifts (e.g., Brinchmann et al., 2004; Bauer et al., 2005; Salim et al., 2007; Amorín et al., 2012; Atek et al., 2014), and spans towards lower values of sSFR, as expected given the values of SFR.

7.1.4 Star Formation Main Sequence

Figure 7.3 shows the SFR as a function of stellar mass for our sample. We include galaxies with log $M_*/M_{\odot}<8$ as blue points, while we use red points for galaxies with log $M_*/M_{\odot}>8$. We mark the area populated by SDSS with gray contours, and the MSs found by Whitaker et al. (2012, W12) for redshifts 0.2, 0.6, and 1.0 (green lines), and the MS optimized for low-mass galaxies by Whitaker et al. (2014, W14; orange line). As we can see, our sample follows a trend consistent with the MS over 2 dex of stellar mass, with lower mass galaxies presenting lower values of SFR. Due to the differences between the definitions of the MS in the literature and the dispersion of our values, it is not trivial to claim that our sample follows best any of them in particular.

The dispersion of our data could be suggesting that besides "normal" star-forming galaxies (galaxies that belong to the MS), in our sample we include a fraction of galaxies with a SF anomaly, either starbursts or SF deficient systems. This could be a consequence of our selection criteria, in which initially, we do not favor any particular SF level.

It is worth noting that our sample covers a wide range of redshift (0.1–1.3). In this context we need to bear in mind that our sample could be dominated by statistical biases (due to different volumes covered at different redshifts) and observational bias (due to the minimum SFR observable at each redshift). In particular, in the top panel, the galaxies with SFRs below W14 are all

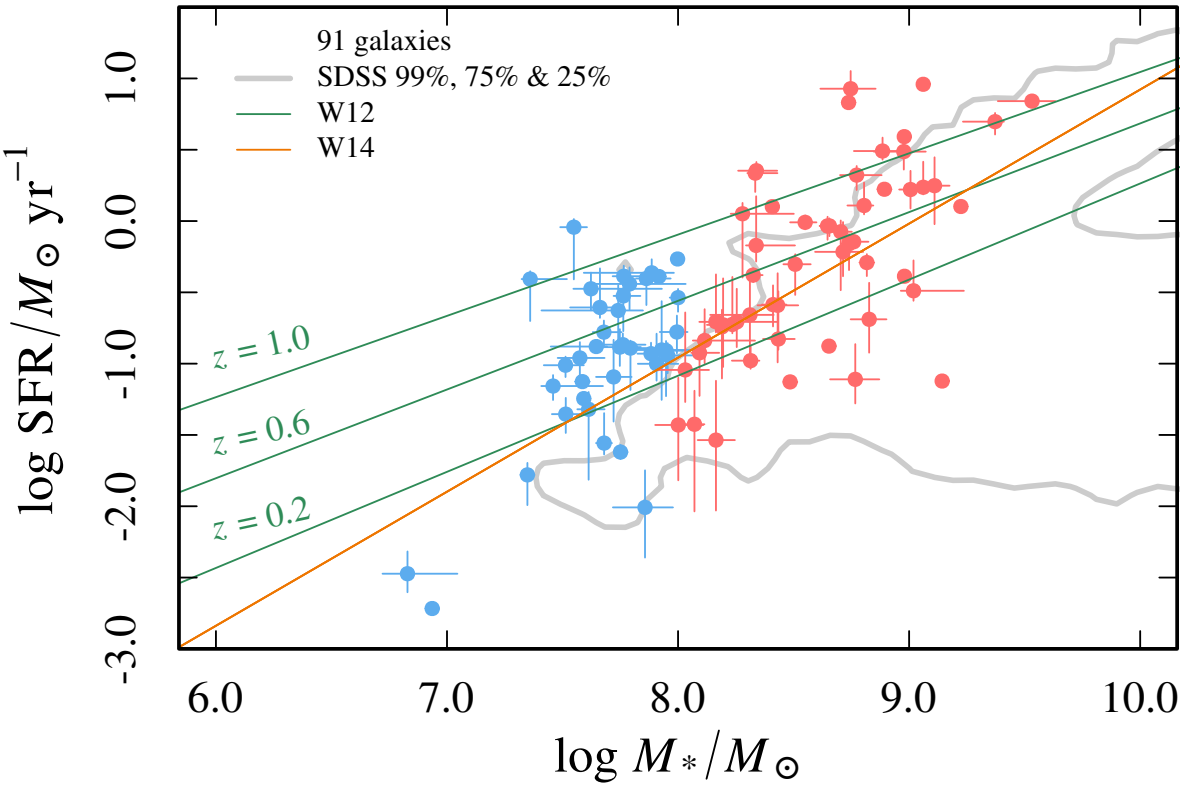

Figure 7.3: Stellar mass-SFR relation for our sample of spectroscopically confirmed low-mass star-forming galaxies color-coded by mass. The plot also shows the SFMS found by Whitaker et al. (2012, W12) for redshifts 0.2, 0.6, and 1.0 (green lines) extended towards lower stellar masses. In addition we show the SFMS derived by Whitaker et al. (2014, W14) for low-mass galaxies in the redshift range between 0.5 and 1.

located at z<0.4 while the galaxies over W14 span the range ∼0.2-0.9. Within this ranges of mass and redshift the further systems present some of the highest SFRs of the subsample, but as we already mention when we described Figure 7.1, we could not observe lower values of SFRs at such redshifts. Hence, the trend with redshift is not clear. The same can be argued for the bottom panel and the most massive galaxies in the sample.

The location of our sample in the MS plane is consistent with the location of the galaxies studied by Atek et al. (2014) in the redshift range between 0.3 and 0.7 (blue points in their Figure 2). However, our sample includes galaxies with 10 times lower SFRs along the whole mass range. The emission line selection they perform to build their sample is probably introducing a lower limit on the SFR, hampering the detection of low-mass and not so strongly star-forming galaxies.

Figure 7.4 shows the relation between sSFR and stellar mass. Our sample populates the area expected, with high values of sSFR (as explained in Section 7.1.3), and a large dispersion. It is clear in this Figure the fact that in this sample we include galaxies with a wide range of SFRs efficiencies. On average our galaxies present SFRs that could double their mass in timescales $\sim 1/3$–1 Gyr, for lower and more massive galaxies (blue and red points in Figure 7.4).

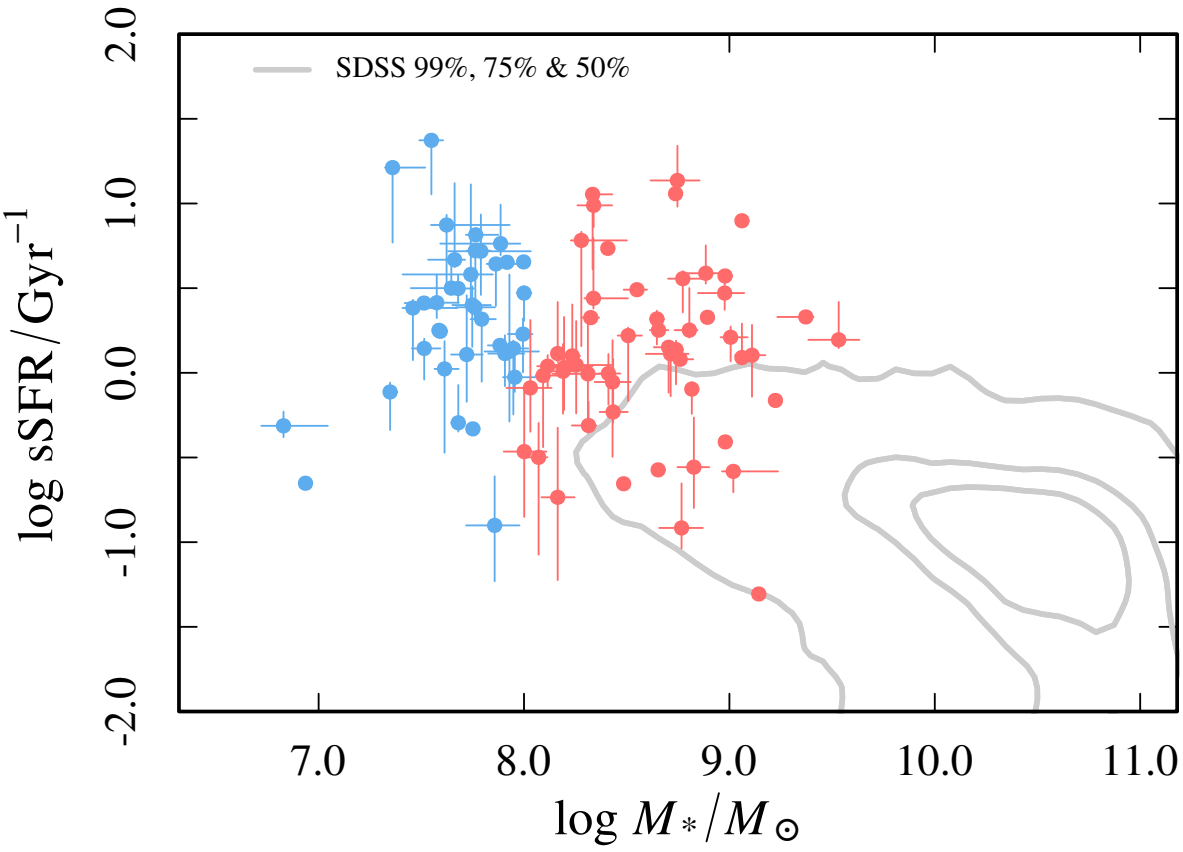

Figure 7.4: sSFR *vs* stellar mass. Our sample is color coded as in Figure 7.3

7.2 Evidence for AGNs

In order to make a right interpretation of the nature of the emission of the galaxies in our sample it is important to identify possible contamination originated by an active galactic nucleus (AGN).

The typical diagnostic diagram used to explore the contamination from AGNs in low redshift ($z \lesssim 0.4$) galaxies is the so-called BPT diagram (Baldwin et al., 1981; Veilleux and Osterbrock, 1987). This diagram uses the [OIII]λ5007/Hβ and [NII]λ6583/Hα emission line ratios. For higher redshifts the later is not available anymore in visible spectroscopy, as [NII]λ6583 and Hα restframe wavelengths are shifted beyond 10.000Å. Then, alternative diagnostics have been defined. Such is the case of the Mass-Excitation (MEx) diagram (Juneau et al., 2011) that assumes a certain relation between stellar mass and metallicity, and then substitutes the [NII]λ6583/Hα by the stellar mass. Both approaches, BPT and MEx diagrams, present a similar appearance, with AGNs and star-forming galaxies populating the top-right and bottom-left areas respectively, and a transition/composite overlapping area.

Figure 7.5 shows both diagnostics for the fraction of galaxies for which the corresponding emission line ratios were able to be measured with a significance larger than 3σ. In both diagrams our sample is represented with colored points (blue and red for $\log M_*/M_\odot < 8.0$ and $\log M_*/M_\odot > 8.0$, respectively), while the distribution of the SDSS is marked with gray con-

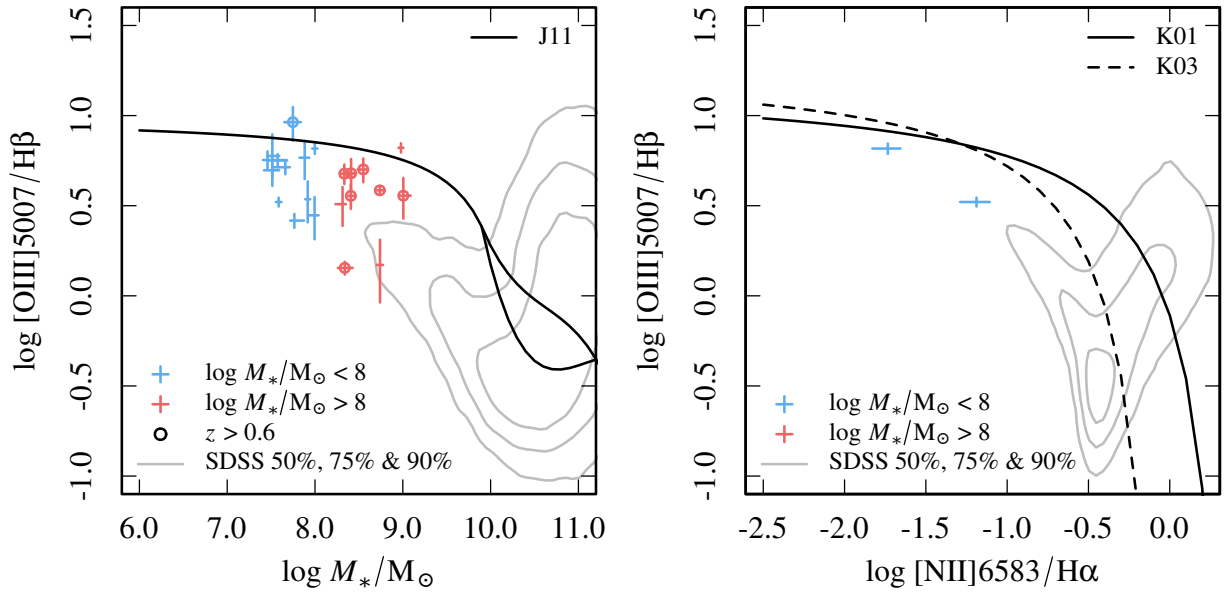

Figure 7.5: Left: MEx diagnostic diagram. The solid black lines show the limit between the areas populated by star-forming galaxies (bottom-left), AGNs (top-right), and composite objects (area enclosed by the black lines) as defined by Juneau et al. (2011, J11). Right: Classic BPT diagram. We use black lines to plot the demarcations found by Kewley et al. (2001, K01) and Kauffmann et al. (2003a, K03). In both panels we show the galaxies for which we are able to measure the emission lines involved in the diagnostics with a significance $>3\sigma$ color-coded by mass (blue and red crosses represent systems with $\log M_*/M_\odot<8$ and $\log M_*/M_\odot>8$, respectively). The distribution of the SDSS data is marked using gray contours.

tours. In each panel, we use black solid lines to represent the demarcations between star-forming galaxies, AGNs, and composite systems.

In principle, we do not expect a large contribution of AGNs in our sample. First of all, low-mass (and low-metallicity) AGNs are extremely rare (at least at very low redshifts) as suggested by Izotov and Thuan (2008). The presence of AGN is negligible even within samples of much more extreme emission-line low-mass systems, such as those studied by van der Wel et al. (2011).

7.2.1 Mass-Excitation Diagram

Left panel in Figure 7.5 shows the MEx diagram for 20 galaxies of our sample. To delimit the areas corresponding to AGNs, star-forming, and transition systems we use the curves provided by Juneau et al. (2011). We can see how our sample remains under the black lines, within the area populated by objects classified as star-forming, except in two cases than we now analyze:

88 (see Appendix B) is actually a rare object within our sample, as it appears to be a merger.

253 (see Appendix B), on the other hand, is a extremely faint system. A glance at its spectra suggests that the measurements of the [OIII]λ5007 and Hβ emission lines could be affected by sky emission features. In fact, the uncertainty for the value of the [OIII]/Hβ goes beyond the demarcation (black line) towards the star-forming region.

In any case, if we consider the possible evolution of the curves (obtained for z$\sim$0 by Juneau et al. (2011)) towards the redshifts of our sample (considering the differences in the stellar mass-metallicity relation as in Henry et al. 2013b), we include both galaxies in the star-forming area.

Given our results we conclude that we do not find clear AGN candidates among those galaxies for which we are able to measure the emission line ratio. We can affirm that the nature of the source of the emission lines we identify in our sample is SF rather than AGN activity.

7.2.2 BPT Diagram

Right panel in Figure 7.5 shows the BPT diagram. Unfortunately, we are only able to locate 2 galaxies of our sample in it. To delimit the areas corresponding to AGNs, star-forming, and transition systems we use the curves defined by Kewley et al. (2001), and Kauffmann et al. (2003a). In this case, even without shifting the boundaries toward higher redshifts (e.g., Kewley et al., 2013a,b), the two objects fall clearly inside the star-forming area, as expected.

7.3 Metallicity

Metallicity is one of the most fundamental properties of galaxies, as it is itself a product of the galactic evolution. The metals abundance reflect how the cycling of gas through stars occurs, and therefore, it is directly linked to the star formation processes, and the gas exchanges (inflows/outflows) between the galaxy and its environment.

In particular, stellar winds and supernovae, also referred to as *feedback*, can physically remove enriched gas from the galaxy via galactic winds, leading to a decrease of the global metallicity of the galaxy. Feedback is believed to play a critical role in regulating star formation also by reheating the cold ISM from which the stars form. Several works have addressed the study of galactic winds indirectly looking for their chemical imprint on galaxies. Inflows of pristine gas from the IGM are also mechanisms that produce a decrease of the average metal content of a galaxy (e.g., Kewley et al. 2010). Inflows are also a mayor ingredient of stellar mass assembly and therefore galaxy evolution.

Therefore, measurements of gas-phase metallicities of galaxies, their evolution with time, and their relation to other parameters, such as stellar mass, luminosity or SFR, can provide indirect insights into their SFHs.

In particular, looking for extremely metal-poor galaxies is a remarkable important task. These galaxies present metallicities that resemble those to be found in the first galaxies formed. Observed at lower redshifts (i.e., Amorín et al., 2014c), even in the very local universe (Guseva et al., 2003c,b,a; Izotov and Thuan, 2004; Guseva et al., 2015), they are the most promising candidates to young galaxies. Indeed, very low metallicity galaxies share properties with high redshift Lyα emitting galaxies and Ly-break galaxies, which are thought to present high ionization parameters and low oxygen abundances, representative of an early stage of galaxy formation dominated by massive stars in compact star-forming regions (e.g., Izotov et al., 2012; Nakajima et al., 2013). There is now some evidence of a metallicity floor, i.e. that even the most metal-deficient star-forming galaxies in the local Universe formed from matter which was already pre-enriched by a

previous star formation episode, e.g. by Population III stars (Thuan et al., 2005).

For more than three decades, one of the first BCD discovered, I Zw 18 (Sargent and Searle, 1970), continued to hold the record as the most metal-deficient emission-line galaxy known, with an oxygen abundance 12+log(O/H)=7.17±0.01 in its northwestern component and 7.22±0.02 in its southeastern component (Thuan et al., 2005). Only very recently, has I Zw 18 been displaced by the BCD SBS 0335–052W which was discovered by (Pustil'nik et al., 1997). This galaxy, with an oxygen abundance 12+log(O/H)=7.12±0.03, is now the emission-line galaxy with the lowest metallicity known (Izotov et al., 2005). Recently, Izotov et al. (2009) derived the oxygen abundance in four HII regions of SBS 0335−052W and found that it varies from region to region in the range 6.86−7.22.

7.3.1 Oxygen Abundances

Measurements of the metallicities of stars and star-forming gas in galaxies have mostly focused on the oxygen abundance of star-forming gas as estimated from a number of empirically calibrated metallicity estimators based on the relative strengths of strong emission lines . Thanks to its strong emission lines in the optical regime, oxygen is the element that can be measured most easily in HII regions, specially important for intermediate to high redshift studies (e.g., Lilly et al., 2003; Zahid et al., 2011; Maier et al., 2015). Oxygen is commonly used as the reference element also because is an α-process element synthesized directly in short-lived massive stars that return material to the IGM faster. Furthermore, it is relatively abundant, it is observed in several ionization states, and line ratios of frequently observed lines can provide good temperature and density diagnostic (Kewley and Dopita, 2002). The O/H abundance in HII regions is typically expressed in terms of 12+log(O/H), where O/H is the ratio of the number of oxygen to hydrogen atomic densities.

To estimate the chemical abundances (i.e. oxygen abundances), a number of calibrations have been developed. Kewley and Ellison (2008) review extensively 10 metallicity calibrations (Figure 7.6), and subdivide them into direct, empirical, theoretical and combined methods. The main difference between the direct methodologies and the rest of them is that it uses the the ratio of the [OIII]λ4363 auroral line to a lower excitation line such as [OIII]λ5007 to estimate the electron temperature of the gas, assuming a classical HII region model, which is afterwards converted into a metallicity. The others use calibrations based on ratios of strong emission lines, such as [OII]λ3727, [OIII]λ5007, Hβ, Hα or [NII]λ6583. In their work, Kewley and Ellison (2008) point out the importance of accounting for the large systematic differences between the metal abundance estimates obtained using different methodologies. In deed, different methods for measuring strong oxygen abundances yield results that are offset by up to 0.7 dex

7.3.2 Dust Correction

The absorption and scattering of light by dust produces a wavelength dependent effect on the SED of a galaxy. Traditionally, diagnostic diagrams (e.g., BPT and MEx diagrams) have tried to avoid correcting for extinction by using the ratios of close emission lines, similarly affected by dust. Nevertheless, since we are using emission lines widely separated for our metallicities estimations (e.g., [OIII]λ5007 and [OII]λ3727) we need to apply a dust correction.

A common way of estimating extinction is the so-called Balmer decrement technique. The

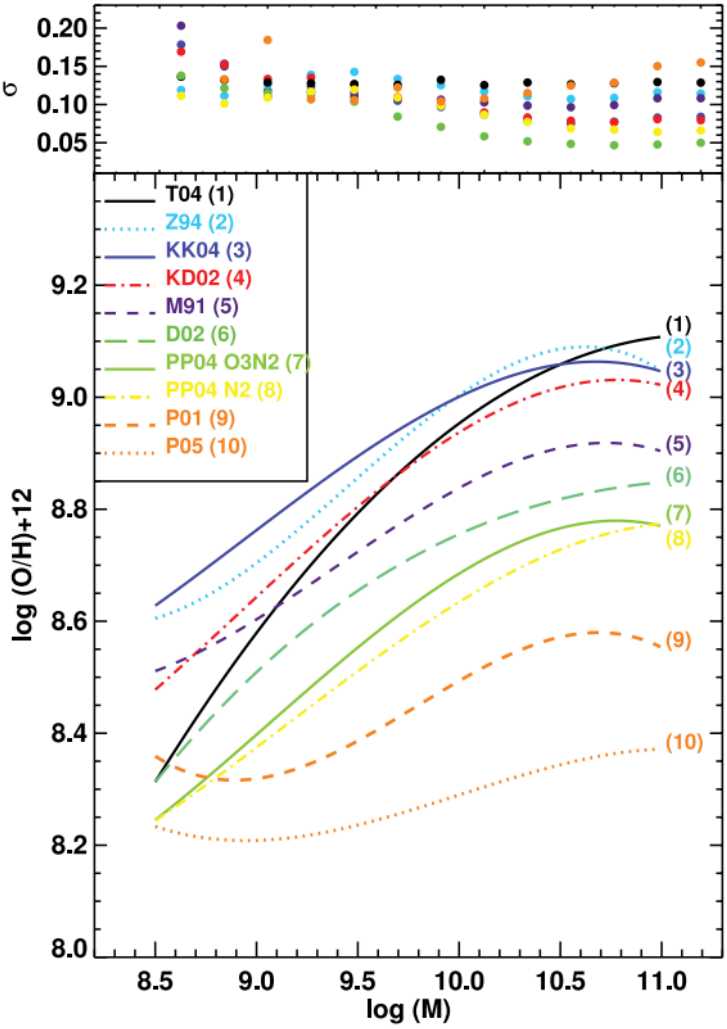

Figure 7.6: Figure 2 by Kewley and Ellison (2008). Best-fit MZ relations calculated applying the different metallicity calibrations they explore to the SDSS: T04, Tremonti et al. 2004; Z94, ; KK04, Kobulnicky and Kewley 2004; KD02, Kewley and Dopita 2002; M91, McGaugh 1991; D02, ; PP04-O3N2, PP04-N2, Pettini and Pagel 2004; P01, Pilyugin 2001; P05, Pilyugin and Thuan 2005. The top panel shows the rms scatter in metallicity for each calibration in 0.1 dex bins of stellar mass.

Balmer emission in most common astrophysical plasmas, such as HII regions, arises from radiative ionization followed by recombination. Downward cascades within the newly recombined atoms produce emission lines whose intensity ratios can be calculated. The Balmer-line intensities (the Balmer decrement) given by Osterbrock (1989) assuming Case B of recombination, with electronic temperature $T_e = 10^4$ K and electronic density $n_e = 10^2$ cm^{-3}, are:

$$H\alpha : H\beta : H\gamma = 2.86 : 1.00 : 0.47 \tag{7.1}$$

By studying how the measured values vary from the tabulated Balmer decrements, and assuming an extinction curve we can estimate the extinction for all the lines measured.

Using only those emission lines with a significance larger than 3σ, we obtain $H\alpha/H\beta = 2.52\,^{2.83}_{2.42}$, and $H\gamma/H\beta = 0.40\,^{0.44}_{0.37}$, which are consistent with no dust scenario. These values are smaller than those obtained by Henry et al. (2013b) and Domínguez et al. (2013) for intermediate redshift star-

forming galaxies with stellar masses reaching $\log M_*/M_\odot \sim 8.5$.

Such Balmer decrements, also compatible with values lower than the theoretical predictions, could be interpreted as a consequence of an incorrect flux calibration of the spectra. In our case we dismiss this option for the following reasons:

- We have checked our flux calibration by comparing spectra of galaxies observed in the different observing runs and reduced independently.
- Low values of dust are reasonable for the type of galaxies we study, characterized by blue colors and low stellar mass (Papaderos et al., 1996, 2008; Gil de Paz and Madore, 2005). For example, Hu et al. (2009) also argues that no correction for dust is appropriate for these faint, low-mass objects.

Despite the low statistics in the estimation of the Balmer decrements (4 and 8 objects for Hα/Hβ and Hγ/Hβ ratios, respectively) we do not expect large deviations from these values in the rest of the sample given the similar properties of the galaxies. Therefore, we decide not to apply the extinction correction. The possible impact of extinction on the values of the metallicities will be mentioned in due time.

7.3.3 Stellar Absorption Correction

Absorption lines from the stellar populations in the galaxy may affect the Balmer emission-line measurements. Domínguez et al. (2013) estimate the Hα and Hβ absorption lines from the best stellar population model from a SED fitting performed on a sample of 128 star-forming galaxies in the redshift range $0.75 \leq z \leq 1.5$. The average Hα EWs and Hβ EWs in absorption they obtain vary between 2–3Å and 3–4Å, respectively within the stellar mass range $\log M_*/M_\odot \sim 8.6$–10.5. These values are similar to the uncertainties of our EWs, with an median of 4Å. For this reason, we decide not to apply a correction for stellar absorption.

7.3.4 R23

Among the different diagnostics developed based on strong lines, we decide to use the $R23$ method, first introduced by Pagel et al. (1979). This technique is based on the ratio of [OII]λ3727, [OIII]λ4959 and [OIII]λ5007 to Hβ, most frequent emission lines available in our observations. $R23$ strong-line diagnostic is expressed as

$$R23 = \frac{I_{[O\text{II}]3727} + I_{[O\text{III}]4959} + I_{[O\text{III}]5007}}{I_{H\beta}} \tag{7.2}$$

The great virtue of $R23$ is that it is based on a few strong emission lines and can therefore be applied in a uniform way over a wide range of redshifts. The relation between $R23$ and the metallicity is double-valued, which means that a single value of $R23$ corresponds to two different metallicities, one on the higher metallicity branch and one on the lower metallicity branch. The physical reason for this $R23$ degeneracy is that the weakening of the oxygen lines is an effective

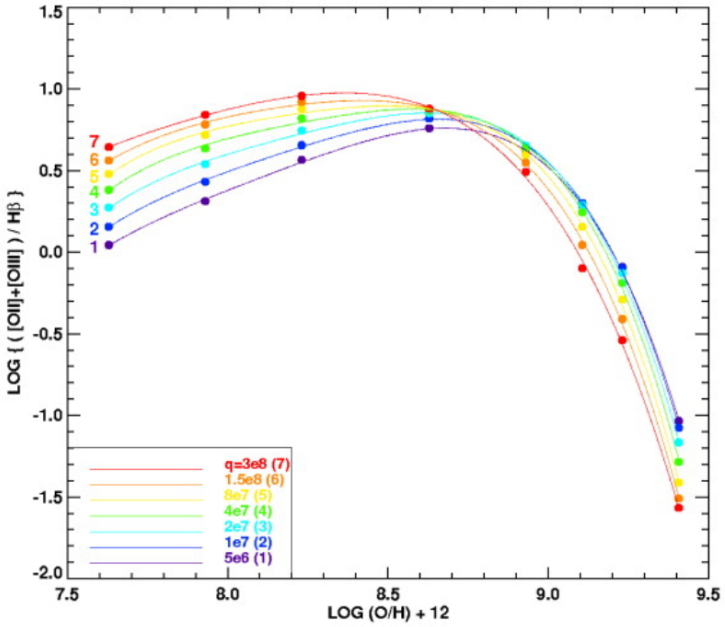

Figure 7.7: R23 diagnostic for abundance vs. metallicity (Figure 5 from Kewley and Dopita, 2002). The plot shows the curves for each ionization parameter between q = 5×10^6 to 3×10^8 cm s^{-1}. Filled circles represent the data points from their models at metallicities from left to right of 0.05, 0.1, 0.2, 0.5, 1.0, 1.5, 2.0, 3.0 $Z_\odot$.

consequence of both low metallicity (at low metallicity the intensity of the forbidden lines scales roughly with the chemical abundance) and efficient nebular cooling (dominated by the infrared fine-structure lines) at high metallicity HII regions that lead to too low electron temperatures to collisionally excite the optical forbidden lines. The "turnover" metallicity that demarcates the transition between the upper and lower branches of $R23$ depends on the calibration used and the physical conditions of the HII region responsible for the emission. In particular, $R23$ strongly depends on the ionization parameter (specially at low abundances), U, defined as the ratio of the ionizing photon density to the hydrogen density:

$$U = Q/4\pi r^2 n_H c \tag{7.3}$$

where Q is the ionizing photon rate, r is the radius of the HII region, n is the hydrogen density, and c is the speed of light. Generally, the ionization parameter is found in the shape of

$$q = U \times c \tag{7.4}$$

Among the different $R23$ calibrations, we apply the one based on the stellar population synthesis and photoionization model calibrations developed by Kewley and Dopita (2002) (Figure 7.7), and updated in Kobulnicky and Kewley (2004, KK04). More precisely, we use the method as described in Kewley and Ellison (2008) (Appendix 2.3), also applied by some of our reference works (e.g., Zahid et al., 2011; Henry et al., 2013a,b). The method consists on the following 3 steps:

1. We determine if our sample of galaxies lies either on the low or the high abundance branches (Section 7.3.4.1).

2. We estimate the ionization parameter using the [OIII]λ5007/[OII]λ3727 line ratio and an initial value for the abundance, [12+log(O/H)], following the next expression:

$$\begin{aligned} logq = &\left\{32.81 - 1.153y^2 + [12 + log(O/H)]\left(-3.396 - 0.025y + 0.1444y^2\right)\right\} \\ &\times \left\{4.603 - 0.3119y - 0.163y^2 + [12 + log(O/H)]\left(-0.48 + 0.0271y + 0.02037y^2\right)\right\}^{-1} \end{aligned} \tag{7.5}$$

where $y = \log \mathrm{O32} = \log([\mathrm{OIII}]\lambda5007/[\mathrm{OII}]\lambda3727)$. The initial value for the abundance is [12+log(O/H)]=8.2 for the lower branch, or [12+log(O/H)]=8.7 for the upper branch.

3. We estimate the metallicity using either the lower or the higher branch:

$$12 + log(O/H)_{lower} = 9.40 + 4.65x - 3.17x^2 - logq\left(0.272 + 0.547x - 0.513x^2\right) \tag{7.6}$$

$$\begin{aligned} 12 + log(O/H)_{upper} = &\ 9.72 + 0.777x - 0.951x^2 - 0.072x^3 - 0.811x^4 \\ &- logq\left(0.0737 + 0.0713x - 0.141x^2 + 0.0373x^3 - 0.058x^4\right) \end{aligned} \tag{7.7}$$

where $x = \log \mathrm{R23}$.

As the metallicity and the ionization parameter are interdependent, an iteration of steps 2 and 3 is used until 12+log (O/H) converges. Normally, three iterations are typically required to reach the final value with a typical uncertainty of 0.15 dex.

7.3.4.1 Determining the Branch of R23

Determining whether a galaxy lies on the low or high metallicity branch is challenging. Among the different techniques suggested in the literature, probably the most reliable are those that use alternative metallicity diagnostics. For instance, Kewley and Ellison (2008) suggest the use of [NII]λ6583/[OII] or [NII]λ6583/Hα. However, this ratios are challenging to obtain for either intermediate to high redshifts ($z \gtrsim 0.5$) and low metallicity galaxies, for which the [NII]λ6583 emission lines are weak. For these reasons, it is crucial that we identify other approaches to break the R23-metallicity degeneracy without observations of [NII]λ6583 and Hα lines. In particular, for analogy with their galaxy sample and redshift range (0.6–0.7), we follow the approach described by Henry et al. (2013a) and use four diagnostics as a function of the stellar mass (Figure 7.8 analogous to Figure 4 in Henry et al. 2013a). In Table 7.1 we give the values used in these diagrams.

1 Top-left panel of Figure 7.8 shows the relation between $R23$ and the stellar mass. Relying on the correlation between metallicity and stellar mass we would expect to identify in this plot a similar trend to the one followed by $R23$ and metallicity. In the top-left panel of their Figure 4, Henry et al. 2013a identify a clear trend in which $R23$ decreases with increasing stellar mass. Assuming that metallicity increases with increasing stellar mass, they interpret such trend as a consequence of their sample of galaxies falling on the upper branch of the $R23$ indicator. Furthermore, they identify a hint of "turnover" at $\log M_*/M_\odot \sim$8.0–8.5. In consequence, they consider that galaxies with stellar masses $\log M_*/M_\odot \lesssim$8.2 fall in the lower metallicity branch. In their paper, Henry et al. 2013a claim that for the ionization parameters

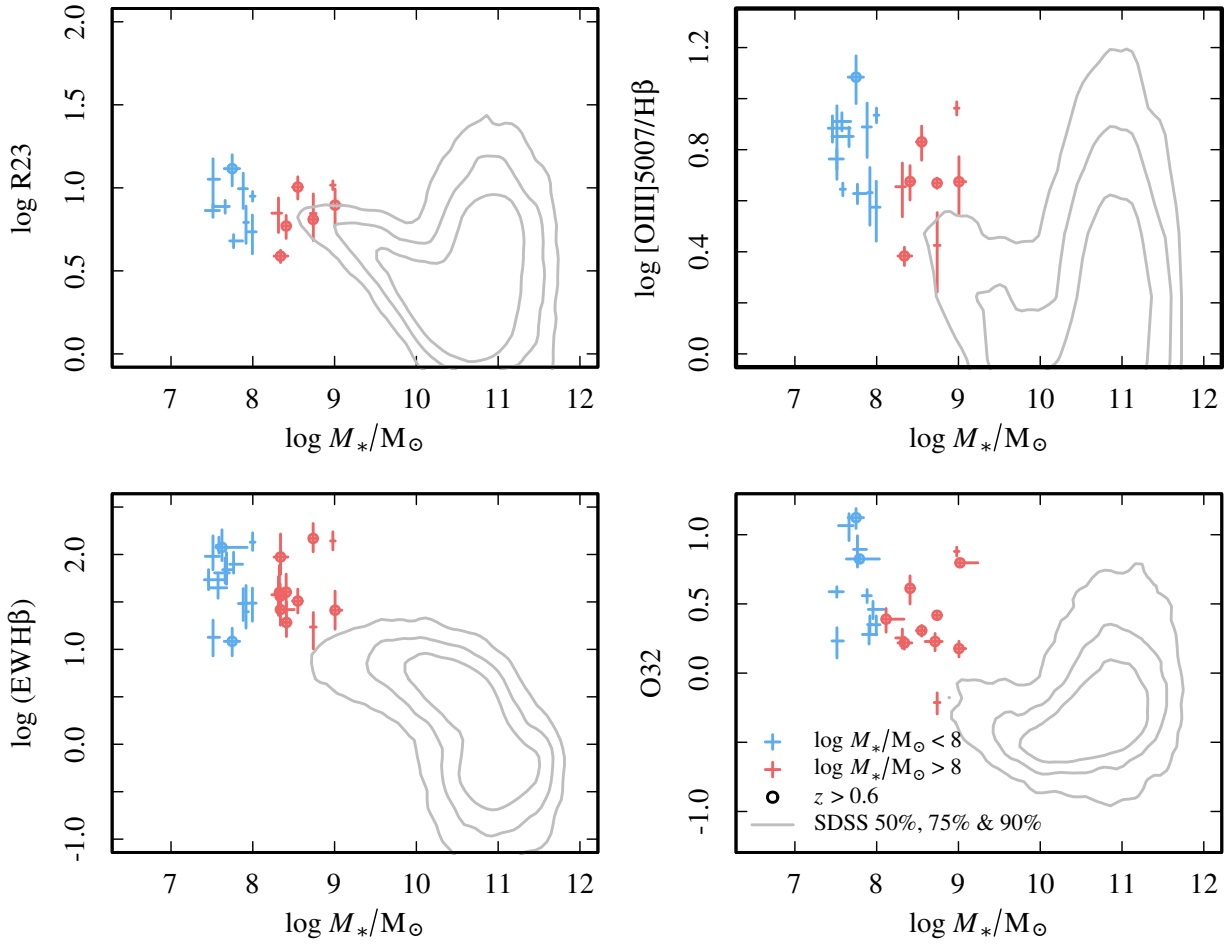

Figure 7.8: From left to right and from top to bottom: measured values of R23, [OIII]/Hβ, log Hβ EW (rest frame), and log ([OIII]/[OII]) $\equiv$ O32 as a function of the stellar mass. To increase the number of points in each plot, all the galaxies for which the corresponding emission lines have been measured are included. This implies that the different panels include different galaxies. For comparison, we also mark with gray contours the area populated by the SDSS DR7 (Abazajian et al., 2009) in each panel (50%, 75%, and 90%).

characteristics of the galaxies in their sample, and using the KK04 calibration, the turnover metallicity is around $12 + \log(\mathrm{O/H}) \sim 8.4$, which is reached when $\log(\mathrm{R23}) \sim 0.9 - 1.0$. In our case, these values of log(R23) are reached along our whole stellar mass range. In fact, we do not identify such decreasing trend of $R23$ with increasing mass for our sample. Nevertheless, our values of $R23$ are consistent with those obtained by Henry et al. 2013a. Very likely, the reason for the lack of trend is the limited range of stellar masses covered towards massive systems ($\log M_*/M_\odot$>9). Something worth to be mentioned is that we expand the lower stellar mass limit of the work by Henry et al. 2013a and we do not find an extension of the incipient decreasing trend they appear to detect for $\log M_*/M_\odot$<8.2.

2 & 3 Maiolino et al. (2008) propose the analysis of the [OIII]/Hβ ratio (top-right panel within Figure 7.8) and the log ([OIII]/[OII]) $\equiv$ O32 (bottom-right panel within Figure 7.8) as a function of the stellar mass to break the $R23$ degeneracy. Maiolino et al. (2008) find that low metallicity branch is favored by [OIII]/Hβ>5 and O32>0.5 cases. In our case, for a clearer visualization, we opt for plotting the values of log [OIII]/Hβ. The values for which the lower metallicities are preferred are log [OIII]/Hβ>0.7. Considering only those more reliable

ratios (emission lines signification >3σ) we realize that such values are mainly covered by galaxies with lower masses. We can see O32 behaves in a similar but much clearer way. Following these criteria, we could set an approximate value of the stellar mass coincident whith the "turnover" point of the R23, log$M_*/M_\odot$∼8.0. This value is consistent with the value considered by Henry et al. (2013a), and much smaller than the obtained and use by Henry et al. (2013b). It is important to take into account that these diagnostics are dependent on the ionization parameter, that can vary from galaxy to galaxy and with increasing redshift (e.g., Brinchmann et al., 2008). As our sample spans a wide range of redshifts, the trends may be affected and vanished by such effect.

4 Finally, we evaluate the use of the Hβ equivalent width (EW) to select low-metallicity galaxies, as suggested by Kakazu et al. (2007) and Hu et al. (2009) in the context of their study of ultrastrong emission line galaxies for which lowest metallicities were found for galaxies that showed Hβ EW>30 Å. Again, for a clearer visualization of the extreme values, we use the log EW Hβ, and therefore, the limit value between lower and higher metallicity solutions would be log EW Hβ ∼ 1.5. In our sample, a handful of galaxies present such high values of EW Hβ but they span the whole stellar mass range, in agreement with the fact we do not see a "turnover" point in the log R23–M_* relation.

Therefore, as a consequence of these results, we do not find clear reasons to use either the upper or lower metallicity branches. These plots do not appear useful to discern between such options given our sample and data.

7.3.4.2 Metallicity Estimation

As initially we do not find a strong evidence to use preferentially any of the branches, we opt for using both. In Table 7.1 we list the oxygen abundances obtained using both the upper and lower branches in each case through the methodology previously explained.

The surprisingly high values of the oxygen abundance obtained using the upper metallicity branch (12+log(O/H)∼8.56-9.23) appear to be not likely for such blue and low-mass galaxies. Indeed, these values are typically obtained for galaxies with a factor of 100 larger stellar masses. We consider the values returned by the low branch approach (12+log(O/H)∼7.16-8.59) more reasonable. Expressed in terms of solar metallicity (solar value of 12+log(O/H)=8.69 from Allende Prieto et al. 2001) the range would corresponds to ∼1-1/34 $Z_\odot$. The ionization parameter ranges log q∼7.3-8.66, corresponding to medium to extreme conditions of the ISM (from light blue to red curves in Figure 7.7).

Guseva et al. 2015 define as extremely metal-deficient galaxies (XMDs) those that qualify 12+log(O/H)≤7.35 (derived through the direct method based on T_e; see also, e.g., Kniazev et al. 2003; Kakazu et al. 2007; Pustilnik and Martin 2007; Ekta and Chengalur 2010b,a. Accounting for the difference of ∼0.3 between the abundance given by the KK04 empirical calibration and that obtained using the direct method (López-Sánchez and Esteban, 2010), we find five galaxies with oxygen abundances compatible with such category: 306, 454, 1126, 1247, and 1860. By compatible we mean that the limit value is within the 16th and 84th percentiles. These galaxies present metallicities (50th percentiles) ranging 12+log(O/H)∼7.16-7.80, which corresponds to 1/34−1/8 $Z_\odot$.

306 is an Irregular galaxy located at $z_{\rm spec}$=0.576 with an absolute rest-fram B-band magnitude $\sim$-17.1, and log$M_*/M_\odot$=7.9. The SED-fitting technique retuns a much higher metallicity for this system with a narrow probability distribution. The 2D spectrum reveals a possible impact of the sky emission on the emission lines measurements. Also, Hβ appear to be affected by the teluric absorption band centered on 7600Å. The low metallicity value could be a consequence of a not adequate sky correction in this case. For these reasons, we do not consider this galaxy as a clear candidate to XMD galaxy.

454 appears to be a disk-like very compact galaxy with a log$M_*/M_\odot\sim$8.0, located at $z_{\rm spec}$=0.536. Its faintness and reasonable EW of the emission lines makes it a more reliable candidate to XMD galaxy. The SED-fitting also returns a low value of oxygen abundance for this system. Interestingly, the SFH of this object appears to be long in absolute terms (t_0=5.5 Gyr), but still short regarding the ammount of mass formed in the last Gyr (more than 50% of the current stellar mass). Furthermore, it is somehow bursty besides an overall increasing trend towards lower lookback times.

1126 is a very distant galaxy ($z_{\rm spec}$=0.864) if we consider its mass (log$M_*/M_\odot\sim$8.3). Its Irr shape is actually very compact. Somehow its SFH resembles the properties of object 454, although it seems to be intrinsically brighter. Nevertheless, [OIII]λ5007 emission line in this galaxy could be affected by sky lines.

1247 Irr galaxy presents a clear enhance of the continuum spectral emission in the bluer wavelengths, and spectral features characteristic of very young populations and extreme physical conditions of the ISM. Given the ratio between the [OIII]λ5007 and [OIII]λ4959 fluxes we suspect the former should be even larger. This might be again an impact of a not well corrected teluric absorption. 1247 presents a stellar mass of log$M_*/M_\odot\sim$7.8 and it is located at $z_{\rm spec}$=0.524. We consider this object one of the clearer candidates to XMD galaxies in our sample.

1860 presents a compact disk-like morphology with a distinguishable and not centered nod of SF. It is a galaxy with log$M_*/M_\odot\sim$8.4 at redshift $z_{\rm spec}$=0.863. Despite the fact the spectrum of this galaxy is noisy, the emission lines appear to be reasonably well recovered. For this reason we consider this to be again a good candidate to XDM, also supported by the SED-fitting metallicity estimation.

The mass-metallicity (MZ) relation is a measure of the average gas-phase oxygen abundance as a function of stellar mass. The correlation between both physical parameters is thought to be shaped by the processes that govern the evolution of galaxies. Lequeux et al. (1979) defined for the first time a total mass-metallicity relation for irregular and blue compact galaxies in the local universe. Years later Tremonti et al. (2004) used the Sloan Digital Sky Survey imaging and spectroscopy of $\sim$53.000 star-forming galaxies to define a MZ at $z\sim$0.1. In this case, the total mass used by Lequeux et al. 1979 was exchanged by the stellar mass.

This important relation has been explored and found at higher redshifts up to $z\sim$3 (e.g., Savaglio et al., 2005; Erb et al., 2006; Maiolino et al., 2008; Mannucci et al., 2009; Moustakas et al., 2011; Zahid et al., 2011; Foster et al., 2012; Zahid et al., 2013; Pérez-Montero et al., 2013; Yuan et al., 2013; Yabe et al., 2014) and over a wide range of stellar masses, reaching $10^7 M_\odot$ (e.g., Lee et al., 2006; Zahid et al., 2012a; Berg et al., 2012; Henry et al., 2013b). These studies

(see Figure 1.7) show that, on the one hand, metallicity increases with stellar mass and flattens out (saturates) for the higher masses. The depletion of metals observed for less massive galaxies has been interpreted as the effect of ubiquitous galactic winds that strip metals more effectively from galaxies with shallow potential wells (low-mass systems). Alternatively, it has been suggested that low-mass systems have yet to convert much of their gas into stars and therefore are less chemically evolved as compared to more massive galaxies which have undergone rapid star formation (Brooks et al., 2007; Mouhcine et al., 2008). The metallicity saturation has been interpreted as the consequence of the chemical equilibrium reached by massive galaxies, in which the mass of oxygen produced by massive stars equals the mass of oxygen locked up by low mass stars. Therefore, the gas-phase oxygen abundance saturates at a metallicity equivalent to the nucleosynthetic stellar yield (Edmunds, 1990). On the other hand, MZ evolves relative to that seen locally shifting towards lower metallicities with increasing redshift for a fixed stellar mass. Interestingly, this apparent shift seems to be larger for lower mass galaxies than more massive systems since $z{\sim}2.3$ (Figure 1.7). This could be interpreted as the chemical version of galaxy *downsizing* (Savaglio et al., 2005; Maier et al., 2006; Maiolino et al., 2008; Zahid et al., 2011), in which more massive galaxies form earlier and faster than dwarf galaxies (Cowie et al., 1996).

However, the observed shape and evolution of the MZ is likely to be affected by the selection of the samples and metallicity estimators used (e.g., Moustakas et al., 2011; Foster et al., 2012; Kewley and Ellison, 2008; López-Sánchez et al., 2012). In fact, Izotov et al. (2011); Guseva et al. (2015), among others, find a common MZ relation at least for compact star-forming galaxies independently of their redshift between $0{<}z{<}3$.

Due to the not enough statistics available in redshift bins in our sample, exploring the evolution of the MZ with redshift is beyond the scope of our work. Instead, we focus on the compatibility between the values of metallicity that we obtain and the MZ found at low stellar masses.

7.3.4.3 Mass-Metallicity Relation for Low-Mass Galaxies

Due to the classical lack of low-mass galaxies ($\log M_*/M_\odot < 9$) in spectroscopic surveys, the MZ relation is still poorly constrained for low mass galaxies outside the local universe. Recently, some works have tried to work on this important missing piece of our picture of low-mass galaxies metallicity evolution. For instance, we highlight the projects by Henry et al. (2013a) and Henry et al. (2013b), in which they derive MZ relations for samples of galaxies with stellar masses $\sim 10^8 M_\odot$ at redshift $\sim$0.65 and $\sim$1.76 respectively. Other interesting works study the metallicity of low mass emission lines galaxies Ly et al. (2014) and Amorín et al. (2014a) at redshifts $<$0.9. Also, there have been some attempts to study the metallicity of low mass strongly lensed high redshift galaxies (e.g., Teplitz et al., 2000; Hainline et al., 2009; Wuyts et al., 2012; Brammer et al., 2012; Yuan et al., 2013; Belli et al., 2013; Amorín et al., 2014c).

In Figures 7.9 and 7.10 we show the MZ relation for the galaxies in our sample for which we are able to measure the emission lines used in the estimation of the metallicity with a significance larger than 3σ. In particular, Figure 7.9 shows on the left panel the values obtained (crosses) using the low metallicity branch approach, while the right panel shows the abundances obtained using the upper metallicity branch. In Figure 7.10 we combine both approaches using as a turnover stellar mass value found by Henry et al. (2013a). The circles mark the galaxies located at redshifts larger than 0.6. Finally, we show the MZ relation obtained by Zahid et al. (2011, grey line; Z11) and Savaglio et al. (2005, black line; S05) for samples in similar redshift ranges than ours. We use

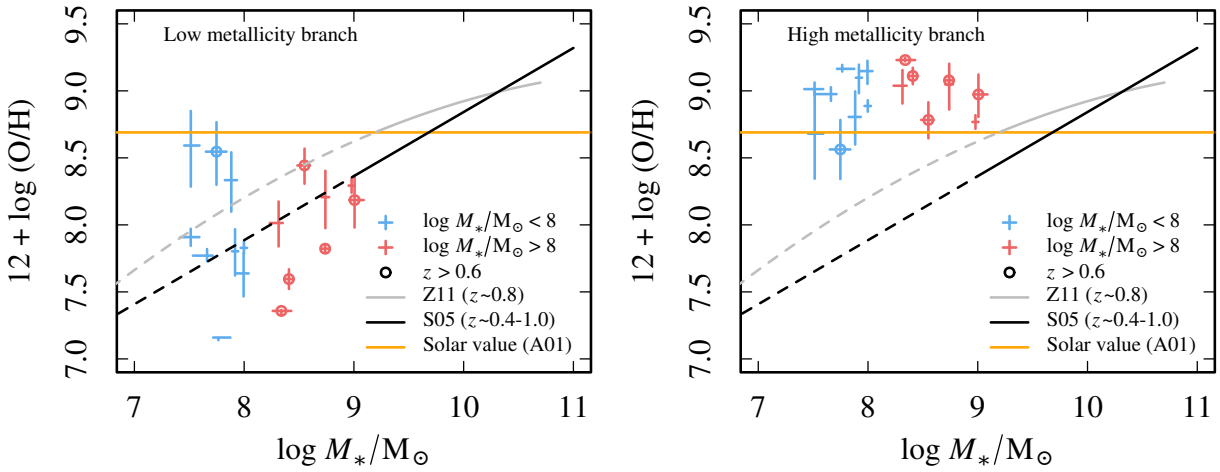

Figure 7.9: Mass-metallicity relation for 17 of the galaxies in our sample. For comparison we show the relation found by Zahid et al. (2011, grey line; Z11) and Savaglio et al. (2005, black line; S05). We use dashed lines for the extensions of both expression towards our stellar mass range. The orange line mark the solar metallicity found by Allende Prieto et al. (2001, A01; 12+log(O/H)=8.69). In the left panel we use the lower metallicity branch for all the galaxies while in the right panel we use the upper branch.

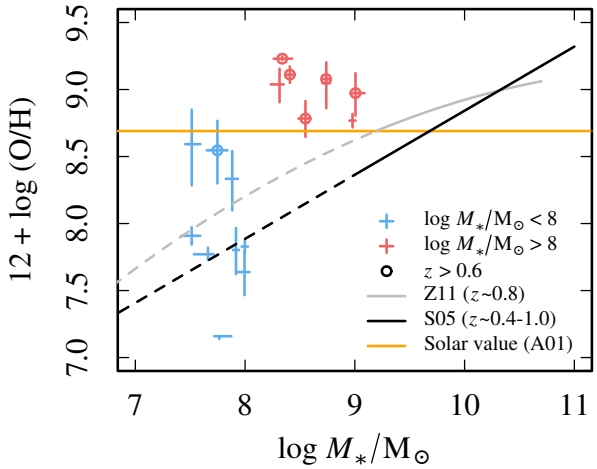

Figure 7.10: MZ relation as in Figure 7.9 but using the lower and upper branches for galaxies with log$M_*/M_\odot$<8.2 and log$M_*/M_\odot$>8.2, respectively, following Henry et al. (2013a).

dashed lines to extend the curves towards lower stellar masses. For comparison, we also mark the solar value with an orange line.

As we can see, both figures point out the incompatibility between the upper metallicity values and the MZ relations. In we focus on the left panel in Figures 7.9, we appreciate a wide dispersion of the oxygen abundances within our sample and no clear increasing trend with stellar mass. Overall, our sample is compatible with both Z11 and S05 MZs. No clear evolution with redshift is found. We wonder whether the behavior of our sample corresponds to a flattening of the MZ towards low mass systems.

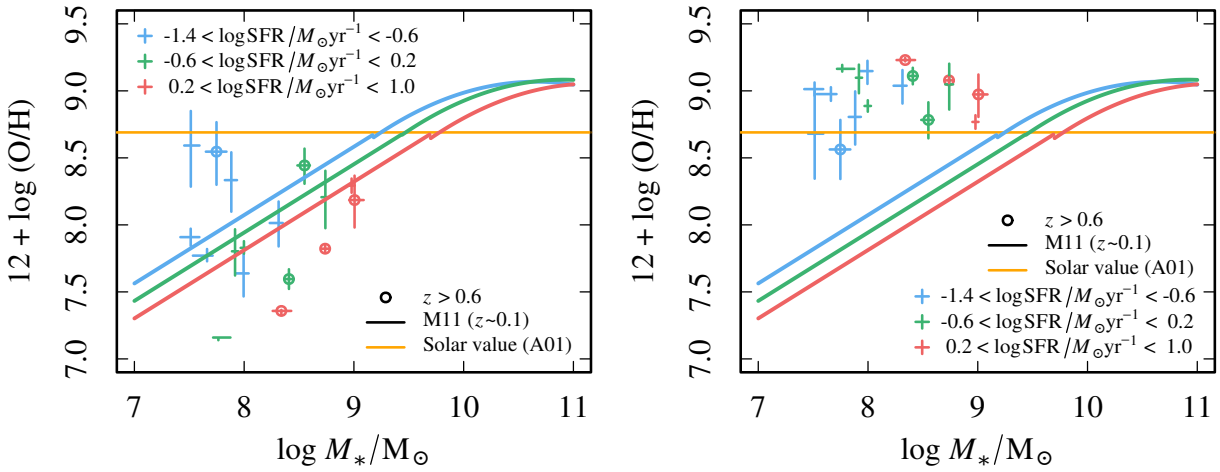

Figure 7.11: Mass-metallicity relation for 17 of the galaxies in our sample, color coded by their SFR as it is specified in the legend. The curves show the local FMR reported by Mannucci et al. (2011) for SFRs -1, -0.2, and 0.6 (blue, green, and red, respectively).

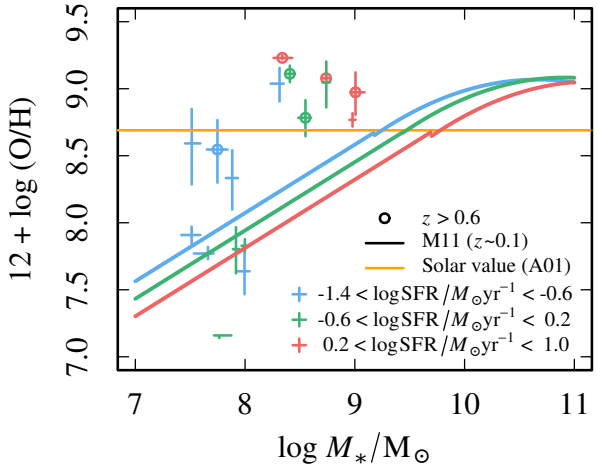

Figure 7.12: MZ color coded by SFR, as in Figure 7.11, but using the lower and upper branches for galaxies with log$M_*/M_\odot$<8.2 and log$M_*/M_\odot$>8.2, respectively, following Henry et al. (2013a).

7.3.5 Fundamental Metallicity Relation

Recently, some authors have found a secondary dependence of the gas metallicity with SFR, in a way that at a given stellar mass the metallicity decreases with increasing SFR (Kewley et al., 2006; Lara-López et al., 2010; Lilly et al., 2013; Pérez-Montero et al., 2013). This tight multidimensional relationship is known as the *fundamental metallicity relation* (FMR; Mannucci et al., 2010; Lara-López et al., 2010, 2013), and it is thought to suggest that there is an interplay between star formation and gas inflows leading to an inverse correlation between SFR and metallicity.

In Figures 7.11 and 7.12 we show the analogous plots of Figures 7.9 and 7.10 showing the FMR relation for the same subsample of galaxies. In particular, the FMR tridimensional relation is represented by the MZs found by Mannucci et al. (2011) for three values of SFR (log SFR/M_*yr^{-1}= -1, -0.2, and 0.6; blue, green, and red lines, respectively). This time, the values obtained (crosses) are colored using the same color code, depending on their SFR. Again,

the circles mark the galaxies located at redshifts larger than 0.6. Despite the huge dispersion, we can see a hint of a trend with those galaxies undergoing a larger SF process (considering absolute values of SFR, and not sSFR) presenting lower metallicities for a given stellar mass.

Table 7.1: Derived metallicities

ID (1)	z_{spec} (2)	$M_*/M_\odot$ (3)	SFR/$M_\odot yr^{-1}$ (4)	log $R23$ (5)	log O32 (6)	EW H$\beta_{rest-frame}$ (7)	[OIII]λ5007/Hβ (8)	logq_{low} (9)	logq_{up} (10)	12+log(O/H)$_{low}$ (11)	12+log(O/H)$_{up}$ (12)
35	0.656	$8.3^{8.5}_{8.3}$	$-0.2^{0.2}_{-0.3}$	–	–	$-26.3^{-18.0}_{-37.6}$	–	–	–	–	–
88	0.553	$9.0^{9.0}_{9.0}$	$0.6^{0.6}_{0.6}$	$1.02^{1.04}_{0.99}$	$0.88^{0.91}_{0.85}$	$-139.0^{-111.8}_{-173.4}$	$0.96^{0.99}_{0.94}$	$8.20^{8.62}_{8.55}$	$8.62^{8.62}_{8.55}$	$8.29^{8.35}_{8.24}$	$8.77^{8.72}_{8.82}$
145	0.521	$8.7^{8.8}_{8.7}$	$-0.2^{-0.1}_{-0.3}$	$0.85^{0.96}_{0.68}$	$-0.21^{-0.14}_{-0.30}$	$-17.2^{-10.1}_{-24.4}$	$0.43^{0.55}_{0.24}$	$7.34^{7.85}_{7.68}$	$7.85^{7.85}_{7.68}$	$8.21^{8.40}_{7.97}$	$9.05^{8.86}_{9.20}$
181	0.759	$9.0^{9.1}_{9.0}$	$0.2^{0.4}_{0.1}$	$0.90^{0.99}_{0.77}$	$0.18^{0.23}_{0.12}$	$-25.9^{-16.3}_{-41.1}$	$0.67^{0.77}_{0.55}$	$7.60^{8.16}_{8.03}$	$8.16^{8.16}_{8.03}$	$8.19^{8.37}_{7.98}$	$8.97^{8.81}_{9.12}$
183	0.532	$7.7^{7.7}_{7.5}$	$-0.6^{-0.3}_{-0.7}$	$0.89^{0.92}_{0.85}$	$1.07^{1.15}_{0.96}$	$-64.0^{-49.7}_{-92.0}$	$0.85^{0.89}_{0.81}$	$8.21^{9.34}_{9.09}$	$9.34^{9.34}_{9.09}$	$7.77^{7.82}_{7.73}$	$8.98^{8.93}_{9.03}$
195	0.538	$7.5^{7.6}_{7.4}$	$-1.0^{-1.0}_{-1.1}$	$0.86^{0.90}_{0.82}$	$0.59^{0.62}_{0.55}$	$-95.6^{-69.0}_{-157.0}$	$0.76^{0.80}_{0.72}$	$7.82^{8.74}_{8.64}$	$8.74^{8.74}_{8.64}$	$7.91^{7.97}_{7.84}$	$9.01^{8.96}_{9.06}$
253	0.760	$7.7^{7.8}_{7.7}$	$-0.9^{-0.8}_{-1.0}$	$1.12^{1.20}_{1.01}$	$1.12^{1.19}_{1.05}$	$-12.2^{-8.6}_{-16.7}$	$1.08^{1.17}_{0.98}$	$8.66^{8.68}_{8.53}$	$8.68^{8.68}_{8.53}$	$8.55^{8.77}_{8.30}$	$8.56^{8.34}_{8.78}$
296	0.261	$7.6^{7.6}_{7.6}$	$-1.1^{-1.1}_{-1.2}$	–	–	$-124.9^{-103.4}_{-152.0}$	$0.65^{0.67}_{0.62}$	–	–	–	–
297	0.446	$7.7^{7.8}_{7.6}$	$-0.8^{-0.7}_{-0.9}$	–	–	$-69.2^{-48.6}_{-104.7}$	–	–	–	–	–
306	0.576	$7.9^{7.9}_{7.9}$	$-0.4^{-0.3}_{-0.4}$	$0.79^{0.89}_{0.67}$	$0.35^{0.41}_{0.28}$	$-24.9^{-16.7}_{-47.1}$	$0.63^{0.73}_{0.50}$	$7.64^{8.68}_{8.48}$	$8.68^{8.68}_{8.48}$	$7.80^{7.97}_{7.62}$	$9.10^{8.98}_{9.20}$
440	0.535	$7.5^{7.6}_{7.5}$	$-1.4^{-1.2}_{-1.5}$	$1.05^{1.17}_{0.88}$	$0.23^{0.33}_{0.11}$	$-13.4^{-8.5}_{-20.3}$	$0.85^{0.97}_{0.68}$	$7.86^{7.92}_{7.73}$	$7.92^{7.92}_{7.73}$	$8.59^{8.85}_{8.29}$	$8.68^{8.34}_{8.99}$
454	0.536	$8.0^{8.0}_{7.9}$	$-0.8^{-0.7}_{-0.9}$	$0.74^{0.84}_{0.60}$	$0.35^{0.41}_{0.28}$	$-30.7^{-19.8}_{-44.2}$	$0.57^{0.68}_{0.44}$	$7.60^{8.85}_{8.63}$	$8.85^{8.85}_{8.63}$	$7.64^{7.79}_{7.47}$	$9.15^{9.05}_{9.22}$
455	0.687	$8.7^{8.8}_{8.6}$	$-0.2^{0.0}_{-0.4}$	–	$0.23^{0.29}_{0.16}$	–	–	–	–	–	–
464	0.729	$8.4^{8.5}_{8.4}$	$-0.6^{-0.5}_{-0.7}$	–	–	$-19.2^{-13.7}_{-31.4}$	–	–	–	–	–
490	0.856	$8.6^{8.6}_{8.5}$	$0.0^{0.0}_{-0.1}$	$1.00^{1.07}_{0.93}$	$0.31^{0.34}_{0.27}$	$-32.3^{-24.2}_{-43.2}$	$0.83^{0.89}_{0.76}$	$7.79^{8.03}_{7.96}$	$8.03^{8.03}_{7.96}$	$8.44^{8.57}_{8.31}$	$8.78^{8.65}_{8.91}$
519	0.909	$8.7^{8.8}_{8.7}$	$0.8^{0.9}_{0.8}$	$0.81^{0.83}_{0.79}$	$0.42^{0.44}_{0.40}$	$-147.7^{-106.8}_{-212.1}$	$0.67^{0.69}_{0.65}$	$7.66^{8.65}_{8.60}$	$8.65^{8.65}_{8.60}$	$7.82^{7.85}_{7.79}$	$9.08^{9.06}_{9.10}$
536	0.578	$7.6^{7.7}_{7.5}$	$-1.0^{-0.8}_{-1.1}$	–	–	$-44.6^{-34.6}_{-61.1}$	$0.91^{0.94}_{0.87}$	–	–	–	–
544	0.436	$8.3^{8.4}_{8.2}$	$-1.0^{-0.9}_{-1.0}$	$0.85^{0.94}_{0.73}$	$0.25^{0.32}_{0.18}$	$-37.6^{-22.9}_{-58.5}$	$0.66^{0.75}_{0.54}$	$7.62^{8.39}_{8.21}$	$8.39^{8.39}_{8.21}$	$8.01^{8.17}_{7.84}$	$9.04^{8.91}_{9.16}$
584	0.767	$8.3^{8.4}_{8.3}$	$0.3^{0.4}_{0.2}$	–	–	$-36.4^{-27.6}_{-48.8}$	–	–	–	–	–
594	0.263	$7.5^{7.7}_{7.4}$	$-1.2^{-1.1}_{-1.3}$	–	–	$-54.2^{-42.6}_{-69.2}$	$0.88^{0.93}_{0.83}$	–	–	–	–
612	0.786	$7.8^{8.0}_{7.6}$	$-0.4^{-0.3}_{-0.6}$	–	$0.82^{0.85}_{0.80}$	–	–	–	–	–	–
626	0.656	$7.6^{7.9}_{7.5}$	$-0.5^{-0.4}_{-0.6}$	–	–	$-118.8^{-86.1}_{-181.9}$	–	–	–	–	–
1126	0.864	$8.3^{8.4}_{8.3}$	$0.4^{0.4}_{0.3}$	$0.59^{0.62}_{0.55}$	$0.22^{0.26}_{0.17}$	$-94.0^{-61.7}_{-164.3}$	$0.38^{0.42}_{0.35}$	$7.46^{8.95}_{8.79}$	$8.95^{8.95}_{8.79}$	$7.36^{7.37}_{7.33}$	$9.23^{9.22}_{9.25}$
1220	0.487	$7.9^{8.0}_{7.8}$	$-1.0^{-0.8}_{-1.1}$	–	$0.28^{0.34}_{0.21}$	–	–	–	–	–	–
1245	0.678	$8.1^{8.3}_{8.1}$	$-0.8^{-0.6}_{-1.0}$	–	$0.39^{0.47}_{0.30}$	–	–	–	–	–	–
1247	0.524	$7.8^{7.9}_{7.7}$	$-0.4^{-0.3}_{-0.4}$	$0.68^{0.72}_{0.64}$	$0.89^{0.99}_{0.77}$	$-79.0^{-63.5}_{-105.4}$	$0.63^{0.66}_{0.59}$	$7.94^{9.91}_{9.52}$	$9.91^{9.91}_{9.52}$	$7.16^{7.14}_{7.15}$	$9.16^{9.14}_{9.19}$
1332	0.339	$8.0^{8.1}_{7.9}$	$-0.9^{-0.9}_{-1.1}$	–	$0.46^{0.52}_{0.39}$	–	–	–	–	–	–
1344	0.374	$8.0^{8.0}_{8.0}$	$-0.3^{-0.2}_{-0.3}$	$0.95^{0.98}_{0.92}$	$1.47^{1.54}_{1.39}$	$-134.9^{-110.5}_{-169.2}$	$0.94^{0.96}_{0.91}$	$8.59^{9.60}_{9.41}$	$9.60^{9.60}_{9.41}$	$7.83^{7.88}_{7.78}$	$8.89^{8.84}_{8.93}$
1605	0.888	$8.3^{8.4}_{8.3}$	$-0.4^{-0.3}_{-0.4}$	–	–	$-39.7^{-26.1}_{-76.4}$	–	–	–	–	–
1765	0.957	$9.0^{9.2}_{9.0}$	$-0.5^{-0.3}_{-0.6}$	–	$0.80^{0.82}_{0.77}$	–	–	–	–	–	–
1860	0.863	$8.4^{8.4}_{8.4}$	$0.1^{0.1}_{0.1}$	$0.77^{0.83}_{0.70}$	$0.61^{0.70}_{0.50}$	$-40.1^{-28.7}_{-62.0}$	$0.68^{0.74}_{0.60}$	$7.80^{9.17}_{8.85}$	$9.17^{9.17}_{8.85}$	$7.60^{7.67}_{7.52}$	$9.11^{9.05}_{9.17}$
2010	0.424	$7.9^{7.9}_{7.8}$	$-0.9^{-0.9}_{-1.0}$	$0.99^{1.09}_{0.88}$	$0.56^{0.60}_{0.51}$	$-30.4^{-20.1}_{-43.7}$	$0.89^{0.98}_{0.77}$	$7.95^{8.33}_{8.23}$	$8.33^{8.33}_{8.23}$	$8.33^{8.54}_{8.10}$	$8.81^{8.60}_{9.00}$

For each galaxy for which we are able to measure the lines included in the ratios and calibrations used ([OII]λ3727, [OIII]λ4959, [OIII]λ5007, and/or Hβ) with a significance $>3\sigma$, we list: (1) ID of the galaxy; (2) spectroscopic redshift; (3) stellar mass from the SED-fitting; (4) SFR from the SED-fitting; (5–6,8) Line ratios; (7) Rest-frame Hβ EW; (9–10) the value of the last iteration ionization parameter (q) using the expressions of the lower and upper metallicity branches; (11–12) the value of the last iteration oxygen abundance using the expressions of the lower and upper metallicity branches. In (3–8,11–12) we report the median and 16th and 84th percentiles. Metallicities and ionization parameters are calculated using the Kobulnicky and Kewley (2004) calibration as described by Kewley and Ellison (2008). No dust and stellar absorption corrections are applied to the measurements of the emission lines as they are expected to be smaller than the uncertainties.

8

Star Formation Histories

In this Chapter we describe the SFHs obtained using the SED-fitting approach presented in Chapter 5. Furthermore, we include the results published in our publication Rodríguez-Muñoz et al. (2015).

8.1 Individual SFHs

It is important to bear in mind that, as we mentioned in Chapter 5, in this study we use physically motivated SFHs derived from the Millenium simulations (Springel et al., 2005), and not simplified functions. The individual SFHs returned by the SED-fitting analysis (Chapter 5) are in fact, the average of the first 10 best-fit model SFHs weighted by their likelihood. In the Appendix B we show the mean SFH and standard deviation found for each galaxy. The resolution in time (steps) is not linear because the SEDs of stars of different ages change more strongly at smaller ages than at older ages (e.g. Gil de Paz and Madore, 2002). It is also worth mentioning that resolution limitations can change the appearance of the SFH. In deed, SFHs composed by high frequency burst cycles can perfectly look constant when averaged over longer time scales. This effect can even be more important when we average the first 10 best-fit model SFHs to give a bes-estimate SFH.

The shapes of the SFHs obtained for our sample are very varied. Still, we can summarize them in four types (Figure 8.1):

- Rising ($\sim$47%). It is characterized by an almost monotonic increase on which sometimes irregularities are superimposed. This is the most typical type within our sample, which is in agreement with what Atek et al. (2014) obtain for a similar sample of emission lines galaxies using the same approach by Pacifici et al. (2012). Interestingly, rising SFHs have been recently proposed as the most likely SFHs for high redshift galaxies (e.g., Finlator et al. 2011).

- Bell-shaped ($\sim$20%): with a maximum at $\gtrsim$2 Gyr followed by a gradual decrease.

- Bursty ($\sim$20%): characterized by a concatenation of bursts.

- Roughly constant ($\sim$11%) over 4$-$6 Gyr.

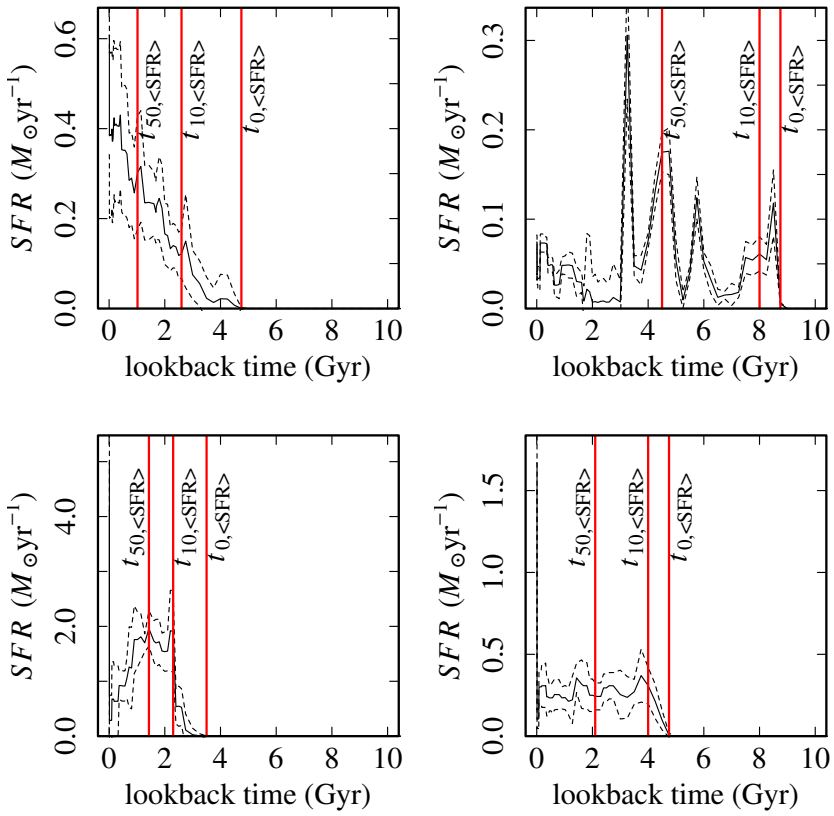

Figure 8.1: Examples of best-estimate SFHs obtained for our targets. From left to right and top to bottom: *rising*, *bell-shaped*, *bursty*, and *roughly constant*. Red vertical lines represent the values of t_0, t_{10}, and t_{50} for each SFH. The solid line represents the weighted average of the 10 best-fitting SFHs. The dash lines show the SFR standard deviation ($\pm$) for each lookback time.

It is worth mentioning that in order to perform a proper classification of the SFHs we need to identify their characteristic trend independently on the scale and order of the values of the SFRs. This is not always easy. On the one hand, for example, some bursty SFHs can appear roughly constant if there is a bright current SF burst, or the constant can appear bursty when there is not a strong burst at the moment of the observation. For this reason, we choose to represent the SFHs in logarithmic scales in certain plots. Nevertheless, we need to be careful because the variations get smoother in such scale, and therefore, we could identify too many roughly constant SFHs. On the other hand, types are not mutually exclusive, which means that, for instance, a bursty trend can appear overlapped on a (e.g.) rising trend. In these cases, we opt for the global trend, which in this example would be the rising trend.

In Figure 8.1 we also show the different stellar mass assembly milestones t_0, t_{10}, and t_{50} described in Chapter 5. Although their absolute positions change in each case, we can see that in the case of bursty and roughly constant SFHs t_0 and t_{10} appear significantly closer to each other than t_{10} and t_{50}. This is a general behavior of both types. Regarding absolute duration, constant and bursty SFHs appear longer than bell-shaped and mainly longer than increasing. It is also worth mentioning that 38% of the galaxies present a steep decrease immediately followed by a steep increase of SFR just before their observed, as can be seen in the examples shown. We refer to the combination of both features as *drop*. The 68% of the galaxies that present the *drop* have

SFHs classified as rising.

We have checked if there is an inclination of more or less massive galaxies to present preferentially any of these SFHs types. Bell-shaped SFHs present the largest median stellar mass $\log M_*/M_\odot \sim 8.7^{9.1}_{8.0}$. Rising, constant and bursty types are populated on average by mainly less massive galaxies $\log M_*/M_\odot \sim 8.0^{8.5}_{7.6}$, $\log M_*/M_\odot \sim 7.9^{8.9}_{7.7}$, and $\log M_*/M_\odot \sim 8.3^{8.8}_{7.7}$, respectively. Pacifici et al. (2013) found bell-shaped SFHs to be more characteristic of higher stellar mass galaxies, which appear to be in agreement with our results.

To probe whether these different SFHs are linked to specific features in the SEDs we compare the median best-fit spectra of each SFH type. In Figure 8.2 we show the median (first panel), percentile 16th (P16; second panel), and percentile 84th (P84; third panel) of the models fitted to each galaxy with SFHs rising (pink), bell-shaped (orange), constant (green), and bursty (blue). To obtain these composite models we calculate the median and percentiles at each wavelength of the best-fit spectra. We need to take into account that the average stellar masses for each type are different, so we should focus on differences in slopes and colors, rather than vertical offsets. If we focus on the top panel we identify a few differences and similarities between the composite SEDs. Rising and bell-shaped SFHs present a very similar average behavior except in the near-UV wavelength range (~ 0.2 μm), where bell-shaped present an excess. This difference could be due to the lower past SFR experienced by rising SFHs compared to bell shaped, which have already experienced the maximum level of SF (if we do not account for the sudden burst we identify at the time they are observed). Bursty and constant SFHs also present a similar behavior except bellow ~ 0.2 μm. Constant SFHs present a steeper median UV slope, consequence of a lower intensity of the current SF process. The second and third panel show the large dispersions found for the SEDs of each SFH type. A good example of this is the difference in the blue color found for the P16 and P84 constant SFH SEDs.

8.1.1 The *Drop* Feature

Now, we focus on the *drop* feature, and carry out the same exercise to identify evidences of intrinsic differences in the SEDs of galaxies for which it is identified. In the bottom panel of Figure 8.2 we show the median and percentiles of the templates used to fit the galaxies with rising SFHs, that present (black) and do not present (grey) the *drop*. Although other SFH types present also this *drop* we have decided to use only the SEDs of the rising SFHs, which are the more numerous, to study the impact of the feature independently. In this plot, we can see how the *drop* produces mainly a decrease of the emission in the nUV ($\lambda < 0.3\mu$m) wavelength range in the median SED, which can be explained by a deficit of SFR in timescales of about 10–100 Myr.

In order to explore these variations we can also use a color-color diagram, searching for a segregation of the galaxies with a *drop*. In Figure 8.3 we show a rest-frame infrared color (K - IRAC 3.6 μ) against a rest-frame visible color (U - b) for our sample. We use the same color code for the different SFH types, and open and filled circles for galaxies which do and do not show the *drop* feature, respectivelly. To obtain these colors we calculate the rest-frame synthetic photometry of the best-fit templates for the MUSYC K and U bands, IRAC 3.6 μ and ACS b band. We select these colors because they trace the most important differences detected in Figure 8.2. We do not identify clear differences depending on the SFH type, but we see that SFHs which present *drop* are located in the upper right quadrant of the plot. This area corresponds to those objects redder in both colors, which is compatible with a recent decrease of the SFR.

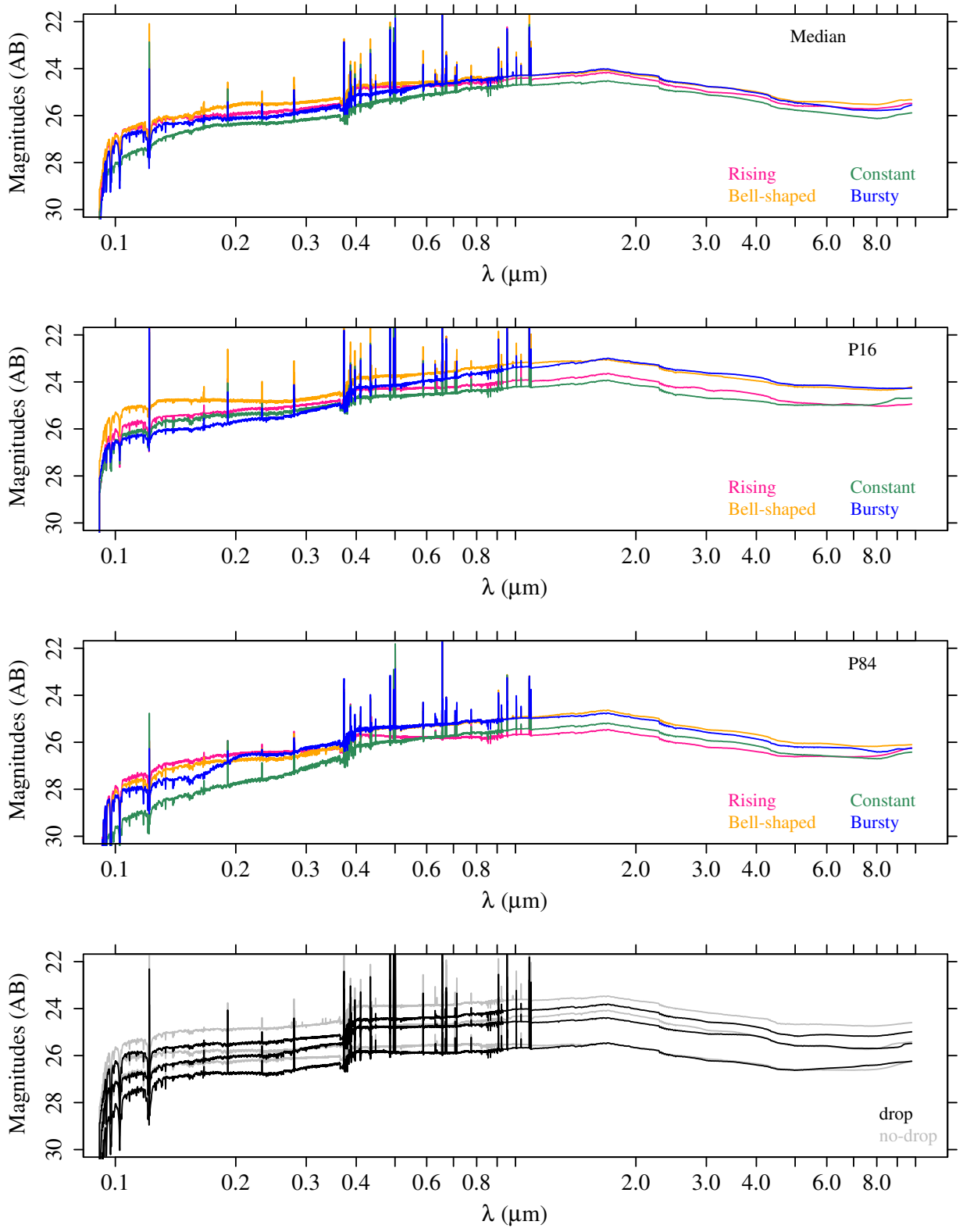

Figure 8.2: From top to bottom: Median (first panel), percentile 16th (second panel), and percentile 84th (third panel) of the magnitudes at each wavelength of the templates fitted to the galaxies characterized by rising (pink), bell-shaped (orange), constant (green), and bursty (blue) SFHs. The fourth panel shows the median and percentiles for the galaxies with rising SFH that present (black) and do not present (grey) the so called *drop* feature.

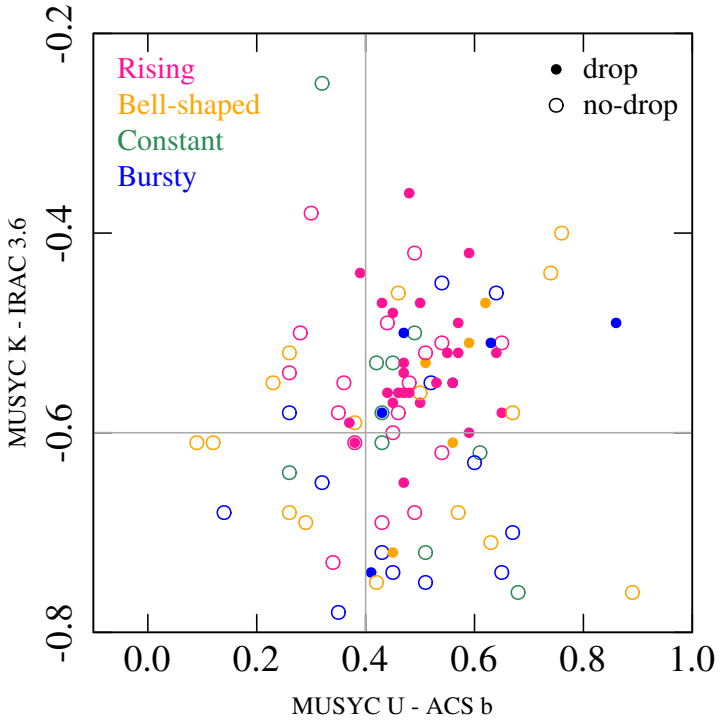

Figure 8.3: Color-color diagram. Points represent galaxies characterized by rising (pink), bell-shaped (orange), constant (green), and bursty (blue) SFHs. Solid and open points represent galaxies with and without *drop*, respectively.

While evidences of different behaviors can be appreciated in the synthetic photometry, it is not clear whether we would find the same trend using the observational data, as the K-correction uncertainties, and photometric errors themselves are likely to vanish any clear behavior in the color-color plot.

8.1.2 Timescales of Individual Stellar Mass Assembly

To characterize the SFHs obtained through the SED-fitting approach we use the same stellar mass assembly milestones described in Chapter 5: t_0, t_{10}, and t_{50}. Figure 8.4 shows the distribution in redshift of t_0 (left panel), t_{10} (central panel), and t_{50} (right panel) for the whole sample. In each plot, the black solid line shows the lookback times corresponding to each redshift (t_z), and therefore, it marks the maximum lengths of the possible SFHs at each redshift, given the age of the Universe. Uncertainties for t_0, t_{10} and t_{50} are difficult to derive because the resolution of the SFH models decreases not linearly with lookback time (varying between 0.10–0.25 Gyr), and uncertainties of the stellar masses should also be taken into account. We can see how the dispersion is larger in t_0 than in t_{50}. This might be a consequence of the different robustness of each milestone. t_0 could be further more difficult to constrain than t_{50}, as at early times in the SFH of the galaxy, the values of mass and SFR are inevitably more uncertain. At first glance, we derive an important fact to take into account from this plot. The age of the universe at each redshift limits the maximum length of the SFH of a galaxy located at such redshift. Therefore, we need to be careful when we compare the SFHs of galaxies observed at different epochs of the universe. Despite the dispersions the vast majority of our sample appears to have formed the last 50% of their current stellar mass within the $\sim$2Gyr previous to their t_z, which can be interpreted as a rather late or recent stellar

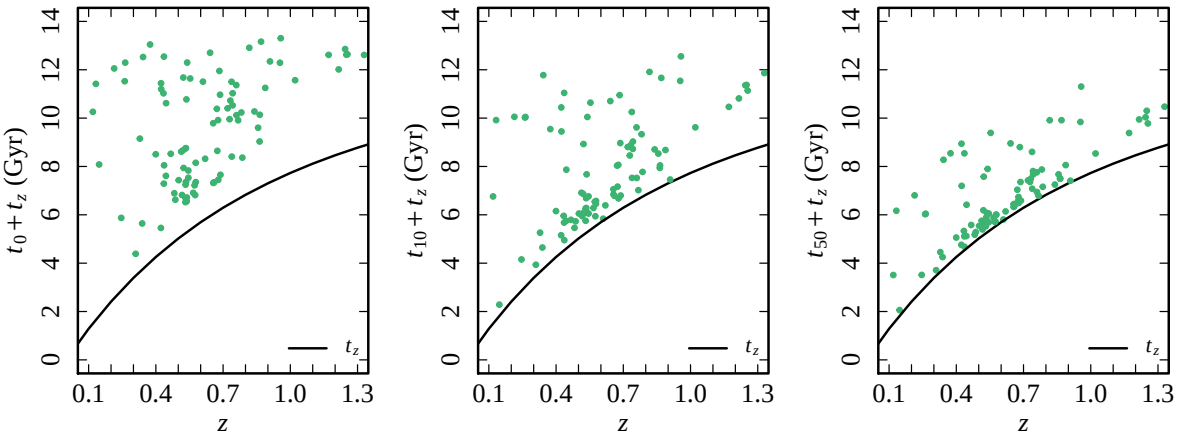

Figure 8.4: From left to right t_0, t_{10}, and t_{50} against the redshift for each of the galaxies in our total sample. The black solid line represents the lookback time at each redshift, t_z.

mass assembly.

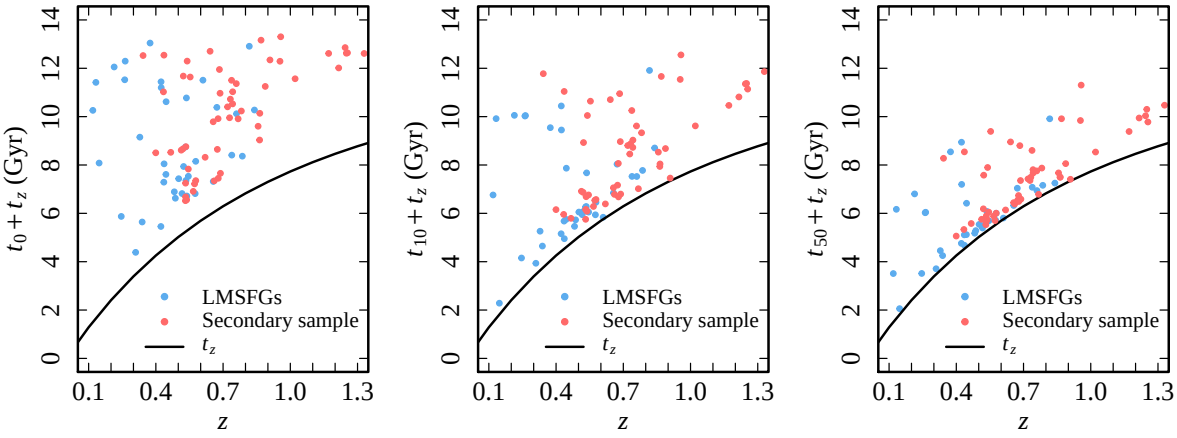

Figure 8.5: From left to right t_0, t_{10}, and t_{50} against the redshift for the galaxies in the LMSFGs sample (blue points) and and the more massive sample (red points). The black solid line represents the lookback time at each redshift, t_z.

We check now whether the current stellar mass of each of the galaxies in our sample is linked to the different mass acquisition *rythms* defined by the values of t_0, t_{10}, and t_{50}. To this aim, we analyze the behavior in the Figure 8.4 of galaxies within two subsamples identified by mass:

1. Low-mass Star-forming galaxies (LMSFGs): $\log M_*/M_\odot \leq 8$
2. Secondary and more massive sample: $\log M_*/M_\odot \leq 8$

Figure 8.5 shows the result. The red points represent the LMSFGs sample, while blue points show the more massive sample. In this plot we can clearly see that the larger redshifts are populated mainly by more massive galaxies ($z > 0.9$). As higher redshifts lead to shorter maximum SFHs by default, we need to take into account that we could be biasing the conclusions for highest mass galaxies. Said that, we do not identify a significant difference between the behavior of both

samples. A likely reason for this absence of significant difference may rely of the fact that the mass difference between the samples is small ($\sim$0.7 dex). We will analyze in more detail the average SFHs of the whole sample and the two subsamples in Section 8.2.

8.2 Median SFHs

Since it is very challenging to accurately constrain the full SFH of individual galaxies we decide to combine them in order to identify common behaviors and general trends. We assume the hypothesis that the galaxies behave in a similar way, regardless of redshift, which is reasonable because all our targets present similar properties and undergo a strong current SF process.

In this section we calculate the mean SFHs of different subsamples within our sample of 91 galaxies. Our objective is to identify common features in the SFHs depending on redshift, physical properties, and morphology. To obtain the composite mean SFHs for each subsample we follow the next steps:

1. First, we normalize the individual SFHs to the median stellar mass of the corresponding subsample. The normalization avoids weighting by mass the composite SFHs, as the highest-mass galaxies could pull the mean SFR towards higher values.

2. Second, we set each SFH to a common reference system where $t_z = 0$, which means that we put together the *current* starburst.

3. Third, we co-add the individual SFHs and for each step in lookback time we derive median (50% of the distribution, SFH-P50) and confidence ranges (16% and 84% of the distribution, SFH-P16 and SFH-P84, respectively) of the SFRs from the co-added SFHs. We refer to the path defined by the median along the lookback time as SFH-P50. We use SFH-P16 and SFH-P84 for the paths outlined by the percentiles 16th and 84th, respectively. We use a similar approach to obtain the median sSFR history (sSFRH). Actually, in this case we use the median, 16 th, and 84 th percentiles of the distribution of sSFR at each lookback time step (sSFRH-P50, sSFRH-P16, and sSFRH-P84 respectively).

4. Consecutively, we characterize these composite SFHs using the milestones t_0, t_{10}, and t_{50} as described in Chapter 5.

5. We derive the uncertainties on the milestones that arise from the ensemble averaging using the bootstrapping method. For each sample, we build 10^3 bootstrap samples (i.e. of the same size of the original) that include individual SFHs randomly selected from the subsample and allowing for repetitions. Then, we obtain SFH-P50, SFH-P16 and SFH-P84 for each random sample and we calculate their t_0, t_{10} and t_{50}. The final values are retrieved as the means and standard deviations of the milestones obtained for the 10^3 bootstrap samples.

8.2.1 SFH-type Dependence

First of all, to better appreciate the differences between the types of SFHs identified in the previous section we average the SFHs within each of the SFH types. Figure 8.6 shows the median SFHs

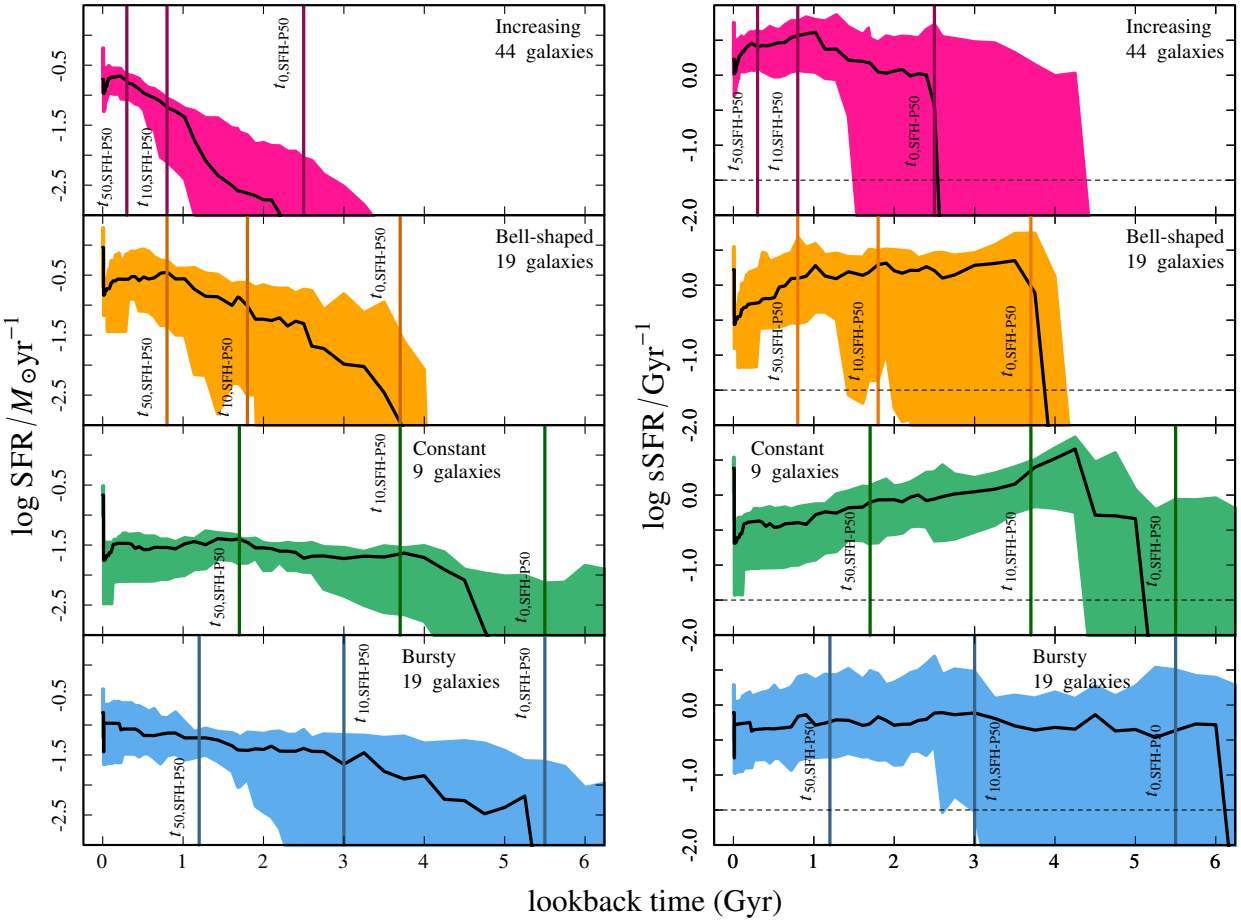

Figure 8.6: Left: Median SFHs (SFH-P50, black solid line) of the four SFH types identified (increasing, bell-shaped, constant and bursty are shown in pink, orange, green, and blue, respectively). Individual SFHs are normalized to the median mass of the corresponding bin before being combined, and put in a common reference system (t_z=0). The colored areas represent the corresponding 16th and 84th percentiles of the SFR per lookback time step (SFH-P16 and SFH-P84 respectively). Right: Median sSFRHs. The horizontal dash lines mark the threshold between star-forming and quiescent galaxies as in Kimm et al. (2009). In each panel, the vertical lines indicate the values of $t_{0,SFH-P50}$, $t_{10,SFH-P50}$, and $t_{50,SFH-P50}$. The number of galaxies included in each stellar mass bin is also indicated.

(SFH-P50; left panels) and median sSFRHs (SFH-P50; right panels) corresponding to each type of SFH using black solid curves. Each panel also shows the t_0, t_{10}, and t_{50} derived from the corresponding median SFH-P50 ($t_{0,\mathrm{SFH-P50}}$, $t_{10,\mathrm{SFH-P50}}$, and $t_{50,\mathrm{SFH-P50}}$). On average, increasing and bell-shaped SFHs appear to be shorter than constant and bursty. The total mean length of the SFH defined as the t_0 of SFH-P50 is minimized by the increasing SFHs and maximized by bursty SFHs, though the dispersion is large in t_0 specially for this last type. Furthermore, increasing SFHs appear to assemble the stellar mass in the rapidest way (i.e. the time interval between t_{10} and t_{50} is in this case the shortest, $\sim$0.5 Gyr), followed by bell-shaped, bursty and constant SFHs. Both of them exhibit inefficient early SFH, that speed up after reaching the 10% of stellar mass (t_{10}). We can see how the burstiness of the bursty SFHs is smoothed when we "average" the SFHs. This effect is already present in the individual SFHs and it needs to be taken into account in every averaging approach we use. With regard sSFR, the maximum value in the first three SFHs modes is reached before they are observed. Increasing SFHs are able to reach the highest sSFRs. Galaxies growing following such trends should therefore be the systems for which larger EWs are measured.

Table 8.1: Average properties of the final subsamples.

Sample	#	$z_{\rm spec}$	$\log M_*/{\rm M}_\odot$	log SFR	log sSFR
(1)	(2)	(3)	(4)	(5)	(6)
LMSFGs	31	0.517 (0.374, 0.672)	7.7 (7.5, 7.9)	-0.9 (-1.3, -0.4)	0.4 (0.0, 0.7)
Secondary	43	0.656 (0.521, 0.743)	8.4 (8.2, 8.8)	-0.4 (-1.0, 0.1)	0.0 (-0.5, 0.3)

For each sample, we report: (1) name; (2) number of galaxies; (3) spectroscopic redshift; (4) stellar mass ($\rm M_\odot$); (5) star formation rate ($\rm M_\odot yr^{-1}$); (6) specific star formation rate ($\rm Gyr^{-1}$); Columns (3–6) show median values, and 16th & and 84th percentiles (within parenthesis) of the distributions.

We notice that the *drop* feature appears in all the panels. As we noticed in Section 8.1 not all individual galaxies present such feature, which suggests that this is not an artifact. In fact, in the library, the prior in sSFR is flat (smoothly declining on the edges) between -2 and 2 (logsSFR/$\rm Gyr^{-1}$), thus we should not be biasing the fit towards bursty solutions. It is interesting anyway that the four SFH types exhibit such feature.

8.2.2 Stellar Mass Dependence

To identify differences in the SFHs of galaxies with different stellar masses, we consider the subsamples described in the previous section: LMSFGs and the secondary more massive sample. To avoid weighting the results with the properties of the galaxies located on areas not (approximately) uniformly covered by the whole mass range, we limit our redshift range to $0.3< z <0.9$. Bellow $z \sim 0.3$ we only observe LMSFGs while over $z \sim 0.9$ there are not LMSFGs observed. Then, our final sample is conformed of 74 galaxies, 31 LMSFGs with stellar masses between $7.3 \leq \log M_*/{\rm M}_\odot \leq 8.0$, and 43 more massive systems with stellar masses between $8.0 < \log M_*/{\rm M}_\odot \leq 9.1$. Table 8.1 gives the median values and 16th–84th percentiles of the stellar mass, SFR, and the sSFR for both final subsamples.

In Table 8.2 we report the final values of the milestones and the associated standard deviations for the SFH-P50, SFH-P16 and SFH-P84 of both subsamples. The two left panels in Figure 8.7 show for each sample the SFH-P50 (black solid line), SFH-P16 (lower limit of the shaded area) and SFH-P84 (upper limit of the shaded area). The right panels in Figure 8.7 present the analogous plot for the composite sSFRH. Probably, the main conclusion we can derive from this plot and the values of the milestones in Table 8.2 is that the galaxies in both our samples appear to have formed a large fraction of their stellar mass recently. Given our reference system is t_z, this means that at any redshift low-mass galaxies appear to be intrinsically ''young" objects. The recent formation of the low-mass galaxies within our sample matches the downsizing cosmological trend of galaxy formation (Cowie et al., 1996). Recent formation refers to the individual time reference system of each galaxy. In any case, early SF activity is not dismissed given the large dispersion in t0. Despite the dispersion in the milestones and the similar properties between the two subsamples (there is only a 0.7 dex difference in the mean stellar mass) we notice that more massive galaxies tend to present longer SFH. Nevertheless, the relative differences between the milestones remain similar implying that the mass assembly can be longer or shorter but somehow similar (actually, as we will see later, both mean SFH can be reproduce approximately with the same function).

Also in this case the *drop* feature appears in both cases. Therefore, we conclude it is neither

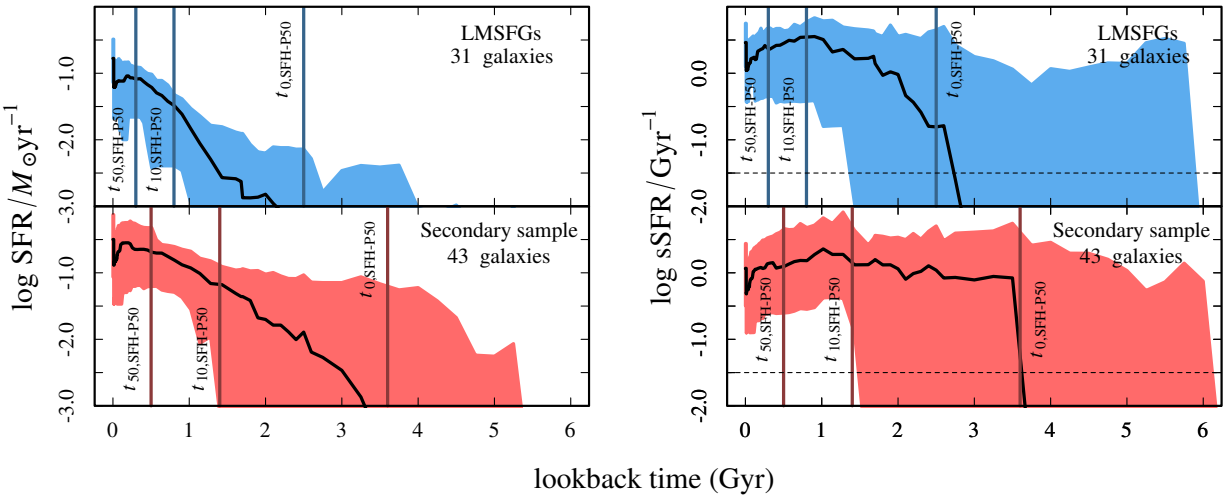

Figure 8.7: Left: Median SFHs of the final samples (SFH-P50, black solid line). Individual SFHs are normalized to the median mass of the corresponding bin before being combined. The colored areas represent the corresponding 16th and 84th percentiles of the SFR per lookback time step (SFH-P16 and SFH-P84 respectively). Right: Median sSFRHs. The horizontal dash lines mark the threshold between star-forming and quiescent galaxies as in Kimm et al. (2009). In each panel, the vertical lines indicate the lookback time of the first SF burst of the SFH-P50 corresponding to each stellar mass bin ($t_{0,SFH-P50}$), and when SFH-P50 forms 10% and 50% of the final stellar mass ($t_{10,SFH-P50}$ and $t_{50,SFH-P50}$). The number of galaxies included in each stellar mass bin is also indicated.

a mass dependent feature.

Our galaxies appear to be much younger than Local Volume dwarfs studied by Weisz et al. (2011a) (ACS Nearby Galaxy Survey Treasury, ANGST; Dalcanton et al. 2009) and Local Group dwarf galaxies from Mateo (1998) (For a complete list of the studies on the SFHs of these galaxies see Weisz et al. 2011b). Both samples include several tens of quiescent and star-forming galaxies with different morphologies. Despite the differences between such samples (analyzed by Weisz et al. 2011b) for both of them long SFHs are found. In deed, the galaxies in these samples had already formed the first half of the current stellar mass by $z \sim$1. This means that their t_{50} would be larger than $\sim$7 Gyr, when our results point in the direction of t_{50} <1 Gyr. It is worth noting that our lowest redshift bin contains a few SFHs with larger t_{50}, reaching values of the same order within the uncertainties. Among the nearby dwarfs studied in detail by the aforementioned works, we find that the typical isolated LG dwarf Leo A is the galaxy with the most delayed stellar mass assembly (Madau et al. 2014). Leo A appears to reach t_50 $\sim$4 Gyr ago, certainly, still earlier than the galaxies in our sample. On the contrary, the work carried out by Leitner (2012) obtained delayed stellar mass assemblies for SDSS star-forming galaxies through a SED-fitting analysis and using an main sequence integration approach. It particular, he inferred a late assembly (z <1) of 70% of the stellar mass for low-mass star-forming galaxies with 8.0<log$M_*/M_\odot$<8.5, more in agreement with our results.

We cannot compare our results to those obtained by Pacifici et al. (2013) for a sample of 4517 blue galaxies in the redshift range 0.2< z <1.4 from All-Wavelength Extended Groth Strip International Survey (AEGIS). In such work, the average SFH is actually obtained as the mean SFR of the SFRs$\neq$0 at each lookback time. This *a priori* slight difference in the averaging approach implies automatically that the t_0 of the average SFH is equal to the largest t_0 of the sample. Therefore, the milestones obtained in their work are neither comparable with ours.

Table 8.2: SFHs Timescales of the Final Samples

Sample	SFH-P50		
	t_0	t_{10}	t_{50}
(1)	(2)	(3)	(4)
LMSFGs	2.5±0.4	0.8±0.1	0.3±0.0
Secondary	3.6±0.3	1.4±0.3	0.5±0.1

Sample	SFH-P16		
	t_0	t_{10}	t_{50}
(1)	(5)	(6)	(7)
LMSFGs	1.3±0.2	0.5±0.2	0.3±0.1
Secondary	1.7±0.3	0.9±0.1	0.4±0.1

Sample	SFH-P84		
	t_0	t_{10}	t_{50}
(1)	(8)	(9)	(10)
LMSFGs	5.0±1.0	1.8±1.0	0.5±0.1
Secondary	5.9±0.7	3.4±0.7	0.8±0.2

For each sample, we report: (1) name; (2–4) t_0, t_{10}, and t_{50} (Gyr) for SFH-P50; (5–7) t_0, t_{10}, and t_{50} (Gyr) for SFH-P16; (8–10) t_0, t_{10}, and t_{50} (Gyr) for SFH-P84; We present the average and standard deviations of the t_0, t_{10}, and t_{50} of the SFH-P50, SFH-P16, and SFH-P84 obtained for 10^3 different bootstrap samples of SFHs drawn from each mass bin.

8.2.3 Stellar Mass and Redshift Dependence. Relative Lookback Times

We now divide the two subsamples into bins of redshift to try to identify an evolution of the values of the milestones and also the shapes of the median SFHs. We consider three bins within the range $0.3< z <0.9$ ($0.3< z <0.5$, $0.5< z <0.6$, and $0.6< z <0.9$), an extra bin bellow 0.3 (populated only by LMSFGs), and another one over 0.9 (populated exclusively by more massive galaxies). We try to define the bins in a way that the number of galaxies in each of them is reasonable to be able to average.

In Figure 8.8 we show the median SFH obtained for each bin and sample following the methodology already described. We also show the number of galaxies in each bin and the t_0, t_{10}, and t_{50}. For each redshift bin we can see that the LMSFGs form their mass later than more massive galaxies, and therefore, all the average stellar mass assembly milestones present lower values for the former. This result was the expected after the conclusions extracted from Figure 8.7. Now we focus on the evolution with redshift of each subsample. If the length of the SFH were determined by the mass (exclusively), we would expect to obtain similar curves for all the redshifts bins. For the sample of LMSFGs the SFHs appear to be extremely similar and short ($t_0 \sim 2.5$ Gyr) in the three highest redshift bins. Surprisingly, LMSFGs in the lowest redshift bin present the longest composite SFH ($t_0 \sim 8.2$ Gyr), with a great dispersion. We enumerate and explain some possible explanations for this behavior:

1 At this low redshifts those galaxies that remain low-mass systems are preferentially those

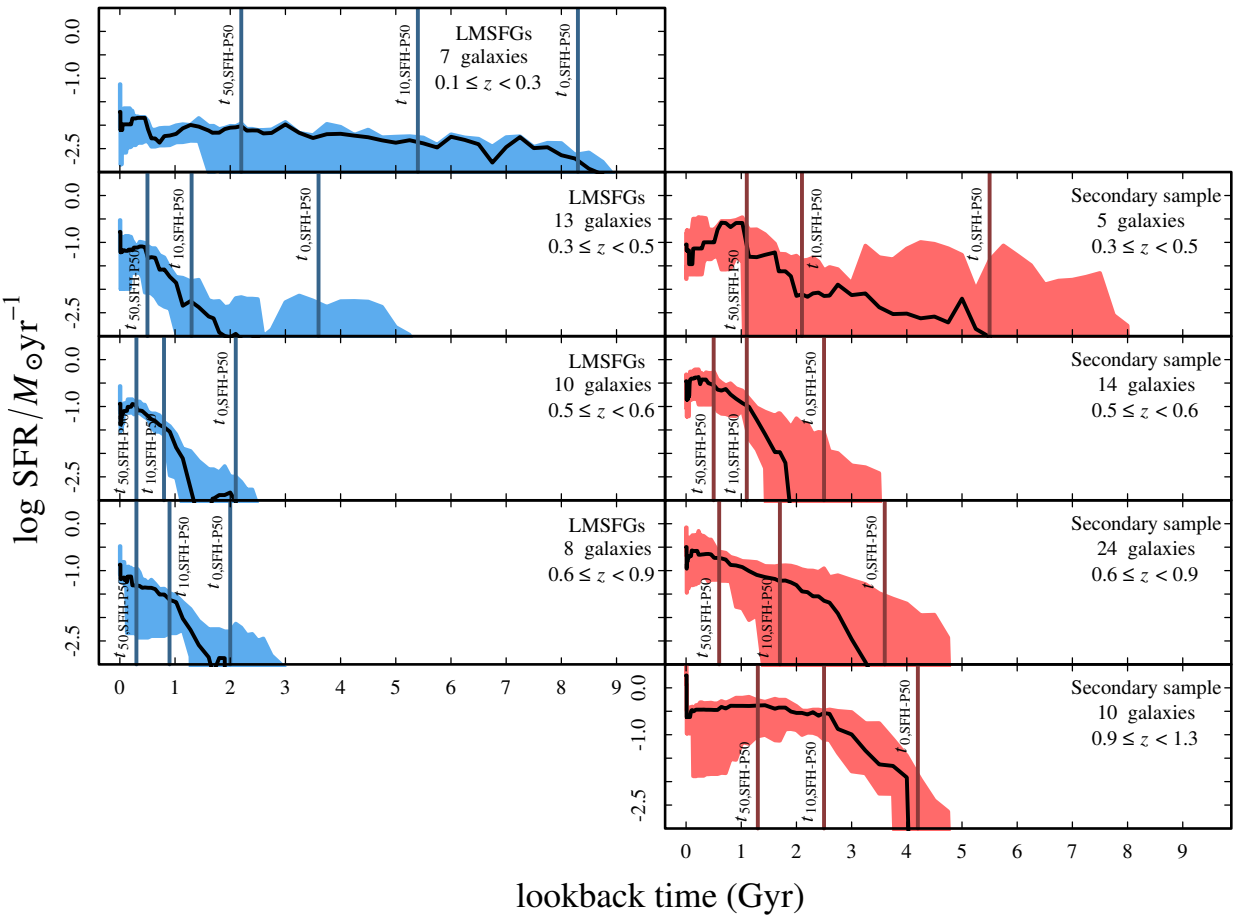

Figure 8.8: Median SFHs (SFH-P50, black solid line) of the two subsamples (LMSFGs and secondary sample in blue and red, respectively) divided into redshift bins. Individual SFHs are normalized to the median mass of the corresponding bin before being combined, and put in a common reference system (t_z=0). The colored areas represent the corresponding 16th and 84th percentiles of the SFR per lookback time step (SFH-P16 and SFH-P84 respectively). In each panel, the vertical lines indicate the values of $t_{0,SFH-P50}$, $t_{10,SFH-P50}$, and $t_{50,SFH-P50}$. The number of galaxies included in each stellar mass bin is also indicated.

that have undergone long and inefficient SFHs. In this case, then, there should be a reason why we do not detect a majority of objects that have followed similar trends to those found at higher redshits.

2 The characteristic lower current sSFR (i.e. weaker emission lines) to which such longer SFHs lead (despite the increase in the current SFR), hampers the observation of galaxies formed through this SF process at higher redshifts than ∼0.5.

3 The longer SFH is a simple consequence of the longer possible SFHs at lower lookback times. We dismiss this possibility as the SFHs library built for this work is characterized by a uniform distribution of t_0 at any redshift.

4 We are only able to detect the older SPs in the lowest redshift ranges. Therefore, higher redshift galaxies present shorter SFHs. One of the consequences of using physically motivated SFHs is that the models fitted can include SPs for which the data has not enough resolution. This effect guaranties that t_0 is very unlikely to be underestimated. Under this assumptions, it is surprising that not detectable SP appear only in the lowest redshifts.

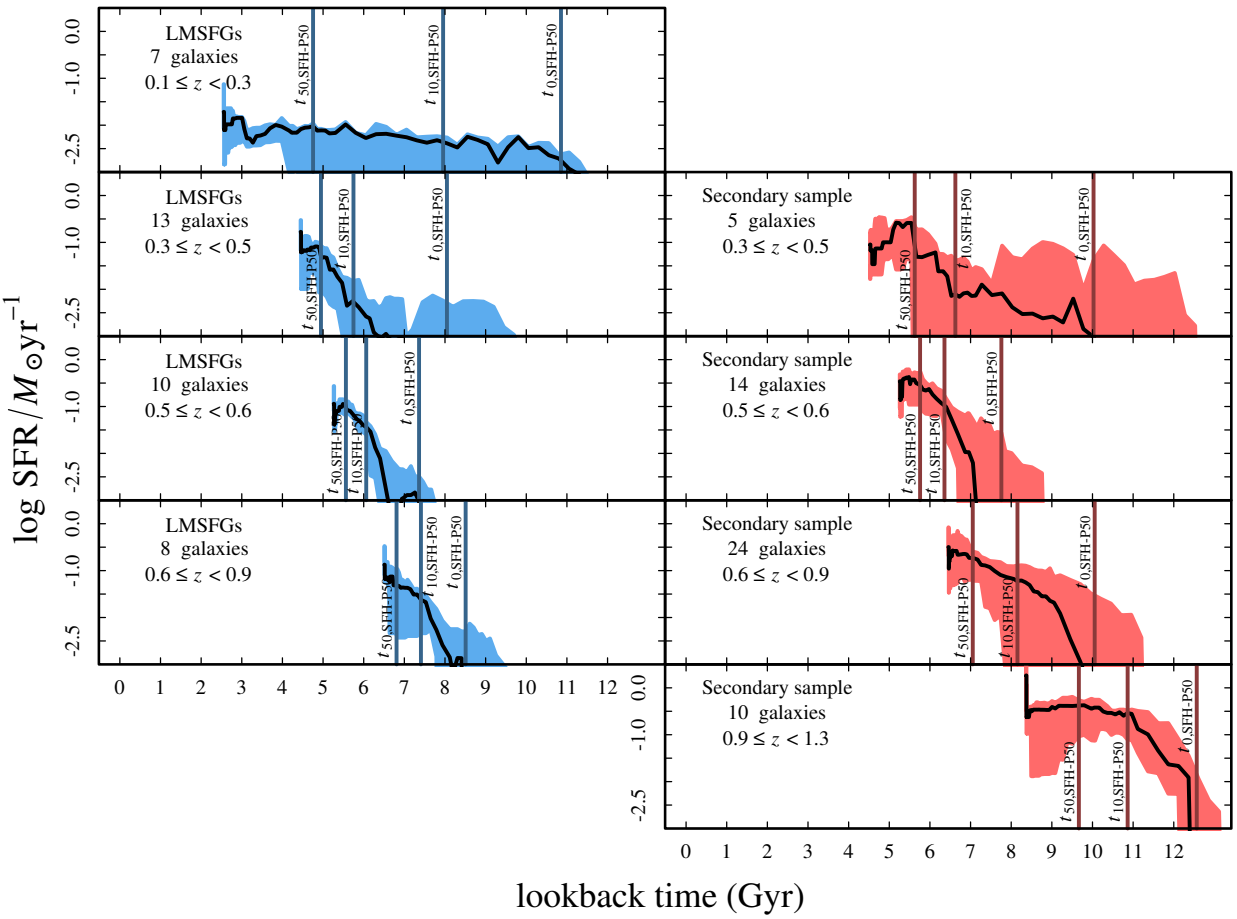

Figure 8.9: Median SFHs as in Figure 8.8. In this case, the composite SFHs are put on the median t_z of each bin.

In the case of the secondary subsample, we again obtain the longest SFH in the lowest redshift bin ($t_0 \sim 5.5$ Gyr). Now the length of the SFHs appears to increase from the second lower redshift bin towards higher redshifts. We need here to keep in mind that the most massive galaxies lie on the further redshift range. Although the difference in the average mass is not large, it could be biasing the higher redshift bin average SFH toward longer SFHs.

8.2.4 Stellar Mass and Redshift Dependence. Absolute Lookback Times

To have a clearer idea of when the SFHs of our sample take place in terms of absolute cosmic time, we shift the composite SFHs of each panel in Figure 8.8 to the lookback time corresponding to the median redshift of each subsample. We plot the result in Figure 8.9. Apparently, we do not identify a common epoch in which all the galaxies in our sample form the bulk of their stellar mass. Our selection rather gathers galaxies characterized (at each redshift) by a recent assembly of most of their observed stellar mass.

8.2.5 Morphology Dependence

To explore whether there is a link between the SFH and the morphology of the galaxies, or alternatively, if each morphology is characterized by a specific type of SFH, we calculate the median

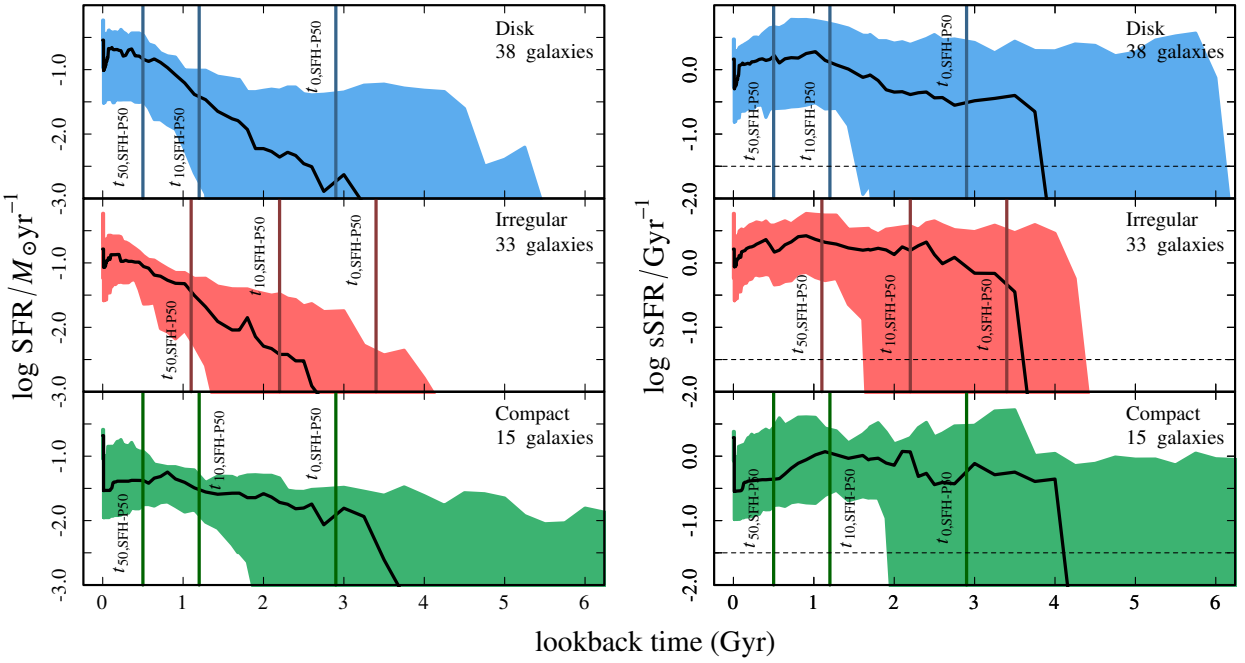

Figure 8.10: Left: Median SFHs (SFH-P50, black solid line) of the three morphological types identified in Chapter 6 (disks, irregulars and compacts are shown in blue red, and green, respectively). Individual SFHs are normalized to the median mass of the corresponding bin before being combined, and put in a common reference system (t_z=0). The colored areas represent the corresponding 16th and 84th percentiles of the SFR per lookback time step (SFH-P16 and SFH-P84 respectively). Right: Median sSFRHs. The horizontal dash lines mark the threshold between star-forming and quiescent galaxies as in Kimm et al. (2009). In each panel, the vertical lines indicate the values of $t_{0,SFH-P50}$, $t_{10,SFH-P50}$, and $t_{50,SFH-P50}$. The number of galaxies included in each stellar mass bin is also indicated.

SFHs of the galaxies that present the same morphology following the same methodology described. In Chapter 6 we classified visually the galaxies into disks, irregulars and compact systems. In the left panels of Figure 8.10, we show the median SFH for each of these types (blue, red, and green, respectively). In the right panels we show their median sSFRHs. In each panel we mark the values of their mass assembly milestones, and we show the number of galaxies included. Disks and irregular galaxies present very similar slopes in the SFHs and sSFHs. Nevertheless, the values of the milestones suggest that disks form their mass slightly more recently than irregulars. On the contrary, compact galaxies present a flatter median SFH (resembling roughly constant or bursty types) and decreasing slope in sSFRH, but very similar milestones to disks. In Chapter 6 we already suggested that we could be misclassifying some compact as disks and the opposite. Interestingly, compact galaxies appear to undergo the strongest current burst with respect their global SFHs, which is in agreement with the properties of BCDs.

8.2.6 Stellar Mass Fraction

Another interesting way to check and compare the stellar mass assembly of the galaxies is the fraction of the total final mass formed at each lookback time. This is what we represent in Figure 8.11. In order to be able to compare the SFHs of all the galaxies, we do not use the absolute values of the lookback time, but we normalize them to the value of t_0. Thus, we actually plot the fraction of final stellar mass against the fraction of the total length of each individual SFH. In the left panel we show the mass assembly of the individual galaxies (grey curves), the median and percentiles

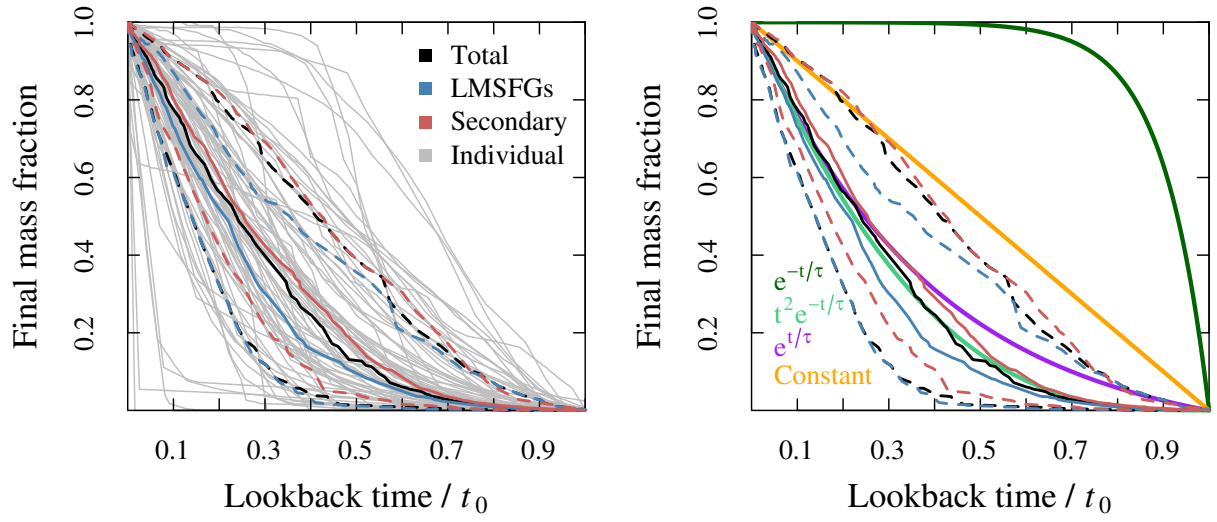

Figure 8.11: Fraction of the final stellar mass formed at each lookback time in units of t_0. Left: Individual SFHs (grey), median SFH and percentiles for the whole sample (black solid and dashed lines), LMSFGs (blue solid and dashed lines), and the secondary sample (red solid and dashed lines). Right: Comparison between the mean SFHs obtained for our sample and subsamples and simplified functions: Constant (orange), exponentially decreasing (age = 10 Gyr, τ = 1 Gyr; dark green), delayed (age = 2 Gyr, τ = 5 Gyr; light green), exponentially increasing (age = 10 Gyr, τ = 4 Gyr; purple).

for LMSFGs (blue solid and dashed lines) and the secondary sample (red solid and dashed lines), and the total sample (black solid and dashed lines). In the right panel we show the composite SFHs obtained (black, blue and red solid and dashed lines) and the curves corresponding to simple parametric SFHs: constant (orange), exponentially decreasing (age = 10 Gyr, τ = 1 Gyr; dark green), delayed (age = 2 Gyr, τ = 5 Gyr; light green), exponentially increasing (age = 10 Gyr, τ = 4 Gyr; purple). From this comparison we deduce that exponentially decreasing with age$\gg \tau$ is not representative of our whole sample. The more representative parametric SFHs of both of our samples vary between constant and exponentially increasing. The simplified SFH that better follows the mean curves obtained for the samples is the delayed ($t^2e^{-t/\tau}$) with τ larger than the age. The function $te^{-t/\tau}$ does not fit the curves independently of the fraction age/τ. Despite exponentially increasing fits reasonably well the curves, it produces an excess of stellar mass at early times with respect what we observe.

8.2.7 Main Sequence and SFHs

In Figure 8.12 we show the MS for the subsamples within the two stellar mass bins we have been using along this *Thesis*. As in Chapter 7, we show the systems with $logM_*/M_\odot \leq 8.0$ in the top panel (blue points), while those targets with $\log M_*/M_\odot > 8.0$ are included in the lower panel (red points). The plot also shows the SFMS found by Whitaker et al. (2012, W12) for redshifts 0.2, 0.6, and 1.0 (green lines) extended towards lower stellar masses, and the SFMS derived by Whitaker et al. (2014, W14) for low-mass galaxies in the redshift range between 0.5 and 1 (orange lines). Blue and red curves represent the median SFHs of our LMSFGs and secondary samples, respectively. As we can see, the SFHs present a deficit of SFR at earlier ages with respect what is predicted by W12 MS. On the contrary, the SFHs obtained follow W14 MS (optimized for low-mass galaxies) backward in lookback time (marked with vertical black lines).

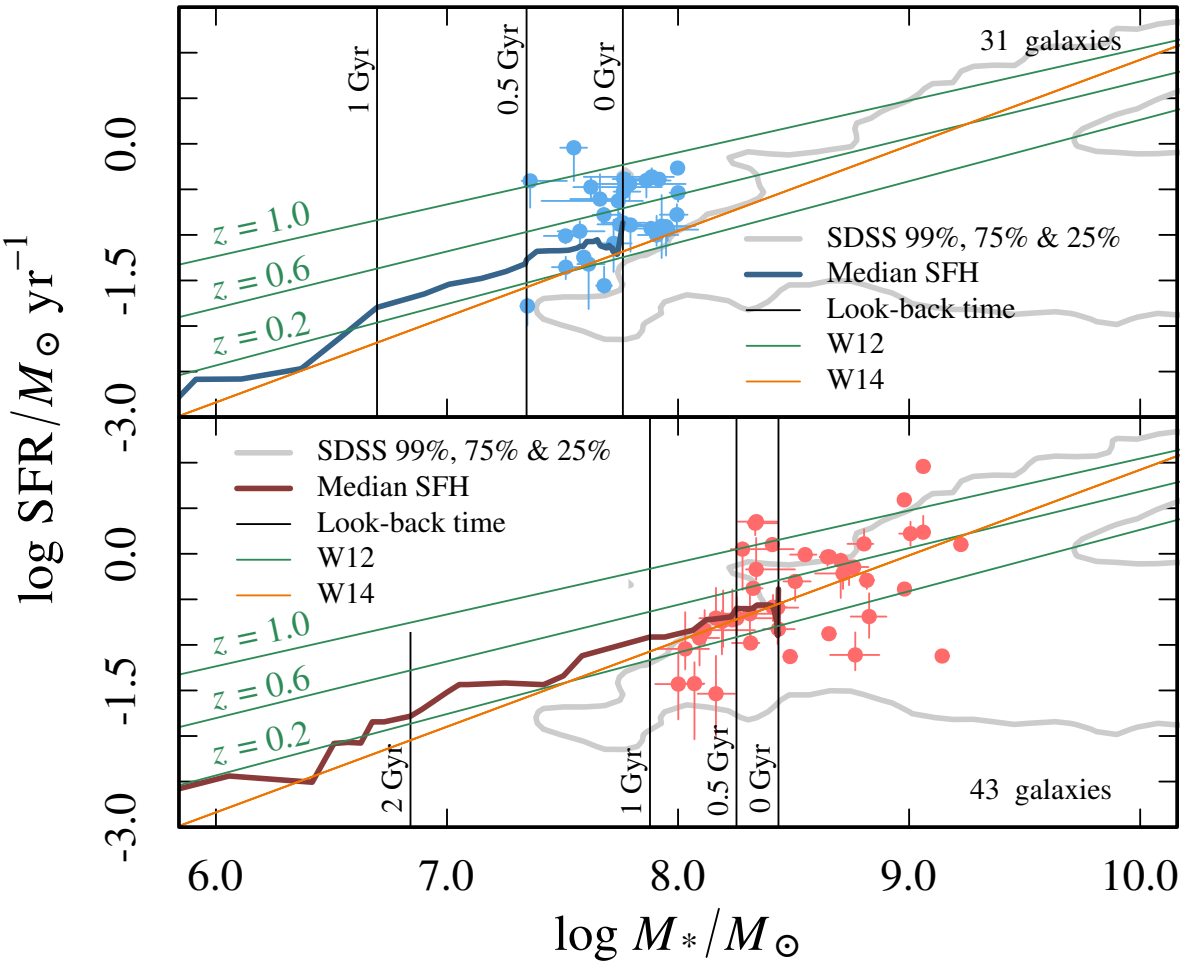

Figure 8.12: Stellar mass-SFR relation for two samples of spectroscopically confirmed low-mass star-forming galaxies. The upper panel presents the systems with $logM_*/M_\odot \leq 8.0$, while those targets with $logM_*/M_\odot > 8.0$ are included in the lower panel. The plot also shows the SFMS found by Whitaker et al. (2012, W12) for redshifts 0.2, 0.6, and 1.0 (green lines) extended towards lower stellar masses. In addition we show the SFMS derived by Whitaker et al. (2014, W14) for low-mass galaxies in the redshift range between 0.5 and 1. The solid curve in each panel represents the median SFH for each mass bin (median stellar mass $logM_*/M_\odot \sim 7.7$ and 8.4 for the top and bottom panels, respectively). The vertical lines mark the lookback time in the median SFH reference system. Both samples present a 1 dex stellar mass growth within the 2 Gyr prior their observation, which would suggest a recent stellar mass assembly for these low-mass star-forming systems.

The average SFH found by Atek et al. (2014, , their Figure 5) applying our approach to a sample of intermediate redshift emission line selected galaxies, clearly presents a burst (SFR sudden increase) at the time the galaxies are observed. On the contrary, we do not find such feature. This is probably due to the fact that we average more plural properties of the galaxies included in our sample. As Atek et al. (2014) points out, high-resolution simulations of dwarf galaxies (e.g., Shen et al., 2013) favor extended SFHs governed by stochastic SF processes with timescales of ∼10–100 Myr. These SF processes are thought to move temporally the galaxies outside the MS. Nevertheless, our approach does not allow to constrain past burst, and tend to smooth the SFHs of these galaxies. This could be the reason we obtain these average SFHs along the MS.

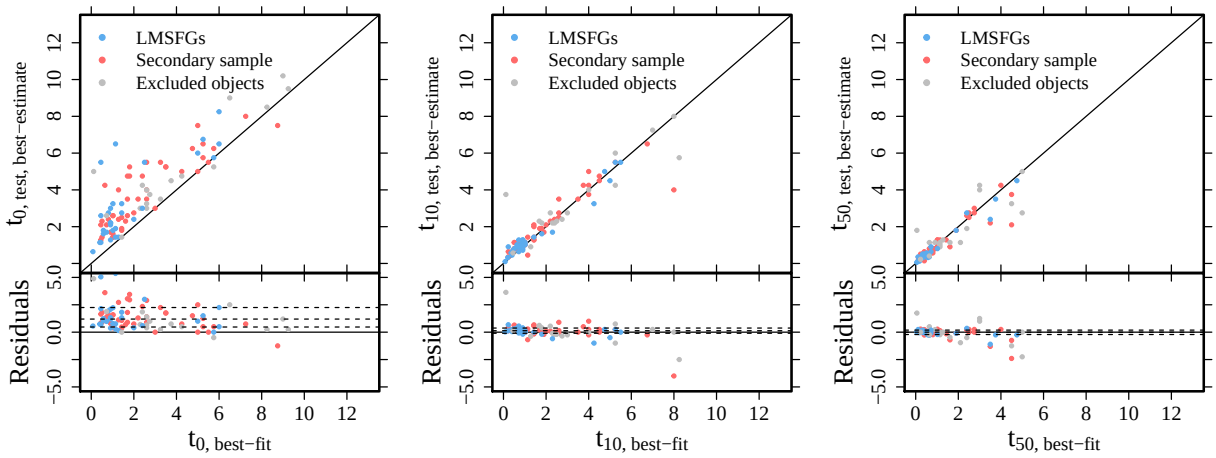

Figure 8.13: Comparison between t_0, t_{10}, and t_{50} of the best-fitting models ($t_{\mathrm{X,best-fit}}$) and those corresponding to the best-estimate model obtained for the synthetic galaxies ($t_{\mathrm{X,test,best-estimate}}$).The LMSFGs and the secondary sample are represented with blue and red points respectively. The gray points show the galaxies outside the final redshift range considered.

8.3 Reliability Test

Considering that the SFHs present in the libraries are adequate and representative of the galaxy population, a question remains whether, and how well, SFHs can be reconstructed from the observations, even when averaging over the ensemble. This is of special importance in our case, as given that the majority of the galaxies in the observed samples are characterized by a high sSFR, the most recent burst of SF can outshine the older stellar populations (especially at ultraviolet and optical rest-frame wavelengths). This would inevitably make our galaxies look younger. To avoid such effect we try to better constrain the emission by more evolved stars (older than $\sim$2 Gyr) we include photometry at larger wavelengths. Furthermore, to evaluate our ability to reconstruct the SFHs given our data and library of SF and metal enrichment histories, we perform the following test. Using the same procedure described in Section 3, we fit the synthetic photometry of the best-fitting model of each of our targets assuming the same photometric uncertainties as in the data and excluding such model from the library. In other words, we apply our methodology to synthetic galaxies for which we previously know the values of t_0, t_{10}, and t_{50}. As we can see in Figure 8.13, the retrieved t_{10} and t_{50} present in general good agreement with the real values for any timescale with median deviations in Gyr (16 th and 84 th percentiles) of 0.2 (-0.1, 0.4), and 0.0 (-0.2, 0.2) respectively. Actually, our methodology tends to overestimate t_0 by 1.2 (0.5, 2.3) Gyr. This happens because the derived SFHs can include masses that could have been formed at early stages without leaving any trace in the photometry.

The power of this approach relies on the fact that the fit is not a mere scaling of the templates to the observed magnitudes, but it is a conversion of different observables (4.000Åbreak [D4000] for the age, NIR photometry for the mass, emission lines and colors for the sSFR) into physical parameters that have to be fully consistent. The key factor is that we have such a variety of SFHs that an average will take into account the hidden populations.

9

Conclusions and Future Work

In this section we describe the main conclusions of our work and the future perspectives for our study of dwarf galaxies at intermediate redshift.

9.1 Conclusions

The global objective of this *Thesis* has been shedding light on the formation and evolution of dwarf galaxies by (1) studying the SFHs (Rodríguez-Muñoz et al., 2015) and (2) analyzing the physical properties (e.g. stellar mass, SFR, metallicities, excitation, extinction; Rodríguez-Muñoz et al. in prep) of a sample of star-forming low-mass galaxies spread out over a wide range of intermediate redshifts. Now, we summarize the main conclusions achieved in this work:

- The criterion based on stellar mass ($\log M_*/M_\odot < 8$) applied at intermediate redshifts selects mainly galaxies that generally match the rest-frame B band absolute magnitude, and rest-frame $B-V$ color criteria of BCDs. The main difference between both low-mass and BCDs initial samples is that the former gathers galaxies in a wider range of surface brightness, including those characteristic of the later. The impact of our selection criteria is clear along the whole work. Compact galaxies normally exhibit more extreme properties: higher SFR and sSFR, what is normally interpreted as the consequence of the starburst they undergo. Therefore, using a mass selection criterion, presumably, we are able to include among our targets galaxies with a wider range of evolutionary stages. This is of key importance because in these heterogeneous samples we can find hypothetical evolutionary links between populations.

- Regarding the ancillary data, we conclude that the optimization of the photometry is very important in order to obtain reliable physical parameters through the analysis of the SEDs of low-mass galaxies. The photometry of low-mass and therefore low-luminosity galaxies in surveys such as MUSYC and CANDELS needs to be remeasured, as they are obtained normally using settings more adequate for the general galaxy population. Summarizing, apertures need to be narrowed to get less noisy SEDs.

- The comparison between photometric redshifts and spectroscopic redshifts shows the importance of obtaining the later for a correct determination of the physical properties of our targets. Given their blue colors, their characteristic flat continuum can hamper a correct

determination of their photometric redshifts. The latest improved photometric redshifts derived by the 3D-HST team (Skelton et al., 2014) appear to match perfectly our spectroscopic redshift measurements. This implies that our approach could now be applied extensively to the numerous samples of dwarfs observed by large surveys.

- We do not find clear candidates for AGNs in our sample using any of the diagnostic diagrams. Then, we conclude that the source of the emission lines of our galaxies is dominated by SF processes. This is in agreement with previous works that claim that the AGN contamination in dwarfs is rare (Izotov and Thuan, 2008).

- The estimated SFRs and stellar masses of the galaxies in our final sample are consistent with the star forming MS over 2 dex in stellar mass, and results from other studies, such as Atek et al. (2014) in the redshift range between 0.3 and 0.7. Due to the differences between the definitions of the MS in the literature and the dispersion of our values, it is not clear which is the MS that best fits our data points. We think that the mentioned dispersion is a consequence of our mass selection criteria, that includes in the sample galaxies that belong to the MS and a fraction of galaxies with a SF anomaly, either starbursts or SF deficient systems.

- The galaxies in our sample for which we are able to measure emission lines with a level of significance over 3σ, populate the area of the Excitation-Mass diagram corresponding to high excited ISM, reaching values similar to high redshift galaxies such as Lyα emitters. Furthermore, they present low metallicities in the range $\sim$1-1/34 $Z_{\odot}$. These results are in agreement with the general idea that dwarf star-forming galaxies resemble the galactic population in the primitive universe.

- The expected SFH of dwarf galaxies is dominated by stochastic processes. Therefore, initially, it can barely be reproduced by simplified functions. However, although we clearly see that most frequent SFHs in our sample are not consistent on average with typical τ-models, they appear to be represented on average by a delayed decreasing exponential such as $t^2e^{-t/\tau}$ with a large value of τ. The median SFH of our sample of LMSFGs suggests that 90% of the stellar mass observed is formed in a 0.5–1.8 Gyr ($t_{10,\mathrm{SFH-P16}}$–$t_{10,\mathrm{SFH-P84}}$) period prior the observation. Our results reinforce the idea of a recent stellar-mass formation for LMSFGs at intermediate redshifts. They are consistent with the previous work about SFHs of star forming galaxies carried out by e.g., Leitner (2012) and with the downsizing cosmological frame (Cowie et al., 1996).

9.2 Future Work

The motivations for pursuing the study of dwarfs are as numerous as the questions regarding their properties and evolution along cosmological time that still nowadays remain unanswered. Do dwarfs follow the scale relations defined by giant galaxies (e.g., Whitaker et al. 2014)? What is the importance of their role in cosmic evolution (e.g., Bouwens et al. 2012b)? When and how do they assemble their stellar mass (e.g., Atek et al. 2014)? The answers to all these questions are crucial for our understanding of the Universe, and key tests for cosmological simulations.

The next and most immediate steps to be taken in order to deepen our knowledge on this type of galaxies would be the following:

1. To complete the available data for each of the galaxies already studied. In particular, given more than half of the galaxies in our sample are located beyond $z \sim 0.5$, we would be extremely interested in NIR spectroscopy to measure Hα and [NII]6584 emission lines. Such emission lines enable breaking the degeneracy of the $R23$ method, and therefore derive unambiguously gas metallicities. Hα fluxes would also allow us to better estimate star formation rates (SFRs) and dust extinctions. With the objective of better characterizing the current star formation process the galaxies in our sample undergo (i.e. their younger SPs), solving degeneracies, and better constrain their SFHs, we have sent proposals to perform spectroscopy with KMOS (K-band Multi-Object Spectrograph) at the VLT. We would also be interested in the kinematics of these galaxies to better understand their nature. This is something we could only acquire through higher resolution spectroscopy.

2. To enlarge the sample of dwarfs always preserving our strategy of selecting samples by intrinsic parameters and features that are not determined by specific extreme evolutionary stages. In this sense, we intend to carry out future mass-limited samples selections in deep IR images.

3. To extend our approach to other fields. In fact, we have already carried out two spectroscopic campaigns with OSIRIS at the GTC (127-GTC54/13A, 164-GTC78/14B; Chapter 3) on GOODS-N and UDS. Our plan is to apply to the data obtained a similar approach to that explained along this work.

4. To push back our upper redshift limit to $z \sim 3 - 4$. This is allowed by the ultra-deep and extended coverage of recent imaging surveys, which provide improved photometric redshifts and physical properties for an extraordinarily numerous sample of galaxies all the way to the early universe. CANDELS (Grogin et al., 2011; Koekemoer et al., 2011), Hawk-I UDS and GOODS Survey (HUGS; Fontana et al., 2014), GOODS Re-ionization Era wide-Area Treasury from *Spitzer* project (GREATS; Labbe et al., 2014), *Spitzer* Large Area Survey with Hyper-Suprime-Cam (SPLASH; Takada, 2010), for instance, are or will be able to reach thousands of dwarf galaxies up to $z \sim 4$.

5. To perform an environmental study of the low-mass star-forming galaxies, to better understand the nature of their star-formation process.

6. To study the gas content of these low-mass systems with the high resolution achievable by Atacama Large Millimeter/submillimeter Array (ALMA). Furthermore, high spatial resolution spectroscopic observations would be useful to identify the hypothetical gas accretion of these galaxies by means of radial gas-phase metallicity profiles.

9.2.1 A Scientific Case for Future Generation Spectrographs

The study of dwarf star-forming galaxies is one of the key motivations for future astronomical facilities generation (e.g. European Extremely Large Telescope, E-ELT). Large photometric surveys have revealed a large population of this type of galaxies up to redshift 4 awaiting to be explored. For instance, the photometric catalogs published by 3D-HST (Skelton et al., 2014) include $\sim$20.000 galaxies with stellar mass $7<\log M_*/M_\odot<9.5$, $J<29$ AB mag, at $z<2$ in GOODS-S. Within this framework, and during the last few years, we have designed scientific cases to exploit the capabilities for the observation of dwarf galaxies of the future generation optical and near-infrared

spectrographs for the 10.4-m GTC (Gran Telescopio Canarias), MEGARA[1] (Multi-Espectrógrafo en GTC de Alta Resolución para Astronomía; PI: A. Gil de Paz), MIRADAS[2] (Mid-resolution InfRAreD Astronomical Spectrograph; PI: S. Eikenberry) respectively, and EMIR[3] (PI: F. Garzón).

In particular, MEGARA and MIRADAS working on GTC will allow the structural and kinematical analysis of numerous samples of dwarfs at intermediate redshifts ($0.5<z\lesssim1.3$), tracing their evolution along cosmological timescales. Their mutiplexing and high spectral resolution are ideal for this scientific case. Apart from spectroscopic redshifts and measurements of emission lines such as [OII]λ3727, Hβ, [OIII]$\lambda\lambda$4959, 5007, MEGARA and MIRADAS spectroscopic data will provide average properties from full-spectrum fitting and spectral indexes (stacked per redshift bins) tightly related to the ages of their underlying stellar populations. This analysis will be crucial for our better understanding of the main processes involved in galaxy assembly and will provide valuable constraints to models of galaxy formation and evolution. The main goals of this scientific case would be to exploit the high spectral resolution and high multiplexing to measure the emission line widths (at least for [OII]λ3727 or Hα, depending on the redshift and the wavelength range available) of a representative sample of low-mass galaxies and BCDs at different redshifts to study the evolution of their kinematics. Line widths will allow us to estimate velocity dispersions and dynamical masses and/or winds/turbulence of the systems. This analysis will be complementary to those massive surveys as ALHAMBRA (Moles et al., 2008) using medium band filters to obtain SEDs and high quality photometric redshifts for the overall population of galaxies up to $z\sim1$.

As another example of the future projection of dwarf galaxies observations, we can also mention GOYA[4] project, a near-IR spectroscopic survey to be carried out with the wide-field multi-object spectrograph EMIR at the GTC. GOYA has been granted with 30 guaranteed nights to observe $\sim$2.500 galaxies in the intermediate-high redshift universe with the aim of "characterize the star-forming galaxies at the epoch of maximum SFR activity ($1< z <5.5$)".

Finally, we have also contributed to the design of a scientific case for the study of low-mass/faint systems using the future E-ELT spectrograph MOSAIC[5] (Multi-Object Spectrograph for Astrophysics, IGM and Cosmology; Evans et al., 2015).

[1] http://guaix.fis.ucm.es/megara
[2] http://www.astro.ufl.edu/miradas/
[3] http://guaix.fis.ucm.es/emir/
[4] http://www.astro.ufl.edu/GOYA/home.html
[5] http://mosaic.obspm.fr/

A

SED-fitting. Additional Material

In this Appendix we show some additional information regarding the SED-fitting approach we follow:

- The distribution of t_0, t_{10}, and t_{50} (Figure A.1, Figure A.2, Figure A.3) of the library of models used in the SED-fitting (Chapter 5). In particular, we show the distribution for subsample of 5000 models randomly extracted from the library.
- Photometry residuals obtained as $(\mathrm{phot}_{\mathrm{obs}} - \mathrm{phot}_{\mathrm{synth}})/\Delta\mathrm{phot}_{\mathrm{obs}}$, where $\mathrm{phot}_{\mathrm{obs}}$ and $\Delta\mathrm{phot}_{\mathrm{obs}}$ are the observational photometric data and uncertainties, respectively, and $\mathrm{phot}_{\mathrm{synth}}$ is the synthetic photometry obtained using the spectral templates and the filters transmission curves. Figure A.4.
- Models χ^2 distributions for each target in our sample (Figure A.5, Figure A.6, Figure A.7, Figure A.8, and Figure A.9). In each plot we show the number of photometric bands (red text) and emission lines EWs (blue text) fitted. There are 7 galaxies for which no emission lines was fitted. In these cases the emission lines were identified in the 2D spectra but they were too affected by sky emissions to be measured. For most of them, the redshift flag is 2 (see Chapter 4).

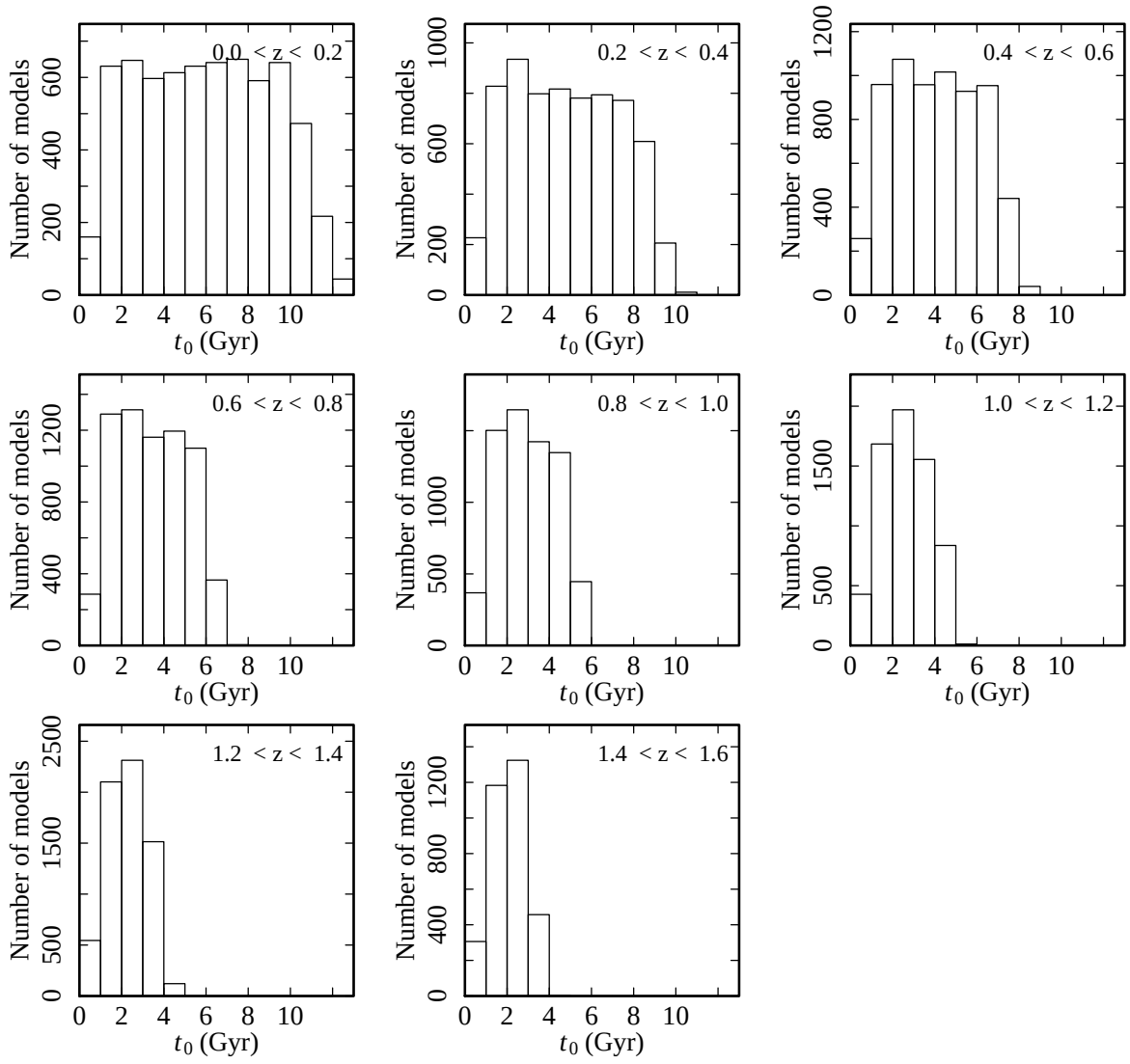

Figure A.1: Distribution of t_0 for a subsample of 5000 random models extracted from the new library of SF and enrichment histories. The distribution is approximately uniform for each redshift bin.

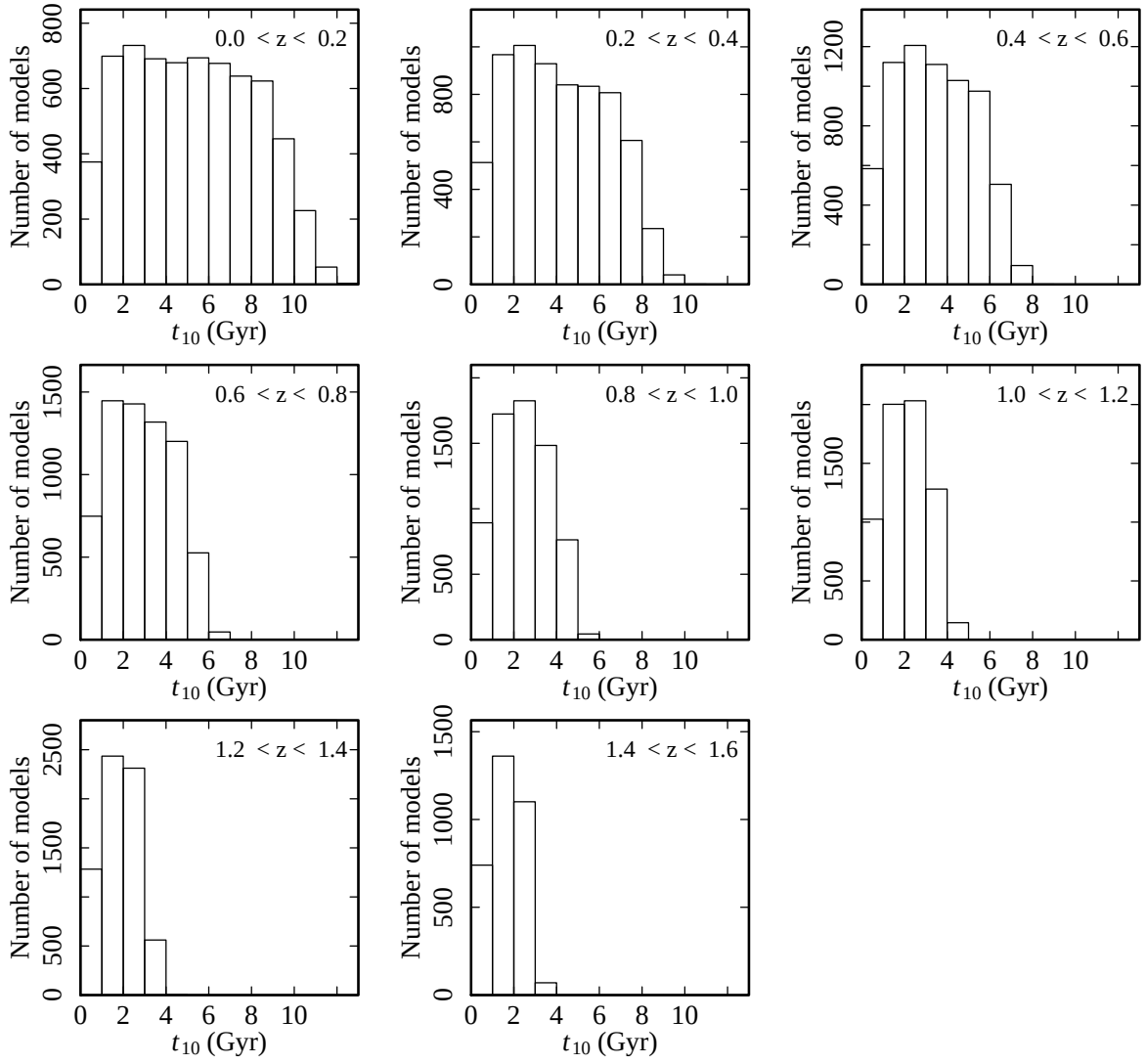

Figure A.2: Distribution of t_{10} for a subsample of 5000 random models extracted from the new library of SF and enrichment histories. The distribution is approximately uniform for each redshift bin.

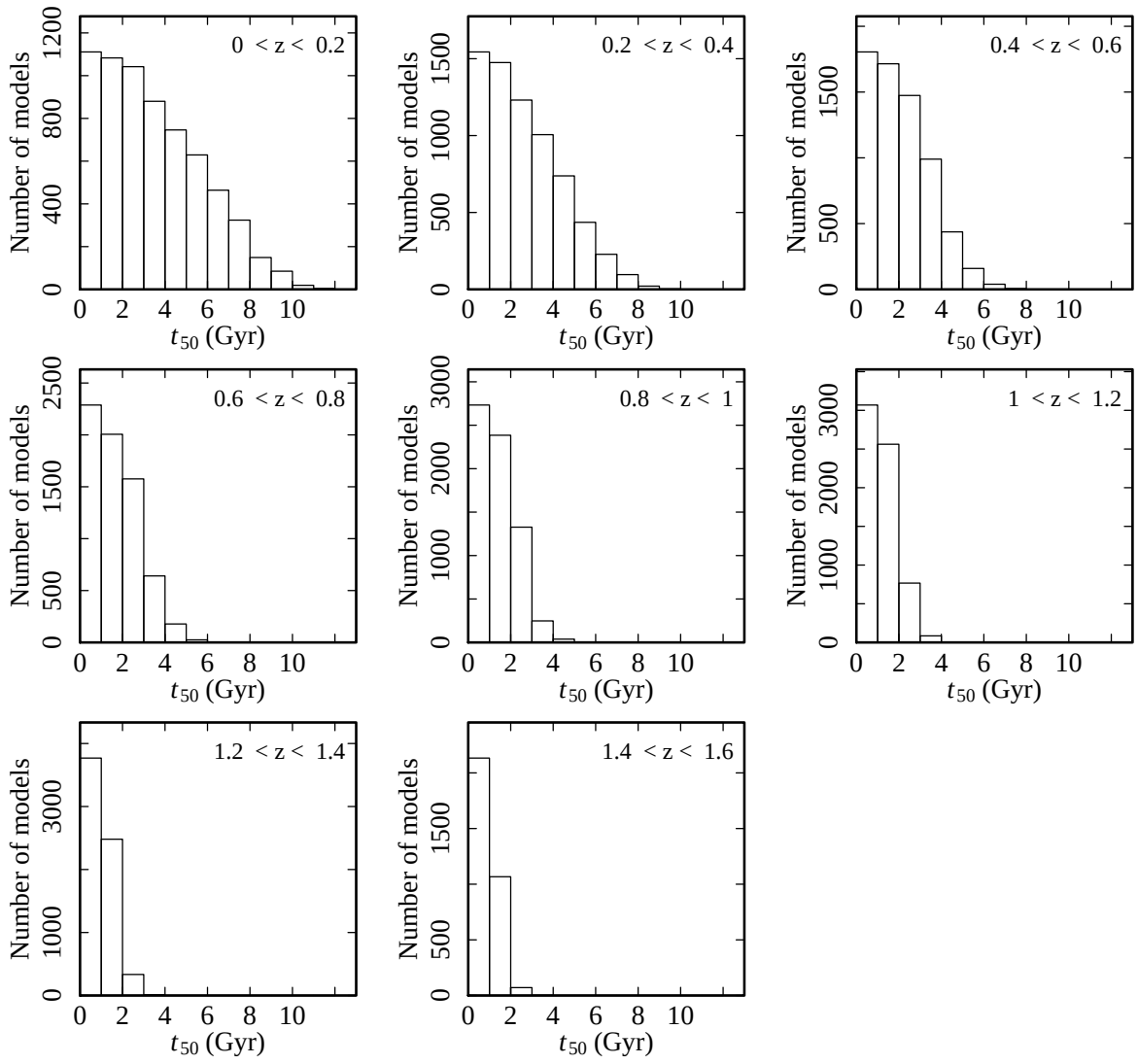

Figure A.3: Distribution of t_0 for a subsample of 5000 random models extracted from the new library of SF and enrichment histories. The distribution is approximately uniform for each redshift bin.

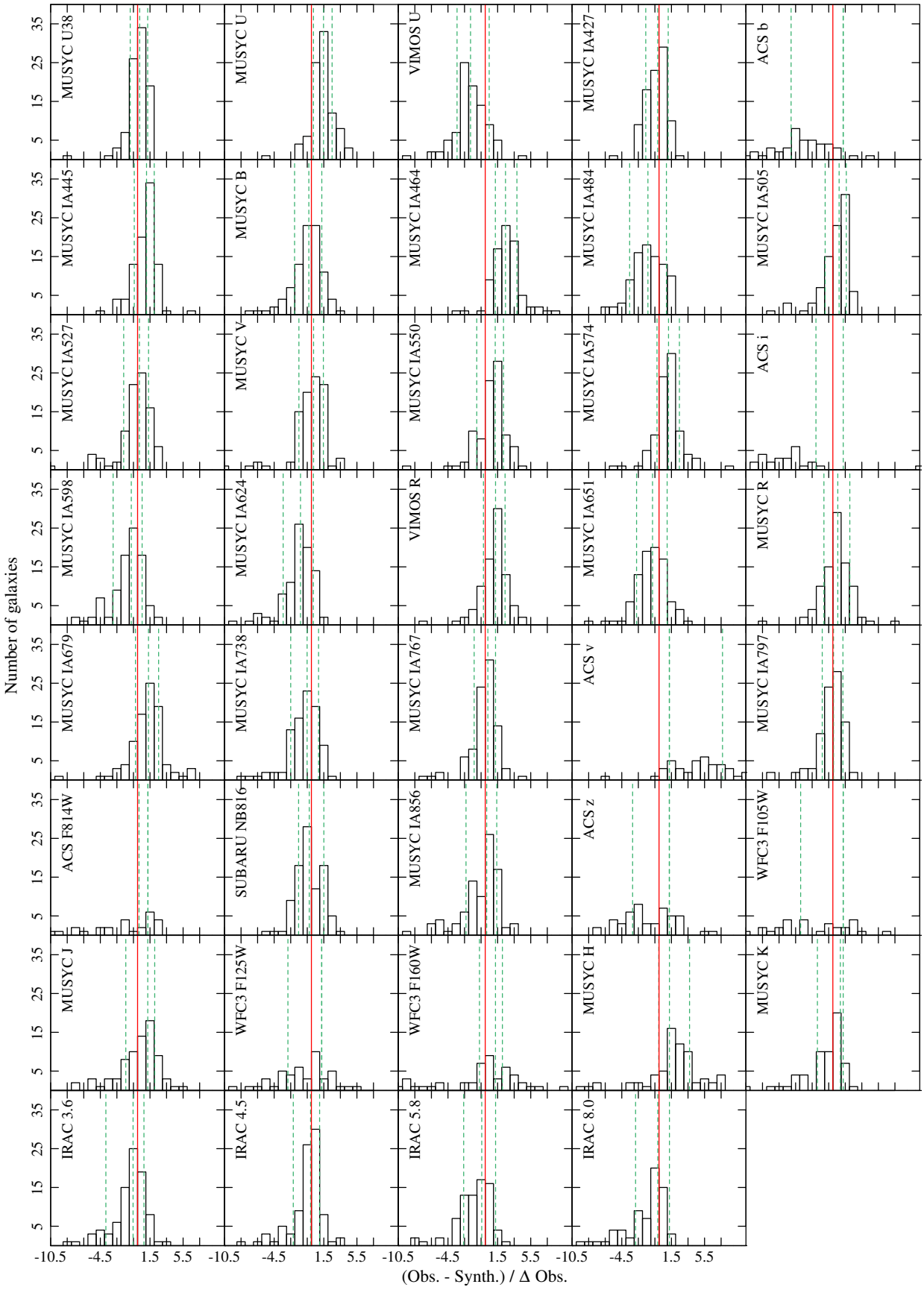

Figure A.4: Each histogram shows the residuals of the photometry for each of the bands. Red vertical lines mark where the zero is. Green dashed lines show for each band the median, and percentiles.

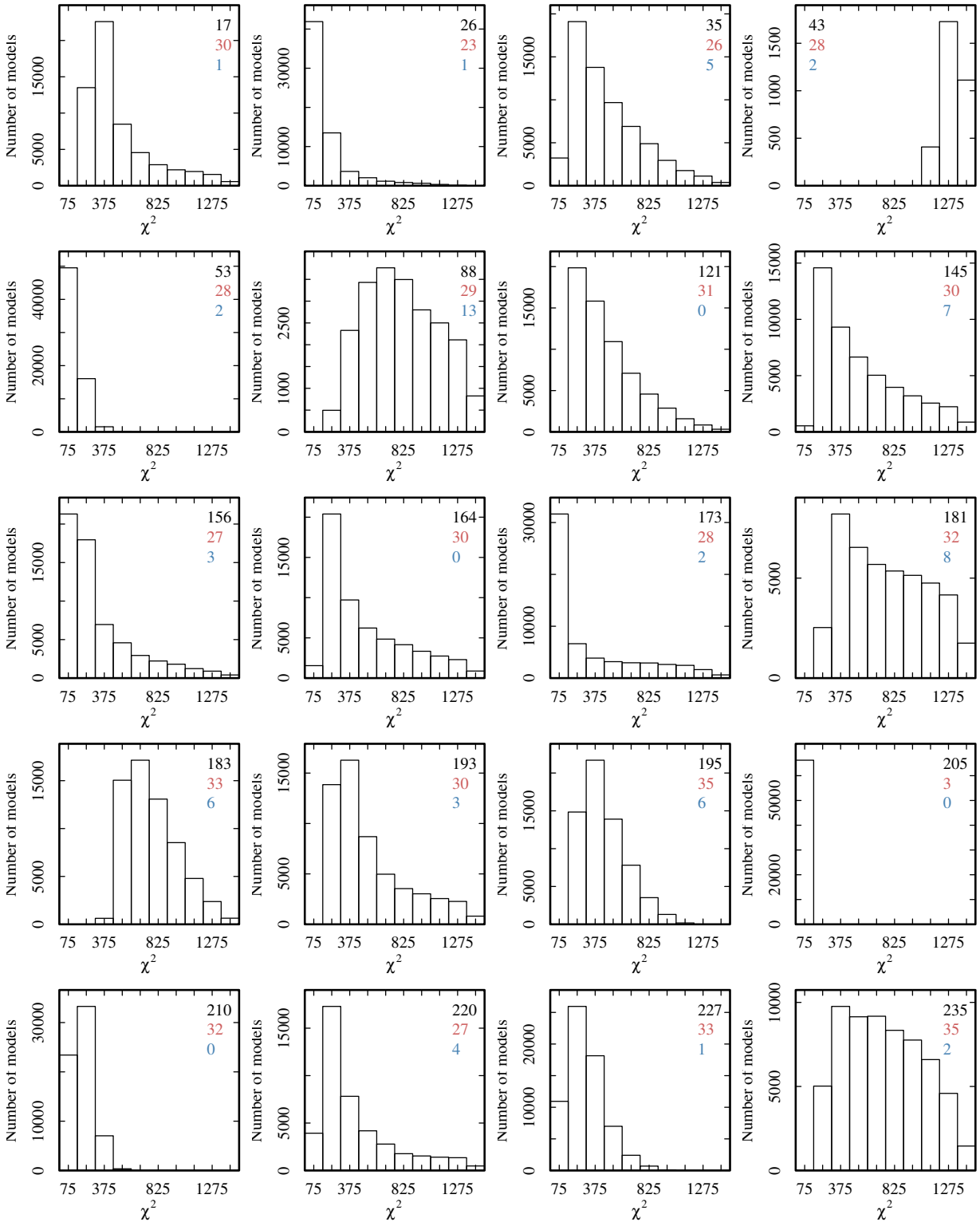

Figure A.5: For each galaxy (the ID is shown in black text) we show the χ^2 that contribute to the probability density functions (i.e. those for which a probability larger than 0 is obtained). We also report the number of bands (red text) and lines (blue text) fitted in each case.

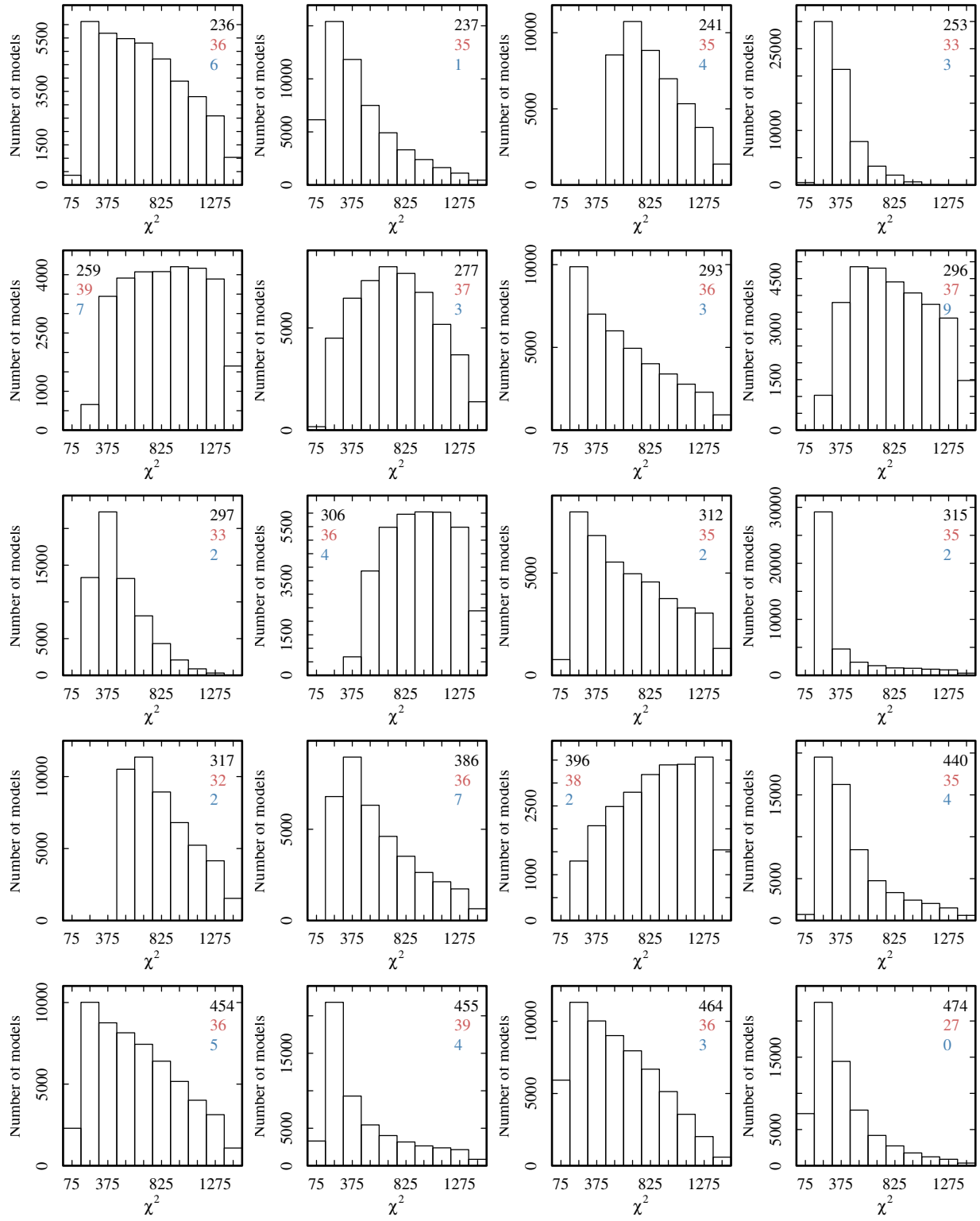

Figure A.6: For each galaxy (the ID is shown in black text) we show the χ^2 that contribute to the probability density functions (i.e. those for which a probability larger than 0 is obtained). We also report the number of bands (red text) and lines (blue text) fitted in each case.

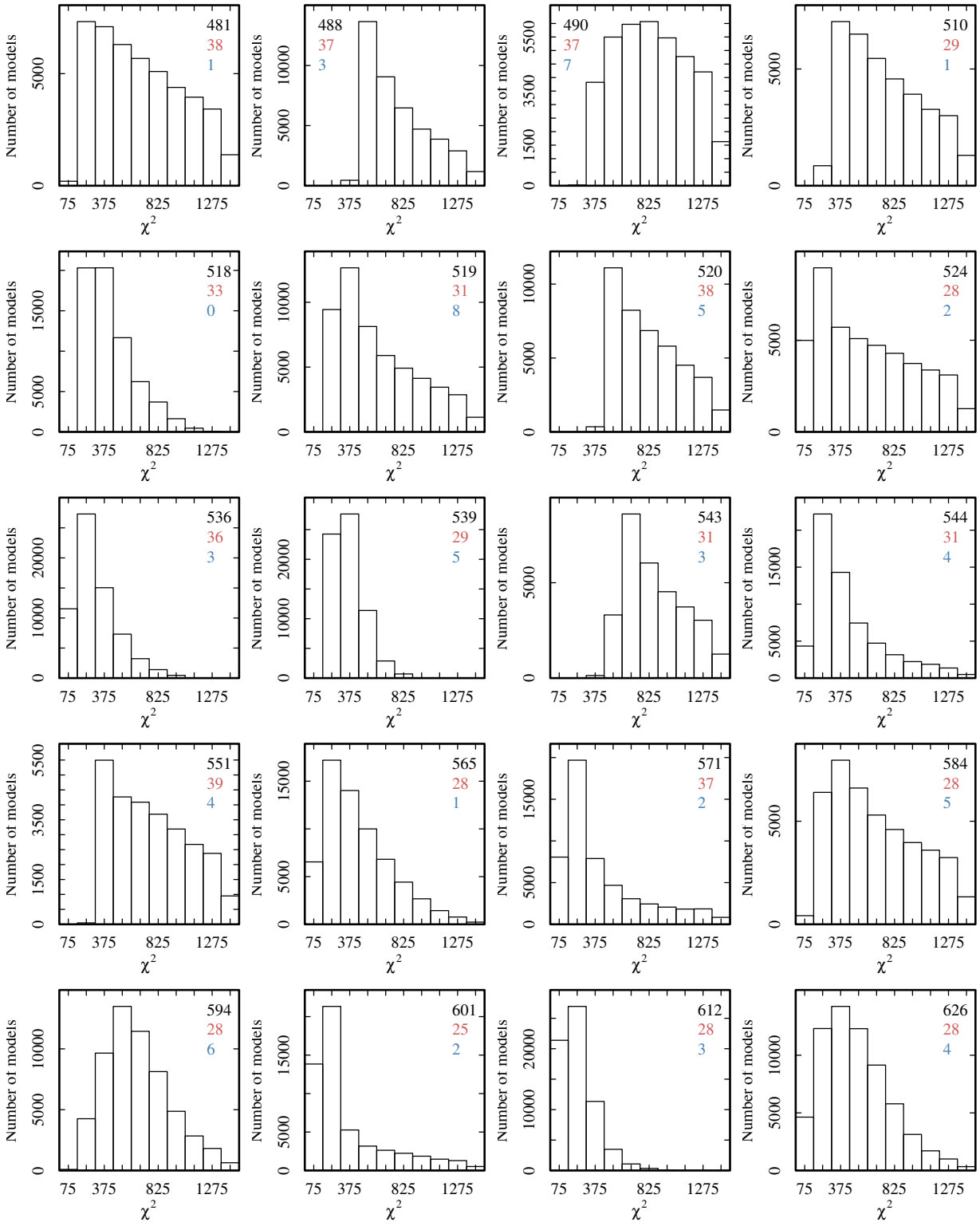

Figure A.7: For each galaxy (the ID is shown in black text) we show the χ^2 that contribute to the probability density functions (i.e. those for which a probability larger than 0 is obtained). We also report the number of bands (red text) and lines (blue text) fitted in each case.

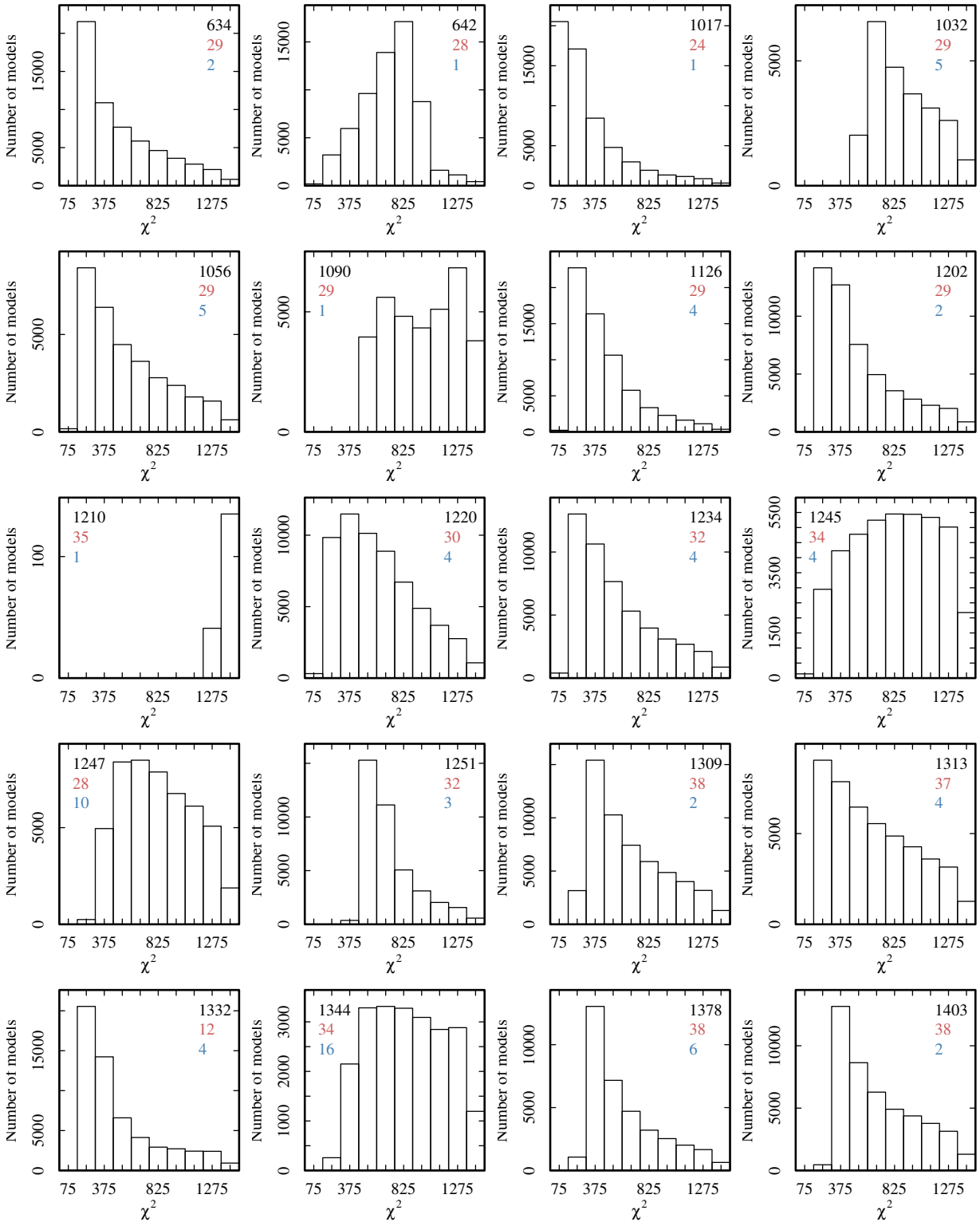

Figure A.8: For each galaxy (the ID is shown in black text) we show the χ^2 that contribute to the probability density functions (i.e. those for which a probability larger than 0 is obtained). We also report the number of bands (red text) and lines (blue text) fitted in each case.

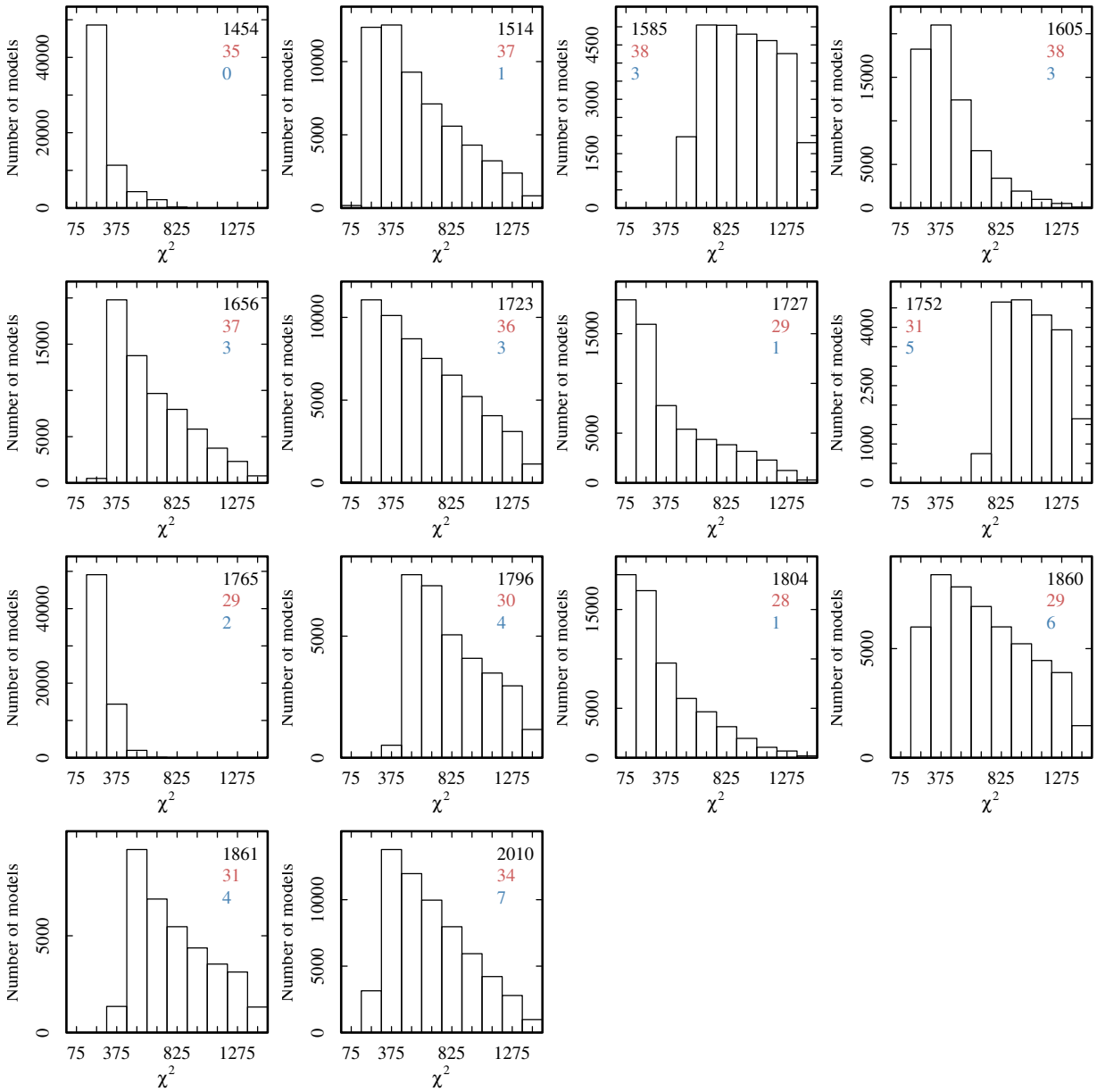

Figure A.9: For each galaxy (the ID is shown in black text) we show the χ^2 that contribute to the probability density functions (i.e. those for which a probability larger than 0 is obtained). We also report the number of bands (red text) and lines (blue text) fitted in each case.

B

Postage Stamps

In this Appendix we include a summary of the results for each of the 94 galaxies spectroscopically confirmed. Each summary contains the following information:

1. A table with the following data, including uncertainties: the ID; the right ascension (α; deg; J2000); the declination (δ; deg; J2000); apparent magnitude in i band (mag); apparent magnitude in J band (mag); spectroscopic redshift (z_{spec} / flag); morphological type (following Chapter 6 classification); Sèrsic index (n) in v-band (Griffith et al., 2012); effective radius in v-band ($R_{eff,v,0}$ Griffith et al., 2012); absolute magnitude in rest-frame B band; rest-frame B band surface brightness ($\mu_{eff,B,0}$) within the effective radius; rest-frame $(B-V)$ color; flux (F; $erg/s\,cm^{-2}$) and equivalent widths (EW; Å) of Hβ, [OII]$\lambda\lambda$3727, [OIII]λ4959, [OIII]λ5007, and Hα emission lines; physical parameters of the SED-fitting output such as stellar mass ($\log M_*/M_\odot$), SFR ($\log$ SFR$/M_\odot$ yr^{-1}), sSFR ($\log$ sSFR/Gyr^{-1}), total optical depth of the dust ($\hat{\tau}_V$), oxygen abundance (12+log(O/H)); the lookback time when the SFH first starts (t_0) and the lookback time when the galaxy forms 10% and 50% of the final stellar mass (t_{10} and t_{50}, respectively).

2. A panel showing the VIMOS spectroscopy (1D and 2D) and a postage stamp wih a ACS 5"×5" RGB image (North up and west left) for each galaxy. We use v, and z bands images for those galaxies within the GEMS area, and b, v, and z bands for those that fall in GOODS.

3. A panel showing the photometry available and used for the SED-fitting analysis. Open and filled circles are used for broad and mid/narrow bands, respectively. Yellow points represent ground based photometric values. We use pink to mark MUSYC survey photometric bands. HST and IRAC observations are shown in blue and green color, respectively. We dismiss IRAC bands that could present contamination by dust emission, and we plot them in grey color. We also show the best-fit template (grey line) and its synthetic photometry in the bands of the observational data (black crosses).

4. A row of panels with the SED-fitting resultant probability density functions for each of the parameters obtained: stellar mass ($\log M_*/M_\odot$), SFR ($\log$ SFR$/M_\odot$ yr^{-1}), sSFR ($\log$ sSFR/Gyr^{-1}), oxygen abundance (12+log(O/H)), total optical depth of the dust ($\hat{\tau}_V$). In each case, the final value and percentiles are marked with solid and dashed vertical lines respectively. This vertical line is blue for those galaxies with $\log M_*/M_\odot < 8$, and red for those galaxies with $\log M_*/M_\odot > 8$.

5. A row of three panels with the variation of the SFR, the sSFR, and the fraction of the final stellar mass with the lookback time. For each lookback time step, we show the median, and

16th and 84th percentiles with solid and dashed lines, respectively. In the three panels we mark the position of t_0, t_{10}, and t_{50} using vertical lines. Again, we use blue color for those galaxies with $\log M_*/M_\odot < 8$, and red for those galaxies with $\log M_*/M_\odot > 8$.

Summary ID 00017

ID	00017	$\mu_{eff,B,0}$	33.9±5.0	F Hα ($\times10^{17}$)	–
α (deg; J2000)	52.941199	$(B-V)_0$	0.41	EW Hα	–
δ (deg; J2000)	-27.925098	F Hβ ($\times10^{17}$)	–	log $M_*/M_\odot$	$8.8^{8.8}_{8.8}$
i (mag)	24.80±0.11	EW Hβ	–	log SFR$/M_\odot\,yr^{-1}$	$-0.3^{-0.2}_{-0.4}$
J (mag)	24.44±0.42	F [OII]$\lambda\lambda$3727 ($\times10^{17}$)	$0.3^{0.5}_{0.1}$	log sSFR$/Gyr^{-1}$	$-0.1^{-0.1}_{-0.2}$
z_{spec}	0.642/2	EW [OII]$\lambda\lambda$3727	$13.8^{28.6}_{5.7}$	$\hat{\tau}_V$	$0.3^{0.3}_{0.2}$
Morph.	Irr	F [OIII]λ4959 ($\times10^{17}$)	$0.3^{0.5}_{0.1}$	12+log(O/H)	$7.4^{7.4}_{7.1}$
n	0.9±0.1	EW [OIII]λ4959	$13.8^{28.6}_{5.7}$	t_0 (Gyr)	6.8
$R_{eff,v,0}$	4.0±0.2	F [OIII]λ5007 ($\times10^{17}$)	$0.3^{0.5}_{0.1}$	t_{10} (Gyr)	4.8
$M_{B,0}$	-16.97	EW [OIII]λ5007	$13.8^{28.6}_{5.7}$	t_{50} (Gyr)	3.0

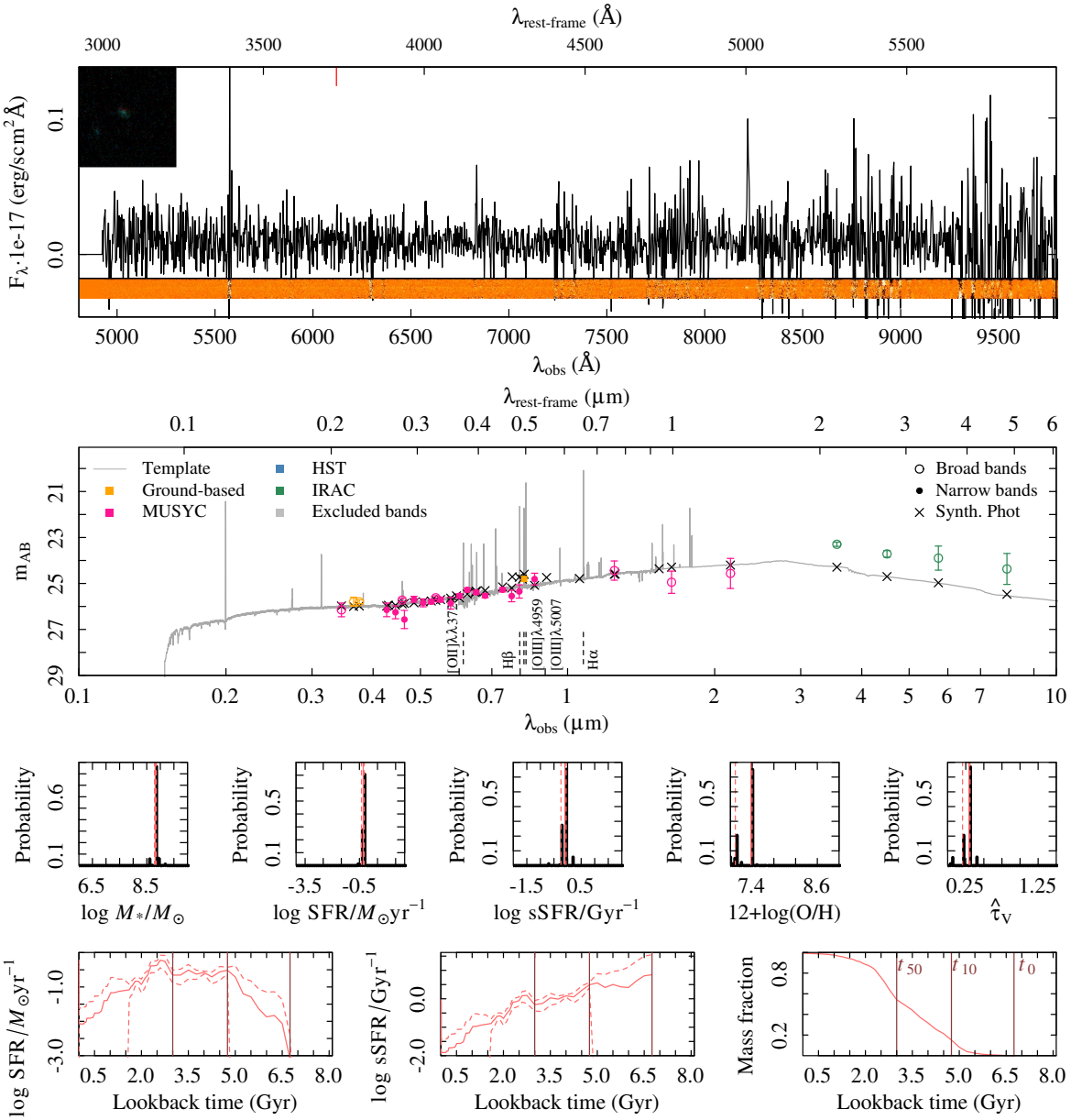

Summary ID 00026

ID	00026	$\mu_{eff,B,0}$	23.5±1.1	F Hα ($\times10^{17}$)	–
α (deg; J2000)	52.945469	$(B-V)_0$	0.67	EW Hα	–
δ (deg; J2000)	-27.917446	F Hβ ($\times10^{17}$)	–	log $M_*/M_\odot$	$7.9^{8.1}_{7.8}$
i (mag)	25.04±0.15	EW Hβ	–	log SFR/$M_\odot\,yr^{-1}$	$-0.9^{-0.6}_{-1.3}$
J (mag)	-99.99±-99.99	F [OII]$\lambda\lambda$3727 ($\times10^{17}$)	$0.3^{0.3}_{0.2}$	log sSFR/Gyr^{-1}	$0.1^{0.6}_{-0.3}$
z_{spec}	0.517/3	EW [OII]$\lambda\lambda$3727	$32.4^{44.7}_{24.0}$	$\hat{\tau}_V$	$0.4^{0.8}_{0.1}$
Morph.	Irr	F [OIII]λ4959 ($\times10^{17}$)	$0.3^{0.3}_{0.2}$	12+log(O/H)	$8.0^{8.3}_{7.7}$
n	0.7±0.1	EW [OIII]λ4959	$32.4^{44.7}_{24.0}$	t_0 (Gyr)	1.7
$R_{eff,v,0}$	1.2±0.0	F [OIII]λ5007 ($\times10^{17}$)	$0.3^{0.3}_{0.2}$	t_{10} (Gyr)	0.8
$M_{B,0}$	-16.31	EW [OIII]λ5007	$32.4^{44.7}_{24.0}$	t_{50} (Gyr)	0.3

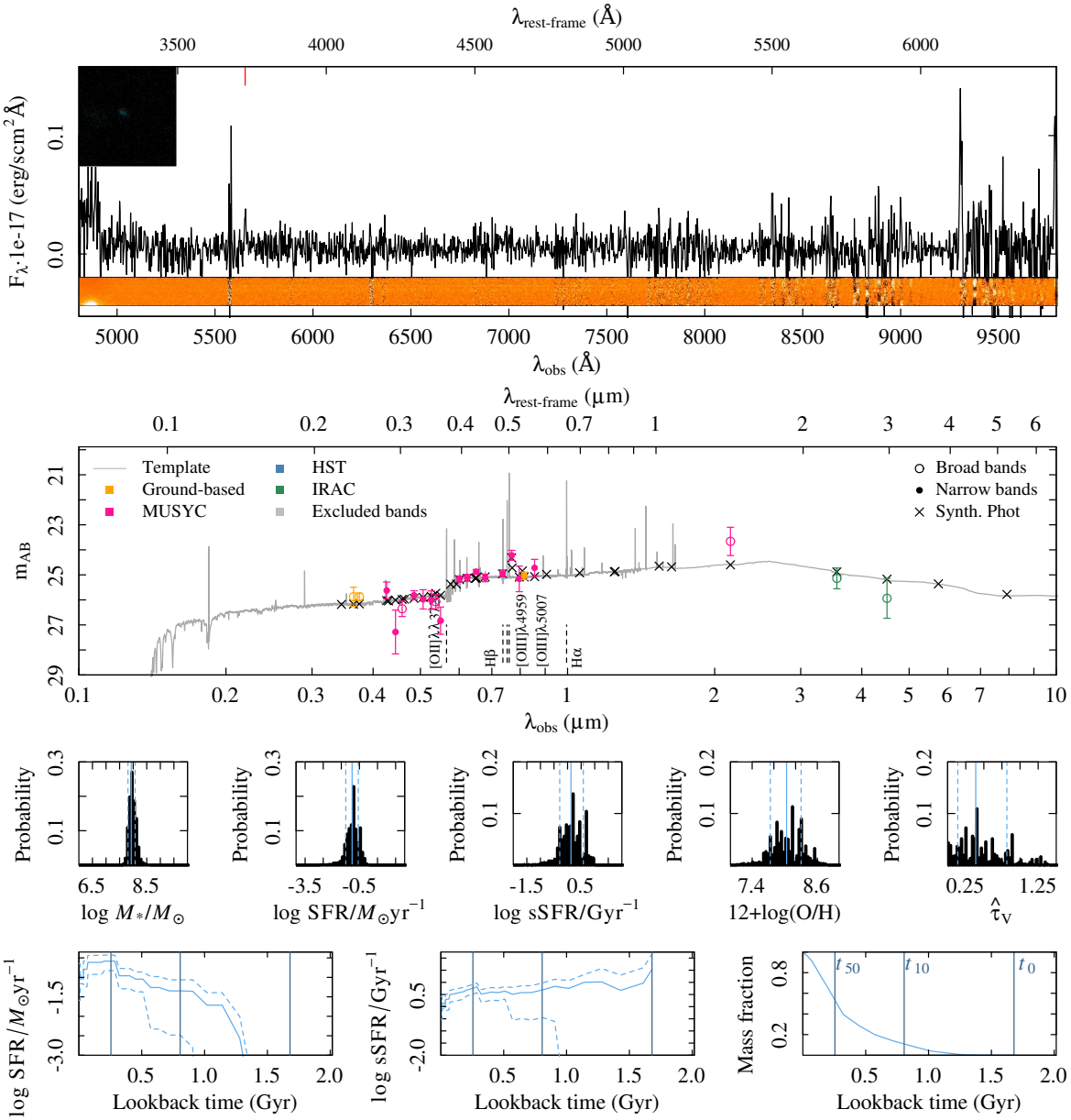

Summary ID 00035

ID	00035	$\mu_{eff,B,0}$	22.8±0.5	F Hα ($\times 10^{17}$)	–
α (deg; J2000)	52.948144	$(B-V)_0$	0.63	EW Hα	–
δ (deg; J2000)	-27.940153	F Hβ ($\times 10^{17}$)	$1.1^{1.3}_{0.8}$	log $M_*/M_\odot$	$8.3^{8.5}_{8.3}$
i (mag)	24.04±0.10	EW Hβ	$26.3^{37.6}_{18.0}$	log SFR/$M_\odot\, yr^{-1}$	$-0.2^{0.2}_{-0.3}$
J (mag)	23.83±0.30	F [OII]$\lambda\lambda$3727 ($\times 10^{17}$)	$1.9^{2.1}_{1.6}$	log sSFR/Gyr^{-1}	$0.4^{0.8}_{0.4}$
z_{spec}	0.656/4	EW [OII]$\lambda\lambda$3727	$50.5^{70.5}_{37.4}$	$\hat{\tau}_V$	$0.5^{0.8}_{0.5}$
Morph.	Irr	F [OIII]λ4959 ($\times 10^{17}$)	$1.9^{2.1}_{1.6}$	12+log(O/H)	$8.1^{8.4}_{7.6}$
n	0.5±0.0	EW [OIII]λ4959	$50.5^{70.5}_{37.4}$	t_0 (Gyr)	3.8
$R_{eff,v,0}$	3.3±0.1	F [OIII]λ5007 ($\times 10^{17}$)	$1.9^{2.1}_{1.6}$	t_{10} (Gyr)	1.0
$M_{B,0}$	-17.60	EW [OIII]λ5007	$50.5^{70.5}_{37.4}$	t_{50} (Gyr)	0.4

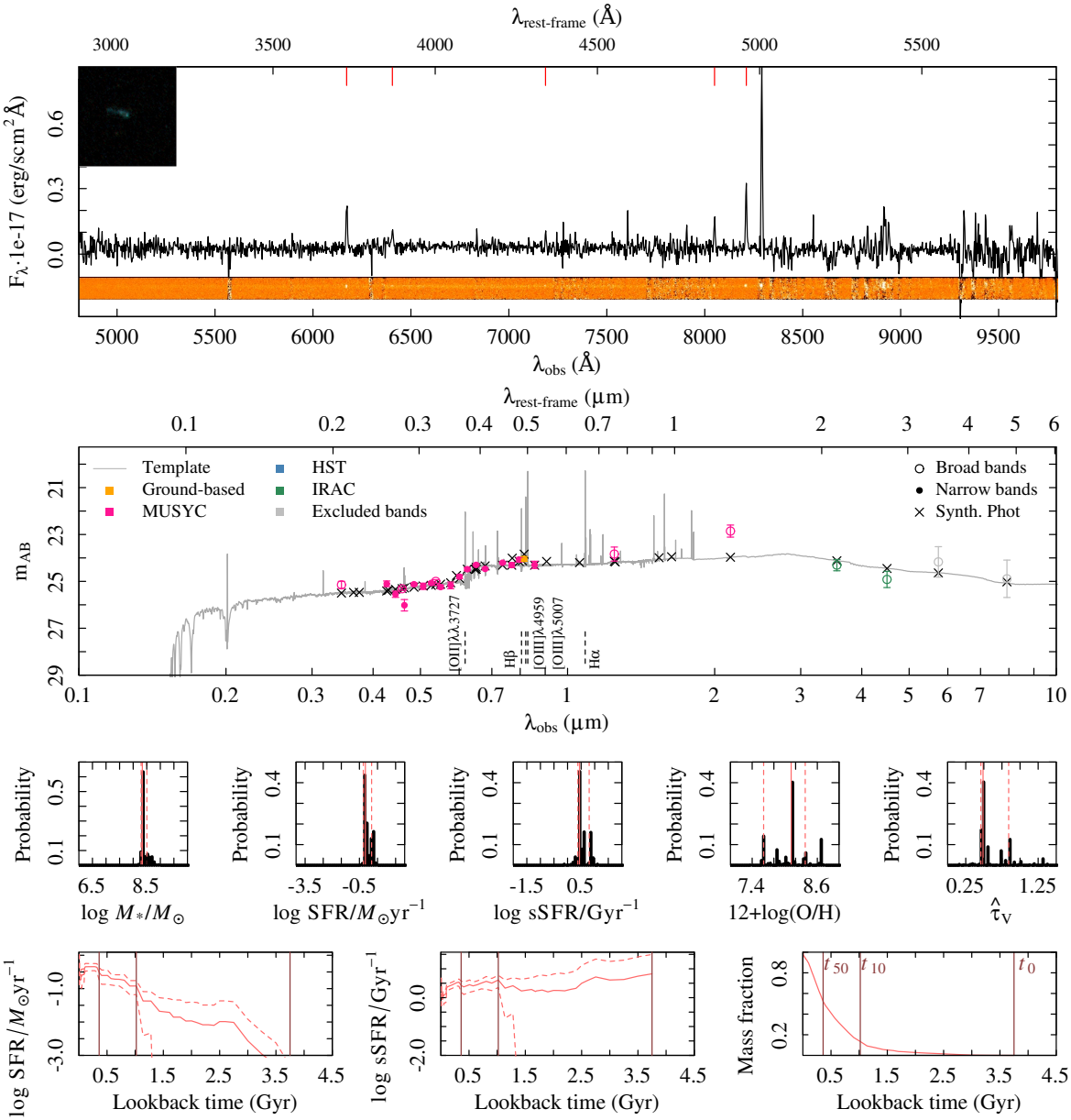

Summary ID 00043

ID	00043	$\mu_{eff,B,0}$	33.0±5.0	F Hα ($\times 10^{17}$)	–
α (deg; J2000)	52.951647	$(B-V)_0$	0.07	EW Hα	–
δ (deg; J2000)	-27.752975	F Hβ ($\times 10^{17}$)	–	log $M_*/M_\odot$	NA^{NA}_{NA}
i (mag)	24.24±0.10	EW Hβ	–	log SFR/$M_\odot\, yr^{-1}$	NA^{NA}_{NA}
J (mag)	23.91±0.18	F [OII]$\lambda\lambda$3727 ($\times 10^{17}$)	$0.7^{0.9}_{0.6}$	log sSFR/Gyr^{-1}	NA^{NA}_{NA}
z_{spec}	0.658/3	EW [OII]$\lambda\lambda$3727	$25.8^{34.9}_{18.8}$	$\hat{\tau}_V$	NA^{NA}_{NA}
Morph.	Irr	F [OIII]λ4959 ($\times 10^{17}$)	$0.7^{0.9}_{0.6}$	12+log(O/H)	NA^{NA}_{NA}
n	0.3±0.0	EW [OIII]λ4959	$25.8^{34.9}_{18.8}$	t_0 (Gyr)	7.2
$R_{eff,v,0}$	NA±NA	F [OIII]λ5007 ($\times 10^{17}$)	$0.7^{0.9}_{0.6}$	t_{10} (Gyr)	5.5
$M_{B,0}$	-18.03	EW [OIII]λ5007	$25.8^{34.9}_{18.8}$	t_{50} (Gyr)	3.5

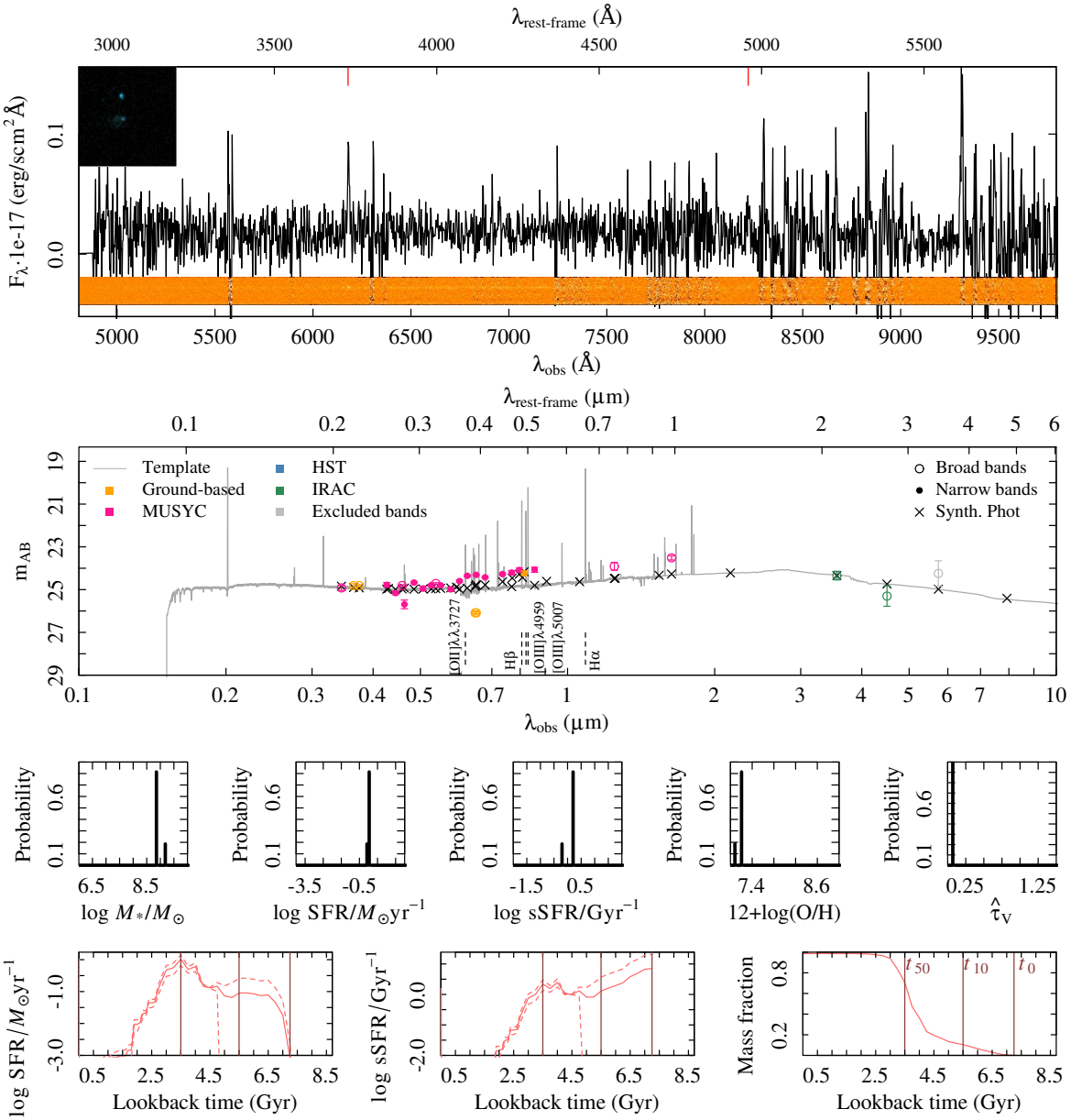

Summary ID 00053

ID	00053	$\mu_{eff,B,0}$	34.6±5.0	F Hα ($\times10^{17}$)	–
α (deg; J2000)	52.957006	$(B-V)_0$	0.52	EW Hα	–
δ (deg; J2000)	-27.896275	F Hβ ($\times10^{17}$)	–	log $M_*/M_\odot$	$8.3^{8.4}_{8.1}$
i (mag)	25.80±0.16	EW Hβ	–	log SFR/$M_\odot\,yr^{-1}$	$-0.7^{-0.5}_{-0.9}$
J (mag)	25.68±0.91	F [OII]$\lambda\lambda$3727 ($\times10^{17}$)	$0.5^{0.6}_{0.5}$	log sSFR/Gyr^{-1}	$0.0^{0.3}_{-0.2}$
z_{spec}	0.742/3	EW [OII]$\lambda\lambda$3727	$62.8^{93.0}_{46.3}$	$\hat{\tau}_V$	$0.3^{0.5}_{0.1}$
Morph.	Irr	F [OIII]λ4959 ($\times10^{17}$)	$0.5^{0.6}_{0.5}$	12+log(O/H)	$7.9^{8.3}_{7.6}$
n	1.4±0.2	EW [OIII]λ4959	$62.8^{93.0}_{46.3}$	t_0 (Gyr)	4.0
$R_{eff,v,0}$	2.1±0.1	F [OIII]λ5007 ($\times10^{17}$)	$0.5^{0.6}_{0.5}$	t_{10} (Gyr)	2.1
$M_{B,0}$	-16.61	EW [OIII]λ5007	$62.8^{93.0}_{46.3}$	t_{50} (Gyr)	1.3

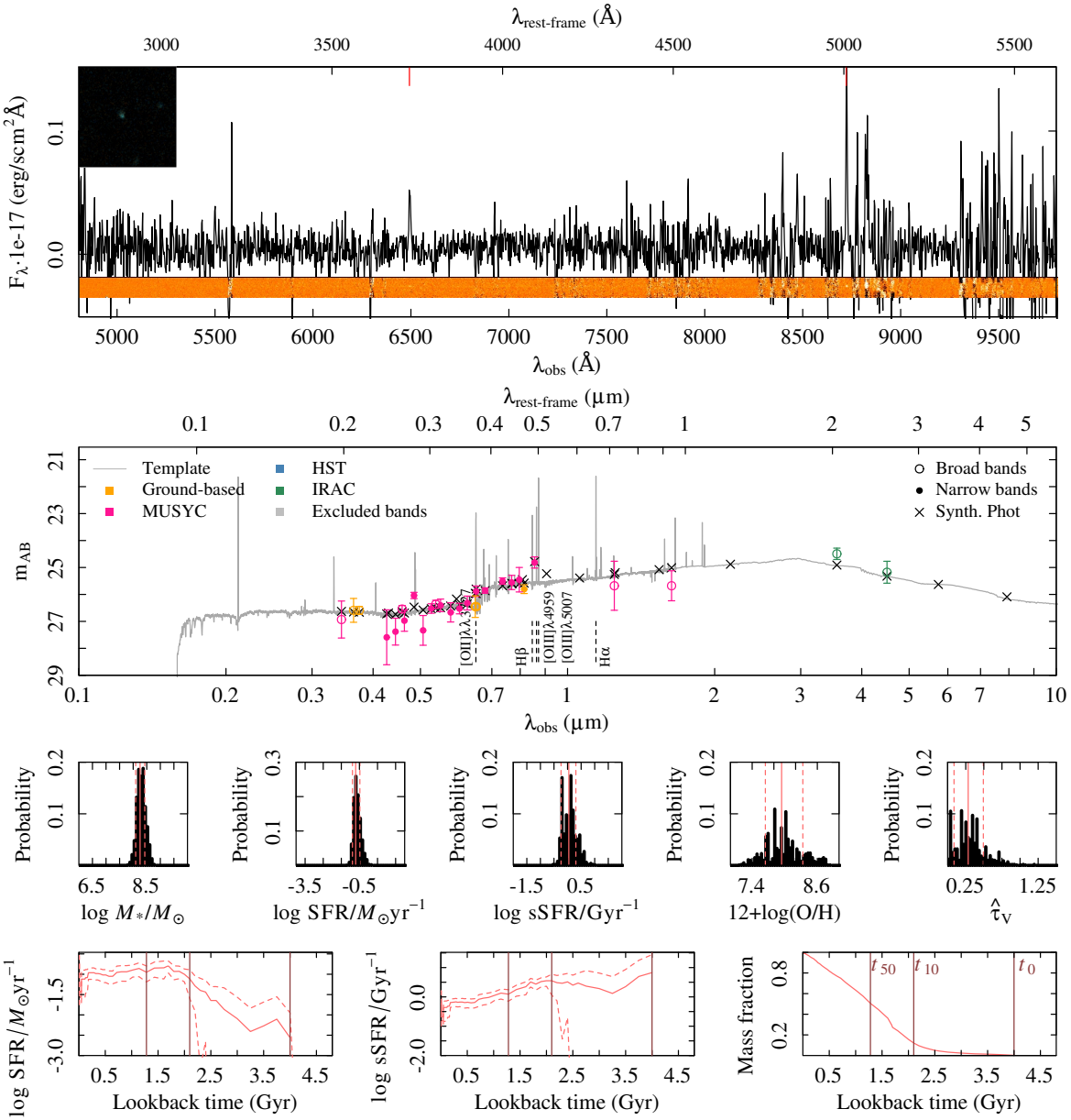

Summary ID 00088

ID	00088	$\mu_{eff,B,0}$	21.7±0.1	F Hα ($\times10^{17}$)	–
α (deg; J2000)	52.972798	$(B-V)_0$	0.23	EW Hα	–
δ (deg; J2000)	-27.749585	F Hβ ($\times10^{17}$)	$16.3^{17.3}_{15.4}$	log $M_*/M_\odot$	$9.0^{9.0}_{9.0}$
i (mag)	23.20±0.10	EW Hβ	$139.0^{173.4}_{111.8}$	log SFR/$M_\odot\,yr^{-1}$	$0.6^{0.6}_{0.6}$
J (mag)	23.56±0.28	F [OII]$\lambda\lambda$3727 ($\times10^{17}$)	$19.7^{21.2}_{18.3}$	log sSFR/Gyr^{-1}	$0.6^{0.6}_{0.5}$
z_{spec}	0.553/4	EW [OII]$\lambda\lambda$3727	$106.3^{139.4}_{84.9}$	$\hat{\tau}_V$	$0.3^{0.3}_{0.3}$
Morph.	U	F [OIII]λ4959 ($\times10^{17}$)	$19.7^{21.2}_{18.3}$	12+log(O/H)	$7.7^{7.7}_{7.7}$
n	3.3±0.2	EW [OIII]λ4959	$106.3^{139.4}_{84.9}$	t_0 (Gyr)	6.2
$R_{eff,v,0}$	1.8±0.0	F [OIII]λ5007 ($\times10^{17}$)	$19.7^{21.2}_{18.3}$	t_{10} (Gyr)	5.2
$M_{B,0}$	-19.24	EW [OIII]λ5007	$106.3^{139.4}_{84.9}$	t_{50} (Gyr)	4.0

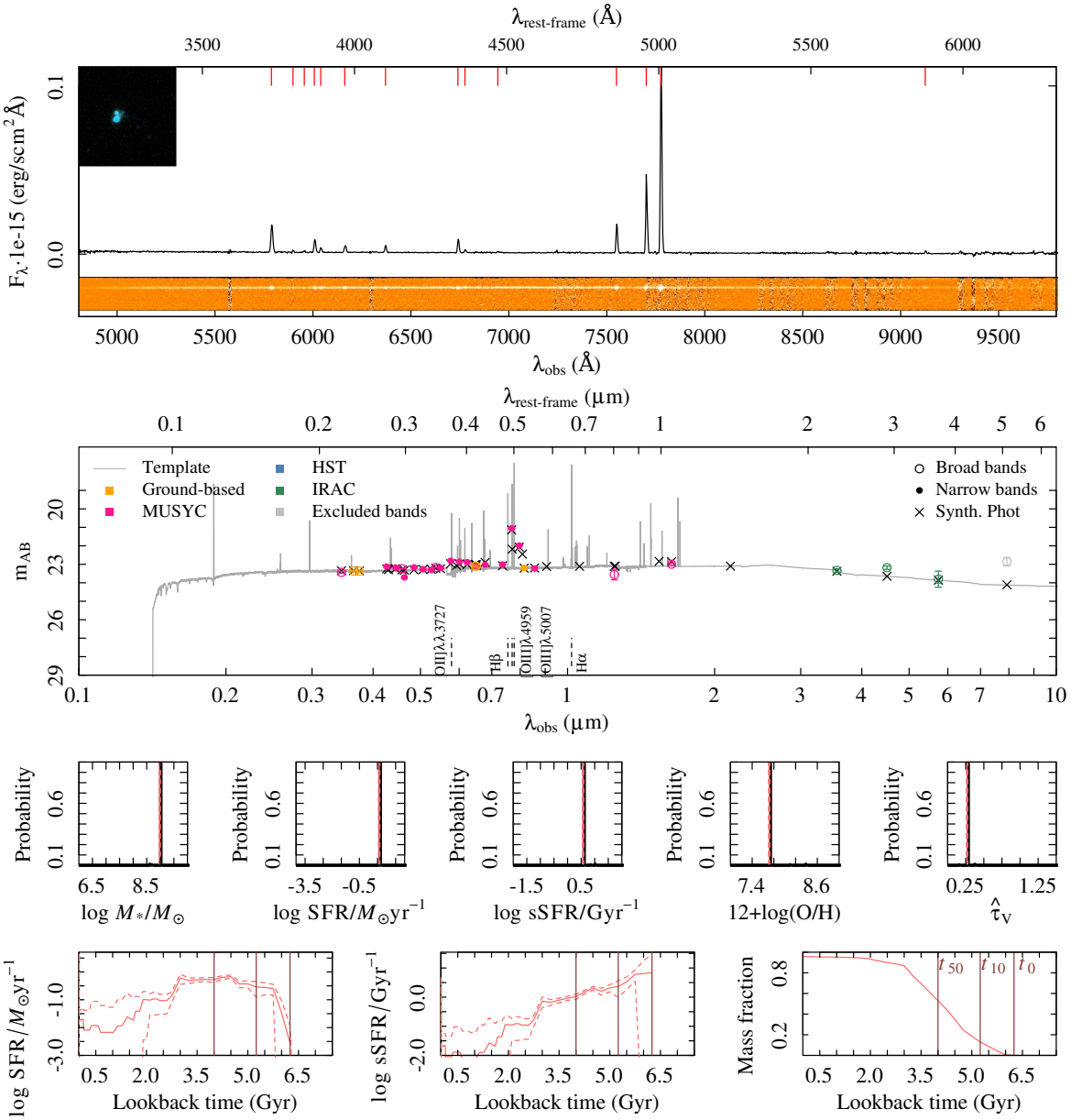

Summary ID 00121

ID	00121	$\mu_{eff,B,0}$	18.7±0.6	F Hα ($\times 10^{17}$)	–
α (deg; J2000)	52.986767	$(B-V)_0$	0.34	EW Hα	–
δ (deg; J2000)	-27.718900	F Hβ ($\times 10^{17}$)	–	log $M_*/M_\odot$	$9.1^{9.2}_{9.0}$
i (mag)	23.98±0.10	EW Hβ	–	log SFR/$M_\odot\, yr^{-1}$	$0.2^{0.4}_{0.0}$
J (mag)	23.95±0.12	F [OII]$\lambda\lambda$3727 ($\times 10^{17}$)	–	log sSFR/Gyr^{-1}	$0.1^{0.3}_{-0.1}$
z_{spec}	1.022/2	EW [OII]$\lambda\lambda$3727	–	$\hat{\tau}_V$	$0.5^{0.9}_{0.4}$
Morph.	D	F [OIII]λ4959 ($\times 10^{17}$)	–	12+log(O/H)	$7.9^{8.6}_{7.5}$
n	1.9±0.2	EW [OIII]λ4959	–	t_0 (Gyr)	3.8
$R_{eff,v,0}$	6.5±0.5	F [OIII]λ5007 ($\times 10^{17}$)	–	t_{10} (Gyr)	1.8
$M_{B,0}$	-18.72	EW [OIII]λ5007	–	t_{50} (Gyr)	0.6

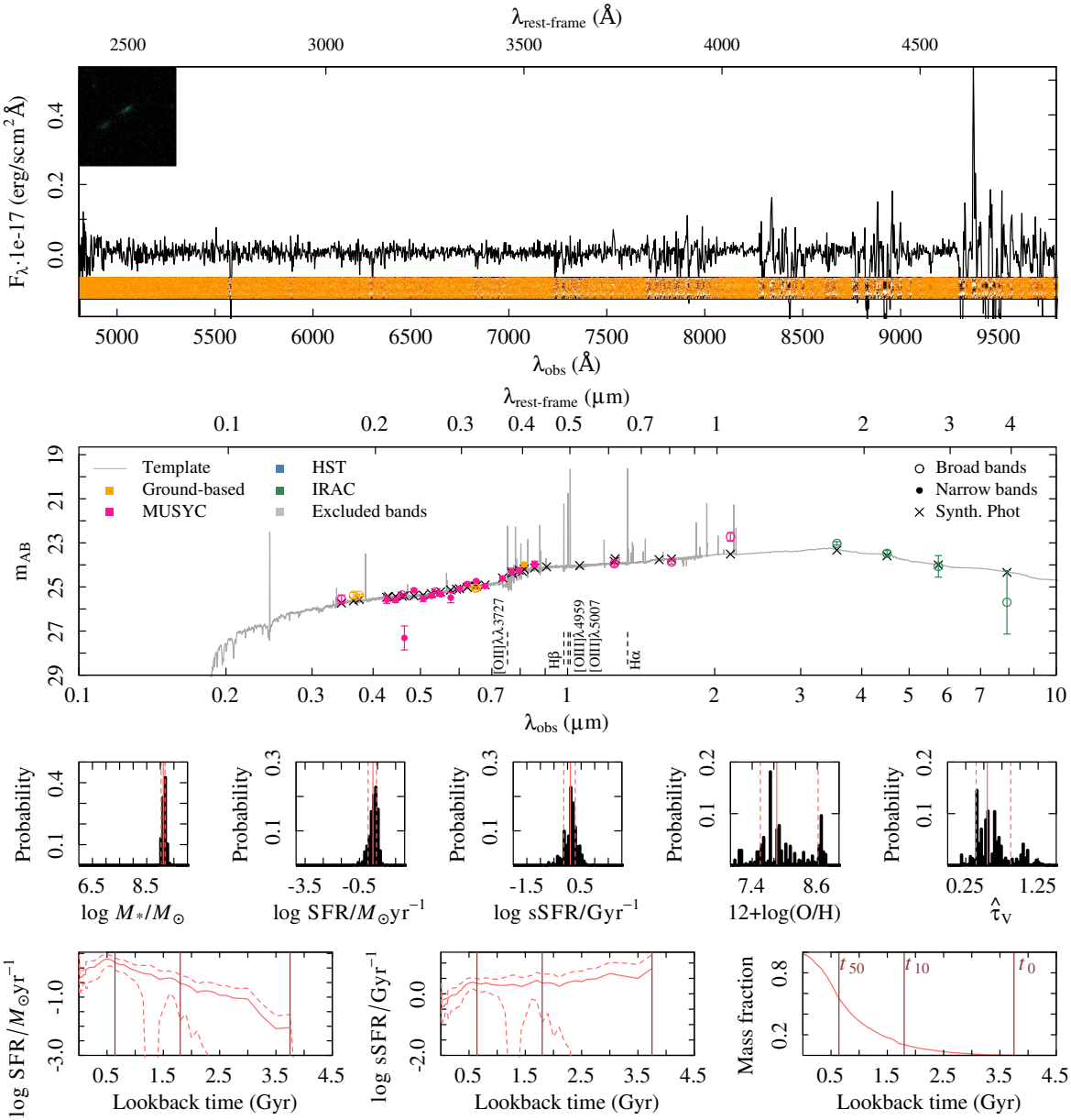

Summary ID 00145

ID	00145	$\mu_{eff,B,0}$	22.9±0.4	F Hα ($\times10^{17}$)	$1.9^{4.8}_{0.4}$
α (deg; J2000)	52.999720	$(B-V)_0$	0.76	EW Hα	$16.3^{13.3}_{38.5}$
δ (deg; J2000)	-27.675425	F Hβ ($\times10^{17}$)	$0.5^{0.6}_{0.3}$	log $M_*/M_\odot$	$8.7^{8.8}_{8.7}$
i (mag)	23.55±0.10	EW Hβ	$17.2^{24.5}_{10.1}$	log SFR/$M_\odot\,yr^{-1}$	$-0.2^{-0.1}_{-0.3}$
J (mag)	23.17±0.07	F [OII]$\lambda\lambda$3727 ($\times10^{17}$)	$2.1^{2.2}_{1.9}$	log sSFR/Gyr^{-1}	$0.1^{0.2}_{-0.1}$
z_{spec}	0.521/4	EW [OII]$\lambda\lambda$3727	$97.1^{128.2}_{79.3}$	$\hat{\tau}_V$	$0.6^{0.6}_{0.3}$
Morph.	D	F [OIII]λ4959 ($\times10^{17}$)	$2.1^{2.2}_{1.9}$	12+log(O/H)	$7.5^{7.6}_{7.3}$
n	1.7±0.1	EW [OIII]λ4959	$97.1^{128.2}_{79.3}$	t_0 (Gyr)	3.5
$R_{eff,v,0}$	1.6±0.0	F [OIII]λ5007 ($\times10^{17}$)	$2.1^{2.2}_{1.9}$	t_{10} (Gyr)	1.7
$M_{B,0}$	-17.46	EW [OIII]λ5007	$97.1^{128.2}_{79.3}$	t_{50} (Gyr)	1.0

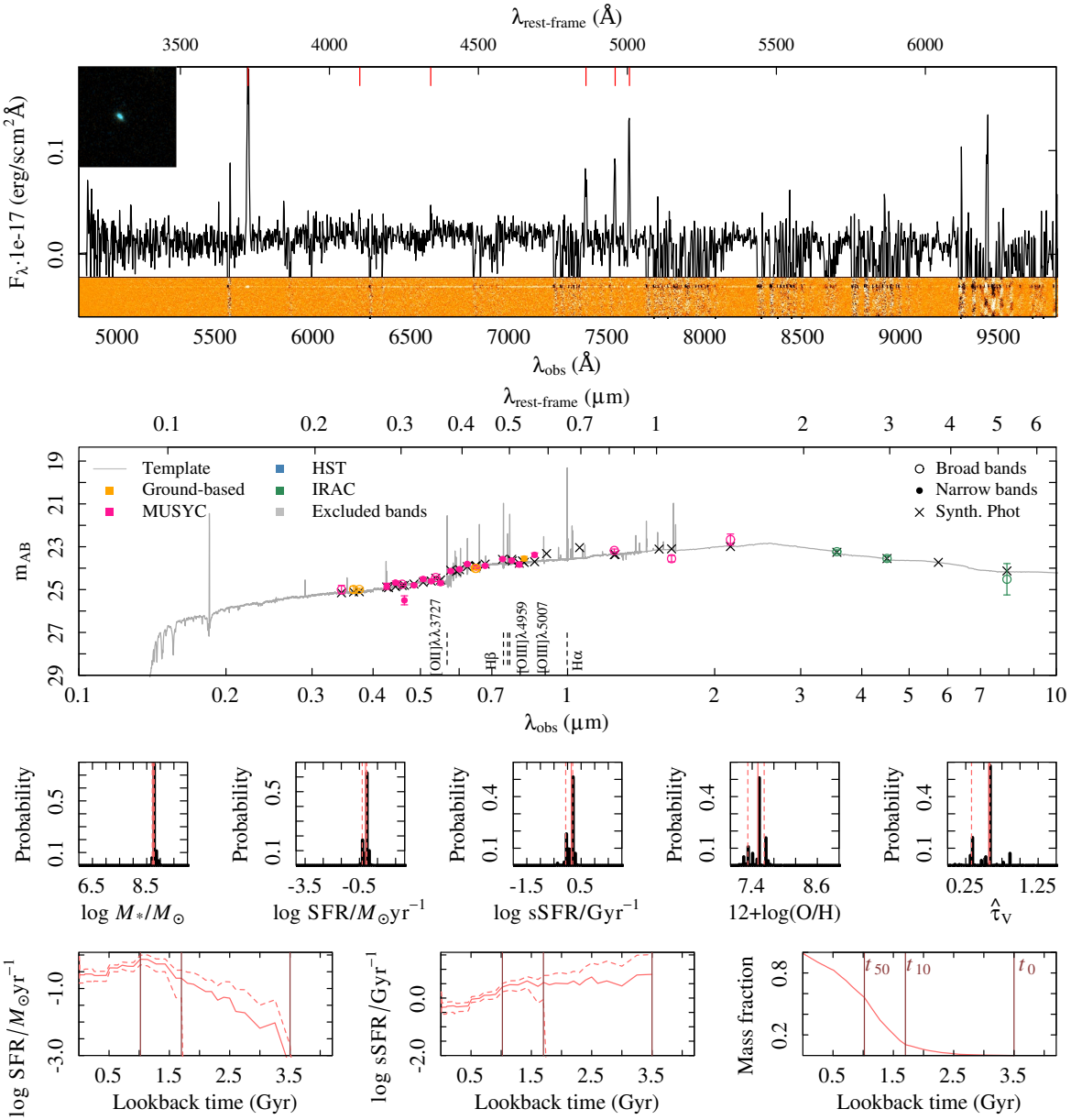

Summary ID 00156

ID	00156	$\mu_{eff,B,0}$	23.4±0.3	F Hα ($\times10^{17}$)	–
α (deg; J2000)	53.005248	$(B-V)_0$	0.82	EW Hα	–
δ (deg; J2000)	-27.973550	F Hβ ($\times10^{17}$)	–	log $M_*/M_\odot$	$8.0^{8.1}_{7.9}$
i (mag)	24.94±0.11	EW Hβ	–	log SFR$/M_\odot\,yr^{-1}$	$-1.0^{-0.6}_{-1.3}$
J (mag)	24.57±0.54	F [OII]$\lambda\lambda$3727 ($\times10^{17}$)	$0.8^{0.9}_{0.7}$	log sSFR$/Gyr^{-1}$	$-0.1^{0.3}_{-0.3}$
z_{spec}	0.513/3	EW [OII]$\lambda\lambda$3727	$47.2^{62.8}_{36.5}$	$\hat{\tau}_V$	$0.5^{1.0}_{0.2}$
Morph.	C	F [OIII]λ4959 ($\times10^{17}$)	$0.8^{0.9}_{0.7}$	12+log(O/H)	$8.0^{8.5}_{7.7}$
n	1.6±0.2	EW [OIII]λ4959	$47.2^{62.8}_{36.5}$	t_0 (Gyr)	3.5
$R_{eff,v,0}$	0.6±0.0	F [OIII]λ5007 ($\times10^{17}$)	$0.8^{0.9}_{0.7}$	t_{10} (Gyr)	1.8
$M_{B,0}$	-16.14	EW [OIII]λ5007	$47.2^{62.8}_{36.5}$	t_{50} (Gyr)	0.6

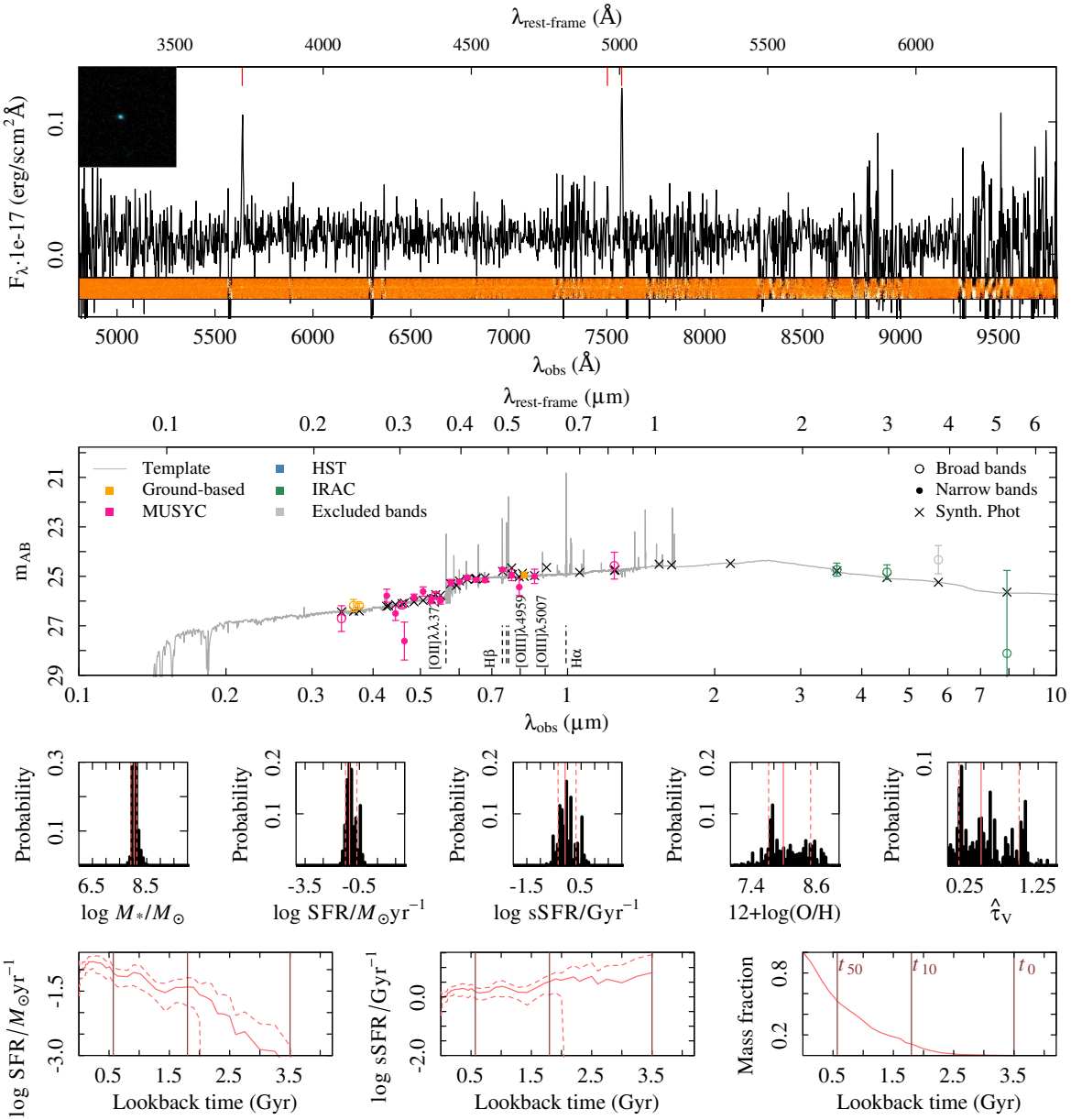

Summary ID 00164

ID	00164	$\mu_{eff,B,0}$	21.8±0.2	F Hα ($\times 10^{17}$)	–
α (deg; J2000)	53.008860	$(B-V)_0$	0.08	EW Hα	–
δ (deg; J2000)	-27.811450	F Hβ ($\times 10^{17}$)	–	log $M_*/M_\odot$	$9.0^{9.1}_{8.8}$
i (mag)	25.13±0.12	EW Hβ	–	log SFR/$M_\odot\, yr^{-1}$	$0.5^{0.6}_{0.4}$
J (mag)	24.57±0.39	F [OII]$\lambda\lambda$3727 ($\times 10^{17}$)	–	log sSFR/Gyr^{-1}	$0.5^{0.6}_{0.4}$
z_{spec}	1.245/2	EW [OII]$\lambda\lambda$3727	–	$\hat{\tau}_V$	$0.3^{0.4}_{0.2}$
Morph.	Irr	F [OIII]λ4959 ($\times 10^{17}$)	–	12+log(O/H)	$7.4^{7.7}_{7.2}$
n	1.3±0.1	EW [OIII]λ4959	–	t_0 (Gyr)	4.2
$R_{eff,v,0}$	5.0±0.2	F [OIII]λ5007 ($\times 10^{17}$)	–	t_{10} (Gyr)	2.8
$M_{B,0}$	-19.44	EW [OIII]λ5007	–	t_{50} (Gyr)	1.4

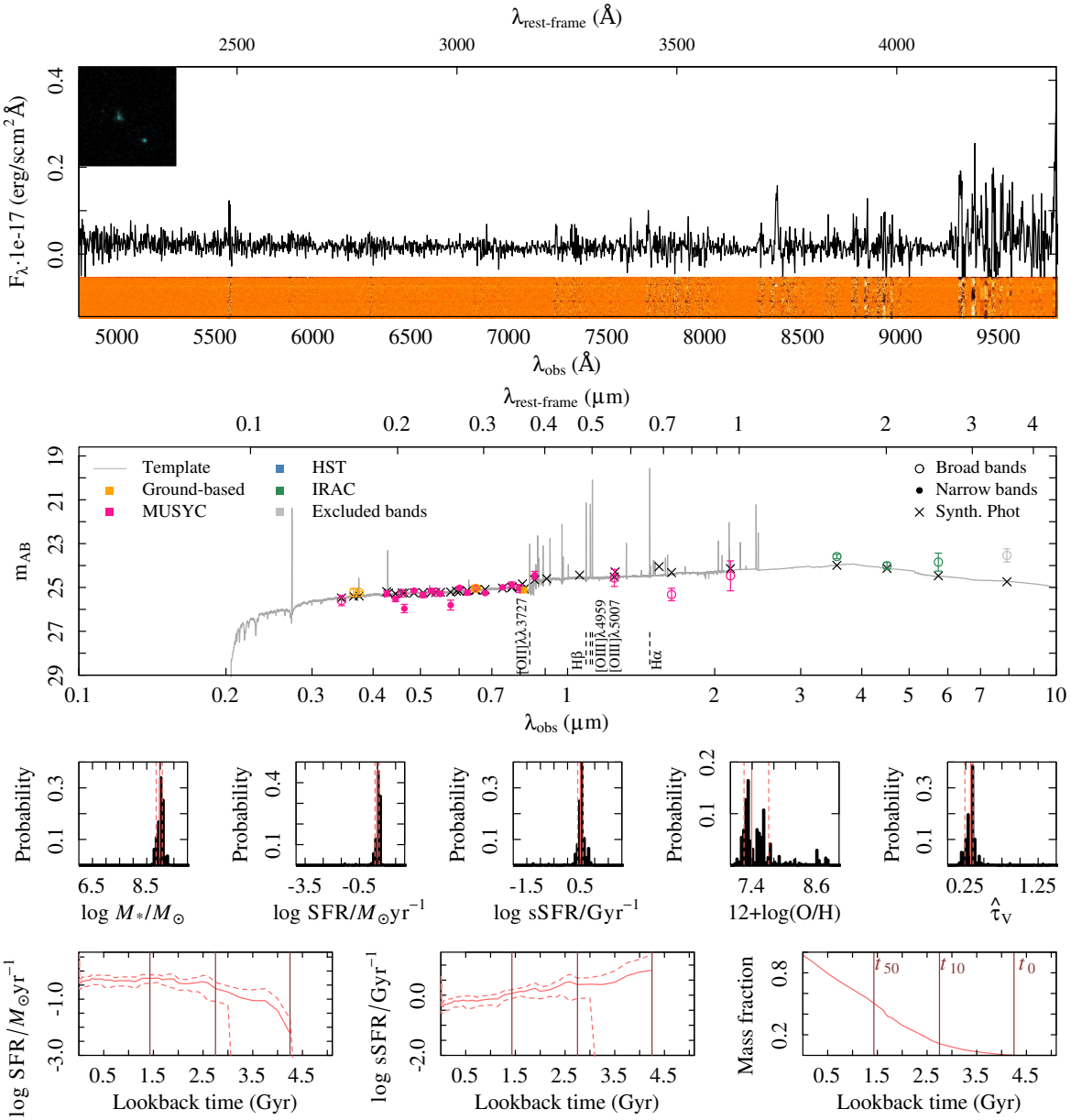

Summary ID 00173

ID	00173	$\mu_{eff,B,0}$	34.6±5.0	F Hα ($\times 10^{17}$)	$0.8^{0.9}_{0.8}$
α (deg; J2000)	53.013867	$(B-V)_0$	1.14	EW Hα	$85.5^{126.4}_{65.5}$
δ (deg; J2000)	-27.633553	F Hβ ($\times 10^{17}$)	–	log $M_*/M_\odot$	$7.9^{8.0}_{7.7}$
i (mag)	24.75±0.17	EW Hβ	–	log SFR/$M_\odot\, yr^{-1}$	$-2.0^{-1.7}_{-2.4}$
J (mag)	23.67±0.12	F [OII]$\lambda\lambda$3727 ($\times 10^{17}$)	–	log sSFR/Gyr^{-1}	$-0.9^{-0.6}_{-1.2}$
z_{spec}	0.214/2	EW [OII]$\lambda\lambda$3727	–	$\hat{\tau}_V$	$0.8^{1.1}_{0.4}$
Morph.	Irr	F [OIII]λ4959 ($\times 10^{17}$)	–	12+log(O/H)	$8.2^{8.5}_{7.6}$
n	0.5±0.1	EW [OIII]λ4959	–	t_0 (Gyr)	9.5
$R_{eff,v,0}$	1.6±0.1	F [OIII]λ5007 ($\times 10^{17}$)	–	t_{10} (Gyr)	7.5
$M_{B,0}$	-13.60	EW [OIII]λ5007	–	t_{50} (Gyr)	4.0

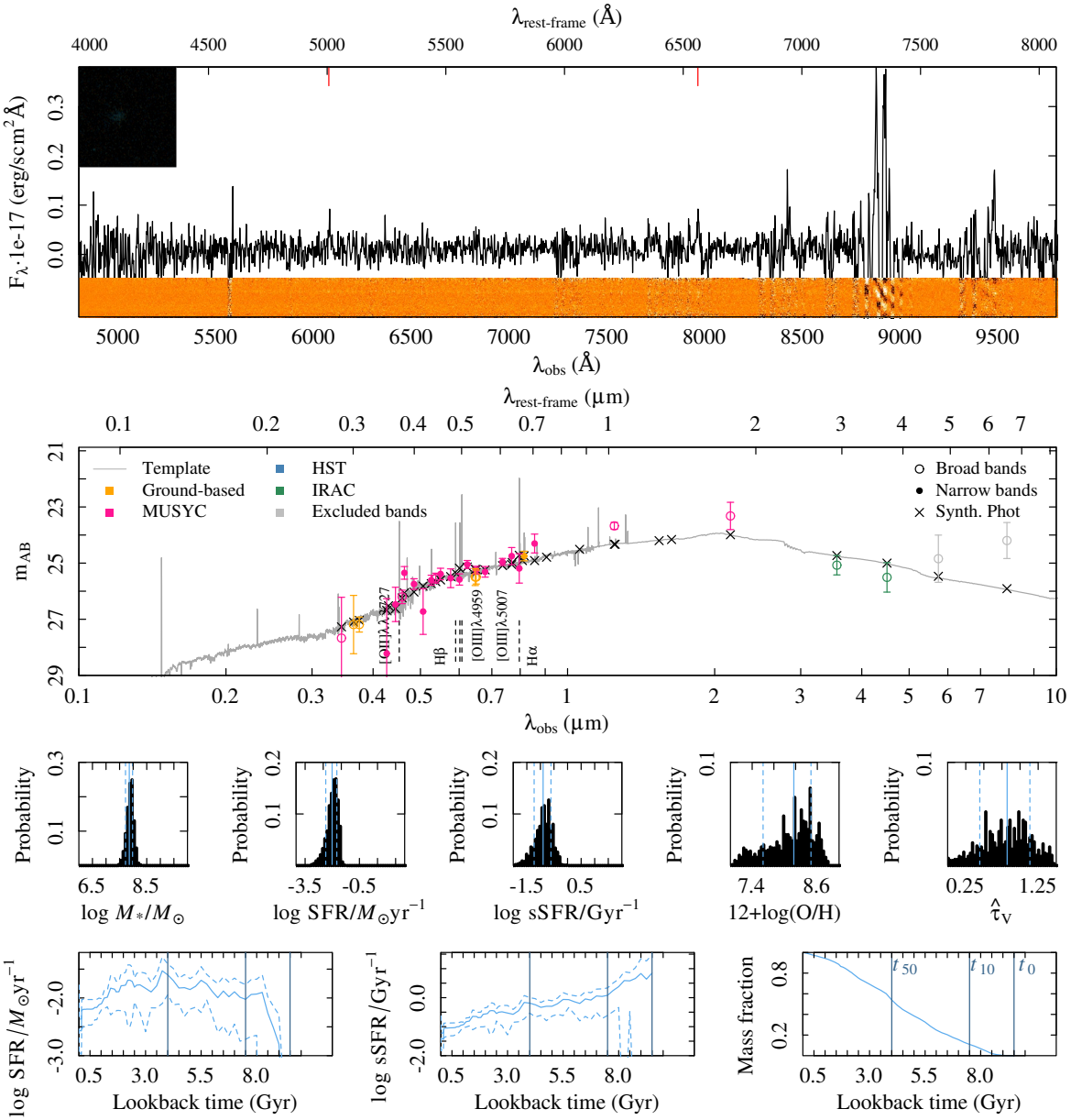

Summary ID 00181

ID	00181	$\mu_{eff,B,0}$	18.3±1.8	F Hα ($\times10^{17}$)	–
α (deg; J2000)	53.017981	$(B-V)_0$	0.45	EW Hα	–
δ (deg; J2000)	-27.863126	F Hβ ($\times10^{17}$)	$2.2^{2.7}_{1.6}$	log $M_*/M_\odot$	$9.0^{9.1}_{9.0}$
i (mag)	23.56±0.10	EW Hβ	$25.9^{41.0}_{16.3}$	log SFR/$M_\odot\,yr^{-1}$	$0.2^{0.4}_{0.1}$
J (mag)	23.68±0.15	F [OII]$\lambda\lambda$3727 ($\times10^{17}$)	$6.9^{7.6}_{6.3}$	log sSFR/Gyr^{-1}	$0.2^{0.3}_{0.1}$
z_{spec}	0.759/4	EW [OII]$\lambda\lambda$3727	$70.2^{93.7}_{57.2}$	$\hat{\tau}_V$	$0.3^{0.4}_{0.3}$
Morph.	Irr	F [OIII]λ4959 ($\times10^{17}$)	$6.9^{7.6}_{6.3}$	12+log(O/H)	$7.8^{8.5}_{7.6}$
n	3.0±0.2	EW [OIII]λ4959	$70.2^{93.7}_{57.2}$	t_0 (Gyr)	4.8
$R_{eff,v,0}$	1.9±0.0	F [OIII]λ5007 ($\times10^{17}$)	$6.9^{7.6}_{6.3}$	t_{10} (Gyr)	3.0
$M_{B,0}$	-18.77	EW [OIII]λ5007	$70.2^{93.7}_{57.2}$	t_{50} (Gyr)	1.0

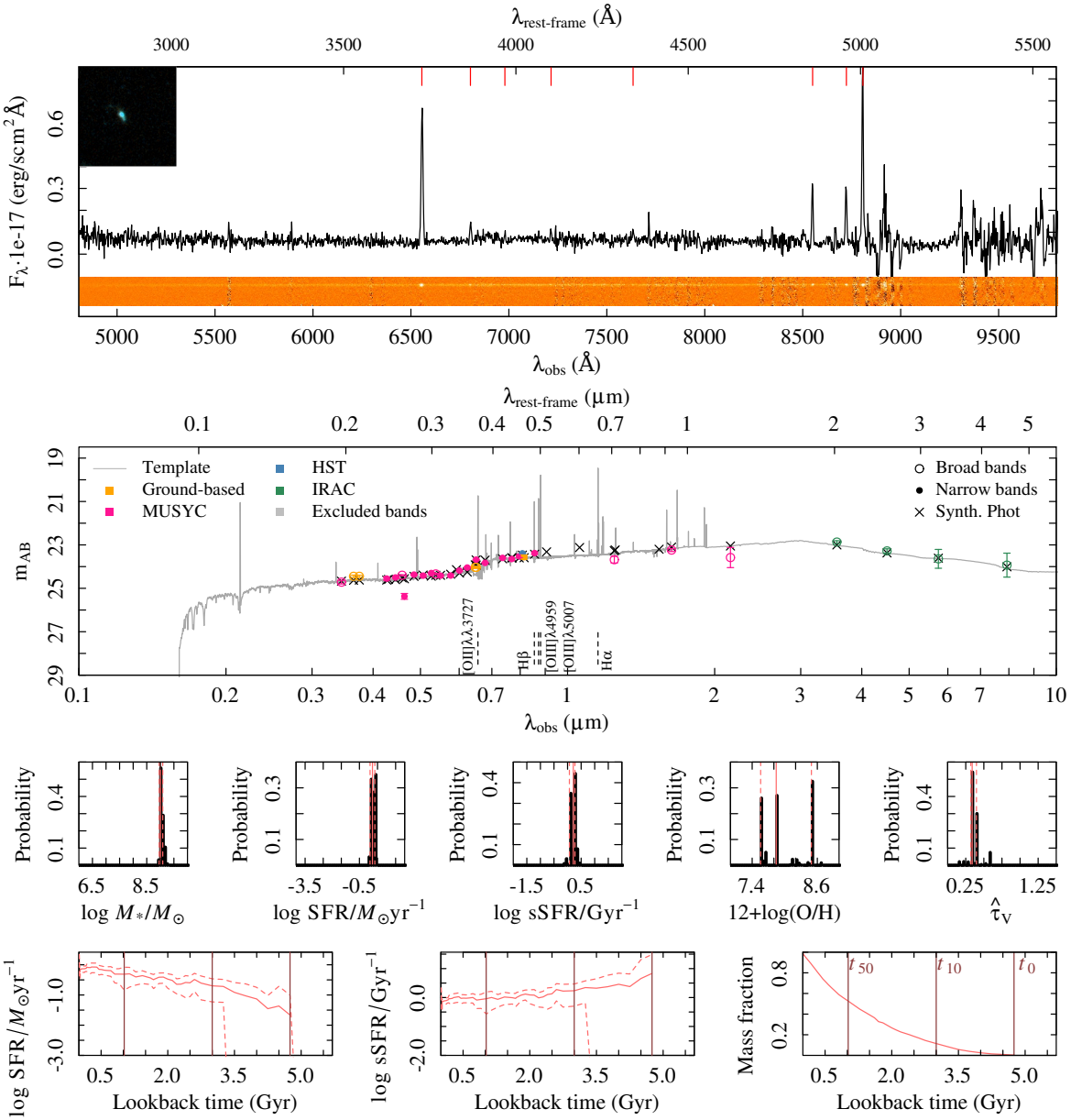

Summary ID 00183

ID	00183	$\mu_{eff,B,0}$	23.2±0.2	F Hα ($\times10^{17}$)	–
α (deg; J2000)	53.019854	$(B-V)_0$	0.64	EW Hα	–
δ (deg; J2000)	-27.721868	F Hβ ($\times10^{17}$)	$0.6^{0.6}_{0.6}$	log $M_*/M_\odot$	$7.7^{7.7}_{7.5}$
i (mag)	25.85±0.17	EW Hβ	$64.0^{92.0}_{49.7}$	log SFR/$M_\odot\,yr^{-1}$	$-0.6^{-0.3}_{-0.7}$
J (mag)	25.33±0.34	F [OII]$\lambda\lambda$3727 ($\times10^{17}$)	$0.4^{0.4}_{0.3}$	log sSFR/Gyr^{-1}	$0.7^{1.1}_{0.6}$
z_{spec}	0.532/4	EW [OII]$\lambda\lambda$3727	$37.1^{61.6}_{23.3}$	$\hat{\tau}_V$	$0.6^{0.9}_{0.6}$
Morph.	Irr	F [OIII]λ4959 ($\times10^{17}$)	$0.4^{0.4}_{0.3}$	12+log(O/H)	$7.8^{7.8}_{7.5}$
n	1.1±0.2	EW [OIII]λ4959	$37.1^{61.6}_{23.3}$	t_0 (Gyr)	3.5
$R_{eff,v,0}$	0.7±0.0	F [OIII]λ5007 ($\times10^{17}$)	$0.4^{0.4}_{0.3}$	t_{10} (Gyr)	1.0
$M_{B,0}$	-15.79	EW [OIII]λ5007	$37.1^{61.6}_{23.3}$	t_{50} (Gyr)	0.5

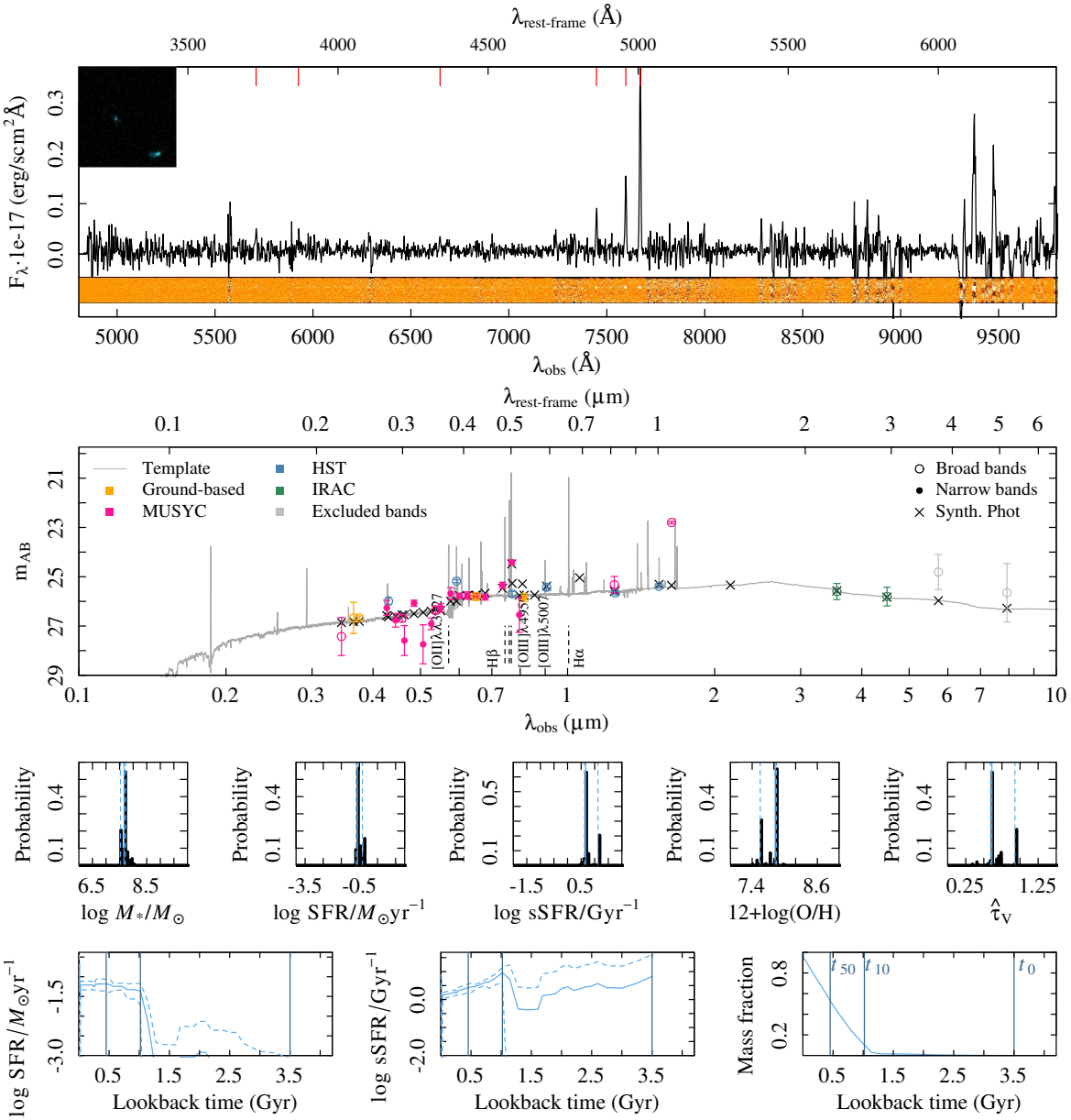

Summary ID 00193

ID	00193	$\mu_{eff,B,0}$	25.0±0.2	F Hα ($\times10^{17}$)	–
α (deg; J2000)	53.027513	$(B-V)_0$	0.79	EW Hα	–
δ (deg; J2000)	-27.899148	F Hβ ($\times10^{17}$)	$0.3^{0.4}_{0.1}$	log $M_*/M_\odot$	$7.8^{7.8}_{7.7}$
i (mag)	24.63±0.11	EW Hβ	$11.5^{19.7}_{5.5}$	log SFR/$M_\odot\,yr^{-1}$	$-0.5^{-0.5}_{-0.8}$
J (mag)	24.08±0.35	F [OII]$\lambda\lambda$3727 ($\times10^{17}$)	$0.6^{0.7}_{0.5}$	log sSFR/Gyr^{-1}	$0.7^{0.8}_{0.4}$
z_{spec}	0.482/3	EW [OII]$\lambda\lambda$3727	$34.3^{54.8}_{21.3}$	$\hat{\tau}_V$	$1.4^{1.4}_{0.8}$
Morph.	Irr	F [OIII]λ4959 ($\times10^{17}$)	$0.6^{0.7}_{0.5}$	12+log(O/H)	$7.9^{7.9}_{7.9}$
n	1.0±0.1	EW [OIII]λ4959	$34.3^{54.8}_{21.3}$	t_0 (Gyr)	2.0
$R_{eff,v,0}$	0.6±0.0	F [OIII]λ5007 ($\times10^{17}$)	$0.6^{0.7}_{0.5}$	t_{10} (Gyr)	0.6
$M_{B,0}$	-16.14	EW [OIII]λ5007	$34.3^{54.8}_{21.3}$	t_{50} (Gyr)	0.3

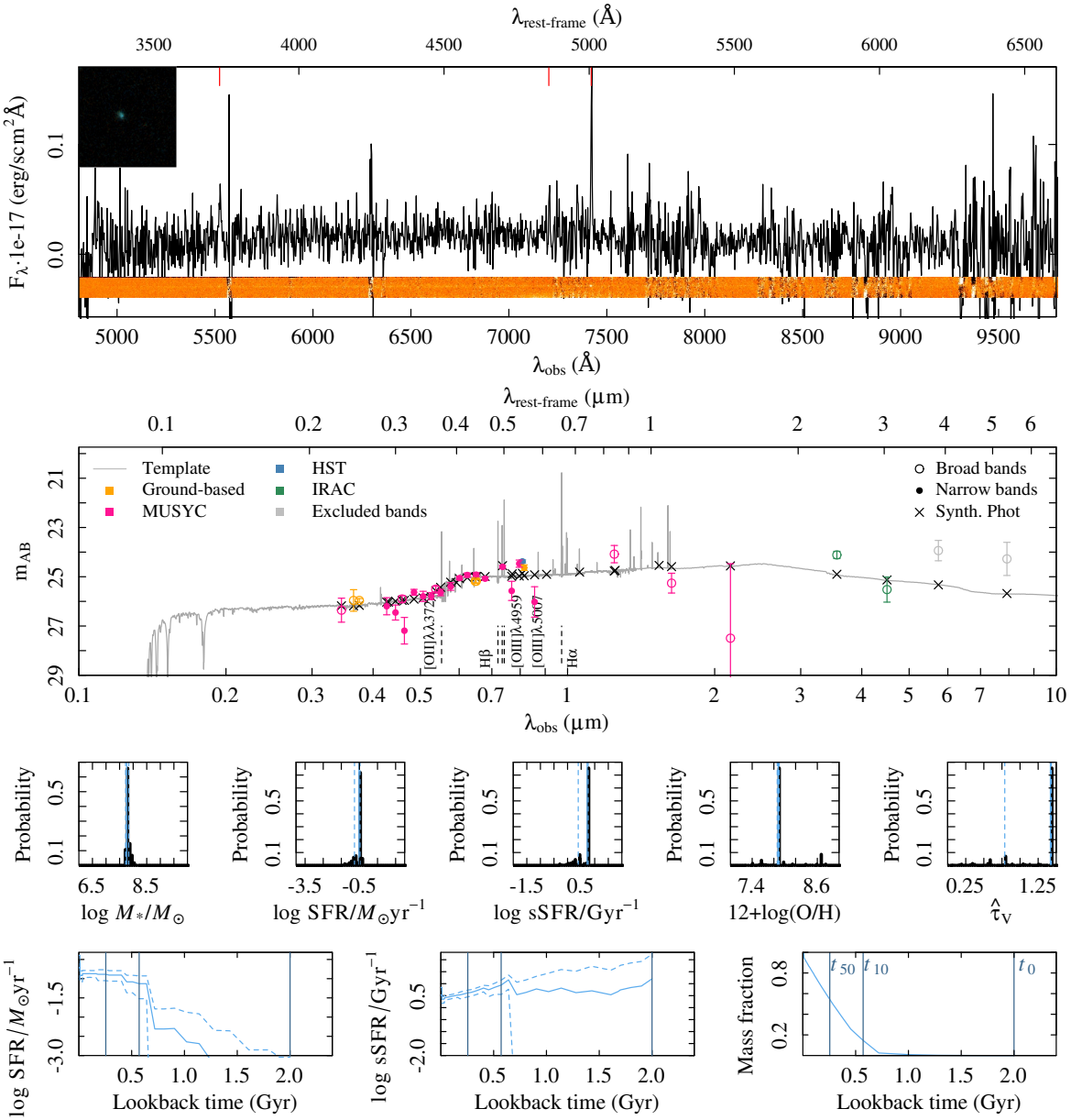

Summary ID 00195

ID	00195	$\mu_{eff,B,0}$	22.9±0.4	F Hα ($\times10^{17}$)	–
α (deg; J2000)	53.029319	$(B-V)_0$	0.46	EW Hα	–
δ (deg; J2000)	-27.740477	F Hβ ($\times10^{17}$)	$0.5^{0.5}_{0.4}$	log $M_*/M_\odot$	$7.5^{7.6}_{7.4}$
i (mag)	25.98±0.20	EW Hβ	$95.6^{157.0}_{69.0}$	log SFR/$M_\odot\,yr^{-1}$	$-1.0^{-1.0}_{-1.1}$
J (mag)	24.87±0.41	F [OII]$\lambda\lambda$3727 ($\times10^{17}$)	$0.7^{0.7}_{0.6}$	log sSFR/Gyr^{-1}	$0.4^{0.4}_{0.4}$
z_{spec}	0.538/4	EW [OII]$\lambda\lambda$3727	$71.4^{94.1}_{57.0}$	$\hat{\tau}_V$	$0.1^{0.1}_{0.1}$
Morph.	D	F [OIII]λ4959 ($\times10^{17}$)	$0.7^{0.7}_{0.6}$	12+log(O/H)	$7.9^{7.9}_{7.9}$
n	0.2±0.1	EW [OIII]λ4959	$71.4^{94.1}_{57.0}$	t_0 (Gyr)	1.4
$R_{eff,v,0}$	0.8±0.0	F [OIII]λ5007 ($\times10^{17}$)	$0.7^{0.7}_{0.6}$	t_{10} (Gyr)	0.8
$M_{B,0}$	-15.93	EW [OIII]λ5007	$71.4^{94.1}_{57.0}$	t_{50} (Gyr)	0.4

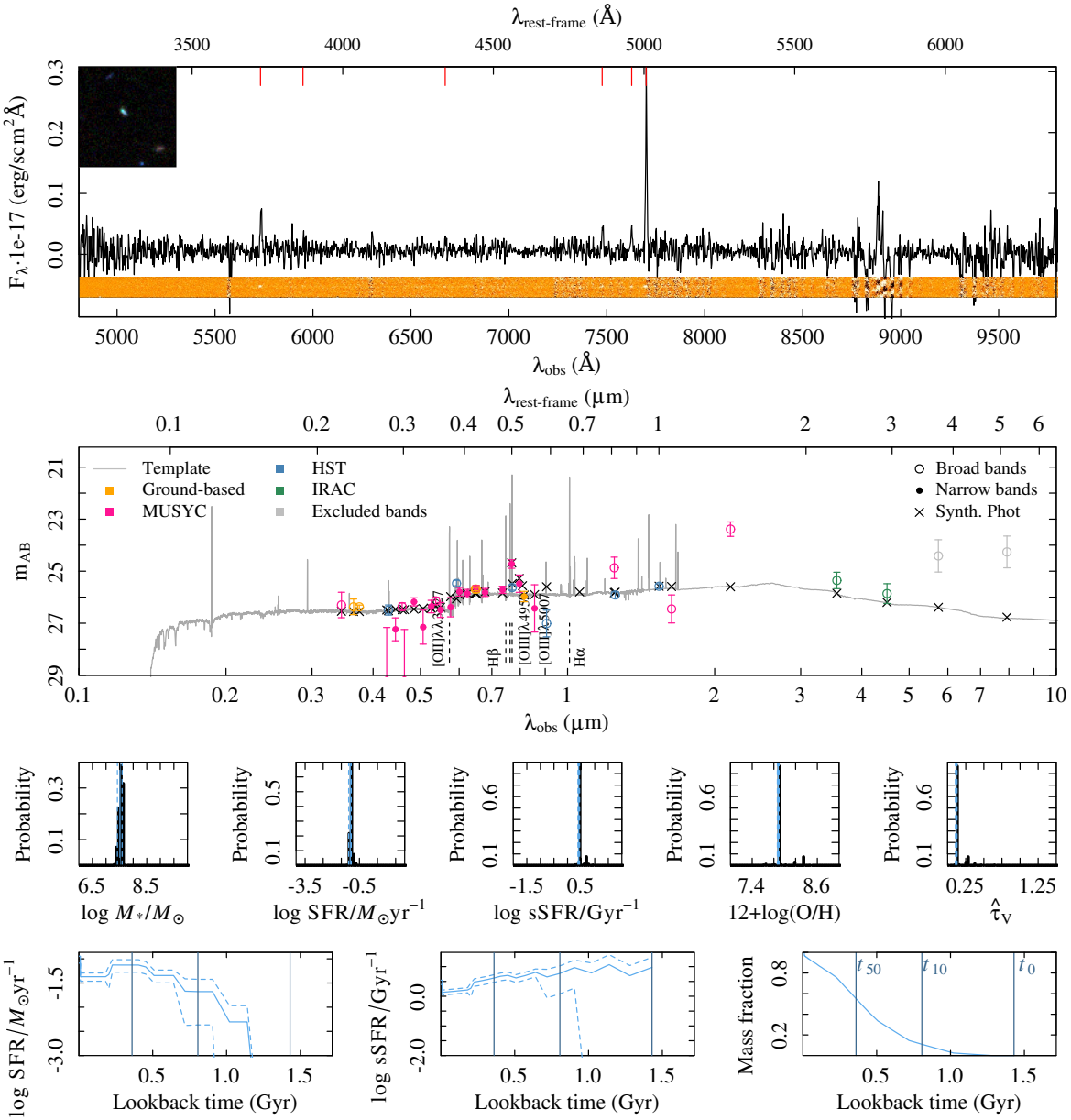

Summary ID 00205

ID	00205	$\mu_{eff,B,0}$	19.3±0.2	F Hα ($\times 10^{17}$)	–
α (deg; J2000)	53.034195	$(B-V)_0$	0.22	EW Hα	–
δ (deg; J2000)	-27.871233	F Hβ ($\times 10^{17}$)	–	log $M_*/M_\odot$	NA^{NA}_{NA}
i (mag)	24.29±0.10	EW Hβ	–	log SFR/$M_\odot\, yr^{-1}$	NA^{NA}_{NA}
J (mag)	-99.99±-99.99	F [OII]$\lambda\lambda$3727 ($\times 10^{17}$)	–	log sSFR/Gyr^{-1}	NA^{NA}_{NA}
z_{spec}	1.088/3	EW [OII]$\lambda\lambda$3727	–	$\hat{\tau}_V$	NA^{NA}_{NA}
Morph.	D	F [OIII]λ4959 ($\times 10^{17}$)	–	12+log(O/H)	NA^{NA}_{NA}
n	1.4±0.1	EW [OIII]λ4959	–	t_0 (Gyr)	4.0
$R_{eff,v,0}$	NA±NA	F [OIII]λ5007 ($\times 10^{17}$)	–	t_{10} (Gyr)	2.6
$M_{B,0}$	-18.95	EW [OIII]λ5007	–	t_{50} (Gyr)	1.3

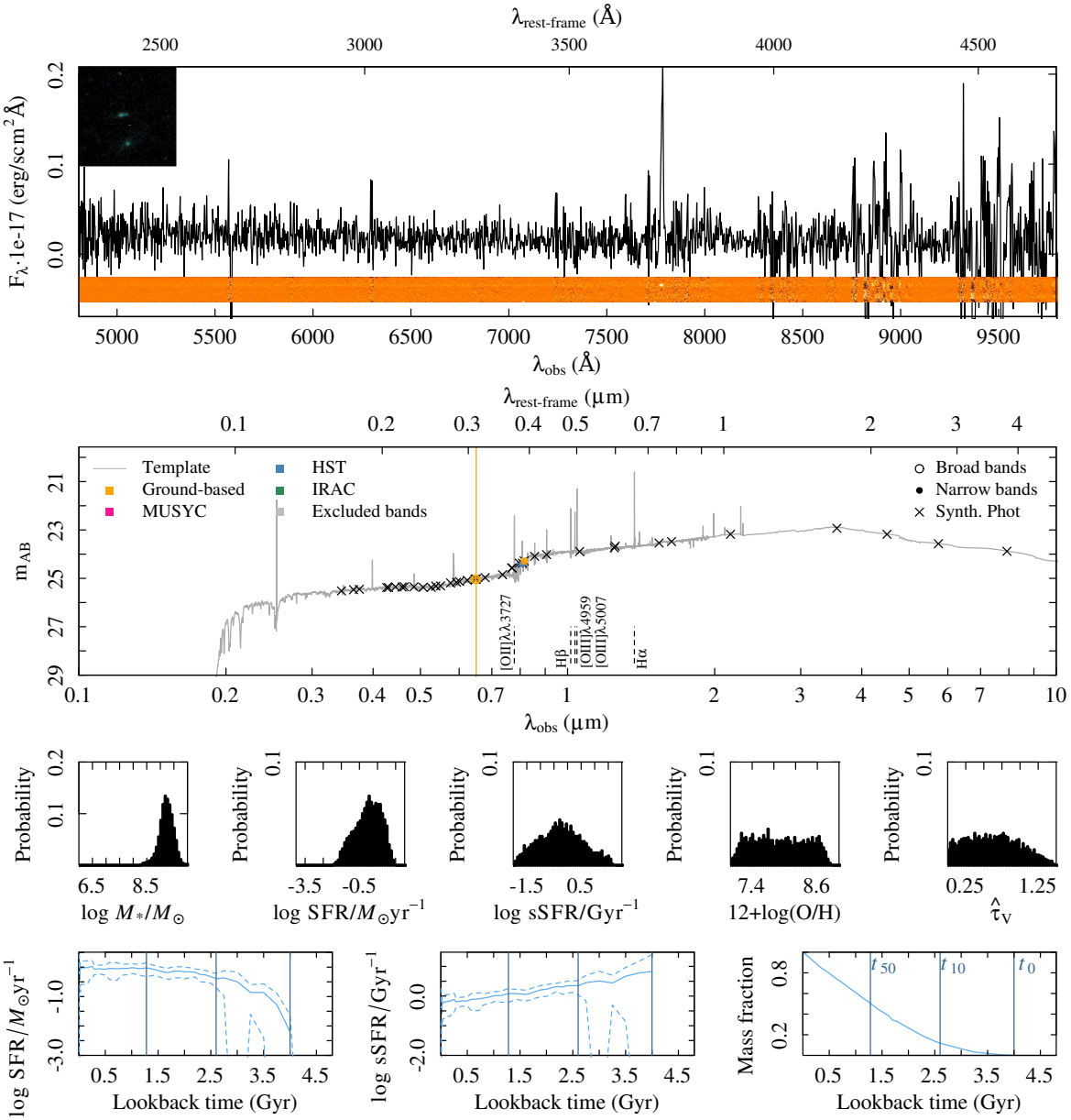

Summary ID 00210

ID	00210	$\mu_{eff,B,0}$	25.4±0.9	F Hα ($\times 10^{17}$)	–
α (deg; J2000)	53.035969	$(B-V)_0$	0.79	EW Hα	–
δ (deg; J2000)	-27.734102	F Hβ ($\times 10^{17}$)	–	log $M_*/M_\odot$	$7.7^{7.8}_{7.4}$
i (mag)	26.04±0.21	EW Hβ	–	log SFR$/M_\odot\, yr^{-1}$	$-0.6^{-0.4}_{-0.9}$
J (mag)	26.27±0.94	F [OII]$\lambda\lambda$3727 ($\times 10^{17}$)	–	log sSFR$/Gyr^{-1}$	$0.6^{1.1}_{0.4}$
z_{spec}	0.423/3	EW [OII]$\lambda\lambda$3727	–	$\hat{\tau}_V$	$0.9^{1.2}_{0.7}$
Morph.	C	F [OIII]λ4959 ($\times 10^{17}$)	–	12+log(O/H)	$7.5^{7.7}_{7.3}$
n	1.9±0.6	EW [OIII]λ4959	–	t_0 (Gyr)	7.0
$R_{eff,v,0}$	0.7±0.1	F [OIII]λ5007 ($\times 10^{17}$)	–	t_{10} (Gyr)	6.0
$M_{B,0}$	-14.75	EW [OIII]λ5007	–	t_{50} (Gyr)	4.5

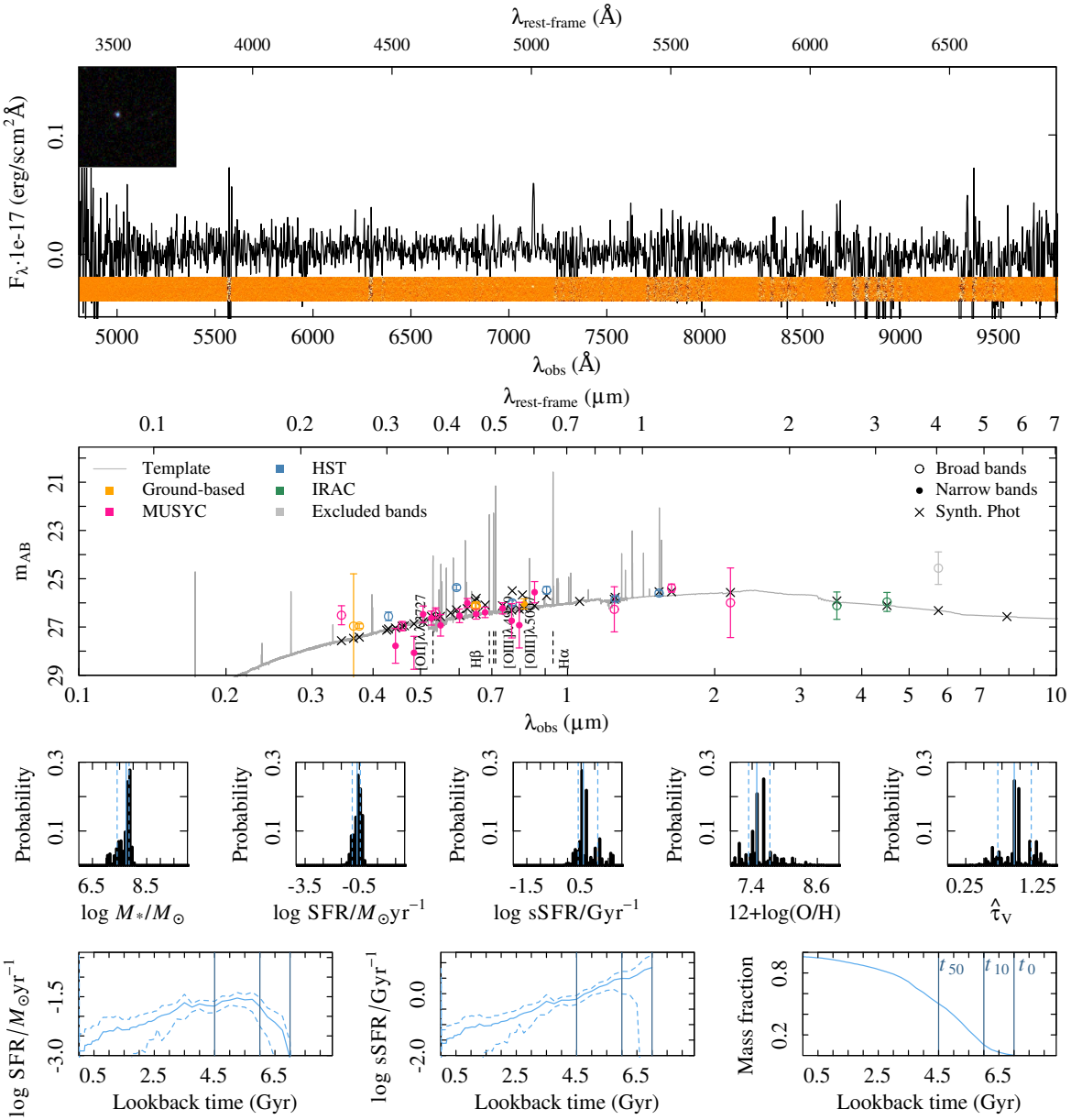

Summary ID 00220

ID	00220	$\mu_{eff,B,0}$	21.0±0.2	F Hα ($\times 10^{17}$)	$1.4^{1.6}_{1.3}$
α (deg; J2000)	53.041173	$(B-V)_0$	0.34	EW Hα	$108.4^{138.9}_{87.4}$
δ (deg; J2000)	-27.638770	F Hβ ($\times 10^{17}$)	$0.3^{0.3}_{0.2}$	log $M_*/M_\odot$	$6.8^{7.0}_{6.7}$
i (mag)	25.01±0.12	EW Hβ	$14.4^{22.4}_{8.2}$	log SFR/$M_\odot\, yr^{-1}$	$-2.5^{-2.3}_{-2.6}$
J (mag)	-99.99±-99.99	F [OII]$\lambda\lambda$3727 ($\times 10^{17}$)	–	log sSFR/Gyr^{-1}	$-0.3^{-0.2}_{-0.4}$
z_{spec}	0.119/3	EW [OII]$\lambda\lambda$3727	–	$\hat{\tau}_V$	$0.1^{0.2}_{0.1}$
Morph.	Irr	F [OIII]λ4959 ($\times 10^{17}$)	–	12+log(O/H)	$7.9^{8.0}_{7.6}$
n	0.6±0.1	EW [OIII]λ4959	–	t_0 (Gyr)	8.8
$R_{eff,v,0}$	0.9±0.0	F [OIII]λ5007 ($\times 10^{17}$)	–	t_{10} (Gyr)	5.2
$M_{B,0}$	-13.43	EW [OIII]λ5007	–	t_{50} (Gyr)	1.9

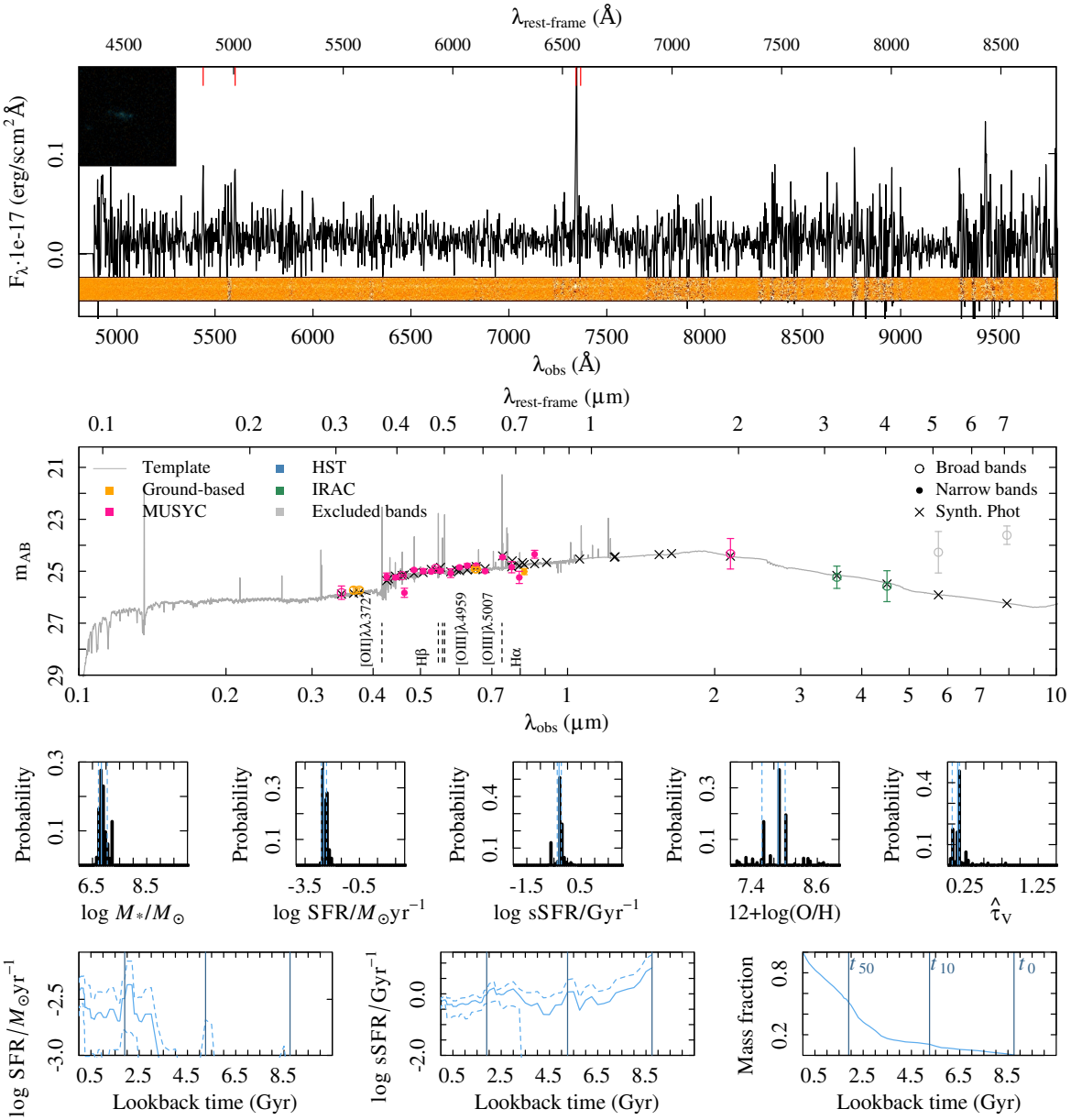

Summary ID 00227

ID	00227	$\mu_{eff,B,0}$	NaN±2.5	F Hα ($\times10^{17}$)	–
α (deg; J2000)	53.044752	$(B-V)_0$	0.41	EW Hα	–
δ (deg; J2000)	-27.834502	F Hβ ($\times10^{17}$)	–	log $M_*/M_\odot$	$7.9^{8.0}_{7.9}$
i (mag)	26.04±0.18	EW Hβ	–	log SFR/$M_\odot\,yr^{-1}$	$-0.9^{-0.8}_{-1.2}$
J (mag)	-99.99±-99.99	F [OII]$\lambda\lambda$3727 ($\times10^{17}$)	$0.4^{0.4}_{0.3}$	log sSFR/Gyr^{-1}	$0.1^{0.2}_{-0.2}$
z_{spec}	0.672/2	EW [OII]$\lambda\lambda$3727	$50.1^{69.4}_{35.8}$	$\hat{\tau}_V$	$0.1^{0.2}_{0.0}$
Morph.	Irr	F [OIII]λ4959 ($\times10^{17}$)	$0.4^{0.4}_{0.3}$	12+log(O/H)	$7.8^{8.3}_{7.8}$
n	-999.0±-999.0	EW [OIII]λ4959	$50.1^{69.4}_{35.8}$	t_0 (Gyr)	4.2
$R_{eff,v,0}$	-355.2±-355.2	F [OIII]λ5007 ($\times10^{17}$)	$0.4^{0.4}_{0.3}$	t_{10} (Gyr)	1.8
$M_{B,0}$	-16.44	EW [OIII]λ5007	$50.1^{69.4}_{35.8}$	t_{50} (Gyr)	0.9

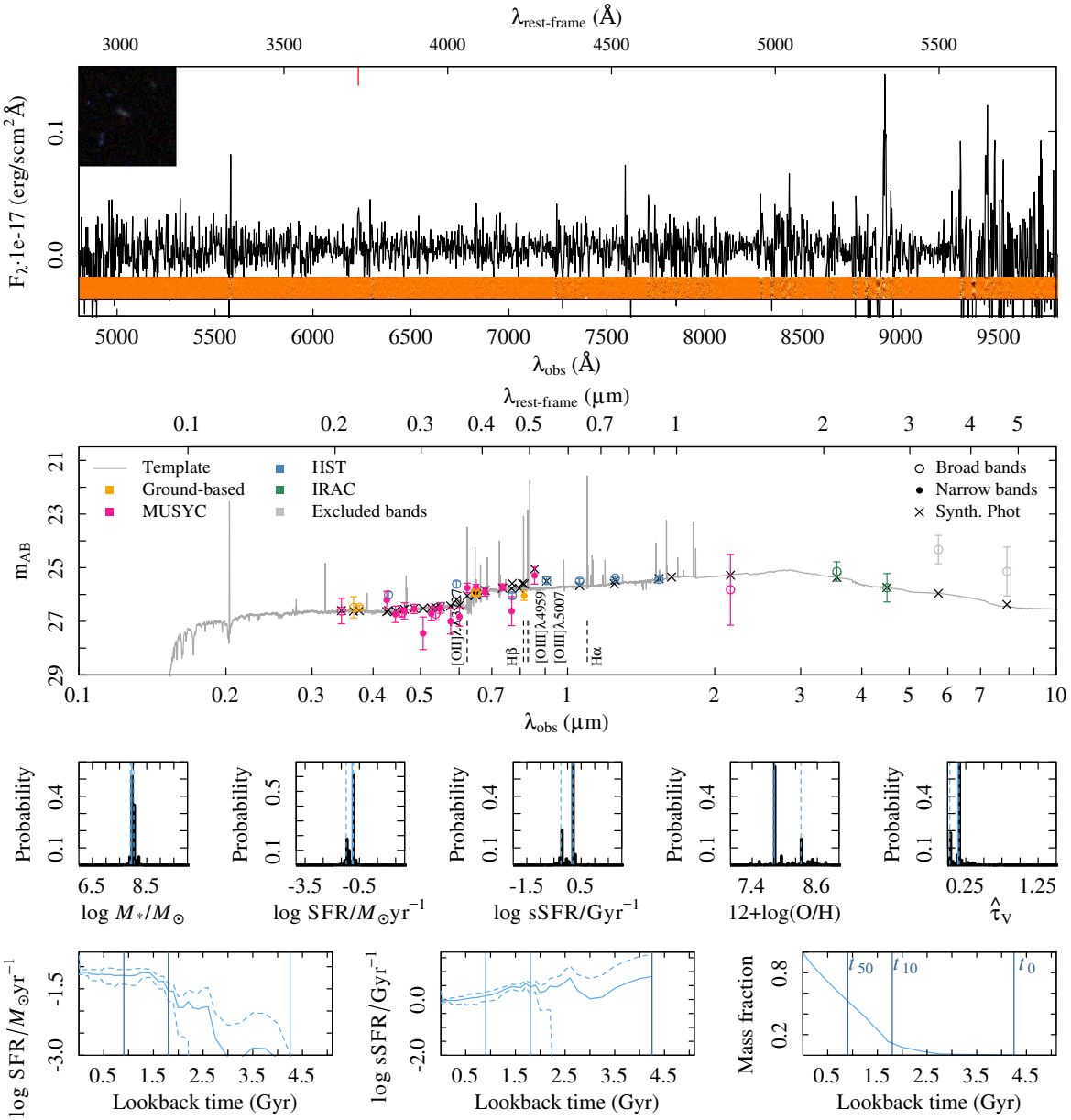

Summary ID 00235

ID	00235	$\mu_{eff,B,0}$	19.7±10.0	F Hα ($\times 10^{17}$)	–
α (deg; J2000)	53.050663	$(B-V)_0$	0.10	EW Hα	–
δ (deg; J2000)	-27.741784	F Hβ ($\times 10^{17}$)	–	log $M_*/M_\odot$	$7.9^{8.0}_{7.6}$
i (mag)	25.93±0.18	EW Hβ	–	log SFR/$M_\odot\, yr^{-1}$	$-0.4^{-0.3}_{-0.4}$
J (mag)	26.58±1.23	F [OII]$\lambda\lambda$3727 ($\times 10^{17}$)	–	log sSFR/Gyr^{-1}	$0.8^{1.0}_{0.7}$
z_{spec}	0.840/3	EW [OII]$\lambda\lambda$3727	–	$\hat{\tau}_V$	$0.2^{0.3}_{0.1}$
Morph.	Irr	F [OIII]λ4959 ($\times 10^{17}$)	–	12+log(O/H)	$7.4^{7.6}_{7.2}$
n	5.1±108.7	EW [OIII]λ4959	–	t_0 (Gyr)	3.2
$R_{eff,v,0}$	0.1±7.3	F [OIII]λ5007 ($\times 10^{17}$)	–	t_{10} (Gyr)	1.6
$M_{B,0}$	-17.50	EW [OIII]λ5007	–	t_{50} (Gyr)	0.2

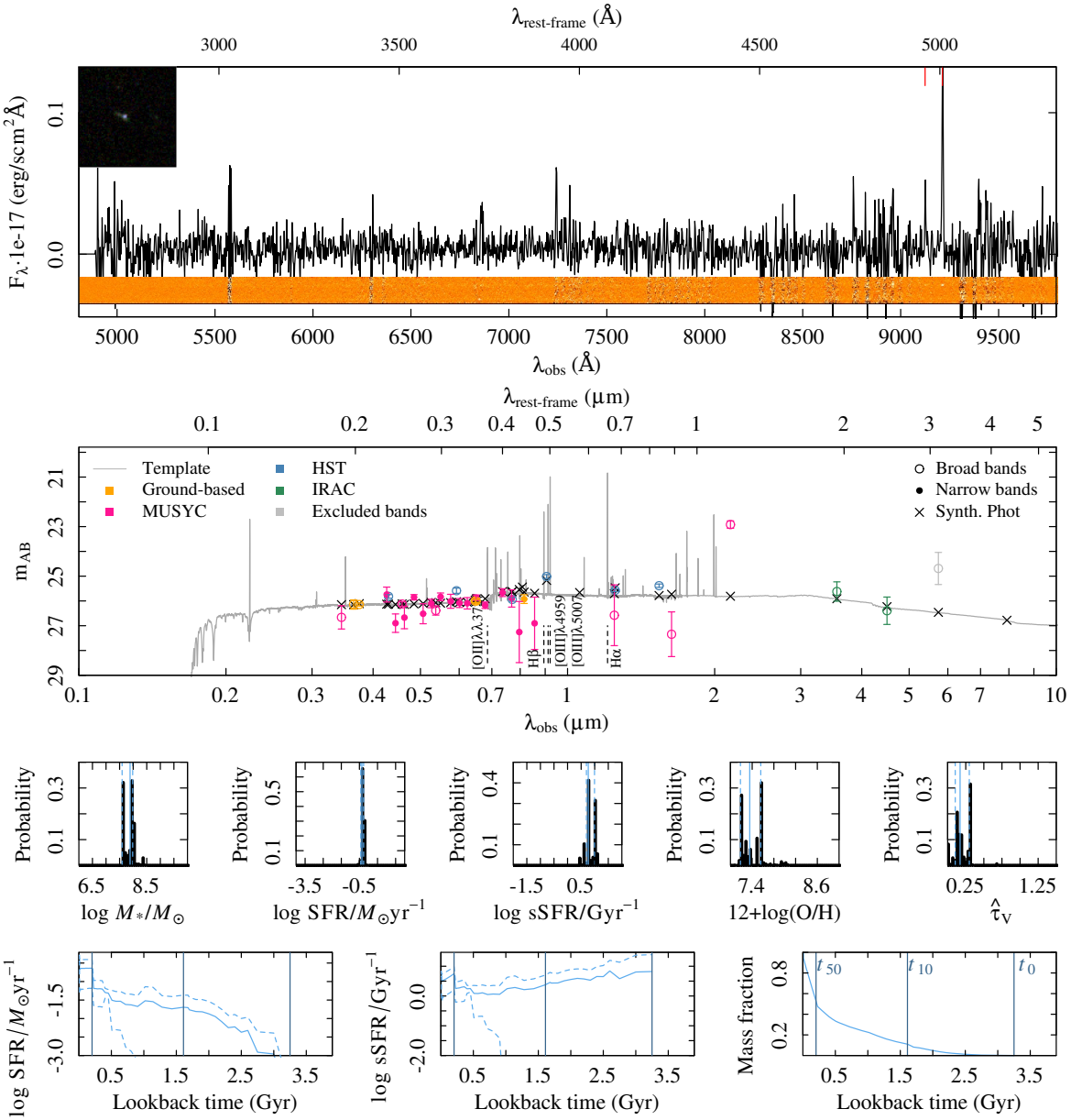

Summary ID 00236

ID	00236	$\mu_{eff,B,0}$	23.4±0.2	F Hα ($\times 10^{17}$)	$1.8^{2}_{1.6}$
α (deg; J2000)	53.050473	$(B-V)_0$	0.87	EW Hα	$78.3^{104.4}_{61.3}$
δ (deg; J2000)	-27.821149	F Hβ ($\times 10^{17}$)	$0.4^{0.6}_{0.1}$	log $M_*/M_\odot$	$7.7^{7.7}_{7.6}$
i (mag)	24.86±0.12	EW Hβ	$9.6^{18.1}_{2.8}$	log SFR/$M_\odot\, yr^{-1}$	$-1.6^{-1.3}_{-1.6}$
J (mag)	25.33±0.66	F [OII]$\lambda\lambda$3727 ($\times 10^{17}$)	$0.4^{0.6}_{0.2}$	log sSFR/Gyr^{-1}	$-0.3^{-0.1}_{-0.3}$
z_{spec}	0.329/4	EW [OII]$\lambda\lambda$3727	$9.4^{15.4}_{3.9}$	$\hat{\tau}_V$	$0.2^{0.4}_{0.2}$
Morph.	Irr	F [OIII]λ4959 ($\times 10^{17}$)	$0.4^{0.6}_{0.2}$	12+log(O/H)	$8.2^{8.7}_{7.8}$
n	0.4±0.0	EW [OIII]λ4959	$9.4^{15.4}_{3.9}$	t_0 (Gyr)	5.5
$R_{eff,v,0}$	1.5±0.0	F [OIII]λ5007 ($\times 10^{17}$)	$0.4^{0.6}_{0.2}$	t_{10} (Gyr)	1.6
$M_{B,0}$	-15.56	EW [OIII]λ5007	$9.4^{15.4}_{3.9}$	t_{50} (Gyr)	0.7

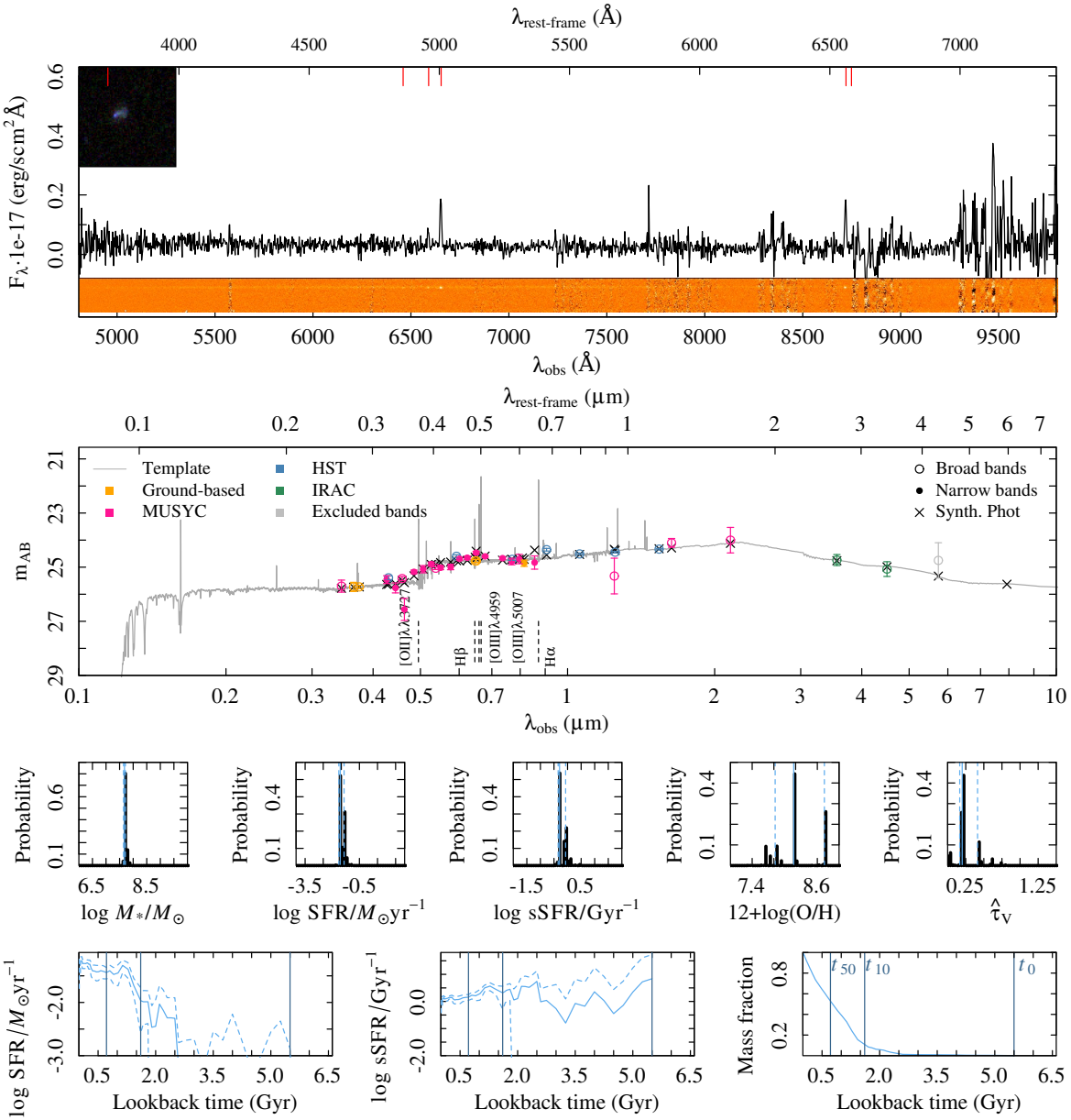

Summary ID 00237

ID	00237	$\mu_{eff,B,0}$	NaN±2.5	F Hα ($\times 10^{17}$)	–
α (deg; J2000)	53.050713	$(B-V)_0$	0.90	EW Hα	–
δ (deg; J2000)	-27.727468	F Hβ ($\times 10^{17}$)	–	log $M_*/M_\odot$	$7.6^{7.7}_{7.6}$
i (mag)	25.30±0.14	EW Hβ	–	log SFR/$M_\odot\, yr^{-1}$	$-1.3^{-1.2}_{-1.8}$
J (mag)	26.38±0.80	F [OII]$\lambda\lambda$3727 ($\times 10^{17}$)	–	log sSFR/Gyr^{-1}	$0.0^{0.2}_{-0.5}$
z_{spec}	0.423/2	EW [OII]$\lambda\lambda$3727	–	$\hat{\tau}_V$	$0.7^{0.9}_{0.2}$
Morph.	D	F [OIII]λ4959 ($\times 10^{17}$)	–	12+log(O/H)	$8.4^{8.7}_{7.8}$
n	-999.0±-999.0	EW [OIII]λ4959	–	t_0 (Gyr)	1.0
$R_{eff,v,0}$	-128.7±-128.7	F [OIII]λ5007 ($\times 10^{17}$)	–	t_{10} (Gyr)	0.7
$M_{B,0}$	-15.33	EW [OIII]λ5007	–	t_{50} (Gyr)	0.3

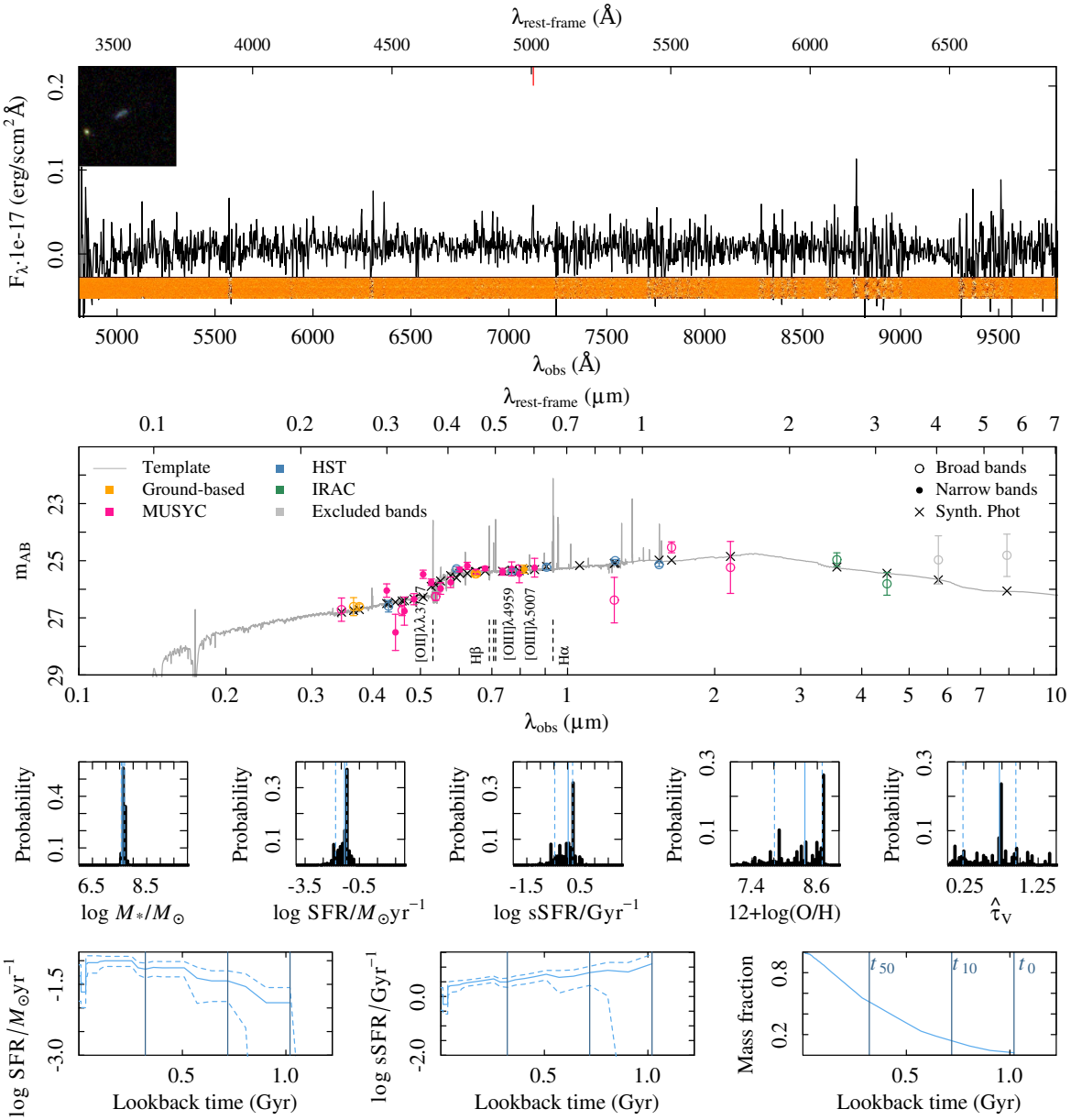

Summary ID 00241

ID	00241	$\mu_{eff,B,0}$	22.9±0.6	F Hα ($\times10^{17}$)	–
α (deg; J2000)	53.052905	$(B-V)_0$	0.79	EW Hα	–
δ (deg; J2000)	-27.759811	F Hβ ($\times10^{17}$)	$0.2^{0.3}_{0.2}$	log $M_*/M_\odot$	$7.8^{7.9}_{7.7}$
i (mag)	25.36±0.14	EW Hβ	$14.2^{24.6}_{7.9}$	log SFR$/M_\odot\,yr^{-1}$	$-0.9^{-0.8}_{-1.2}$
J (mag)	26.74±1.37	F [OII]$\lambda\lambda$3727 ($\times10^{17}$)	$0.3^{0.4}_{0.3}$	log sSFR$/Gyr^{-1}$	$0.3^{0.4}_{-0.1}$
z_{spec}	0.545/3	EW [OII]$\lambda\lambda$3727	$26.0^{138.9}_{133.6}$	$\hat{\tau}_V$	$0.8^{0.8}_{0.4}$
Morph.	D	F [OIII]λ4959 ($\times10^{17}$)	$0.3^{0.4}_{0.3}$	12+log(O/H)	$8.0^{8.0}_{7.9}$
n	1.2±0.2	EW [OIII]λ4959	$26.0^{138.9}_{133.6}$	t_0 (Gyr)	2.2
$R_{eff,v,0}$	0.8±0.0	F [OIII]λ5007 ($\times10^{17}$)	$0.3^{0.4}_{0.3}$	t_{10} (Gyr)	0.7
$M_{B,0}$	-16.05	EW [OIII]λ5007	$26.0^{138.9}_{133.6}$	t_{50} (Gyr)	0.4

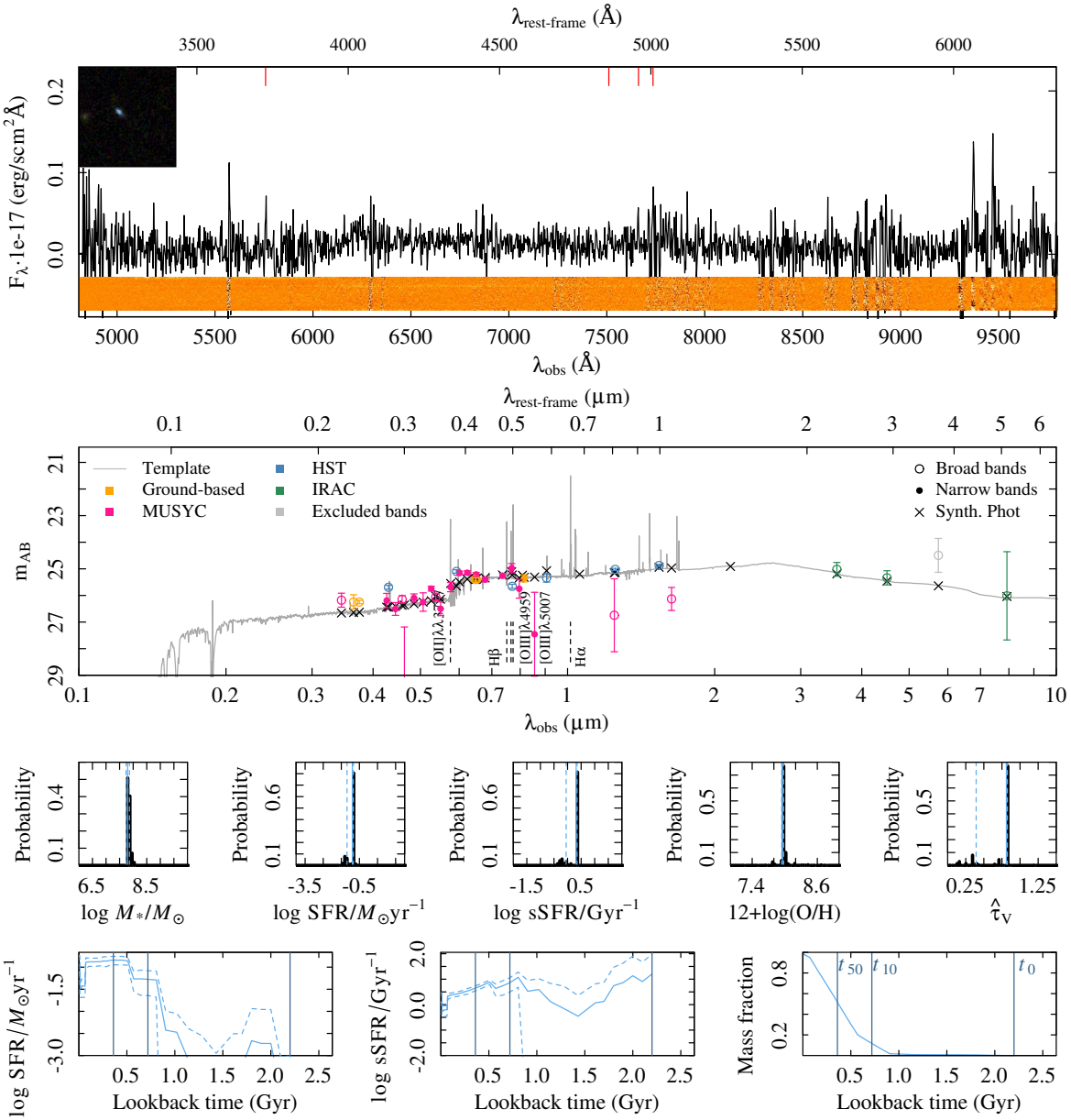

Summary ID 00253

ID	00253	$\mu_{eff,B,0}$	-Inf±NaN	F Hα ($\times 10^{17}$)	–
α (deg; J2000)	53.058174	$(B-V)_0$	0.37	EW Hα	–
δ (deg; J2000)	-27.853634	F Hβ ($\times 10^{17}$)	$0.2^{0.3}_{0.2}$	log $M_*/M_\odot$	$7.7^{7.8}_{7.7}$
i (mag)	25.86±0.22	EW Hβ	$12.2^{16.7}_{8.6}$	log SFR/$M_\odot\, yr^{-1}$	$-0.9^{-0.8}_{-1.0}$
J (mag)	24.07±0.23	F [OII]$\lambda\lambda$3727 ($\times 10^{17}$)	$0.2^{0.2}_{0.2}$	log sSFR/Gyr^{-1}	$0.4^{0.5}_{0.2}$
z_{spec}	0.760/3	EW [OII]$\lambda\lambda$3727	$64.4^{39.3}_{143.4}$	$\hat{\tau}_V$	$0.4^{0.7}_{0.2}$
Morph.	C	F [OIII]λ4959 ($\times 10^{17}$)	$0.2^{0.2}_{0.2}$	12+log(O/H)	$8.1^{8.2}_{7.9}$
n	0.0±0.0	EW [OIII]λ4959	$64.4^{39.3}_{143.4}$	t_0 (Gyr)	3.5
$R_{eff,v,0}$	0.0±0.0	F [OIII]λ5007 ($\times 10^{17}$)	$0.2^{0.2}_{0.2}$	t_{10} (Gyr)	0.9
$M_{B,0}$	-16.35	EW [OIII]λ5007	$64.4^{39.3}_{143.4}$	t_{50} (Gyr)	0.3

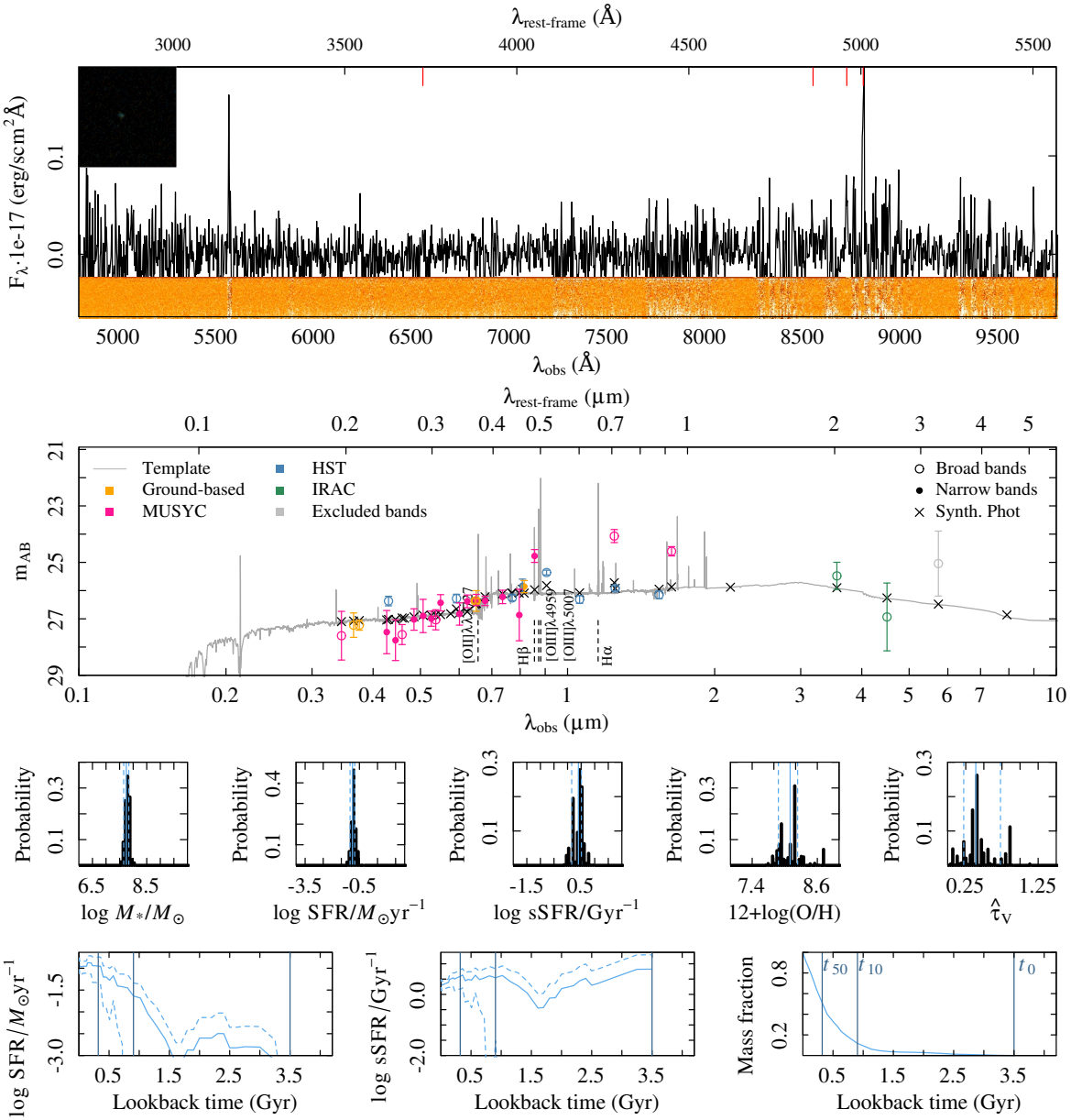

Summary ID 00259

ID	00259	$\mu_{eff,B,0}$	21.4±0.3	F Hα ($\times 10^{17}$)	–
α (deg; J2000)	53.060438	$(B-V)_0$	0.57	EW Hα	–
δ (deg; J2000)	-27.864026	F Hβ ($\times 10^{17}$)	$1.1^{2}_{0.4}$	log $M_*/M_\odot$	$8.3^{8.5}_{8.2}$
i (mag)	23.89±0.10	EW Hβ	$10.7^{23.4}_{3.0}$	log SFR/$M_\odot\, yr^{-1}$	$0.1^{0.1}_{-0.4}$
J (mag)	24.36±0.27	F [OII]$\lambda\lambda$3727 ($\times 10^{17}$)	$5.3^{6}_{4.6}$	log sSFR/Gyr^{-1}	$0.8^{0.8}_{0.2}$
z_{spec}	0.573/4	EW [OII]$\lambda\lambda$3727	$46.6^{62.8}_{35.9}$	$\hat{\tau}_V$	$1.3^{1.3}_{0.4}$
Morph.	D	F [OIII]λ4959 ($\times 10^{17}$)	$5.3^{6}_{4.6}$	12+log(O/H)	$8.2^{8.2}_{7.9}$
n	1.5±0.1	EW [OIII]λ4959	$46.6^{62.8}_{35.9}$	t_0 (Gyr)	1.7
$R_{eff,v,0}$	0.7±0.0	F [OIII]λ5007 ($\times 10^{17}$)	$5.3^{6}_{4.6}$	t_{10} (Gyr)	0.9
$M_{B,0}$	-17.82	EW [OIII]λ5007	$46.6^{62.8}_{35.9}$	t_{50} (Gyr)	0.2

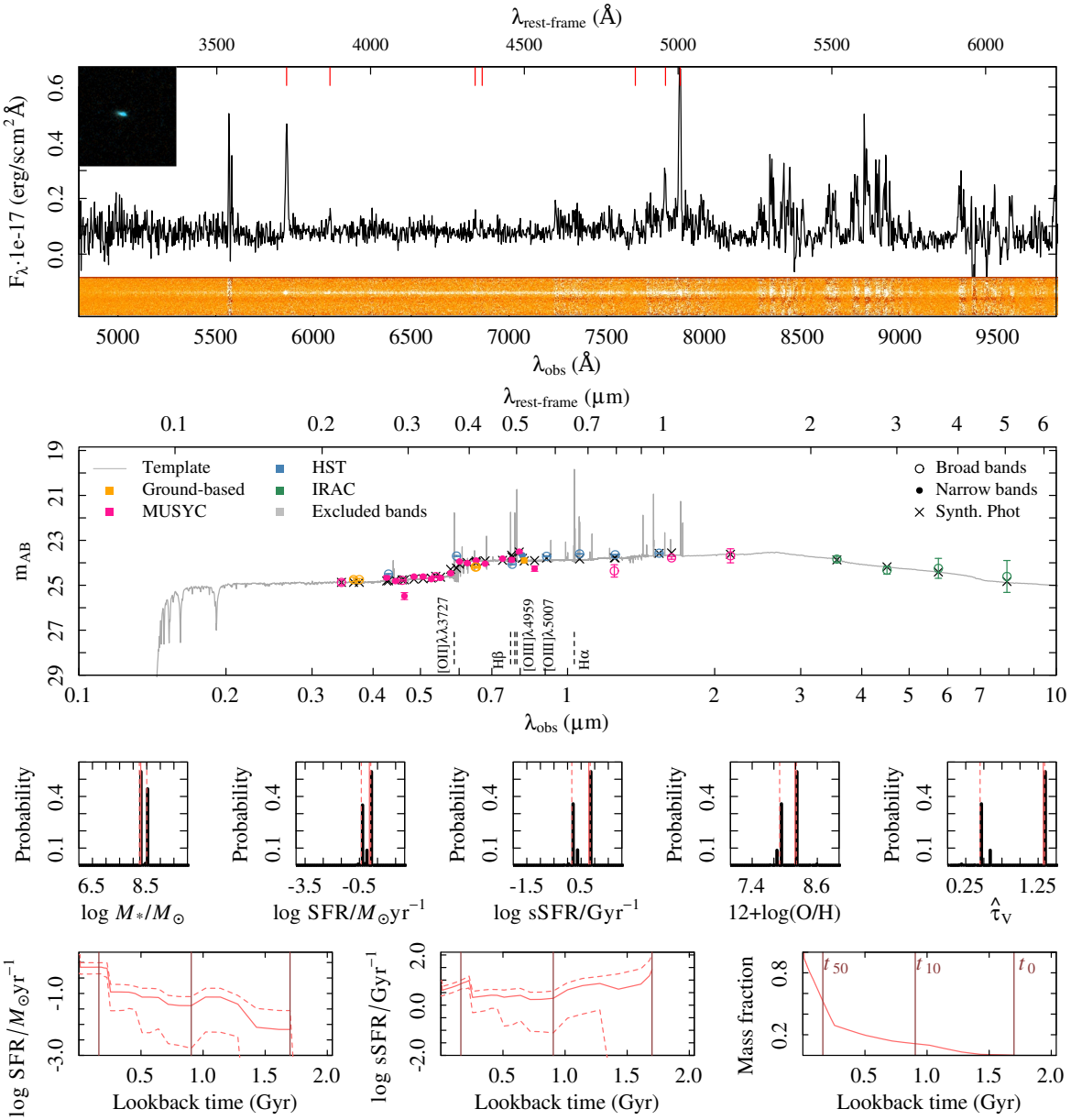

Summary ID 00277

ID	00277	$\mu_{eff,B,0}$	20.4±0.3	F Hα ($\times10^{17}$)	–
α (deg; J2000)	53.069947	$(B-V)_0$	0.63	EW Hα	–
δ (deg; J2000)	-27.847012	F Hβ ($\times10^{17}$)	–	log $M_*/M_\odot$	$7.4^{7.5}_{7.3}$
i (mag)	25.57±0.14	EW Hβ	–	log SFR/$M_\odot\,yr^{-1}$	$-0.4^{-0.4}_{-0.7}$
J (mag)	-99.99±-99.99	F [OII]$\lambda\lambda$3727 ($\times10^{17}$)	$0.3^{0.4}_{0.2}$	log sSFR/Gyr^{-1}	$1.2^{1.2}_{0.8}$
z_{spec}	0.437/3	EW [OII]$\lambda\lambda$3727	$18.0^{31.7}_{9.1}$	$\hat{\tau}_V$	$1.0^{1.0}_{0.5}$
Morph.	Irr	F [OIII]λ4959 ($\times10^{17}$)	$0.3^{0.4}_{0.2}$	12+log(O/H)	$7.1^{7.2}_{7.1}$
n	1.8±0.2	EW [OIII]λ4959	$18.0^{31.7}_{9.1}$	t_0 (Gyr)	3.5
$R_{eff,v,0}$	0.4±0.0	F [OIII]λ5007 ($\times10^{17}$)	$0.3^{0.4}_{0.2}$	t_{10} (Gyr)	0.4
$M_{B,0}$	-15.84	EW [OIII]λ5007	$18.0^{31.7}_{9.1}$	t_{50} (Gyr)	0.1

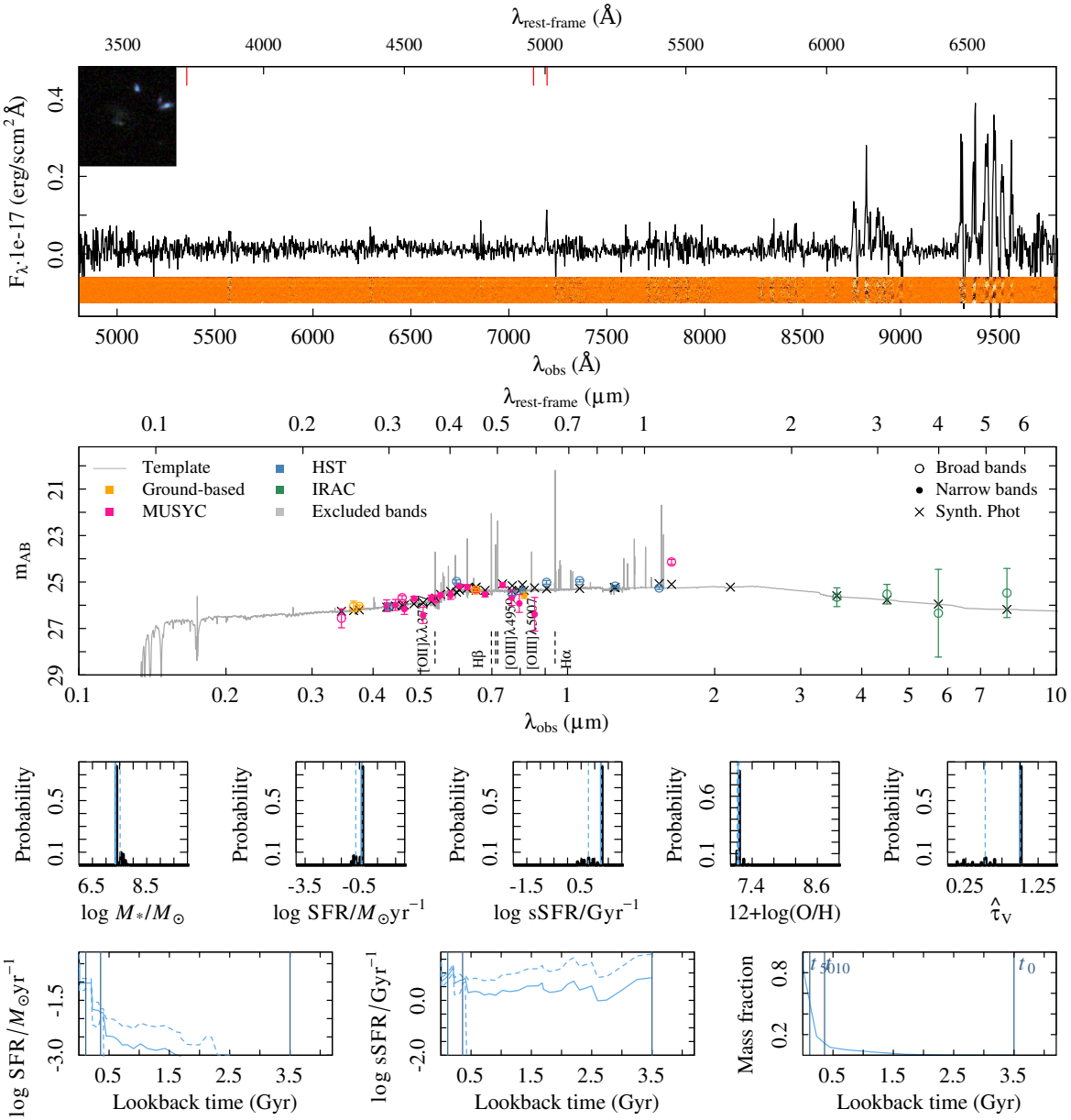

Summary ID 00293

ID	00293	$\mu_{eff,B,0}$	21.0±0.4	F Hα ($\times10^{17}$)	–
α (deg; J2000)	53.081321	$(B-V)_0$	0.74	EW Hα	–
δ (deg; J2000)	-27.712291	F Hβ ($\times10^{17}$)	$0.2^{0.3}_{0.1}$	log $M_*/M_\odot$	$8.2^{8.3}_{8.1}$
i (mag)	24.93±0.11	EW Hβ	$13.7^{21.4}_{8.2}$	log SFR/$M_\odot\,yr^{-1}$	$-0.7^{-0.4}_{-1.0}$
J (mag)	-99.99±-99.99	F [OII]$\lambda\lambda$3727 ($\times10^{17}$)	$0.4^{0.5}_{0.3}$	log sSFR/Gyr^{-1}	$0.0^{0.3}_{-0.2}$
z_{spec}	0.545/3	EW [OII]$\lambda\lambda$3727	$39.8^{70.1}_{27.3}$	$\hat{\tau}_V$	$0.6^{0.9}_{0.3}$
Morph.	Irr	F [OIII]λ4959 ($\times10^{17}$)	$0.4^{0.5}_{0.3}$	12+log(O/H)	$7.7^{8.2}_{7.6}$
n	2.2±0.3	EW [OIII]λ4959	$39.8^{70.1}_{27.3}$	t_0 (Gyr)	2.5
$R_{eff,v,0}$	4.7±0.9	F [OIII]λ5007 ($\times10^{17}$)	$0.4^{0.5}_{0.3}$	t_{10} (Gyr)	1.4
$M_{B,0}$	-16.61	EW [OIII]λ5007	$39.8^{70.1}_{27.3}$	t_{50} (Gyr)	0.7

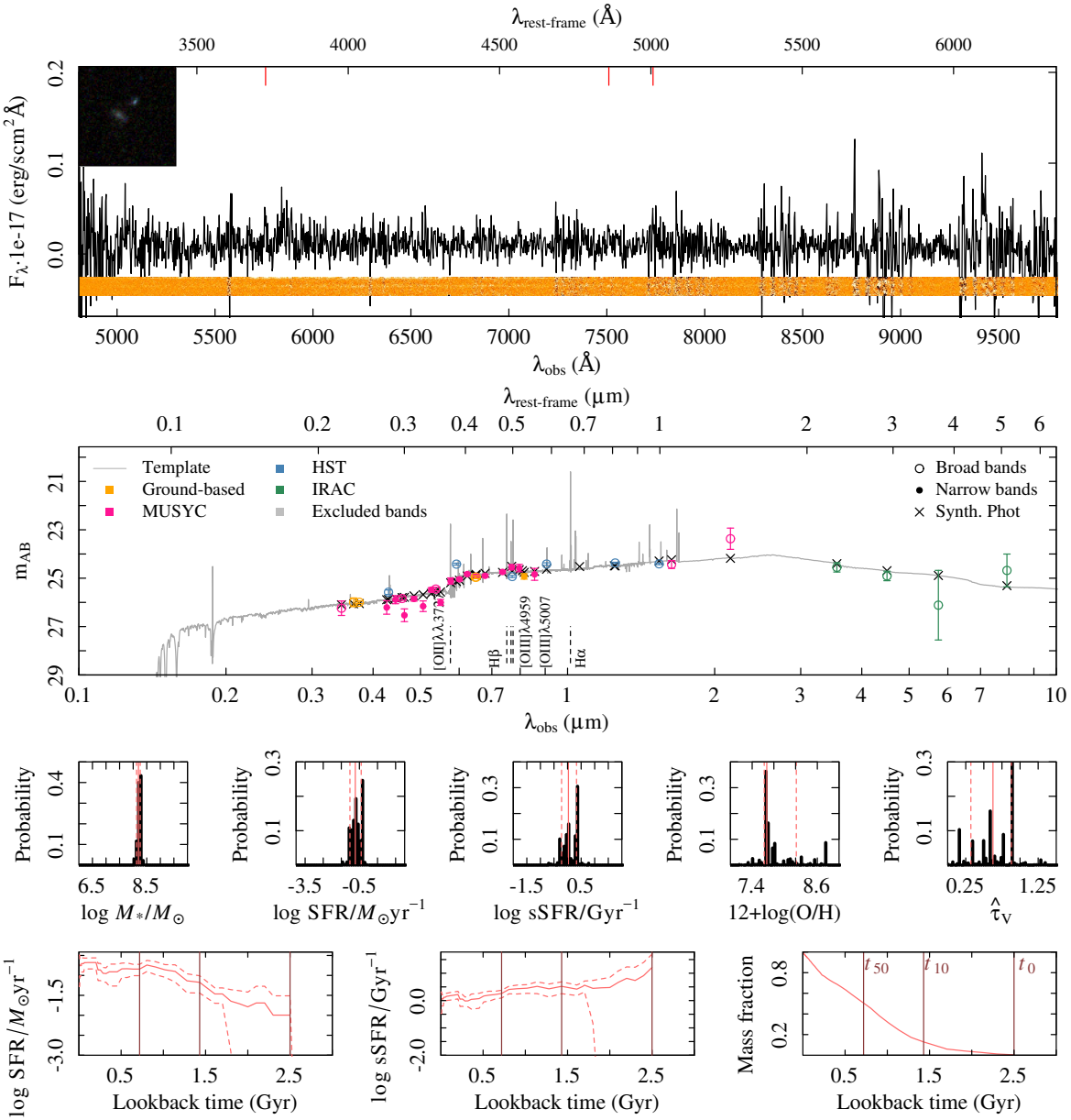

Summary ID 00296

ID	00296	$\mu_{eff,B,0}$	20.1±0.3	F Hα ($\times 10^{17}$)	$3.5^{3.6}_{3.5}$
α (deg; J2000)	53.085689	$(B-V)_0$	0.34	EW Hα	$433.6^{582.9}_{347.4}$
δ (deg; J2000)	-27.852992	F Hβ ($\times 10^{17}$)	$1.5^{1.5}_{1.4}$	log $M_*/M_\odot$	$7.6^{7.6}_{7.6}$
i (mag)	25.23±0.12	EW Hβ	$124.9^{152.0}_{103.4}$	log SFR/$M_\odot\, yr^{-1}$	$-1.1^{-1.1}_{-1.2}$
J (mag)	24.80±0.27	F [OII]$\lambda\lambda$3727 ($\times 10^{17}$)	–	log sSFR/Gyr^{-1}	$0.3^{0.3}_{0.2}$
z_{spec}	0.261/4	EW [OII]$\lambda\lambda$3727	–	$\hat{\tau}_V$	$0.1^{0.1}_{0.0}$
Morph.	C	F [OIII]λ4959 ($\times 10^{17}$)	–	12+log(O/H)	$7.6^{7.6}_{7.6}$
n	8.0±1.9	EW [OIII]λ4959	–	t_0 (Gyr)	8.5
$R_{eff,v,0}$	0.4±0.0	F [OIII]λ5007 ($\times 10^{17}$)	–	t_{10} (Gyr)	6.8
$M_{B,0}$	-15.25	EW [OIII]λ5007	–	t_{50} (Gyr)	3.0

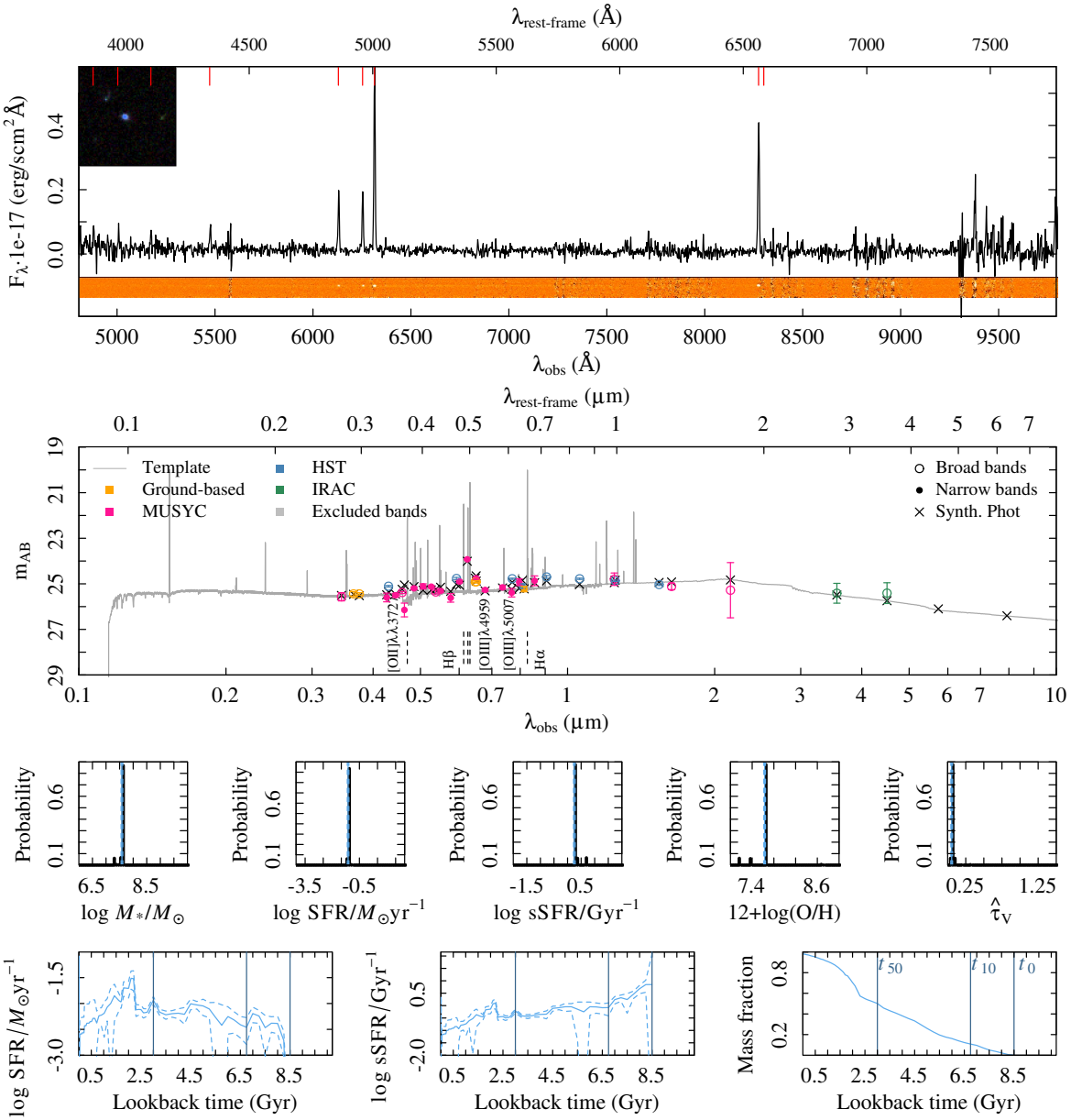

Summary ID 00297

ID	00297	$\mu_{eff,B,0}$	21.5±0.3	F Hα ($\times10^{17}$)	–
α (deg; J2000)	53.087576	$(B-V)_0$	0.64	EW Hα	–
δ (deg; J2000)	-27.856864	F Hβ ($\times10^{17}$)	$0.3^{0.4}_{0.3}$	log $M_*/M_\odot$	$7.7^{7.8}_{7.6}$
i (mag)	25.69±0.14	EW Hβ	$69.2^{104.6}_{48.6}$	log SFR/$M_\odot\,yr^{-1}$	$-0.8^{-0.7}_{-0.9}$
J (mag)	25.36±0.31	F [OII]$\lambda\lambda$3727 ($\times10^{17}$)	–	log sSFR/Gyr^{-1}	$0.5^{0.6}_{0.4}$
z_{spec}	0.446/3	EW [OII]$\lambda\lambda$3727	–	$\hat{\tau}_V$	$0.5^{0.6}_{0.4}$
Morph.	C	F [OIII]λ4959 ($\times10^{17}$)	–	12+log(O/H)	$7.1^{7.2}_{7.1}$
n	3.3±0.7	EW [OIII]λ4959	–	t_0 (Gyr)	6.0
$R_{eff,v,0}$	2.2±0.5	F [OIII]λ5007 ($\times10^{17}$)	–	t_{10} (Gyr)	3.2
$M_{B,0}$	-15.30	EW [OIII]λ5007	–	t_{50} (Gyr)	1.7

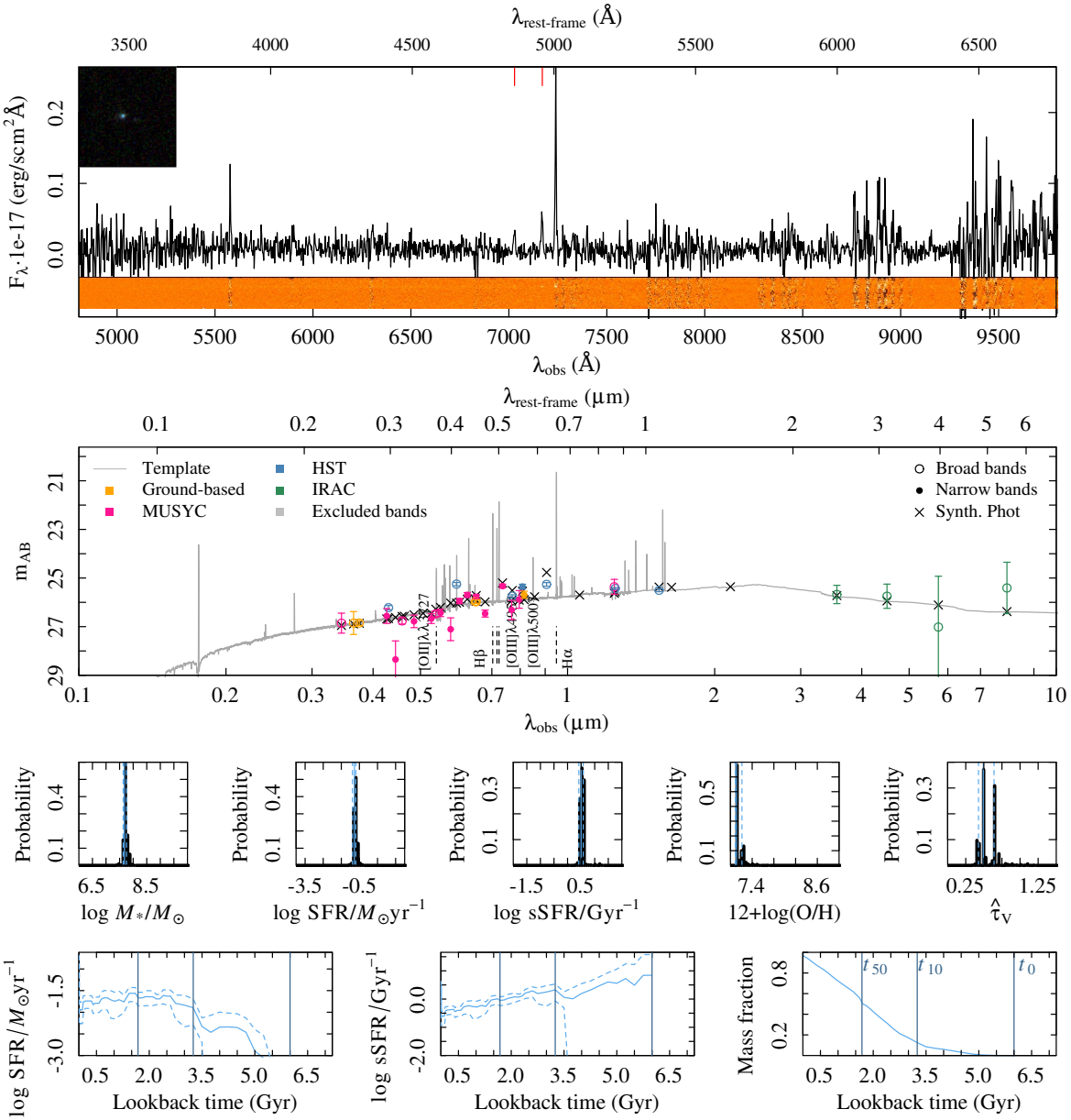

Summary ID 00306

ID	00306	$\mu_{eff,B,0}$	16.4±83755655.5	F Hα ($\times10^{17}$)	–
α (deg; J2000)	53.090336	$(B-V)_0$	0.54	EW Hα	–
δ (deg; J2000)	-27.779161	F Hβ ($\times10^{17}$)	$0.6^{0.8}_{0.5}$	log $M_*/M_\odot$	$7.9^{7.9}_{7.9}$
i (mag)	24.71±0.11	EW Hβ	$24.9^{47.1}_{16.8}$	log SFR/$M_\odot\,yr^{-1}$	$-0.4^{-0.3}_{-0.4}$
J (mag)	-99.99±-99.99	F [OII]$\lambda\lambda$3727 ($\times10^{17}$)	$1.2^{1.3}_{1.0}$	log sSFR/Gyr^{-1}	$0.7^{0.7}_{0.6}$
z_{spec}	0.576/3	EW [OII]$\lambda\lambda$3727	$45.5^{61.1}_{34.8}$	$\hat{\tau}_V$	$0.8^{0.8}_{0.8}$
Morph.	Irr	F [OIII]λ4959 ($\times10^{17}$)	$1.2^{1.3}_{1.0}$	12+log(O/H)	$8.2^{8.3}_{8.2}$
n	2.2±0.2	EW [OIII]λ4959	$45.5^{61.1}_{34.8}$	t_0 (Gyr)	1.3
$R_{eff,v,0}$	1.4±0.1	F [OIII]λ5007 ($\times10^{17}$)	$1.2^{1.3}_{1.0}$	t_{10} (Gyr)	0.4
$M_{B,0}$	-17.11	EW [OIII]λ5007	$45.5^{61.1}_{34.8}$	t_{50} (Gyr)	0.2

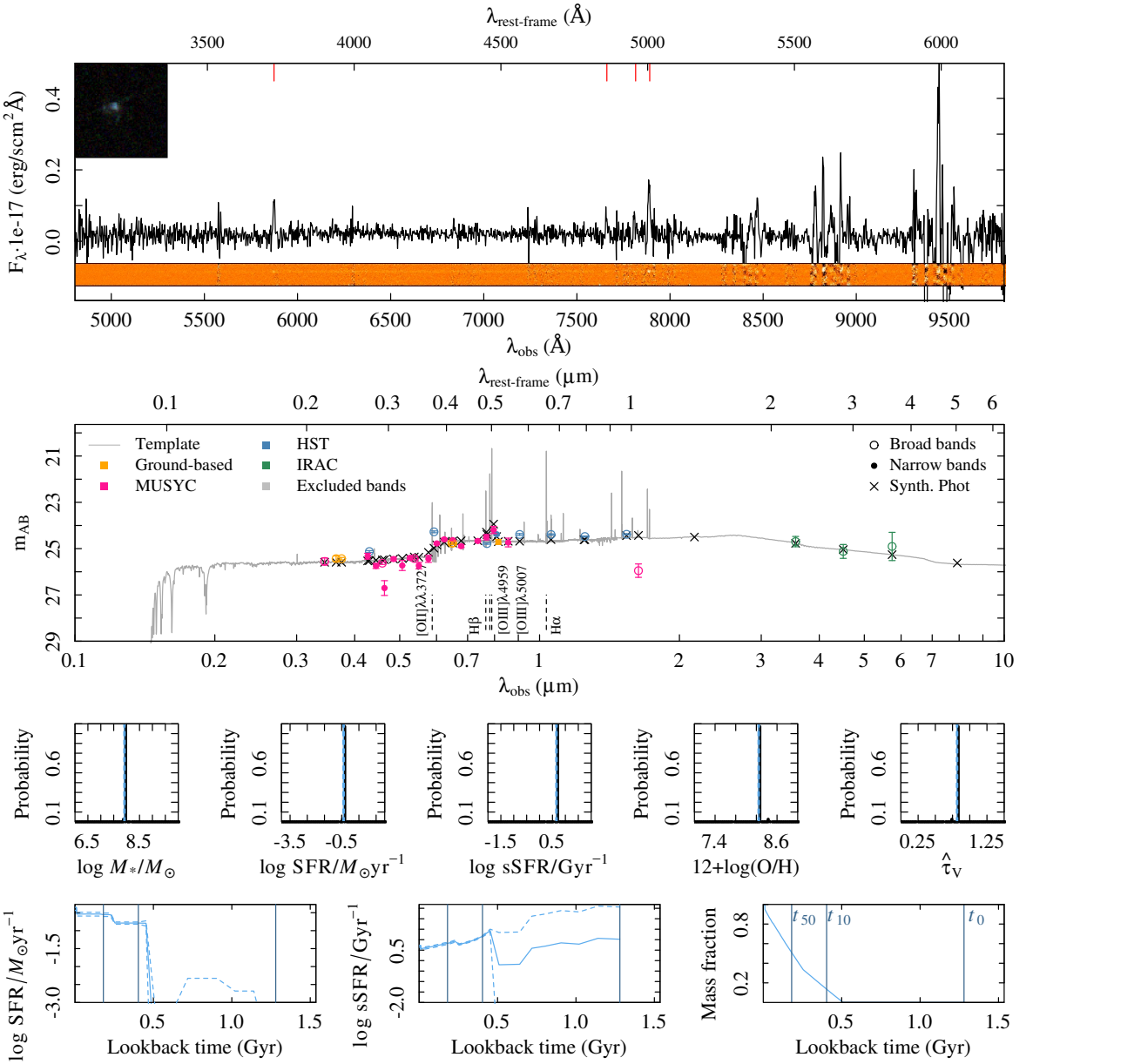

Summary ID 00312

ID	00312	$\mu_{eff,B,0}$	21.9±0.4	F Hα ($\times 10^{17}$)	–
α (deg; J2000)	53.093497	$(B-V)_0$	0.21	EW Hα	–
δ (deg; J2000)	-27.702559	F Hβ ($\times 10^{17}$)	–	log $M_*/M_\odot$	$9.4^{9.4}_{9.2}$
i (mag)	24.73±0.11	EW Hβ	–	log SFR/$M_\odot\, yr^{-1}$	$0.7^{0.8}_{0.6}$
J (mag)	23.78±0.09	F [OII]$\lambda\lambda$3727 ($\times 10^{17}$)	$2.7^{2.9}_{2.6}$	log sSFR/Gyr^{-1}	$0.3^{0.4}_{0.3}$
z_{spec}	1.216/2	EW [OII]$\lambda\lambda$3727	$77.0^{101.3}_{60.3}$	$\hat{\tau}_V$	$0.3^{0.3}_{0.3}$
Morph.	C	F [OIII]λ4959 ($\times 10^{17}$)	$2.7^{2.9}_{2.6}$	12+log(O/H)	$8.7^{8.7}_{8.7}$
n	4.2±0.8	EW [OIII]λ4959	$77.0^{101.3}_{60.3}$	t_0 (Gyr)	3.5
$R_{eff,v,0}$	1.6±0.1	F [OIII]λ5007 ($\times 10^{17}$)	$2.7^{2.9}_{2.6}$	t_{10} (Gyr)	2.3
$M_{B,0}$	-19.62	EW [OIII]λ5007	$77.0^{101.3}_{60.3}$	t_{50} (Gyr)	1.4

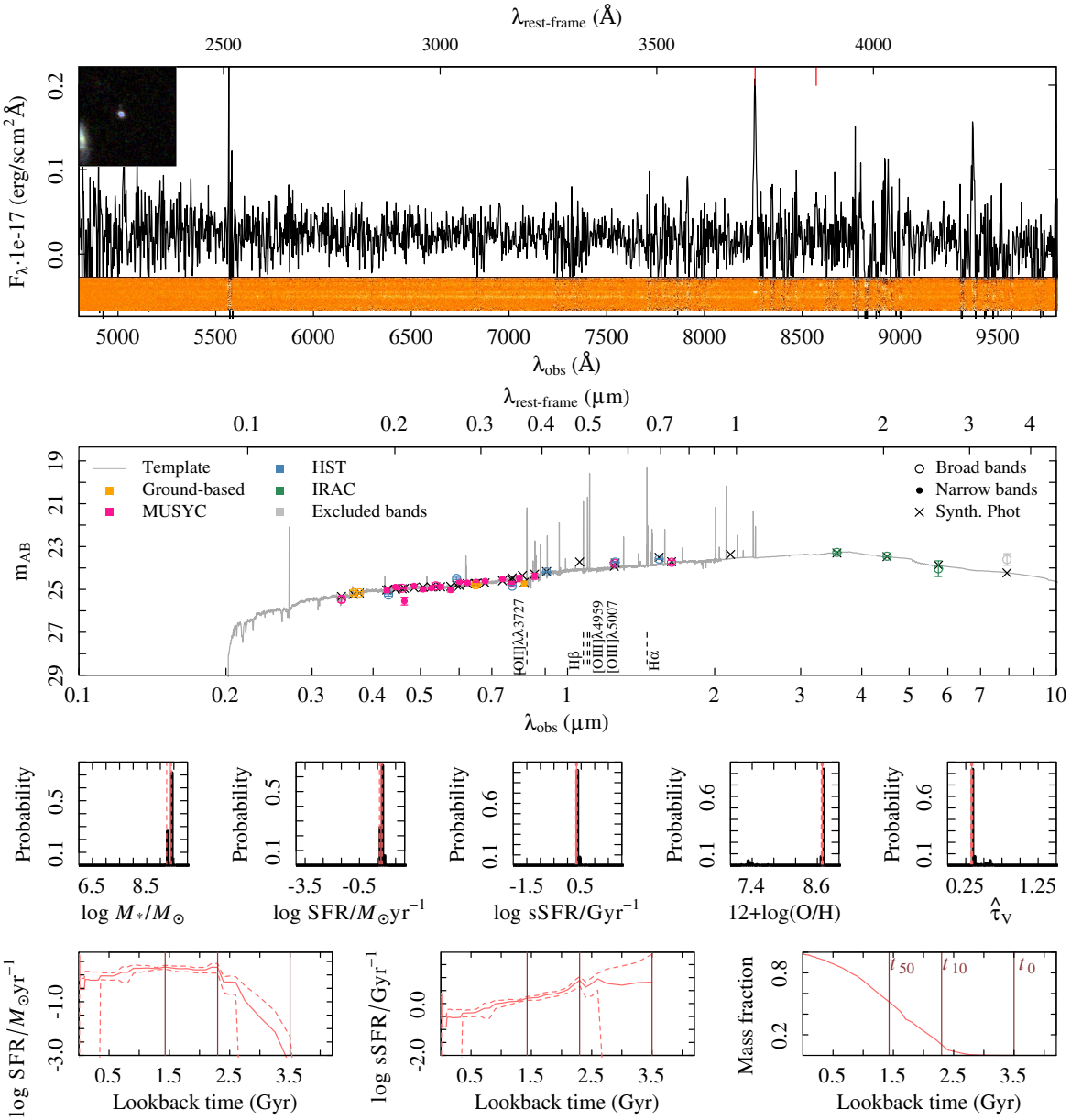

Summary ID 00315

ID	00315	$\mu_{eff,B,0}$	23.4±0.3	F Hα ($\times 10^{17}$)	$0.4^{0.5}_{0.3}$
α (deg; J2000)	53.096709	$(B-V)_0$	0.52	EW Hα	$41.3^{176.9}_{16.6}$
δ (deg; J2000)	-27.868291	F Hβ ($\times 10^{17}$)	–	log $M_*/M_\odot$	$6.9^{7.0}_{6.9}$
i (mag)	26.05±0.19	EW Hβ	–	log SFR/$M_\odot\, yr^{-1}$	$-2.7^{-2.7}_{-2.8}$
J (mag)	-99.99±-99.99	F [OII]$\lambda\lambda$3727 ($\times 10^{17}$)	–	log sSFR/Gyr^{-1}	$-0.7^{-0.6}_{-0.7}$
z_{spec}	0.132/2	EW [OII]$\lambda\lambda$3727	–	$\hat{\tau}_V$	$0.2^{0.2}_{0.2}$
Morph.	D	F [OIII]λ4959 ($\times 10^{17}$)	–	12+log(O/H)	$8.6^{8.6}_{8.6}$
n	1.3±0.2	EW [OIII]λ4959	–	t_0 (Gyr)	9.8
$R_{eff,v,0}$	0.6±0.1	F [OIII]λ5007 ($\times 10^{17}$)	–	t_{10} (Gyr)	8.2
$M_{B,0}$	-12.06	EW [OIII]λ5007	–	t_{50} (Gyr)	4.5

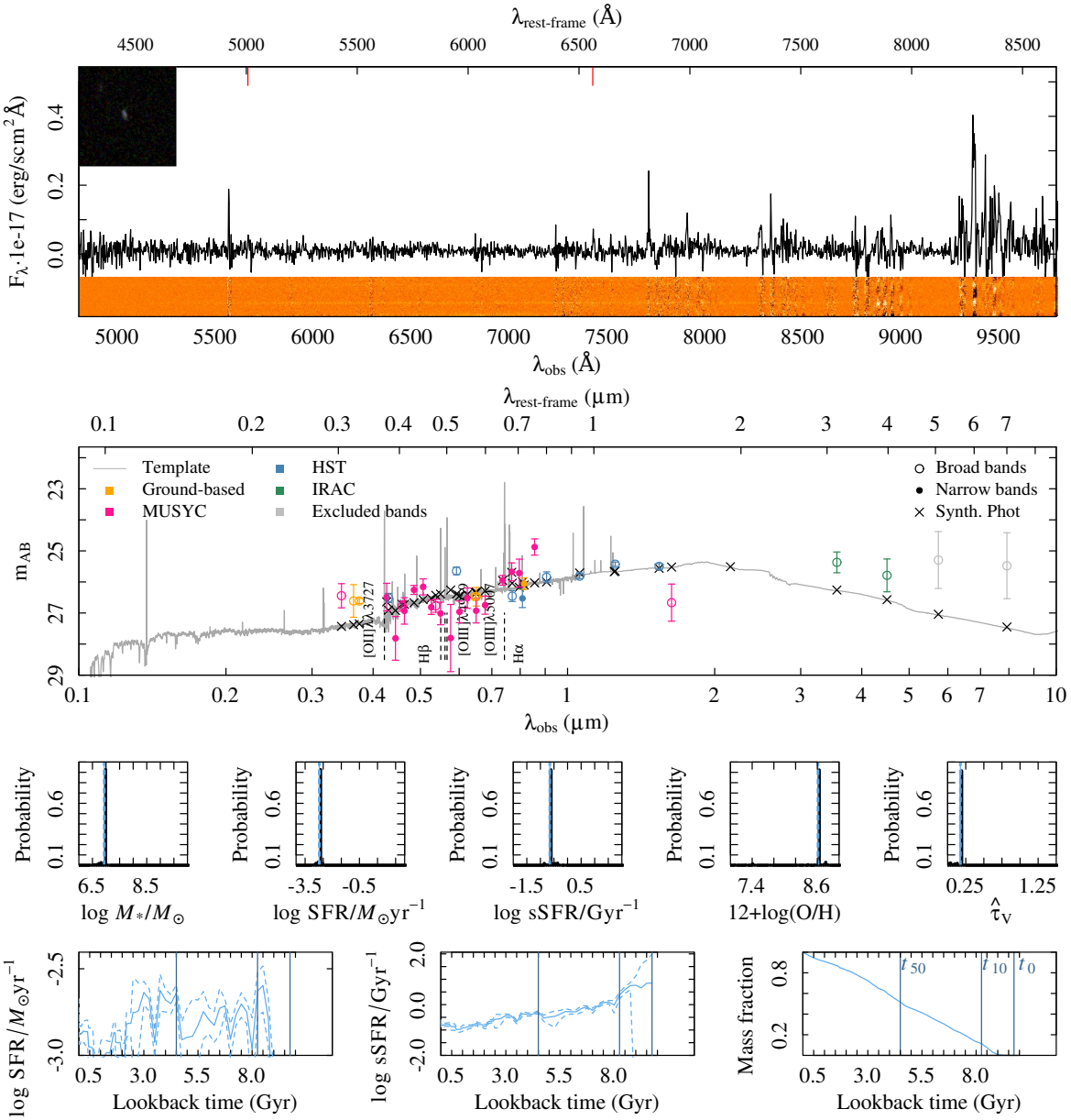

Summary ID 00317

ID	00317	$\mu_{eff,B,0}$	23.4±0.3	F Hα ($\times10^{17}$)	–
α (deg; J2000)	53.100644	$(B-V)_0$	0.65	EW Hα	–
δ (deg; J2000)	-27.662545	F Hβ ($\times10^{17}$)	–	log $M_*/M_\odot$	$8.2^{8.3}_{8.1}$
i (mag)	24.34±0.10	EW Hβ	–	log SFR/$M_\odot\,yr^{-1}$	$-0.7^{-0.6}_{-1.1}$
J (mag)	25.34±0.35	F [OII]$\lambda\lambda$3727 ($\times10^{17}$)	$1^{1.2}_{0.8}$	log sSFR/Gyr^{-1}	$0.0^{0.2}_{-0.2}$
z_{spec}	0.620/3	EW [OII]$\lambda\lambda$3727	$44.5^{71.1}_{29.5}$	$\hat{\tau}_V$	$0.5^{0.7}_{0.5}$
Morph.	Irr	F [OIII]λ4959 ($\times10^{17}$)	$1^{1.2}_{0.8}$	12+log(O/H)	$7.8^{8.4}_{7.6}$
n	0.2±0.0	EW [OIII]λ4959	$44.5^{71.1}_{29.5}$	t_0 (Gyr)	2.5
$R_{eff,v,0}$	2.4±0.1	F [OIII]λ5007 ($\times10^{17}$)	$1^{1.2}_{0.8}$	t_{10} (Gyr)	0.6
$M_{B,0}$	-17.05	EW [OIII]λ5007	$44.5^{71.1}_{29.5}$	t_{50} (Gyr)	0.3

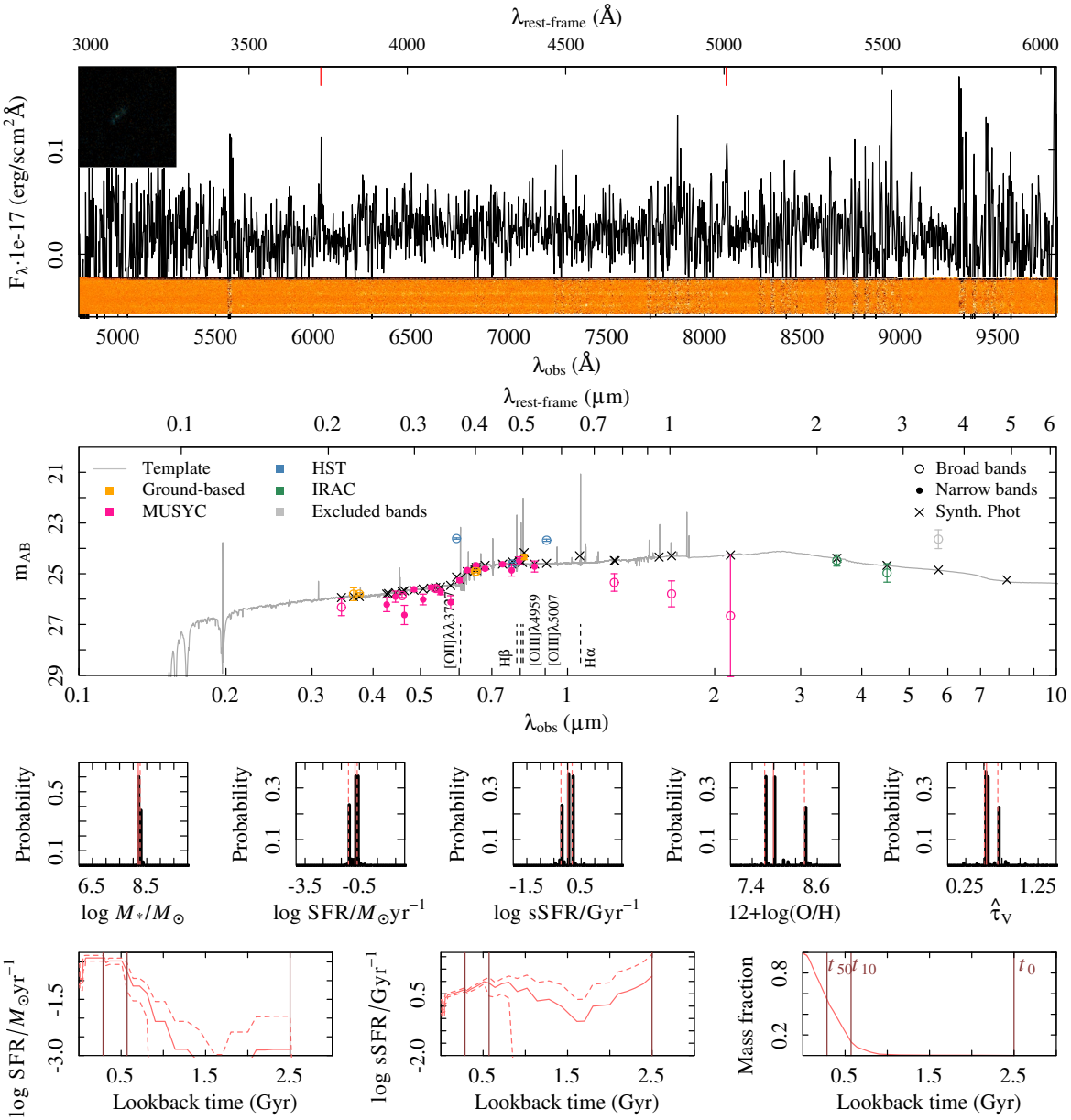

Summary ID 00386

ID	00386	$\mu_{eff,B,0}$	22.6±0.2	F Hα ($\times10^{17}$)	$1^{1.1}_{0.8}$
α (deg; J2000)	53.132339	$(B-V)_0$	1.00	EW Hα	$61.9^{101.6}_{39.9}$
δ (deg; J2000)	-27.736744	F Hβ ($\times10^{17}$)	$0.3^{0.5}_{0}$	log $M_*/M_\odot$	$8.1^{8.2}_{8.1}$
i (mag)	24.25±0.11	EW Hβ	$6.2^{13.4}_{0.9}$	log SFR/$M_\odot\,yr^{-1}$	$-0.9^{-0.8}_{-1.2}$
J (mag)	24.07±0.22	F [OII]$\lambda\lambda$3727 ($\times10^{17}$)	$0.7^{0.8}_{0.5}$	log sSFR/Gyr^{-1}	$0.0^{0.0}_{-0.4}$
z_{spec}	0.400/4	EW [OII]$\lambda\lambda$3727	$23.7^{35.3}_{15.8}$	$\hat{\tau}_V$	$0.9^{1.1}_{0.4}$
Morph.	D	F [OIII]λ4959 ($\times10^{17}$)	$0.7^{0.8}_{0.5}$	12+log(O/H)	$8.3^{8.5}_{8.3}$
n	0.4±0.1	EW [OIII]λ4959	$23.7^{35.3}_{15.8}$	t_0 (Gyr)	4.2
$R_{eff,v,0}$	2.0±0.0	F [OIII]λ5007 ($\times10^{17}$)	$0.7^{0.8}_{0.5}$	t_{10} (Gyr)	1.8
$M_{B,0}$	-16.00	EW [OIII]λ5007	$23.7^{35.3}_{15.8}$	t_{50} (Gyr)	0.8

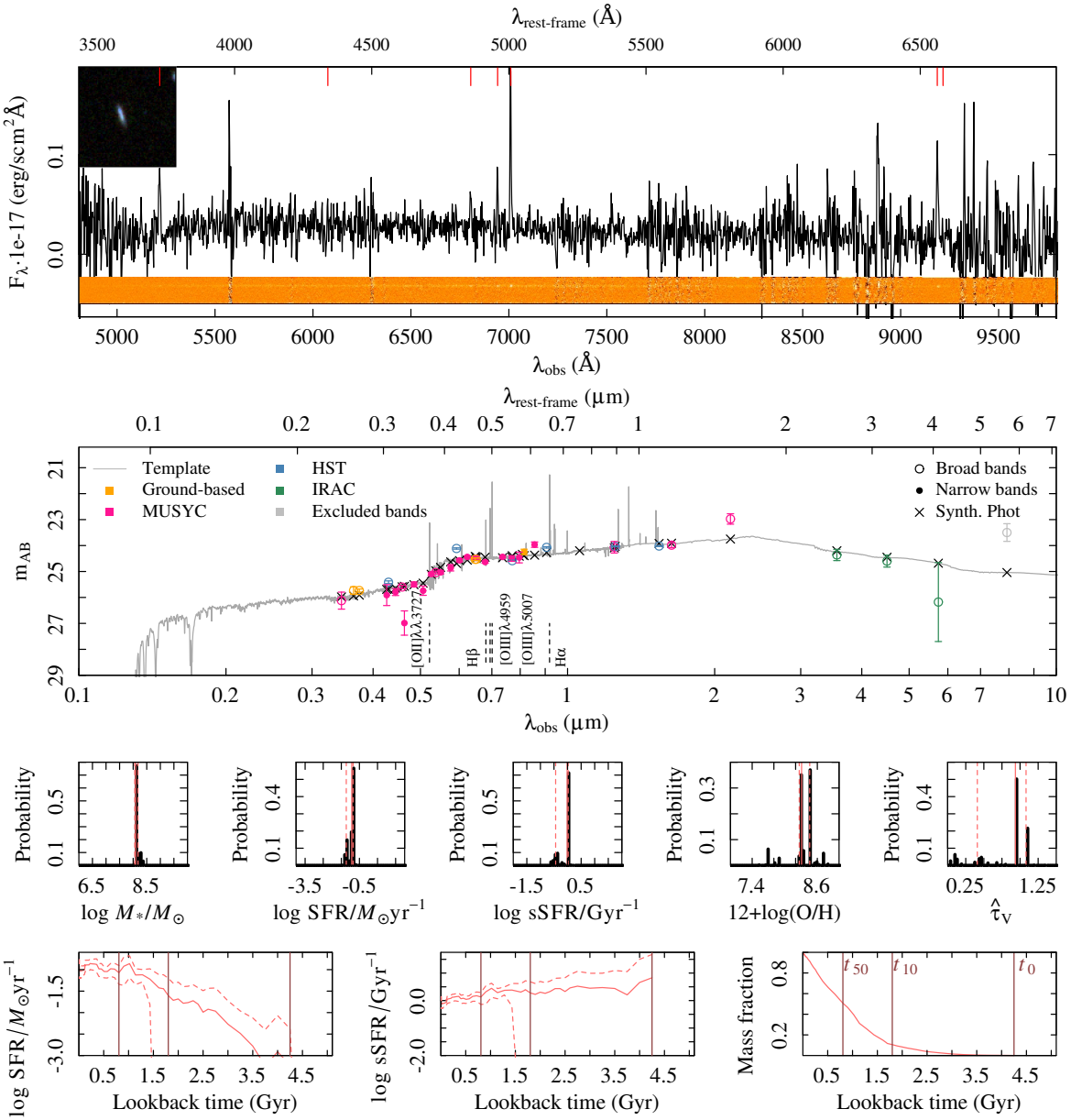

Summary ID 00396

ID	00396	$\mu_{eff,B,0}$	23.0±0.1	F Hα ($\times10^{17}$)	$0.7^{0.8}_{0.5}$
α (deg; J2000)	53.141056	$(B-V)_0$	0.76	EW Hα	$38.9^{54.0}_{27.3}$
δ (deg; J2000)	-27.881795	F Hβ ($\times10^{17}$)	–	log $M_*/M_\odot$	$7.3^{7.4}_{7.3}$
i (mag)	24.71±0.12	EW Hβ	–	log SFR/$M_\odot\,yr^{-1}$	$-1.8^{-1.7}_{-2.0}$
J (mag)	24.17±0.14	F [OII]$\lambda\lambda$3727 ($\times10^{17}$)	–	log sSFR/Gyr^{-1}	$-0.1^{-0.1}_{-0.3}$
z_{spec}	0.310/3	EW [OII]$\lambda\lambda$3727	–	$\hat{\tau}_V$	$0.4^{0.5}_{0.0}$
Morph.	Irr	F [OIII]λ4959 ($\times10^{17}$)	–	12+log(O/H)	$7.7^{7.9}_{7.7}$
n	0.4±0.0	EW [OIII]λ4959	–	t_0 (Gyr)	0.9
$R_{eff,v,0}$	0.7±0.0	F [OIII]λ5007 ($\times10^{17}$)	–	t_{10} (Gyr)	0.5
$M_{B,0}$	-15.51	EW [OIII]λ5007	–	t_{50} (Gyr)	0.2

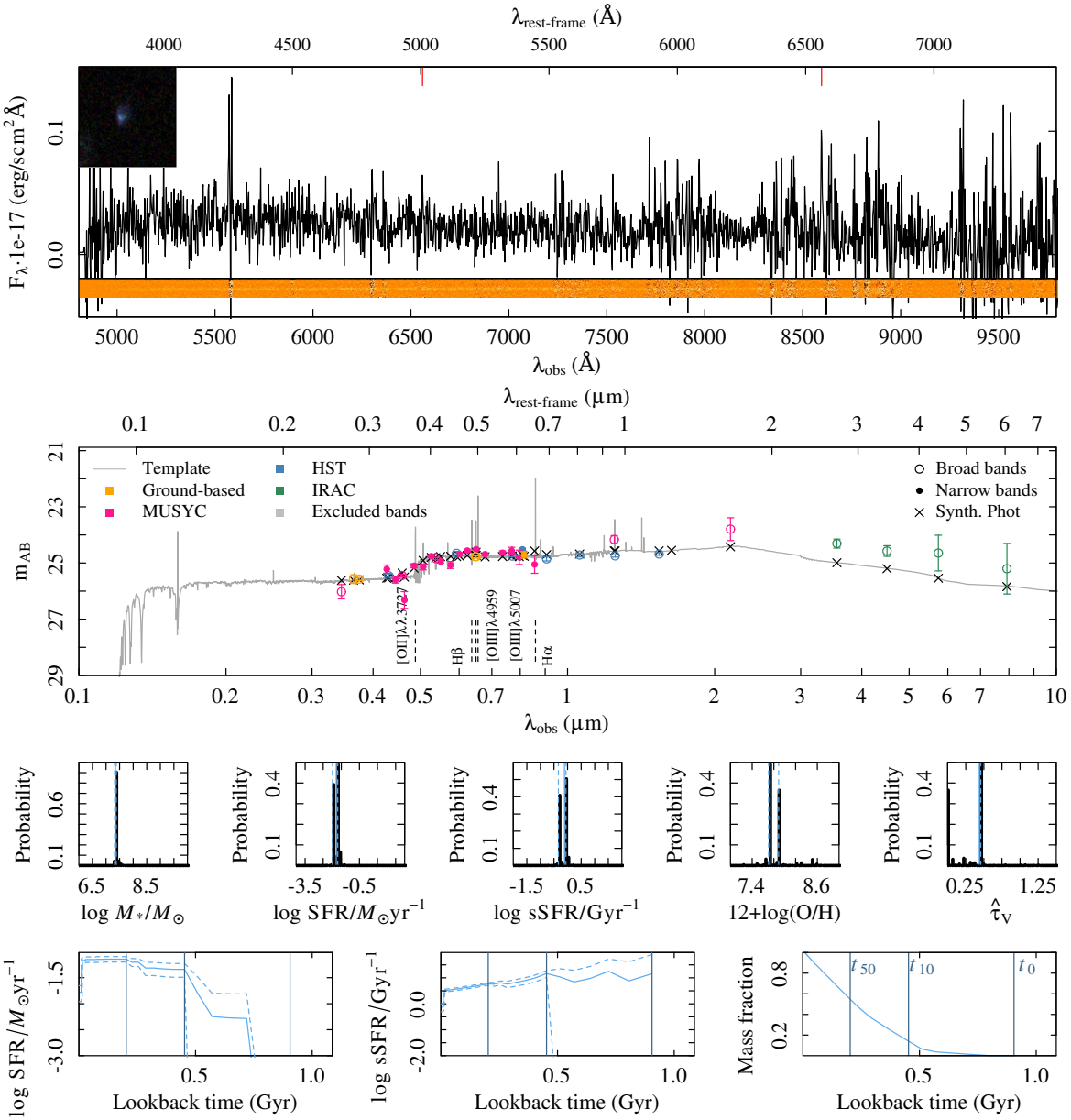

Summary ID 00440

ID	00440	$\mu_{eff,B,0}$	25.1±0.2	F Hα ($\times10^{17}$)	–
α (deg; J2000)	53.160653	$(B-V)_0$	0.54	EW Hα	–
δ (deg; J2000)	-27.917633	F Hβ ($\times10^{17}$)	$0.1^{0.2}_{0.1}$	log $M_*/M_\odot$	$7.5^{7.6}_{7.5}$
i (mag)	26.20±0.19	EW Hβ	$13.4^{20.3}_{8.5}$	log SFR/$M_\odot\,yr^{-1}$	$-1.4^{-1.2}_{-1.5}$
J (mag)	-99.99±-99.99	F [OII]$\lambda\lambda$3727 ($\times10^{17}$)	$0.5^{0.6}_{0.4}$	log sSFR/Gyr^{-1}	$0.1^{0.2}_{0.0}$
z_{spec}	0.535/3	EW [OII]$\lambda\lambda$3727	$35.2^{65.9}_{21.4}$	$\hat{\tau}_V$	$0.1^{0.3}_{0.1}$
Morph.	Irr	F [OIII]λ4959 ($\times10^{17}$)	$0.5^{0.6}_{0.4}$	12+log(O/H)	$7.6^{8.1}_{7.4}$
n	0.6±0.1	EW [OIII]λ4959	$35.2^{65.9}_{21.4}$	t_0 (Gyr)	2.1
$R_{eff,v,0}$	1.0±0.1	F [OIII]λ5007 ($\times10^{17}$)	$0.5^{0.6}_{0.4}$	t_{10} (Gyr)	1.0
$M_{B,0}$	-15.73	EW [OIII]λ5007	$35.2^{65.9}_{21.4}$	t_{50} (Gyr)	0.4

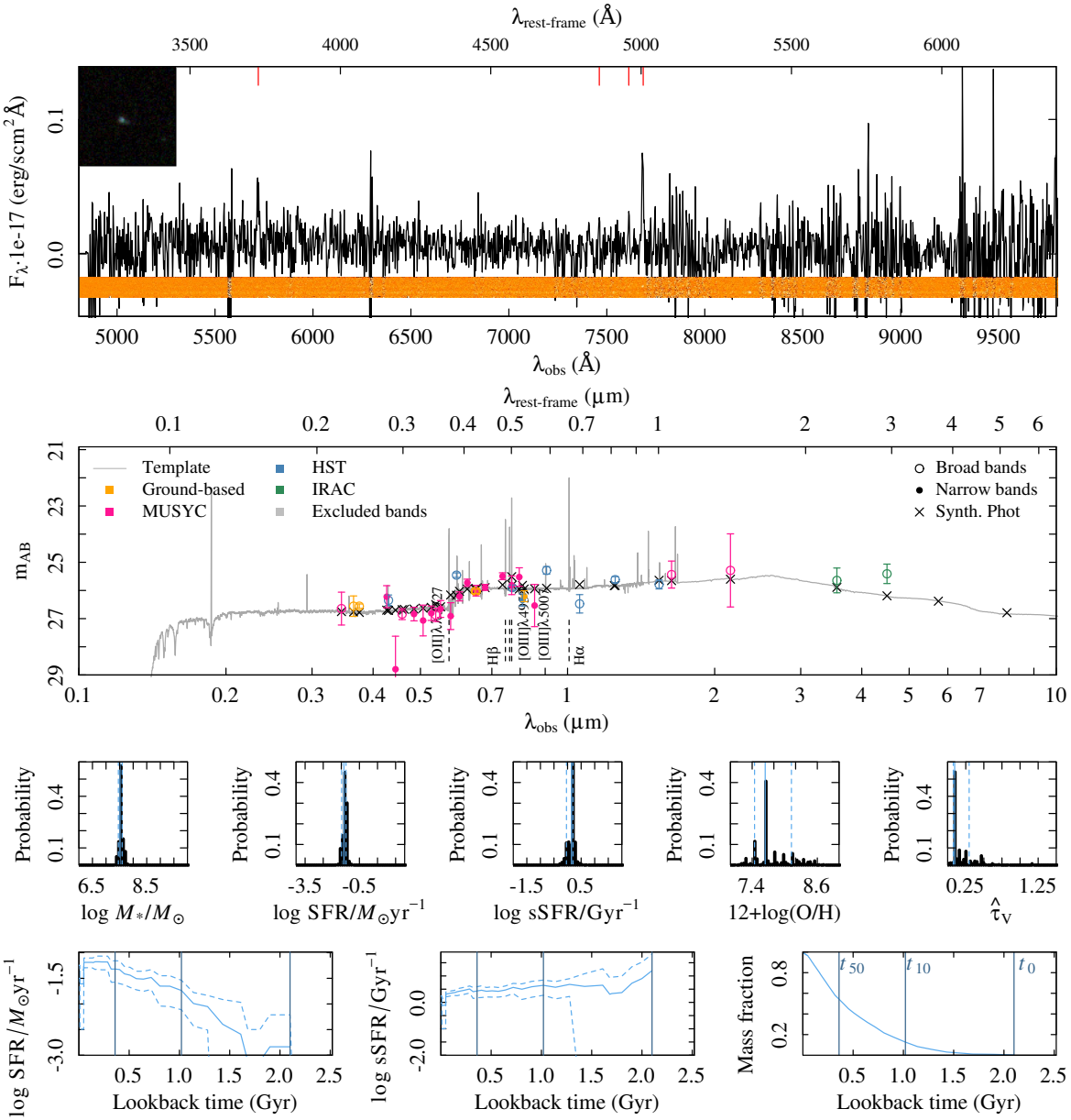

Summary ID 00454

ID	00454	$\mu_{eff,B,0}$	22.5±0.3	F Hα ($\times10^{17}$)	–
α (deg; J2000)	53.166669	$(B-V)_0$	0.61	EW Hα	–
δ (deg; J2000)	-27.733578	F Hβ ($\times10^{17}$)	$0.6^{0.8}_{0.5}$	log $M_*/M_\odot$	$8.0^{8.0}_{7.9}$
i (mag)	25.29±0.12	EW Hβ	$30.7^{44.3}_{19.8}$	log SFR/$M_\odot\,yr^{-1}$	$-0.8^{-0.7}_{-0.9}$
J (mag)	25.21±0.36	F [OII]$\lambda\lambda$3727 ($\times10^{17}$)	$1.1^{1.2}_{0.9}$	log sSFR/Gyr^{-1}	$0.2^{0.3}_{0.0}$
z_{spec}	0.536/4	EW [OII]$\lambda\lambda$3727	$50.2^{71.1}_{36.5}$	$\hat{\tau}_V$	$0.2^{0.3}_{0.1}$
Morph.	D	F [OIII]λ4959 ($\times10^{17}$)	$1.1^{1.2}_{0.9}$	12+log(O/H)	$7.6^{8.6}_{7.5}$
n	0.6±0.1	EW [OIII]λ4959	$50.2^{71.1}_{36.5}$	t_0 (Gyr)	5.5
$R_{eff,v,0}$	1.1±0.0	F [OIII]λ5007 ($\times10^{17}$)	$1.1^{1.2}_{0.9}$	t_{10} (Gyr)	2.4
$M_{B,0}$	-16.49	EW [OIII]λ5007	$50.2^{71.1}_{36.5}$	t_{50} (Gyr)	0.7

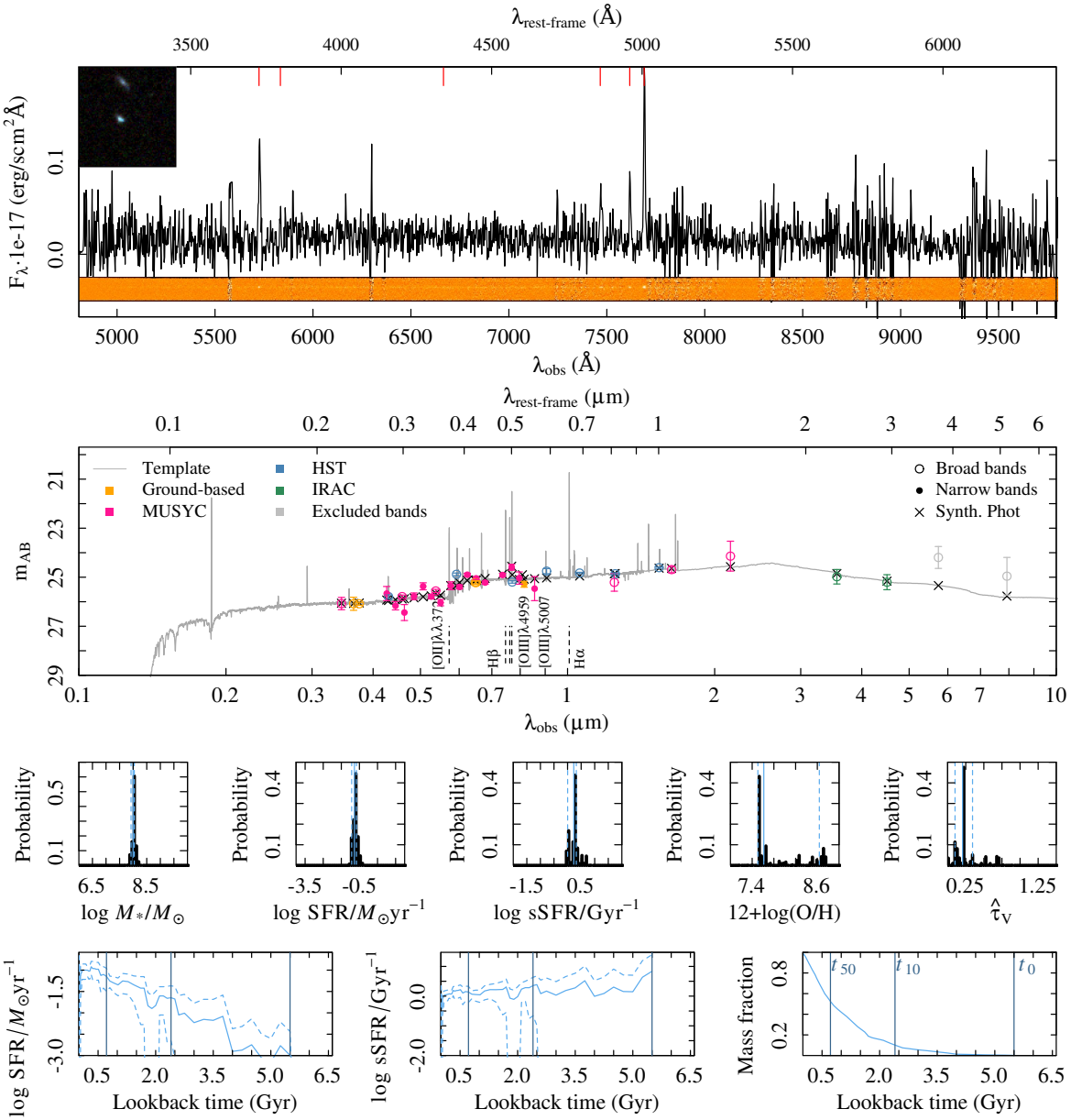

Summary ID 00455

ID	00455	$\mu_{eff,B,0}$	34.1±5.0	F Hα ($\times10^{17}$)	–
α (deg; J2000)	53.167001	$(B-V)_0$	0.71	EW Hα	–
δ (deg; J2000)	-27.915028	F Hβ ($\times10^{17}$)	$0.1^{0.2}_{0}$	log $M_*/M_\odot$	$8.7^{8.8}_{8.6}$
i (mag)	24.64±0.11	EW Hβ	$5.7^{17.3}_{1.1}$	log SFR/$M_\odot\,yr^{-1}$	$-0.2^{0.0}_{-0.4}$
J (mag)	24.92±0.24	F [OII]$\lambda\lambda$3727 ($\times10^{17}$)	$0.6^{0.6}_{0.5}$	log sSFR/Gyr^{-1}	$0.1^{0.2}_{-0.1}$
z_{spec}	0.687/3	EW [OII]$\lambda\lambda$3727	$48.5^{62.3}_{36.0}$	$\hat{\tau}_V$	$1.0^{1.2}_{0.8}$
Morph.	C	F [OIII]λ4959 ($\times10^{17}$)	$0.6^{0.6}_{0.5}$	12+log(O/H)	$7.5^{8.6}_{7.3}$
n	1.9±0.3	EW [OIII]λ4959	$48.5^{62.3}_{36.0}$	t_0 (Gyr)	4.8
$R_{eff,v,0}$	1.5±0.1	F [OIII]λ5007 ($\times10^{17}$)	$0.6^{0.6}_{0.5}$	t_{10} (Gyr)	2.6
$M_{B,0}$	-16.90	EW [OIII]λ5007	$48.5^{62.3}_{36.0}$	t_{50} (Gyr)	1.0

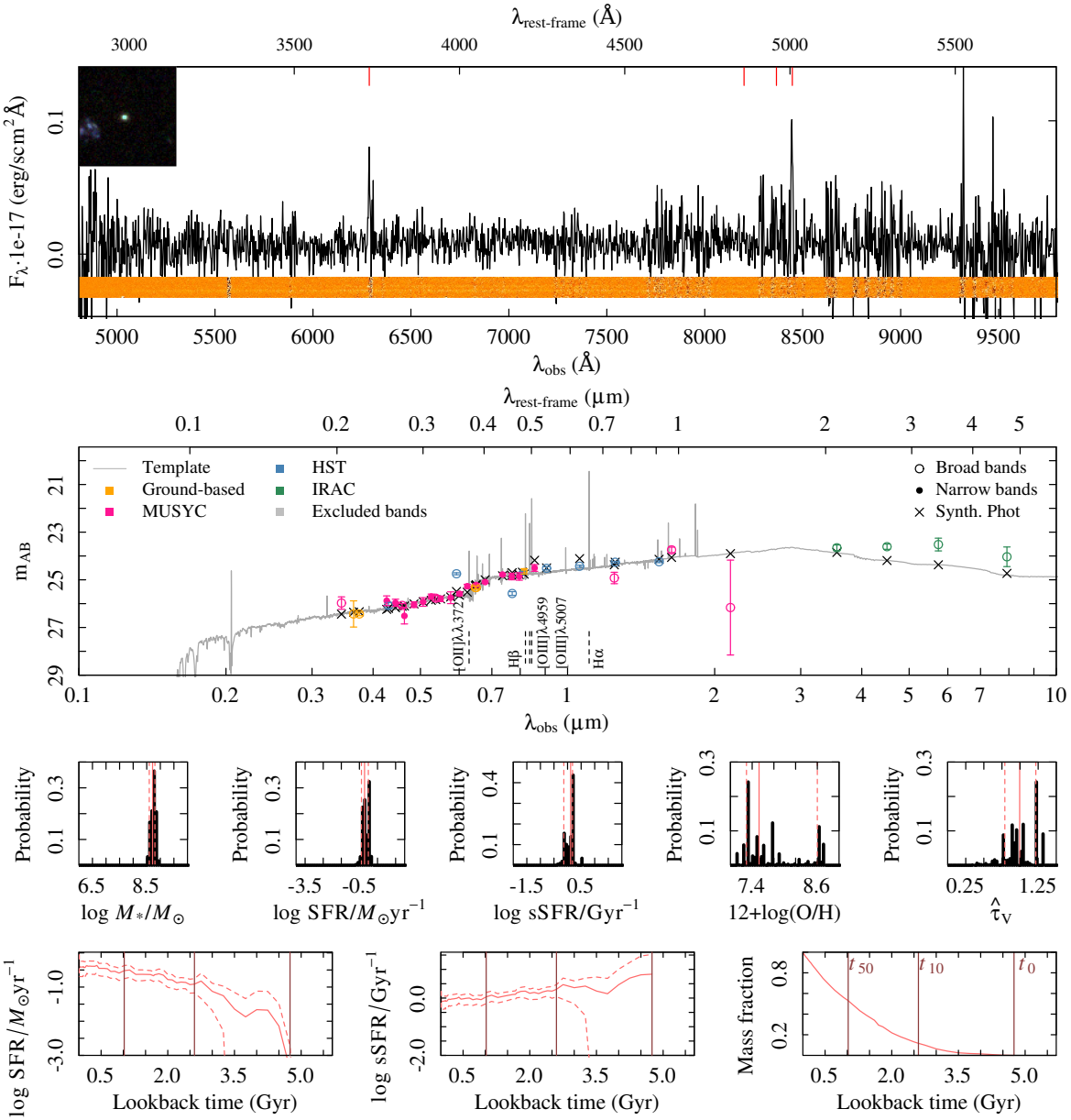

Summary ID 00464

ID	00464	$\mu_{eff,B,0}$	26.2±2.0	F Hα ($\times10^{17}$)	–
α (deg; J2000)	53.172069	$(B-V)_0$	0.44	EW Hα	–
δ (deg; J2000)	-27.676844	F Hβ ($\times10^{17}$)	$0.3^{0.4}_{0.3}$	log $M_*/M_\odot$	$8.4^{8.5}_{8.4}$
i (mag)	25.00±0.14	EW Hβ	$19.2^{31.4}_{13.6}$	log SFR/$M_\odot\,yr^{-1}$	$-0.6^{-0.5}_{-0.7}$
J (mag)	25.17±0.35	F [OII]$\lambda\lambda$3727 ($\times10^{17}$)	$1^{1.1}_{0.9}$	log sSFR/Gyr^{-1}	$0.0^{0.1}_{-0.2}$
z_{spec}	0.729/3	EW [OII]$\lambda\lambda$3727	$65.0^{109.0}_{46.8}$	$\hat{\tau}_V$	$0.2^{0.5}_{0.1}$
Morph.	Irr	F [OIII]λ4959 ($\times10^{17}$)	$1^{1.1}_{0.9}$	12+log(O/H)	$8.6^{8.7}_{7.8}$
n	0.2±0.0	EW [OIII]λ4959	$65.0^{109.0}_{46.8}$	t_0 (Gyr)	3.5
$R_{eff,v,0}$	4.3±0.1	F [OIII]λ5007 ($\times10^{17}$)	$1^{1.1}_{0.9}$	t_{10} (Gyr)	2.0
$M_{B,0}$	-17.39	EW [OIII]λ5007	$65.0^{109.0}_{46.8}$	t_{50} (Gyr)	0.8

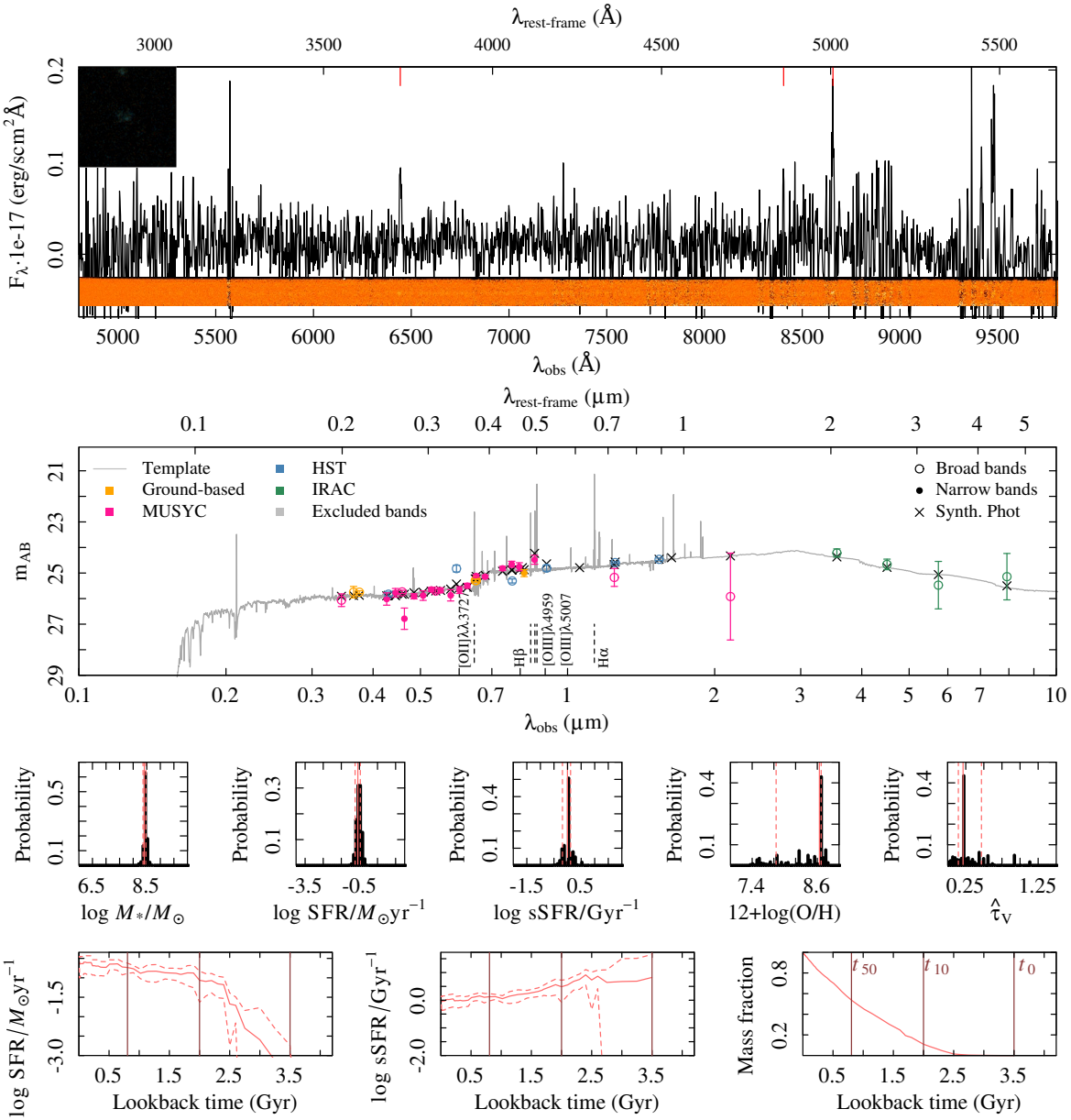

Summary ID 00474

ID	00474	$\mu_{eff,B,0}$	32.8±5.0	F Hα ($\times 10^{17}$)	–
α (deg; J2000)	53.175554	$(B-V)_0$	0.56	EW Hα	–
δ (deg; J2000)	-27.970997	F Hβ ($\times 10^{17}$)	–	log $M_*/M_\odot$	$8.7^{8.9}_{8.6}$
i (mag)	25.04±0.15	EW Hβ	–	log SFR/$M_\odot\, yr^{-1}$	$0.9^{1.1}_{0.8}$
J (mag)	24.77±0.24	F [OII]$\lambda\lambda$3727 ($\times 10^{17}$)	–	log sSFR/Gyr^{-1}	$1.1^{1.3}_{1.0}$
z_{spec}	1.171/2	EW [OII]$\lambda\lambda$3727	–	$\hat{\tau}_V$	$0.9^{1.1}_{0.7}$
Morph.	U	F [OIII]λ4959 ($\times 10^{17}$)	–	12+log(O/H)	$7.4^{7.6}_{7.2}$
n	1.3±0.2	EW [OIII]λ4959	–	t_0 (Gyr)	4.2
$R_{eff,v,0}$	4.0±0.2	F [OIII]λ5007 ($\times 10^{17}$)	–	t_{10} (Gyr)	2.1
$M_{B,0}$	-18.63	EW [OIII]λ5007	–	t_{50} (Gyr)	0.9

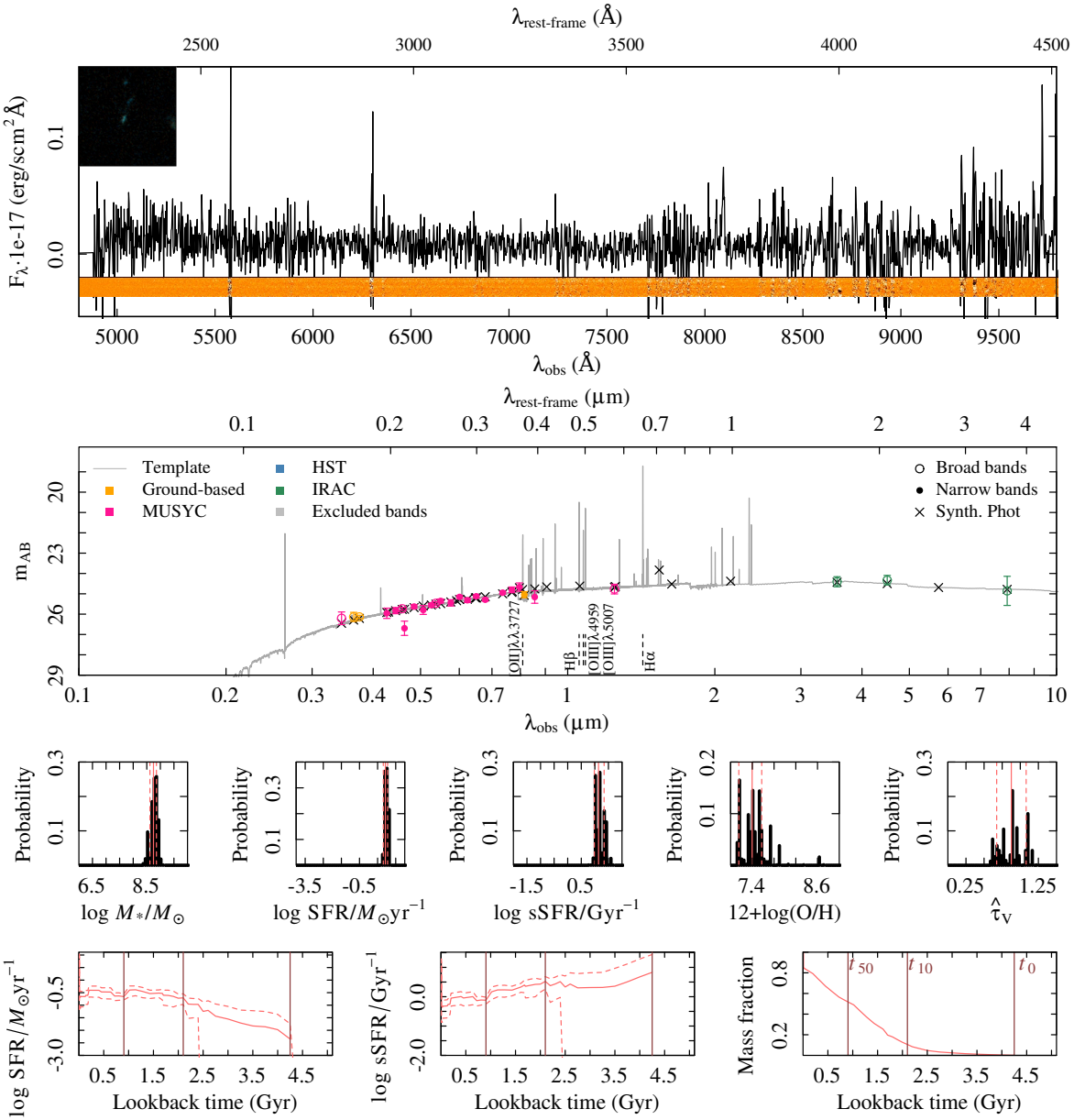

Summary ID 00481

ID	00481	$\mu_{eff,B,0}$	-Inf±NaN	F Hα ($\times 10^{17}$)	–
α (deg; J2000)	53.177753	$(B-V)_0$	0.15	EW Hα	–
δ (deg; J2000)	-27.787045	F Hβ ($\times 10^{17}$)	–	log $M_*/M_\odot$	$8.9^{8.9}_{8.9}$
i (mag)	24.84±0.11	EW Hβ	–	log SFR/$M_\odot\, yr^{-1}$	$0.2^{0.3}_{0.2}$
J (mag)	23.73±0.15	F [OII]$\lambda\lambda$3727 ($\times 10^{17}$)	$2.1^{2.3}_{1.9}$	log sSFR/Gyr^{-1}	$0.3^{0.4}_{0.3}$
z_{spec}	0.954/2	EW [OII]$\lambda\lambda$3727	$62.9^{81.1}_{49.8}$	$\hat{\tau}_V$	$0.2^{0.2}_{0.2}$
Morph.	D	F [OIII]λ4959 ($\times 10^{17}$)	$2.1^{2.3}_{1.9}$	12+log(O/H)	$8.7^{8.7}_{8.7}$
n	0.2±0.1	EW [OIII]λ4959	$62.9^{81.1}_{49.8}$	t_0 (Gyr)	4.8
$R_{eff,v,0}$	7.9±0.1	F [OIII]λ5007 ($\times 10^{17}$)	$2.1^{2.3}_{1.9}$	t_{10} (Gyr)	4.0
$M_{B,0}$	-18.63	EW [OIII]λ5007	$62.9^{81.1}_{49.8}$	t_{50} (Gyr)	2.1

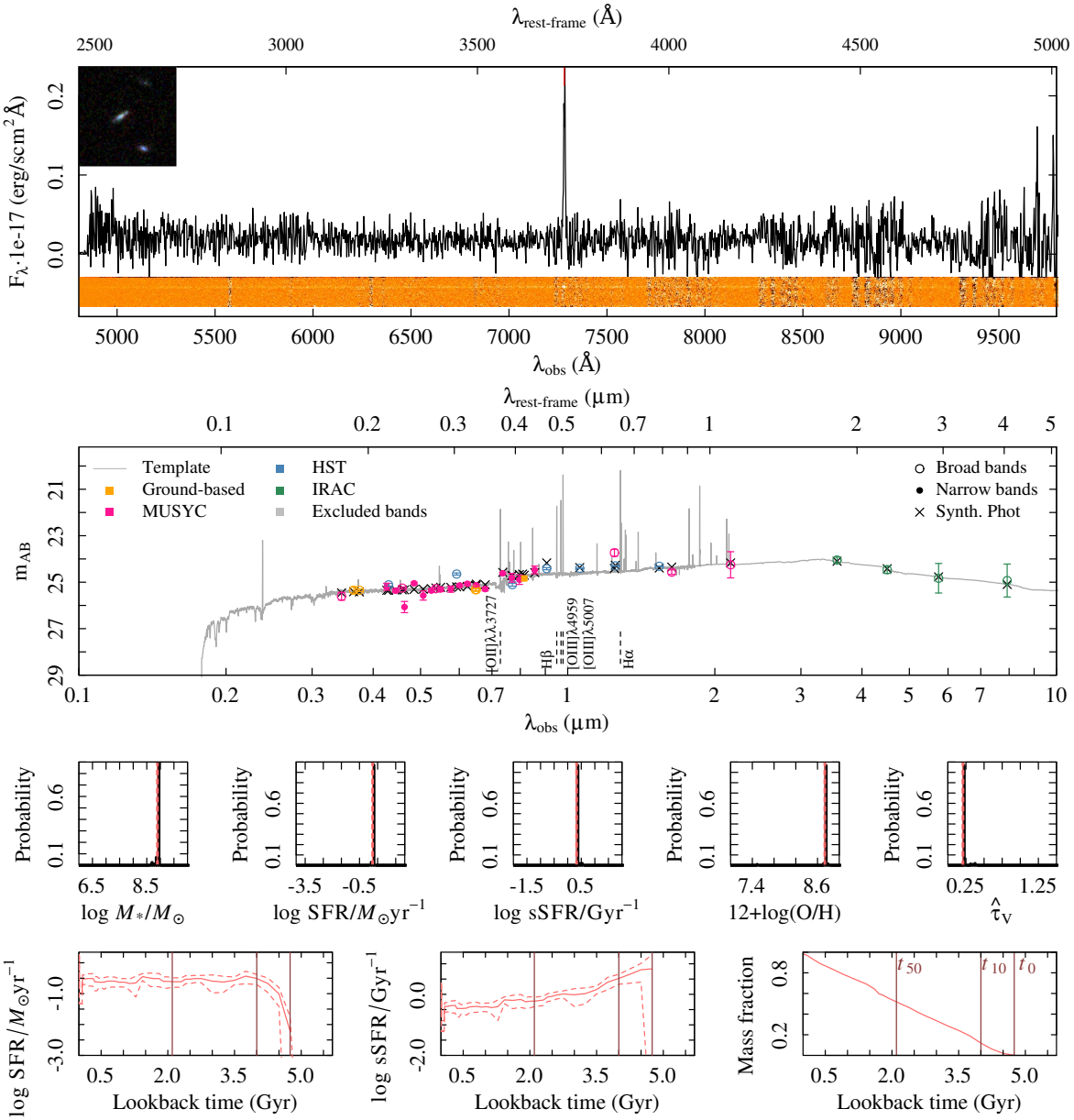

Summary ID 00488

ID	00488	$\mu_{eff,B,0}$	21.7±0.3	F Hα ($\times10^{17}$)	–
α (deg; J2000)	53.180220	$(B-V)_0$	0.95	EW Hα	–
δ (deg; J2000)	-27.752439	F Hβ ($\times10^{17}$)	$0.2^{0.4}_{0.1}$	log $M_*/M_\odot$	$8.2^{8.2}_{8.1}$
i (mag)	24.61±0.11	EW Hβ	$5.2^{11.9}_{1.6}$	log SFR/$M_\odot\,yr^{-1}$	$-0.7^{-0.4}_{-0.8}$
J (mag)	-99.99±-99.99	F [OII]$\lambda\lambda$3727 ($\times10^{17}$)	$1.5^{1.7}_{1.4}$	log sSFR/Gyr^{-1}	$0.1^{0.4}_{0.1}$
z_{spec}	0.533/3	EW [OII]$\lambda\lambda$3727	$58.9^{77.2}_{45.0}$	$\hat{\tau}_V$	$0.7^{1.1}_{0.7}$
Morph.	D	F [OIII]λ4959 ($\times10^{17}$)	$1.5^{1.7}_{1.4}$	12+log(O/H)	$8.4^{8.4}_{7.7}$
n	1.2±0.1	EW [OIII]λ4959	$58.9^{77.2}_{45.0}$	t_0 (Gyr)	2.0
$R_{eff,v,0}$	0.9±0.0	F [OIII]λ5007 ($\times10^{17}$)	$1.5^{1.7}_{1.4}$	t_{10} (Gyr)	0.9
$M_{B,0}$	-16.40	EW [OIII]λ5007	$58.9^{77.2}_{45.0}$	t_{50} (Gyr)	0.4

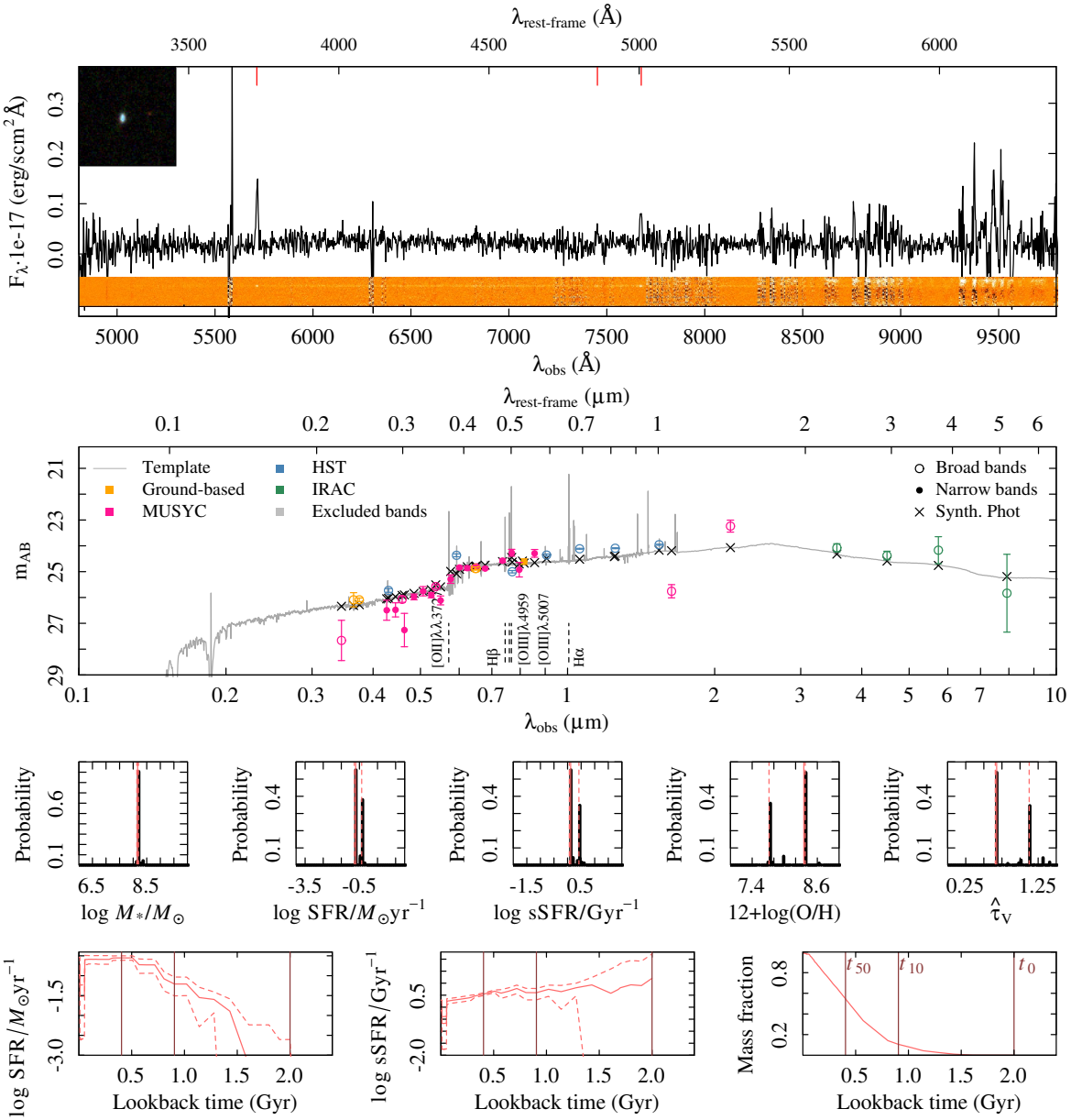

Summary ID 00490

ID	00490	$\mu_{eff,B,0}$	19.8±0.3	F Hα ($\times10^{17}$)	–
α (deg; J2000)	53.180775	$(B-V)_0$	0.22	EW Hα	–
δ (deg; J2000)	-27.865190	F Hβ ($\times10^{17}$)	$1.1^{1.2}_{0.9}$	log $M_*/M_\odot$	$8.6^{8.6}_{8.5}$
i (mag)	24.43±0.10	EW Hβ	$32.3^{43.1}_{24.2}$	log SFR/$M_\odot\,yr^{-1}$	$0.0^{0.0}_{-0.1}$
J (mag)	24.94±0.28	F [OII]$\lambda\lambda$3727 ($\times10^{17}$)	$3.5^{3.8}_{3.3}$	log sSFR/Gyr^{-1}	$0.5^{0.5}_{0.5}$
z_{spec}	0.856/4	EW [OII]$\lambda\lambda$3727	$80.9^{100.5}_{66.2}$	$\hat{\tau}_V$	$0.2^{0.2}_{0.2}$
Morph.	D	F [OIII]λ4959 ($\times10^{17}$)	$3.5^{3.8}_{3.3}$	12+log(O/H)	$7.8^{7.8}_{7.8}$
n	4.9±0.8	EW [OIII]λ4959	$80.9^{100.5}_{66.2}$	t_0 (Gyr)	2.5
$R_{eff,v,0}$	0.8±0.0	F [OIII]λ5007 ($\times10^{17}$)	$3.5^{3.8}_{3.3}$	t_{10} (Gyr)	1.3
$M_{B,0}$	-18.56	EW [OIII]λ5007	$80.9^{100.5}_{66.2}$	t_{50} (Gyr)	0.6

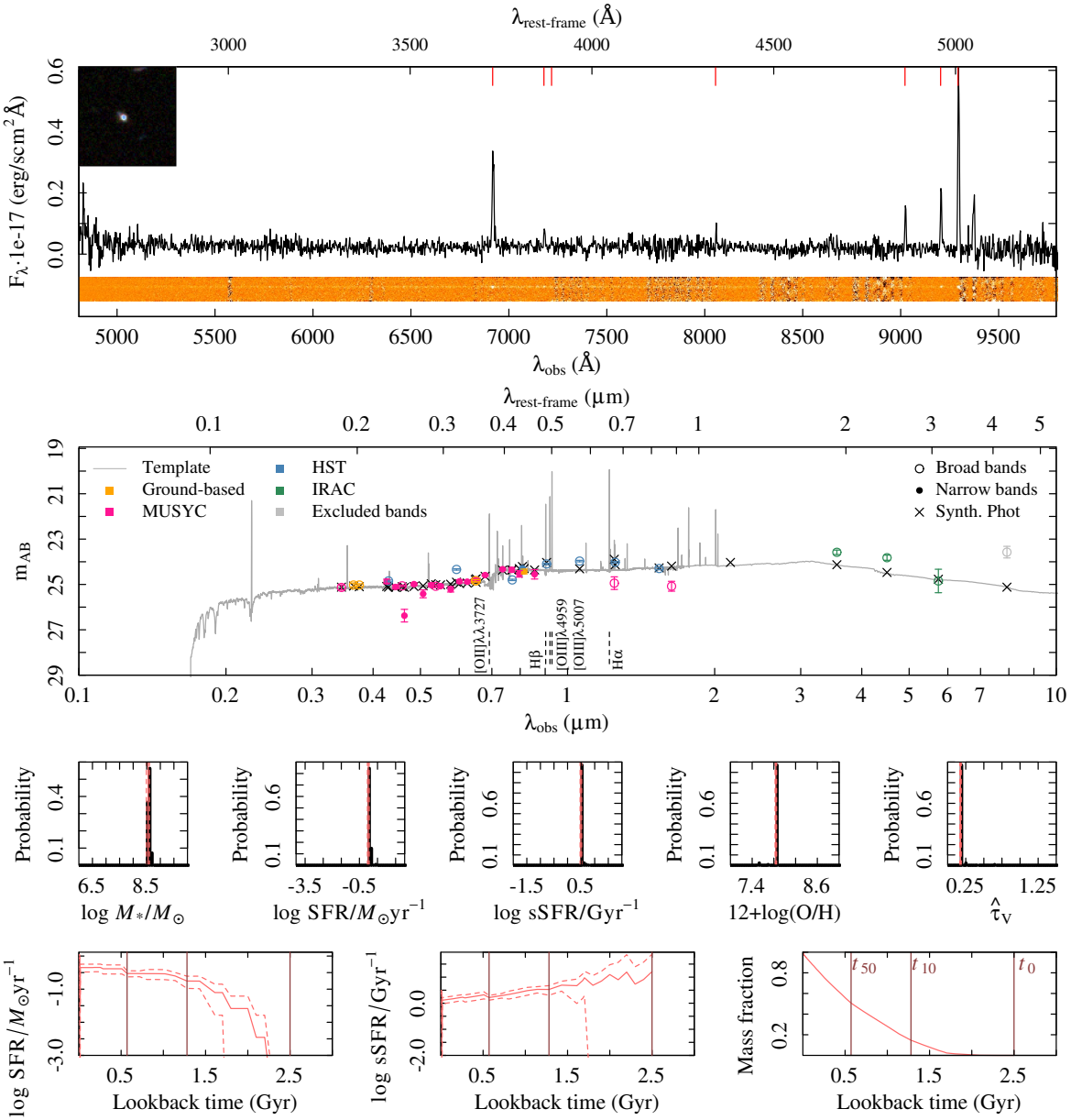

Summary ID 00510

ID	00510	$\mu_{eff,B,0}$	14.6±1683.3	F Hα ($\times10^{17}$)	–
α (deg; J2000)	53.194294	$(B-V)_0$	0.08	EW Hα	–
δ (deg; J2000)	-27.673538	F Hβ ($\times10^{17}$)	–	log $M_*/M_\odot$	$9.5^{9.6}_{9.4}$
i (mag)	24.31±0.10	EW Hβ	–	log SFR/$M_\odot\ yr^{-1}$	$0.8^{0.9}_{0.8}$
J (mag)	24.59±0.21	F [OII]$\lambda\lambda$3727 ($\times10^{17}$)	$1.2^{1.4}_{1.1}$	log sSFR/Gyr^{-1}	$0.2^{0.4}_{0.1}$
z_{spec}	1.329/2	EW [OII]$\lambda\lambda$3727	$33.1^{45.6}_{24.4}$	$\hat{\tau}_V$	$0.2^{0.4}_{0.2}$
Morph.	U	F [OIII]λ4959 ($\times10^{17}$)	$1.2^{1.4}_{1.1}$	12+log(O/H)	$7.2^{7.3}_{7.2}$
n	1.5±0.1	EW [OIII]λ4959	$33.1^{45.6}_{24.4}$	t_0 (Gyr)	3.8
$R_{eff,v,0}$	7.9±0.2	F [OIII]λ5007 ($\times10^{17}$)	$1.2^{1.4}_{1.1}$	t_{10} (Gyr)	3.0
$M_{B,0}$	-20.43	EW [OIII]λ5007	$33.1^{45.6}_{24.4}$	t_{50} (Gyr)	1.4

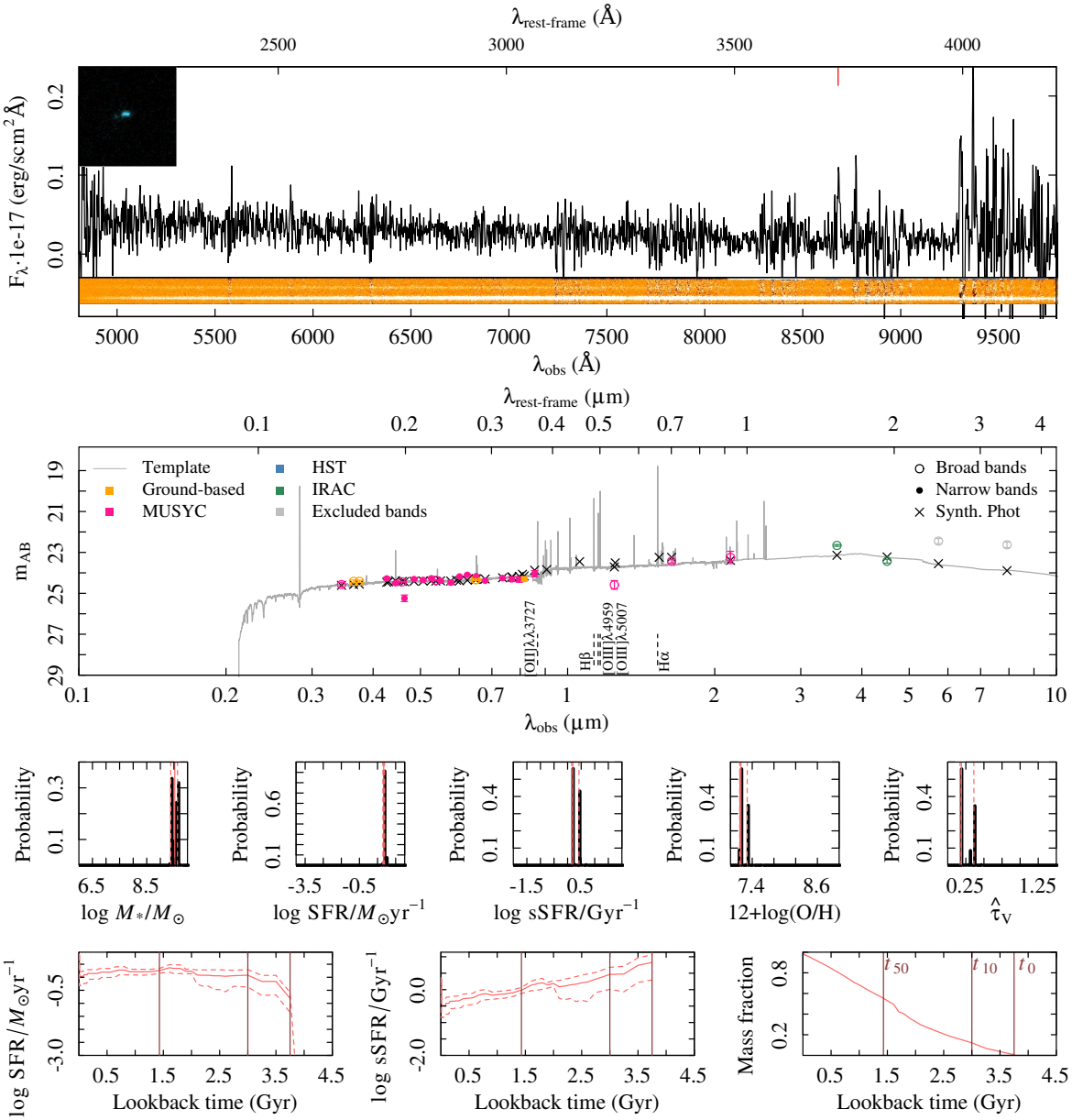

Summary ID 00518

ID	00518	$\mu_{eff,B,0}$	21.4±0.4	F Hα ($\times 10^{17}$)	–
α (deg; J2000)	53.198254	$(B-V)_0$	0.86	EW Hα	–
δ (deg; J2000)	-27.746025	F Hβ ($\times 10^{17}$)	–	log $M_*/M_\odot$	$7.7^{7.8}_{7.6}$
i (mag)	25.29±0.12	EW Hβ	–	log SFR/$M_\odot\, yr^{-1}$	$-1.1^{-0.8}_{-1.4}$
J (mag)	-99.99±-99.99	F [OII]$\lambda\lambda$3727 ($\times 10^{17}$)	–	log sSFR/Gyr^{-1}	$0.1^{0.5}_{-0.2}$
z_{spec}	0.502/2	EW [OII]$\lambda\lambda$3727	–	$\hat{\tau}_V$	$0.8^{1.0}_{0.4}$
Morph.	C	F [OIII]λ4959 ($\times 10^{17}$)	–	12+log(O/H)	$8.0^{8.3}_{7.8}$
n	2.0±0.4	EW [OIII]λ4959	–	t_0 (Gyr)	2.4
$R_{eff,v,0}$	0.6±0.0	F [OIII]λ5007 ($\times 10^{17}$)	–	t_{10} (Gyr)	1.0
$M_{B,0}$	-15.51	EW [OIII]λ5007	–	t_{50} (Gyr)	0.5

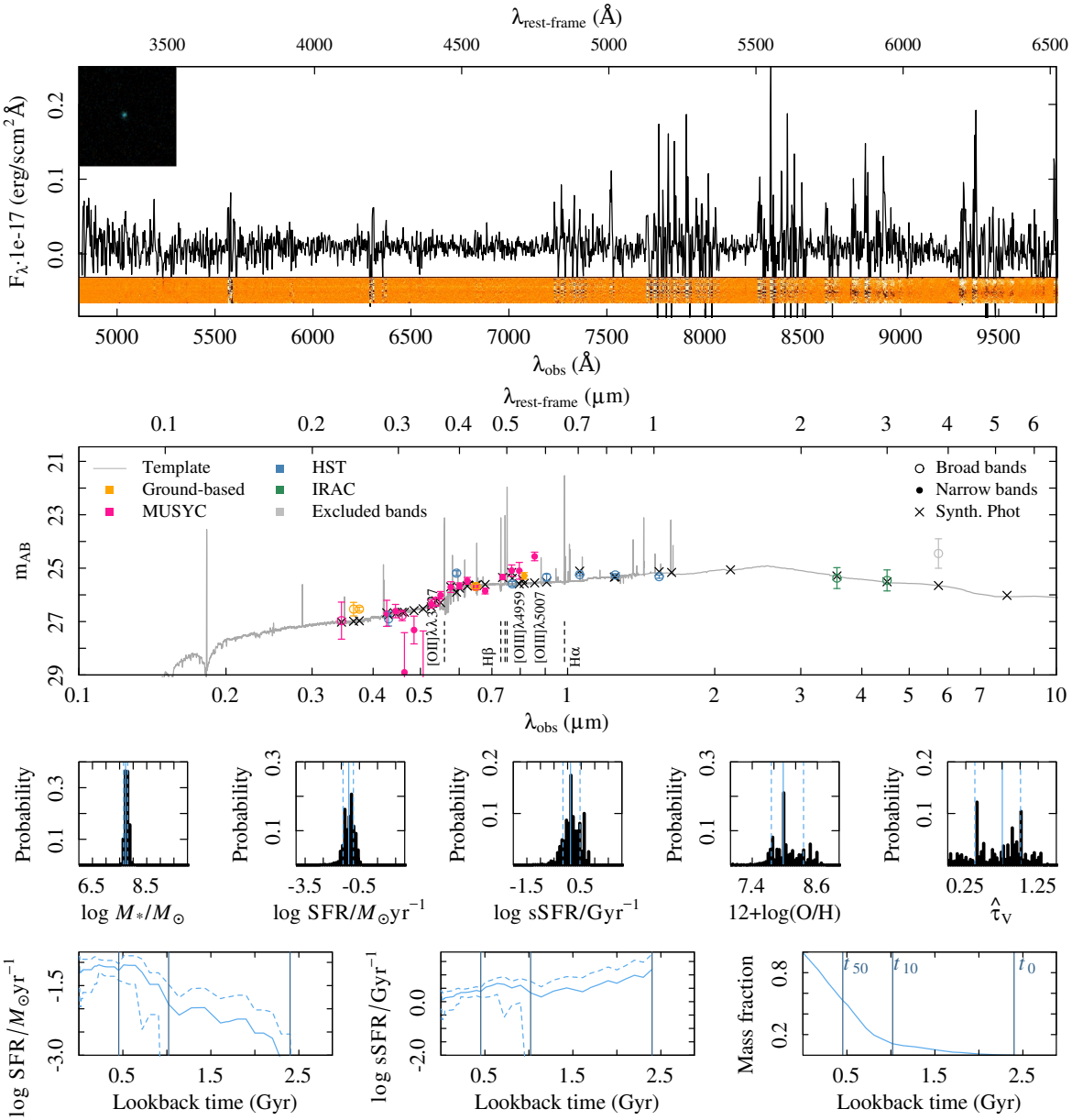

Summary ID 00519

ID	00519	$\mu_{eff,B,0}$	31.1±3.7	F Hα ($\times10^{17}$)	–
α (deg; J2000)	53.198736	$(B-V)_0$	0.28	EW Hα	–
δ (deg; J2000)	-27.948377	F Hβ ($\times10^{17}$)	$2.2^{2.3}_{2.1}$	log $M_*/M_\odot$	$8.7^{8.8}_{8.7}$
i (mag)	24.68±0.11	EW Hβ	$147.7^{212.2}_{106.8}$	log SFR/$M_\odot\,yr^{-1}$	$0.8^{0.9}_{0.8}$
J (mag)	24.37±0.20	F [OII]$\lambda\lambda$3727 ($\times10^{17}$)	$3.9^{4.1}_{3.8}$	log sSFR/Gyr^{-1}	$1.1^{1.1}_{1.0}$
z_{spec}	0.909/4	EW [OII]$\lambda\lambda$3727	$146.4^{187.6}_{119.4}$	$\hat{\tau}_V$	$1.3^{1.3}_{1.3}$
Morph.	D	F [OIII]λ4959 ($\times10^{17}$)	$3.9^{4.1}_{3.8}$	12+log(O/H)	$7.3^{7.3}_{7.3}$
n	0.8±0.1	EW [OIII]λ4959	$146.4^{187.6}_{119.4}$	t_0 (Gyr)	5.0
$R_{eff,v,0}$	0.9±0.0	F [OIII]λ5007 ($\times10^{17}$)	$3.9^{4.1}_{3.8}$	t_{10} (Gyr)	0.1
$M_{B,0}$	-18.69	EW [OIII]λ5007	$146.4^{187.6}_{119.4}$	t_{50} (Gyr)	0.1

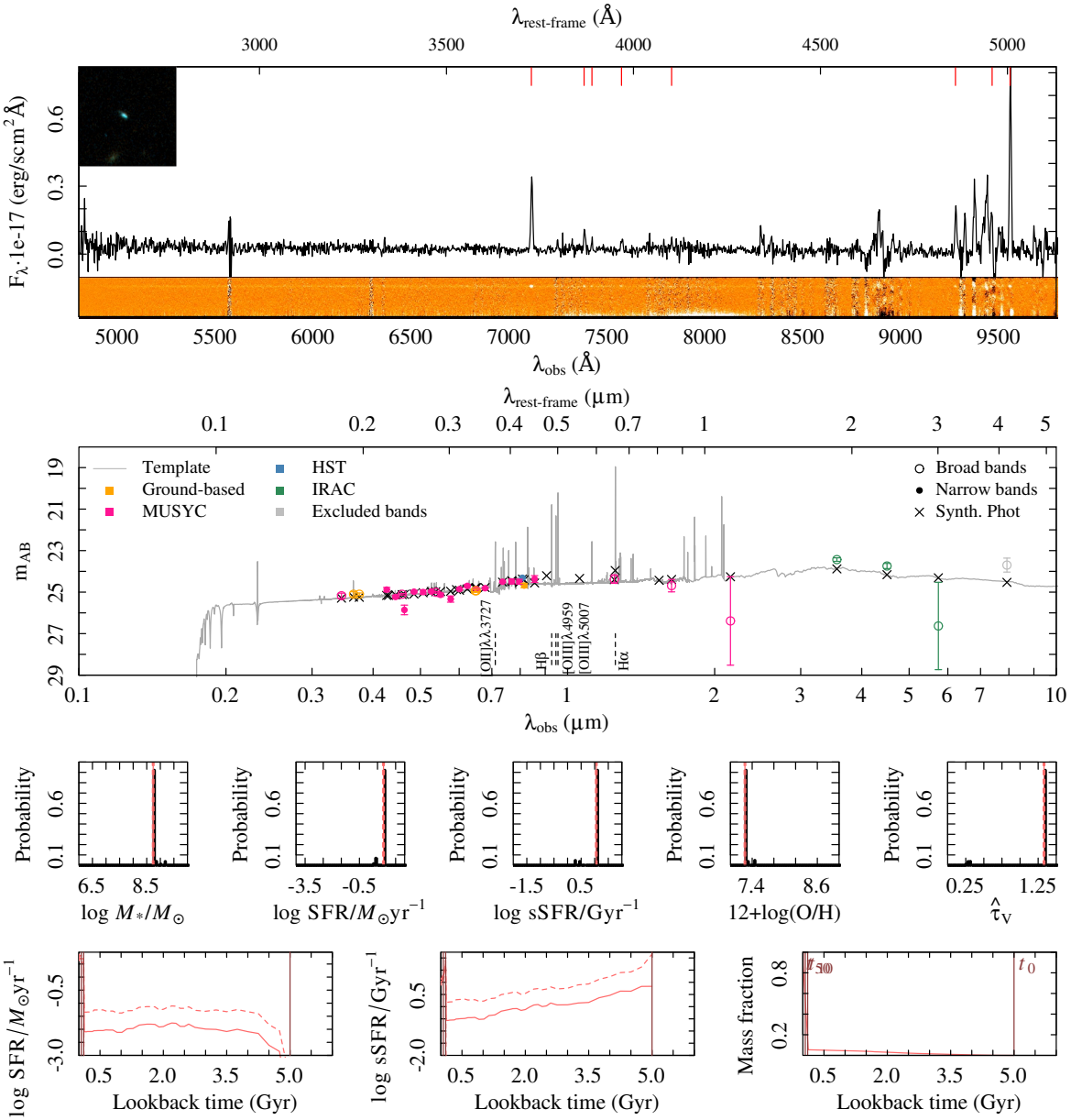

Summary ID 00520

ID	00520	$\mu_{eff,B,0}$	20.5±0.7	F Hα ($\times 10^{17}$)	–
α (deg; J2000)	53.198647	$(B-V)_0$	0.90	EW Hα	–
δ (deg; J2000)	-27.858181	F Hβ ($\times 10^{17}$)	$0.4^{0.6}_{0.2}$	log $M_*/M_\odot$	$7.9^{8.0}_{7.8}$
i (mag)	24.54±0.11	EW Hβ	$9.7^{18.1}_{4.2}$	log SFR/$M_\odot\, yr^{-1}$	$-0.4^{-0.4}_{-0.6}$
J (mag)	-99.99±-99.99	F [OII]$\lambda\lambda$3727 ($\times 10^{17}$)	$1.1^{1.4}_{0.9}$	log sSFR/Gyr^{-1}	$0.6^{0.7}_{0.4}$
z_{spec}	0.445/3	EW [OII]$\lambda\lambda$3727	$31.2^{45.3}_{20.3}$	$\hat{\tau}_V$	$1.1^{1.1}_{1.0}$
Morph.	D	F [OIII]λ4959 ($\times 10^{17}$)	$1.1^{1.4}_{0.9}$	12+log(O/H)	$8.7^{8.7}_{8.7}$
n	0.5±0.0	EW [OIII]λ4959	$31.2^{45.3}_{20.3}$	t_0 (Gyr)	3.0
$R_{eff,v,0}$	0.8±0.0	F [OIII]λ5007 ($\times 10^{17}$)	$1.1^{1.4}_{0.9}$	t_{10} (Gyr)	1.0
$M_{B,0}$	-16.16	EW [OIII]λ5007	$31.2^{45.3}_{20.3}$	t_{50} (Gyr)	0.5

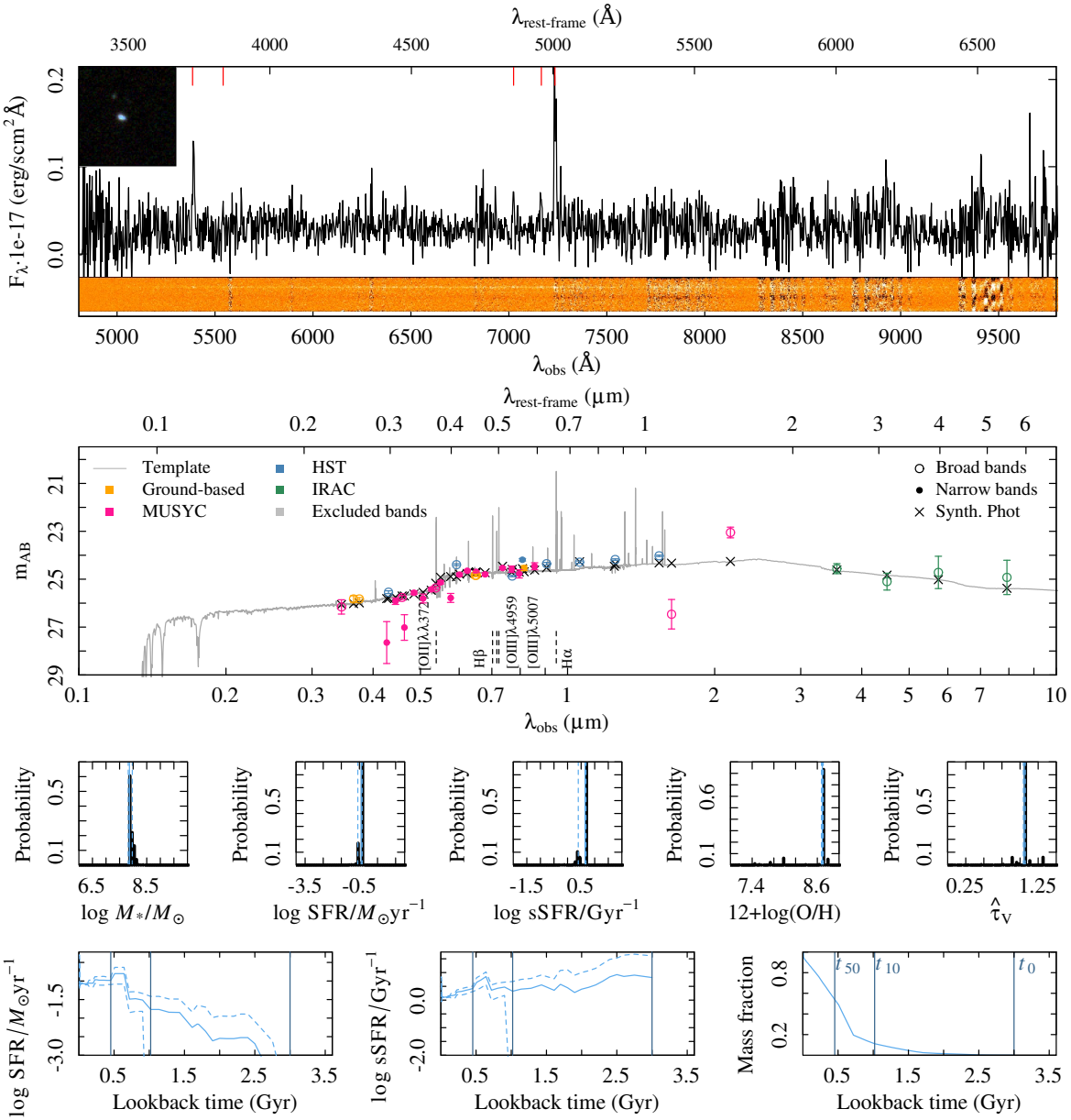

Summary ID 00524

ID	00524	$\mu_{eff,B,0}$	-Inf±NaN	F Hα ($\times 10^{17}$)	–
α (deg; J2000)	53.202959	$(B-V)_0$	-0.02	EW Hα	–
δ (deg; J2000)	-27.979923	F Hβ ($\times 10^{17}$)	–	log $M_*/M_\odot$	$8.9^{9.0}_{8.8}$
i (mag)	24.61±0.13	EW Hβ	–	log SFR/$M_\odot\, yr^{-1}$	$0.5^{0.6}_{0.4}$
J (mag)	24.30±0.22	F [OII]$\lambda\lambda$3727 ($\times 10^{17}$)	–	log sSFR/Gyr^{-1}	$0.6^{0.8}_{0.5}$
z_{spec}	1.250/3	EW [OII]$\lambda\lambda$3727	–	$\hat{\tau}_V$	$0.1^{0.2}_{0.1}$
Morph.	C	F [OIII]λ4959 ($\times 10^{17}$)	–	12+log(O/H)	$8.0^{8.1}_{7.7}$
n	0.0±0.0	EW [OIII]λ4959	–	t_0 (Gyr)	4.0
$R_{eff,v,0}$	0.0±0.0	F [OIII]λ5007 ($\times 10^{17}$)	–	t_{10} (Gyr)	2.8
$M_{B,0}$	-19.96	EW [OIII]λ5007	–	t_{50} (Gyr)	1.6

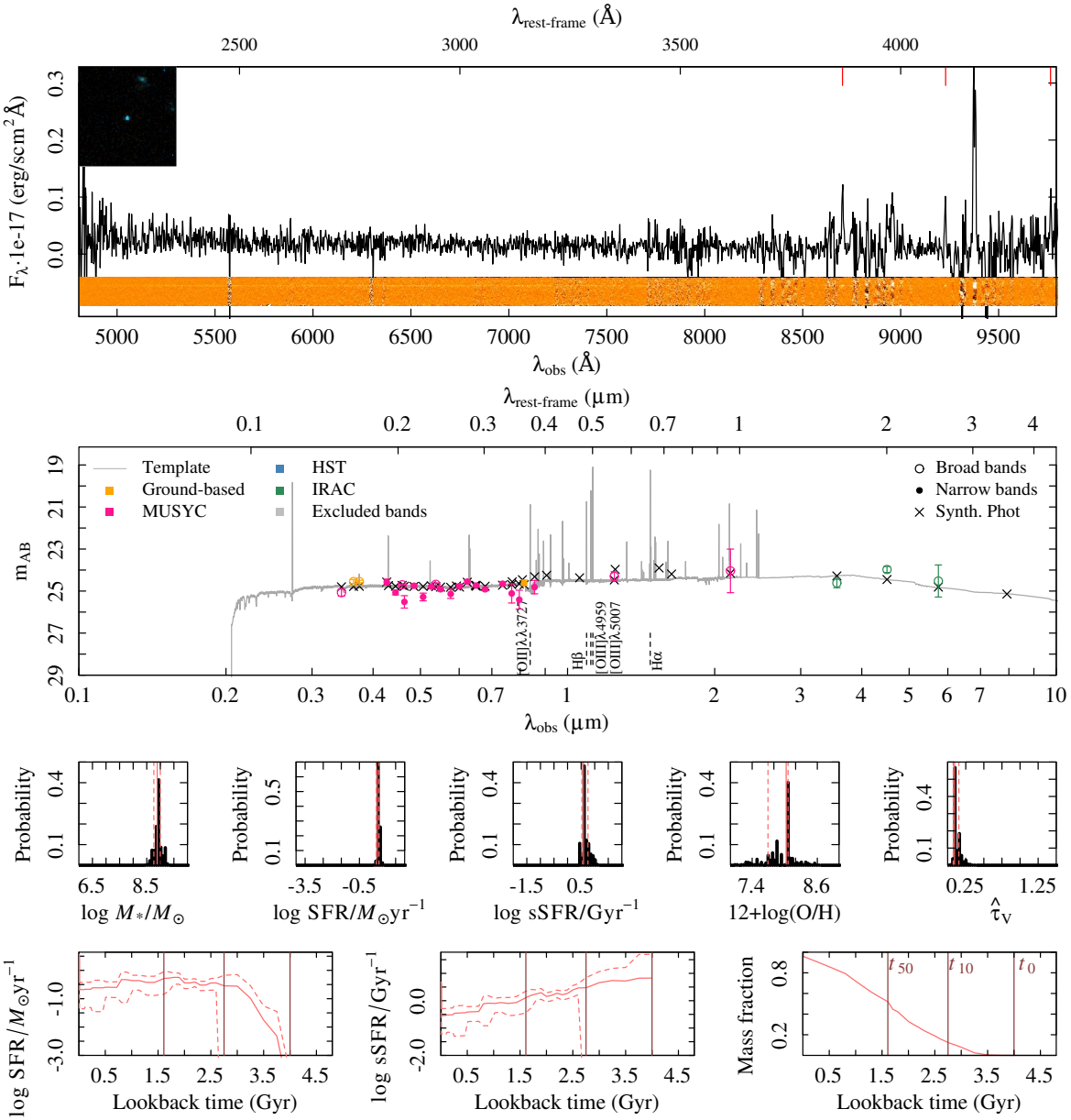

Summary ID 00536

ID	00536	$\mu_{eff,B,0}$	21.9±0.6	F Hα ($\times10^{17}$)	–
α (deg; J2000)	53.209579	$(B-V)_0$	0.50	EW Hα	–
δ (deg; J2000)	-27.846897	F Hβ ($\times10^{17}$)	$0.3^{0.3}_{0.3}$	log $M_*/M_\odot$	$7.6^{7.7}_{7.5}$
i (mag)	25.74±0.14	EW Hβ	$44.6^{61.1}_{34.6}$	log SFR$/M_\odot\,yr^{-1}$	$-1.0^{-0.8}_{-1.1}$
J (mag)	26.96±1.15	F [OII]$\lambda\lambda$3727 ($\times10^{17}$)	–	log sSFR$/Gyr^{-1}$	$0.4^{0.6}_{0.3}$
z_{spec}	0.578/3	EW [OII]$\lambda\lambda$3727	–	$\hat{\tau}_V$	$0.2^{0.5}_{0.1}$
Morph.	D	F [OIII]λ4959 ($\times10^{17}$)	–	12+log(O/H)	$7.9^{8.0}_{7.8}$
n	2.8±0.6	EW [OIII]λ4959	–	t_0 (Gyr)	2.6
$R_{eff,v,0}$	1.2±0.2	F [OIII]λ5007 ($\times10^{17}$)	–	t_{10} (Gyr)	0.9
$M_{B,0}$	-15.95	EW [OIII]λ5007	–	t_{50} (Gyr)	0.4

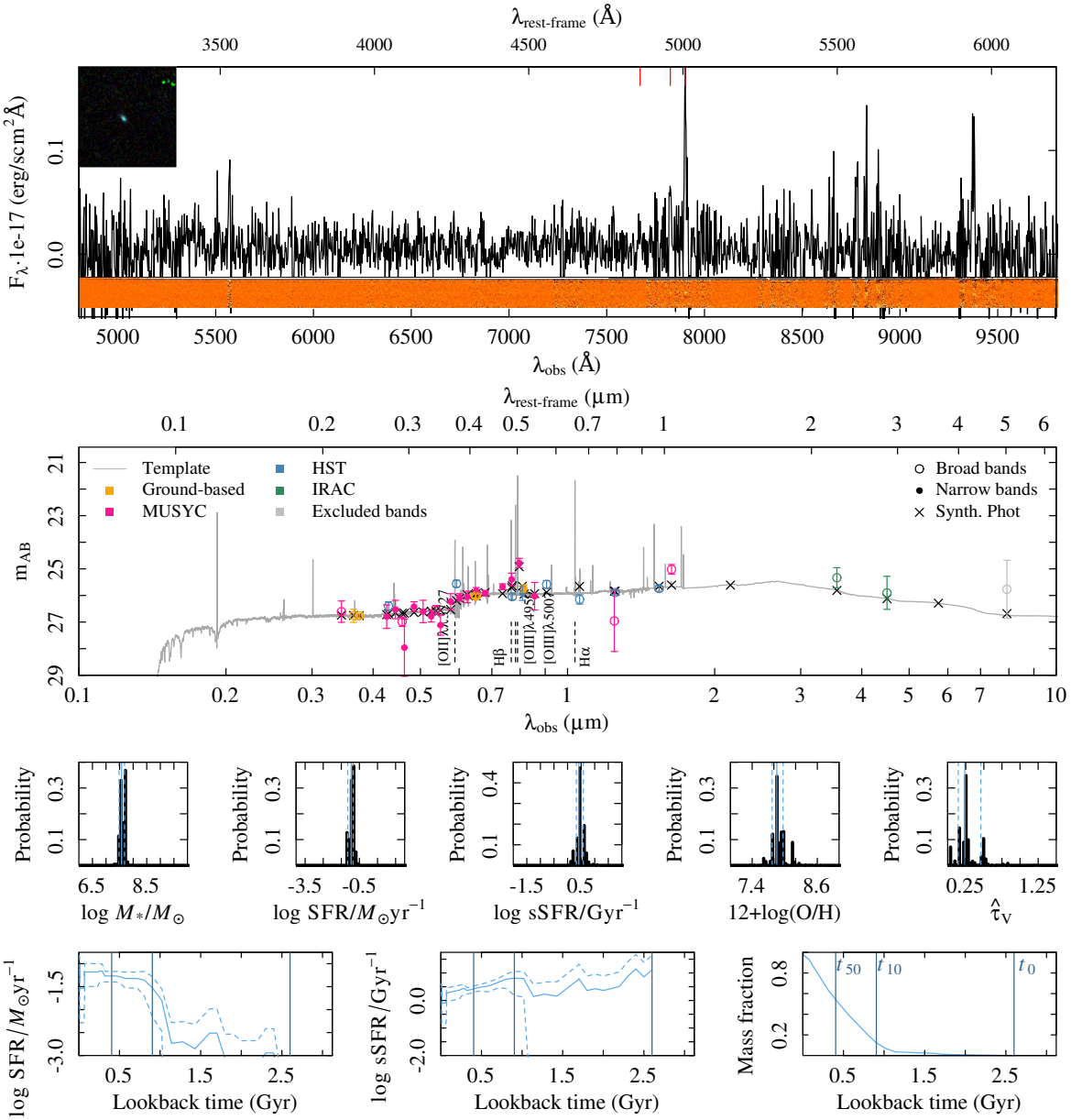

Summary ID 00539

ID	00539	$\mu_{eff,B,0}$	21.5±0.3	F Hα ($\times 10^{17}$)	–
α (deg; J2000)	53.210166	$(B-V)_0$	0.26	EW Hα	–
δ (deg; J2000)	-27.738077	F Hβ ($\times 10^{17}$)	–	log $M_*/M_\odot$	$7.8^{7.9}_{7.7}$
i (mag)	25.80±0.22	EW Hβ	–	log SFR$/M_\odot\, yr^{-1}$	$-0.9^{-0.8}_{-0.9}$
J (mag)	25.17±0.46	F [OII]$\lambda\lambda$3727 ($\times 10^{17}$)	$0.7^{0.8}_{0.6}$	log sSFR$/Gyr^{-1}$	$0.4^{0.4}_{0.3}$
z_{spec}	0.739/3	EW [OII]$\lambda\lambda$3727	$90.1^{149.5}_{59.3}$	$\hat{\tau}_V$	$0.0^{0.1}_{0.0}$
Morph.	Irr	F [OIII]λ4959 ($\times 10^{17}$)	$0.7^{0.8}_{0.6}$	12+log(O/H)	$7.8^{8.0}_{7.8}$
n	0.2±0.1	EW [OIII]λ4959	$90.1^{149.5}_{59.3}$	t_0 (Gyr)	1.9
$R_{eff,v,0}$	2.5±0.1	F [OIII]λ5007 ($\times 10^{17}$)	$0.7^{0.8}_{0.6}$	t_{10} (Gyr)	1.0
$M_{B,0}$	-16.83	EW [OIII]λ5007	$90.1^{149.5}_{59.3}$	t_{50} (Gyr)	0.6

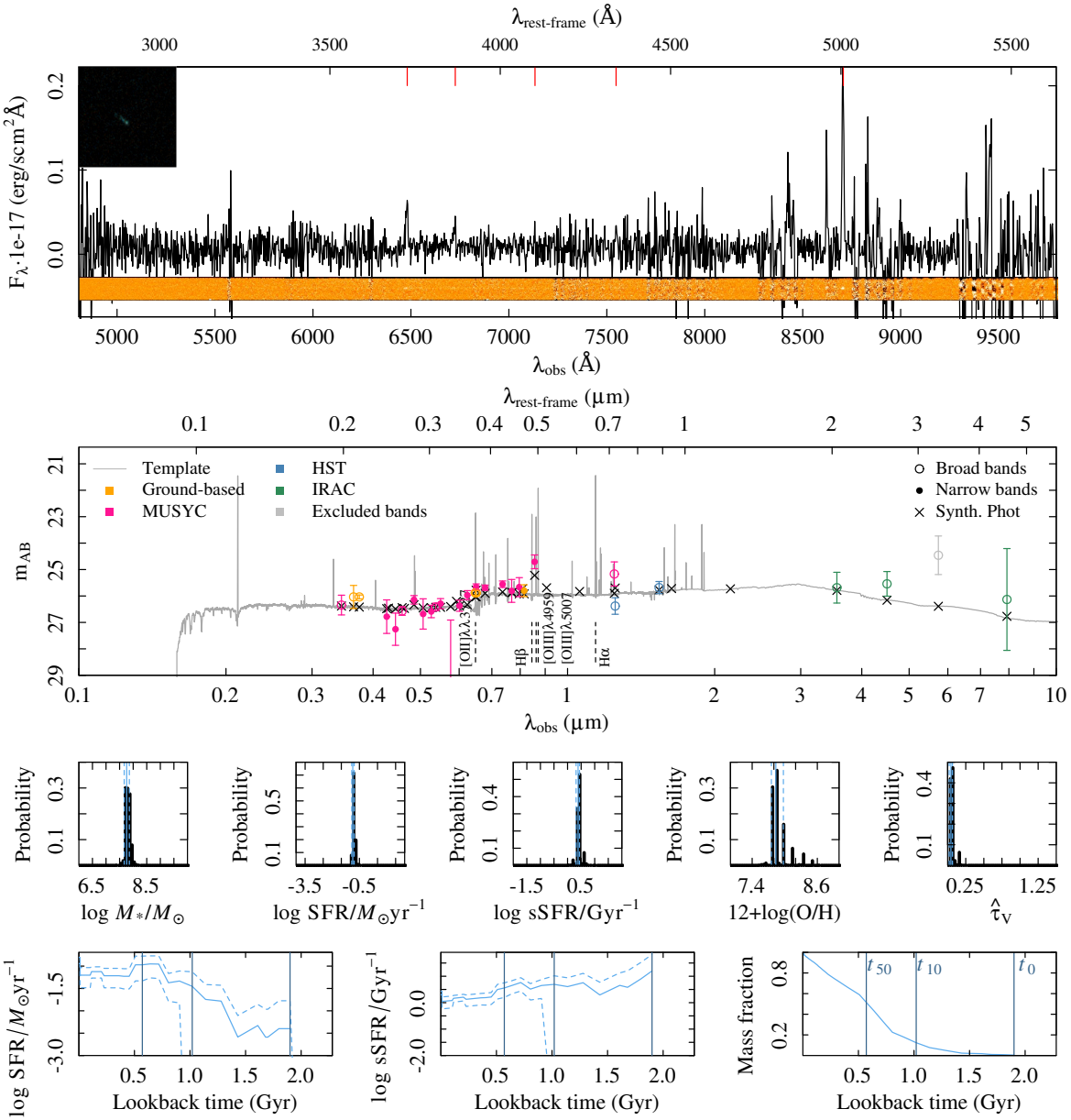

Summary ID 00543

ID	00543	$\mu_{eff,B,0}$	21.9±0.3	F Hα ($\times10^{17}$)	–
α (deg; J2000)	53.213894	$(B-V)_0$	1.27	EW Hα	–
δ (deg; J2000)	-27.735340	F Hβ ($\times10^{17}$)	–	log $M_*/M_\odot$	$9.1^{9.1}_{9.0}$
i (mag)	23.59±0.10	EW Hβ	–	log SFR/$M_\odot\,yr^{-1}$	$1.0^{1.0}_{0.9}$
J (mag)	23.30±0.08	F [OII]$\lambda\lambda$3727 ($\times10^{17}$)	$0.3^{0.6}_{0}$	log sSFR/Gyr^{-1}	$0.9^{0.9}_{0.9}$
z_{spec}	0.720/3	EW [OII]$\lambda\lambda$3727	$7.1^{13.7}_{0.9}$	$\hat{\tau}_V$	$1.4^{1.4}_{1.4}$
Morph.	Irr	F [OIII]λ4959 ($\times10^{17}$)	$0.3^{0.6}_{0}$	12+log(O/H)	$7.1^{7.2}_{7.1}$
n	2.5±0.1	EW [OIII]λ4959	$7.1^{13.7}_{0.9}$	t_0 (Gyr)	4.0
$R_{eff,v,0}$	3.6±0.2	F [OIII]λ5007 ($\times10^{17}$)	$0.3^{0.6}_{0}$	t_{10} (Gyr)	2.4
$M_{B,0}$	-17.36	EW [OIII]λ5007	$7.1^{13.7}_{0.9}$	t_{50} (Gyr)	1.0

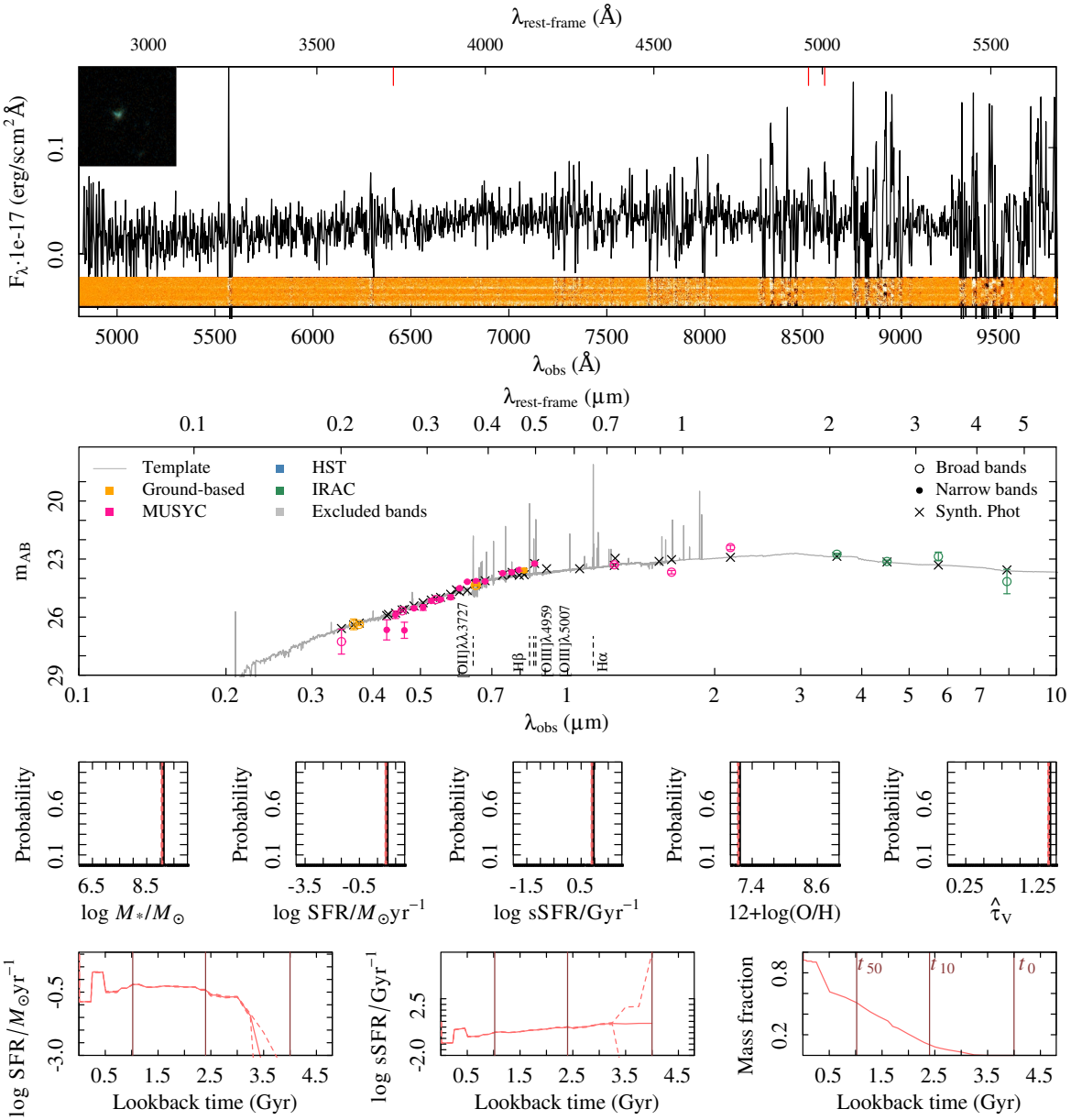

Summary ID 00544

ID	00544	$\mu_{eff,B,0}$	22.9±0.2	F Hα ($\times10^{17}$)	–
α (deg; J2000)	53.217863	$(B-V)_0$	0.62	EW Hα	–
δ (deg; J2000)	-27.928164	F Hβ ($\times10^{17}$)	$0.3^{0.4}_{0.3}$	log $M_*/M_\odot$	$8.3^{8.4}_{8.2}$
i (mag)	25.35±0.12	EW Hβ	$37.6^{58.5}_{22.8}$	log SFR/$M_\odot\,yr^{-1}$	$-1.0^{-0.9}_{-1.0}$
J (mag)	24.06±0.16	F [OII]$\lambda\lambda$3727 ($\times10^{17}$)	$0.8^{1.0}_{0.7}$	log sSFR/Gyr^{-1}	$-0.3^{-0.2}_{-0.3}$
z_{spec}	0.436/4	EW [OII]$\lambda\lambda$3727	$56.1^{80.1}_{39.4}$	$\hat{\tau}_V$	$0.1^{0.2}_{0.1}$
Morph.	C	F [OIII]λ4959 ($\times10^{17}$)	$0.8^{1.0}_{0.7}$	12+log(O/H)	$7.3^{7.3}_{7.2}$
n	1.3±0.2	EW [OIII]λ4959	$56.1^{80.1}_{39.4}$	t_0 (Gyr)	8.0
$R_{eff,v,0}$	0.8±0.0	F [OIII]λ5007 ($\times10^{17}$)	$0.8^{1.0}_{0.7}$	t_{10} (Gyr)	6.5
$M_{B,0}$	-15.94	EW [OIII]λ5007	$56.1^{80.1}_{39.4}$	t_{50} (Gyr)	3.8

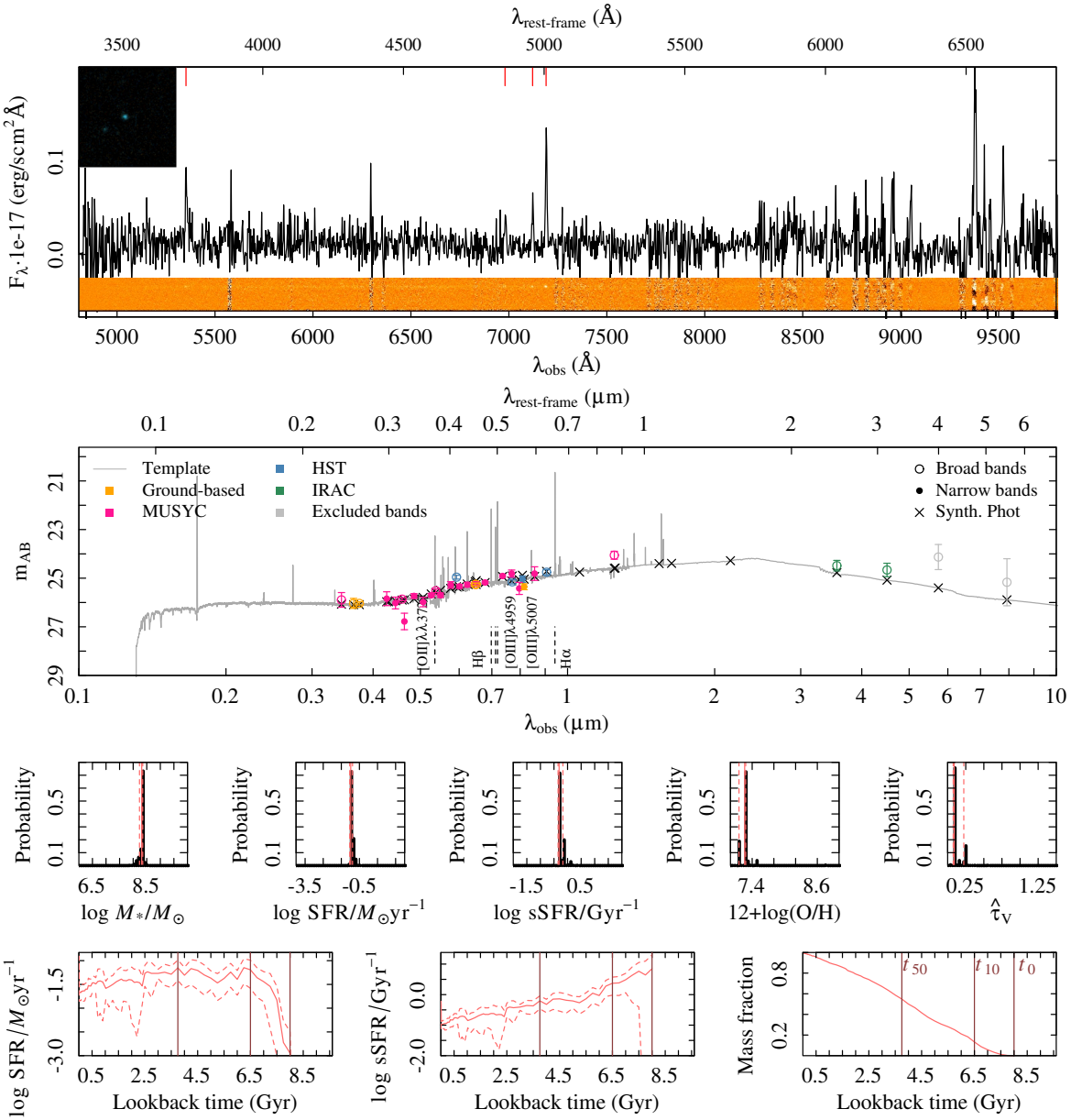

Summary ID 00551

ID	00551	$\mu_{eff,B,0}$	22.4±0.1	F Hα ($\times 10^{17}$)	$0.5^{0.8}_{0.2}$
α (deg; J2000)	53.219341	$(B-V)_0$	0.86	EW Hα	$15.7^{29.0}_{7.1}$
δ (deg; J2000)	-27.862219	F Hβ ($\times 10^{17}$)	$0.1^{0.4}_{0.2}$	log $M_*/M_\odot$	$7.8^{7.8}_{7.7}$
i (mag)	23.89±0.10	EW Hβ	$1.9^{8.2}_{3.0}$	log SFR/$M_\odot\,yr^{-1}$	$-1.6^{-1.6}_{-1.7}$
J (mag)	25.21±0.39	F [OII]$\lambda\lambda$3727 ($\times 10^{17}$)	–	log sSFR/Gyr^{-1}	$-0.3^{-0.3}_{-0.4}$
z_{spec}	0.246/3	EW [OII]$\lambda\lambda$3727	–	$\hat{\tau}_V$	$0.6^{0.6}_{0.6}$
Morph.	U	F [OIII]λ4959 ($\times 10^{17}$)	–	12+log(O/H)	$8.4^{8.4}_{8.4}$
n	0.2±0.0	EW [OIII]λ4959	–	t_0 (Gyr)	3.0
$R_{eff,v,0}$	1.9±0.1	F [OIII]λ5007 ($\times 10^{17}$)	–	t_{10} (Gyr)	1.1
$M_{B,0}$	-15.38	EW [OIII]λ5007	–	t_{50} (Gyr)	0.6

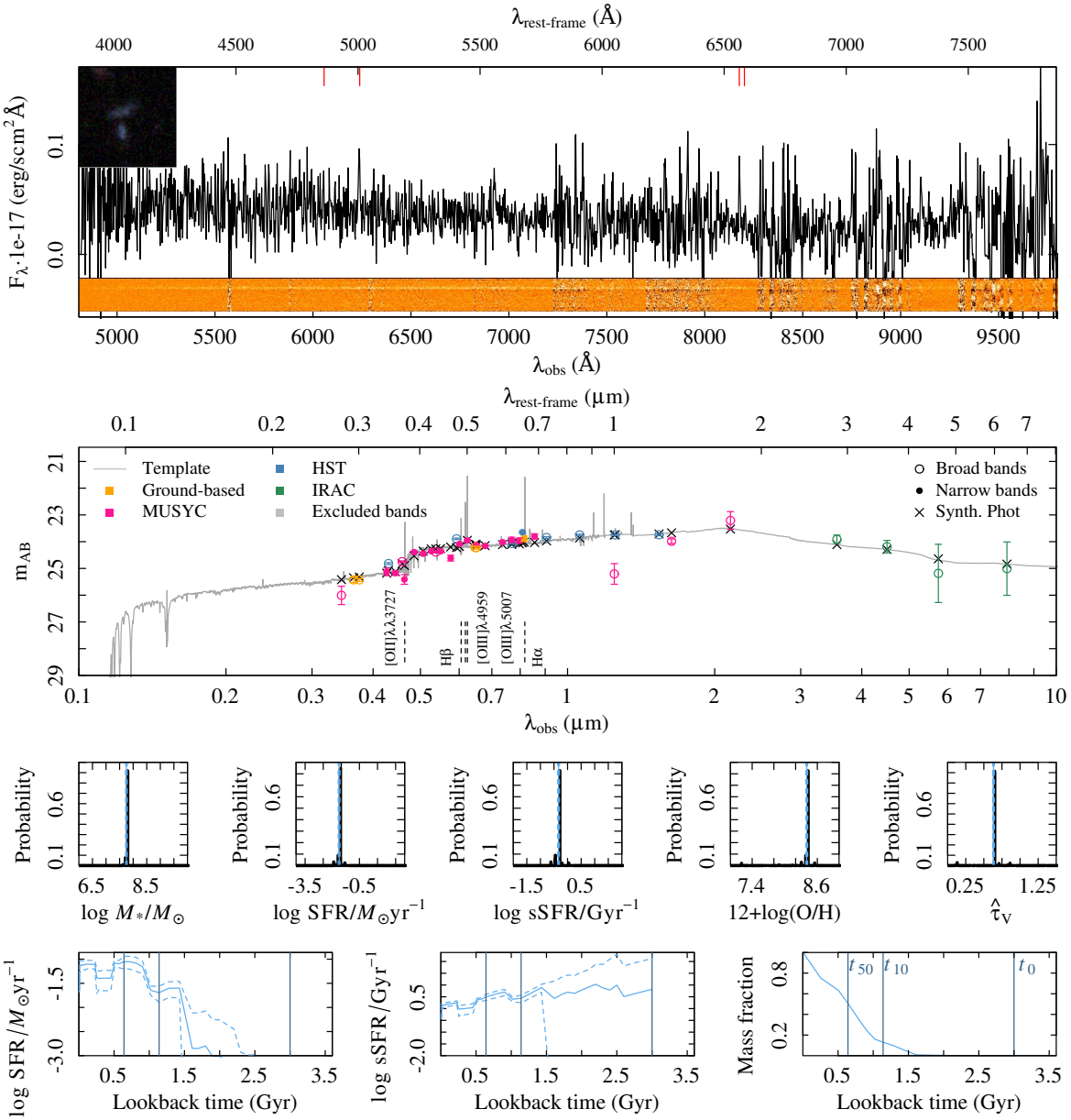

Summary ID 00565

ID	00565	$\mu_{eff,B,0}$	19.7±0.8	F Hα ($\times 10^{17}$)	–
α (deg; J2000)	53.232244	$(B-V)_0$	0.74	EW Hα	–
δ (deg; J2000)	-27.698200	F Hβ ($\times 10^{17}$)	–	log $M_*/M_\odot$	$8.1^{8.1}_{8.0}$
i (mag)	24.78±0.12	EW Hβ	–	log SFR/$M_\odot\, yr^{-1}$	$-1.4^{-1.2}_{-2.0}$
J (mag)	-99.99±-99.99	F [OII]$\lambda\lambda$3727 ($\times 10^{17}$)	$1.1^{1.3}_{1.0}$	log sSFR/Gyr^{-1}	$-0.5^{-0.3}_{-1.1}$
z_{spec}	0.567/3	EW [OII]$\lambda\lambda$3727	$44.0^{62.2}_{32.0}$	$\hat{\tau}_V$	$0.3^{0.5}_{0.1}$
Morph.	Irr	F [OIII]λ4959 ($\times 10^{17}$)	$1.1^{1.3}_{1.0}$	12+log(O/H)	$8.4^{8.5}_{8.0}$
n	0.4±0.0	EW [OIII]λ4959	$44.0^{62.2}_{32.0}$	t_0 (Gyr)	1.4
$R_{eff,v,0}$	1.9±0.0	F [OIII]λ5007 ($\times 10^{17}$)	$1.1^{1.3}_{1.0}$	t_{10} (Gyr)	0.8
$M_{B,0}$	-16.68	EW [OIII]λ5007	$44.0^{62.2}_{32.0}$	t_{50} (Gyr)	0.4

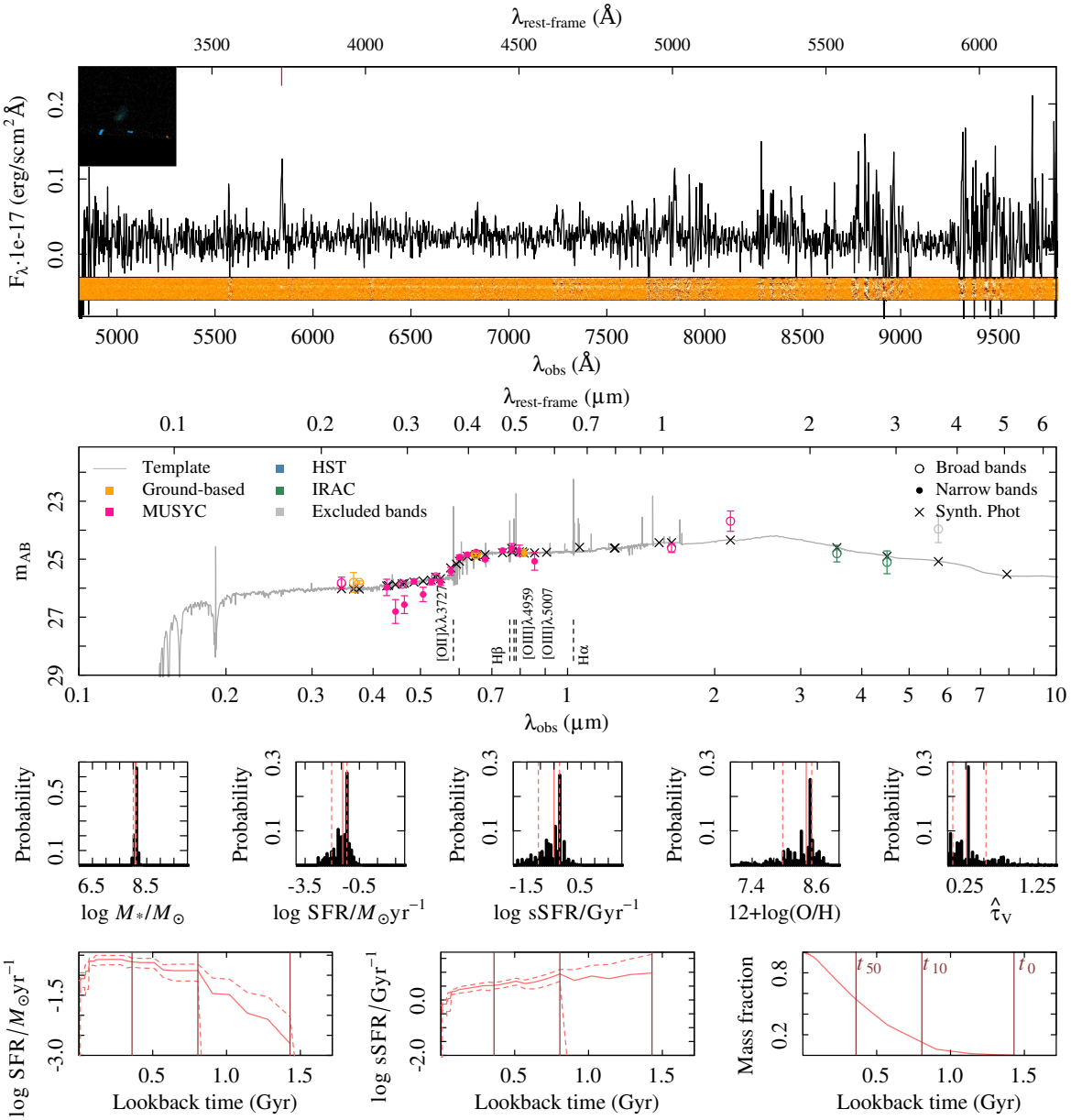

Summary ID 00571

ID	00571	$\mu_{eff,B,0}$	23.1±2.0	F Hα ($\times10^{17}$)	–
α (deg; J2000)	53.235705	$(B-V)_0$	0.97	EW Hα	–
δ (deg; J2000)	-27.906338	F Hβ ($\times10^{17}$)	$0.1^{0.2}_{0}$	log $M_*/M_\odot$	$8.8^{8.9}_{8.7}$
i (mag)	24.80±0.11	EW Hβ	$5.6^{11.5}_{1.4}$	log SFR/$M_\odot\,yr^{-1}$	$-0.7^{-0.4}_{-0.9}$
J (mag)	24.77±0.19	F [OII]$\lambda\lambda$3727 ($\times10^{17}$)	$0.4^{0.5}_{0.4}$	log sSFR/Gyr^{-1}	$-0.6^{-0.3}_{-0.8}$
z_{spec}	0.684/2	EW [OII]$\lambda\lambda$3727	$40.1^{55.8}_{29.6}$	$\hat{\tau}_V$	$0.6^{1.1}_{0.4}$
Morph.	C	F [OIII]λ4959 ($\times10^{17}$)	$0.4^{0.5}_{0.4}$	12+log(O/H)	$8.4^{8.7}_{7.7}$
n	4.9±1.6	EW [OIII]λ4959	$40.1^{55.8}_{29.6}$	t_0 (Gyr)	5.8
$R_{eff,v,0}$	0.8±0.1	F [OIII]λ5007 ($\times10^{17}$)	$0.4^{0.5}_{0.4}$	t_{10} (Gyr)	4.5
$M_{B,0}$	-16.20	EW [OIII]λ5007	$40.1^{55.8}_{29.6}$	t_{50} (Gyr)	2.6

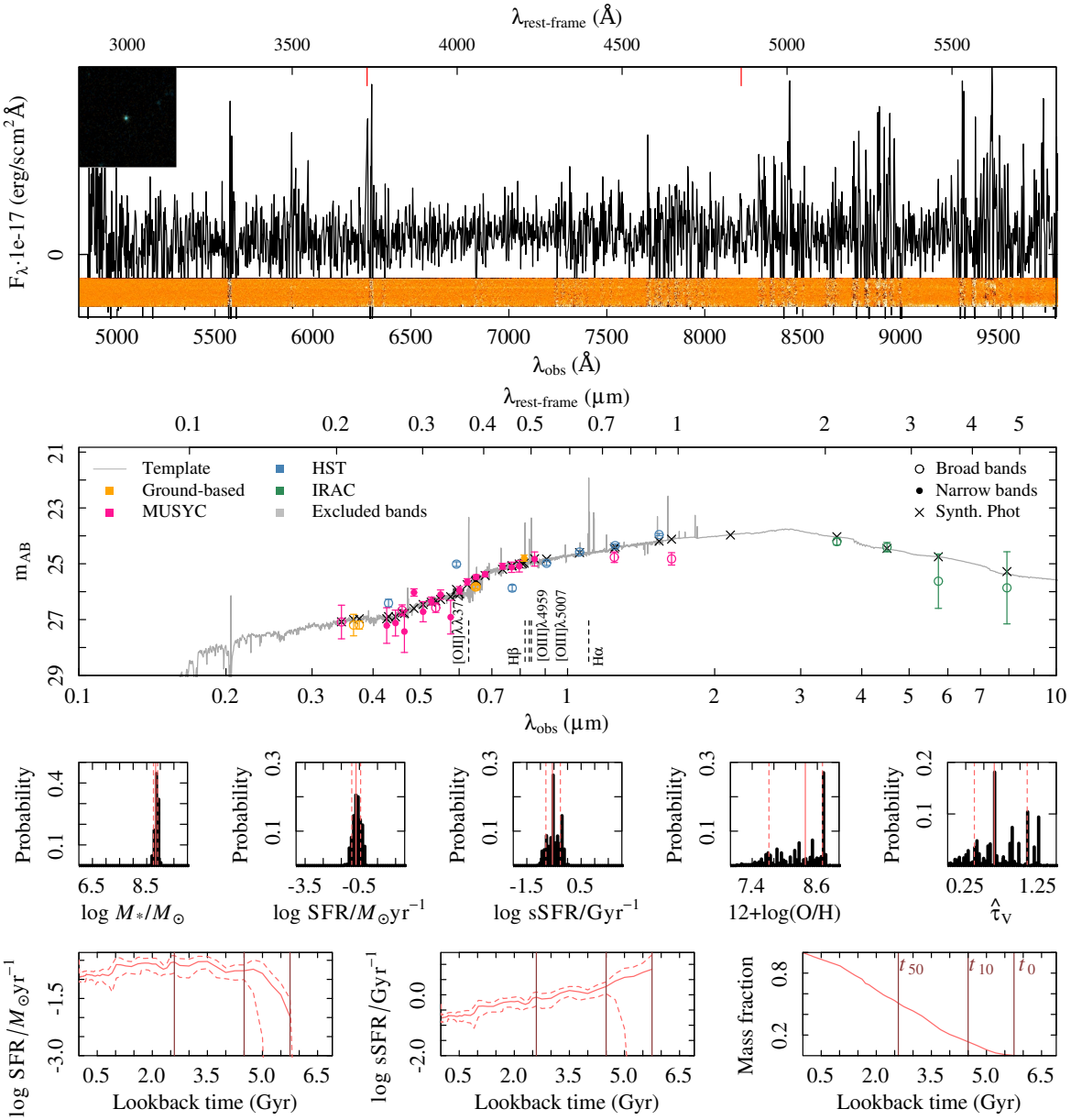

Summary ID 00584

ID	00584	$\mu_{eff,B,0}$	21.7±0.1	F Hα ($\times10^{17}$)	–
α (deg; J2000)	53.246076	$(B-V)_0$	0.39	EW Hα	–
δ (deg; J2000)	-27.642419	F Hβ ($\times10^{17}$)	$1.6^{1.8}_{1.4}$	log $M_*/M_\odot$	$8.3^{8.4}_{8.3}$
i (mag)	23.91±0.10	EW Hβ	$36.3^{48.8}_{27.6}$	log SFR/$M_\odot\,yr^{-1}$	$0.3^{0.4}_{0.2}$
J (mag)	24.12±0.19	F [OII]$\lambda\lambda$3727 ($\times10^{17}$)	$4.3^{4.8}_{4}$	log sSFR/Gyr^{-1}	$1.1^{1.1}_{0.6}$
z_{spec}	0.767/4	EW [OII]$\lambda\lambda$3727	$73.6^{99.8}_{59.8}$	$\hat{\tau}_V$	$0.7^{0.7}_{0.3}$
Morph.	Irr	F [OIII]λ4959 ($\times10^{17}$)	$4.3^{4.8}_{4}$	12+log(O/H)	$7.8^{7.8}_{7.8}$
n	0.9±0.0	EW [OIII]λ4959	$73.6^{99.8}_{59.8}$	t_0 (Gyr)	3.2
$R_{eff,v,0}$	1.4±0.0	F [OIII]λ5007 ($\times10^{17}$)	$4.3^{4.8}_{4}$	t_{10} (Gyr)	0.3
$M_{B,0}$	-18.77	EW [OIII]λ5007	$73.6^{99.8}_{59.8}$	t_{50} (Gyr)	0.1

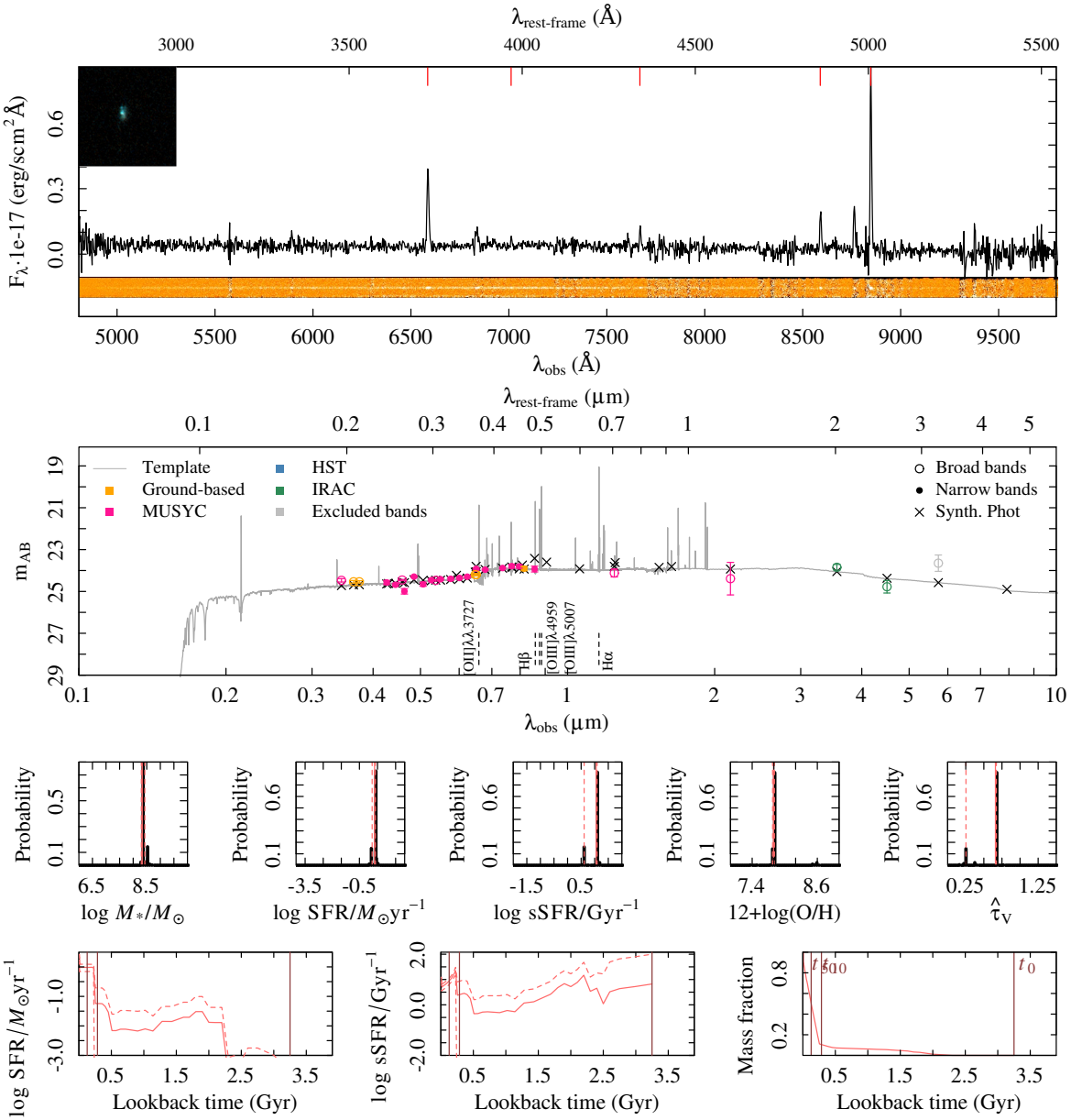

Summary ID 00594

ID	00594	$\mu_{eff,B,0}$	22.0±0.2	F Hα ($\times 10^{17}$)	$4.2^{4.3}_{4.1}$
α (deg; J2000)	53.252631	$(B-V)_0$	0.70	EW Hα	$327.9^{468.9}_{263.8}$
δ (deg; J2000)	-27.704223	F Hβ ($\times 10^{17}$)	$1.2^{1.3}_{1.1}$	log $M_*/M_\odot$	$7.5^{7.7}_{7.4}$
i (mag)	25.03±0.14	EW Hβ	$54.2^{69.3}_{42.7}$	log SFR/$M_\odot\, yr^{-1}$	$-1.2^{-1.1}_{-1.3}$
J (mag)	24.24±0.18	F [OII]$\lambda\lambda$3727 ($\times 10^{17}$)	–	log sSFR/Gyr^{-1}	$0.4^{0.4}_{0.1}$
z_{spec}	0.263/4	EW [OII]$\lambda\lambda$3727	–	$\hat{\tau}_V$	$0.3^{0.3}_{0.2}$
Morph.	C	F [OIII]λ4959 ($\times 10^{17}$)	–	12+log(O/H)	$7.6^{7.8}_{7.5}$
n	2.2±0.3	EW [OIII]λ4959	–	t_0 (Gyr)	9.2
$R_{eff,v,0}$	0.3±0.0	F [OIII]λ5007 ($\times 10^{17}$)	–	t_{10} (Gyr)	6.8
$M_{B,0}$	-14.94	EW [OIII]λ5007	–	t_{50} (Gyr)	3.0

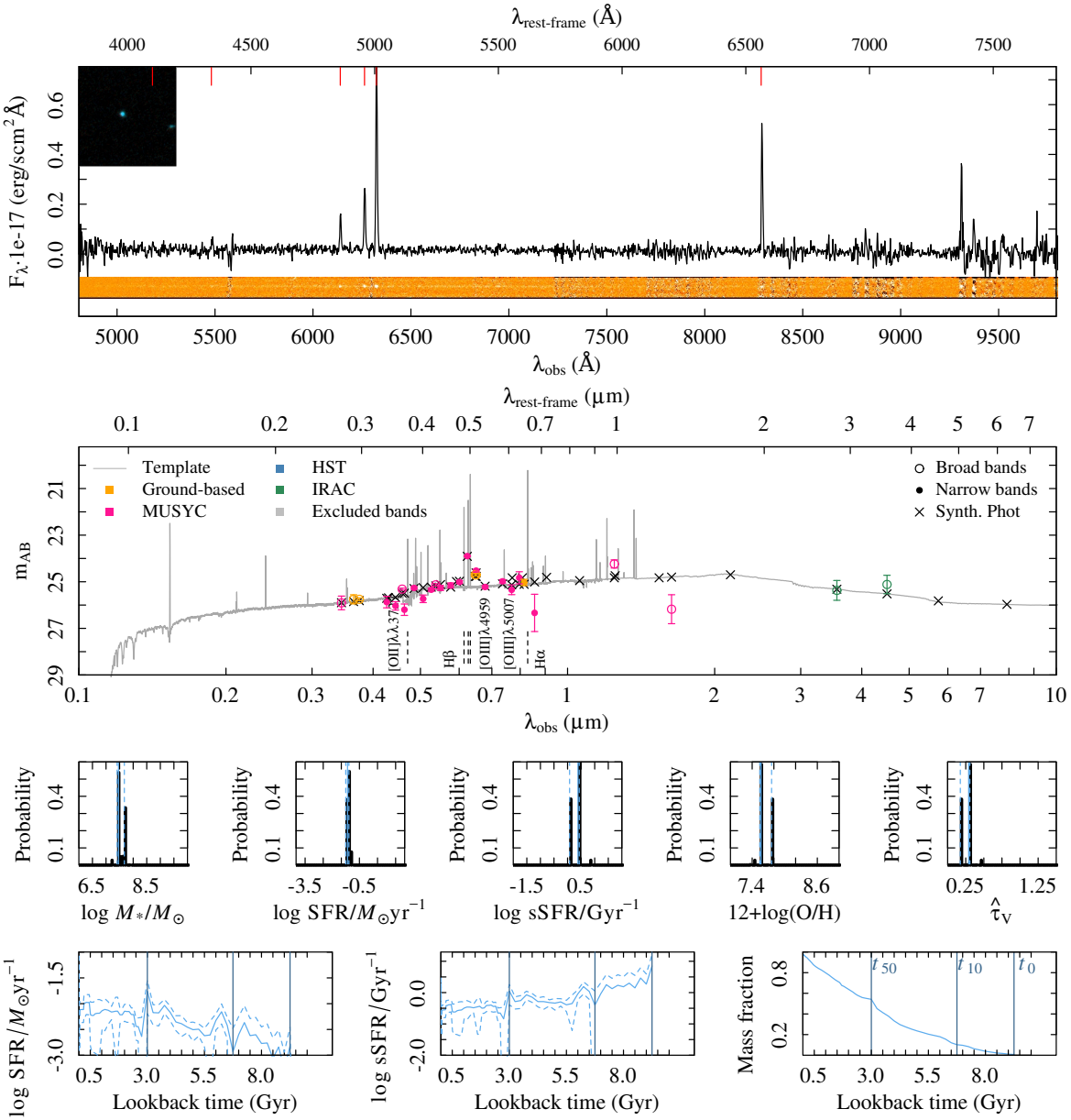

Summary ID 00601

ID	00601	$\mu_{eff,B,0}$	22.0±0.2	F Hα ($\times10^{17}$)	–
α (deg; J2000)	53.257368	$(B-V)_0$	0.99	EW Hα	–
δ (deg; J2000)	-27.731932	F Hβ ($\times10^{17}$)	–	log $M_*/M_\odot$	$8.0^{8.1}_{7.9}$
i (mag)	25.32±0.15	EW Hβ	–	log SFR$/M_\odot\,yr^{-1}$	$-1.4^{-1.1}_{-1.8}$
J (mag)	25.17±0.52	F [OII]$\lambda\lambda$3727 ($\times10^{17}$)	$0.3^{0.4}_{0.2}$	log sSFR$/Gyr^{-1}$	$-0.5^{-0.1}_{-0.9}$
z_{spec}	0.534/3	EW [OII]$\lambda\lambda$3727	$20.5^{31.3}_{12.8}$	$\hat{\tau}_V$	$0.7^{1.0}_{0.2}$
Morph.	Irr	F [OIII]λ4959 ($\times10^{17}$)	$0.3^{0.4}_{0.2}$	12+log(O/H)	$8.2^{8.5}_{7.7}$
n	0.6±0.1	EW [OIII]λ4959	$20.5^{31.3}_{12.8}$	t_0 (Gyr)	3.5
$R_{eff,v,0}$	3.7±0.2	F [OIII]λ5007 ($\times10^{17}$)	$0.3^{0.4}_{0.2}$	t_{10} (Gyr)	1.3
$M_{B,0}$	-15.60	EW [OIII]λ5007	$20.5^{31.3}_{12.8}$	t_{50} (Gyr)	0.6

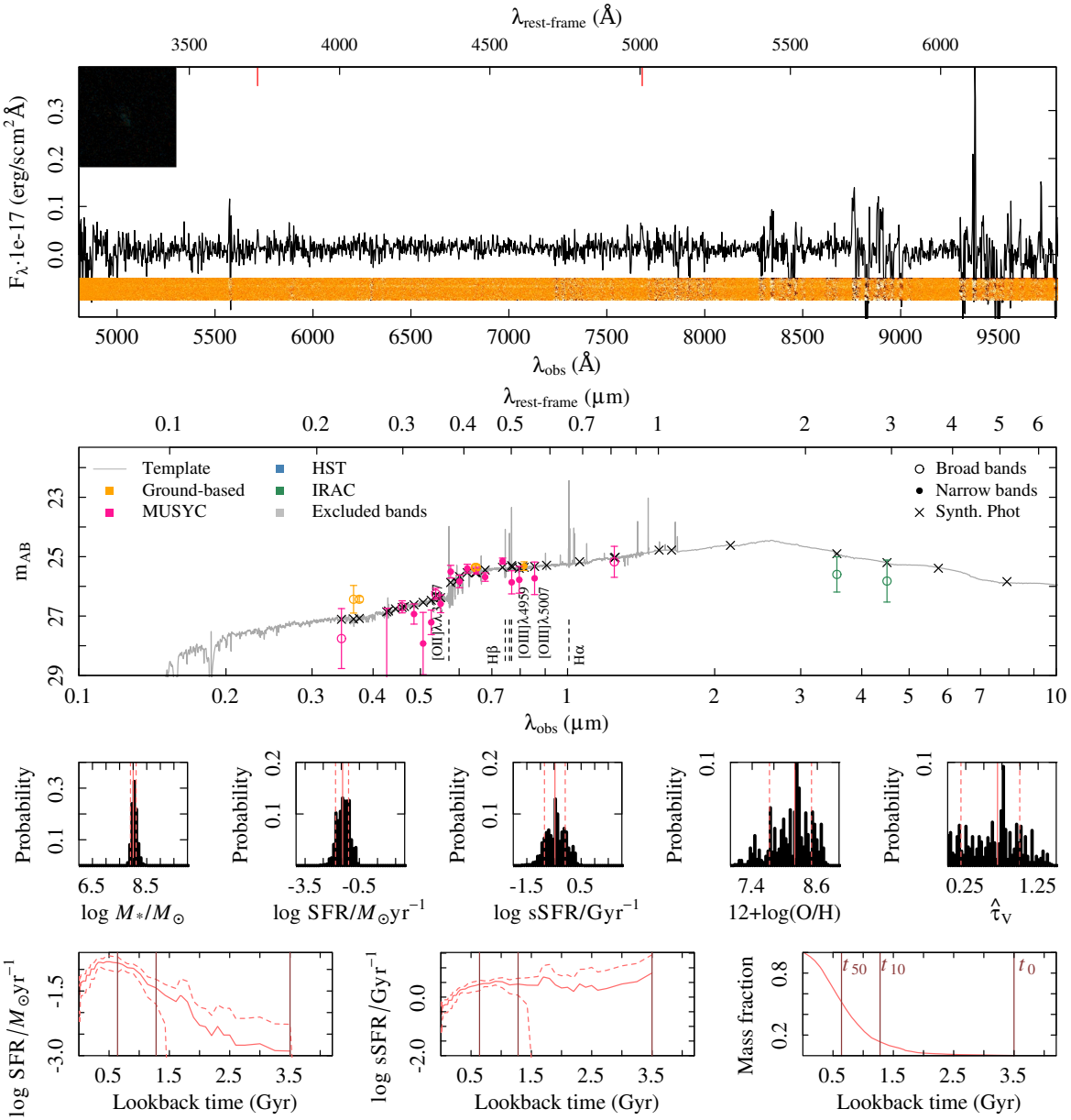

Summary ID 00612

ID	00612	$\mu_{eff,B,0}$	24.4±0.2	F Hα ($\times10^{17}$)	–
α (deg; J2000)	53.262591	$(B-V)_0$	0.25	EW Hα	–
δ (deg; J2000)	-27.697821	F Hβ ($\times10^{17}$)	–	log $M_*/M_\odot$	$7.8^{8.0}_{7.6}$
i (mag)	25.63±0.15	EW Hβ	–	log SFR/$M_\odot\,yr^{-1}$	$-0.4^{-0.3}_{-0.6}$
J (mag)	25.11±0.50	F [OII]$\lambda\lambda$3727 ($\times10^{17}$)	$0.7^{0.8}_{0.7}$	log sSFR/Gyr^{-1}	$0.7^{0.9}_{0.5}$
z_{spec}	0.786/3	EW [OII]$\lambda\lambda$3727	$97.3^{138.6}_{78.3}$	$\hat{\tau}_V$	$0.2^{0.3}_{0.2}$
Morph.	Irr	F [OIII]λ4959 ($\times10^{17}$)	$0.7^{0.8}_{0.7}$	12+log(O/H)	$7.9^{8.1}_{7.7}$
n	1.2±0.2	EW [OIII]λ4959	$97.3^{138.6}_{78.3}$	t_0 (Gyr)	1.6
$R_{eff,v,0}$	1.6±0.1	F [OIII]λ5007 ($\times10^{17}$)	$0.7^{0.8}_{0.7}$	t_{10} (Gyr)	1.0
$M_{B,0}$	-17.06	EW [OIII]λ5007	$97.3^{138.6}_{78.3}$	t_{50} (Gyr)	0.4

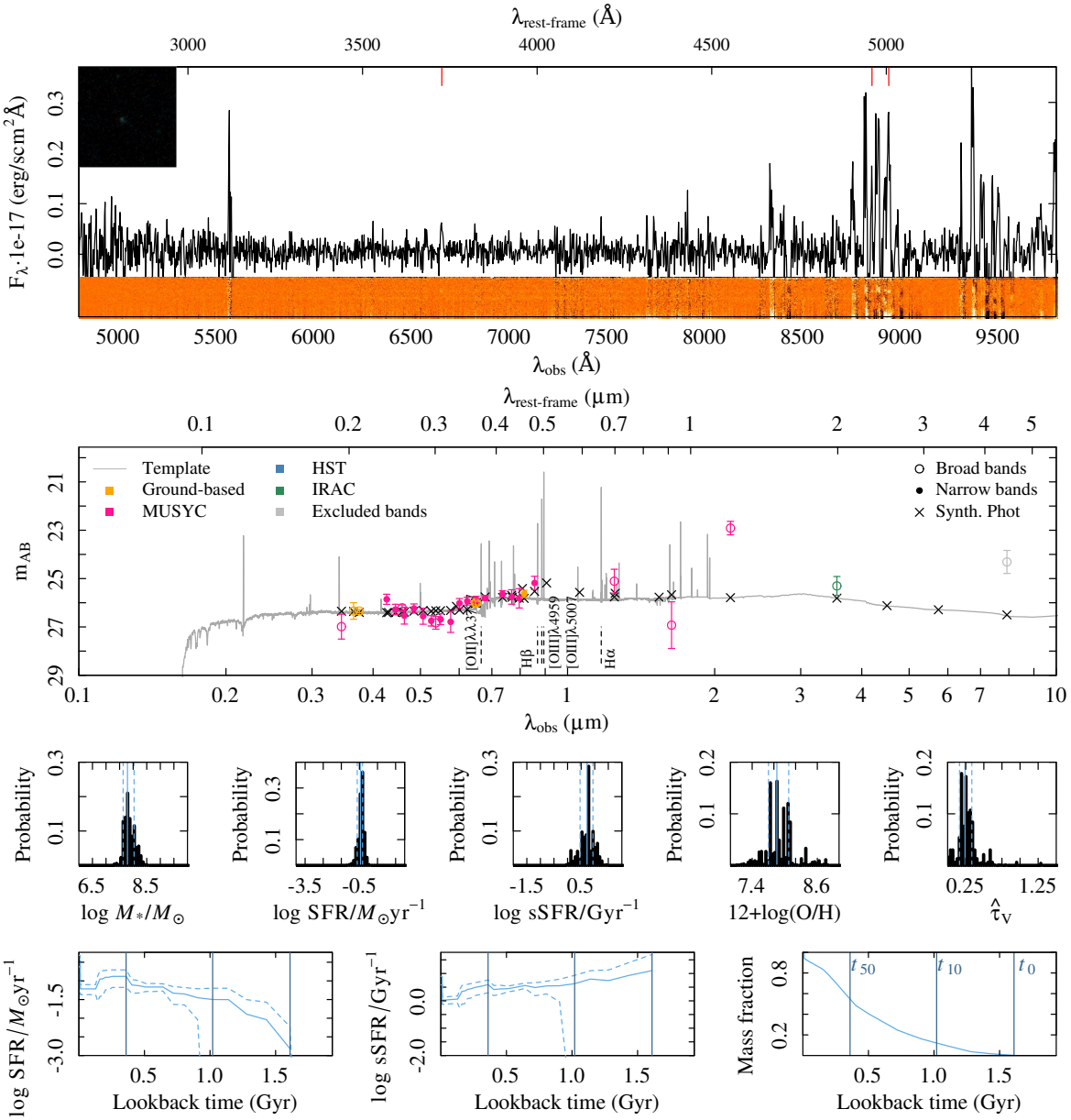

Summary ID 00626

ID	00626	$\mu_{eff,B,0}$	21.7±0.2	F Hα ($\times10^{17}$)	–
α (deg; J2000)	53.271349	$(B-V)_0$	0.25	EW Hα	–
δ (deg; J2000)	-27.725206	F Hβ ($\times10^{17}$)	$0.7^{0.7}_{0.6}$	log $M_*/M_\odot$	$7.6^{7.9}_{7.5}$
i (mag)	25.14±0.14	EW Hβ	$118.8^{181.9}_{86.1}$	log SFR/$M_\odot\,yr^{-1}$	$-0.5^{-0.4}_{-0.6}$
J (mag)	25.57±0.46	F [OII]$\lambda\lambda$3727 ($\times10^{17}$)	$0.8^{0.9}_{0.7}$	log sSFR/Gyr^{-1}	$0.9^{0.9}_{0.5}$
z_{spec}	0.656/4	EW [OII]$\lambda\lambda$3727	$47.8^{73.3}_{34.6}$	$\hat{\tau}_V$	$0.1^{0.2}_{0.0}$
Morph.	Irr	F [OIII]λ4959 ($\times10^{17}$)	$0.8^{0.9}_{0.7}$	12+log(O/H)	$7.7^{7.8}_{7.4}$
n	0.7±0.1	EW [OIII]λ4959	$47.8^{73.3}_{34.6}$	t_0 (Gyr)	1.3
$R_{eff,v,0}$	0.9±0.0	F [OIII]λ5007 ($\times10^{17}$)	$0.8^{0.9}_{0.7}$	t_{10} (Gyr)	0.7
$M_{B,0}$	-17.22	EW [OIII]λ5007	$47.8^{73.3}_{34.6}$	t_{50} (Gyr)	0.3

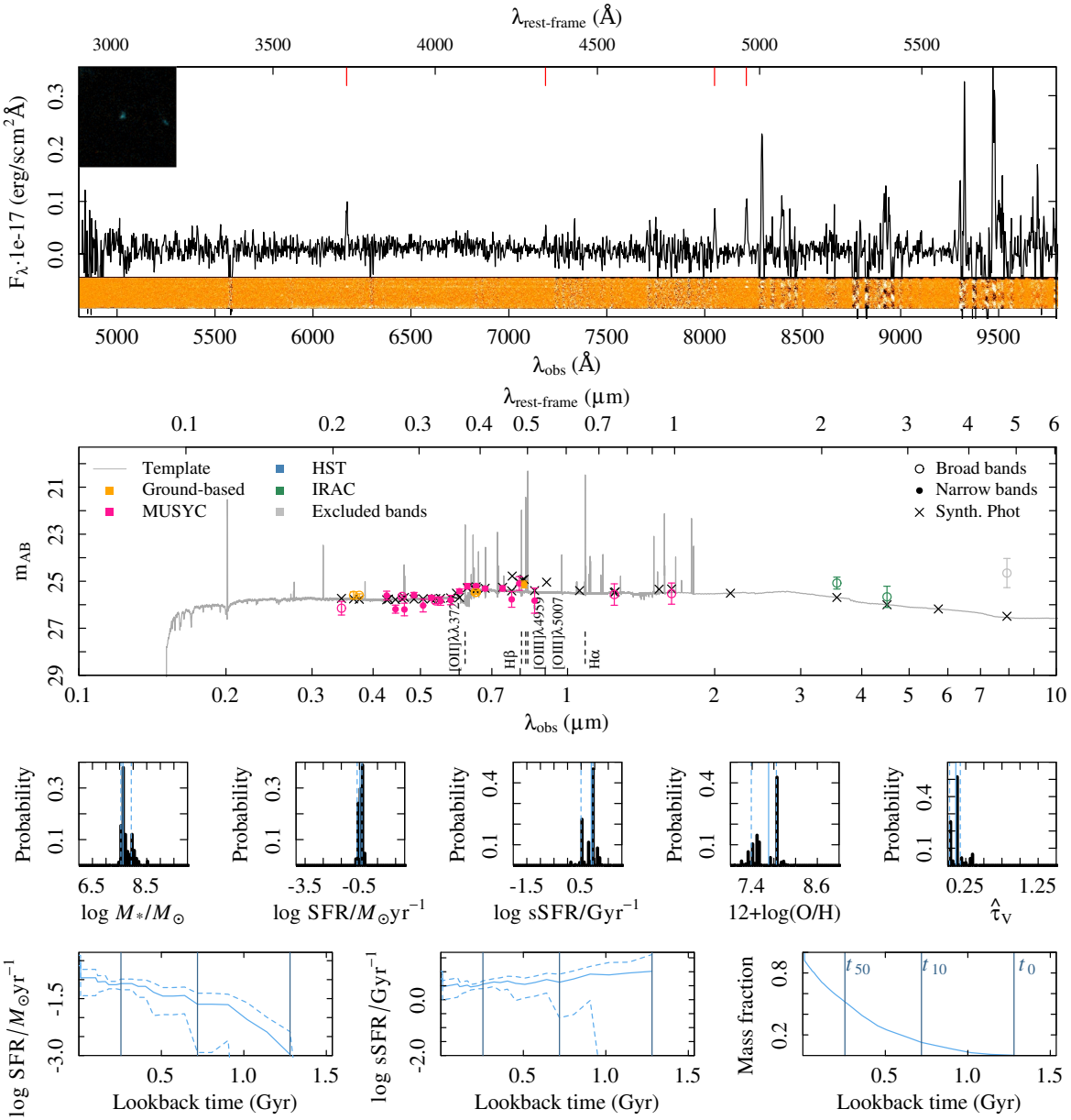

Summary ID 00634

ID	00634	$\mu_{eff,B,0}$	26.1±4.6	F Hα ($\times 10^{17}$)	–
α (deg; J2000)	53.275932	$(B-V)_0$	0.05	EW Hα	–
δ (deg; J2000)	-27.847659	F Hβ ($\times 10^{17}$)	–	log $M_*/M_\odot$	$8.8^{8.9}_{8.7}$
i (mag)	25.12±0.12	EW Hβ	–	log SFR/$M_\odot\, yr^{-1}$	$0.3^{0.4}_{0.2}$
J (mag)	26.72±1.09	F [OII]$\lambda\lambda$3727 ($\times 10^{17}$)	$4.6^{4.7}_{4.4}$	log sSFR/Gyr^{-1}	$0.6^{0.6}_{0.4}$
z_{spec}	1.255/2	EW [OII]$\lambda\lambda$3727	$154.1^{192.3}_{126.9}$	$\hat{\tau}_V$	$0.2^{0.2}_{0.2}$
Morph.	Irr	F [OIII]λ4959 ($\times 10^{17}$)	$4.6^{4.7}_{4.4}$	12+log(O/H)	$7.7^{7.9}_{7.7}$
n	1.1±0.1	EW [OIII]λ4959	$154.1^{192.3}_{126.9}$	t_0 (Gyr)	4.0
$R_{eff,v,0}$	4.0±0.1	F [OIII]λ5007 ($\times 10^{17}$)	$4.6^{4.7}_{4.4}$	t_{10} (Gyr)	2.5
$M_{B,0}$	-19.22	EW [OIII]λ5007	$154.1^{192.3}_{126.9}$	t_{50} (Gyr)	1.1

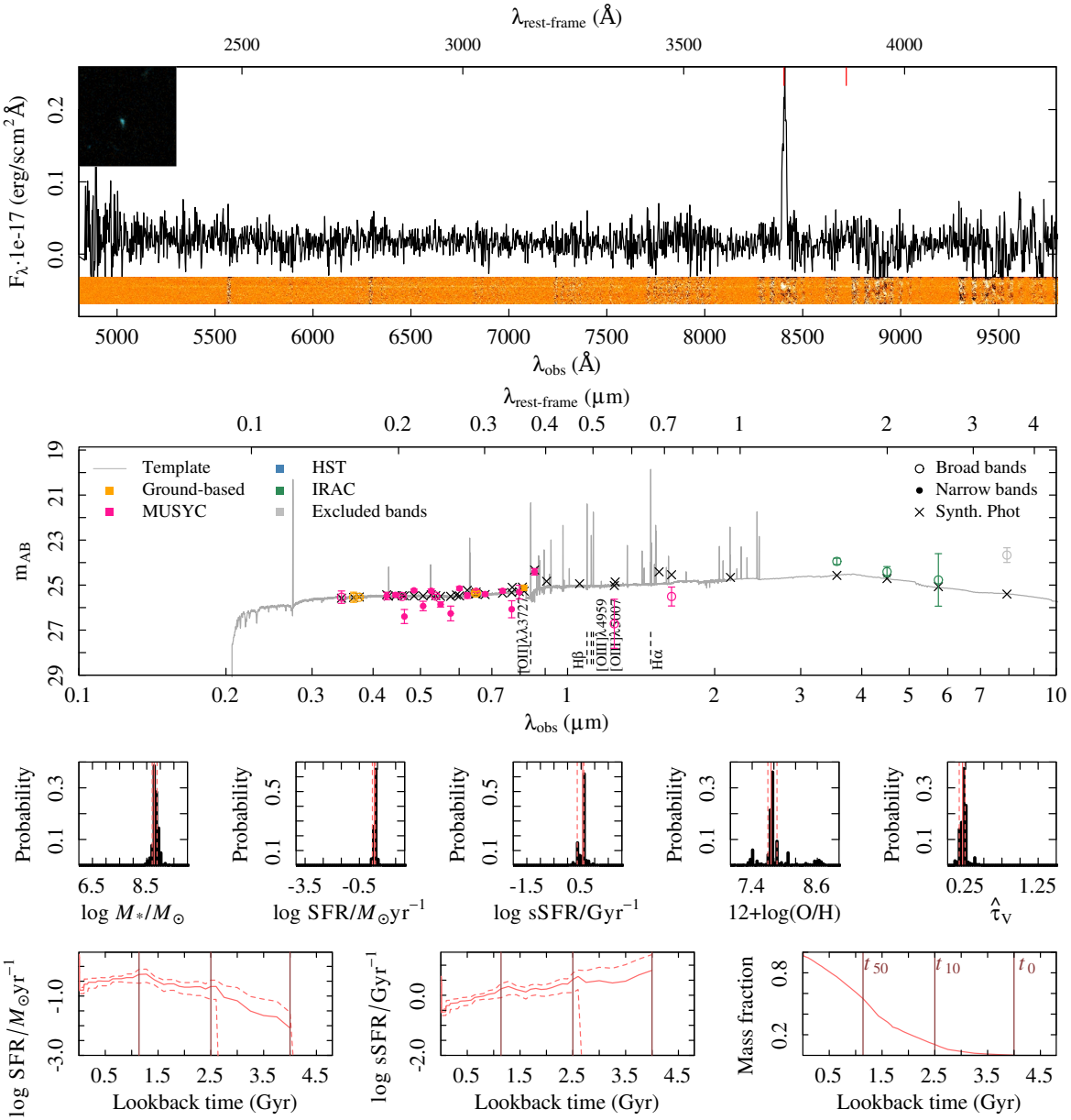

Summary ID 00642

ID	00642	$\mu_{eff,B,0}$	14.9±7.3	F Hα ($\times 10^{17}$)	–
α (deg; J2000)	53.280529	$(B-V)_0$	0.18	EW Hα	–
δ (deg; J2000)	-27.888326	F Hβ ($\times 10^{17}$)	–	log $M_*/M_\odot$	$7.5^{7.6}_{7.5}$
i (mag)	25.70±0.20	EW Hβ	–	log SFR/$M_\odot\, yr^{-1}$	$0.0^{0.0}_{-0.4}$
J (mag)	28.39±2.11	F [OII]$\lambda\lambda$3727 ($\times 10^{17}$)	$0.4^{0.5}_{0.2}$	log sSFR/Gyr^{-1}	$1.4^{1.4}_{1.1}$
z_{spec}	0.817/3	EW [OII]$\lambda\lambda$3727	$13.0^{26.5}_{7.0}$	$\hat{\tau}_V$	$0.6^{0.6}_{0.1}$
Morph.	D	F [OIII]λ4959 ($\times 10^{17}$)	$0.4^{0.5}_{0.2}$	12+log(O/H)	$7.1^{7.8}_{7.1}$
n	2.8±1.1	EW [OIII]λ4959	$13.0^{26.5}_{7.0}$	t_0 (Gyr)	6.0
$R_{eff,v,0}$	0.5±0.1	F [OIII]λ5007 ($\times 10^{17}$)	$0.4^{0.5}_{0.2}$	t_{10} (Gyr)	4.8
$M_{B,0}$	-17.17	EW [OIII]λ5007	$13.0^{26.5}_{7.0}$	t_{50} (Gyr)	2.3

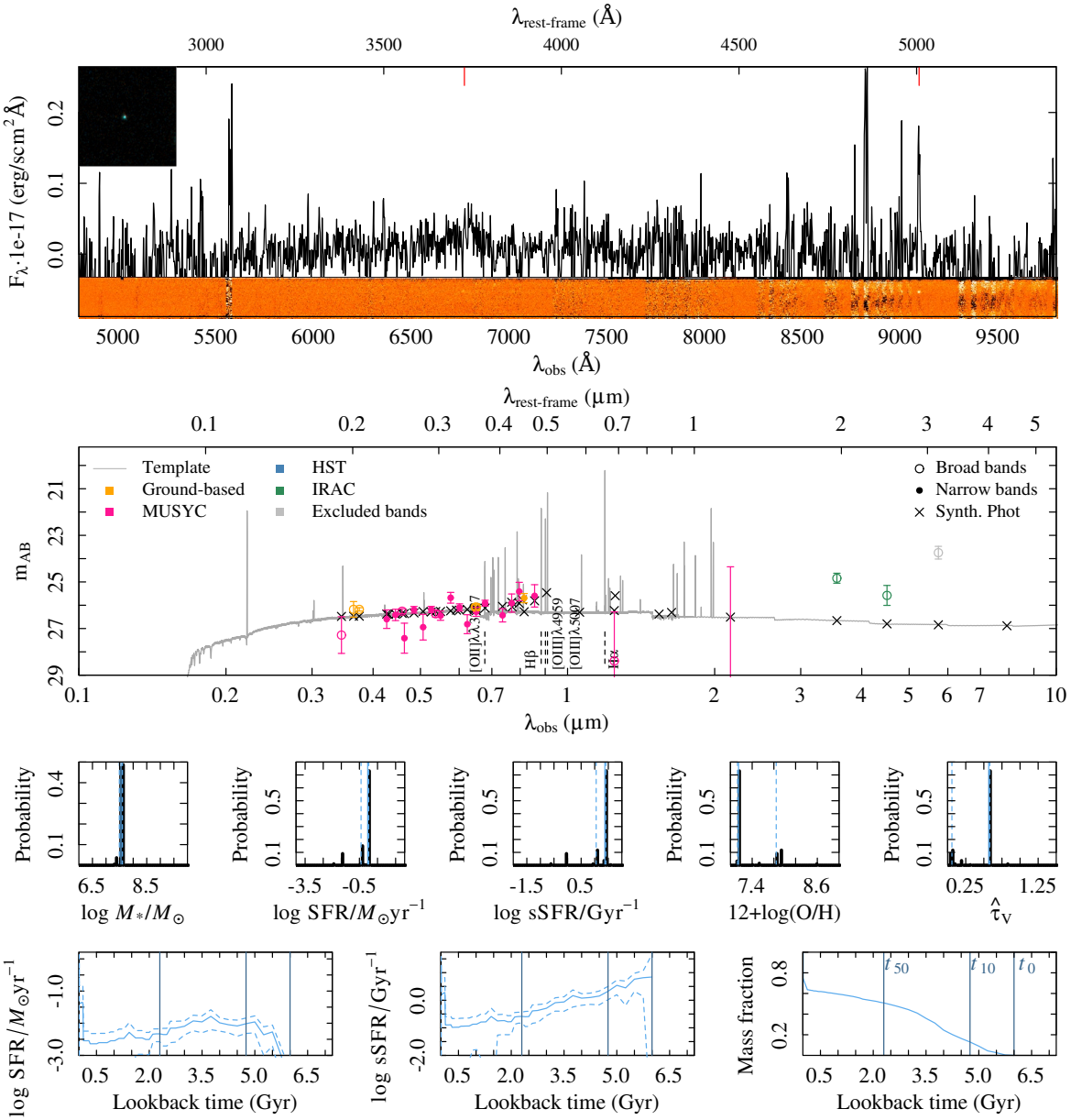

Summary ID 01017

ID	01017	$\mu_{eff,B,0}$	21.8±0.2	F Hα ($\times 10^{17}$)	–
α (deg; J2000)	52.945856	$(B-V)_0$	0.66	EW Hα	–
δ (deg; J2000)	-27.937501	F Hβ ($\times 10^{17}$)	–	log $M_*/M_\odot$	$8.4^{8.5}_{8.3}$
i (mag)	24.28±0.12	EW Hβ	–	log SFR/$M_\odot\, yr^{-1}$	$-0.6^{-0.4}_{-1.0}$
J (mag)	-99.99±-99.99	F [OII]$\lambda\lambda$3727 ($\times 10^{17}$)	$0.3^{0.5}_{0.1}$	log sSFR/Gyr^{-1}	$-0.1^{0.2}_{-0.5}$
z_{spec}	0.674/3	EW [OII]$\lambda\lambda$3727	$13.6^{26.3}_{5.0}$	$\hat{\tau}_V$	$0.6^{0.9}_{0.2}$
Morph.	D	F [OIII]λ4959 ($\times 10^{17}$)	$0.3^{0.5}_{0.1}$	12+log(O/H)	$8.1^{8.4}_{7.7}$
n	0.8±0.1	EW [OIII]λ4959	$13.6^{26.3}_{5.0}$	t_0 (Gyr)	2.5
$R_{eff,v,0}$	1.4±0.0	F [OIII]λ5007 ($\times 10^{17}$)	$0.3^{0.5}_{0.1}$	t_{10} (Gyr)	1.0
$M_{B,0}$	-17.39	EW [OIII]λ5007	$13.6^{26.3}_{5.0}$	t_{50} (Gyr)	0.4

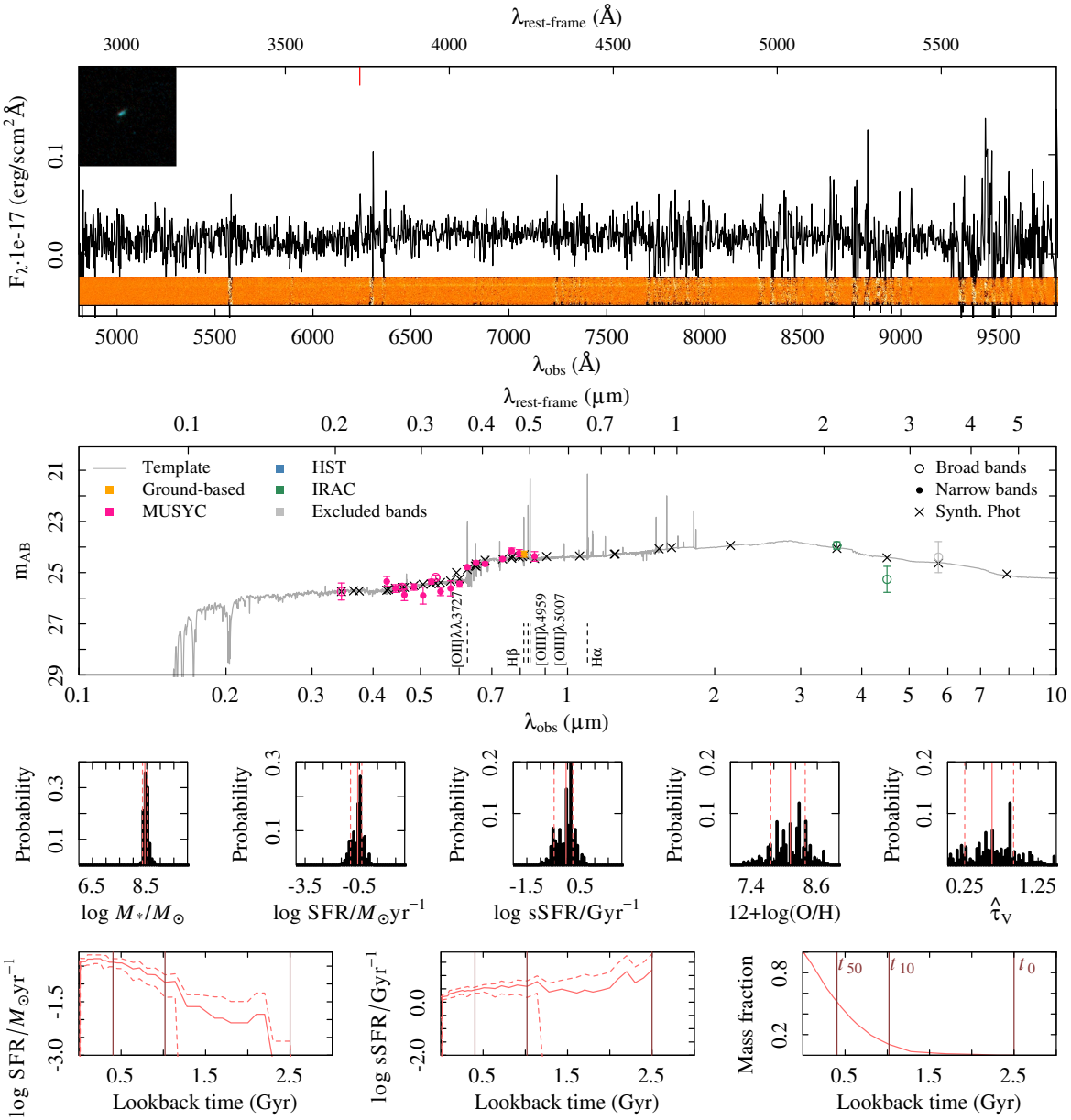

Summary ID 01032

ID	01032	$\mu_{eff,B,0}$	31.9±5.0	F Hα ($\times 10^{17}$)	$2.7^{4}_{1.5}$
α (deg; J2000)	52.950095	$(B-V)_0$	1.12	EW Hα	$17.0^{34.6}_{7.8}$
δ (deg; J2000)	-27.833122	F Hβ ($\times 10^{17}$)	$1.1^{2.6}_{0.6}$	log $M_*/M_\odot$	$9.1^{9.2}_{9.1}$
i (mag)	21.93±0.10	EW Hβ	$4.2^{12.9}_{2.2}$	log SFR/$M_\odot\,yr^{-1}$	$-1.1^{-1.1}_{-1.2}$
J (mag)	21.89±0.05	F [OII]$\lambda\lambda$3727 ($\times 10^{17}$)	$3.7^{5.7}_{1.9}$	log sSFR/Gyr^{-1}	$-1.3^{-1.3}_{-1.3}$
z_{spec}	0.467/3	EW [OII]$\lambda\lambda$3727	$14.4^{25.0}_{6.7}$	$\hat{\tau}_V$	$0.2^{0.2}_{0.2}$
Morph.	U	F [OIII]λ4959 ($\times 10^{17}$)	$3.7^{5.7}_{1.9}$	12+log(O/H)	$7.5^{7.5}_{7.5}$
n	3.1±0.1	EW [OIII]λ4959	$14.4^{25.0}_{6.7}$	t_0 (Gyr)	3.8
$R_{eff,v,0}$	3.0±0.1	F [OIII]λ5007 ($\times 10^{17}$)	$3.7^{5.7}_{1.9}$	t_{10} (Gyr)	1.0
$M_{B,0}$	-18.41	EW [OIII]λ5007	$14.4^{25.0}_{6.7}$	t_{50} (Gyr)	0.8

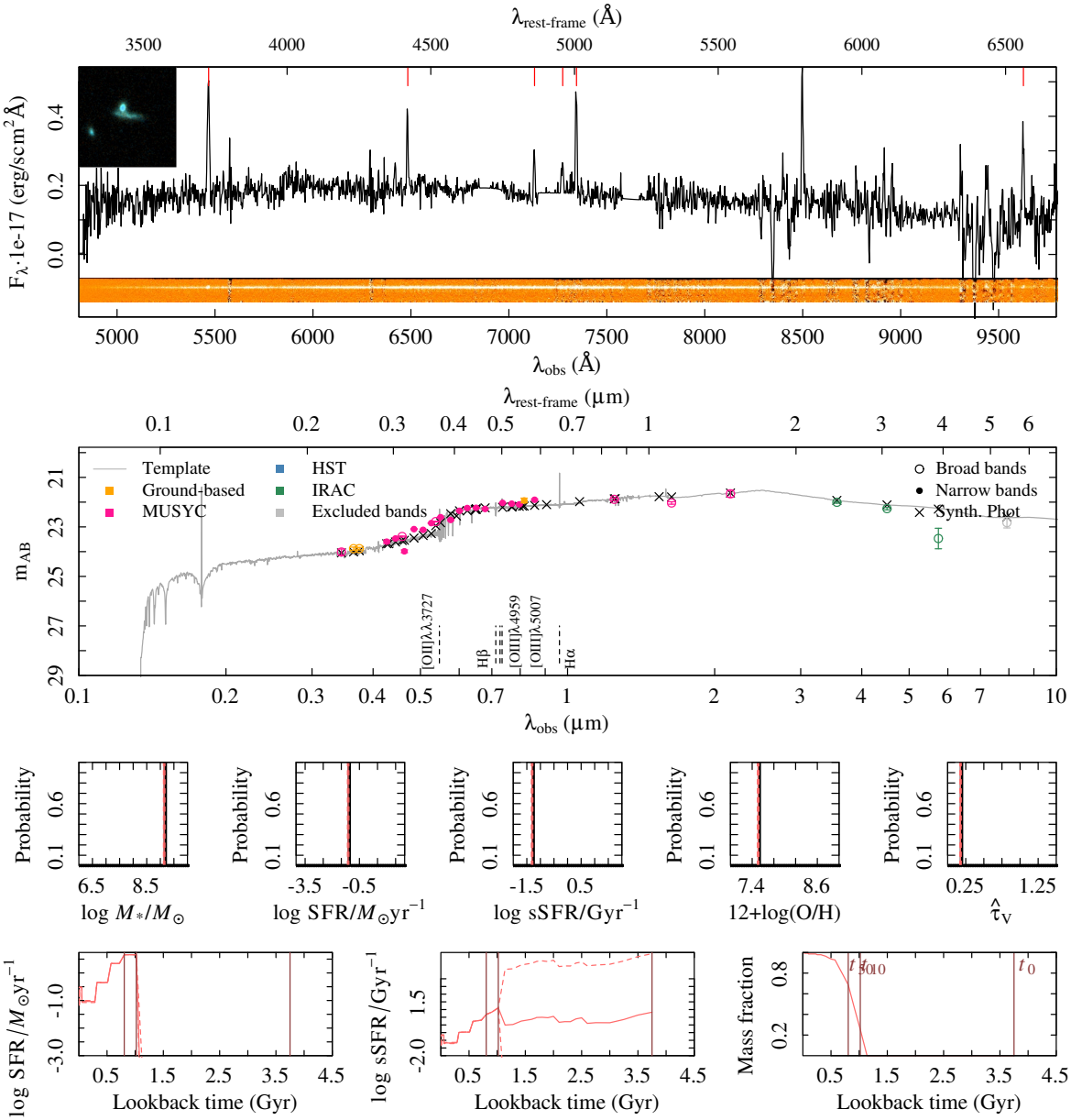

Summary ID 01056

ID	01056	$\mu_{eff,B,0}$	23.4±0.1	F Hα ($\times10^{17}$)	–
α (deg; J2000)	52.961075	$(B-V)_0$	0.78	EW Hα	–
δ (deg; J2000)	-27.755775	F Hβ ($\times10^{17}$)	$0.6^{0.9}_{0.2}$	log $M_*/M_\odot$	$9.2^{9.3}_{9.2}$
i (mag)	22.82±0.10	EW Hβ	$5.6^{11.0}_{1.8}$	log SFR/$M_\odot\,yr^{-1}$	$0.1^{0.1}_{0.1}$
J (mag)	23.03±0.14	F [OII]$\lambda\lambda$3727 ($\times10^{17}$)	$3^{3.5}_{2.4}$	log sSFR/Gyr^{-1}	$-0.2^{-0.1}_{-0.2}$
z_{spec}	0.522/3	EW [OII]$\lambda\lambda$3727	$40.3^{55.3}_{28.7}$	$\hat{\tau}_V$	$0.8^{0.8}_{0.7}$
Morph.	D	F [OIII]λ4959 ($\times10^{17}$)	$3^{3.5}_{2.4}$	12+log(O/H)	$7.2^{7.2}_{7.2}$
n	1.8±0.1	EW [OIII]λ4959	$40.3^{55.3}_{28.7}$	t_0 (Gyr)	6.5
$R_{eff,v,0}$	2.3±0.0	F [OIII]λ5007 ($\times10^{17}$)	$3^{3.5}_{2.4}$	t_{10} (Gyr)	3.8
$M_{B,0}$	-18.14	EW [OIII]λ5007	$40.3^{55.3}_{28.7}$	t_{50} (Gyr)	2.3

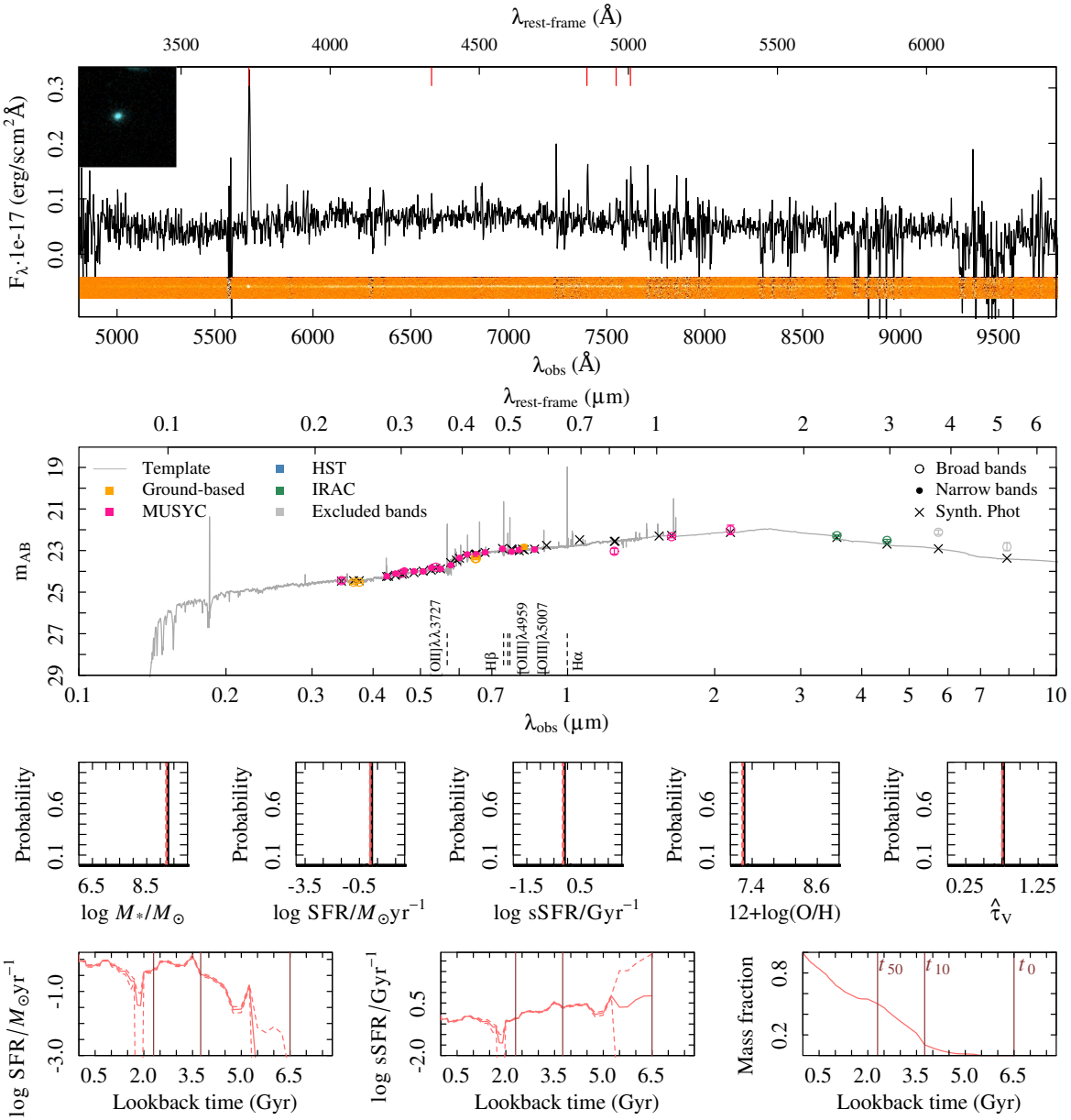

Summary ID 01090

ID	01090	$\mu_{eff,B,0}$	22.6±0.3	F Hα ($\times 10^{17}$)	–
α (deg; J2000)	52.972494	$(B-V)_0$	0.20	EW Hα	–
δ (deg; J2000)	-27.888551	F Hβ ($\times 10^{17}$)	–	log $M_*/M_\odot$	$7.6^{7.6}_{7.6}$
i (mag)	24.99±0.13	EW Hβ	–	log SFR/$M_\odot\, yr^{-1}$	$-1.2^{-1.2}_{-1.3}$
J (mag)	-99.99±-99.99	F [OII]$\lambda\lambda$3727 ($\times 10^{17}$)	$0.6^{0.6}_{0.5}$	log sSFR/Gyr^{-1}	$0.2^{0.3}_{0.2}$
z_{spec}	0.610/2	EW [OII]$\lambda\lambda$3727	$70.2^{102.8}_{52.0}$	$\hat{\tau}_V$	$0.9^{0.9}_{0.9}$
Morph.	D	F [OIII]λ4959 ($\times 10^{17}$)	$0.6^{0.6}_{0.5}$	12+log(O/H)	$7.2^{7.2}_{7.2}$
n	1.6±0.4	EW [OIII]λ4959	$70.2^{102.8}_{52.0}$	t_0 (Gyr)	5.8
$R_{eff,v,0}$	0.3±0.0	F [OIII]λ5007 ($\times 10^{17}$)	$0.6^{0.6}_{0.5}$	t_{10} (Gyr)	0.1
$M_{B,0}$	-16.65	EW [OIII]λ5007	$70.2^{102.8}_{52.0}$	t_{50} (Gyr)	0.0

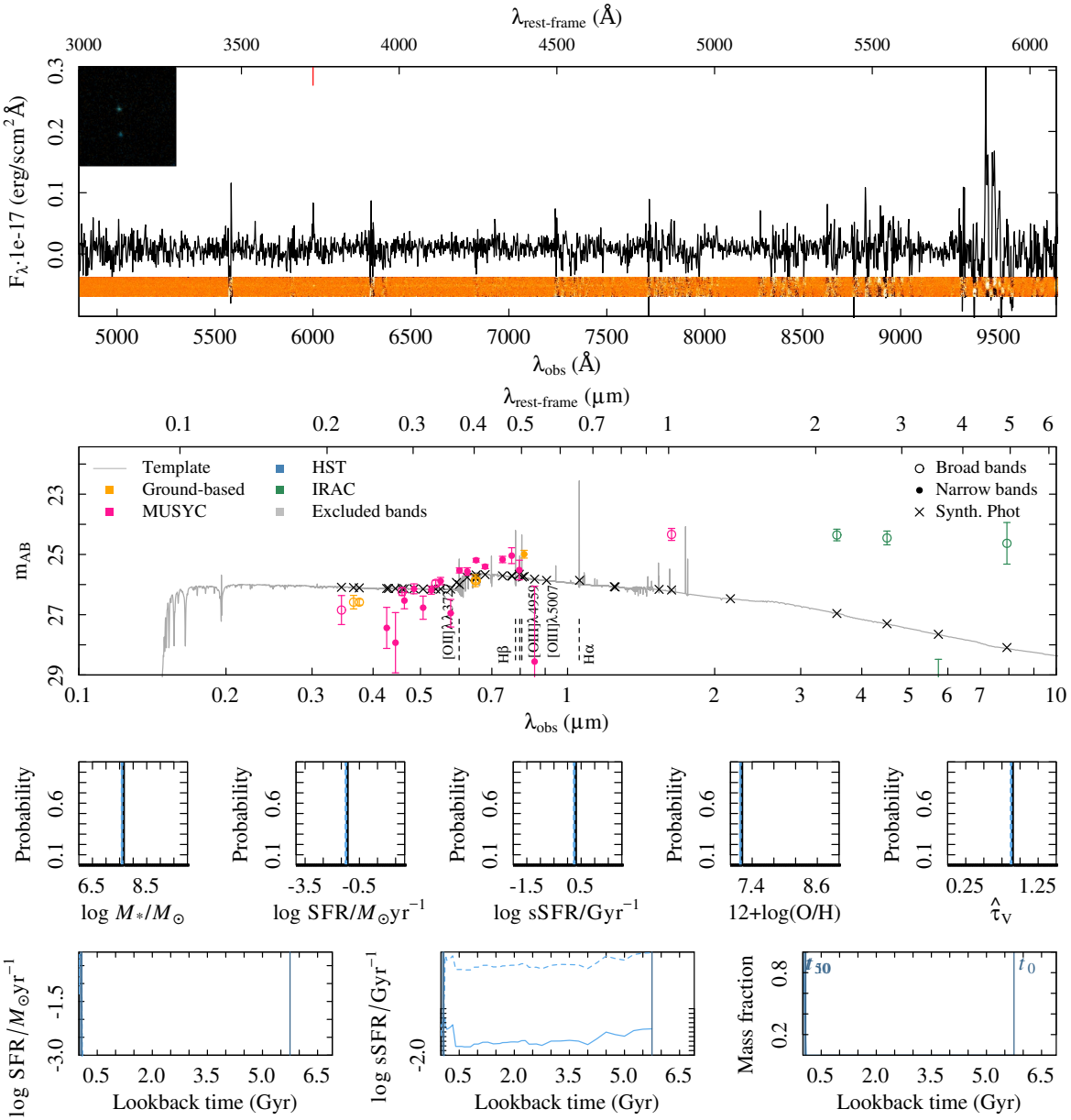

Summary ID 01126

ID	01126	$\mu_{eff,B,0}$	25.5±3.2	F Hα ($\times 10^{17}$)	–
α (deg; J2000)	52.982541	$(B-V)_0$	0.42	EW Hα	–
δ (deg; J2000)	-27.727385	F Hβ ($\times 10^{17}$)	$1.2^{1.3}_{1.1}$	log $M_*/M_\odot$	$8.3^{8.4}_{8.3}$
i (mag)	24.39±0.11	EW Hβ	$94.0^{164.3}_{61.6}$	log SFR/$M_\odot\, yr^{-1}$	$0.4^{0.4}_{0.3}$
J (mag)	23.97±0.13	F [OII]$\lambda\lambda$3727 ($\times 10^{17}$)	$1.8^{2}_{1.7}$	log sSFR/Gyr^{-1}	$1.0^{1.1}_{0.9}$
z_{spec}	0.864/3	EW [OII]$\lambda\lambda$3727	$155.6^{408.4}_{79.3}$	$\hat{\tau}_V$	$0.7^{0.8}_{0.6}$
Morph.	Irr	F [OIII]λ4959 ($\times 10^{17}$)	$1.8^{2}_{1.7}$	12+log(O/H)	$7.8^{8.0}_{7.4}$
n	1.4±0.2	EW [OIII]λ4959	$155.6^{408.4}_{79.3}$	t_0 (Gyr)	3.0
$R_{eff,v,0}$	1.3±0.0	F [OIII]λ5007 ($\times 10^{17}$)	$1.8^{2}_{1.7}$	t_{10} (Gyr)	0.8
$M_{B,0}$	-17.87	EW [OIII]λ5007	$155.6^{408.4}_{79.3}$	t_{50} (Gyr)	0.3

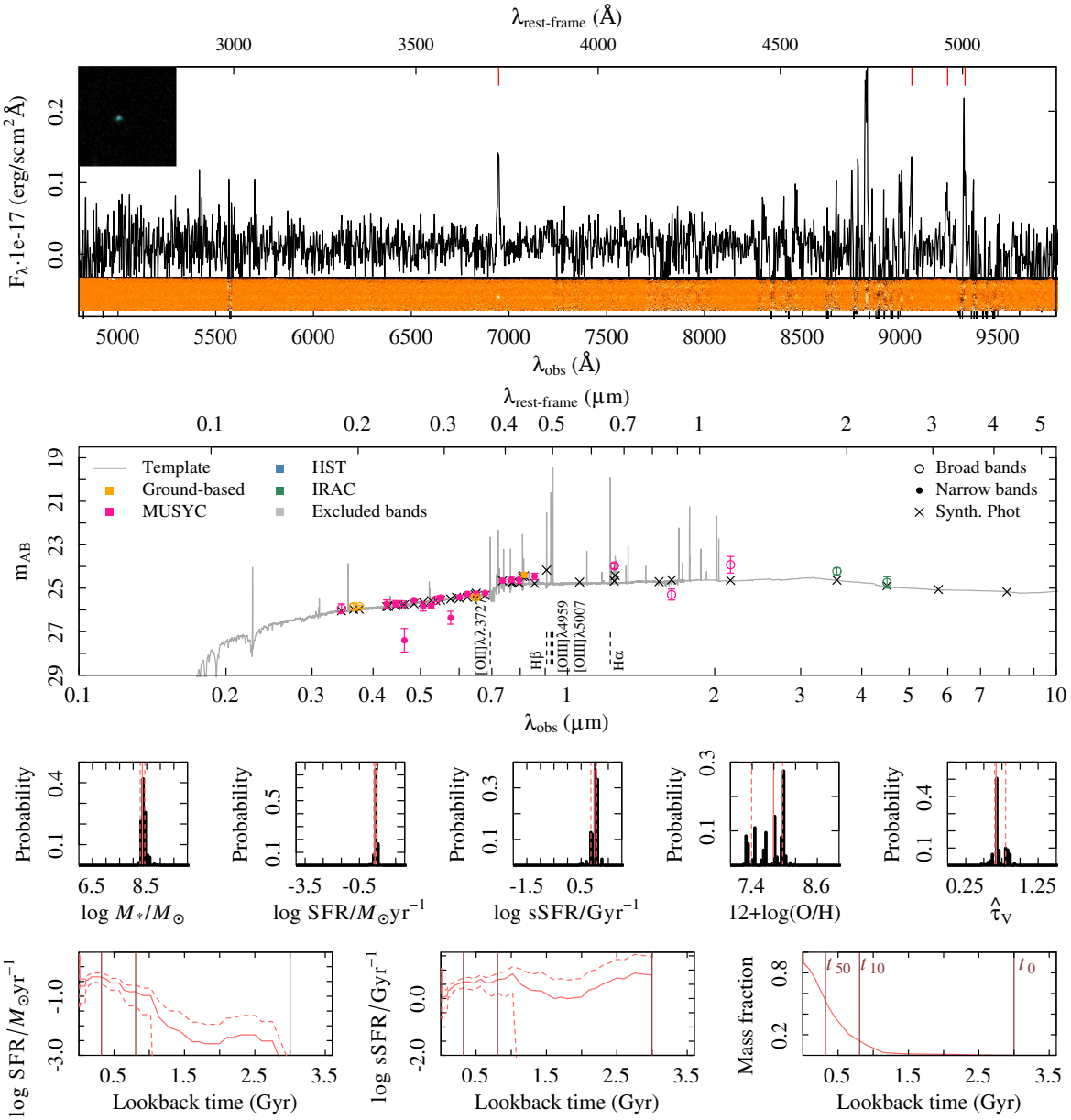

Summary ID 01202

ID	01202	$\mu_{eff,B,0}$	34.3±5.0	F Hα ($\times 10^{17}$)	–
α (deg; J2000)	53.009269	$(B-V)_0$	0.72	EW Hα	–
δ (deg; J2000)	-27.794656	F Hβ ($\times 10^{17}$)	$0.2^{0.4}_{0}$	log $M_*/M_\odot$	$8.2^{8.3}_{8.2}$
i (mag)	24.32±0.10	EW Hβ	$4.2^{9.8}_{0.0}$	log SFR$/M_\odot\,yr^{-1}$	$-0.7^{-0.4}_{-0.8}$
J (mag)	25.77±0.86	F [OII]$\lambda\lambda$3727 ($\times 10^{17}$)	$0.8^{1.0}_{0.5}$	log sSFR$/Gyr^{-1}$	$0.1^{0.4}_{0.1}$
z_{spec}	0.679/3	EW [OII]$\lambda\lambda$3727	$21.5^{34.0}_{12.9}$	$\hat{\tau}_V$	$0.6^{0.8}_{0.6}$
Morph.	C	F [OIII]λ4959 ($\times 10^{17}$)	$0.8^{1.0}_{0.5}$	12+log(O/H)	$8.7^{8.7}_{8.2}$
n	1.8±0.2	EW [OIII]λ4959	$21.5^{34.0}_{12.9}$	t_0 (Gyr)	1.3
$R_{eff,v,0}$	0.5±0.0	F [OIII]λ5007 ($\times 10^{17}$)	$0.8^{1.0}_{0.5}$	t_{10} (Gyr)	0.5
$M_{B,0}$	-17.08	EW [OIII]λ5007	$21.5^{34.0}_{12.9}$	t_{50} (Gyr)	0.3

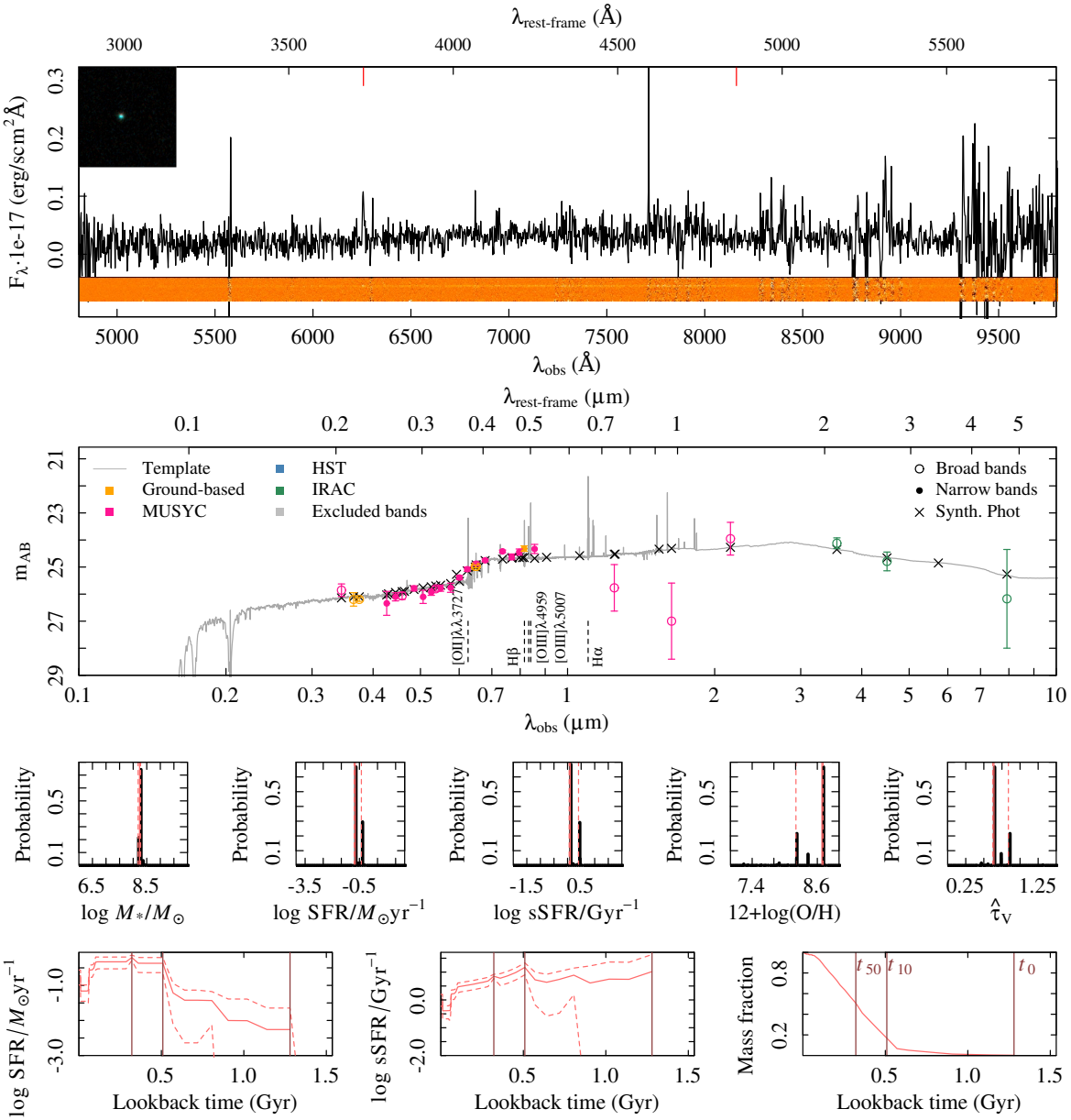

Summary ID 01210

ID	01210	$\mu_{eff,B,0}$	22.9±0.7	F Hα ($\times10^{17}$)	–
α (deg; J2000)	53.011996	$(B-V)_0$	1.50	EW Hα	–
δ (deg; J2000)	-27.737994	F Hβ ($\times10^{17}$)	–	log $M_*/M_\odot$	NA^{NA}_{NA}
i (mag)	24.72±0.11	EW Hβ	–	log SFR/$M_\odot\,yr^{-1}$	NA^{NA}_{NA}
J (mag)	24.82±0.49	F [OII]$\lambda\lambda$3727 ($\times10^{17}$)	$0.5^{0.6}_{0.4}$	log sSFR/Gyr^{-1}	NA^{NA}_{NA}
z_{spec}	0.816/2	EW [OII]$\lambda\lambda$3727	$24.1^{33.1}_{15.7}$	$\hat{\tau}_V$	NA^{NA}_{NA}
Morph.	C	F [OIII]λ4959 ($\times10^{17}$)	$0.5^{0.6}_{0.4}$	12+log(O/H)	NA^{NA}_{NA}
n	0.9±0.5	EW [OIII]λ4959	$24.1^{33.1}_{15.7}$	t_0 (Gyr)	5.5
$R_{eff,v,0}$	NA±NA	F [OIII]λ5007 ($\times10^{17}$)	$0.5^{0.6}_{0.4}$	t_{10} (Gyr)	2.2
$M_{B,0}$	-15.90	EW [OIII]λ5007	$24.1^{33.1}_{15.7}$	t_{50} (Gyr)	1.7

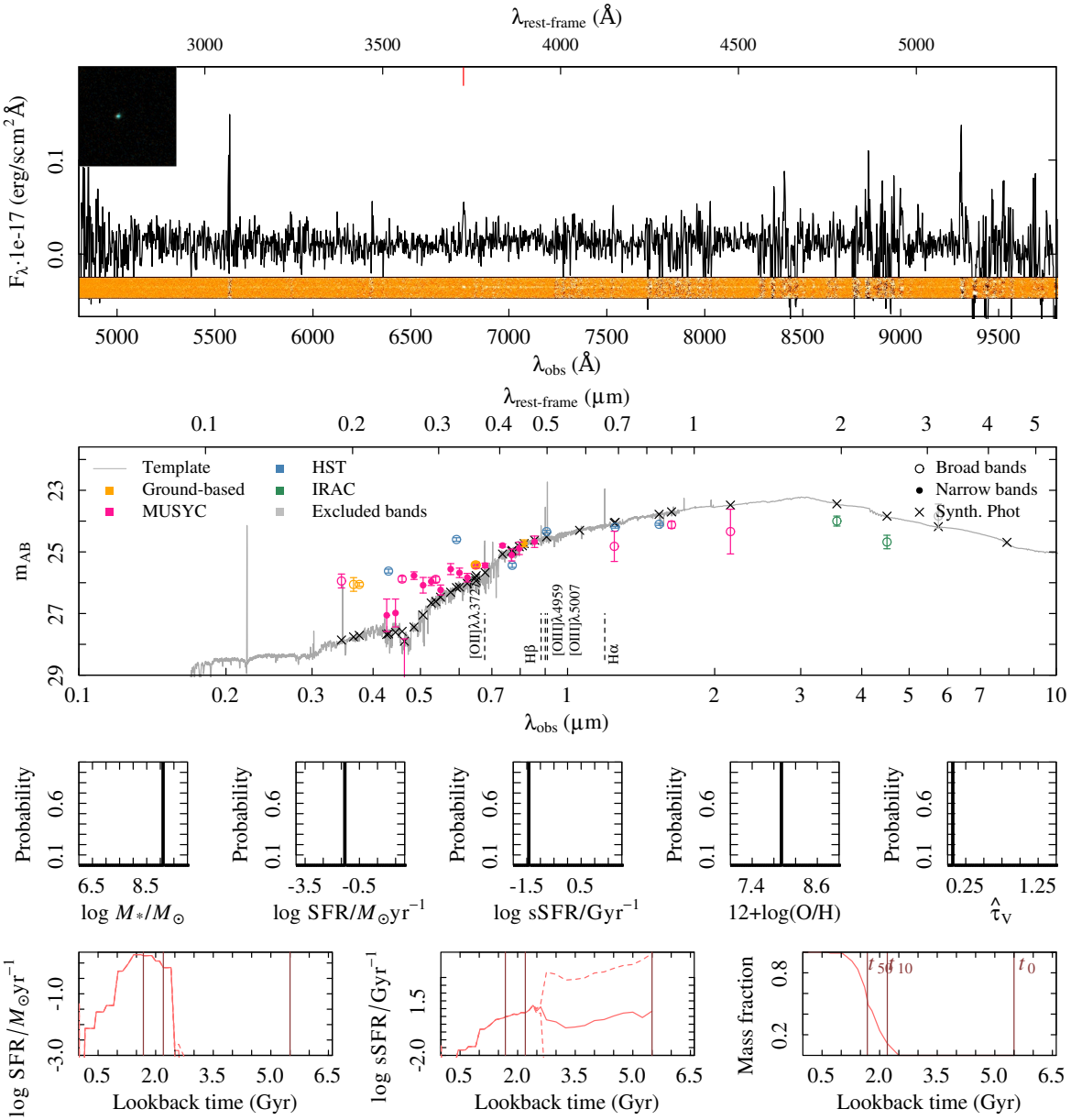

Summary ID 01220

ID	01220	$\mu_{eff,B,0}$	22.8±0.4	F Hα ($\times10^{17}$)	$1.5^{1.6}_{1.4}$
α (deg; J2000)	53.017372	$(B-V)_0$	0.65	EW Hα	$88.8^{71.5}_{119.3}$
δ (deg; J2000)	-27.679994	F Hβ ($\times10^{17}$)	$0.2^{0.3}_{0.1}$	log $M_*/M_\odot$	$7.9^{8.0}_{7.8}$
i (mag)	24.49±0.12	EW Hβ	$7.1^{11.4}_{3.0}$	log SFR$/M_\odot\,yr^{-1}$	$-1.0^{-0.8}_{-1.1}$
J (mag)	24.77±0.24	F [OII]$\lambda\lambda$3727 ($\times10^{17}$)	$1.9^{2.2}_{1.7}$	log sSFR$/Gyr^{-1}$	$0.1^{0.2}_{-0.1}$
z_{spec}	0.487/4	EW [OII]$\lambda\lambda$3727	$59.9^{87.6}_{46.3}$	$\hat{\tau}_V$	$0.2^{0.6}_{0.1}$
Morph.	D	F [OIII]λ4959 ($\times10^{17}$)	$1.9^{2.2}_{1.7}$	12+log(O/H)	$8.4^{8.4}_{8.1}$
n	1.1±0.1	EW [OIII]λ4959	$59.9^{87.6}_{46.3}$	t_0 (Gyr)	1.7
$R_{eff,v,0}$	0.6±0.0	F [OIII]λ5007 ($\times10^{17}$)	$1.9^{2.2}_{1.7}$	t_{10} (Gyr)	0.8
$M_{B,0}$	-16.64	EW [OIII]λ5007	$59.9^{87.6}_{46.3}$	t_{50} (Gyr)	0.4

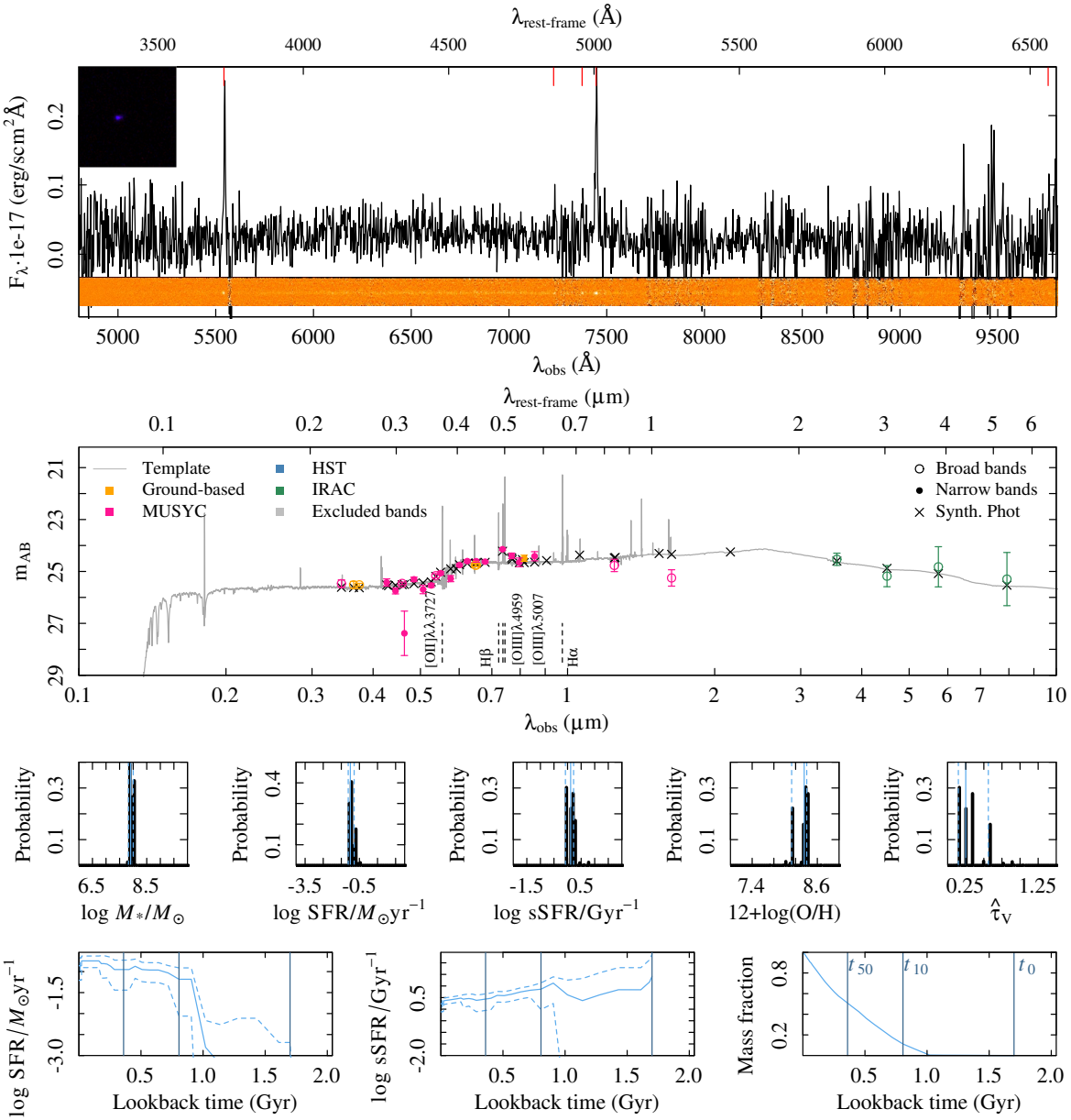

Summary ID 01234

ID	01234	$\mu_{eff,B,0}$	24.1±0.1	F Hα ($\times10^{17}$)	–
α (deg; J2000)	53.022946	$(B-V)_0$	0.86	EW Hα	–
δ (deg; J2000)	-27.826548	F Hβ ($\times10^{17}$)	$0.4^{0.7}_{0.1}$	log $M_*/M_\odot$	$8.0^{8.0}_{8.0}$
i (mag)	24.39±0.10	EW Hβ	$10.5^{19.6}_{3.1}$	log SFR/$M_\odot\,yr^{-1}$	$-0.5^{-0.5}_{-0.6}$
J (mag)	23.93±0.20	F [OII]$\lambda\lambda$3727 ($\times10^{17}$)	$1.9^{2.2}_{1.6}$	log sSFR/Gyr^{-1}	$0.5^{0.5}_{0.3}$
z_{spec}	0.436/4	EW [OII]$\lambda\lambda$3727	$61.9^{90.8}_{40.5}$	$\hat{\tau}_V$	$0.9^{0.9}_{0.8}$
Morph.	D	F [OIII]λ4959 ($\times10^{17}$)	$1.9^{2.2}_{1.6}$	12+log(O/H)	$8.6^{8.7}_{8.1}$
n	0.6±0.0	EW [OIII]λ4959	$61.9^{90.8}_{40.5}$	t_0 (Gyr)	2.8
$R_{eff,v,0}$	0.8±0.0	F [OIII]λ5007 ($\times10^{17}$)	$1.9^{2.2}_{1.6}$	t_{10} (Gyr)	1.1
$M_{B,0}$	-16.39	EW [OIII]λ5007	$61.9^{90.8}_{40.5}$	t_{50} (Gyr)	0.5

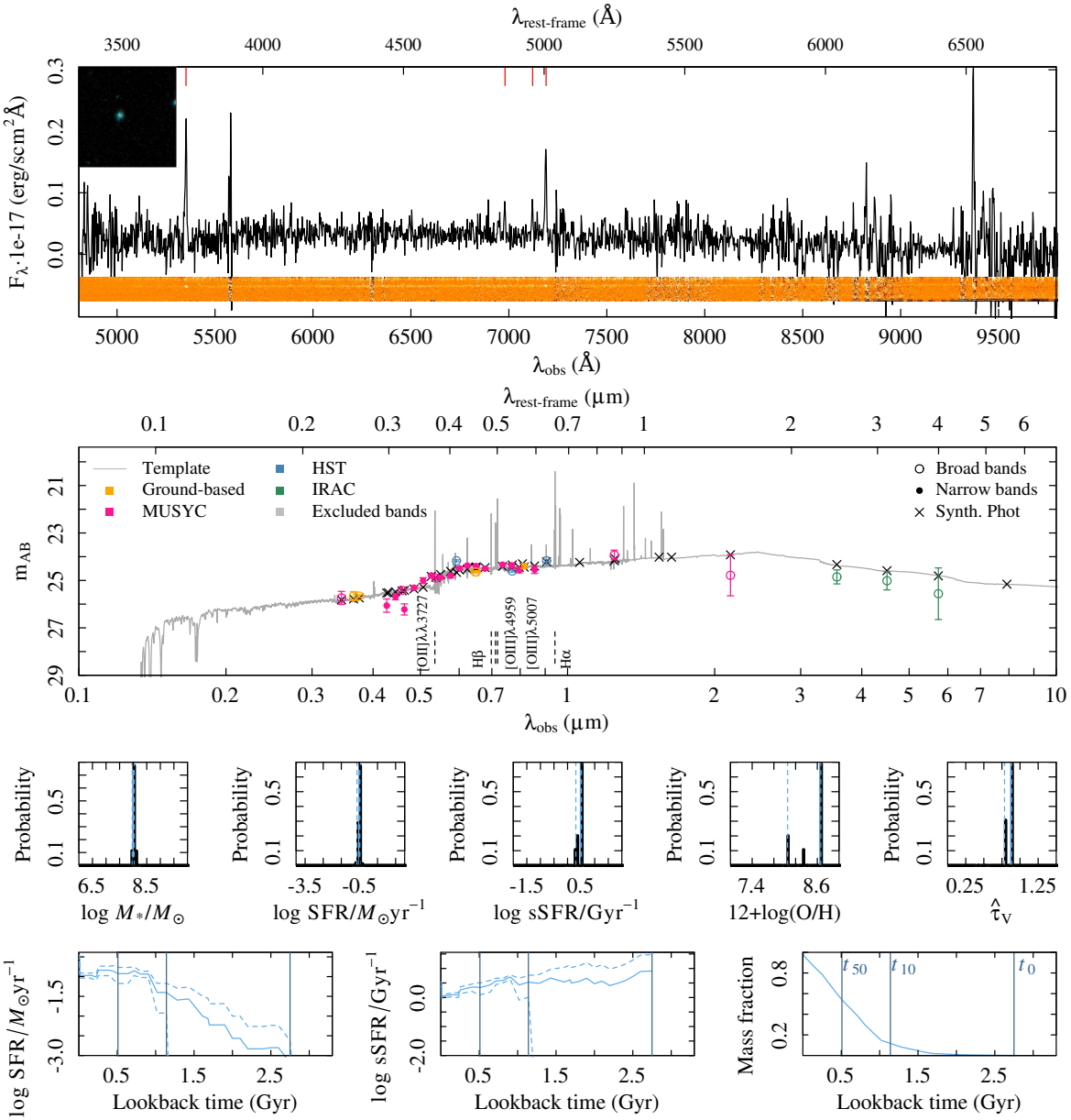

Summary ID 01245

ID	01245	$\mu_{eff,B,0}$	22.8±0.8	F Hα ($\times10^{17}$)	–
α (deg; J2000)	53.025685	$(B-V)_0$	0.35	EW Hα	–
δ (deg; J2000)	-27.705562	F Hβ ($\times10^{17}$)	$0.3^{0.5}_{0.1}$	log $M_*/M_\odot$	$8.1^{8.3}_{8.1}$
i (mag)	24.61±0.11	EW Hβ	$9.6^{19.5}_{3.0}$	log SFR/$M_\odot\,yr^{-1}$	$-0.8^{-0.6}_{-1.0}$
J (mag)	25.46±0.39	F [OII]$\lambda\lambda$3727 ($\times10^{17}$)	$1.1^{1.4}_{0.9}$	log sSFR/Gyr^{-1}	$0.0^{0.1}_{-0.1}$
z_{spec}	0.678/4	EW [OII]$\lambda\lambda$3727	$34.3^{49.2}_{25.7}$	$\hat{\tau}_V$	$0.0^{0.1}_{0.0}$
Morph.	D	F [OIII]λ4959 ($\times10^{17}$)	$1.1^{1.4}_{0.9}$	12+log(O/H)	$8.1^{8.2}_{7.5}$
n	1.4±0.2	EW [OIII]λ4959	$34.3^{49.2}_{25.7}$	t_0 (Gyr)	3.8
$R_{eff,v,0}$	0.7±0.0	F [OIII]λ5007 ($\times10^{17}$)	$1.1^{1.4}_{0.9}$	t_{10} (Gyr)	1.8
$M_{B,0}$	-17.49	EW [OIII]λ5007	$34.3^{49.2}_{25.7}$	t_{50} (Gyr)	0.6

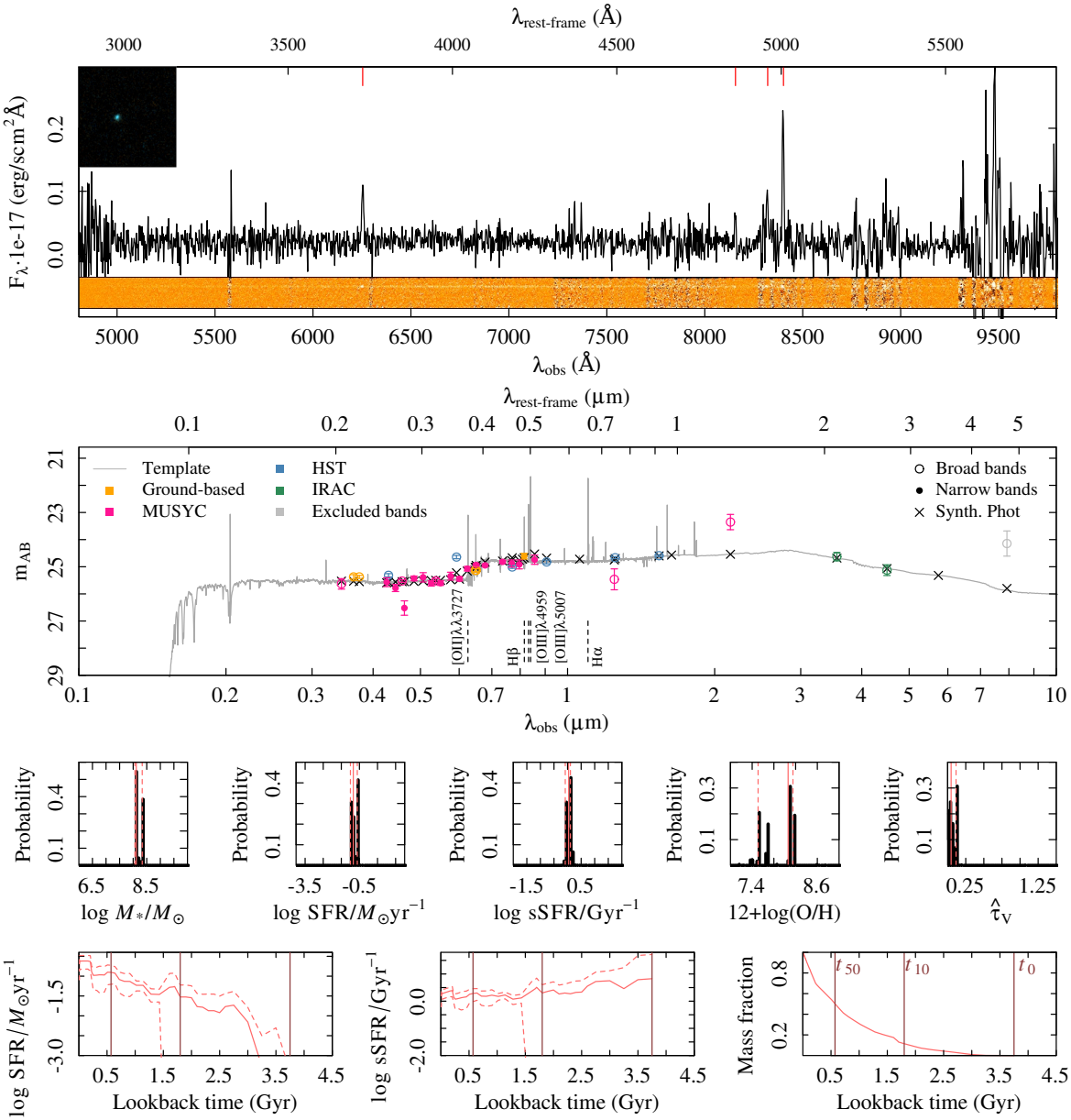

Summary ID 01247

ID	01247	$\mu_{eff,B,0}$	-Inf±NaN	F Hα ($\times 10^{17}$)	–
α (deg; J2000)	53.026255	$(B-V)_0$	0.40	EW Hα	–
δ (deg; J2000)	-27.670498	F Hβ ($\times 10^{17}$)	$1.8^{2}_{1.7}$	log $M_*/M_\odot$	$7.8^{7.9}_{7.7}$
i (mag)	25.05±0.12	EW Hβ	$78.9^{105.5}_{63.5}$	log SFR/$M_\odot\, yr^{-1}$	$-0.4^{-0.3}_{-0.4}$
J (mag)	23.95±0.12	F [OII]$\lambda\lambda$3727 ($\times 10^{17}$)	$1^{1.2}_{0.8}$	log sSFR/Gyr^{-1}	$0.8^{0.9}_{0.8}$
z_{spec}	0.524/4	EW [OII]$\lambda\lambda$3727	$28.2^{40.8}_{19.7}$	$\hat{\tau}_V$	$0.3^{0.3}_{0.3}$
Morph.	Irr	F [OIII]λ4959 ($\times 10^{17}$)	$1^{1.2}_{0.8}$	12+log(O/H)	$7.4^{7.7}_{7.4}$
n	1.4±0.1	EW [OIII]λ4959	$28.2^{40.8}_{19.7}$	t_0 (Gyr)	2.8
$R_{eff,v,0}$	0.7±0.0	F [OIII]λ5007 ($\times 10^{17}$)	$1^{1.2}_{0.8}$	t_{10} (Gyr)	0.8
$M_{B,0}$	-17.11	EW [OIII]λ5007	$28.2^{40.8}_{19.7}$	t_{50} (Gyr)	0.3

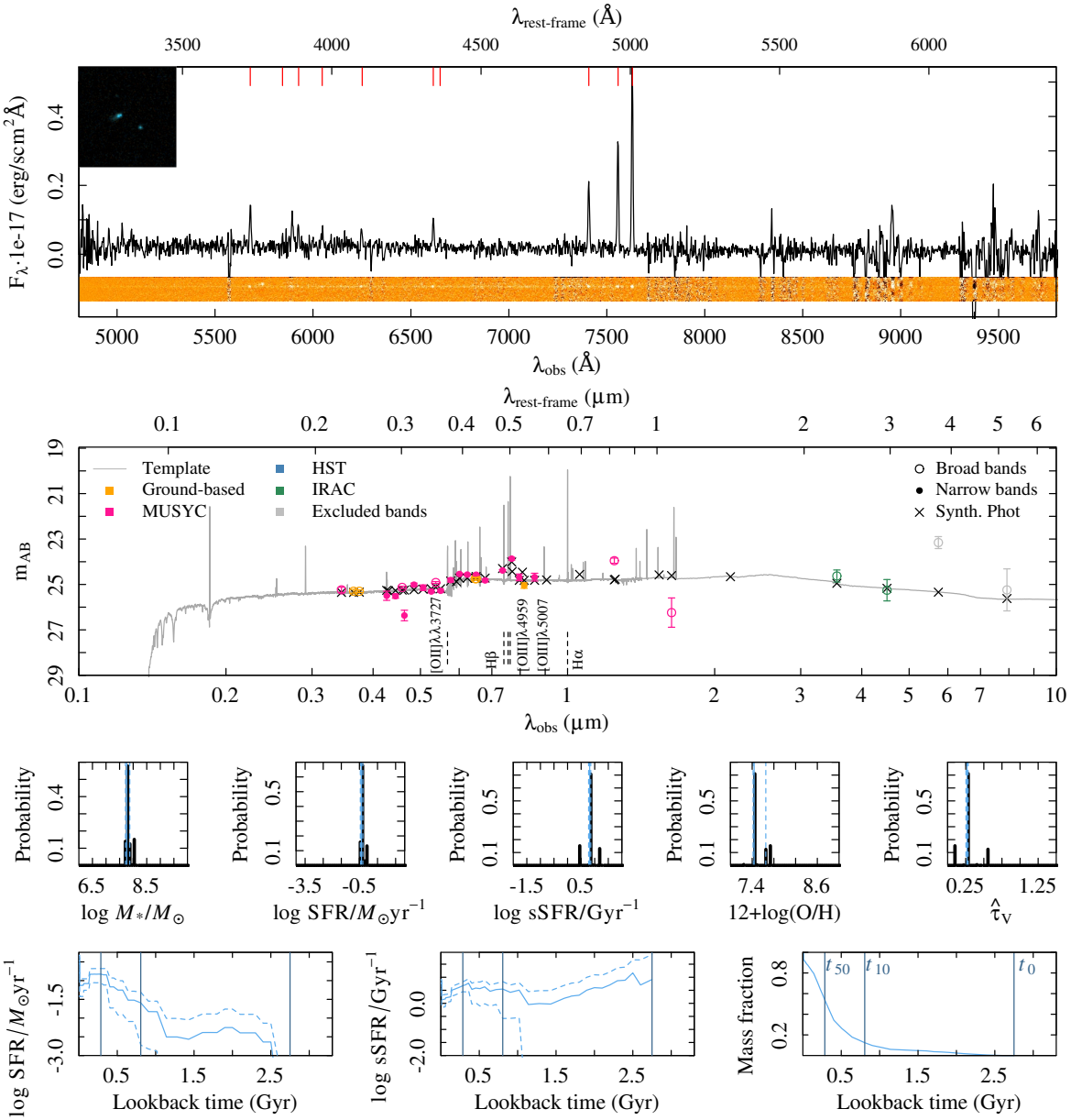

Summary ID 01251

ID	01251	$\mu_{eff,B,0}$	23.3±0.2	F Hα ($\times10^{17}$)	$0.4^{0.4}_{0.3}$
α (deg; J2000)	53.026680	$(B-V)_0$	1.39	EW Hα	$33.8^{51.2}_{24.1}$
δ (deg; J2000)	-27.878836	F Hβ ($\times10^{17}$)	$0.2^{0.3}_{0.1}$	log $M_*/M_\odot$	$8.7^{8.7}_{8.6}$
i (mag)	24.29±0.10	EW Hβ	$10.5^{17.2}_{5.6}$	log SFR/$M_\odot\,yr^{-1}$	$-0.9^{-0.8}_{-0.9}$
J (mag)	23.35±0.16	F [OII]$\lambda\lambda$3727 ($\times10^{17}$)	–	log sSFR/Gyr^{-1}	$-0.6^{-0.5}_{-0.6}$
z_{spec}	0.434/3	EW [OII]$\lambda\lambda$3727	–	$\hat{\tau}_V$	$1.4^{1.4}_{1.4}$
Morph.	D	F [OIII]λ4959 ($\times10^{17}$)	–	12+log(O/H)	$8.2^{8.2}_{8.2}$
n	1.1±0.1	EW [OIII]λ4959	–	t_0 (Gyr)	6.5
$R_{eff,v,0}$	0.8±0.0	F [OIII]λ5007 ($\times10^{17}$)	–	t_{10} (Gyr)	1.4
$M_{B,0}$	-15.70	EW [OIII]λ5007	–	t_{50} (Gyr)	0.8

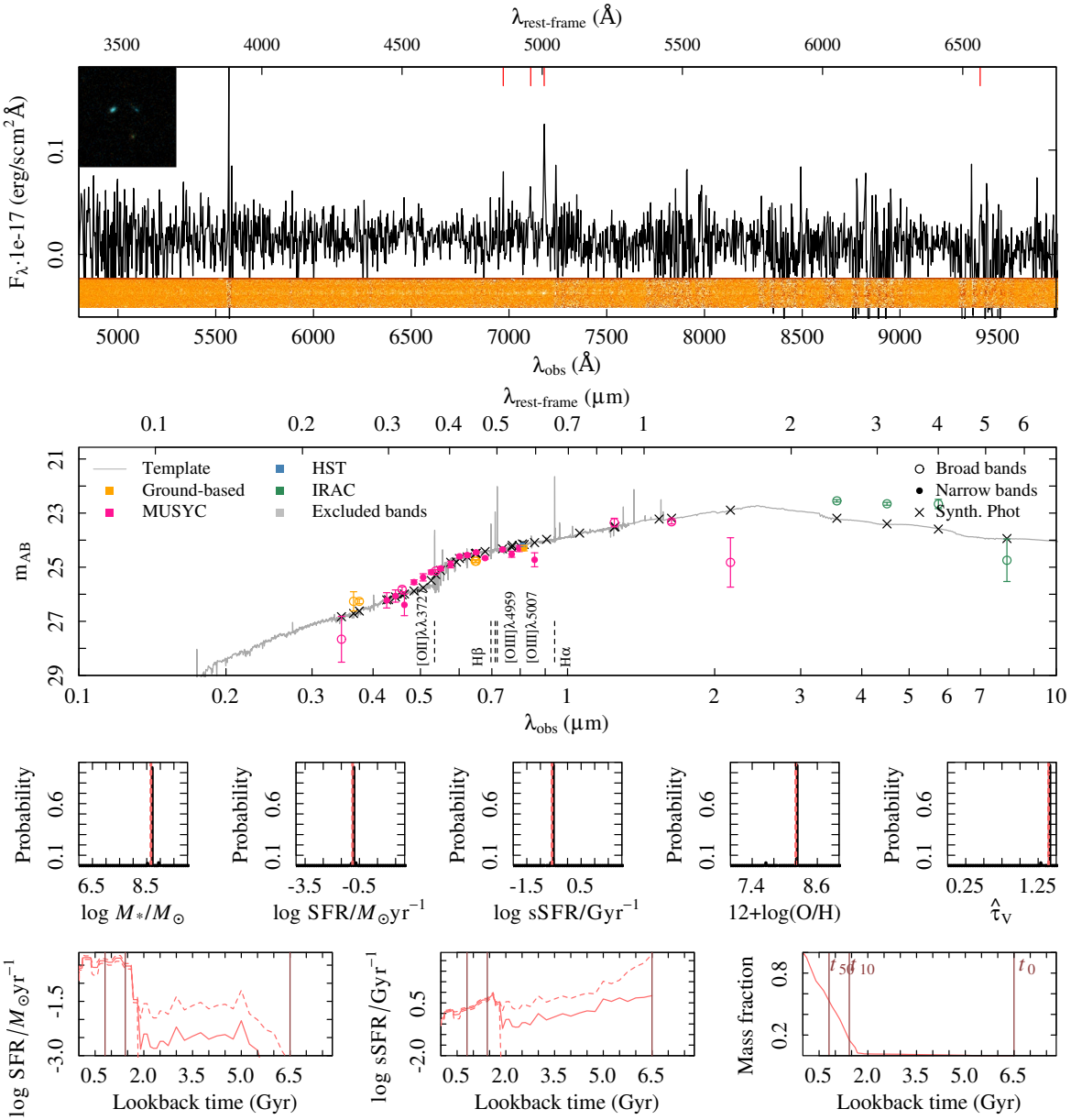

Summary ID 01309

ID	01309	$\mu_{eff,B,0}$	33.6±5.0	F Hα ($\times 10^{17}$)	–
α (deg; J2000)	53.050108	$(B-V)_0$	0.69	EW Hα	–
δ (deg; J2000)	-27.805533	F Hβ ($\times 10^{17}$)	–	log $M_*/M_\odot$	$8.8^{8.8}_{8.7}$
i (mag)	24.39±0.10	EW Hβ	–	log SFR/$M_\odot\, yr^{-1}$	$0.1^{0.3}_{0.0}$
J (mag)	25.42±0.54	F [OII]$\lambda\lambda$3727 ($\times 10^{17}$)	$1^{1.1}_{0.9}$	log sSFR/Gyr^{-1}	$0.3^{0.5}_{0.2}$
z_{spec}	0.743/3	EW [OII]$\lambda\lambda$3727	$75.4^{99.2}_{60.0}$	$\hat{\tau}_V$	$0.7^{0.8}_{0.7}$
Morph.	D	F [OIII]λ4959 ($\times 10^{17}$)	$1^{1.1}_{0.9}$	12+log(O/H)	$7.7^{8.6}_{7.7}$
n	4.1±0.8	EW [OIII]λ4959	$75.4^{99.2}_{60.0}$	t_0 (Gyr)	4.5
$R_{eff,v,0}$	1.0±0.1	F [OIII]λ5007 ($\times 10^{17}$)	$1^{1.1}_{0.9}$	t_{10} (Gyr)	2.4
$M_{B,0}$	-17.75	EW [OIII]λ5007	$75.4^{99.2}_{60.0}$	t_{50} (Gyr)	1.1

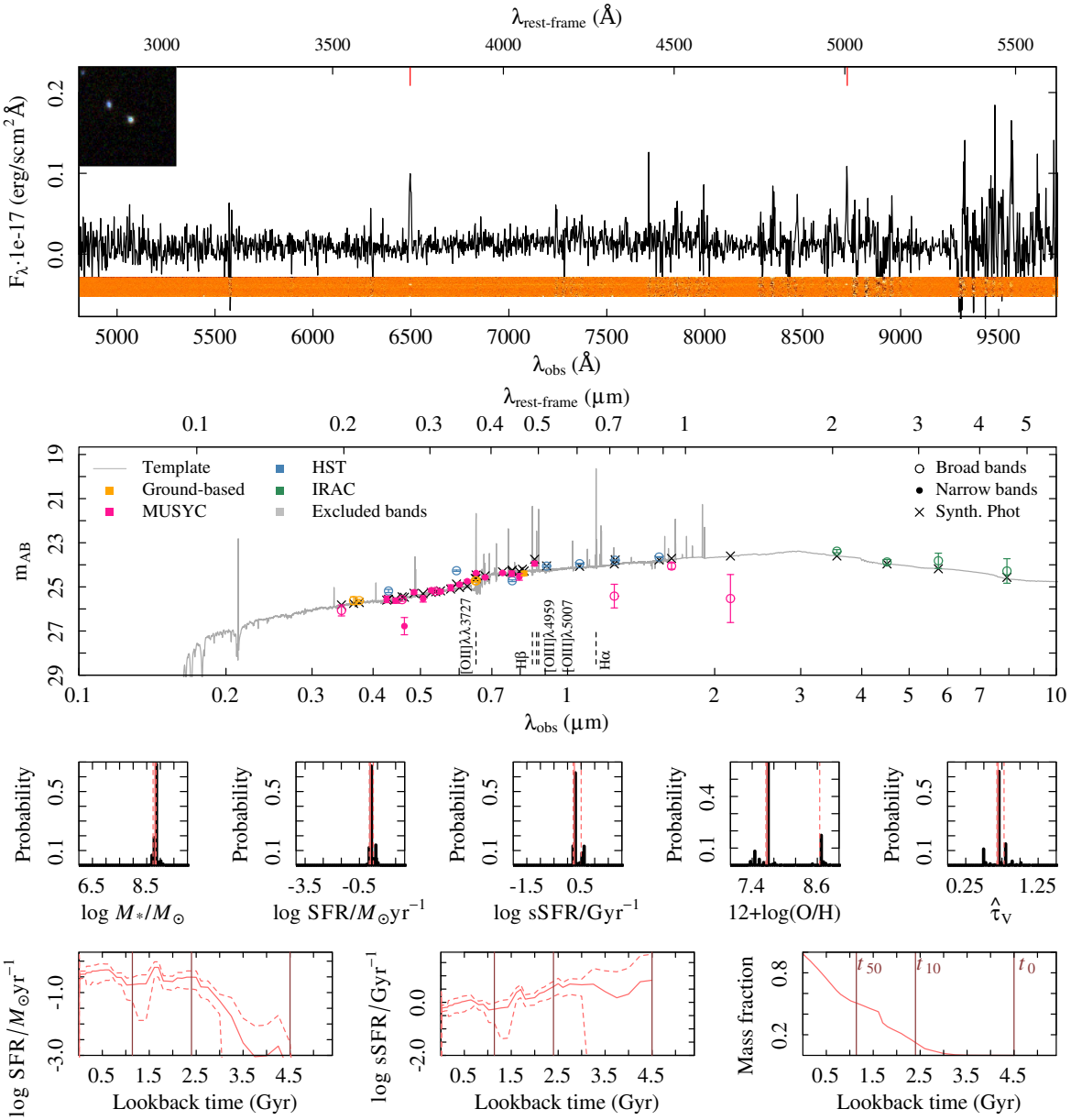

Summary ID 01313

ID	01313	$\mu_{eff,B,0}$	19.8±0.5	F Hα ($\times 10^{17}$)	–
α (deg; J2000)	53.051197	$(B-V)_0$	0.74	EW Hα	–
δ (deg; J2000)	-27.787284	F Hβ ($\times 10^{17}$)	$0.8^{1.2}_{0.4}$	log $M_*/M_\odot$	$8.6^{8.7}_{8.6}$
i (mag)	23.64±0.10	EW Hβ	$10.8^{19.7}_{4.2}$	log SFR/$M_\odot\,yr^{-1}$	$0.0^{0.0}_{-0.1}$
J (mag)	24.08±0.41	F [OII]$\lambda\lambda$3727 ($\times 10^{17}$)	$2.4^{2.8}_{2.1}$	log sSFR/Gyr^{-1}	$0.3^{0.4}_{0.2}$
z_{spec}	0.578/4	EW [OII]$\lambda\lambda$3727	$43.3^{59.1}_{31.3}$	$\hat{\tau}_V$	$1.1^{1.1}_{0.8}$
Morph.	C	F [OIII]λ4959 ($\times 10^{17}$)	$2.4^{2.8}_{2.1}$	12+log(O/H)	$7.8^{7.8}_{7.7}$
n	2.6±0.3	EW [OIII]λ4959	$43.3^{59.1}_{31.3}$	t_0 (Gyr)	1.8
$R_{eff,v,0}$	0.5±0.0	F [OIII]λ5007 ($\times 10^{17}$)	$2.4^{2.8}_{2.1}$	t_{10} (Gyr)	1.0
$M_{B,0}$	-17.72	EW [OIII]λ5007	$43.3^{59.1}_{31.3}$	t_{50} (Gyr)	0.4

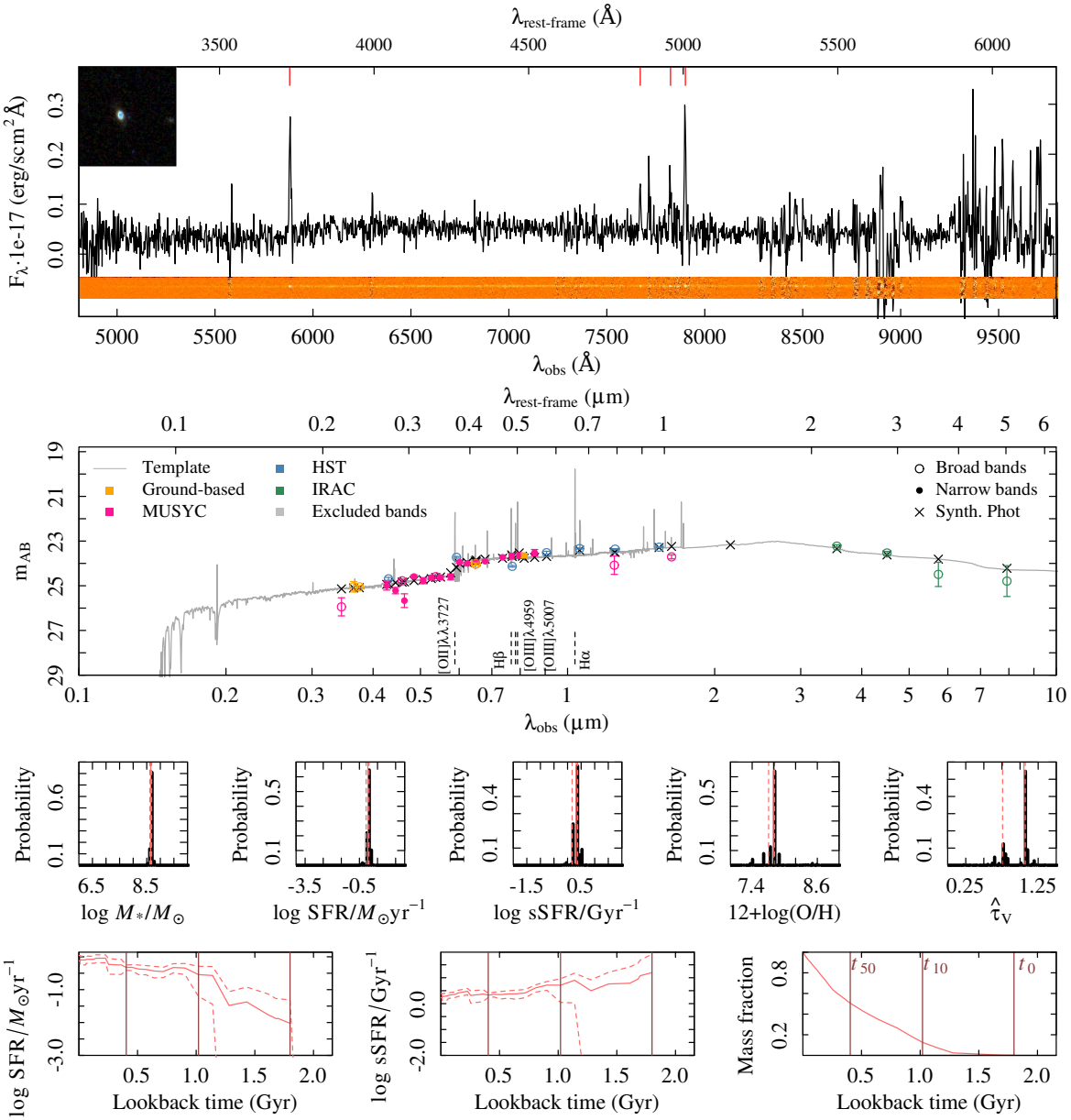

Summary ID 01332

ID	01332	$\mu_{eff,B,0}$	-Inf±NaN	F Hα ($\times 10^{17}$)	–
α (deg; J2000)	53.058327	$(B-V)_0$	1.09	EW Hα	–
δ (deg; J2000)	-27.829482	F Hβ ($\times 10^{17}$)	$0.7^{0.9}_{0.4}$	log $M_*/M_\odot$	$8.0^{8.1}_{7.9}$
i (mag)	24.61±0.11	EW Hβ	$19.5^{30.8}_{11.7}$	log SFR/$M_\odot\, yr^{-1}$	$-0.9^{-0.9}_{-1.1}$
J (mag)	-99.99±-99.99	F [OII]$\lambda\lambda$3727 ($\times 10^{17}$)	$1.4^{1.6}_{1.2}$	log sSFR/Gyr^{-1}	$0.0^{0.1}_{-0.1}$
z_{spec}	0.339/4	EW [OII]$\lambda\lambda$3727	$54.1^{74.7}_{41.0}$	$\hat{\tau}_V$	$1.0^{1.2}_{1.0}$
Morph.	C	F [OIII]λ4959 ($\times 10^{17}$)	$1.4^{1.6}_{1.2}$	12+log(O/H)	$7.7^{8.5}_{7.3}$
n	1.3±0.2	EW [OIII]λ4959	$54.1^{74.7}_{41.0}$	t_0 (Gyr)	1.9
$R_{eff,v,0}$	0.3±0.0	F [OIII]λ5007 ($\times 10^{17}$)	$1.4^{1.6}_{1.2}$	t_{10} (Gyr)	0.9
$M_{B,0}$	-15.29	EW [OIII]λ5007	$54.1^{74.7}_{41.0}$	t_{50} (Gyr)	0.5

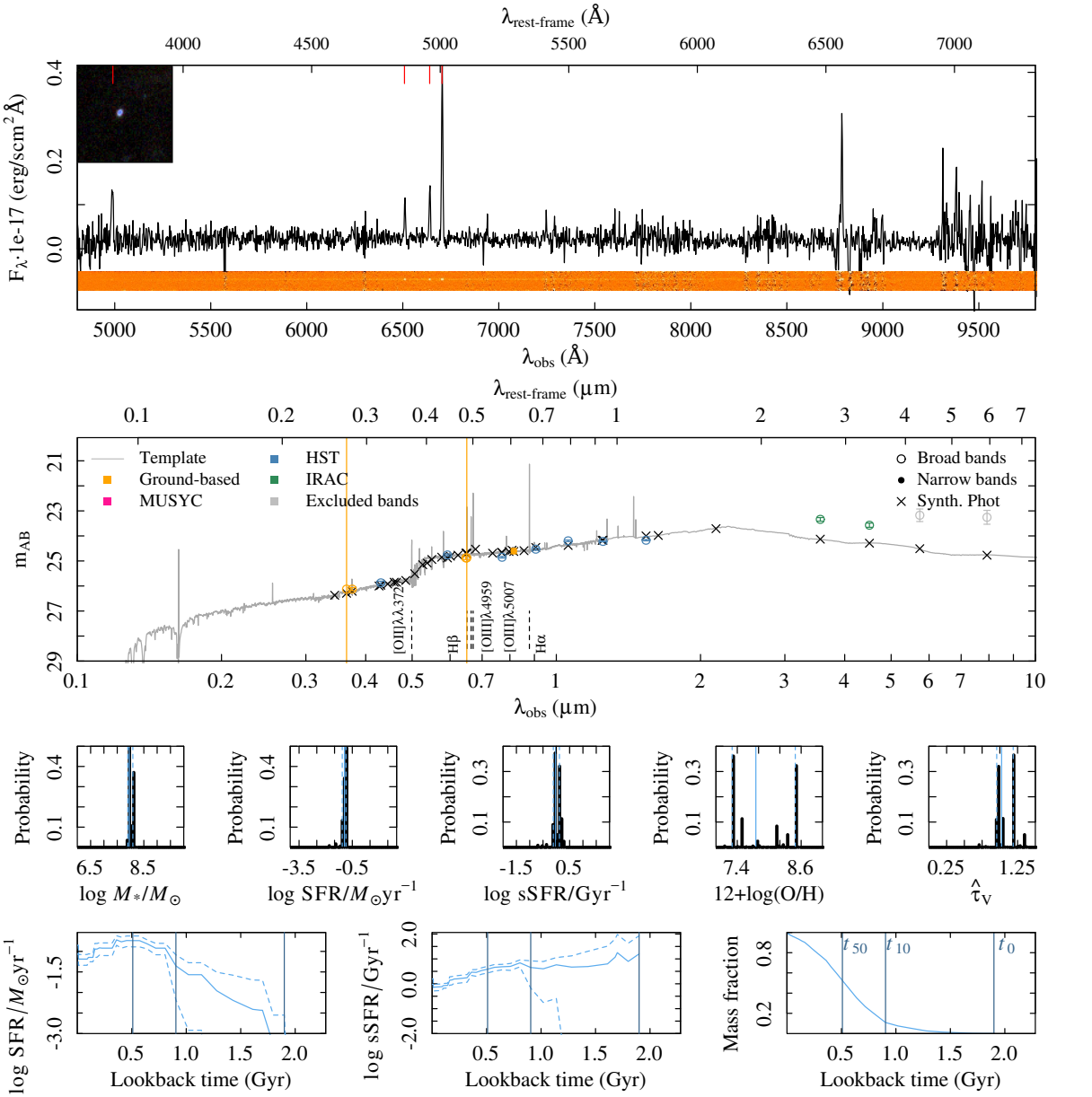

Summary ID 01344

ID	01344	$\mu_{eff,B,0}$	19.2±2.1	F Hα ($\times 10^{17}$)	$14^{14.2}_{13.8}$
α (deg; J2000)	53.066000	$(B-V)_0$	0.88	EW Hα	$1047.3^{1450.9}_{785.0}$
δ (deg; J2000)	-27.730996	F Hβ ($\times 10^{17}$)	$5.8^{6.2}_{5.5}$	log $M_*/M_\odot$	$8.0^{8.0}_{8.0}$
i (mag)	24.53±0.10	EW Hβ	$134.8^{169.2}_{110.5}$	log SFR/$M_\odot\,yr^{-1}$	$-0.3^{-0.2}_{-0.3}$
J (mag)	25.28±0.43	F [OII]$\lambda\lambda$3727 ($\times 10^{17}$)	$1.7^{2}_{1.4}$	log sSFR/Gyr^{-1}	$0.7^{0.7}_{0.6}$
z_{spec}	0.374/4	EW [OII]$\lambda\lambda$3727	$46.6^{64.3}_{33.5}$	$\hat{\tau}_V$	$0.4^{0.4}_{0.3}$
Morph.	D	F [OIII]λ4959 ($\times 10^{17}$)	$1.7^{2}_{1.4}$	12+log(O/H)	$7.8^{7.8}_{7.8}$
n	8.0±1.1	EW [OIII]λ4959	$46.6^{64.3}_{33.5}$	t_0 (Gyr)	9.0
$R_{eff,v,0}$	0.6±0.0	F [OIII]λ5007 ($\times 10^{17}$)	$1.7^{2}_{1.4}$	t_{10} (Gyr)	5.5
$M_{B,0}$	-16.65	EW [OIII]λ5007	$46.6^{64.3}_{33.5}$	t_{50} (Gyr)	4.5

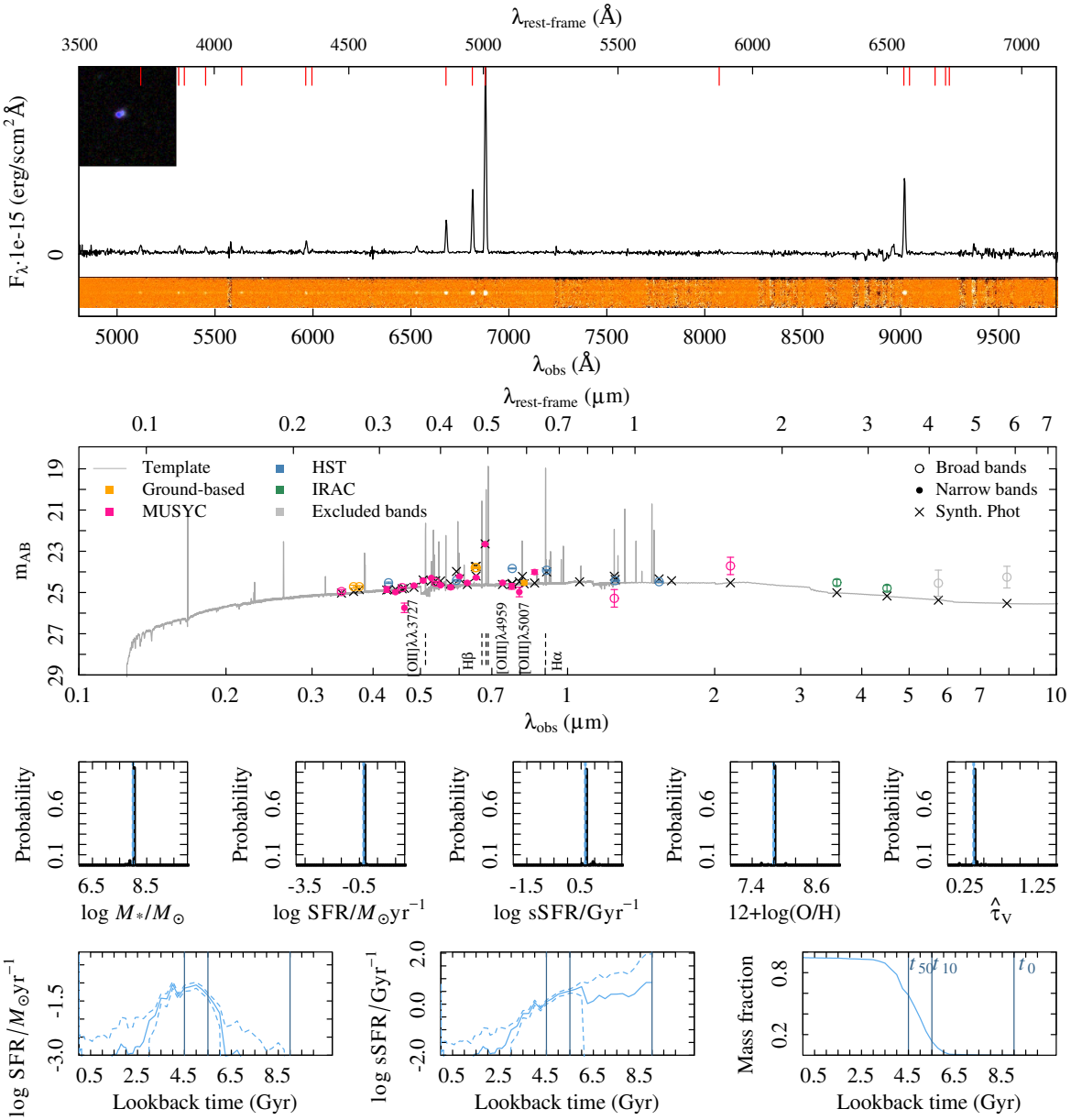

Summary ID 01378

ID	01378	$\mu_{eff,B,0}$	22.1±0.2	F Hα ($\times10^{17}$)	$2.3^{2.6}_{1.9}$
α (deg; J2000)	53.080138	$(B-V)_0$	1.06	EW Hα	$46.0^{60.1}_{35.1}$
δ (deg; J2000)	-27.867174	F Hβ ($\times10^{17}$)	$0.1^{0.4}_{0.2}$	log $M_*/M_\odot$	$8.5^{8.5}_{8.5}$
i (mag)	23.82±0.10	EW Hβ	$1.9^{7.1}_{2.4}$	log SFR/$M_\odot\,yr^{-1}$	$-1.1^{-1.1}_{-1.2}$
J (mag)	23.41±0.08	F [OII]$\lambda\lambda$3727 ($\times10^{17}$)	$1.5^{1.8}_{1.2}$	log sSFR/Gyr^{-1}	$-0.7^{-0.6}_{-0.7}$
z_{spec}	0.343/3	EW [OII]$\lambda\lambda$3727	$30.9^{46.1}_{21.4}$	$\hat{\tau}_V$	$0.5^{0.5}_{0.5}$
Morph.	D	F [OIII]λ4959 ($\times10^{17}$)	$1.5^{1.8}_{1.2}$	12+log(O/H)	$7.6^{7.6}_{7.5}$
n	1.4±0.1	EW [OIII]λ4959	$30.9^{46.1}_{21.4}$	t_0 (Gyr)	8.8
$R_{eff,v,0}$	1.2±0.0	F [OIII]λ5007 ($\times10^{17}$)	$1.5^{1.8}_{1.2}$	t_{10} (Gyr)	8.0
$M_{B,0}$	-15.94	EW [OIII]λ5007	$30.9^{46.1}_{21.4}$	t_{50} (Gyr)	4.5

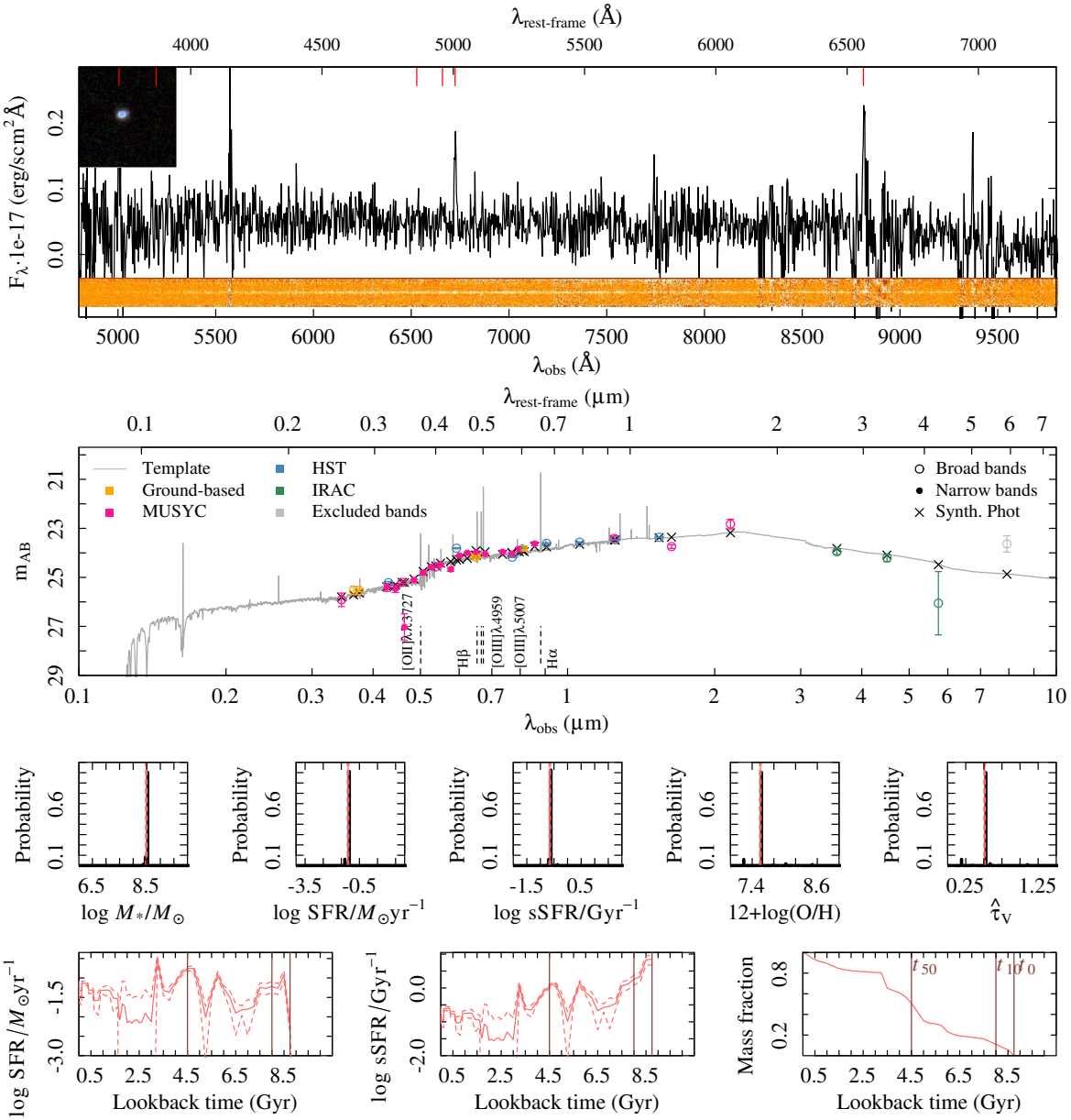

Summary ID 01403

ID	01403	$\mu_{eff,B,0}$	21.5±0.1	F Hα ($\times10^{17}$)	–
α (deg; J2000)	53.091122	$(B-V)_0$	0.80	EW Hα	–
δ (deg; J2000)	-27.878697	F Hβ ($\times10^{17}$)	$0.7^{1.0}_{0.3}$	log $M_*/M_\odot$	$8.8^{8.8}_{8.7}$
i (mag)	23.89±0.10	EW Hβ	$10.7^{19.2}_{4.1}$	log SFR/$M_\odot\,yr^{-1}$	$-0.1^{-0.1}_{-0.2}$
J (mag)	23.97±0.15	F [OII]$\lambda\lambda$3727 ($\times10^{17}$)	$2.6^{3.1}_{2.1}$	log sSFR/Gyr^{-1}	$0.1^{0.1}_{0.0}$
z_{spec}	0.688/3	EW [OII]$\lambda\lambda$3727	$43.5^{62.6}_{30.7}$	$\hat{\tau}_V$	$0.9^{1.2}_{0.9}$
Morph.	D	F [OIII]λ4959 ($\times10^{17}$)	$2.6^{3.1}_{2.1}$	12+log(O/H)	$8.4^{8.5}_{8.0}$
n	0.8±0.1	EW [OIII]λ4959	$43.5^{62.6}_{30.7}$	t_0 (Gyr)	1.4
$R_{eff,v,0}$	1.0±0.0	F [OIII]λ5007 ($\times10^{17}$)	$2.6^{3.1}_{2.1}$	t_{10} (Gyr)	0.6
$M_{B,0}$	-17.64	EW [OIII]λ5007	$43.5^{62.6}_{30.7}$	t_{50} (Gyr)	0.3

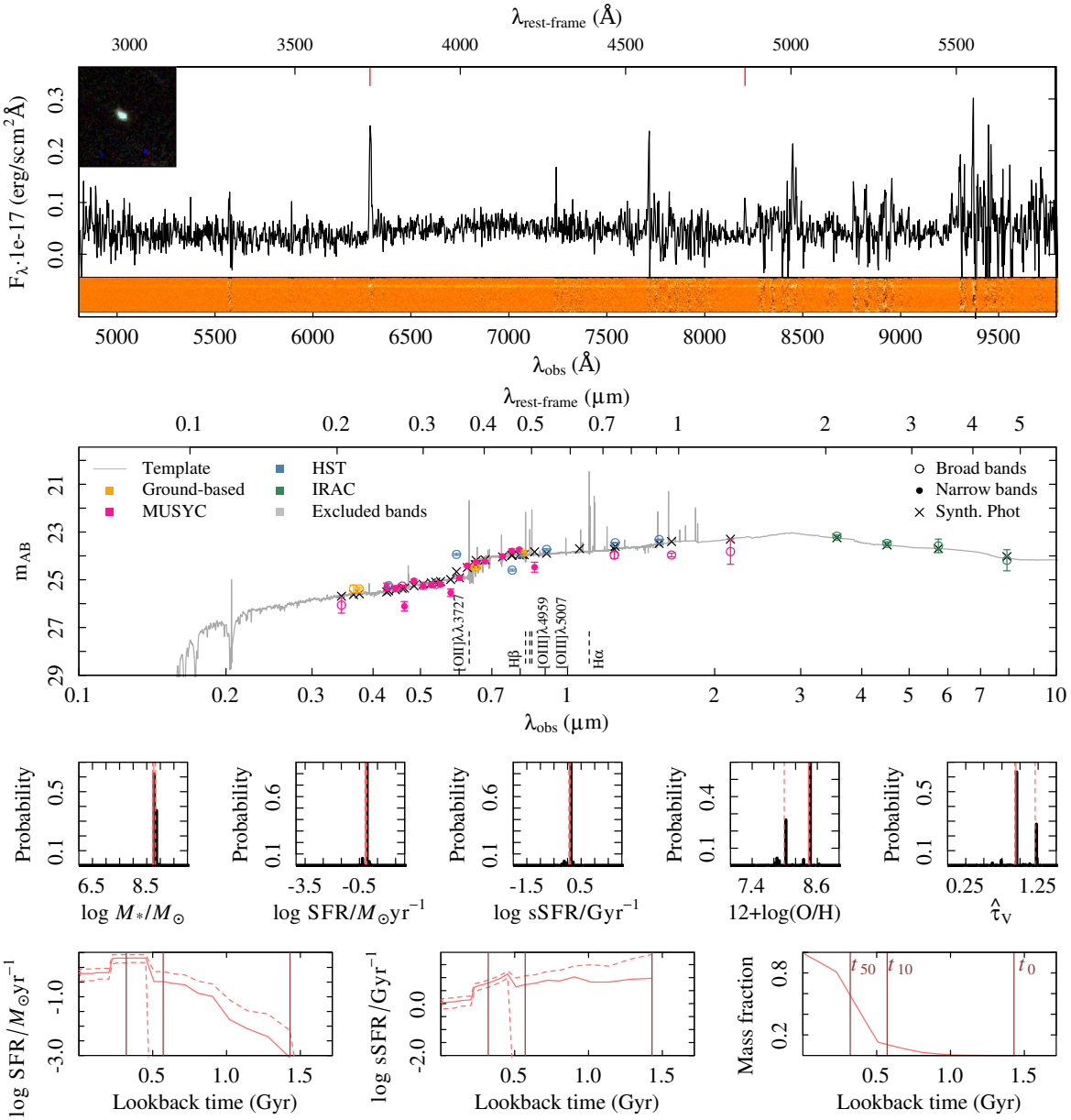

Summary ID 01454

ID	01454	$\mu_{eff,B,0}$	25.1±0.3	F Hα ($\times10^{17}$)	–
α (deg; J2000)	53.111832	$(B-V)_0$	0.74	EW Hα	–
δ (deg; J2000)	-27.776048	F Hβ ($\times10^{17}$)	–	log $M_*/M_\odot$	$8.3^{8.4}_{8.1}$
i (mag)	26.00±0.16	EW Hβ	–	log SFR/$M_\odot\,yr^{-1}$	$-0.7^{-0.4}_{-1.0}$
J (mag)	-99.99±-99.99	F [OII]$\lambda\lambda$3727 ($\times10^{17}$)	$0.7^{0.8}_{0.7}$	log sSFR/Gyr^{-1}	$0.0^{0.4}_{-0.4}$
z_{spec}	0.738/2	EW [OII]$\lambda\lambda$3727	$113.8^{707.1}_{556.6}$	$\hat{\tau}_V$	$0.5^{1.0}_{0.3}$
Morph.	D	F [OIII]λ4959 ($\times10^{17}$)	$0.7^{0.8}_{0.7}$	12+log(O/H)	$8.1^{8.4}_{7.6}$
n	0.6±0.1	EW [OIII]λ4959	$113.8^{707.1}_{556.6}$	t_0 (Gyr)	5.0
$R_{eff,v,0}$	6.8±0.5	F [OIII]λ5007 ($\times10^{17}$)	$0.7^{0.8}_{0.7}$	t_{10} (Gyr)	3.8
$M_{B,0}$	-15.82	EW [OIII]λ5007	$113.8^{707.1}_{556.6}$	t_{50} (Gyr)	2.0

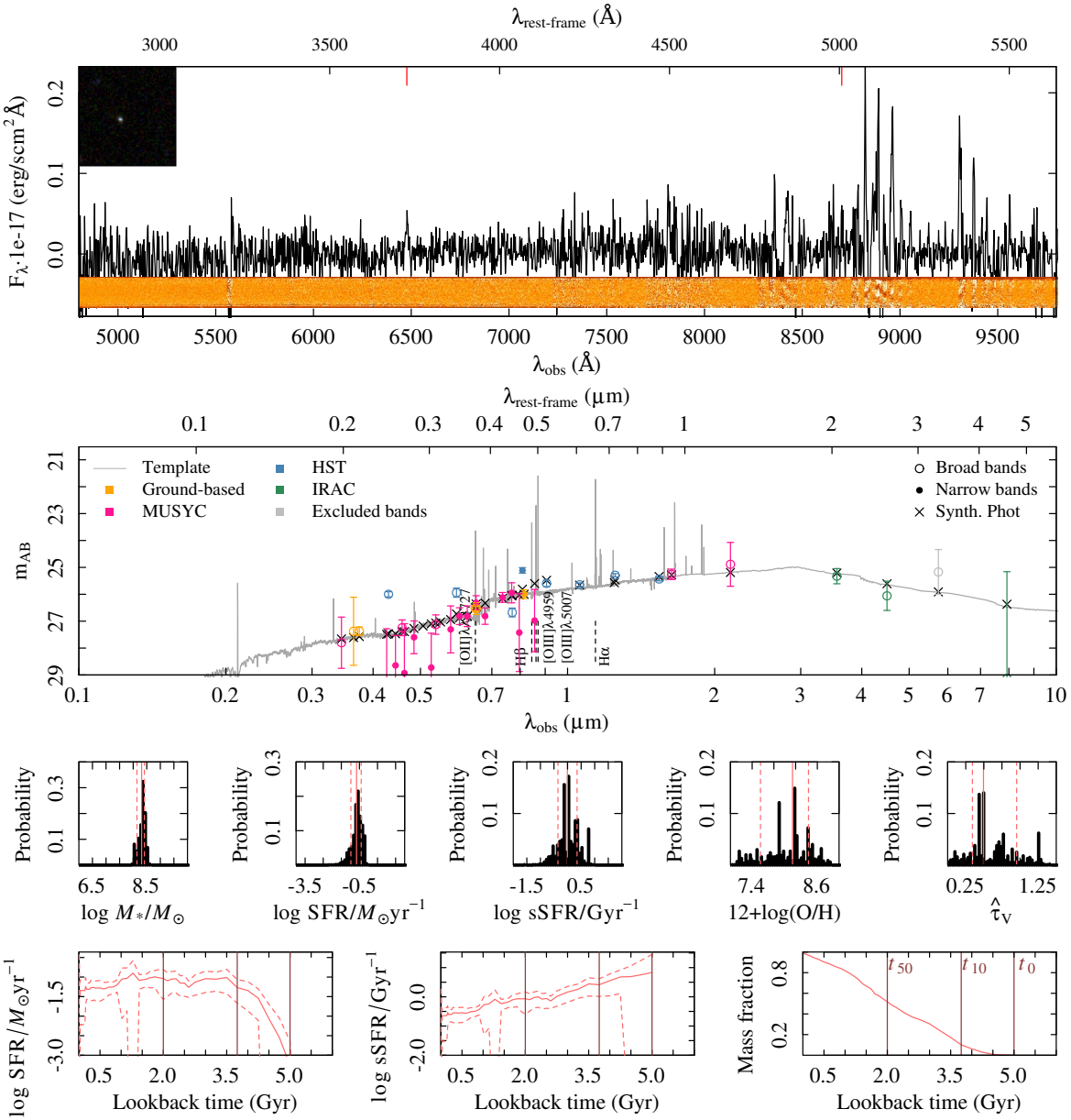

Summary ID 01514

ID	01514	$\mu_{eff,B,0}$	22.4±0.3	F Hα ($\times 10^{17}$)	–
α (deg; J2000)	53.143874	$(B-V)_0$	0.47	EW Hα	–
δ (deg; J2000)	-27.875205	F Hβ ($\times 10^{17}$)	–	log $M_*/M_\odot$	$8.7^{8.7}_{8.6}$
i (mag)	24.92±0.11	EW Hβ	–	log SFR/$M_\odot\, yr^{-1}$	$0.0^{0.0}_{-0.1}$
J (mag)	24.43±0.24	F [OII]$\lambda\lambda$3727 ($\times 10^{17}$)	$0.1^{0.1}_{0}$	log sSFR/Gyr^{-1}	$0.3^{0.3}_{0.2}$
z_{spec}	0.782/2	EW [OII]$\lambda\lambda$3727	$3.3^{7.7}_{0.2}$	$\hat{\tau}_V$	$0.5^{0.5}_{0.5}$
Morph.	D	F [OIII]λ4959 ($\times 10^{17}$)	$0.1^{0.1}_{0}$	12+log(O/H)	$7.8^{7.9}_{7.8}$
n	1.1±0.1	EW [OIII]λ4959	$3.3^{7.7}_{0.2}$	t_0 (Gyr)	3.5
$R_{eff,v,0}$	1.4±0.0	F [OIII]λ5007 ($\times 10^{17}$)	$0.1^{0.1}_{0}$	t_{10} (Gyr)	2.6
$M_{B,0}$	-17.74	EW [OIII]λ5007	$3.3^{7.7}_{0.2}$	t_{50} (Gyr)	1.1

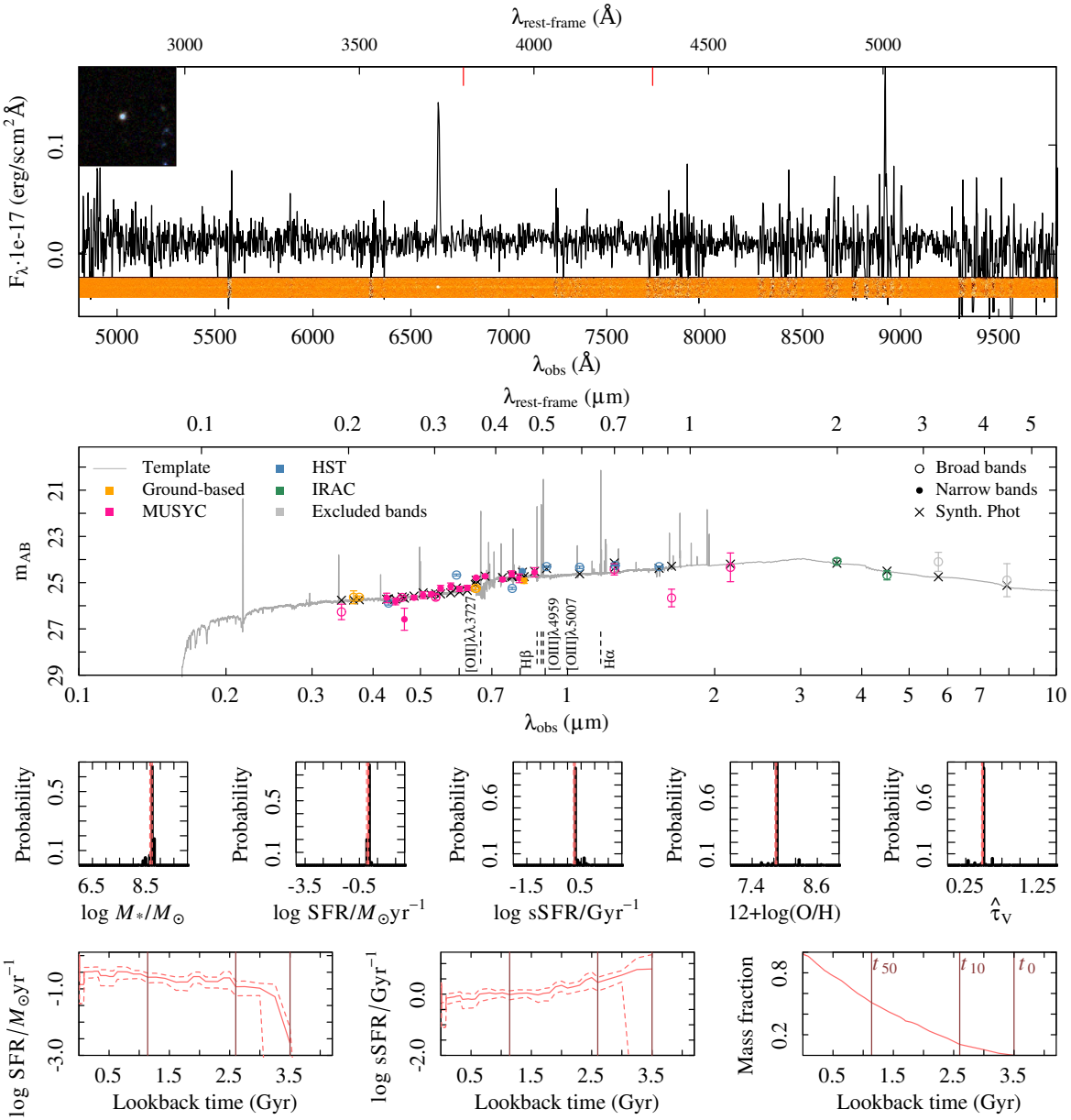

Summary ID 01585

ID	01585	$\mu_{eff,B,0}$	22.4±3.5	F Hα ($\times10^{17}$)	–
α (deg; J2000)	53.170545	$(B-V)_0$	0.57	EW Hα	–
δ (deg; J2000)	-27.924223	F Hβ ($\times10^{17}$)	–	log $M_*/M_\odot$	$8.5^{8.6}_{8.5}$
i (mag)	24.01±0.10	EW Hβ	–	log SFR$/M_\odot\,yr^{-1}$	$-0.3^{-0.2}_{-0.5}$
J (mag)	26.98±1.08	F [OII]$\lambda\lambda$3727 ($\times10^{17}$)	$1.7^{2.1}_{1.3}$	log sSFR$/Gyr^{-1}$	$0.2^{0.3}_{-0.2}$
z_{spec}	0.661/3	EW [OII]$\lambda\lambda$3727	$37.3^{54.2}_{25.0}$	$\hat{\tau}_V$	$0.8^{0.8}_{0.1}$
Morph.	Irr	F [OIII]λ4959 ($\times10^{17}$)	$1.7^{2.1}_{1.3}$	12+log(O/H)	$8.4^{8.4}_{7.8}$
n	2.0±1.7	EW [OIII]λ4959	$37.3^{54.2}_{25.0}$	t_0 (Gyr)	1.3
$R_{eff,v,0}$	1.0±1.7	F [OIII]λ5007 ($\times10^{17}$)	$1.7^{2.1}_{1.3}$	t_{10} (Gyr)	0.7
$M_{B,0}$	-17.91	EW [OIII]λ5007	$37.3^{54.2}_{25.0}$	t_{50} (Gyr)	0.3

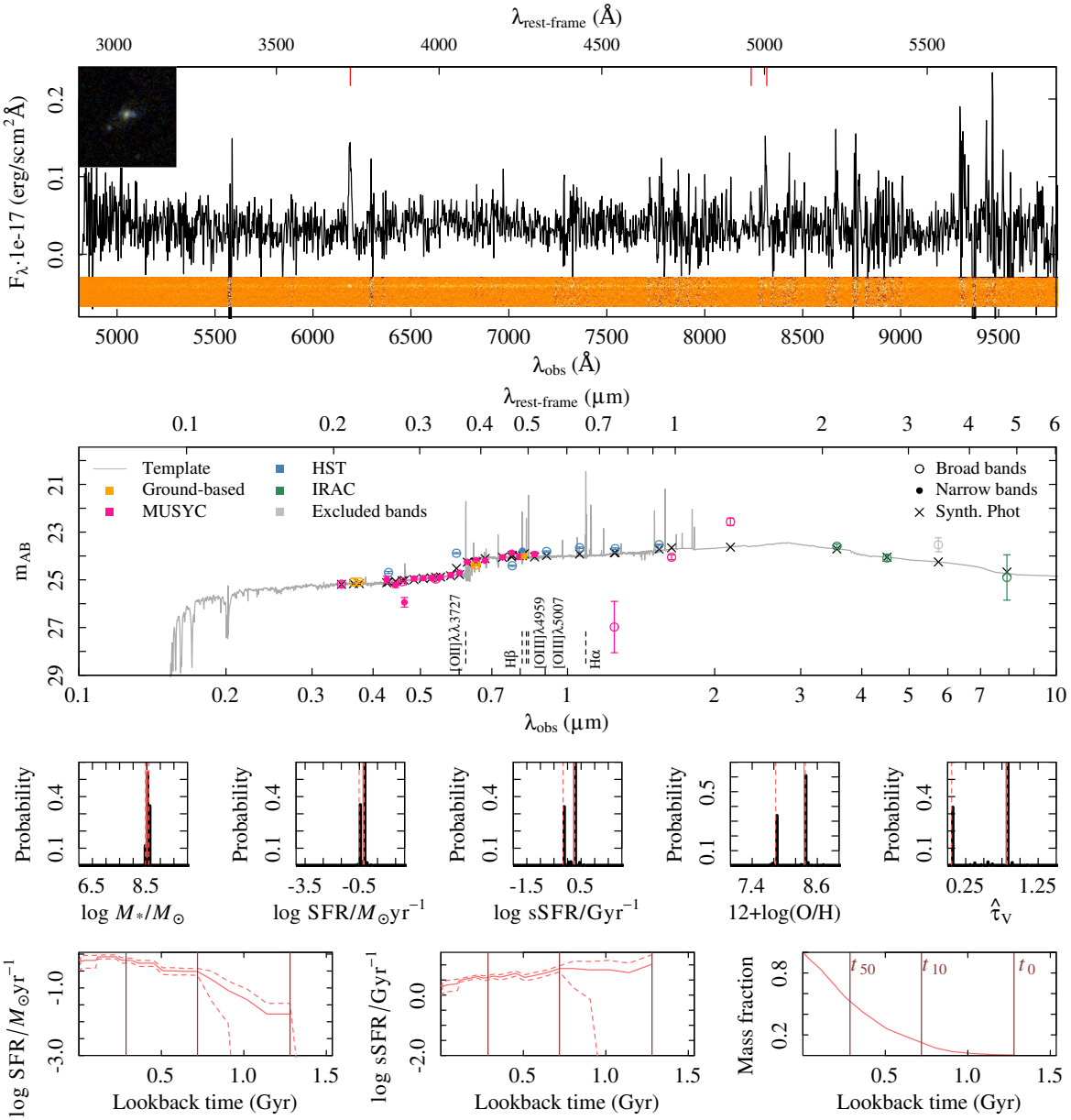

Summary ID 01605

ID	01605	$\mu_{eff,B,0}$	20.1±1764.4	F Hα ($\times 10^{17}$)	–
α (deg; J2000)	53.180598	$(B-V)_0$	0.36	EW Hα	–
δ (deg; J2000)	-27.870065	F Hβ ($\times 10^{17}$)	$0.1^{0.1}_{0.1}$	log $M_*/M_\odot$	$8.3^{8.4}_{8.3}$
i (mag)	25.40±0.13	EW Hβ	$39.7^{76.4}_{26.1}$	log SFR/$M_\odot\, yr^{-1}$	$-0.4^{-0.3}_{-0.4}$
J (mag)	24.39±0.19	F [OII]$\lambda\lambda$3727 ($\times 10^{17}$)	$0.3^{0.4}_{0.2}$	log sSFR/Gyr^{-1}	$0.3^{0.4}_{0.3}$
z_{spec}	0.888/2	EW [OII]$\lambda\lambda$3727	$45.7^{84.7}_{26.0}$	$\hat{\tau}_V$	$0.4^{0.4}_{0.4}$
Morph.	Irr	F [OIII]λ4959 ($\times 10^{17}$)	$0.3^{0.4}_{0.2}$	12+log(O/H)	$8.0^{8.1}_{8.0}$
n	1.7±421.3	EW [OIII]λ4959	$45.7^{84.7}_{26.0}$	t_0 (Gyr)	4.0
$R_{eff,v,0}$	0.2±52.8	F [OIII]λ5007 ($\times 10^{17}$)	$0.3^{0.4}_{0.2}$	t_{10} (Gyr)	1.4
$M_{B,0}$	-17.06	EW [OIII]λ5007	$45.7^{84.7}_{26.0}$	t_{50} (Gyr)	0.7

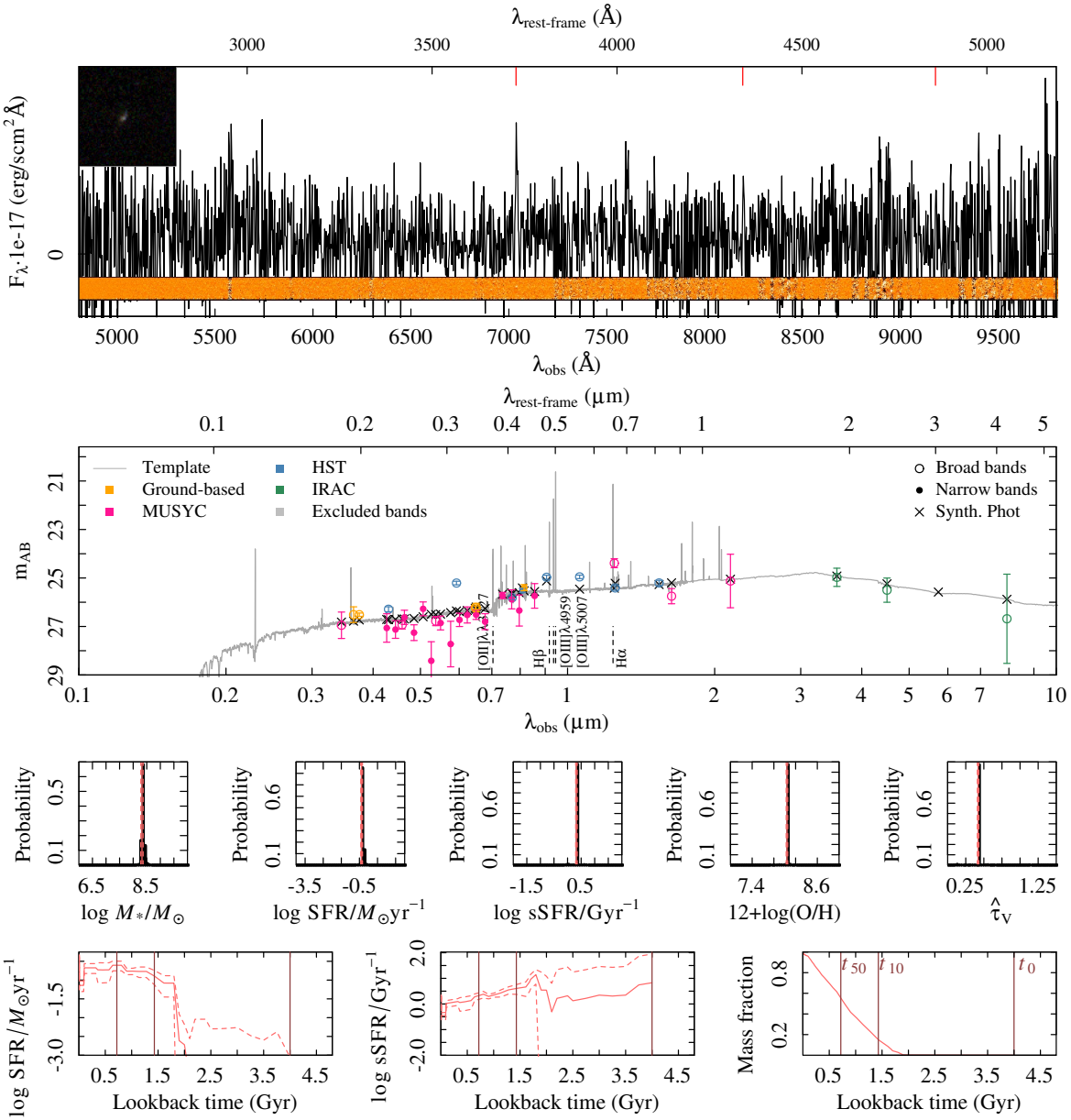

Summary ID 01656

ID	01656	$\mu_{eff,B,0}$	34.3±5.0	F Hα ($\times10^{17}$)	–
α (deg; J2000)	53.200094	$(B-V)_0$	0.29	EW Hα	–
δ (deg; J2000)	-27.813245	F Hβ ($\times10^{17}$)	–	log $M_*/M_\odot$	$9.0^{9.0}_{9.0}$
i (mag)	25.00±0.11	EW Hβ	–	log SFR/$M_\odot\,yr^{-1}$	$-0.4^{-0.3}_{-0.4}$
J (mag)	24.88±0.36	F [OII]$\lambda\lambda$3727 ($\times10^{17}$)	$0.8^{0.9}_{0.7}$	log sSFR/Gyr^{-1}	$-0.4^{-0.4}_{-0.4}$
z_{spec}	0.870/2	EW [OII]$\lambda\lambda$3727	$62.3^{87.9}_{45.9}$	$\hat{\tau}_V$	$0.1^{0.1}_{0.1}$
Morph.	D	F [OIII]λ4959 ($\times10^{17}$)	$0.8^{0.9}_{0.7}$	12+log(O/H)	$7.3^{7.4}_{7.3}$
n	1.6±0.3	EW [OIII]λ4959	$62.3^{87.9}_{45.9}$	t_0 (Gyr)	6.0
$R_{eff,v,0}$	2.1±0.1	F [OIII]λ5007 ($\times10^{17}$)	$0.8^{0.9}_{0.7}$	t_{10} (Gyr)	4.5
$M_{B,0}$	-17.62	EW [OIII]λ5007	$62.3^{87.9}_{45.9}$	t_{50} (Gyr)	2.8

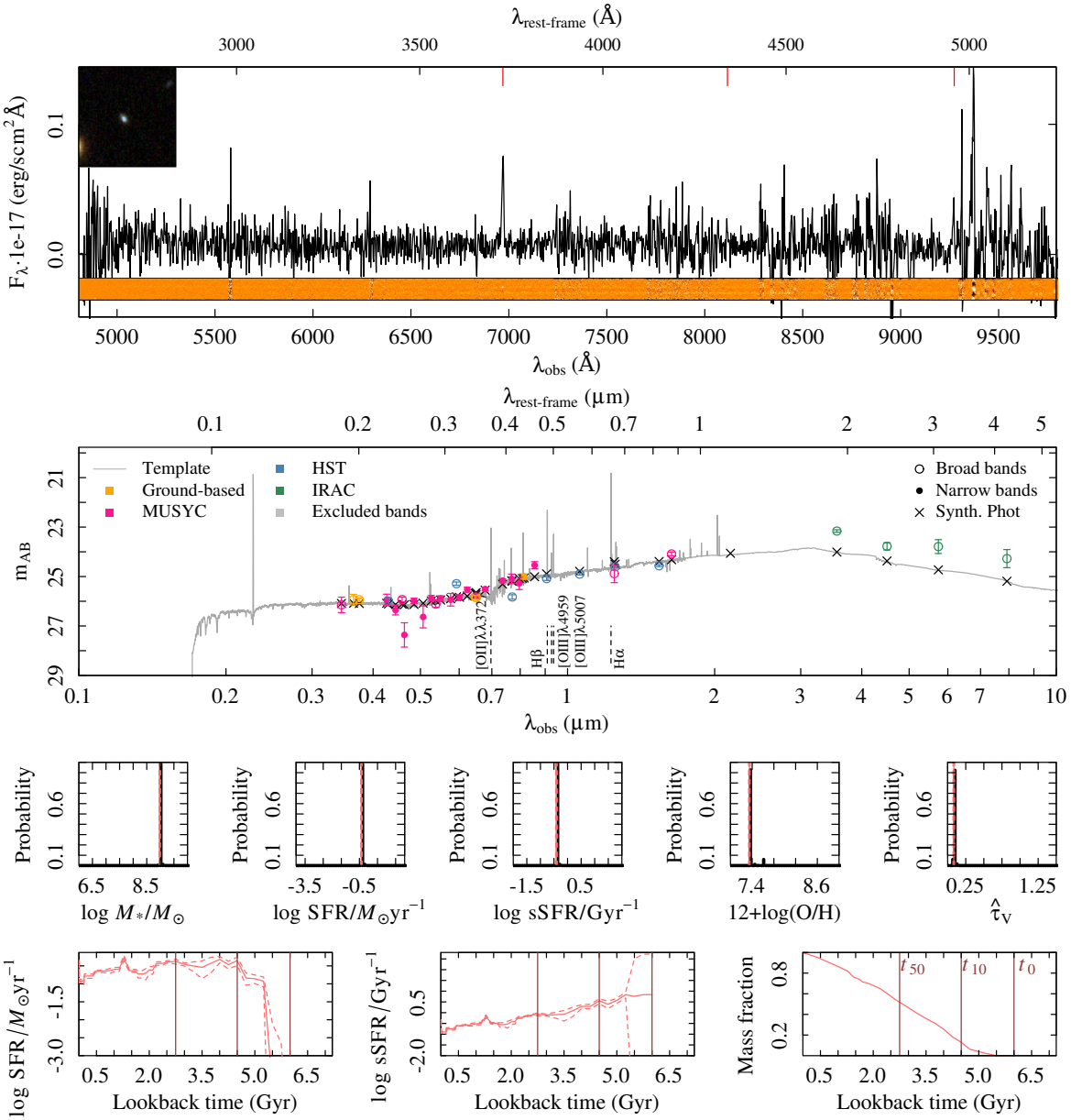

Summary ID 01723

ID	01723	$\mu_{eff,B,0}$	20.4±0.5	F Hα ($\times10^{17}$)	–
α (deg; J2000)	53.234593	$(B-V)_0$	0.42	EW Hα	–
δ (deg; J2000)	-27.884144	F Hβ ($\times10^{17}$)	–	log $M_*/M_\odot$	$8.4^{8.5}_{8.4}$
i (mag)	24.73±0.11	EW Hβ	–	log SFR/$M_\odot\,yr^{-1}$	$-0.8^{-0.5}_{-0.9}$
J (mag)	24.98±0.27	F [OII]$\lambda\lambda$3727 ($\times10^{17}$)	$0.5^{0.6}_{0.4}$	log sSFR/Gyr^{-1}	$-0.2^{0.1}_{-0.3}$
z_{spec}	0.733/3	EW [OII]$\lambda\lambda$3727	$28.9^{47.0}_{18.9}$	$\hat{\tau}_V$	$0.1^{0.3}_{0.0}$
Morph.	D	F [OIII]λ4959 ($\times10^{17}$)	$0.5^{0.6}_{0.4}$	12+log(O/H)	$7.9^{8.0}_{7.6}$
n	1.0±0.2	EW [OIII]λ4959	$28.9^{47.0}_{18.9}$	t_0 (Gyr)	4.2
$R_{eff,v,0}$	1.6±0.1	F [OIII]λ5007 ($\times10^{17}$)	$0.5^{0.6}_{0.4}$	t_{10} (Gyr)	2.3
$M_{B,0}$	-17.32	EW [OIII]λ5007	$28.9^{47.0}_{18.9}$	t_{50} (Gyr)	1.0

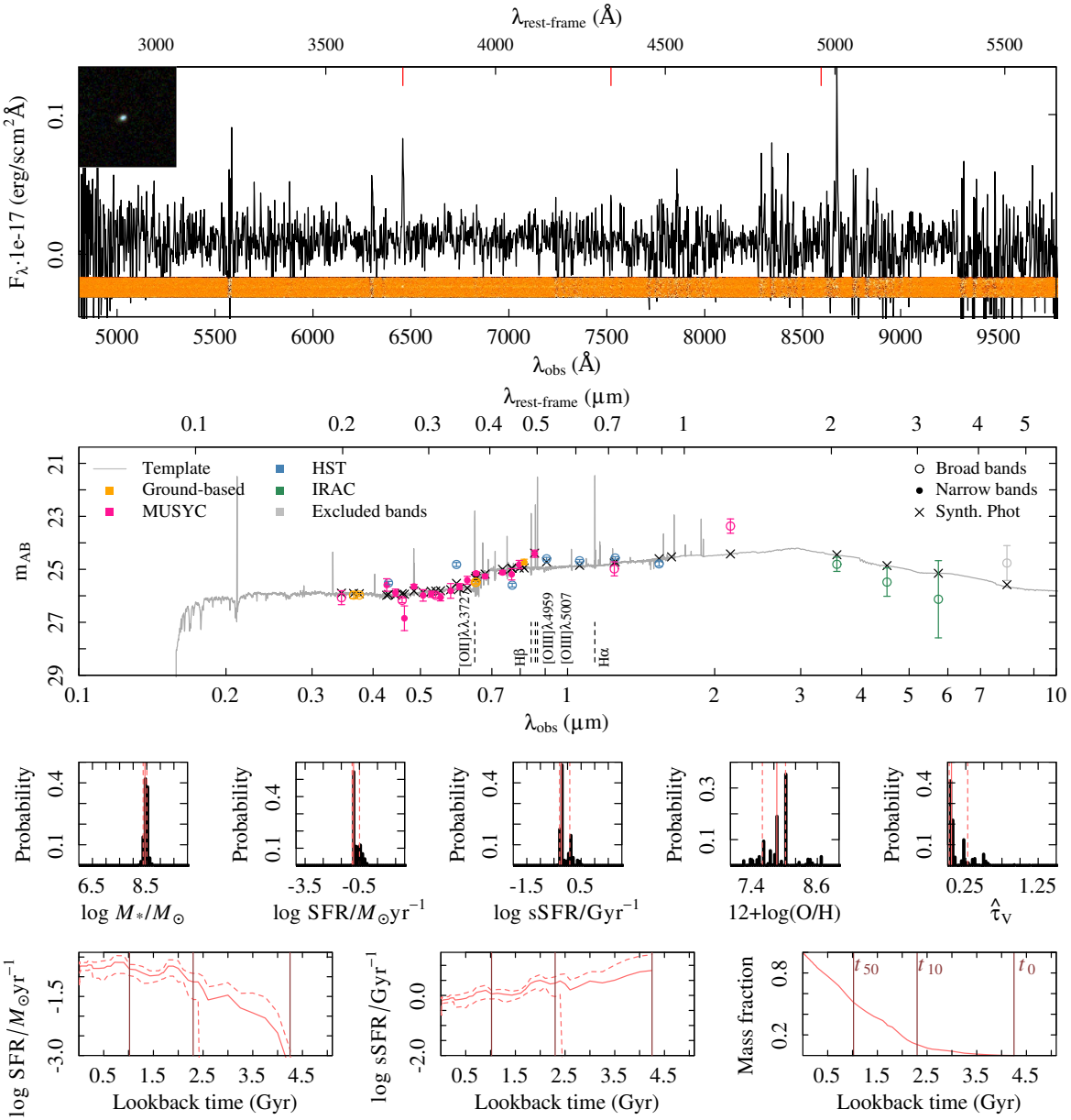

Summary ID 01727

ID	01727	$\mu_{eff,B,0}$	21.2±0.3	F Hα ($\times10^{17}$)	–
α (deg; J2000)	53.235372	$(B-V)_0$	0.91	EW Hα	–
δ (deg; J2000)	-27.654885	F Hβ ($\times10^{17}$)	–	log $M_*/M_\odot$	$8.8^{8.9}_{8.7}$
i (mag)	24.24±0.10	EW Hβ	–	log SFR/$M_\odot\,yr^{-1}$	$-1.1^{-0.9}_{-1.3}$
J (mag)	23.83±0.11	F [OII]$\lambda\lambda$3727 ($\times10^{17}$)	$1.2^{1.4}_{1.0}$	log sSFR/Gyr^{-1}	$-0.9^{-0.7}_{-1.0}$
z_{spec}	0.540/3	EW [OII]$\lambda\lambda$3727	$47.0^{65.8}_{34.1}$	$\hat{\tau}_V$	$0.1^{0.3}_{0.0}$
Morph.	Irr	F [OIII]λ4959 ($\times10^{17}$)	$1.2^{1.4}_{1.0}$	12+log(O/H)	$8.0^{8.5}_{7.5}$
n	1.4±0.3	EW [OIII]λ4959	$47.0^{65.8}_{34.1}$	t_0 (Gyr)	7.0
$R_{eff,v,0}$	1.3±0.1	F [OIII]λ5007 ($\times10^{17}$)	$1.2^{1.4}_{1.0}$	t_{10} (Gyr)	4.8
$M_{B,0}$	-16.61	EW [OIII]λ5007	$47.0^{65.8}_{34.1}$	t_{50} (Gyr)	2.5

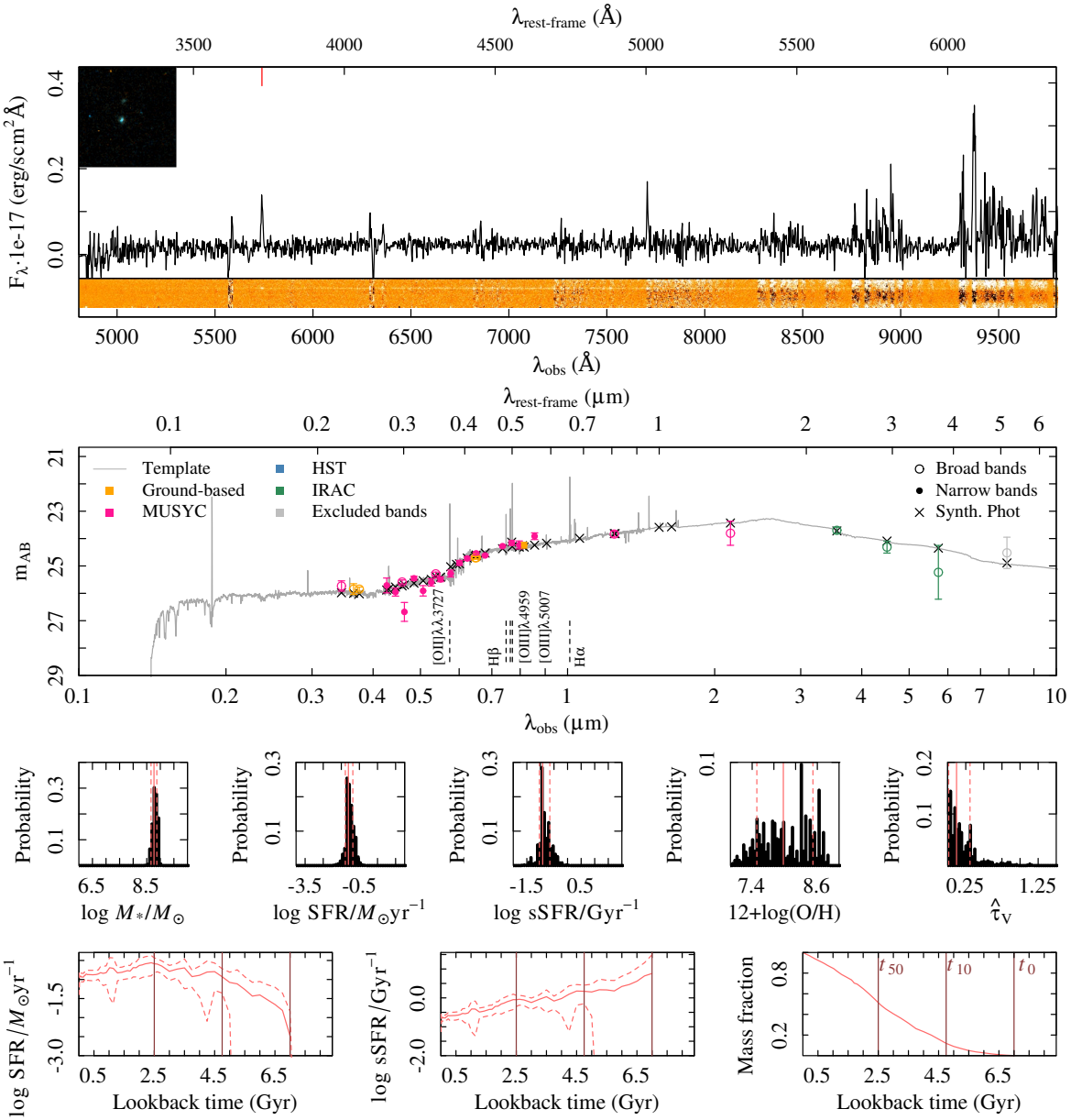

Summary ID 01752

ID	01752	$\mu_{eff,B,0}$	18.9±0.2	F Hα ($\times10^{17}$)	$4.9^{5.7}_{4.2}$
α (deg; J2000)	53.250208	$(B-V)_0$	0.52	EW Hα	$44.5^{59.7}_{35.0}$
δ (deg; J2000)	-27.690871	F Hβ ($\times10^{17}$)	$0.5^{1.1}_{0}$	log $M_*/M_\odot$	$7.6^{7.7}_{7.4}$
i (mag)	22.69±0.10	EW Hβ	$3.8^{8.7}_{0.2}$	log SFR$/M_\odot\,yr^{-1}$	$-0.9^{-0.8}_{-0.9}$
J (mag)	23.07±0.06	F [OII]$\lambda\lambda$3727 ($\times10^{17}$)	–	log sSFR$/Gyr^{-1}$	$0.5^{0.6}_{0.5}$
z_{spec}	0.147/4	EW [OII]$\lambda\lambda$3727	–	$\hat{\tau}_V$	$1.4^{1.4}_{1.3}$
Morph.	D	F [OIII]λ4959 ($\times10^{17}$)	–	12+log(O/H)	$8.4^{8.5}_{8.4}$
n	1.5±0.0	EW [OIII]λ4959	–	t_0 (Gyr)	6.2
$R_{eff,v,0}$	0.3±0.0	F [OIII]λ5007 ($\times10^{17}$)	–	t_{10} (Gyr)	0.5
$M_{B,0}$	-15.53	EW [OIII]λ5007	–	t_{50} (Gyr)	0.2

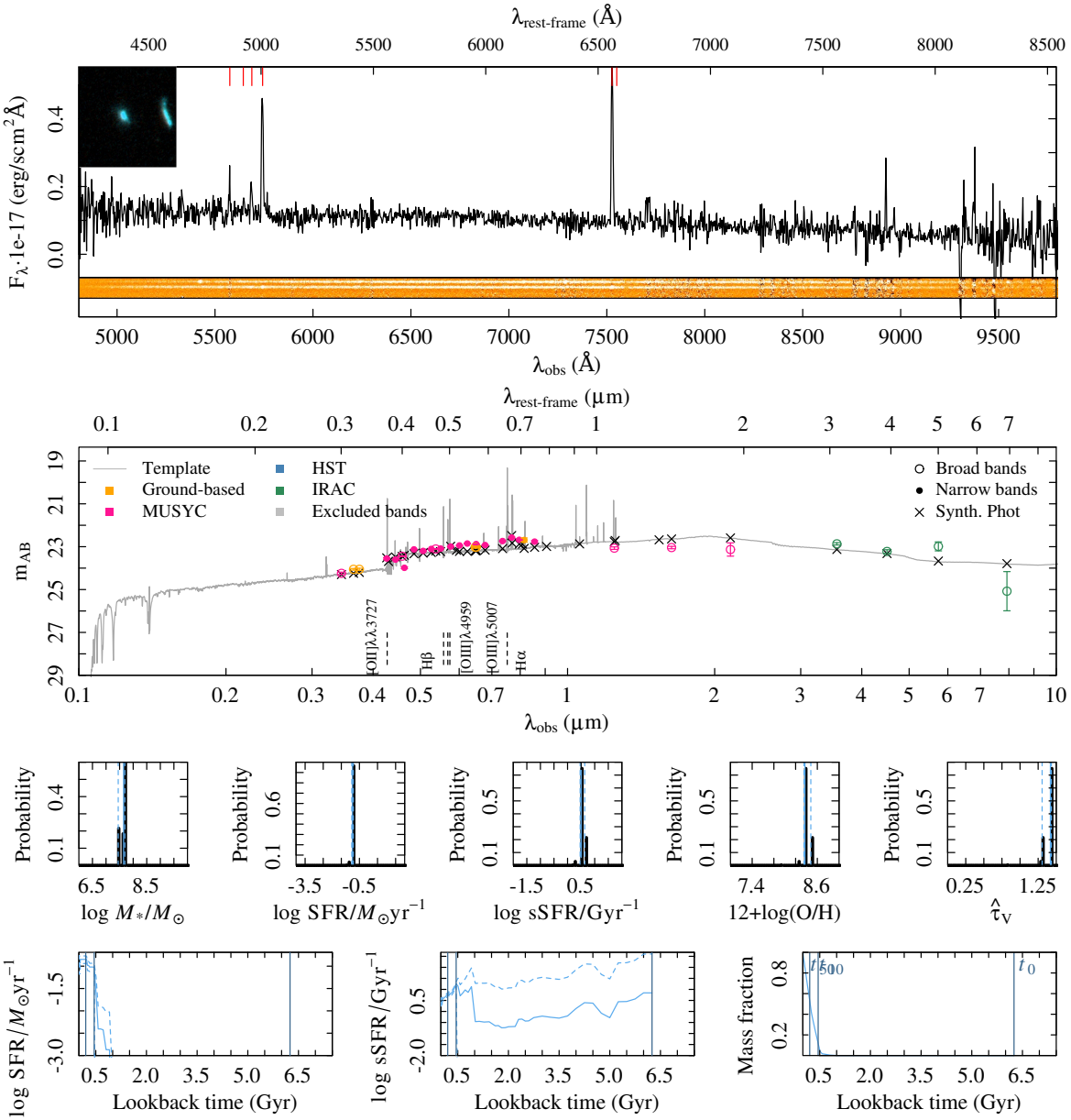

Summary ID 01765

ID	01765	$\mu_{eff,B,0}$	22.3±0.5	F Hα ($\times10^{17}$)	–
α (deg; J2000)	53.259785	$(B-V)_0$	0.22	EW Hα	–
δ (deg; J2000)	-27.680972	F Hβ ($\times10^{17}$)	–	log $M_*/M_\odot$	$9.0^{9.2}_{9.0}$
i (mag)	26.17±0.20	EW Hβ	–	log SFR/$M_\odot\,yr^{-1}$	$-0.5^{-0.3}_{-0.6}$
J (mag)	25.81±0.69	F [OII]$\lambda\lambda$3727 ($\times10^{17}$)	$0.5^{0.5}_{0.5}$	log sSFR/Gyr^{-1}	$-0.6^{-0.5}_{-0.7}$
z_{spec}	0.957/3	EW [OII]$\lambda\lambda$3727	$73.7^{110.9}_{57.6}$	$\hat{\tau}_V$	$0.1^{0.2}_{0.0}$
Morph.	D	F [OIII]λ4959 ($\times10^{17}$)	$0.5^{0.5}_{0.5}$	12+log(O/H)	$7.3^{7.6}_{7.2}$
n	8.0±3.5	EW [OIII]λ4959	$73.7^{110.9}_{57.6}$	t_0 (Gyr)	5.8
$R_{eff,v,0}$	1.3±0.2	F [OIII]λ5007 ($\times10^{17}$)	$0.5^{0.5}_{0.5}$	t_{10} (Gyr)	5.0
$M_{B,0}$	-17.24	EW [OIII]λ5007	$73.7^{110.9}_{57.6}$	t_{50} (Gyr)	3.8

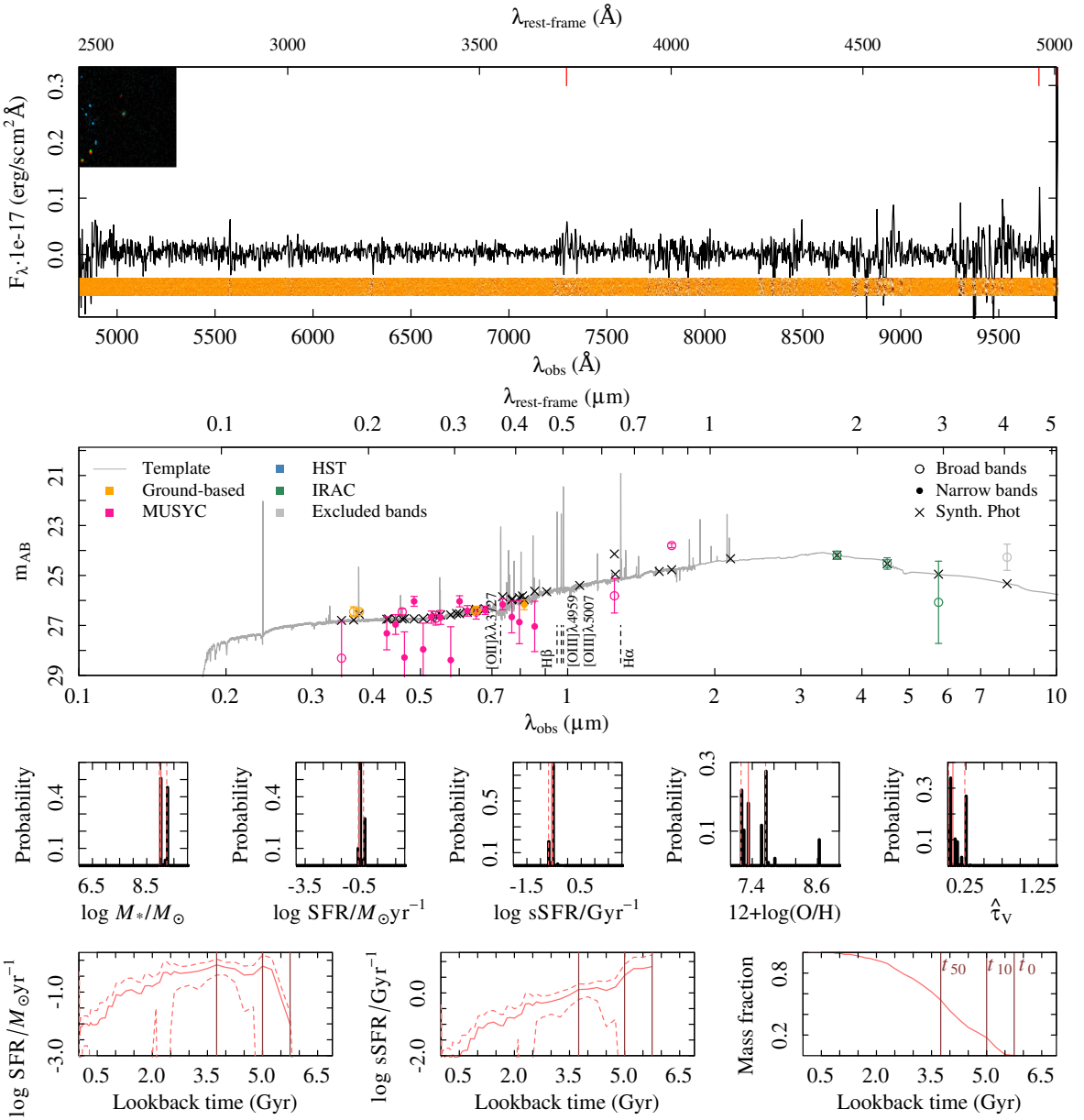

Summary ID 01796

ID	01796	$\mu_{eff,B,0}$	21.0±0.4	F Hα ($\times10^{17}$)	–
α (deg; J2000)	53.271301	$(B-V)_0$	0.97	EW Hα	–
δ (deg; J2000)	-27.805797	F Hβ ($\times10^{17}$)	$2.3^{3.5}_{0.9}$	log $M_*/M_\odot$	$9.1^{9.1}_{9.0}$
i (mag)	22.45±0.10	EW Hβ	$9.7^{16.8}_{3.6}$	log SFR/$M_\odot\,yr^{-1}$	$0.2^{0.4}_{0.2}$
J (mag)	22.47±0.03	F [OII]$\lambda\lambda$3727 ($\times10^{17}$)	$6.3^{7.4}_{5.1}$	log sSFR/Gyr^{-1}	$0.1^{0.3}_{0.1}$
z_{spec}	0.532/4	EW [OII]$\lambda\lambda$3727	$35.3^{49.7}_{26.4}$	$\hat{\tau}_V$	$1.3^{1.4}_{1.3}$
Morph.	D	F [OIII]λ4959 ($\times10^{17}$)	$6.3^{7.4}_{5.1}$	12+log(O/H)	$8.2^{8.2}_{7.6}$
n	0.6±0.0	EW [OIII]λ4959	$35.3^{49.7}_{26.4}$	t_0 (Gyr)	1.3
$R_{eff,v,0}$	0.9±0.0	F [OIII]λ5007 ($\times10^{17}$)	$6.3^{7.4}_{5.1}$	t_{10} (Gyr)	0.5
$M_{B,0}$	-18.28	EW [OIII]λ5007	$35.3^{49.7}_{26.4}$	t_{50} (Gyr)	0.3

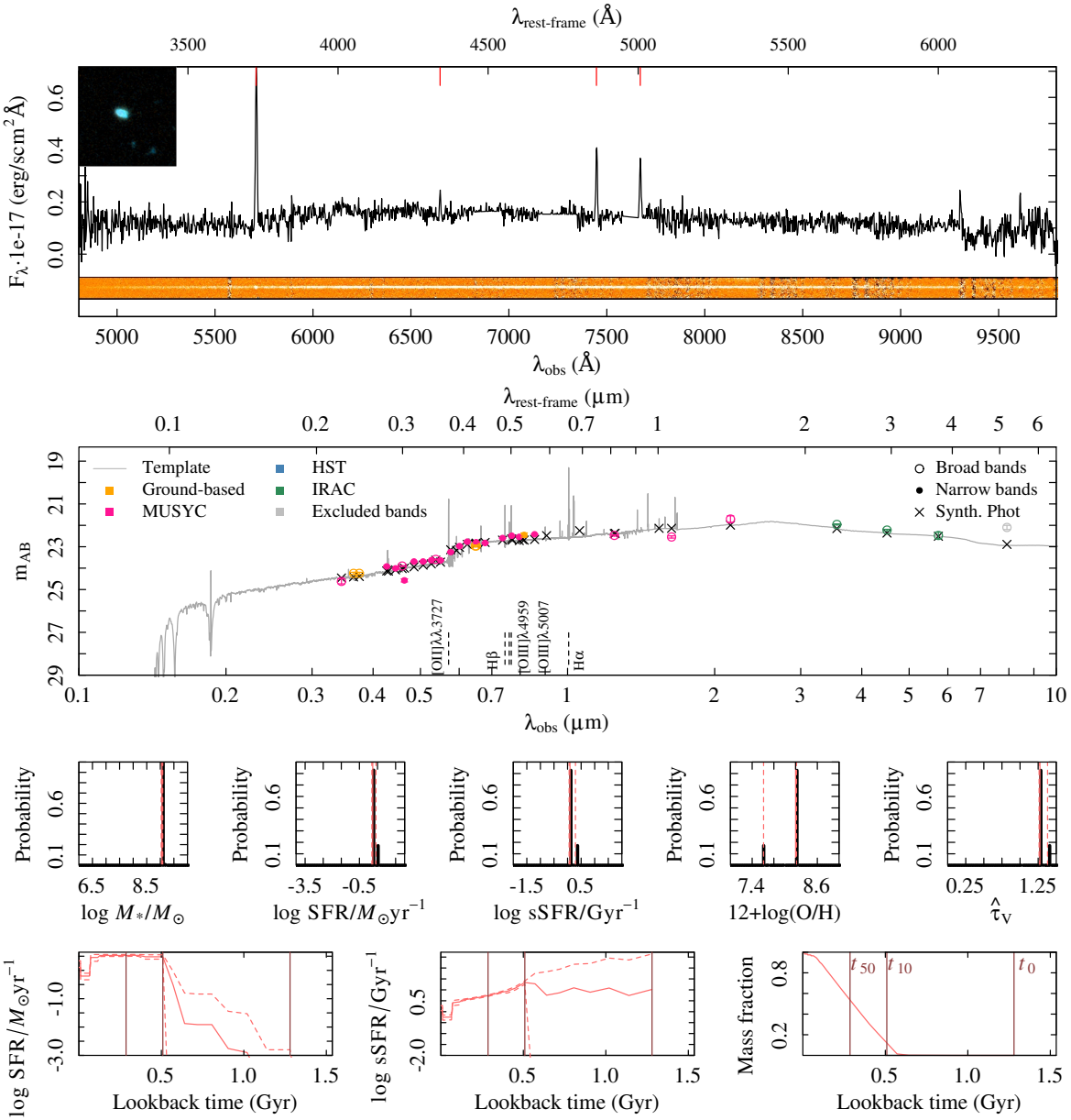

Summary ID 01804

ID	01804	$\mu_{eff,B,0}$	19.6±0.9	F Hα ($\times10^{17}$)	–
α (deg; J2000)	53.275468	$(B-V)_0$	0.86	EW Hα	–
δ (deg; J2000)	-27.803242	F Hβ ($\times10^{17}$)	–	log $M_*/M_\odot$	$8.2^{8.2}_{8.1}$
i (mag)	24.62±0.11	EW Hβ	–	log SFR/$M_\odot\,yr^{-1}$	$-1.5^{-1.1}_{-2.0}$
J (mag)	24.71±0.24	F [OII]$\lambda\lambda$3727 ($\times10^{17}$)	$0.7^{0.9}_{0.5}$	log sSFR/Gyr^{-1}	$-0.7^{-0.3}_{-1.2}$
z_{spec}	0.533/2	EW [OII]$\lambda\lambda$3727	$35.7^{53.6}_{23.8}$	$\hat{\tau}_V$	$0.4^{0.9}_{0.1}$
Morph.	D	F [OIII]λ4959 ($\times10^{17}$)	$0.7^{0.9}_{0.5}$	12+log(O/H)	$8.1^{8.6}_{7.5}$
n	0.6±0.1	EW [OIII]λ4959	$35.7^{53.6}_{23.8}$	t_0 (Gyr)	1.4
$R_{eff,v,0}$	0.9±0.0	F [OIII]λ5007 ($\times10^{17}$)	$0.7^{0.9}_{0.5}$	t_{10} (Gyr)	0.9
$M_{B,0}$	-16.33	EW [OIII]λ5007	$35.7^{53.6}_{23.8}$	t_{50} (Gyr)	0.4

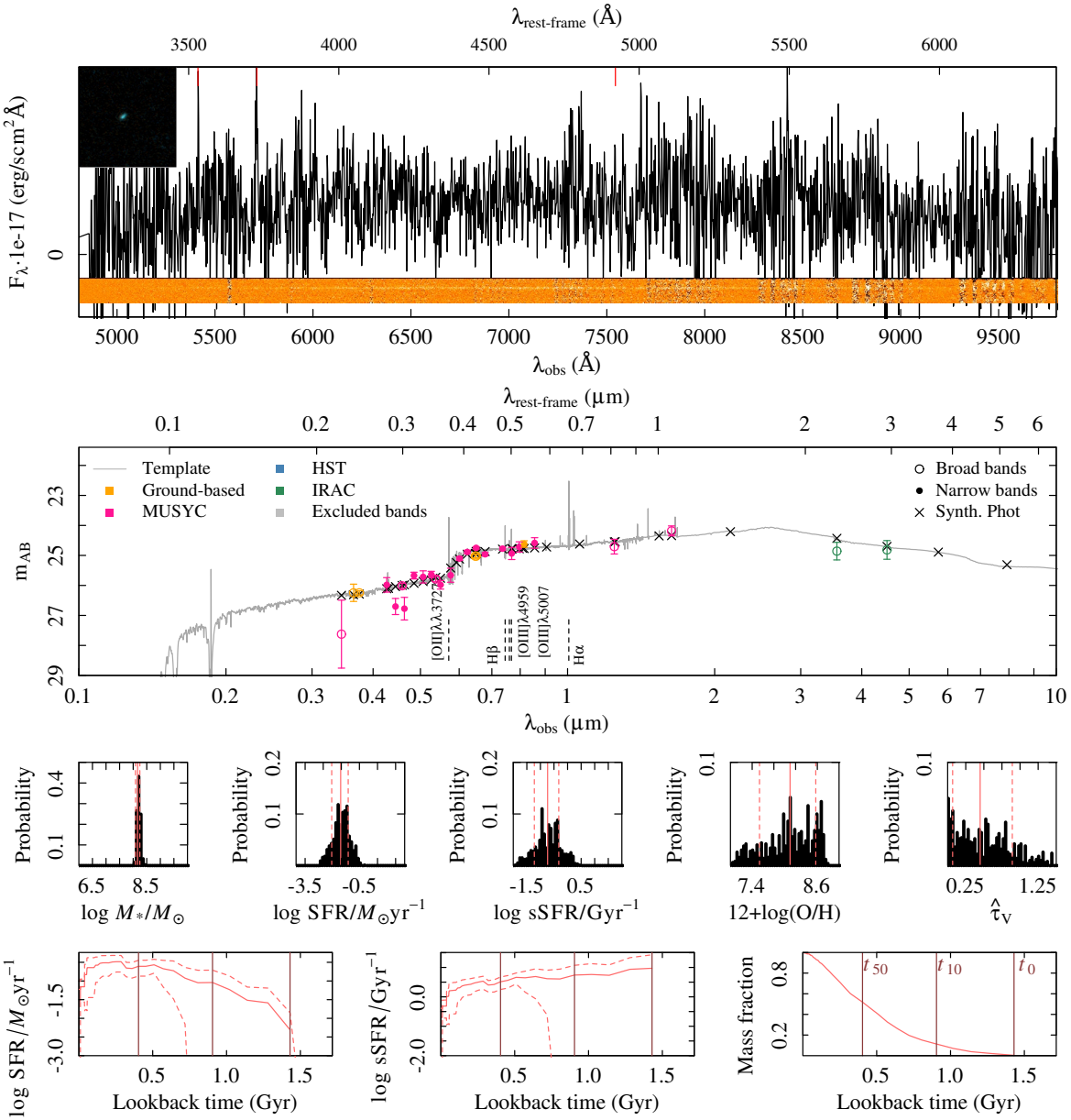

Summary ID 01860

ID	01860	$\mu_{eff,B,0}$	20.9±0.8	F Hα ($\times 10^{17}$)	–
α (deg; J2000)	53.297399	$(B-V)_0$	0.30	EW Hα	–
δ (deg; J2000)	-27.685623	F Hβ ($\times 10^{17}$)	$1.1^{1.3}_{1.0}$	log $M_*/M_\odot$	$8.4^{8.4}_{8.4}$
i (mag)	24.25±0.10	EW Hβ	$40.2^{62.0}_{28.7}$	log SFR/$M_\odot\,yr^{-1}$	$0.1^{0.1}_{0.1}$
J (mag)	24.77±0.27	F [OII]$\lambda\lambda$3727 ($\times 10^{17}$)	$1.3^{1.6}_{1.0}$	log sSFR/Gyr^{-1}	$0.7^{0.8}_{0.7}$
z_{spec}	0.863/4	EW [OII]$\lambda\lambda$3727	$19.1^{27.4}_{13.6}$	$\hat{\tau}_V$	$0.4^{0.4}_{0.4}$
Morph.	D	F [OIII]λ4959 ($\times 10^{17}$)	$1.3^{1.6}_{1.0}$	12+log(O/H)	$7.5^{7.5}_{7.5}$
n	0.7±0.1	EW [OIII]λ4959	$19.1^{27.4}_{13.6}$	t_0 (Gyr)	1.9
$R_{eff,v,0}$	1.2±0.0	F [OIII]λ5007 ($\times 10^{17}$)	$1.3^{1.6}_{1.0}$	t_{10} (Gyr)	0.7
$M_{B,0}$	-18.44	EW [OIII]λ5007	$19.1^{27.4}_{13.6}$	t_{50} (Gyr)	0.3

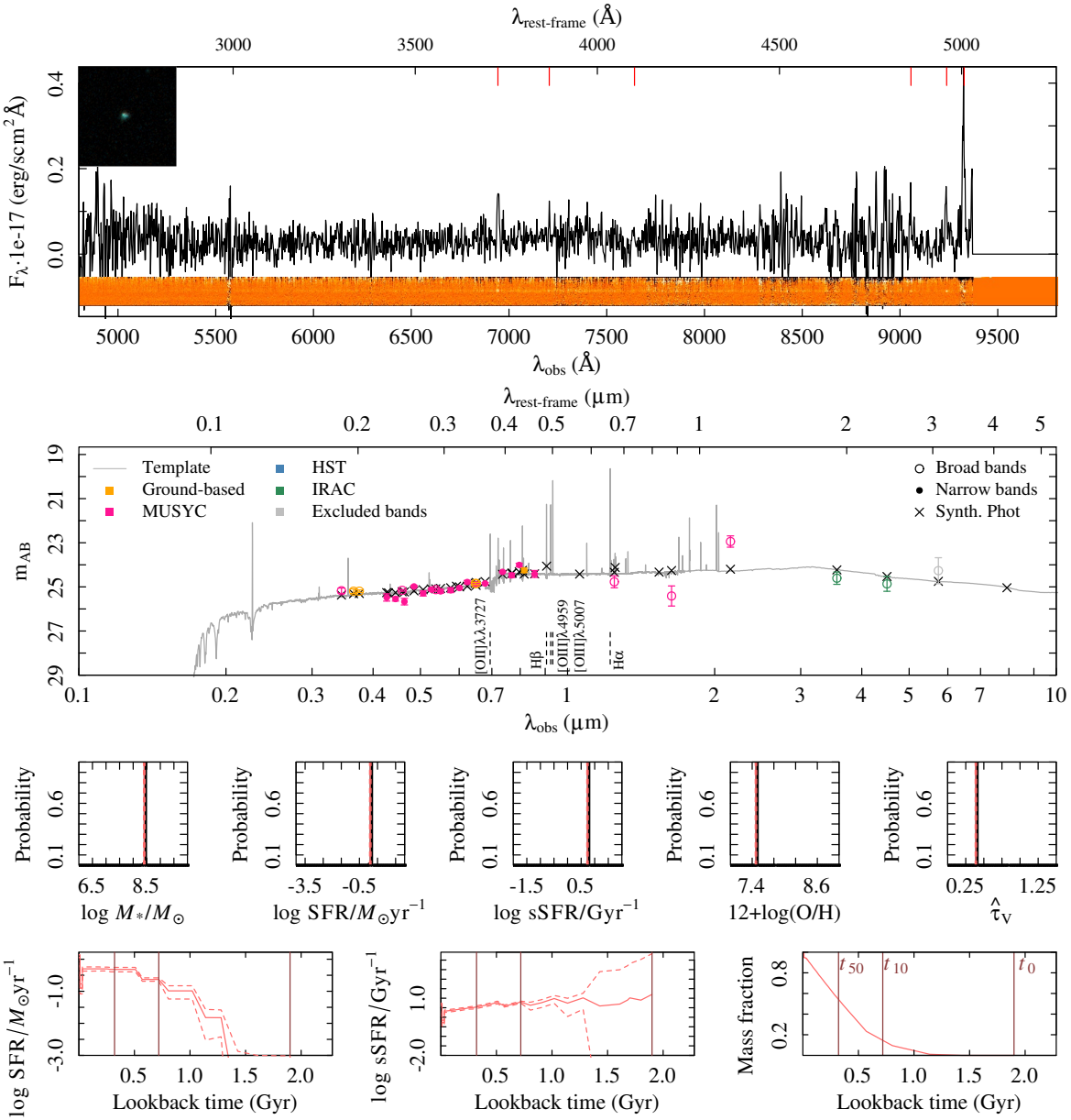

Summary ID 01861

ID	01861	$\mu_{eff,B,0}$	21.6±0.3	F Hα ($\times10^{17}$)	–
α (deg; J2000)	53.297825	$(B-V)_0$	0.97	EW Hα	–
δ (deg; J2000)	-27.695697	F Hβ ($\times10^{17}$)	$0.8^{1.4}_{0.4}$	log $M_*/M_\odot$	$8.7^{8.8}_{8.6}$
i (mag)	23.25±0.10	EW Hβ	$9.3^{17.0}_{4.0}$	log SFR/$M_\odot\,yr^{-1}$	$-0.1^{0.0}_{-0.5}$
J (mag)	23.10±0.08	F [OII]$\lambda\lambda$3727 ($\times10^{17}$)	$2.3^{2.7}_{1.9}$	log sSFR/Gyr^{-1}	$0.2^{0.2}_{-0.1}$
z_{spec}	0.538/4	EW [OII]$\lambda\lambda$3727	$30.2^{41.9}_{22.6}$	$\hat{\tau}_V$	$1.3^{1.3}_{0.9}$
Morph.	D	F [OIII]λ4959 ($\times10^{17}$)	$2.3^{2.7}_{1.9}$	12+log(O/H)	$8.0^{8.1}_{7.1}$
n	2.1±0.1	EW [OIII]λ4959	$30.2^{41.9}_{22.6}$	t_0 (Gyr)	1.3
$R_{eff,v,0}$	0.7±0.0	F [OIII]λ5007 ($\times10^{17}$)	$2.3^{2.7}_{1.9}$	t_{10} (Gyr)	0.8
$M_{B,0}$	-17.51	EW [OIII]λ5007	$30.2^{41.9}_{22.6}$	t_{50} (Gyr)	0.5

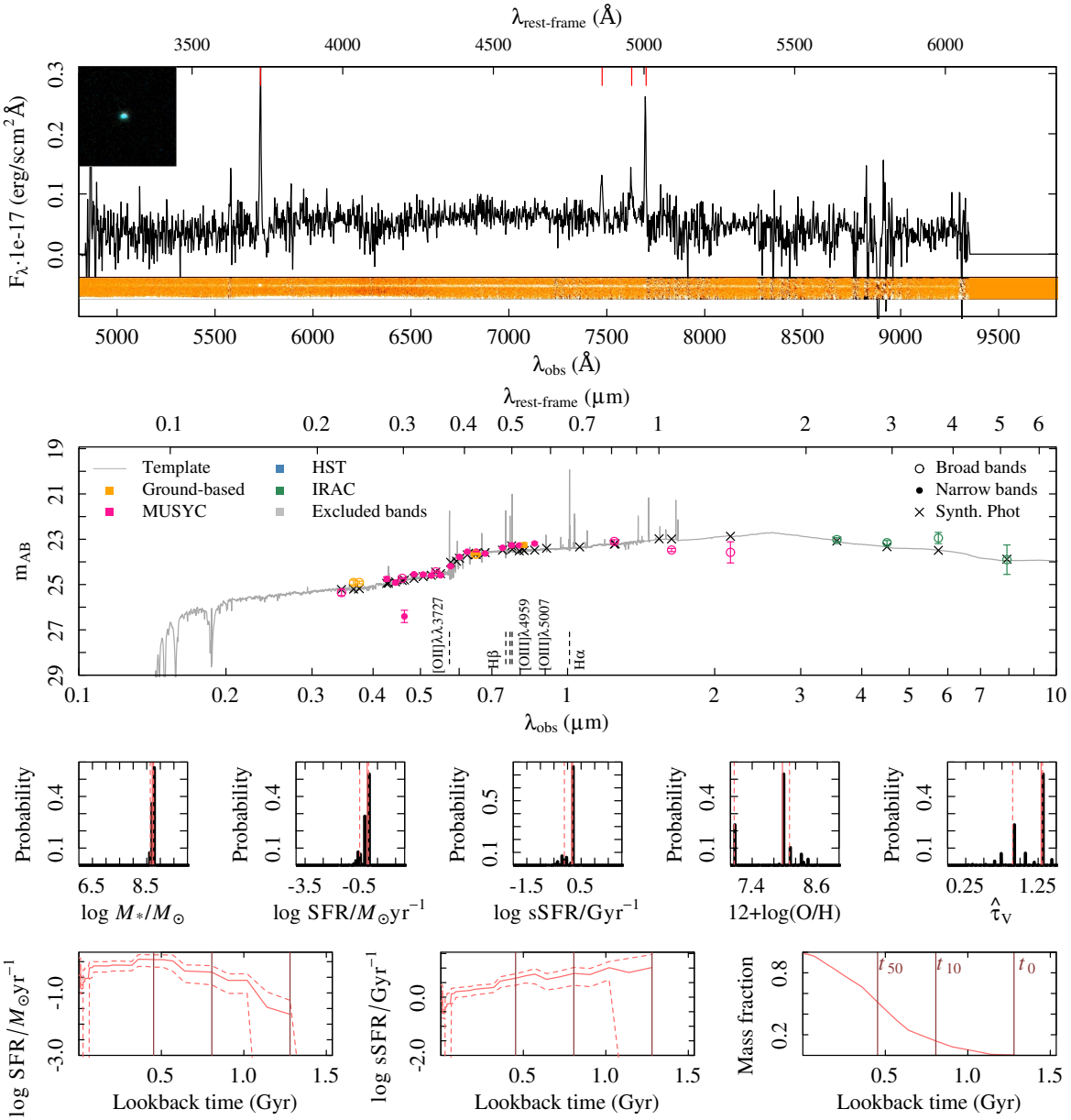

Summary ID 02010

ID	02010	$\mu_{eff,B,0}$	25.9±0.9	F Hα ($\times10^{17}$)	$1.2^{1.2}_{1.1}$
α (deg; J2000)	53.176486	$(B-V)_0$	0.61	EW Hα	$340.4^{876.8}_{170.9}$
δ (deg; J2000)	-27.789775	F Hβ ($\times10^{17}$)	$0.5^{0.6}_{0.4}$	log $M_*/M_\odot$	$7.9^{7.9}_{7.8}$
i (mag)	25.92±0.15	EW Hβ	$31.1^{43.3}_{21.8}$	log SFR/$M_\odot\,yr^{-1}$	$-0.9^{-0.9}_{-1.0}$
J (mag)	-99.99±-99.99	F [OII]$\lambda\lambda$3727 ($\times10^{17}$)	$0.6^{0.8}_{0.5}$	log sSFR/Gyr^{-1}	$0.2^{0.2}_{0.1}$
z_{spec}	0.424/4	EW [OII]$\lambda\lambda$3727	$46.6^{67.3}_{32.2}$	$\hat{\tau}_V$	$0.2^{0.2}_{0.2}$
Morph.	D	F [OIII]λ4959 ($\times10^{17}$)	$0.6^{0.8}_{0.5}$	12+log(O/H)	$8.6^{8.6}_{8.6}$
n	1.2±0.3	EW [OIII]λ4959	$46.6^{67.3}_{32.2}$	t_0 (Gyr)	6.8
$R_{eff,v,0}$	0.6±0.0	F [OIII]λ5007 ($\times10^{17}$)	$0.6^{0.8}_{0.5}$	t_{10} (Gyr)	4.8
$M_{B,0}$	-15.63	EW [OIII]λ5007	$46.6^{67.3}_{32.2}$	t_{50} (Gyr)	2.5

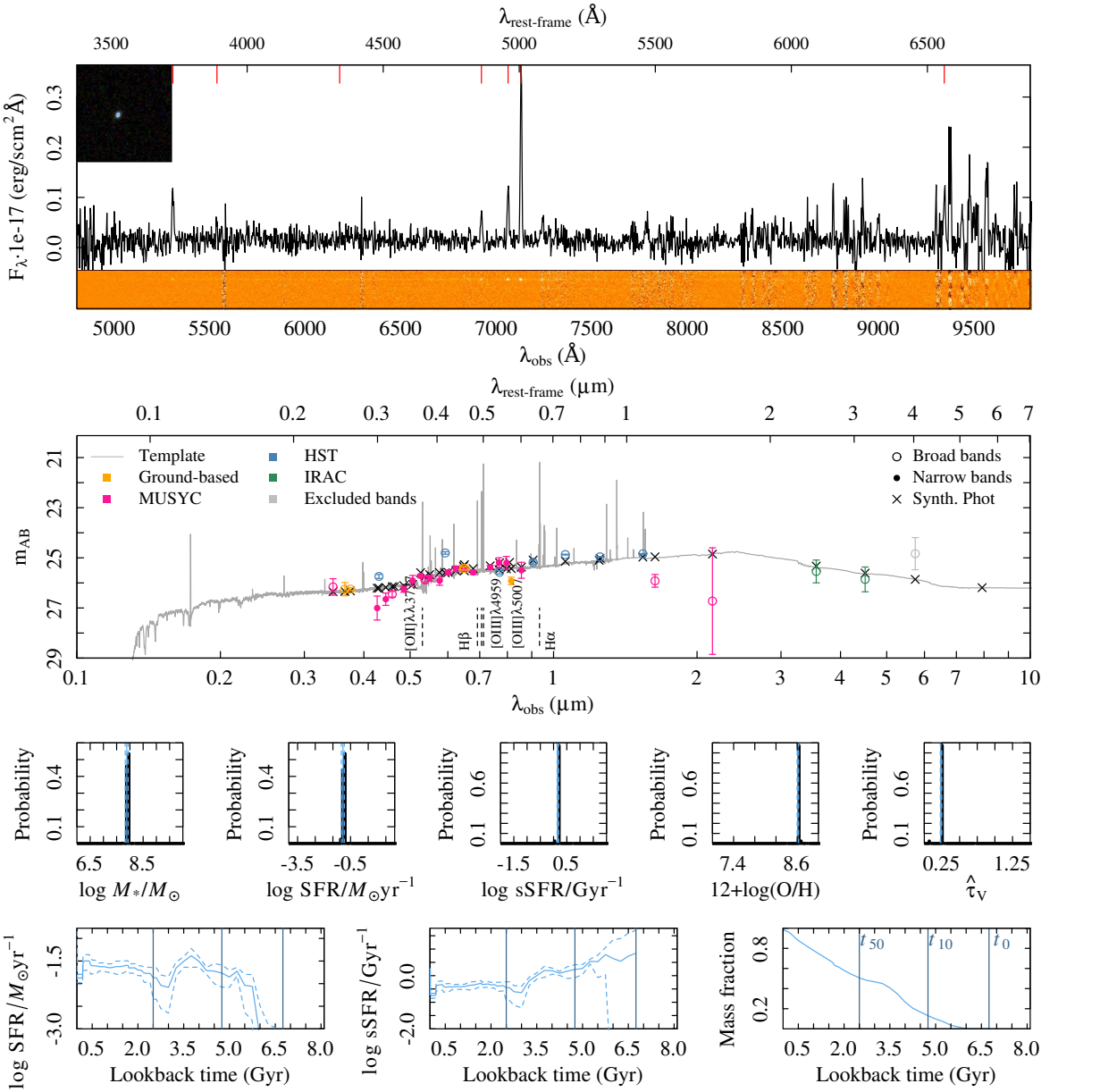

Bibliography

K. N. Abazajian, J. K. Adelman-McCarthy, M. A. Agüeros, S. S. Allam, C. Allende Prieto, D. An, K. S. J. Anderson, S. F. Anderson, J. Annis, N. A. Bahcall, and et al. The Seventh Data Release of the Sloan Digital Sky Survey. *ApJS*, 182:543, June 2009. doi: 10.1088/0067-0049/182/2/543.

M. Ajiki, B. Mobasher, Y. Taniguchi, Y. Shioya, T. Nagao, T. Murayama, and S. S. Sasaki. Narrowband Survey of the GOODS Fields: Search for Lyα Emitters at z = 5.7. *ApJ*, 638:596–602, February 2006. doi: 10.1086/499097.

C. Allende Prieto, D. L. Lambert, and M. Asplund. The Forbidden Abundance of Oxygen in the Sun. *ApJ*, 556:L63–L66, July 2001. doi: 10.1086/322874.

R. Amorín, J. M. Vílchez, G. F. Hägele, V. Firpo, E. Pérez-Montero, and P. Papaderos. Complex Gas Kinematics in Compact, Rapidly Assembling Star-forming Galaxies. *ApJ*, 754:L22, August 2012. doi: 10.1088/2041-8205/754/2/L22.

R. Amorín, A. Grazian, M. Castellano, L. Pentericci, A. Fontana, V. Sommariva, A. van der Wel, M. Maseda, and E. Merlin. Evidence of Very Low Metallicity and High Ionization State in a Strongly Lensed, Star-forming Dwarf Galaxy at z= 3.417. *ApJ*, 788:L4, June 2014a. doi: 10.1088/2041-8205/788/1/L4.

R. Amorín, E. Pérez-Montero, T. Contini, J. M. Vílchez, M. Bolzonella, L. A. M. Tasca, F. Lamareille, G. Zamorani, C. Maier, C. M. Carollo, J.-P. Kneib, O. Le Fèvre, S. Lilly, V. Mainieri, A. Renzini, M. Scodeggio, S. Bardelli, A. Bongiorno, K. Caputi, O. Cucciati, S. de la Torre, L. de Ravel, P. Franzetti, B. Garilli, A. Iovino, P. Kampczyk, C. Knobel, K. Kovač, J.-F. Le Borgne, V. L. B. M. Mignoli, R. Pellò, Y. Peng, V. Presotto, E. Ricciardelli, J. D. Silverman, M. Tanaka, L. Tresse, D. Vergani, and E. Zucca. Extreme emission-line galaxies out to z$\sim$1 in zCOSMOS-20k. I. Sample and characterization of global properties. *ArXiv e-prints*, March 2014b.

R. Amorín, V. Sommariva, M. Castellano, A. Grazian, L. A. M. Tasca, A. Fontana, L. Pentericci, P. Cassata, B. Garilli, V. Le Brun, O. Le Fèvre, D. Maccagni, R. Thomas, E. Vanzella, G. Zamorani, E. Zucca, S. Bardelli, P. Capak, L. P. Cassará, A. Cimatti, J. G. Cuby, O. Cucciati, S. de la Torre, A. Durkalec, M. Giavalisco, N. P. Hathi, O. Ilbert, B. C. Lemaux, C. Moreau, S. Paltani, B. Ribeiro, M. Salvato, D. Schaerer, M. Scodeggio, M. Talia, Y. Taniguchi, L. Tresse, D. Vergani, P. W. Wang, S. Charlot, T. Contini, S. Fotopoulou, C. López-Sanjuan, Y. Mellier, and N. Scoville. Discovering extremely compact and metal-poor, star-forming dwarf galaxies out to z ˜ 0.9 in the VIMOS Ultra-Deep Survey. *A&A*, 568: L8, August 2014c. doi: 10.1051/0004-6361/201423816.

F. Annibali, M. Cignoni, M. Tosi, R. P. van der Marel, A. Aloisi, G. Clementini, R. Contreras Ramos, G. Fiorentino, M. Marconi, and I. Musella. The Star Formation History of the Very Metal-poor Blue Compact Dwarf I Zw 18 from HST/ACS Data. *AJ*, 146:144, December 2013. doi: 10.1088/0004-6256/146/6/144.

M. L. N. Ashby, S. P. Willner, G. G. Fazio, J.-S. Huang, R. Arendt, P. Barmby, G. Barro, E. F. Bell, R. Bouwens, A. Cattaneo, D. Croton, R. Davé, J. S. Dunlop, E. Egami, S. Faber, K. Finlator, N. A. Grogin, P. Guhathakurta, L. Hernquist, J. L. Hora, G. Illingworth, A. Kashlinsky, A. M. Koekemoer, D. C. Koo, I. Labbé, Y. Li, L. Lin, H. Moseley, K. Nandra, J. Newman, K. Noeske, M. Ouchi, M. Peth, D. Rigopoulou, B. Robertson, V. Sarajedini, L. Simard, H. A. Smith, Z. Wang, R. Wechsler, B. Weiner, G. Wilson, S. Wuyts, T. Yamada, and H. Yan. SEDS: The Spitzer Extended Deep Survey. Survey Design, Photometry, and Deep IRAC Source Counts. *ApJ*, 769:80, May 2013. doi: 10.1088/0004-637X/769/1/80.

H. Atek, B. Siana, C. Scarlata, M. Malkan, P. McCarthy, H. Teplitz, A. Henry, J. Colbert, C. Bridge, A. J. Bunker, A. Dressler, R. A. E. Fosbury, N. P. Hathi, C. Martin, N. R. Ross, and H. Shim. Very Strong Emission-line Galaxies in the WFC3 Infrared Spectroscopic Parallel Survey and Implications for High-redshift Galaxies. *ApJ*, 743:121, December 2011. doi: 10.1088/0004-637X/743/2/121.

H. Atek, J.-P. Kneib, C. Pacifici, M. Malkan, S. Charlot, J. Lee, A. Bedregal, A. J. Bunker, J. W. Colbert, A. Dressler, N. Hathi, M. Lehnert, C. L. Martin, P. McCarthy, M. Rafelski, N. Ross, B. Siana, and H. I. Teplitz. Hubble Space Telescope Grism Spectroscopy of Extreme Starbursts across Cosmic Time: The Role of Dwarf Galaxies in the Star Formation History of the Universe. *ApJ*, 789:96, July 2014. doi: 10.1088/0004-637X/789/2/96.

A. Babul and M. J. Rees. On dwarf elliptical galaxies and the faint blue counts. *MNRAS*, 255:346–350, March 1992.

J. A. Baldwin, M. M. Phillips, and R. Terlevich. Classification parameters for the emission-line spectra of extragalactic objects. *PASP*, 93:5–19, February 1981. doi: 10.1086/130766.

F. D. Barazza, S. Jogee, H.-W. Rix, M. Barden, E. F. Bell, J. A. R. Caldwell, D. H. McIntosh, K. Meisenheimer, C. Y. Peng, and C. Wolf. Color, Structure, and Star Formation History of Dwarf Galaxies over the Last ˜3 Gyr with GEMS and SDSS. *ApJ*, 643:162–172, May 2006. doi: 10.1086/501447.

G. Barro, P. G. Pérez-González, J. Gallego, M. L. N. Ashby, M. Kajisawa, S. Miyazaki, V. Villar, T. Yamada, and J. Zamorano. UV-to-FIR Analysis of Spitzer/IRAC Sources in the Extended Groth Strip. I. Multi-wavelength Photometry and Spectral Energy Distributions. *ApJS*, 193:13, March 2011a. doi: 10.1088/0067-0049/193/1/13.

G. Barro, P. G. Pérez-González, J. Gallego, M. L. N. Ashby, M. Kajisawa, S. Miyazaki, V. Villar, T. Yamada, and J. Zamorano. UV-to-FIR Analysis of Spitzer/IRAC Sources in the Extended Groth Strip. II. Photometric Redshifts, Stellar Masses, and Star Formation Rates. *ApJS*, 193:30, April 2011b. doi: 10.1088/0067-0049/193/2/30.

A. E. Bauer, N. Drory, G. J. Hill, and G. Feulner. Specific Star Formation Rates to Redshift 1.5. *ApJ*, 621: L89–L92, March 2005. doi: 10.1086/429289.

S. Belli, T. Jones, R. S. Ellis, and J. Richard. Testing the Universality of the Fundamental Metallicity Relation at High Redshift Using Low-mass Gravitationally Lensed Galaxies. *ApJ*, 772:141, August 2013. doi: 10.1088/0004-637X/772/2/141.

A. Benítez-Llambay, J. F. Navarro, M. G. Abadi, S. Gottlöber, G. Yepes, Y. Hoffman, and M. Steinmetz. The imprint of reionization on the star formation histories of dwarf galaxies. *MNRAS*, 450:4207–4220, July 2015. doi: 10.1093/mnras/stv925.

C. Benn, K. Dee, and T. Agócs. ACAM: a new imager/spectrograph for the William Herschel Telescope. In *Society of Photo-Optical Instrumentation Engineers (SPIE) Conference Series*, volume 7014 of *Society of Photo-Optical Instrumentation Engineers (SPIE) Conference Series*, page 6, July 2008. doi: 10.1117/12.788694.

D. A. Berg, E. D. Skillman, A. R. Marble, L. van Zee, C. W. Engelbracht, J. C. Lee, R. C. Kennicutt, Jr., D. Calzetti, D. A. Dale, and B. D. Johnson. Direct Oxygen Abundances for Low-luminosity LVL Galaxies. *ApJ*, 754:98, August 2012. doi: 10.1088/0004-637X/754/2/98.

E. Bertin and S. Arnouts. SExtractor: Software for source extraction. *A&AS*, 117:393–404, June 1996. doi: 10.1051/aas:1996164.

B. Binggeli. A Note on the Definition and Nomenclature of Dwarf Galaxies. In G. Meylan and P. Prugniel, editors, *European Southern Observatory Conference and Workshop Proceedings*, volume 49 of *European Southern Observatory Conference and Workshop Proceedings*, page 13, January 1994.

G. R. Blumenthal, S. M. Faber, J. R. Primack, and M. J. Rees. Formation of galaxies and large-scale structure with cold dark matter. *Nature*, 311:517–525, October 1984. doi: 10.1038/311517a0.

D. Bottini, B. Garilli, D. Maccagni, L. Tresse, V. Le Brun, O. Le Fèvre, J. P. Picat, R. Scaramella, M. Scodeggio, G. Vettolani, A. Zanichelli, C. Adami, M. Arnaboldi, S. Arnouts, S. Bardelli, M. Bolzonella, A. Cappi, S. Charlot, P. Ciliegi, T. Contini, S. Foucaud, P. Franzetti, L. Guzzo, O. Ilbert, A. Iovino, H. J. McCracken, B. Marano, C. Marinoni, G. Mathez, A. Mazure, B. Meneux, R. Merighi, S. Paltani, A. Pollo, L. Pozzetti, M. Radovich, G. Zamorani, and E. Zucca. The Very Large Telescope Visible Multi-Object Spectrograph Mask Preparation Software. *PASP*, 117:996–1103, September 2005. doi: 10.1086/432150.

R. J. Bouwens, G. D. Illingworth, P. A. Oesch, M. Franx, I. Labbé, M. Trenti, P. van Dokkum, C. M. Carollo, V. González, R. Smit, and D. Magee. UV-continuum Slopes at z ˜ 4-7 from the HUDF09+ERS+CANDELS Observations: Discovery of a Well-defined UV Color-Magnitude Relationship for z $\geq$ 4 Star-forming Galaxies. *ApJ*, 754:83, August 2012a. doi: 10.1088/0004-637X/754/2/83.

R. J. Bouwens, G. D. Illingworth, P. A. Oesch, M. Trenti, I. Labbé, M. Franx, M. Stiavelli, C. M. Carollo, P. van Dokkum, and D. Magee. Lower-luminosity Galaxies Could Reionize the Universe: Very Steep Faint-end Slopes to the UV Luminosity Functions at z $\geq$ 5-8 from the HUDF09 WFC3/IR Observations. *ApJ*, 752:L5, June 2012b. doi: 10.1088/2041-8205/752/1/L5.

G. B. Brammer, R. Sánchez-Janssen, I. Labbé, E. da Cunha, D. K. Erb, M. Franx, M. Fumagalli, B. Lundgren, D. Marchesini, I. Momcheva, E. Nelson, S. Patel, R. Quadri, H.-W. Rix, R. E. Skelton, K. B. Schmidt, A. van der Wel, P. G. van Dokkum, D. A. Wake, and K. E. Whitaker. 3D-HST Grism Spectroscopy of a Gravitationally Lensed, Low-metallicity Starburst Galaxy at z = 1.847. *ApJ*, 758:L17, October 2012. doi: 10.1088/2041-8205/758/1/L17.

J. Brinchmann, S. Charlot, S. D. M. White, C. Tremonti, G. Kauffmann, T. Heckman, and J. Brinkmann. The physical properties of star-forming galaxies in the low-redshift Universe. *MNRAS*, 351:1151–1179, July 2004. doi: 10.1111/j.1365-2966.2004.07881.x.

J. Brinchmann, M. Pettini, and S. Charlot. New insights into the stellar content and physical conditions of star-forming galaxies at z = 2-3 from spectral modelling. *MNRAS*, 385:769–782, April 2008. doi: 10.1111/j.1365-2966.2008.12914.x.

A. M. Brooks, F. Governato, C. M. Booth, B. Willman, J. P. Gardner, J. Wadsley, G. Stinson, and T. Quinn. The Origin and Evolution of the Mass-Metallicity Relationship for Galaxies: Results from Cosmological N-Body Simulations. *ApJ*, 655:L17–L20, January 2007. doi: 10.1086/511765.

G. Bruzual and S. Charlot. Stellar population synthesis at the resolution of 2003. *MNRAS*, 344:1000–1028, October 2003. doi: 10.1046/j.1365-8711.2003.06897.x.

J. S. Bullock, A. V. Kravtsov, and D. H. Weinberg. Reionization and the Abundance of Galactic Satellites. *ApJ*, 539:517–521, August 2000. doi: 10.1086/309279.

K. Bundy, R. S. Ellis, C. J. Conselice, J. E. Taylor, M. C. Cooper, C. N. A. Willmer, B. J. Weiner, A. L. Coil, K. G. Noeske, and P. R. M. Eisenhardt. The Mass Assembly History of Field Galaxies: Detection of an Evolving Mass Limit for Star-Forming Galaxies. *ApJ*, 651:120–141, November 2006. doi: 10.1086/507456.

C. Cardamone, K. Schawinski, M. Sarzi, S. P. Bamford, N. Bennert, C. M. Urry, C. Lintott, W. C. Keel, J. Parejko, R. C. Nichol, D. Thomas, D. Andreescu, P. Murray, M. J. Raddick, A. Slosar, A. Szalay, and J. Vandenberg. Galaxy Zoo Green Peas: discovery of a class of compact extremely star-forming galaxies. *MNRAS*, 399:1191–1205, November 2009. doi: 10.1111/j.1365-2966.2009.15383.x.

C. N. Cardamone, P. G. van Dokkum, C. M. Urry, Y. Taniguchi, E. Gawiser, G. Brammer, E. Taylor, M. Damen, E. Treister, B. E. Cobb, N. Bond, K. Schawinski, P. Lira, T. Murayama, T. Saito, and K. Sumikawa. The Multiwavelength Survey by Yale-Chile (MUSYC): Deep Medium-band Optical Imaging and High-quality 32-band Photometric Redshifts in the ECDF-S. *ApJS*, 189:270–285, August 2010. doi: 10.1088/0067-0049/189/2/270.

N. Cardiel. *Formación estelar en galaxias dominantes de cúmulos*. PhD thesis, Universidad Complutense de Madrid, 1999.

J. Cepa, M. Aguiar, V. G. Escalera, I. Gonzalez-Serrano, E. Joven-Alvarez, L. Peraza, J. L. Rasilla, L. F. Rodriguez-Ramos, J. J. Gonzalez, F. J. Cobos Duenas, B. Sanchez, C. Tejada, J. Bland-Hawthorn, C. Militello, and F. Rosa. OSIRIS tunable imager and spectrograph. In M. Iye and A. F. Moorwood, editors, *Optical and IR Telescope Instrumentation and Detectors*, volume 4008 of *Society of Photo-Optical Instrumentation Engineers (SPIE) Conference Series*, pages 623–631, August 2000.

G. Chabrier. Galactic Stellar and Substellar Initial Mass Function. *PASP*, 115:763–795, July 2003. doi: 10.1086/376392.

S. Charlot and S. M. Fall. A Simple Model for the Absorption of Starlight by Dust in Galaxies. *ApJ*, 539: 718–731, August 2000. doi: 10.1086/309250.

S. Charlot and M. Longhetti. Nebular emission from star-forming galaxies. *MNRAS*, 323:887–903, May 2001. doi: 10.1046/j.1365-8711.2001.04260.x.

J. Chevallard, S. Charlot, B. Wandelt, and V. Wild. Insights into the content and spatial distribution of dust from the integrated spectral properties of galaxies. *MNRAS*, 432:2061–2091, July 2013. doi: 10.1093/mnras/stt523.

D. Coe, A. Zitrin, M. Carrasco, X. Shu, W. Zheng, M. Postman, L. Bradley, A. Koekemoer, R. Bouwens, T. Broadhurst, A. Monna, O. Host, L. A. Moustakas, H. Ford, J. Moustakas, A. van der Wel, M. Donahue, S. A. Rodney, N. Benítez, S. Jouvel, S. Seitz, D. D. Kelson, and P. Rosati. CLASH: Three Strongly Lensed Images of a Candidate z $\sim$ 11 Galaxy. *ApJ*, 762:32, January 2013. doi: 10.1088/0004-637X/762/1/32.

M. R. Corbin, W. D. Vacca, R. Cid Fernandes, J. E. Hibbard, R. S. Somerville, and R. A. Windhorst. Ultracompact Blue Dwarf Galaxies: Hubble Space Telescope Imaging and Stellar Population Analysis. *ApJ*, 651:861–873, November 2006. doi: 10.1086/507575.

L. L. Cowie, A. Songaila, E. M. Hu, and J. G. Cohen. New Insight on Galaxy Formation and Evolution From Keck Spectroscopy of the Hawaii Deep Fields. *AJ*, 112:839, September 1996. doi: 10.1086/118058.

O. Cucciati, L. Tresse, O. Ilbert, O. Le Fèvre, B. Garilli, V. Le Brun, P. Cassata, P. Franzetti, D. Maccagni, M. Scodeggio, E. Zucca, G. Zamorani, S. Bardelli, M. Bolzonella, R. M. Bielby, H. J. McCracken, A. Zanichelli, and D. Vergani. The star formation rate density and dust attenuation evolution over 12 Gyr with the VVDS surveys. *A&A*, 539:A31, March 2012. doi: 10.1051/0004-6361/201118010.

E. Daddi, M. Dickinson, G. Morrison, R. Chary, A. Cimatti, D. Elbaz, D. Frayer, A. Renzini, A. Pope, D. M. Alexander, F. E. Bauer, M. Giavalisco, M. Huynh, J. Kurk, and M. Mignoli. Multiwavelength Study of Massive Galaxies at z˜2. I. Star Formation and Galaxy Growth. *ApJ*, 670:156–172, November 2007. doi: 10.1086/521818.

T. Dahlen, B. Mobasher, M. Dickinson, H. C. Ferguson, M. Giavalisco, C. Kretchmer, and S. Ravindranath. Evolution of the Luminosity Function, Star Formation Rate, Morphology, and Size of Star-forming Galaxies Selected at Rest-Frame 1500 and 2800 Å. *ApJ*, 654:172–185, January 2007. doi: 10.1086/508854.

J. J. Dalcanton, B. F. Williams, A. C. Seth, A. Dolphin, J. Holtzman, K. Rosema, E. D. Skillman, A. Cole, L. Girardi, S. M. Gogarten, I. D. Karachentsev, K. Olsen, D. Weisz, C. Christensen, K. Freeman, K. Gilbert, C. Gallart, J. Harris, P. Hodge, R. S. de Jong, V. Karachentseva, M. Mateo, P. B. Stetson, M. Tavarez, D. Zaritsky, F. Governato, and T. Quinn. The ACS Nearby Galaxy Survey Treasury. *ApJS*, 183:67–108, July 2009. doi: 10.1088/0067-0049/183/1/67.

M. Damen, I. Labbé, P. G. van Dokkum, M. Franx, E. N. Taylor, W. N. Brandt, M. Dickinson, E. Gawiser, G. D. Illingworth, M. Kriek, D. Marchesini, A. Muzzin, C. Papovich, and H.-W. Rix. The SIMPLE Survey: Observations, Reduction, and Catalog. *ApJ*, 727:1, January 2011. doi: 10.1088/0004-637X/727/1/1.

J. I. Davies and S. Phillipps. The evolution of dwarf galaxies. *MNRAS*, 233:553–559, August 1988.

M. Davis, P. Guhathakurta, N. P. Konidaris, J. A. Newman, M. L. N. Ashby, A. D. Biggs, P. Barmby, K. Bundy, S. C. Chapman, A. L. Coil, C. J. Conselice, M. C. Cooper, D. J. Croton, P. R. M. Eisenhardt, R. S. Ellis, S. M. Faber, T. Fang, G. G. Fazio, A. Georgakakis, B. F. Gerke, W. M. Goss, S. Gwyn, J. Harker, A. M. Hopkins, J.-S. Huang, R. J. Ivison, S. A. Kassin, E. N. Kirby, A. M. Koekemoer, D. C. Koo, E. S. Laird, E. Le Floc'h, L. Lin, J. M. Lotz, P. J. Marshall, D. C. Martin, A. J. Metevier, L. A. Moustakas, K. Nandra, K. G. Noeske, C. Papovich, A. C. Phillips, R. M. Rich, G. H. Rieke, D. Rigopoulou, S. Salim, D. Schiminovich, L. Simard, I. Smail, T. A. Small, B. J. Weiner, C. N. A. Willmer, S. P. Willner, G. Wilson, E. L. Wright, and R. Yan. The All-Wavelength Extended Groth Strip International Survey (AEGIS) Data Sets. *ApJ*, 660:L1–L6, May 2007. doi: 10.1086/517931.

G. De Lucia and J. Blaizot. The hierarchical formation of the brightest cluster galaxies. *MNRAS*, 375:2–14, February 2007. doi: 10.1111/j.1365-2966.2006.11287.x.

A. Dekel and J. Silk. The origin of dwarf galaxies, cold dark matter, and biased galaxy formation. *ApJ*, 303:39–55, April 1986. doi: 10.1086/164050.

A. Domínguez, B. Siana, A. L. Henry, C. Scarlata, A. G. Bedregal, M. Malkan, H. Atek, N. R. Ross, J. W. Colbert, H. I. Teplitz, M. Rafelski, P. McCarthy, A. Bunker, N. P. Hathi, A. Dressler, C. L. Martin, and D. Masters. Dust Extinction from Balmer Decrements of Star-forming Galaxies at 0.75 <= z <= 1.5 with Hubble Space Telescope/Wide-Field-Camera 3 Spectroscopy from the WFC3 Infrared Spectroscopic Parallel Survey. *ApJ*, 763:145, February 2013. doi: 10.1088/0004-637X/763/2/145.

S. Dong, D. N. C. Lin, and S. D. Murray. Star Formation and Feedback in Dwarf Galaxies. *ApJ*, 596:930–943, October 2003. doi: 10.1086/378091.

S. P. Driver, D. T. Hill, L. S. Kelvin, A. S. G. Robotham, J. Liske, P. Norberg, I. K. Baldry, S. P. Bamford, A. M. Hopkins, J. Loveday, J. A. Peacock, E. Andrae, J. Bland-Hawthorn, S. Brough, M. J. I. Brown, E. Cameron, J. H. Y. Ching, M. Colless, C. J. Conselice, S. M. Croom, N. J. G. Cross, R. de Propris, S. Dye, M. J. Drinkwater, S. Ellis, A. W. Graham, M. W. Grootes, M. Gunawardhana, D. H. Jones, E. van Kampen, C. Maraston, R. C. Nichol, H. R. Parkinson, S. Phillipps, K. Pimbblet, C. C. Popescu, M. Prescott, I. G. Roseboom, E. M. Sadler, A. E. Sansom, R. G. Sharp, D. J. B. Smith, E. Taylor, D. Thomas, R. J. Tuffs, D. Wijesinghe, L. Dunne, C. S. Frenk, M. J. Jarvis, B. F. Madore, M. J. Meyer, M. Seibert, L. Staveley-Smith, W. J. Sutherland, and S. J. Warren. Galaxy and Mass Assembly (GAMA): survey diagnostics and core data release. *MNRAS*, 413:971–995, May 2011. doi: 10.1111/j.1365-2966.2010.18188.x.

N. Drory, K. Bundy, A. Leauthaud, N. Scoville, P. Capak, O. Ilbert, J. S. Kartaltepe, J. P. Kneib, H. J. McCracken, M. Salvato, D. B. Sanders, D. Thompson, and C. J. Willott. The Bimodal Galaxy Stellar Mass Function in the COSMOS Survey to z ˜ 1: A Steep Faint End and a New Galaxy Dichotomy. *ApJ*, 707:1595–1609, December 2009. doi: 10.1088/0004-637X/707/2/1595.

M. G. Edmunds. General Constraints on the Effect of Gas Flows in the Chemical Evolution of Galaxies. *MNRAS*, 246:678, October 1990.

B. Ekta and J. N. Chengalur. HI in isolated extremely metal-deficient galaxies. *MNRAS*, 403:295–299, March 2010a. doi: 10.1111/j.1365-2966.2009.16108.x.

B. Ekta and J. N. Chengalur. When are extremely metal-deficient galaxies extremely metal deficient? *MNRAS*, 406:1238–1247, August 2010b. doi: 10.1111/j.1365-2966.2010.16756.x.

D. Elbaz, E. Daddi, D. Le Borgne, M. Dickinson, D. M. Alexander, R.-R. Chary, J.-L. Starck, W. N. Brandt, M. Kitzbichler, E. MacDonald, M. Nonino, P. Popesso, D. Stern, and E. Vanzella. The reversal of the star formation-density relation in the distant universe. *A&A*, 468:33–48, June 2007. doi: 10.1051/0004-6361:20077525.

D. K. Erb, A. E. Shapley, M. Pettini, C. C. Steidel, N. A. Reddy, and K. L. Adelberger. The Mass-Metallicity Relation at z>˜2. *ApJ*, 644:813–828, June 2006. doi: 10.1086/503623.

C. Evans, M. Puech, J. Afonso, O. Almaini, P. Amram, H. Aussel, B. Barbuy, A. Basden, N. Bastian, G. Battaglia, B. Biller, P. Bonifacio, N. Bouché, A. Bunker, E. Caffau, S. Charlot, M. Cirasuolo, Y. Clenet, F. Combes, C. Conselice, T. Contini, J.-G. Cuby, G. Dalton, B. Davies, A. de Koter, K. Disseau, J. Dunlop, B. Epinat, F. Fiore, S. Feltzing, A. Ferguson, H. Flores, A. Fontana, T. Fusco, D. Gadotti, A. Gallazzi, J. Gallego, E. Giallongo, T. Gonçalves, D. Gratadour, E. Guenther, F. Hammer, V. Hill, M. Huertas-Company, R. Ibata, L. Kaper, A. Korn, S. Larsen, O. Le Fèvre, B. Lemasle, C. Maraston, S. Mei, Y. Mellier, S. Morris, G. Östlin, T. Paumard, R. Pello, L. Pentericci, C. Peroux, P. Petitjean, M. Rodrigues, L. Rodríguez-Muñoz, D. Rouan, H. Sana, D. Schaerer, E. Telles, S. Trager, L. Tresse, N. Welikala, S. Zibetti, and B. Ziegler. The Science Case for Multi-Object Spectroscopy on the European ELT. *ArXiv e-prints*, January 2015.

G. J. Ferland. *Hazy, A Brief Introduction to Cloudy 90*. 1996.

A. Ferrara and E. Tolstoy. The role of stellar feedback and dark matter in the evolution of dwarf galaxies. *MNRAS*, 313:291–309, April 2000. doi: 10.1046/j.1365-8711.2000.03209.x.

K. Finlator, B. D. Oppenheimer, and R. Davé. Smoothly rising star formation histories during the reionization epoch. *MNRAS*, 410:1703–1724, January 2011. doi: 10.1111/j.1365-2966.2010.17554.x.

A. Fontana, J. S. Dunlop, D. Paris, T. A. Targett, K. Boutsia, M. Castellano, A. Galametz, A. Grazian, R. McLure, E. Merlin, L. Pentericci, S. Wuyts, O. Almaini, K. Caputi, R.-R. Chary, M. Cirasuolo, C. J. Conselice, A. Cooray, E. Daddi, M. Dickinson, S. M. Faber, G. Fazio, H. C. Ferguson, E. Giallongo, M. Giavalisco, N. A. Grogin, N. Hathi, A. M. Koekemoer, D. C. Koo, R. A. Lucas, M. Nonino, H. W. Rix, A. Renzini, D. Rosario, P. Santini, C. Scarlata, V. Sommariva, D. P. Stark, A. van der Wel, E. Vanzella, V. Wild, H. Yan, and S. Zibetti. The Hawk-I UDS and GOODS Survey (HUGS): Survey design and deep K-band number counts. *A&A*, 570:A11, October 2014. doi: 10.1051/0004-6361/201423543.

C. Foster, A. M. Hopkins, M. Gunawardhana, M. A. Lara-López, R. G. Sharp, O. Steele, E. N. Taylor, S. P. Driver, I. K. Baldry, S. P. Bamford, J. Liske, J. Loveday, P. Norberg, J. A. Peacock, M. Alpaslan, A. E. Bauer, J. Bland-Hawthorn, S. Brough, E. Cameron, M. Colless, C. J. Conselice, S. M. Croom, C. S. Frenk, D. T. Hill, D. H. Jones, L. S. Kelvin, K. Kuijken, R. C. Nichol, M. S. Owers, H. R. Parkinson, K. A. Pimbblet, C. C. Popescu, M. Prescott, A. S. G. Robotham, A. R. Lopez-Sanchez, W. J. Sutherland, D. Thomas, R. J. Tuffs, E. van Kampen, and D. Wijesinghe. Galaxy And Mass Assembly (GAMA): the mass-metallicity relationship. *A&A*, 547:A79, November 2012. doi: 10.1051/0004-6361/201220050.

M. Fukugita, K. Shimasaku, and T. Ichikawa. Galaxy Colors in Various Photometric Band Systems. *PASP*, 107:945, October 1995. doi: 10.1086/133643.

C. Gallart. *Constraints on the Effects of Reionization in the Star Formation History of Dwarf Galaxies: Some Conclusions from the LCID Project*, page 103. 2012. doi: 10.1007/978-3-642-22018-0_10.

M. Geha, M. R. Blanton, R. Yan, and J. L. Tinker. A Stellar Mass Threshold for Quenching of Field Galaxies. *ApJ*, 757:85, September 2012. doi: 10.1088/0004-637X/757/1/85.

M. Giavalisco, H. C. Ferguson, A. M. Koekemoer, M. Dickinson, D. M. Alexander, F. E. Bauer, J. Bergeron, C. Biagetti, W. N. Brandt, S. Casertano, C. Cesarsky, E. Chatzichristou, C. Conselice, S. Cristiani, L. Da Costa, T. Dahlen, D. de Mello, P. Eisenhardt, T. Erben, S. M. Fall, C. Fassnacht, R. Fosbury, A. Fruchter, J. P. Gardner, N. Grogin, R. N. Hook, A. E. Hornschemeier, R. Idzi, S. Jogee, C. Kretchmer, V. Laidler, K. S. Lee, M. Livio, R. Lucas, P. Madau, B. Mobasher, L. A. Moustakas, M. Nonino, P. Padovani, C. Papovich, Y. Park, S. Ravindranath, A. Renzini, M. Richardson, A. Riess, P. Rosati, M. Schirmer, E. Schreier, R. S. Somerville, H. Spinrad, D. Stern, M. Stiavelli, L. Strolger, C. M. Urry, B. Vandame, R. Williams, and C. Wolf. The Great Observatories Origins Deep Survey: Initial Results from Optical and Near-Infrared Imaging. *ApJ*, 600:L93–L98, January 2004. doi: 10.1086/379232.

A. Gil de Paz and B. F. Madore. On the Optimization of Broadband Photometry for Galaxy Evolution Studies. *AJ*, 123:1864–1880, April 2002. doi: 10.1086/339480.

A. Gil de Paz and B. F. Madore. Palomar/Las Campanas Imaging Atlas of Blue Compact Dwarf Galaxies. II. Surface Photometry and the Properties of the Underlying Stellar Population. *ApJS*, 156:345–360, February 2005. doi: 10.1086/427068.

V. González, I. Labbé, R. J. Bouwens, G. Illingworth, M. Franx, M. Kriek, and G. B. Brammer. The Stellar Mass Density and Specific Star Formation Rate of the Universe at z ˜ 7. *ApJ*, 713:115–130, April 2010. doi: 10.1088/0004-637X/713/1/115.

A. W. Graham and S. P. Driver. A Concise Reference to (Projected) Sérsic $R^{1/n}$ Quantities, Including Concentration, Profile Slopes, Petrosian Indices, and Kron Magnitudes. *PASA*, 22:118–127, 2005. doi: 10.1071/AS05001.

E. K. Grebel. Star Formation Histories of Nearby Dwarf Galaxies. *Astrophysics and Space Science Supplement*, 277:231–239, 2001. doi: 10.1023/A:1012742903265.

E. K. Grebel and J. S. Gallagher, III. The Impact of Reionization on the Stellar Populations of Nearby Dwarf Galaxies. *ApJ*, 610:L89–L92, August 2004. doi: 10.1086/423339.

R. L. Griffith, M. C. Cooper, J. A. Newman, L. A. Moustakas, D. Stern, J. M. Comerford, M. Davis, J. M. Lotz, M. Barden, C. J. Conselice, P. L. Capak, S. M. Faber, J. D. Kirkpatrick, A. M. Koekemoer, D. C. Koo, K. G. Noeske, N. Scoville, K. Sheth, P. Shopbell, C. N. A. Willmer, and B. Weiner. The Advanced Camera for Surveys General Catalog: Structural Parameters for Approximately Half a Million Galaxies. *ApJS*, 200:9, May 2012. doi: 10.1088/0067-0049/200/1/9.

N. A. Grogin, D. D. Kocevski, S. M. Faber, H. C. Ferguson, A. M. Koekemoer, A. G. Riess, V. Acquaviva, D. M. Alexander, O. Almaini, M. L. N. Ashby, M. Barden, E. F. Bell, F. Bournaud, T. M. Brown, K. I. Caputi, S. Casertano, P. Cassata, M. Castellano, P. Challis, R.-R. Chary, E. Cheung, M. Cirasuolo, C. J. Conselice, A. Roshan Cooray, D. J. Croton, E. Daddi, T. Dahlen, R. Davé, D. F. de Mello, A. Dekel, M. Dickinson, T. Dolch, J. L. Donley, J. S. Dunlop, A. A. Dutton, D. Elbaz, G. G. Fazio, A. V. Filippenko, S. L. Finkelstein, A. Fontana, J. P. Gardner, P. M. Garnavich, E. Gawiser, M. Giavalisco, A. Grazian, Y. Guo, N. P. Hathi, B. Häussler, P. F. Hopkins, J.-S. Huang, K.-H. Huang, S. W. Jha, J. S. Kartaltepe, R. P. Kirshner, D. C. Koo, K. Lai, K.-S. Lee, W. Li, J. M. Lotz, R. A. Lucas, P. Madau, P. J. McCarthy, E. J. McGrath, D. H. McIntosh, R. J. McLure, B. Mobasher, L. A. Moustakas, M. Mozena, K. Nandra, J. A. Newman, S.-M. Niemi, K. G. Noeske, C. J. Papovich, L. Pentericci, A. Pope, J. R. Primack, A. Rajan, S. Ravindranath, N. A. Reddy, A. Renzini, H.-W. Rix, A. R. Robaina, S. A. Rodney, D. J. Rosario, P. Rosati, S. Salimbeni, C. Scarlata, B. Siana, L. Simard, J. Smidt, R. S. Somerville, H. Spinrad, A. N. Straughn, L.-G. Strolger, O. Telford, H. I. Teplitz, J. R. Trump, A. van der Wel, C. Villforth, R. H. Wechsler, B. J. Weiner, T. Wiklind, V. Wild, G. Wilson, S. Wuyts, H.-J. Yan, and M. S. Yun. CANDELS: The Cosmic Assembly Near-infrared Deep Extragalactic Legacy Survey. *ApJS*, 197:35, December 2011. doi: 10.1088/0067-0049/197/2/35.

C. Gruppioni, F. Pozzi, G. Rodighiero, I. Delvecchio, S. Berta, L. Pozzetti, G. Zamorani, P. Andreani, A. Cimatti, O. Ilbert, E. Le Floc'h, D. Lutz, B. Magnelli, L. Marchetti, P. Monaco, R. Nordon, S. Oliver, P. Popesso, L. Riguccini, I. Roseboom, D. J. Rosario, M. Sargent, M. Vaccari, B. Altieri, H. Aussel, A. Bongiovanni, J. Cepa, E. Daddi, H. Domínguez-Sánchez, D. Elbaz, N. Förster Schreiber, R. Genzel, A. Iribarrem, M. Magliocchetti, R. Maiolino, A. Poglitsch, A. Pérez García, M. Sanchez-Portal, E. Sturm, L. Tacconi, I. Valtchanov, A. Amblard, V. Arumugam, M. Bethermin, J. Bock, A. Boselli, V. Buat, D. Burgarella, N. Castro-Rodríguez, A. Cava, P. Chanial, D. L. Clements, A. Conley, A. Cooray, C. D. Dowell, E. Dwek, S. Eales, A. Franceschini, J. Glenn, M. Griffin, E. Hatziminaoglou, E. Ibar, K. Isaak, R. J. Ivison, G. Lagache, L. Levenson, N. Lu, S. Madden, B. Maffei, G. Mainetti, H. T. Nguyen, B. O'Halloran, M. J. Page, P. Panuzzo, A. Papageorgiou, C. P. Pearson, I. Pérez-Fournon, M. Pohlen, D. Rigopoulou, M. Rowan-Robinson, B. Schulz, D. Scott, N. Seymour, D. L. Shupe, A. J. Smith, J. A. Stevens, M. Symeonidis, M. Trichas, K. E. Tugwell, L. Vigroux, L. Wang, G. Wright, C. K. Xu, M. Zemcov, S. Bardelli, M. Carollo, T. Contini, O. Le Févre, S. Lilly, V. Mainieri, A. Renzini, M. Scodeggio, and E. Zucca. The Herschel PEP/HerMES luminosity function - I. Probing the evolution of PACS selected Galaxies to z $\simeq$ 4. *MNRAS*, 432:23–52, June 2013. doi: 10.1093/mnras/stt308.

Y. Guo, H. C. Ferguson, M. Giavalisco, G. Barro, S. P. Willner, M. L. N. Ashby, T. Dahlen, J. L. Donley, S. M. Faber, A. Fontana, A. Galametz, A. Grazian, K.-H. Huang, D. D. Kocevski, A. M. Koekemoer, D. C. Koo, E. J. McGrath, M. Peth, M. Salvato, S. Wuyts, M. Castellano, A. R. Cooray, M. E. Dickinson, J. S. Dunlop, G. G. Fazio, J. P. Gardner, E. Gawiser, N. A. Grogin, N. P. Hathi, L.-T. Hsu, K.-S. Lee, R. A. Lucas, B. Mobasher, K. Nandra, J. A. Newman, and A. van der Wel. CANDELS Multi-wavelength Catalogs: Source Detection and Photometry in the GOODS-South Field. *ApJS*, 207:24, August 2013. doi: 10.1088/0067-0049/207/2/24.

N. G. Guseva, P. Papaderos, Y. I. Izotov, R. F. Green, K. J. Fricke, T. X. Thuan, and K. G. Noeske. Spectro-

scopic and photometric studies of low-metallicity star-forming dwarf galaxies . I. SBS 1129+576. *A&A*, 407:75–90, August 2003a. doi: 10.1051/0004-6361:20030806.

N. G. Guseva, P. Papaderos, Y. I. Izotov, R. F. Green, K. J. Fricke, T. X. Thuan, and K. G. Noeske. Spectroscopic and photometric studies of low-metallicity star-forming dwarf galaxies. II. HS 1442+4250. *A&A*, 407:91–104, August 2003b. doi: 10.1051/0004-6361:20030807.

N. G. Guseva, P. Papaderos, Y. I. Izotov, R. F. Green, K. J. Fricke, T. X. Thuan, and K. G. Noeske. Spectroscopic and photometric studies of low-metallicity star-forming dwarf galaxies. III. SBS 1415+437. *A&A*, 407:105–120, August 2003c. doi: 10.1051/0004-6361:20030808.

N. G. Guseva, Y. I. Izotov, K. J. Fricke, and C. Henkel. New candidates for extremely metal-poor emission-line galaxies in the SDSS/BOSS DR10. *ArXiv e-prints*, May 2015.

K. N. Hainline, A. E. Shapley, K. A. Kornei, M. Pettini, E. Buckley-Geer, S. S. Allam, and D. L. Tucker. Rest-Frame Optical Spectra of Three Strongly Lensed Galaxies at z ˜ 2. *ApJ*, 701:52–65, August 2009. doi: 10.1088/0004-637X/701/1/52.

B. Häußler, M. Barden, S. P. Bamford, and A. Rojas. Galapagos: A Semi-Automated Tool for Galaxy Profile Fitting. In I. N. Evans, A. Accomazzi, D. J. Mink, and A. H. Rots, editors, *Astronomical Data Analysis Software and Systems XX*, volume 442 of *Astronomical Society of the Pacific Conference Series*, page 155, July 2011.

S. Heap, J.-C. Bouret, and I. Hubeny. Population III Stars in I Zw 18. *ArXiv e-prints*, April 2015.

A. Heavens, B. Panter, R. Jimenez, and J. Dunlop. The star-formation history of the Universe from the stellar populations of nearby galaxies. *Nature*, 428:625–627, April 2004. doi: 10.1038/nature02474.

A. Henry, C. L. Martin, K. Finlator, and A. Dressler. The Metallicity Evolution of Low-mass Galaxies: New Constraints at Intermediate Redshift. *ApJ*, 769:148, June 2013a. doi: 10.1088/0004-637X/769/2/148.

A. Henry, C. Scarlata, A. Domínguez, M. Malkan, C. L. Martin, B. Siana, H. Atek, A. G. Bedregal, J. W. Colbert, M. Rafelski, N. Ross, H. Teplitz, A. J. Bunker, A. Dressler, N. Hathi, D. Masters, P. McCarthy, and A. Straughn. Low Masses and High Redshifts: The Evolution of the Mass-Metallicity Relation. *ApJ*, 776:L27, October 2013b. doi: 10.1088/2041-8205/776/2/L27.

H. Hildebrandt, T. Erben, J. P. Dietrich, O. Cordes, L. Haberzettl, M. Hetterscheidt, M. Schirmer, O. Schmithuesen, P. Schneider, P. Simon, and C. Trachternach. GaBoDS: The Garching-Bonn Deep Survey. V. Data release of the ESO Deep-Public-Survey. *A&A*, 452:1121–1128, June 2006. doi: 10.1051/0004-6361:20054278.

P. W. Hodge. Dwarf Galaxies. *ARA&A*, 9:35, 1971. doi: 10.1146/annurev.aa.09.090171.000343.

C. Hoyos, D. C. Koo, A. C. Phillips, C. N. A. Willmer, and P. Guhathakurta. The DEEP2 Galaxy Redshift Survey: Discovery of Luminous, Metal-poor Star-forming Galaxies at Redshifts z ˜ 0.7. *ApJ*, 635:L21–L24, December 2005. doi: 10.1086/499232.

E. M. Hu, L. L. Cowie, Y. Kakazu, and A. J. Barger. Deep Spectroscopy of Ultra-Strong Emission-Line Galaxies. *ApJ*, 698:2014–2022, June 2009. doi: 10.1088/0004-637X/698/2/2014.

S. Huang, M. P. Haynes, R. Giovanelli, and J. Brinchmann. The Arecibo Legacy Fast ALFA Survey: The Galaxy Population Detected by ALFALFA. *ApJ*, 756:113, September 2012. doi: 10.1088/0004-637X/756/2/113.

E. P. Hubble. *Realm of the Nebulae*. 1936.

O. Ilbert, M. Salvato, E. Le Floc'h, H. Aussel, P. Capak, H. J. McCracken, B. Mobasher, J. Kartaltepe, N. Scoville, D. B. Sanders, S. Arnouts, K. Bundy, P. Cassata, J.-P. Kneib, A. Koekemoer, O. Le Fèvre, S. Lilly, J. Surace, Y. Taniguchi, L. Tasca, D. Thompson, L. Tresse, M. Zamojski, G. Zamorani, and E. Zucca. Galaxy Stellar Mass Assembly Between 0.2 z 2 from the S-COSMOS Survey. *ApJ*, 709: 644–663, February 2010. doi: 10.1088/0004-637X/709/2/644.

O. Ilbert, H. J. McCracken, O. Le Fèvre, P. Capak, J. Dunlop, A. Karim, M. A. Renzini, K. Caputi, S. Boissier, S. Arnouts, H. Aussel, J. Comparat, Q. Guo, P. Hudelot, J. Kartaltepe, J. P. Kneib, J. K. Krogager, E. Le Floc'h, S. Lilly, Y. Mellier, B. Milvang-Jensen, T. Moutard, M. Onodera, J. Richard, M. Salvato, D. B. Sanders, N. Scoville, J. D. Silverman, Y. Taniguchi, L. Tasca, R. Thomas, S. Toft, L. Tresse, D. Vergani, M. Wolk, and A. Zirm. Mass assembly in quiescent and star-forming galaxies since z 4 from UltraVISTA. *A&A*, 556:A55, August 2013. doi: 10.1051/0004-6361/201321100.

Y. I. Izotov and T. X. Thuan. Deep Hubble Space Telescope ACS Observations of I Zw 18: a Young Galaxy in Formation. *ApJ*, 616:768–782, December 2004. doi: 10.1086/424990.

Y. I. Izotov and T. X. Thuan. Active Galactic Nuclei in Four Metal-poor Dwarf Emission-Line Galaxies. *ApJ*, 687:133–140, November 2008. doi: 10.1086/591660.

Y. I. Izotov, F. H. Chaffee, C. B. Foltz, R. F. Green, N. G. Guseva, and T. X. Thuan. Helium Abundance in the Most Metal-deficient Blue Compact Galaxies: I ZW 18 and SBS 0335-052. *ApJ*, 527:757–777, December 1999. doi: 10.1086/308119.

Y. I. Izotov, T. X. Thuan, and N. G. Guseva. SBS 0335-052W: The Lowest Metallicity Star-forming Galaxy Known. *ApJ*, 632:210–216, October 2005. doi: 10.1086/432874.

Y. I. Izotov, N. G. Guseva, K. J. Fricke, and P. Papaderos. SBS 0335-052E+W: deep VLT/FORS+UVES spectroscopy of the pair of the lowest-metallicity blue compact dwarf galaxies. *A&A*, 503:61–72, August 2009. doi: 10.1051/0004-6361/200911965.

Y. I. Izotov, N. G. Guseva, and T. X. Thuan. Green Pea Galaxies and Cohorts: Luminous Compact Emission-line Galaxies in the Sloan Digital Sky Survey. *ApJ*, 728:161, February 2011. doi: 10.1088/0004-637X/728/2/161.

Y. I. Izotov, T. X. Thuan, and N. G. Guseva. Hunting for extremely metal-poor emission-line galaxies in the Sloan Digital Sky Survey: MMT and 3.5 m APO observations. *A&A*, 546:A122, October 2012. doi: 10.1051/0004-6361/201219733.

L. Jamet, M. Cerviño, V. Luridiana, E. Pérez, and T. Yakobchuk. The distance to the C component of I Zw 18 and its star formation history. A probabilistic approach. *A&A*, 509:A10, January 2010. doi: 10.1051/0004-6361/20078239.

S. Juneau, K. Glazebrook, D. Crampton, P. J. McCarthy, S. Savaglio, R. Abraham, R. G. Carlberg, H.-W. Chen, D. Le Borgne, R. O. Marzke, K. Roth, I. Jørgensen, I. Hook, and R. Murowinski. Cosmic Star Formation History and Its Dependence on Galaxy Stellar Mass. *ApJ*, 619:L135–L138, February 2005. doi: 10.1086/427937.

S. Juneau, M. Dickinson, D. M. Alexander, and S. Salim. A New Diagnostic of Active Galactic Nuclei: Revealing Highly Absorbed Systems at Redshift >0.3. *ApJ*, 736:104, August 2011. doi: 10.1088/0004-637X/736/2/104.

Y. Kakazu, L. L. Cowie, and E. M. Hu. Mapping Extremely Low Metallicity Galaxies to Redshift One. *ApJ*, 668:853–875, October 2007. doi: 10.1086/521333.

J. S. Kalirai, J. MacKenty, R. Bohlin, T. Brown, S. Deustua, R. A. Kimble, and A. Riess. WFC3 SMOV Proposal 11451: The Photometric Performance and Calibration of WFC3/IR. Technical report, November 2009.

A. Karim, E. Schinnerer, A. Martínez-Sansigre, M. T. Sargent, A. van der Wel, H.-W. Rix, O. Ilbert, V. Smolčić, C. Carilli, M. Pannella, A. M. Koekemoer, E. F. Bell, and M. Salvato. The Star Formation History of Mass-selected Galaxies in the COSMOS Field. *ApJ*, 730:61, April 2011. doi: 10.1088/0004-637X/730/2/61.

J. S. Kartaltepe, M. Mozena, D. Kocevski, D. H. McIntosh, J. Lotz, E. F. Bell, S. Faber, H. Ferguson, D. Koo, R. Bassett, M. Bernyk, K. Blancato, F. Bournaud, P. Cassata, M. Castellano, E. Cheung, C. J. Conselice, D. Croton, T. Dahlen, D. F. de Mello, L. DeGroot, J. Donley, J. Guedes, N. Grogin, N. Hathi, M. Hilton, B. Hollon, H. Inami, S. Kassin, A. Koekemoer, C. Lani, N. Liu, R. A. Lucas, M. Martig, E. McGrath, C. McPartland, B. Mobasher, A. Morlock, S. Mutch, E. O'Leary, M. Peth, J. Pforr, A. Pillepich, G. B. Poole, Z. Rizer, D. Rosario, E. Soto, A. Straughn, O. Telford, B. Sunnquist, B. Weiner, and S. Wuyts. CANDELS Visual Classifications: Scheme, Data Release, and First Results. *ArXiv e-prints*, January 2014.

G. Kauffmann, T. M. Heckman, C. Tremonti, J. Brinchmann, S. Charlot, S. D. M. White, S. E. Ridgway, J. Brinkmann, M. Fukugita, P. B. Hall, Ž. Ivezić, G. T. Richards, and D. P. Schneider. The host galaxies of active galactic nuclei. *MNRAS*, 346:1055–1077, December 2003a. doi: 10.1111/j.1365-2966.2003.07154.x.

G. Kauffmann, T. M. Heckman, S. D. M. White, S. Charlot, C. Tremonti, J. Brinchmann, G. Bruzual, E. W. Peng, M. Seibert, M. Bernardi, M. Blanton, J. Brinkmann, F. Castander, I. Csábai, M. Fukugita, Z. Ivezic, J. A. Munn, R. C. Nichol, N. Padmanabhan, A. R. Thakar, D. H. Weinberg, and D. York. Stellar masses and star formation histories for 10^5 galaxies from the Sloan Digital Sky Survey. *MNRAS*, 341:33–53, May 2003b. doi: 10.1046/j.1365-8711.2003.06291.x.

C. Kehrig, J. M. Vílchez, E. Pérez-Montero, J. Iglesias-Páramo, J. Brinchmann, D. Kunth, F. Durret, and F. M. Bayo. The Extended He II λ4686-emitting Region in IZw 18 Unveiled: Clues for Peculiar Ionizing Sources. *ApJ*, 801:L28, March 2015. doi: 10.1088/2041-8205/801/2/L28.

D. D. Kelson. Decoding the Star-Forming Main Sequence or: How I Learned to Stop Worrying and Love the Central Limit Theorem. *ArXiv e-prints*, June 2014.

J. V. Kepner, A. Babul, and D. N. Spergel. The Delayed Formation of Dwarf Galaxies. *ApJ*, 487:61, September 1997. doi: 10.1086/304602.

L. J. Kewley and M. A. Dopita. Using Strong Lines to Estimate Abundances in Extragalactic H II Regions and Starburst Galaxies. *ApJS*, 142:35–52, September 2002. doi: 10.1086/341326.

L. J. Kewley and S. L. Ellison. Metallicity Calibrations and the Mass-Metallicity Relation for Star-forming Galaxies. *ApJ*, 681:1183–1204, July 2008. doi: 10.1086/587500.

L. J. Kewley, M. A. Dopita, R. S. Sutherland, C. A. Heisler, and J. Trevena. Theoretical Modeling of Starburst Galaxies. *ApJ*, 556:121–140, July 2001. doi: 10.1086/321545.

L. J. Kewley, M. J. Geller, and E. J. Barton. Metallicity and Nuclear Star Formation in Nearby Galaxy Pairs: Evidence for Tidally Induced Gas Flows. *AJ*, 131:2004–2017, April 2006. doi: 10.1086/500295.

L. J. Kewley, M. A. Dopita, C. Leitherer, R. Davé, T. Yuan, M. Allen, B. Groves, and R. Sutherland. Theoretical Evolution of Optical Strong Lines across Cosmic Time. *ApJ*, 774:100, September 2013a. doi: 10.1088/0004-637X/774/2/100.

L. J. Kewley, C. Maier, K. Yabe, K. Ohta, M. Akiyama, M. A. Dopita, and T. Yuan. The Cosmic BPT Diagram: Confronting Theory with Observations. *ApJ*, 774:L10, September 2013b. doi: 10.1088/2041-8205/774/1/L10.

T. Kimm, R. S. Somerville, S. K. Yi, F. C. van den Bosch, S. Salim, F. Fontanot, P. Monaco, H. Mo, A. Pasquali, R. M. Rich, and X. Yang. The correlation of star formation quenching with internal galaxy properties and environment. *MNRAS*, 394:1131–1147, April 2009. doi: 10.1111/j.1365-2966.2009.14414.x.

A. L. Kinney, D. Calzetti, R. C. Bohlin, K. McQuade, T. Storchi-Bergmann, and H. R. Schmitt. Template Ultraviolet to Near-Infrared Spectra of Star-forming Galaxies and Their Application to K-Corrections. *ApJ*, 467:38, August 1996. doi: 10.1086/177583.

A. Klypin, A. V. Kravtsov, O. Valenzuela, and F. Prada. Where Are the Missing Galactic Satellites? *ApJ*, 522:82–92, September 1999. doi: 10.1086/307643.

A. Y. Kniazev, E. K. Grebel, L. Hao, M. A. Strauss, J. Brinkmann, and M. Fukugita. Discovery of Eight New Extremely Metal Poor Galaxies in the Sloan Digital Sky Survey. *ApJ*, 593:L73–L76, August 2003. doi: 10.1086/378259.

A. Y. Kniazev, S. A. Pustilnik, E. K. Grebel, H. Lee, and A. G. Pramskij. Strong Emission Line H II Galaxies in the Sloan Digital Sky Survey. I. Catalog of DR1 Objects with Oxygen Abundances from T_e Measurements. *ApJS*, 153:429–445, August 2004. doi: 10.1086/421519.

H. A. Kobulnicky and L. J. Kewley. Metallicities of 0.3<z<1.0 Galaxies in the GOODS-North Field. *ApJ*, 617:240–261, December 2004. doi: 10.1086/425299.

I. Kochiashvili, P. Møller, B. Milvang-Jensen, L. Christensen, J. P. U. Fynbo, W. Freudling, B. Clément, J.-G. Cuby, J. Zabl, and S. Zibetti. Emission line selected galaxies at $z=0.6-2$ in GOODS South: Stellar masses, SFRs, and large scale structure. *ArXiv e-prints*, April 2015.

A. M. Koekemoer, S. M. Faber, H. C. Ferguson, N. A. Grogin, D. D. Kocevski, D. C. Koo, K. Lai, J. M. Lotz, R. A. Lucas, E. J. McGrath, S. Ogaz, A. Rajan, A. G. Riess, S. A. Rodney, L. Strolger, S. Casertano, M. Castellano, T. Dahlen, M. Dickinson, T. Dolch, A. Fontana, M. Giavalisco, A. Grazian, Y. Guo, N. P. Hathi, K.-H. Huang, A. van der Wel, H.-J. Yan, V. Acquaviva, D. M. Alexander, O. Almaini, M. L. N. Ashby, M. Barden, E. F. Bell, F. Bournaud, T. M. Brown, K. I. Caputi, P. Cassata, P. J. Challis, R.-R. Chary, E. Cheung, M. Cirasuolo, C. J. Conselice, A. Roshan Cooray, D. J. Croton, E. Daddi, R. Davé, D. F. de Mello, L. de Ravel, A. Dekel, J. L. Donley, J. S. Dunlop, A. A. Dutton, D. Elbaz, G. G. Fazio, A. V. Filippenko, S. L. Finkelstein, C. Frazer, J. P. Gardner, P. M. Garnavich, E. Gawiser, R. Gruetzbauch, W. G. Hartley, B. Häussler, J. Herrington, P. F. Hopkins, J.-S. Huang, S. W. Jha, A. Johnson, J. S. Kartaltepe, A. A. Khostovan, R. P. Kirshner, C. Lani, K.-S. Lee, W. Li, P. Madau, P. J. McCarthy, D. H. McIntosh, R. J. McLure, C. McPartland, B. Mobasher, H. Moreira, A. Mortlock, L. A. Moustakas, M. Mozena, K. Nandra, J. A. Newman, J. L. Nielsen, S. Niemi, K. G. Noeske, C. J. Papovich, L. Pentericci, A. Pope, J. R. Primack, S. Ravindranath, N. A. Reddy, A. Renzini, H.-W. Rix, A. R. Robaina, D. J. Rosario, P. Rosati, S. Salimbeni, C. Scarlata, B. Siana, L. Simard, J. Smidt, D. Snyder, R. S. Somerville, H. Spinrad, A. N. Straughn, O. Telford, H. I. Teplitz, J. R. Trump, C. Vargas, C. Villforth, C. R. Wagner, P. Wandro, R. H. Wechsler, B. J. Weiner, T. Wiklind, V. Wild, G. Wilson, S. Wuyts, and M. S. Yun. CANDELS: The Cosmic Assembly Near-infrared Deep Extragalactic Legacy Survey – The Hubble

Space Telescope Observations, Imaging Data Products, and Mosaics. *ApJS*, 197:36, December 2011. doi: 10.1088/0067-0049/197/2/36.

M. Kriek, A. E. Shapley, N. A. Reddy, B. Siana, A. L. Coil, B. Mobasher, W. R. Freeman, L. de Groot, S. H. Price, R. Sanders, I. Shivaei, G. B. Brammer, I. G. Momcheva, R. E. Skelton, P. G. van Dokkum, K. E. Whitaker, J. Aird, M. Azadi, M. Kassis, J. S. Bullock, C. Conroy, R. Dave, D. Keres, and M. Krumholz. The MOSFIRE Deep Evolution Field (MOSDEF) Survey: Rest-Frame Optical Spectroscopy For ˜1500 H-Selected Galaxies at 1.37 < z < 3.8. *ArXiv e-prints*, December 2014.

R. G. Kron. Photometry of a complete sample of faint galaxies. *ApJS*, 43:305–325, June 1980. doi: 10.1086/190669.

P. Kroupa. On the variation of the initial mass function. *MNRAS*, 322:231–246, April 2001. doi: 10.1046/j.1365-8711.2001.04022.x.

D. Kunth and G. Östlin. The most metal-poor galaxies. *A&A Rev.*, 10:1–79, 2000. doi: 10.1007/s001590000005.

I. Labbé, J. Huang, M. Franx, G. Rudnick, P. Barmby, E. Daddi, P. G. van Dokkum, G. G. Fazio, N. M. F. Schreiber, A. F. M. Moorwood, H.-W. Rix, H. Röttgering, I. Trujillo, and P. van der Werf. IRAC Mid-Infrared Imaging of the Hubble Deep Field-South: Star Formation Histories and Stellar Masses of Red Galaxies at z>2. *ApJ*, 624:L81–L84, May 2005. doi: 10.1086/430700.

I. Labbe, P. Oesch, G. Illingworth, P. van Dokkum, M. Franx, V. Gonzalez, R. Bouwens, D. Magee, R. Smit, B. Holden, M. Stefanon, and M. Stiavelli. GREATS: GOODS Re-ionization Era wide-Area Treasury from Spitzer. Spitzer Proposal, December 2014.

V. G. Laidler, C. Papovich, N. A. Grogin, R. Idzi, M. Dickinson, H. C. Ferguson, B. Hilbert, K. Clubb, and S. Ravindranath. TFIT: A Photometry Package Using Prior Information for Mixed-Resolution Data Sets. *PASP*, 119:1325–1344, November 2007. doi: 10.1086/523898.

M. A. Lara-López, J. Cepa, A. Bongiovanni, A. M. Pérez García, A. Ederoclite, H. Castañeda, M. Fernández Lorenzo, M. Pović, and M. Sánchez-Portal. A fundamental plane for field star-forming galaxies. *A&A*, 521:L53, October 2010. doi: 10.1051/0004-6361/201014803.

M. A. Lara-López, A. M. Hopkins, A. R. López-Sánchez, S. Brough, M. Colless, J. Bland-Hawthorn, S. Driver, C. Foster, J. Liske, J. Loveday, A. S. G. Robotham, R. G. Sharp, O. Steele, and E. N. Taylor. Galaxy And Mass Assembly (GAMA): the connection between metals, specific SFR and H I gas in galaxies: the Z-SSFR relation. *MNRAS*, 433:L35–L39, June 2013. doi: 10.1093/mnrasl/slt054.

O. Le Fèvre, M. Saisse, D. Mancini, S. Brau-Nogue, O. Caputi, L. Castinel, S. D'Odorico, B. Garilli, M. Kissler-Patig, C. Lucuix, G. Mancini, A. Pauget, G. Sciarretta, M. Scodeggio, L. Tresse, and G. Vettolani. Commissioning and performances of the VLT-VIMOS instrument. In M. Iye and A. F. M. Moorwood, editors, *Instrument Design and Performance for Optical/Infrared Ground-based Telescopes*, volume 4841 of *Society of Photo-Optical Instrumentation Engineers (SPIE) Conference Series*, pages 1670–1681, March 2003. doi: 10.1117/12.460959.

O. Le Fèvre, G. Vettolani, B. Garilli, L. Tresse, D. Bottini, V. Le Brun, D. Maccagni, J. P. Picat, R. Scaramella, M. Scodeggio, A. Zanichelli, C. Adami, M. Arnaboldi, S. Arnouts, S. Bardelli, M. Bolzonella, A. Cappi, S. Charlot, P. Ciliegi, T. Contini, S. Foucaud, P. Franzetti, I. Gavignaud, L. Guzzo, O. Ilbert, A. Iovino, H. J. McCracken, B. Marano, C. Marinoni, G. Mathez, A. Mazure, B. Meneux, R. Merighi, S. Paltani, R. Pellò, A. Pollo, L. Pozzetti, M. Radovich, G. Zamorani, E. Zucca, M. Bondi, A. Bongiorno, G. Busarello, F. Lamareille, Y. Mellier, P. Merluzzi, V. Ripepi, and D. Rizzo. The VIMOS

VLT deep survey. First epoch VVDS-deep survey: 11 564 spectra with $17.5 \leq \mathrm{IAB} \leq 24$, and the redshift distribution over $0 \leq z \leq 5$. *A&A*, 439:845–862, September 2005. doi: 10.1051/0004-6361:20041960.

O. Le Fèvre, P. Cassata, O. Cucciati, B. Garilli, O. Ilbert, V. Le Brun, D. Maccagni, C. Moreau, M. Scodeggio, L. Tresse, G. Zamorani, C. Adami, S. Arnouts, S. Bardelli, M. Bolzonella, M. Bondi, A. Bongiorno, D. Bottini, A. Cappi, S. Charlot, P. Ciliegi, T. Contini, S. de la Torre, S. Foucaud, P. Franzetti, I. Gavignaud, L. Guzzo, A. Iovino, B. Lemaux, C. López-Sanjuan, H. J. McCracken, B. Marano, C. Marinoni, A. Mazure, Y. Mellier, R. Merighi, P. Merluzzi, S. Paltani, R. Pellò, A. Pollo, L. Pozzetti, R. Scaramella, L. Tasca, D. Vergani, G. Vettolani, A. Zanichelli, and E. Zucca. The VIMOS VLT Deep Survey final data release: a spectroscopic sample of 35 016 galaxies and AGN out to $z \sim 6.7$ selected with $17.5 \leq i_{AB} \leq 24.75$. *A&A*, 559:A14, November 2013. doi: 10.1051/0004-6361/201322179.

H. Lee, E. D. Skillman, J. M. Cannon, D. C. Jackson, R. D. Gehrz, E. F. Polomski, and C. E. Woodward. On Extending the Mass-Metallicity Relation of Galaxies by 2.5 Decades in Stellar Mass. *ApJ*, 647:970–983, August 2006. doi: 10.1086/505573.

J. C. Lee, J. J. Salzer, D. A. Law, and J. L. Rosenberg. Emission-Line Galaxy Surveys as Probes of the Spatial Distribution of Dwarf Galaxies. I. The University of Michigan Survey. *ApJ*, 536:606–622, June 2000. doi: 10.1086/308967.

J. C. Lee, J. J. Salzer, and J. Melbourne. Metal Abundances of KISS Galaxies. III. Nebular Abundances for Fourteen Galaxies and the Luminosity-Metallicity Relationship for H II Galaxies. *ApJ*, 616:752–767, December 2004. doi: 10.1086/425156.

J. C. Lee, R. C. Kennicutt, Jr., S. J. J. G. Funes, S. Sakai, and S. Akiyama. Dwarf Galaxy Starburst Statistics in the Local Volume. *ApJ*, 692:1305, February 2009. doi: 10.1088/0004-637X/692/2/1305.

F. Legrand, D. Kunth, J.-R. Roy, J. M. Mas-Hesse, and J. R. Walsh. A continuous low star formation rate in IZw 18? *A&A*, 355:891–899, March 2000.

B. D. Lehmer, W. N. Brandt, D. M. Alexander, F. E. Bauer, D. P. Schneider, P. Tozzi, J. Bergeron, G. P. Garmire, R. Giacconi, R. Gilli, G. Hasinger, A. E. Hornschemeier, A. M. Koekemoer, V. Mainieri, T. Miyaji, M. Nonino, P. Rosati, J. D. Silverman, G. Szokoly, and C. Vignali. The Extended Chandra Deep Field-South Survey: Chandra Point-Source Catalogs. *ApJS*, 161:21–40, November 2005. doi: 10.1086/444590.

S. N. Leitner. On the Last 10 Billion Years of Stellar Mass Growth in Star-forming Galaxies. *ApJ*, 745:149, February 2012. doi: 10.1088/0004-637X/745/2/149.

J. Lequeux, M. Peimbert, J. F. Rayo, A. Serrano, and S. Torres-Peimbert. Chemical composition and evolution of irregular and blue compact galaxies. *A&A*, 80:155–166, December 1979.

S. J. Lilly, C. M. Carollo, and A. N. Stockton. The Metallicities of Star-forming Galaxies at Intermediate Redshifts $0.47 < z < 0.92$. *ApJ*, 597:730–750, November 2003. doi: 10.1086/378389.

S. J. Lilly, O. Le Fèvre, A. Renzini, G. Zamorani, M. Scodeggio, T. Contini, C. M. Carollo, G. Hasinger, J.-P. Kneib, A. Iovino, V. Le Brun, C. Maier, V. Mainieri, M. Mignoli, J. Silverman, L. A. M. Tasca, M. Bolzonella, A. Bongiorno, D. Bottini, P. Capak, K. Caputi, A. Cimatti, O. Cucciati, E. Daddi, R. Feldmann, P. Franzetti, B. Garilli, L. Guzzo, O. Ilbert, P. Kampczyk, K. Kovac, F. Lamareille, A. Leauthaud, J.-F. L. Borgne, H. J. McCracken, C. Marinoni, R. Pello, E. Ricciardelli, C. Scarlata, D. Vergani, D. B. Sanders, E. Schinnerer, N. Scoville, Y. Taniguchi, S. Arnouts, H. Aussel, S. Bardelli, M. Brusa, A. Cappi, P. Ciliegi, A. Finoguenov, S. Foucaud, A. Franceschini, C. Halliday, C. Impey, C. Knobel, A. Koekemoer, J. Kurk, D. Maccagni, S. Maddox, B. Marano, G. Marconi, B. Meneux, B. Mobasher, C. Moreau, J. A.

Peacock, C. Porciani, L. Pozzetti, R. Scaramella, D. Schiminovich, P. Shopbell, I. Smail, D. Thompson, L. Tresse, G. Vettolani, A. Zanichelli, and E. Zucca. zCOSMOS: A Large VLT/VIMOS Redshift Survey Covering 0 < z < 3 in the COSMOS Field. *ApJS*, 172:70–85, September 2007. doi: 10.1086/516589.

S. J. Lilly, C. M. Carollo, A. Pipino, A. Renzini, and Y. Peng. Gas Regulation of Galaxies: The Evolution of the Cosmic Specific Star Formation Rate, the Metallicity-Mass-Star-formation Rate Relation, and the Stellar Content of Halos. *ApJ*, 772:119, August 2013. doi: 10.1088/0004-637X/772/2/119.

C. J. Lintott, K. Schawinski, A. Slosar, K. Land, S. Bamford, D. Thomas, M. J. Raddick, R. C. Nichol, A. Szalay, D. Andreescu, P. Murray, and J. Vandenberg. Galaxy Zoo: morphologies derived from visual inspection of galaxies from the Sloan Digital Sky Survey. *MNRAS*, 389:1179–1189, September 2008. doi: 10.1111/j.1365-2966.2008.13689.x.

Á. R. López-Sánchez and C. Esteban. Massive star formation in Wolf-Rayet galaxies. IV. Colours, chemical-composition analysis and metallicity-luminosity relations. *A&A*, 517:A85, July 2010. doi: 10.1051/0004-6361/201014156.

Á. R. López-Sánchez, M. A. Dopita, L. J. Kewley, H. J. Zahid, D. C. Nicholls, and J. Scharwächter. Eliminating error in the chemical abundance scale for extragalactic H II regions. *MNRAS*, 426:2630–2651, November 2012. doi: 10.1111/j.1365-2966.2012.21145.x.

C. Ly, M. A. Malkan, T. Nagao, N. Kashikawa, K. Shimasaku, and M. Hayashi. "Direct" Gas-phase Metallicities, Stellar Properties, and Local Environments of Emission-line Galaxies at Redshifts below 0.90. *ApJ*, 780:122, January 2014. doi: 10.1088/0004-637X/780/2/122.

M.-M. Mac Low and A. Ferrara. Starburst-driven Mass Loss from Dwarf Galaxies: Efficiency and Metal Ejection. *ApJ*, 513:142–155, March 1999. doi: 10.1086/306832.

P. Madau and M. Dickinson. Cosmic Star-Formation History. *ARA&A*, 52:415–486, August 2014. doi: 10.1146/annurev-astro-081811-125615.

P. Madau, D. R. Weisz, and C. Conroy. Reversal of Fortune: Increased Star Formation Efficiencies in the Early Histories of Dwarf Galaxies? *ApJ*, 790:L17, August 2014. doi: 10.1088/2041-8205/790/2/L17.

G. E. Magdis, D. Rigopoulou, J.-S. Huang, and G. G. Fazio. On the stellar masses of IRAC detected Lyman Break Galaxies at z ˜ 3. *MNRAS*, 401:1521–1531, January 2010. doi: 10.1111/j.1365-2966.2009.15779.x.

B. Magnelli, D. Elbaz, R. R. Chary, M. Dickinson, D. Le Borgne, D. T. Frayer, and C. N. A. Willmer. Evolution of the dusty infrared luminosity function from z = 0 to z = 2.3 using observations from Spitzer. *A&A*, 528:A35, April 2011. doi: 10.1051/0004-6361/200913941.

B. Magnelli, P. Popesso, S. Berta, F. Pozzi, D. Elbaz, D. Lutz, M. Dickinson, B. Altieri, P. Andreani, H. Aussel, M. Béthermin, A. Bongiovanni, J. Cepa, V. Charmandaris, R.-R. Chary, A. Cimatti, E. Daddi, N. M. Förster Schreiber, R. Genzel, C. Gruppioni, M. Harwit, H. S. Hwang, R. J. Ivison, G. Magdis, R. Maiolino, E. Murphy, R. Nordon, M. Pannella, A. Pérez García, A. Poglitsch, D. Rosario, M. Sanchez-Portal, P. Santini, D. Scott, E. Sturm, L. J. Tacconi, and I. Valtchanov. The deepest Herschel-PACS far-infrared survey: number counts and infrared luminosity functions from combined PEP/GOODS-H observations. *A&A*, 553:A132, May 2013. doi: 10.1051/0004-6361/201321371.

S. Mahajan, M. J. Drinkwater, S. Driver, L. S. Kelvin, A. M. Hopkins, I. Baldry, S. Phillipps, J. Bland-Hawthorn, S. Brough, J. Loveday, S. J. Penny, and A. S. G. Robotham. Galaxy And Mass Assembly (GAMA): the unimodal nature of the dwarf galaxy population. *MNRAS*, 446:2967–2984, January 2015. doi: 10.1093/mnras/stu2009.

C. Maier, S. J. Lilly, C. M. Carollo, K. Meisenheimer, H. Hippelein, and A. Stockton. Oxygen Gas Abundances at z˜1.4: Implications for the Chemical Evolution History of Galaxies. *ApJ*, 639:858–867, March 2006. doi: 10.1086/499518.

C. Maier, B. L. Ziegler, S. J. Lilly, T. Contini, E. Pérez-Montero, F. Lamareille, M. Bolzonella, and E. Le Floc'h. Mass-metallicity relation of zCOSMOS galaxies at z 0.7, its dependence on star formation rate, and the existence of massive low-metallicity galaxies. *A&A*, 577:A14, May 2015. doi: 10.1051/0004-6361/201425224.

R. Maiolino, T. Nagao, A. Grazian, F. Cocchia, A. Marconi, F. Mannucci, A. Cimatti, A. Pipino, S. Ballero, F. Calura, C. Chiappini, A. Fontana, G. L. Granato, F. Matteucci, G. Pastorini, L. Pentericci, G. Risaliti, M. Salvati, and L. Silva. AMAZE. I. The evolution of the mass-metallicity relation at z > 3. *A&A*, 488:463–479, September 2008. doi: 10.1051/0004-6361:200809678.

G. A. Mamon, D. Tweed, T. X. Thuan, and A. Cattaneo. *Predicting the Frequencies of Young and of Tiny Galaxies*, page 39. 2012. doi: 10.1007/978-3-642-22018-0_3.

F. Mannucci, G. Cresci, R. Maiolino, A. Marconi, G. Pastorini, L. Pozzetti, A. Gnerucci, G. Risaliti, R. Schneider, M. Lehnert, and M. Salvati. LSD: Lyman-break galaxies Stellar populations and Dynamics - I. Mass, metallicity and gas at z ˜ 3.1. *MNRAS*, 398:1915–1931, October 2009. doi: 10.1111/j.1365-2966.2009.15185.x.

F. Mannucci, G. Cresci, R. Maiolino, A. Marconi, and A. Gnerucci. A fundamental relation between mass, star formation rate and metallicity in local and high-redshift galaxies. *MNRAS*, 408:2115–2127, November 2010. doi: 10.1111/j.1365-2966.2010.17291.x.

F. Mannucci, R. Salvaterra, and M. A. Campisi. The metallicity of the long GRB hosts and the fundamental metallicity relation of low-mass galaxies. *MNRAS*, 414:1263–1268, June 2011. doi: 10.1111/j.1365-2966.2011.18459.x.

M. L. Martín-Manjón, M. Mollá, A. I. Díaz, and R. Terlevich. Evolution of star-forming dwarf galaxies: characterizing the star formation scenarios. *MNRAS*, 420:1294–1308, February 2012. doi: 10.1111/j.1365-2966.2011.20122.x.

M. V. Maseda, A. van der Wel, E. da Cunha, H.-W. Rix, C. Pacifici, I. Momcheva, G. B. Brammer, M. Franx, P. van Dokkum, E. F. Bell, M. Fumagalli, N. A. Grogin, D. D. Kocevski, A. M. Koekemoer, B. F. Lundgren, D. Marchesini, E. J. Nelson, S. G. Patel, R. E. Skelton, A. N. Straughn, J. R. Trump, B. J. Weiner, K. E. Whitaker, and S. Wuyts. Confirmation of Small Dynamical and Stellar Masses for Extreme Emission Line Galaxies at z ˜ 2. *ApJ*, 778:L22, November 2013. doi: 10.1088/2041-8205/778/1/L22.

M. L. Mateo. Dwarf Galaxies of the Local Group. *ARA&A*, 36:435–506, 1998. doi: 10.1146/annurev.astro.36.1.435.

L. Mayer, F. Governato, M. Colpi, B. Moore, T. Quinn, J. Wadsley, J. Stadel, and G. Lake. Tidal Stirring and the Origin of Dwarf Spheroidals in the Local Group. *ApJ*, 547:L123–L127, February 2001a. doi: 10.1086/318898.

L. Mayer, F. Governato, M. Colpi, B. Moore, T. Quinn, J. Wadsley, J. Stadel, and G. Lake. The Metamorphosis of Tidally Stirred Dwarf Galaxies. *ApJ*, 559:754–784, October 2001b. doi: 10.1086/322356.

L. Mayer, C. Mastropietro, J. Wadsley, J. Stadel, and B. Moore. Simultaneous ram pressure and tidal stripping; how dwarf spheroidals lost their gas. *MNRAS*, 369:1021–1038, July 2006. doi: 10.1111/j.1365-2966.2006.10403.x.

S. S. McGaugh. H II region abundances - Model oxygen line ratios. *ApJ*, 380:140–150, October 1991. doi: 10.1086/170569.

G. E. Miller and J. M. Scalo. The initial mass function and stellar birthrate in the solar neighborhood. *ApJS*, 41:513–547, November 1979. doi: 10.1086/190629.

M. Moles, N. Benítez, J. A. L. Aguerri, E. J. Alfaro, T. Broadhurst, J. Cabrera-Caño, F. J. Castander, J. Cepa, M. Cerviño, D. Cristóbal-Hornillos, A. Fernández-Soto, R. M. González Delgado, L. Infante, I. Márquez, V. J. Martínez, J. Masegosa, A. del Olmo, J. Perea, F. Prada, J. M. Quintana, and S. F. Sánchez. The Alhambra Survey: a Large Area Multimedium-Band Optical and Near-Infrared Photometric Survey. *AJ*, 136:1325–1339, September 2008. doi: 10.1088/0004-6256/136/3/1325.

A. B. Morales-Luis, J. Sánchez Almeida, J. A. L. Aguerri, and C. Muñoz-Tuñón. Systematic Search for Extremely Metal-poor Galaxies in the Sloan Digital Sky Survey. *ApJ*, 743:77, December 2011. doi: 10.1088/0004-637X/743/1/77.

M. Mouhcine, B. K. Gibson, A. Renda, and D. Kawata. Simulating the mass-metallicity relation from z 1. *A&A*, 486:711–720, August 2008. doi: 10.1051/0004-6361:20078190.

J. Moustakas, D. Zaritsky, M. Brown, R. Cool, A. Dey, D. J. Eisenstein, A. H. Gonzalez, B. Jannuzi, C. Jones, C. S. Kochanek, S. S. Murray, and V. Wild. Evolution of the Stellar Mass-Metallicity Relation Since z=0.75. *ArXiv e-prints*, December 2011.

J. Moustakas, A. L. Coil, J. Aird, M. R. Blanton, R. J. Cool, D. J. Eisenstein, A. J. Mendez, K. C. Wong, G. Zhu, and S. Arnouts. PRIMUS: Constraints on Star Formation Quenching and Galaxy Merging, and the Evolution of the Stellar Mass Function from z = 0-1. *ApJ*, 767:50, April 2013. doi: 10.1088/0004-637X/767/1/50.

E. Moy, P. Barmby, D. Rigopoulou, J.-S. Huang, S. P. Willner, and G. G. Fazio. H-band observations of the Chandra Deep Field South. *A&A*, 403:493–499, May 2003. doi: 10.1051/0004-6361:20030245.

K. Nakajima, M. Ouchi, K. Shimasaku, T. Hashimoto, Y. Ono, and J. C. Lee. First Spectroscopic Evidence for High Ionization State and Low Oxygen Abundance in Lyα Emitters. *ApJ*, 769:3, May 2013. doi: 10.1088/0004-637X/769/1/3.

K. G. Noeske, B. J. Weiner, S. M. Faber, C. Papovich, D. C. Koo, R. S. Somerville, K. Bundy, C. J. Conselice, J. A. Newman, D. Schiminovich, E. Le Floc'h, A. L. Coil, G. H. Rieke, J. M. Lotz, J. R. Primack, P. Barmby, M. C. Cooper, M. Davis, R. S. Ellis, G. G. Fazio, P. Guhathakurta, J. Huang, S. A. Kassin, D. C. Martin, A. C. Phillips, R. M. Rich, T. A. Small, C. N. A. Willmer, and G. Wilson. Star Formation in AEGIS Field Galaxies since z=1.1: The Dominance of Gradually Declining Star Formation, and the Main Sequence of Star-forming Galaxies. *ApJ*, 660:L43–L46, May 2007. doi: 10.1086/517926.

M. Nonino, M. Dickinson, P. Rosati, A. Grazian, N. Reddy, S. Cristiani, M. Giavalisco, H. Kuntschner, E. Vanzella, E. Daddi, R. A. E. Fosbury, and C. Cesarsky. Deep U Band and R Imaging of Goods-South: Observations, Data Reduction and First Results. *ApJS*, 183:244–260, August 2009. doi: 10.1088/0067-0049/183/2/244.

J. B. Oke. Absolute Spectral Energy Distributions for White Dwarfs. *ApJS*, 27:21, February 1974. doi: 10.1086/190287.

D. E. Osterbrock. *Astrophysics of gaseous nebulae and active galactic nuclei*. 1989.

G. Östlin. Hubble Space Telescope/NICMOS Observations of I ZW 18: A Population of Old Asymptotic Giant Branch Stars Revealed. *ApJ*, 535:L99–L102, June 2000. doi: 10.1086/312715.

C. Pacifici, S. Charlot, J. Blaizot, and J. Brinchmann. Relative merits of different types of rest-frame optical observations to constrain galaxy physical parameters. *MNRAS*, 421:2002–2024, April 2012. doi: 10.1111/j.1365-2966.2012.20431.x.

C. Pacifici, S. A. Kassin, B. Weiner, S. Charlot, and J. P. Gardner. The Rise and Fall of the Star Formation Histories of Blue Galaxies at Redshifts 0.2 < z < 1.4. *ApJ*, 762:L15, January 2013. doi: 10.1088/2041-8205/762/1/L15.

C. Pacifici, E. da Cunha, S. Charlot, H.-W. Rix, M. Fumagalli, A. v. d. Wel, M. Franx, M. V. Maseda, P. G. van Dokkum, G. B. Brammer, I. Momcheva, R. E. Skelton, K. Whitaker, J. Leja, B. Lundgren, S. A. Kassin, and S. K. Yi. On the importance of using appropriate spectral models to derive physical properties of galaxies at 0.7 < z < 2.8. *MNRAS*, 447:786–805, February 2015. doi: 10.1093/mnras/stu2447.

B. E. J. Pagel, M. G. Edmunds, D. E. Blackwell, M. S. Chun, and G. Smith. On the composition of H II regions in southern galaxies. I - NGC 300 and 1365. *MNRAS*, 189:95–113, October 1979.

P. Papaderos and G. Östlin. I Zw 18 as morphological paradigm for rapidly assembling high-z galaxies. *A&A*, 537:A126, January 2012. doi: 10.1051/0004-6361/201117551.

P. Papaderos, H.-H. Loose, T. X. Thuan, and K. J. Fricke. Optical structure and star formation in blue compact dwarf galaxies. I. Observations and profile decomposition. *A&AS*, 120:207–228, December 1996.

P. Papaderos, Y. I. Izotov, T. X. Thuan, K. G. Noeske, K. J. Fricke, N. G. Guseva, and R. F. Green. The blue compact dwarf galaxy I Zw 18: A comparative study of its low-surface-brightness component. *A&A*, 393:461–483, October 2002. doi: 10.1051/0004-6361:20021023.

P. Papaderos, N. G. Guseva, Y. I. Izotov, and K. J. Fricke. Extremely metal-poor star-forming galaxies. New detections and general morphological and photometric properties. *A&A*, 491:113–129, November 2008. doi: 10.1051/0004-6361:200810028.

C. Papovich, M. Dickinson, and H. C. Ferguson. The Stellar Populations and Evolution of Lyman Break Galaxies. *ApJ*, 559:620–653, October 2001. doi: 10.1086/322412.

F. Patat, S. Moehler, K. O'Brien, E. Pompei, T. Bensby, G. Carraro, A. de Ugarte Postigo, A. Fox, I. Gavignaud, G. James, H. Korhonen, C. Ledoux, S. Randall, H. Sana, J. Smoker, S. Stefl, and T. Szeifert. Optical atmospheric extinction over Cerro Paranal. *A&A*, 527:A91, March 2011. doi: 10.1051/0004-6361/201015537.

S. G. Patel, B. P. Holden, D. D. Kelson, M. Franx, A. van der Wel, and G. D. Illingworth. The UVJ Selection of Quiescent and Star-forming Galaxies: Separating Early- and Late-type Galaxies and Isolating Edge-on Spirals. *ApJ*, 748:L27, April 2012. doi: 10.1088/2041-8205/748/2/L27.

P. J. E. Peebles. Large-scale background temperature and mass fluctuations due to scale-invariant primeval perturbations. *ApJ*, 263:L1–L5, December 1982. doi: 10.1086/183911.

C. Y. Peng, L. C. Ho, C. D. Impey, and H.-W. Rix. Detailed Structural Decomposition of Galaxy Images. *AJ*, 124:266–293, July 2002. doi: 10.1086/340952.

P. G. Pérez-González, G. H. Rieke, E. Egami, A. Alonso-Herrero, H. Dole, C. Papovich, M. Blaylock, J. Jones, M. Rieke, J. Rigby, P. Barmby, G. G. Fazio, J. Huang, and C. Martin. Spitzer View on the Evolution of Star-forming Galaxies from z = 0 to z ˜ 3. *ApJ*, 630:82–107, September 2005. doi: 10.1086/431894.

P. G. Pérez-González, G. H. Rieke, V. Villar, G. Barro, M. Blaylock, E. Egami, J. Gallego, A. Gil de Paz, S. Pascual, J. Zamorano, and J. L. Donley. The Stellar Mass Assembly of Galaxies from z = 0 to z = 4: Analysis of a Sample Selected in the Rest-Frame Near-Infrared with Spitzer. *ApJ*, 675:234–261, March 2008. doi: 10.1086/523690.

E. Pérez-Montero, T. Contini, F. Lamareille, C. Maier, C. M. Carollo, J.-P. Kneib, O. Le Fèvre, S. Lilly, V. Mainieri, A. Renzini, M. Scodeggio, G. Zamorani, S. Bardelli, M. Bolzonella, A. Bongiorno, K. Caputi, O. Cucciati, S. de la Torre, L. de Ravel, P. Franzetti, B. Garilli, A. Iovino, P. Kampczyk, C. Knobel, K. Kovač, J.-F. Le Borgne, V. Le Brun, M. Mignoli, R. Pellò, Y. Peng, V. Presotto, E. Ricciardelli, J. D. Silverman, M. Tanaka, L. A. M. Tasca, L. Tresse, D. Vergani, and E. Zucca. The cosmic evolution of oxygen and nitrogen abundances in star-forming galaxies over the past 10 Gyr. *A&A*, 549:A25, January 2013. doi: 10.1051/0004-6361/201220070.

M. Pettini and B. E. J. Pagel. [OIII]/[NII] as an abundance indicator at high redshift. *MNRAS*, 348:L59–L63, March 2004. doi: 10.1111/j.1365-2966.2004.07591.x.

M. Pettini, A. E. Shapley, C. C. Steidel, J.-G. Cuby, M. Dickinson, A. F. M. Moorwood, K. L. Adelberger, and M. Giavalisco. The Rest-Frame Optical Spectra of Lyman Break Galaxies: Star Formation, Extinction, Abundances, and Kinematics. *ApJ*, 554:981–1000, June 2001. doi: 10.1086/321403.

A. C. Phillips, R. Guzmán, J. Gallego, D. C. Koo, J. D. Lowenthal, N. P. Vogt, S. M. Faber, and G. D. Illingworth. The Nature of Compact Galaxies in the Hubble Deep Field. I. Global Properties1,. *ApJ*, 489: 543–558, November 1997.

L. S. Pilyugin. On the oxygen abundance determination in HII regions. High-metallicity regions. *A&A*, 369: 594–604, April 2001. doi: 10.1051/0004-6361:20010079.

L. S. Pilyugin and T. X. Thuan. Oxygen Abundance Determination in H II Regions: The Strong Line Intensities-Abundance Calibration Revisited. *ApJ*, 631:231–243, September 2005. doi: 10.1086/432408.

S. A. Pustilnik and J.-M. Martin. H I study of extremely metal-deficient dwarf galaxies. I. The Nançay radio telescope observations of twenty-two objects. *A&A*, 464:859–869, March 2007. doi: 10.1051/0004-6361: 20066137.

S. A. Pustil'nik, V. A. Lipovetsky, Y. I. Izotov, E. Brinks, T. X. Thuan, A. Y. Knyazev, S. I. Neizvestnyi, and A. V. Ugryumov. Detection of a second optical component in the H I cloud of the young dwarf galaxy SBS 0335-052: New observations with the 6-m telescope. *Astronomy Letters*, 23:308–311, May 1997.

W. T. Reach, S. T. Megeath, M. Cohen, J. Hora, S. Carey, J. Surace, S. P. Willner, P. Barmby, G. Wilson, W. Glaccum, P. Lowrance, M. Marengo, and G. G. Fazio. Absolute Calibration of the Infrared Array Camera on the Spitzer Space Telescope. *PASP*, 117:978–990, September 2005. doi: 10.1086/432670.

N. A. Reddy and C. C. Steidel. A Steep Faint-End Slope of the UV Luminosity Function at z ˜ 2-3: Implications for the Global Stellar Mass Density and Star Formation in Low-Mass Halos. *ApJ*, 692: 778–803, February 2009. doi: 10.1088/0004-637X/692/1/778.

A. Rémy-Ruyer, S. C. Madden, F. Galliano, M. Galametz, T. T. Takeuchi, R. S. Asano, S. Zhukovska, V. Lebouteiller, D. Cormier, A. Jones, M. Bocchio, M. Baes, G. J. Bendo, M. Boquien, A. Boselli, I. DeLooze, V. Doublier-Pritchard, T. Hughes, O. Ł. Karczewski, and L. Spinoglio. Gas-to-dust mass ratios in local galaxies over a 2 dex metallicity range. *A&A*, 563:A31, March 2014. doi: 10.1051/ 0004-6361/201322803.

A. Renzini and Y.-j. Peng. An Objective Definition for the Main Sequence of Star-forming Galaxies. *ApJ*, 801:L29, March 2015. doi: 10.1088/2041-8205/801/2/L29.

H.-W. Rix, M. Barden, S. V. W. Beckwith, E. F. Bell, A. Borch, J. A. R. Caldwell, B. Häussler, K. Jahnke, S. Jogee, D. H. McIntosh, K. Meisenheimer, C. Y. Peng, S. F. Sanchez, R. S. Somerville, L. Wisotzki, and C. Wolf. GEMS: Galaxy Evolution from Morphologies and SEDs. *ApJS*, 152:163–173, June 2004. doi: 10.1086/420885.

M. S. Roberts and M. P. Haynes. Physical Parameters along the Hubble Sequence. *ARA&A*, 32:115–152, 1994. doi: 10.1146/annurev.aa.32.090194.000555.

A. S. G. Robotham and S. P. Driver. The GALEX-SDSS NUV and FUV flux density and local star formation rate. *MNRAS*, 413:2570–2582, June 2011. doi: 10.1111/j.1365-2966.2011.18327.x.

G. Rodighiero, E. Daddi, I. Baronchelli, A. Cimatti, A. Renzini, H. Aussel, P. Popesso, D. Lutz, P. Andreani, S. Berta, A. Cava, D. Elbaz, A. Feltre, A. Fontana, N. M. Förster Schreiber, A. Franceschini, R. Genzel, A. Grazian, C. Gruppioni, O. Ilbert, E. Le Floch, G. Magdis, M. Magliocchetti, B. Magnelli, R. Maiolino, H. McCracken, R. Nordon, A. Poglitsch, P. Santini, F. Pozzi, L. Riguccini, L. J. Tacconi, S. Wuyts, and G. Zamorani. The Lesser Role of Starbursts in Star Formation at z = 2. *ApJ*, 739:L40, October 2011. doi: 10.1088/2041-8205/739/2/L40.

L. Rodríguez-Muñoz, J. Gallego, C. Pacifici, L. Tresse, S. Charlot, A. Gil de Paz, G. Barro, and V. Villar. Recent Stellar Mass Assembly of Low-mass Star-forming Galaxies at Redshifts $0.3 < z < 0.9$. *ApJ*, 799: 36, January 2015. doi: 10.1088/0004-637X/799/1/36.

S. Salim, R. M. Rich, S. Charlot, J. Brinchmann, B. D. Johnson, D. Schiminovich, M. Seibert, R. Mallery, T. M. Heckman, K. Forster, P. G. Friedman, D. C. Martin, P. Morrissey, S. G. Neff, T. Small, T. K. Wyder, L. Bianchi, J. Donas, Y.-W. Lee, B. F. Madore, B. Milliard, A. S. Szalay, B. Y. Welsh, and S. K. Yi. UV Star Formation Rates in the Local Universe. *ApJS*, 173:267–292, December 2007. doi: 10.1086/519218.

E. E. Salpeter. The Luminosity Function and Stellar Evolution. *ApJ*, 121:161, January 1955. doi: 10.1086/145971.

J. Sánchez Almeida, C. Muñoz-Tuñón, R. Amorín, J. A. Aguerri, R. Sánchez-Janssen, and G. Tenorio-Tagle. Search for Blue Compact Dwarf Galaxies During Quiescence. *ApJ*, 685:194–210, September 2008. doi: 10.1086/590380.

A. Sandage and B. Binggeli. Studies of the Virgo cluster. III - A classification system and an illustrated atlas of Virgo cluster dwarf galaxies. *AJ*, 89:919–931, July 1984. doi: 10.1086/113588.

D. B. Sanders, J. M. Mazzarella, D.-C. Kim, J. A. Surace, and B. T. Soifer. The IRAS Revised Bright Galaxy Sample. *AJ*, 126:1607–1664, October 2003. doi: 10.1086/376841.

W. L. W. Sargent and L. Searle. Isolated Extragalactic H II Regions. *ApJ*, 162:L155, December 1970. doi: 10.1086/180644.

S. Savaglio, K. Glazebrook, D. Le Borgne, S. Juneau, R. G. Abraham, H.-W. Chen, D. Crampton, P. J. McCarthy, R. G. Carlberg, R. O. Marzke, K. Roth, I. Jørgensen, and R. Murowinski. The Gemini Deep Deep Survey. VII. The Redshift Evolution of the Mass-Metallicity Relation. *ApJ*, 635:260–279, December 2005. doi: 10.1086/497331.

M. Sawicki and H. K. C. Yee. Optical-Infrared Spectral Energy Distributions of $Z > 2$ Lyman Break Galaxies. *AJ*, 115:1329–1339, April 1998. doi: 10.1086/300291.

M. A. Schenker, B. E. Robertson, R. S. Ellis, Y. Ono, R. J. McLure, J. S. Dunlop, A. Koekemoer, R. A. A. Bowler, M. Ouchi, E. Curtis-Lake, A. B. Rogers, E. Schneider, S. Charlot, D. P. Stark, S. R. Furlanetto, and M. Cirasuolo. The UV Luminosity Function of Star-forming Galaxies via Dropout Selection at Redshifts z ˜ 7 and 8 from the 2012 Ultra Deep Field Campaign. *ApJ*, 768:196, May 2013. doi: 10.1088/0004-637X/768/2/196.

D. Schiminovich, O. Ilbert, S. Arnouts, B. Milliard, L. Tresse, O. Le Fèvre, M. Treyer, T. K. Wyder, T. Budavári, E. Zucca, G. Zamorani, D. C. Martin, C. Adami, M. Arnaboldi, S. Bardelli, T. Barlow, L. Bianchi, M. Bolzonella, D. Bottini, Y.-I. Byun, A. Cappi, T. Contini, S. Charlot, J. Donas, K. Forster, S. Foucaud, P. Franzetti, P. G. Friedman, B. Garilli, I. Gavignaud, L. Guzzo, T. M. Heckman, C. Hoopes, A. Iovino, P. Jelinsky, V. Le Brun, Y.-W. Lee, D. Maccagni, B. F. Madore, R. Malina, B. Marano, C. Marinoni, H. J. McCracken, A. Mazure, B. Meneux, P. Morrissey, S. Neff, S. Paltani, R. Pellò, J. P. Picat, A. Pollo, L. Pozzetti, M. Radovich, R. M. Rich, R. Scaramella, M. Scodeggio, M. Seibert, O. Siegmund, T. Small, A. S. Szalay, G. Vettolani, B. Welsh, C. K. Xu, and A. Zanichelli. The GALEX-VVDS Measurement of the Evolution of the Far-Ultraviolet Luminosity Density and the Cosmic Star Formation Rate. *ApJ*, 619: L47–L50, January 2005. doi: 10.1086/427077.

M. Scodeggio, P. Franzetti, B. Garilli, A. Zanichelli, S. Paltani, D. Maccagni, D. Bottini, V. Le Brun, T. Contini, R. Scaramella, C. Adami, S. Bardelli, E. Zucca, L. Tresse, O. Ilbert, S. Foucaud, A. Iovino, R. Merighi, G. Zamorani, I. Gavignaud, D. Rizzo, H. J. McCracken, O. Le Fèvre, J. P. Picat, G. Vettolani, M. Arnaboldi, S. Arnouts, M. Bolzonella, A. Cappi, S. Charlot, P. Ciliegi, L. Guzzo, B. Marano, C. Marinoni, G. Mathez, A. Mazure, B. Meneux, R. Pellò, A. Pollo, L. Pozzetti, and M. Radovich. The VVDS Data-Reduction Pipeline: Introducing VIPGI, the VIMOS Interactive Pipeline and Graphical Interface. *PASP*, 117:1284–1295, November 2005. doi: 10.1086/496937.

N. Scoville, H. Aussel, M. Brusa, P. Capak, C. M. Carollo, M. Elvis, M. Giavalisco, L. Guzzo, G. Hasinger, C. Impey, J.-P. Kneib, O. LeFevre, S. J. Lilly, B. Mobasher, A. Renzini, R. M. Rich, D. B. Sanders, E. Schinnerer, D. Schminovich, P. Shopbell, Y. Taniguchi, and N. D. Tyson. The Cosmic Evolution Survey (COSMOS): Overview. *ApJS*, 172:1–8, September 2007. doi: 10.1086/516585.

L. Searle and W. L. W. Sargent. Inferences from the Composition of Two Dwarf Blue Galaxies. *ApJ*, 173: 25, April 1972. doi: 10.1086/151398.

J. L. Sersic. *Atlas de galaxias australes*. 1968.

R. Sharples, R. Bender, A. Agudo Berbel, R. Bennett, N. Bezawada, N. Bouché, D. Bramall, M. Casali, M. Cirasuolo, P. Clark, M. Cliffe, R. Davies, R. Davies, N. Drory, M. Dubbeldam, A. Fairley, G. Finger, R. Genzel, R. Haefner, A. Hess, P. Jeffers, I. Lewis, D. Montgomery, J. Murray, B. Muschielok, N. Förster Schreiber, J. Pirard, S. Ramsey-Howat, P. Rees, J. Richter, D. Robertson, I. Robson, S. Rolt, R. Saglia, J. Schlichter, M. Tecza, S. Todd, M. Wegner, and E. Wiezorrek. Recent Progress on the KMOS Multi-object Integral Field Spectrometer. *The Messenger*, 139:24–27, March 2010.

S. Shen, P. Madau, J. Guedes, L. Mayer, J. X. Prochaska, and J. Wadsley. The Circumgalactic Medium of Massive Galaxies at z ˜ 3: A Test for Stellar Feedback, Galactic Outflows, and Cold Streams. *ApJ*, 765: 89, March 2013. doi: 10.1088/0004-637X/765/2/89.

Y. Shi, L. Armus, G. Helou, S. Stierwalt, Y. Gao, J. Wang, Z.-Y. Zhang, and Q. Gu. Inefficient star formation in extremely metal poor galaxies. *Nature*, 514:335–338, October 2014. doi: 10.1038/nature13820.

M. Sirianni, M. J. Jee, N. Benítez, J. P. Blakeslee, A. R. Martel, G. Meurer, M. Clampin, G. De Marchi, H. C. Ford, R. Gilliland, G. F. Hartig, G. D. Illingworth, J. Mack, and W. J. McCann. The Photometric Performance and Calibration of the Hubble Space Telescope Advanced Camera for Surveys. *PASP*, 117: 1049–1112, October 2005. doi: 10.1086/444553.

R. E. Skelton, K. E. Whitaker, I. G. Momcheva, G. B. Brammer, P. G. van Dokkum, I. Labbé, M. Franx, A. van der Wel, R. Bezanson, E. Da Cunha, M. Fumagalli, N. Förster Schreiber, M. Kriek, J. Leja, B. F. Lundgren, D. Magee, D. Marchesini, M. V. Maseda, E. J. Nelson, P. Oesch, C. Pacifici, S. G. Patel, S. Price, H.-W. Rix, T. Tal, D. A. Wake, and S. Wuyts. 3D-HST WFC3-selected Photometric Catalogs in the Five CANDELS/3D-HST Fields: Photometry, Photometric Redshifts, and Stellar Masses. *ApJS*, 214: 24, October 2014. doi: 10.1088/0067-0049/214/2/24.

R. Sorba and M. Sawicki. Missing Stellar Mass in SED Fitting: Spatially Unresolved Photometry can Underestimate Galaxy Masses. *ArXiv e-prints*, June 2015.

V. Springel. Larger, faster, better: Current trends in cosmological simulations. *Astronomische Nachrichten*, 333:515–522, June 2012. doi: 10.1002/asna.201211701.

V. Springel, S. D. M. White, A. Jenkins, C. S. Frenk, N. Yoshida, L. Gao, J. Navarro, R. Thacker, D. Croton, J. Helly, J. A. Peacock, S. Cole, P. Thomas, H. Couchman, A. Evrard, J. Colberg, and F. Pearce. Simulations of the formation, evolution and clustering of galaxies and quasars. *Nature*, 435:629–636, June 2005. doi: 10.1038/nature03597.

M. Stefanon, D. Marchesini, A. Muzzin, G. Brammer, J. S. Dunlop, M. Franx, J. P. U. Fynbo, I. Labbé, B. Milvang-Jensen, and P. G. van Dokkum. Stellar Mass Functions of Galaxies At 4 z 7 from an IRAC-selected Sample in Cosmos/Ultravista: Limits on the Abundance of Very Massive Galaxies. *ApJ*, 803:11, April 2015. doi: 10.1088/0004-637X/803/1/11.

G. S. Stinson, J. J. Dalcanton, T. Quinn, T. Kaufmann, and J. Wadsley. Breathing in Low-Mass Galaxies: A Study of Episodic Star Formation. *ApJ*, 667:170–175, September 2007. doi: 10.1086/520504.

M. A. Strauss, D. H. Weinberg, R. H. Lupton, V. K. Narayanan, J. Annis, M. Bernardi, M. Blanton, S. Burles, A. J. Connolly, J. Dalcanton, M. Doi, D. Eisenstein, J. A. Frieman, M. Fukugita, J. E. Gunn, Ž. Ivezić, S. Kent, R. S. J. Kim, G. R. Knapp, R. G. Kron, J. A. Munn, H. J. Newberg, R. C. Nichol, S. Okamura, T. R. Quinn, M. W. Richmond, D. J. Schlegel, K. Shimasaku, M. SubbaRao, A. S. Szalay, D. Vanden Berk, M. S. Vogeley, B. Yanny, N. Yasuda, D. G. York, and I. Zehavi. Spectroscopic Target Selection in the Sloan Digital Sky Survey: The Main Galaxy Sample. *AJ*, 124:1810–1824, September 2002. doi: 10.1086/342343.

H. Susa and M. Umemura. Formation of Dwarf Galaxies during the Cosmic Reionization. *ApJ*, 600:1–16, January 2004. doi: 10.1086/379784.

M. Taghizadeh-Popp, S. M. Fall, R. L. White, and A. S. Szalay. Simulating Deep Hubble Images with Semi-empirical Models of Galaxy Formation. *ApJ*, 801:14, March 2015. doi: 10.1088/0004-637X/801/1/14.

M. Takada. Subaru Hyper Suprime-Cam Project. In N. Kawai and S. Nagataki, editors, *American Institute of Physics Conference Series*, volume 1279 of *American Institute of Physics Conference Series*, pages 120–127, October 2010. doi: 10.1063/1.3509247.

T. T. Takeuchi, K. Yoshikawa, and T. T. Ishii. The Luminosity Function of IRAS Point Source Catalog Redshift Survey Galaxies. *ApJ*, 587:L89–L92, April 2003. doi: 10.1086/375181.

G. A. Tammann. Dwarf Galaxies in the Past. In G. Meylan and P. Prugniel, editors, *European Southern Observatory Conference and Workshop Proceedings*, volume 49 of *European Southern Observatory Conference and Workshop Proceedings*, page 3, January 1994.

K. Tassis, T. Abel, G. L. Bryan, and M. L. Norman. Numerical Simulations of High-Redshift Star Formation in Dwarf Galaxies. *ApJ*, 587:13–24, April 2003. doi: 10.1086/368148.

E. N. Taylor, M. Franx, P. G. van Dokkum, R. F. Quadri, E. Gawiser, E. F. Bell, L. F. Barrientos, G. A. Blanc, F. J. Castander, M. Damen, V. Gonzalez-Perez, P. B. Hall, D. Herrera, H. Hildebrandt, M. Kriek, I. Labbé, P. Lira, J. Maza, G. Rudnick, E. Treister, C. M. Urry, J. P. Willis, and S. Wuyts. A Public, K-Selected, Optical-to-Near-Infrared Catalog of the Extended Chandra Deep Field South (ECDFS) from the Multiwavelength Survey by Yale-Chile (MUSYC). *ApJS*, 183:295–319, August 2009. doi: 10.1088/0067-0049/183/2/295.

H. I. Teplitz, I. S. McLean, E. E. Becklin, D. F. Figer, A. M. Gilbert, J. R. Graham, J. E. Larkin, N. A. Levenson, and M. K. Wilcox. The Rest-Frame Optical Spectrum of MS 1512-CB58. *ApJ*, 533:L65–L68, April 2000. doi: 10.1086/312595.

T. X. Thuan and G. E. Martin. Blue compact dwarf galaxies. I - Neutral hydrogen observations of 115 galaxies. *ApJ*, 247:823–848, August 1981. doi: 10.1086/159094.

T. X. Thuan, A. Lecavelier des Etangs, and Y. I. Izotov. Abundances in the H I Envelope of the Extremely Low Metallicity Blue Compact Dwarf Galaxy SBS 0335-052 from Far Ultraviolet Spectroscopic Explorer Observations. *ApJ*, 621:269–277, March 2005. doi: 10.1086/427469.

E. Tolstoy, V. Hill, and M. Tosi. Star-Formation Histories, Abundances, and Kinematics of Dwarf Galaxies in the Local Group. *ARA&A*, 47:371–425, September 2009. doi: 10.1146/annurev-astro-082708-101650.

A. R. Tomczak, R. F. Quadri, K.-V. H. Tran, I. Labbé, C. M. S. Straatman, C. Papovich, K. Glazebrook, R. Allen, G. B. Brammer, G. G. Kacprzak, L. Kawinwanichakij, D. D. Kelson, P. J. McCarthy, N. Mehrtens, A. J. Monson, S. E. Persson, L. R. Spitler, V. Tilvi, and P. van Dokkum. Galaxy Stellar Mass Functions from ZFOURGE/CANDELS: An Excess of Low-mass Galaxies since z = 2 and the Rapid Buildup of Quiescent Galaxies. *ApJ*, 783:85, March 2014. doi: 10.1088/0004-637X/783/2/85.

M. Tosi, L. Greggio, G. Marconi, and P. Focardi. Star formation in dwarf irregular galaxies - Sextans B. *AJ*, 102:951–974, September 1991. doi: 10.1086/115925.

C. A. Tremonti, T. M. Heckman, G. Kauffmann, J. Brinchmann, S. Charlot, S. D. M. White, M. Seibert, E. W. Peng, D. J. Schlegel, A. Uomoto, M. Fukugita, and J. Brinkmann. The Origin of the Mass-Metallicity Relation: Insights from 53,000 Star-forming Galaxies in the Sloan Digital Sky Survey. *ApJ*, 613:898–913, October 2004. doi: 10.1086/423264.

L. Tresse, O. Ilbert, E. Zucca, G. Zamorani, S. Bardelli, S. Arnouts, S. Paltani, L. Pozzetti, D. Bottini, B. Garilli, V. Le Brun, O. Le Fèvre, D. Maccagni, J.-P. Picat, R. Scaramella, M. Scodeggio, G. Vettolani, A. Zanichelli, C. Adami, M. Arnaboldi, M. Bolzonella, A. Cappi, S. Charlot, P. Ciliegi, T. Contini, S. Foucaud, P. Franzetti, I. Gavignaud, L. Guzzo, A. Iovino, H. J. McCracken, B. Marano, C. Marinoni, A. Mazure, B. Meneux, R. Merighi, R. Pellò, A. Pollo, M. Radovich, M. Bondi, A. Bongiorno, G. Busarello, O. Cucciati, F. Lamareille, G. Mathez, Y. Mellier, P. Merluzzi, and V. Ripepi. The cosmic star formation rate evolution from z = 5 to z = 0 from the VIMOS VLT deep survey. *A&A*, 472:403–419, September 2007. doi: 10.1051/0004-6361:20066330.

S. van den Bergh. The galaxies of the Local Group. *Cambridge Astrophysics Series*, 35, 2000.

A. van der Wel, A. N. Straughn, H.-W. Rix, S. L. Finkelstein, A. M. Koekemoer, B. J. Weiner, S. Wuyts, E. F. Bell, S. M. Faber, J. R. Trump, D. C. Koo, H. C. Ferguson, C. Scarlata, N. P. Hathi, J. S. Dunlop, J. A. Newman, M. Dickinson, K. Jahnke, B. W. Salmon, D. F. de Mello, D. D. Kocevski, K. Lai, N. A. Grogin, S. A. Rodney, Y. Guo, E. J. McGrath, K.-S. Lee, G. Barro, K.-H. Huang, A. G. Riess, M. L. N. Ashby, and S. P. Willner. Extreme Emission-line Galaxies in CANDELS: Broadband-selected, Starbursting Dwarf Galaxies at z > 1. *ApJ*, 742:111, December 2011. doi: 10.1088/0004-637X/742/2/111.

S. Veilleux and D. E. Osterbrock. Spectral classification of emission-line galaxies. *ApJS*, 63:295–310, February 1987. doi: 10.1086/191166.

D. R. Weisz, J. J. Dalcanton, B. F. Williams, K. M. Gilbert, E. D. Skillman, A. C. Seth, A. E. Dolphin, K. B. W. McQuinn, S. M. Gogarten, J. Holtzman, K. Rosema, A. Cole, I. D. Karachentsev, and D. Zaritsky. The ACS Nearby Galaxy Survey Treasury. VIII. The Global Star Formation Histories of 60 Dwarf Galaxies in the Local Volume. *ApJ*, 739:5, September 2011a. doi: 10.1088/0004-637X/739/1/5.

D. R. Weisz, A. E. Dolphin, J. J. Dalcanton, E. D. Skillman, J. Holtzman, B. F. Williams, K. M. Gilbert, A. C. Seth, A. Cole, S. M. Gogarten, K. Rosema, I. D. Karachentsev, K. B. W. McQuinn, and D. Zaritsky. How Typical Are the Local Group Dwarf Galaxies? *ApJ*, 743:8, December 2011b. doi: 10.1088/0004-637X/743/1/8.

D. R. Weisz, A. E. Dolphin, E. D. Skillman, J. Holtzman, K. M. Gilbert, J. J. Dalcanton, and B. F. Williams. The Star Formation Histories of Local Group Dwarf Galaxies. I. Hubble Space Telescope/Wide Field Planetary Camera 2 Observations. *ApJ*, 789:147, July 2014a. doi: 10.1088/0004-637X/789/2/147.

D. R. Weisz, A. E. Dolphin, E. D. Skillman, J. Holtzman, K. M. Gilbert, J. J. Dalcanton, and B. F. Williams. The Star Formation Histories of Local Group Dwarf Galaxies. II. Searching For Signatures of Reionization. *ApJ*, 789:148, July 2014b. doi: 10.1088/0004-637X/789/2/148.

K. E. Whitaker, P. G. van Dokkum, G. Brammer, and M. Franx. The Star Formation Mass Sequence Out to z = 2.5. *ApJ*, 754:L29, August 2012. doi: 10.1088/2041-8205/754/2/L29.

K. E. Whitaker, M. Franx, J. Leja, P. G. van Dokkum, A. Henry, R. E. Skelton, M. Fumagalli, I. G. Momcheva, G. B. Brammer, I. Labbé, E. J. Nelson, and J. R. Rigby. Constraining the Low-mass Slope of the Star Formation Sequence at $0.5 < z < 2.5$. *ApJ*, 795:104, November 2014. doi: 10.1088/0004-637X/795/2/104.

S. D. M. White and M. J. Rees. Core condensation in heavy halos - A two-stage theory for galaxy formation and clustering. *MNRAS*, 183:341–358, May 1978.

R. E. Williams, B. Blacker, M. Dickinson, W. V. D. Dixon, H. C. Ferguson, A. S. Fruchter, M. Giavalisco, R. L. Gilliland, I. Heyer, R. Katsanis, Z. Levay, R. A. Lucas, D. B. McElroy, L. Petro, M. Postman, H.-M. Adorf, and R. Hook. The Hubble Deep Field: Observations, Data Reduction, and Galaxy Photometry. *AJ*, 112:1335, October 1996. doi: 10.1086/118105.

R. J. Williams, R. F. Quadri, M. Franx, P. van Dokkum, and I. Labbé. Detection of Quiescent Galaxies in a Bicolor Sequence from Z = 0-2. *ApJ*, 691:1879–1895, February 2009. doi: 10.1088/0004-637X/691/2/1879.

E. Wuyts, J. R. Rigby, K. Sharon, and M. D. Gladders. Constraints on the Low-mass End of the Mass-Metallicity Relation at z = 1-2 from Lensed Galaxies. *ApJ*, 755:73, August 2012. doi: 10.1088/0004-637X/755/1/73.

S. Wuyts, I. Labbé, M. Franx, G. Rudnick, P. G. van Dokkum, G. G. Fazio, N. M. Förster Schreiber, J. Huang, A. F. M. Moorwood, H.-W. Rix, H. Röttgering, and P. van der Werf. What Do We Learn from IRAC Observations of Galaxies at $2 < z < 3.5$? *ApJ*, 655:51–65, January 2007. doi: 10.1086/509708.

T. K. Wyder, M. A. Treyer, B. Milliard, D. Schiminovich, S. Arnouts, T. Budavári, T. A. Barlow, L. Bianchi, Y.-I. Byun, J. Donas, K. Forster, P. G. Friedman, T. M. Heckman, P. N. Jelinsky, Y.-W. Lee, B. F. Madore, R. F. Malina, D. C. Martin, P. Morrissey, S. G. Neff, R. M. Rich, O. H. W. Siegmund, T. Small, A. S. Szalay, and B. Y. Welsh. The Ultraviolet Galaxy Luminosity Function in the Local Universe from GALEX Data. *ApJ*, 619:L15–L18, January 2005. doi: 10.1086/424735.

J. S. B. Wyithe and A. Loeb. Cosmic Variance in the Transparency of the Intergalactic Medium after Reionization. *ApJ*, 646:696–702, August 2006. doi: 10.1086/502620.

K. Yabe, K. Ohta, F. Iwamuro, M. Akiyama, N. Tamura, S. Yuma, M. Kimura, N. Takato, Y. Moritani, M. Sumiyoshi, T. Maihara, J. Silverman, G. Dalton, I. Lewis, D. Bonfield, H. Lee, E. Curtis-Lake, E. Macaulay, and F. Clarke. The mass-metallicity relation at z
1.4 revealed with Subaru/FMOS. *MNRAS*, 437:3647–3663, February 2014. doi: 10.1093/mnras/stt2185.

D. G. York, J. Adelman, J. E. Anderson, Jr., S. F. Anderson, J. Annis, N. A. Bahcall, J. A. Bakken, R. Barkhouser, S. Bastian, E. Berman, W. N. Boroski, S. Bracker, C. Briegel, J. W. Briggs, J. Brinkmann, R. Brunner, S. Burles, L. Carey, M. A. Carr, F. J. Castander, B. Chen, P. L. Colestock, A. J. Connolly, J. H. Crocker, I. Csabai, P. C. Czarapata, J. E. Davis, M. Doi, T. Dombeck, D. Eisenstein, N. Ellman, B. R. Elms, M. L. Evans, X. Fan, G. R. Federwitz, L. Fiscelli, S. Friedman, J. A. Frieman, M. Fukugita, B. Gillespie, J. E. Gunn, V. K. Gurbani, E. de Haas, M. Haldeman, F. H. Harris, J. Hayes, T. M. Heckman, G. S. Hennessy, R. B. Hindsley, S. Holm, D. J. Holmgren, C.-h. Huang, C. Hull, D. Husby, S.-I. Ichikawa, T. Ichikawa, Ž. Ivezić, S. Kent, R. S. J. Kim, E. Kinney, M. Klaene, A. N. Kleinman, S. Kleinman, G. R. Knapp, J. Korienek, R. G. Kron, P. Z. Kunszt, D. Q. Lamb, B. Lee, R. F. Leger, S. Limmongkol, C. Lindenmeyer, D. C. Long, C. Loomis, J. Loveday, R. Lucinio, R. H. Lupton, B. MacKinnon, E. J. Mannery, P. M. Mantsch, B. Margon, P. McGehee, T. A. McKay, A. Meiksin, A. Merelli, D. G. Monet, J. A. Munn, V. K. Narayanan, T. Nash, E. Neilsen, R. Neswold, H. J. Newberg, R. C. Nichol, T. Nicinski, M. Nonino, N. Okada, S. Okamura, J. P. Ostriker, R. Owen, A. G. Pauls, J. Peoples, R. L. Peterson, D. Petravick, J. R. Pier, A. Pope, R. Pordes, A. Prosapio, R. Rechenmacher, T. R. Quinn, G. T. Richards, M. W. Richmond, C. H. Rivetta, C. M. Rockosi, K. Ruthmansdorfer, D. Sandford, D. J. Schlegel, D. P. Schneider, M. Sekiguchi, G. Sergey, K. Shimasaku, W. A. Siegmund, S. Smee, J. A. Smith, S. Snedden, R. Stone, C. Stoughton, M. A. Strauss, C. Stubbs, M. SubbaRao, A. S. Szalay, I. Szapudi, G. P. Szokoly, A. R. Thakar, C. Tremonti, D. L. Tucker, A. Uomoto, D. Vanden Berk, M. S. Vogeley, P. Waddell, S.-i. Wang, M. Watanabe, D. H. Weinberg, B. Yanny, N. Yasuda, and SDSS Collaboration. The Sloan Digital Sky Survey: Technical Summary. *AJ*, 120:1579–1587, September 2000. doi: 10.1086/301513.

T.-T. Yuan, L. J. Kewley, and J. Richard. The Metallicity Evolution of Star-forming Galaxies from Redshift 0 to 3: Combining Magnitude-limited Survey with Gravitational Lensing. *ApJ*, 763:9, January 2013. doi: 10.1088/0004-637X/763/1/9.

H. J. Zahid, L. J. Kewley, and F. Bresolin. The Mass-Metallicity and Luminosity-Metallicity Relations from DEEP2 at z ˜ 0.8. *ApJ*, 730:137, April 2011. doi: 10.1088/0004-637X/730/2/137.

H. J. Zahid, F. Bresolin, L. J. Kewley, A. L. Coil, and R. Davé. The Metallicities of Low Stellar Mass Galaxies and the Scatter in the Mass-Metallicity Relation. *ApJ*, 750:120, May 2012a. doi: 10.1088/0004-637X/750/2/120.

H. J. Zahid, G. I. Dima, L. J. Kewley, D. K. Erb, and R. Davé. A Census of Oxygen in Star-forming Galaxies: An Empirical Model Linking Metallicities, Star Formation Rates, and Outflows. *ApJ*, 757:54, September 2012b. doi: 10.1088/0004-637X/757/1/54.

H. J. Zahid, M. J. Geller, L. J. Kewley, H. S. Hwang, D. G. Fabricant, and M. J. Kurtz. The Chemical Evolution of Star-forming Galaxies over the Last 11 Billion Years. *ApJ*, 771:L19, July 2013. doi: 10.1088/2041-8205/771/2/L19.

S. Zaroubi. The Epoch of Reionization. In T. Wiklind, B. Mobasher, and V. Bromm, editors, *Astrophysics and Space Science Library*, volume 396 of *Astrophysics and Space Science Library*, page 45, 2013. doi: 10.1007/978-3-642-32362-1_2.

F. Zwicky. Blue Compact Galaxies. *ApJ*, 142:1293, October 1965. doi: 10.1086/148411.

F. Zwicky. Compact Galaxies and Compact Parts of Galaxies. II. *ApJ*, 143:192, January 1966. doi: 10.1086/148490.